THE THERMAL PROPERTIES OF AN SF_6 CIRCUIT BREAKER ARC DURING THE CURRENT ZERO PERIOD

A THESIS SUBMITTED IN ACCORDANCE WITH THE REQUIREMENTS OF THE UNIVERSITY OF LIVERPOOL, FOR THE DEGREE OF DOCTOR OF PHILOSOPHY, BY E. LEWIS (B.ENG.)

FEBRUARY 1987

DEPARTMENT OF
ELECTRICAL ENGINEERING
AND ELECTRONICS

ABSTRACT

High speed photographic and time and space resolved spectroscopic investigations have been undertaken to quantify the processes governing arc thermal reignition phenomena.

A fixed nozzle and electrode geometry was used with SF_6 as the host gas. A sonic flow of gas at the nozzle throat was sustained using an upstream vessel pressure of 7.8 psig.

A 35.5mF capacitor bank was used to supply electrical energy for reduced and full power arcing tests using different circuit configurations.

Sophisticated optical diagnostic instrumentation has enabled photographic and spectroscopic investigations with high time and space resolution to be made during the current zero period of both the full and reduced power arcing cases.

The results of above experimental investigations are of value in determining the thermal structure and the processes governing thermal reignition of the circuit breaker arc of the present investigation. In particular, temperature profiles derived from the above investigations have been used to quantify the important terms of the dynamic current zero energy balance.

Experimental investigations have thus been performed during the critical current zero period of a full power circuit breaker arc. The significance of these results has been realised in evaluating the current zero temperature profiles and subsequently the energy conservation equation terms for severe circuit breaking conditions.

ACKNOWLEDGEMENTS

I should like to thank the Science and Engineering Research Council for their financial support that enabled this work to be carried out. My thanks extend also to my supervisor, Dr. G.R. Jones, for his guidance and encouragement, and to Dr. A.N. Prasad and Dr. M.T.C. Fang for many interesting and stimulating conversations. Thanks are also due to S. Taylor and the technical staff of the Department of Electrical Engineering and Electronics of the University of Liverpool for their valuable assistance. Finally, thanks to Mrs. C. Woods for the thesis typing.

To my wife and parents

CONTENTS

CHAPTER 1

INTRODUCTION

Circuit breakers are an integral part of any power transmission system. They serve to protect components within that system which are expensive and easily damaged if subjected to the excessive currents which occur during a typical power system fault. Protection is achieved by isolating a particular part of a circuit or network when a fault occurs. The fault current is interrupted in a manner such that no system damage occurs owing to voltage transients caused by too rapid a rate of current decay. The latter requirement is normally fulfilled by interrupting the alternating fault current as it passes through a zero value naturally at the end of an alternating half cycle.

Most commercial circuit breakers consist of two contacts which are closed together when the power system is in normal operation. However if a fault is detected, the contacts are separated. The instant at which contact occurs varies according to the circuit breaker type and application but in all cases an electrical arc discharge is formed. This arc is contained or manipulated such that when the fault current has decayed to zero, the arc is extinguished and the fault current is successfully interrupted.

To achieve such a successful interruption, sufficient energy must be removed in order to keep the electrical

conductance in the recovering contact gap as low as possible so that reignition due to joule heating caused by residual current flow is avoided. In addition a subsequent recovery of the insulation properties is required to prevent dielectric breakdown by the voltage across the arcing gap produced by the network reaction to current interruption.

For the above reasons the medium in which the arc is formed is important in determining the electrical performance limitations of a circuit breaker. The influence of the medium is manifest through its thermodynamic and aerodynamic properties prior to current zero, the first few microseconds thereafter, and its dielectric properties during the voltage restrike period. Thus as power system voltages have increased, the ability of a circuit breaker to interrupt increasing short circuit fault currents and withstand greater voltages has necessitated improving and changing circuit breaker designs.

Early forms of circuit breakers incorporated a knife switch type mechanism which posed an obvious safety threat for the operator. Further developments of circuit breakers led to a remote operation and an eventual complete immersement in oil. The latter development involved the evolution of hydrogen gas during breaker operation which resulted in an explosion hazzard. Thus such commercial breakers included a minimum amount of oil (Rieder, 1971). These breakers were

superseded by air blast breakers, the further developments of which (e.g. unit stacking and insulation) led to their installation in the 400KV distribution system (Rieder, 1971).

Over the last 25 years, the use of air has been further superseded by SF_6 gas as an arcing medium, the first production breakers being developed by Westinghouse (Friedrich et al) and (Leeds et al, 1957). SF_6 has a low ionization energy and a high affinity for electrons when de-ionizing which makes it an ideal quenching medium. These properties enable a lower pressure or a higher rating per break unit to be used when compared to the equivalent air breaker.

SF_6 breakers have been developed for a large range of power system switching duties. They range from the medium voltage rotary arc switches where the arc is magnetically driven through the SF_6 gas to the higher voltage duties utilising a multi-break puffer style breaker. The latter involves compressing a volume of gas pneumatically forcing it to flow in opposing directions through two back to back nozzles before exhaustion into a collection chamber. With full duoflow operation the two nozzles are also used as the contacts. Any vapourised contact material is removed by the biderctional flow so assisting in providing an efficient performance. However in many other ways the fundamental processes governing arc quenching are similar to those in interruptors using unidirectional flow produced by pressurised gas on one side of a nozzle sustaining a flow into lower

second (or sometimes sub-microsecond) time resolution and precise spatial resolution owing to the rapid rate of change of properties and the small radial dimensions of the arc column respectively during this period.

An extensive investigation using high speed photographic techniques was conducted on both full and reduced power arcing conditions so that the arc column dimensions and structure could be quantified and a direct comparison of the two cases made. The instrumentation pertaining to this section of the work is described in chapter 4 and the results obtained are presented in chapter 6.

The photographic measurements not only allowed a quantitative analysis to be made of the luminous arc column and its properties but also enabled a precise evaluation of the arc column throughout the current zero period. This enabled the more elaborate measurement technique required for the spectroscopic investigation to be executed efficiently with a full knowledge of the arc column's luminous behaviour.

The spectroscopic investigation enabled direct localised arc column intensity measurements with radial (and spectral) resolution and a time exposure of 1.6μs such that radial temperature profiles during the current zero period could be derived. The results of this investigation are presented in chapter 6.

From the radial temperature profiles derived from these diagnostic techniques the transient variation of arc properties

during the current zero period could be derived. The information provided an accurate method of quantifying the energy processes during the current zero period and establishing the existence of LTE conditions. Additionally a quantitative evaluation of the shape factors of the integral analysis could be made. Some of the underlying theoretical aspects of the above properties and processes are discussed in chapter 7 and their implications discussed in chapter 8.

The experimental data required for the solution of the current zero energy conservation equation had previously been inadequate or non-existent. Since it is technically unrealistic to apply such elaborate diagnostic techniques to the hostile environment of a full scale circuit breaker test station, it is hoped that the information presented in this thesis may serve to identify more precisely the physical phenomena governing interruption in commercial high power interruptors.

CHAPTER 2

LITERATURE REVIEW

2.1 Introduction

In this chapter the work published to date by authors working in the field of gas blast circuit breakers is reviewed and particular attention is paid to the current zero period of the current waveform.

A section of this chapter is devoted to the evolution of theoretical models describing the current zero arc behaviour. It is also necessary to include a review of interrupter design and development by means of empirical laws which were derived directly from experimentally observed phenomena. In particular, the development of optical measurements as a useful diagnostic technique and their significance with respect to interrupter development is considered.

2.2 Theoretical Models Describing Current Zero Arc Behaviour

The need for a satisfactory theory to describe current interruption by a circuit breaker became clear in the 1920's when oil and air blast breakers were being used extensively in the power distribution system. It was not understood why identical breakers interrupted currents up to their rated value in some circuits whereas in others arc reignition and failure to interrupt occurred for a peak current level well

below the rated value. Rieder (1972) describes high voltage oscillations (the transient restrike voltage) present just after current zero owing to the combination of the natural frequency of the circuit and the remnant arc column. In 1927 the relatively fast recording capability of the C.R.O. enabled these transients to be observed and the apparent anomaly explained in terms of post current zero severity.

In 1928 Slepian utilised these observations to formulate his 'race theory' to describe the effect of the transient restrike voltage upon breaker performance. The race referred to was between the increasing transient voltage across the circuit breaker and the recovery of the dielectric strength of the arc gap after current zero. Although the 'race' concept remains valid, Slepian's theory was disproved (Kesselring and Koppelman, 1935) through the observation that circuit breakers could withstand a faster rate of rise of recovery voltage (larger dielectric strength) than predicted by Slepian's theory. Slepian (1941) responded to this by accounting for the increased rrrv withstand by the molecular diffusion of cool material by turbulent mixing of the plasma. This explanation was unacceptable on three counts. Firstly, turbulent mixing time scales exceed those involved with the thermal recovery of a plasma column. Also Cassie (1953), through the use of high speed photographs, demonstrated that the nature of the arc column dictated that the turbulence could only be in evidence at the high current levels and not at the current zero. In addition the increase in voltage

required by Slepian's explanation did not evidently coincide with the turbulence.

An independently derived alternative theory which gained notoriety was proposed by Kesselring and Koppelman (1935) and Prince et al (1940). This essentially described the current zero arc column splitting into two electrically isolated axial sections. Although agreement was evident with cross blast circuit breakers, the theory was disproved by Slepian who cited the high speed photographs of Biermanns (1932) showing a continuous arc column at current zero and Cassie's (1953) observation of post current zero (post-arc) current which could not flow according to the displacement theory.

The two theories described above attempted to describe the performance of the breaker in terms of the voltage or dielectric withstand after current zero. Neither theory could accommodate the possibility of a continuous conducting channel giving rise to a post current zero conductance. Thus it was clear that a satisfactory arc model should be capable of describing the conductance decay of the plasma when the current ceases to flow and should be sufficiently simple for combination with the external circuit equations. Two such theories emerged, the first by Cassie (1939) and the second by Mayr (1943). Based on an independent set of assumptions they both describe the dynamic energy equilibrium of the arc plasma column during the current zero period. Both models characterise the column conductivity during the current zero period as some unique function of temperature

which may in turn be related to the energy content per unit volume of the plasma. When applied to the whole cross-section of the arc the conductance could be described as

$$\frac{1}{R} = G = f(Q) \qquad 2.1$$

where

R is the arc resistance per unit length

Q is the energy content per unit length

Both Cassie (1939) and Mayr (1943) established the nature of the dynamic energy content variation as

$$Q = \int_0^t (W-N)\,dt \qquad 2.2$$

where

W = arc power input

N = arc power loss

dt = time derivative

Also with the relationship (Browne, 1948)

$$\frac{1}{R} = f(W,N,t) \qquad 2.3$$

$$\frac{1}{R} = F(Q) = F\left(\int_0^t (W-N)\,dt\right) \qquad 2.4$$

Equation 2.4 can be differentiated to establish a more general form for use in arc modelling i.e.

$$R\frac{d}{dt}\left(\frac{1}{R}\right) = \frac{F^1(Q)}{F(Q)} \cdot \frac{dQ}{dt} = \frac{F^1(Q)}{F(Q)} \quad (W\text{-}N) \qquad 2.5$$

Both Cassie (1939) and Mayr (1943) solved this equation within the context of a set of assumptions regarding the physical nature of the arc column to arrive at their respective arc equations.

Cassie (1939) formulated his model with the following set of assumptions:

(i) The arc cylindrical column is regarded to have uniform temperature with constant electrical resistivity and energy content per unit volume, δ and q respectively. The arc column is enclosed by a well defined boundary outside which the conductivity is zero.

(ii) The arc column is surrounded by an axial flow with no mutual interaction occurring.

(iii) Heat loss across the boundary from the arc is entirely radial in direction.

(iv) The arc cross-sectional area undergoes change to accommodate changes in current but the arc temperature remains constant.

(v) The power loss is proportional to the column cross-section. Thus

$$N = \lambda A$$

where

λ = power loss per unit volume

A = column cross-sectional area

Therefore

$$W-N = \frac{E^2}{R} - \lambda A = \frac{E^2 - \rho\lambda}{R} \qquad 2.6$$

Also

$$Q = qA = \frac{q\rho}{R}$$

Therefore

$$\frac{1}{R} = \frac{Q}{\rho\lambda} = F(Q) \qquad 2.7$$

So, substituting in 2.5 yields

$$R\frac{d}{dt}\frac{1}{R} = \frac{\lambda}{q}\frac{E^2}{\lambda\rho} - 1 = \frac{1}{\theta_c}\frac{E^2}{\lambda\rho} - 1 \qquad 2.8$$

θ_c has units of time and is called the Cassie time constant.

Mayr (1943) evolved his model through a different set of assumptions. Mayr assumed

(i) The arc column is cylindrically symmetrical with a constant area A in space and time.

(ii) There is no external gas flow.

(iii) To accommodate changes in current the conductivity is allowed to vary with temperature according to a much simplified Saha equation (Haydon, pp. 348-356), namely

$$G = K_1 \exp(-\alpha/T)$$

where α = constant

(iv) Thermal losses occur in a radial direction only and obey the Fourier law of heat conduction.

By forming an expression for the conductivity in terms of the stored energy per unit volume and applying it to the whole arc column to obtain the heat content per unit length, Q, the Mayr equation may be formed by substitution into equation 2.5

$$R \frac{d}{dt}\left(\frac{1}{R}\right) = \frac{N_o}{Q_o}\left(\frac{W}{N_o} - 1\right) = \frac{1}{\theta_M}\left(\frac{W}{N_o} - 1\right)$$

Therefore

$$R \frac{d}{dt}\left(\frac{1}{R}\right) = \frac{1}{\theta_M}\left(\frac{E^2}{RN_o} - 1\right) \qquad 2.9$$

Where,

E is the instantaneous electric field

N_o is the power dissipated by thermal heat conduction and is constant

$\theta_M\left(= \frac{Q_o}{N_o} \right)$ is the Mayr time constant

Q_o is a constant and is determined from the equation

$$\frac{1}{R} = K \exp\left(\frac{Q}{Q_o}\right)$$

K is a constant

Browne (1948) proposed a composite model by describing the arc decay towards current zero using Cassie's model and then characterising the arc during the post current zero period when the column still has some conductance and is subject to the restrike voltage using Mayr's model. Browne claimed his model demonstrated good qualitative agreement with experimental observations when special cases of simple current and voltage waveforms were used.

However, Browne's (1948) model was open to criticism in three ways. Initially, if the steady state condition is applied to the Cassie model before current zero (equation 2.8) then the relationship $E = (\rho\lambda)^{1/2}$ emerges with ρ and λ constant and independent of instantaneous current. Consequently the Cassie equation cannot predict the increase in electric field which occurs just before current zero in the case of a good interruption. Secondly, Browne (1948) defines his criterion for the critical electric field to cause reignition as being the instantaneous voltage required to hold the conductance constant, a condition synonymous with the dielectric definition quoted originally by Slepian (1930) rather than continuing the original theme of a power balance. This criterion yielded incorrect values of critical electric field strength when either the Cassie or Mayr equation was applied to the real circuit breaking case. A further criticism was put forward by Skeats (1948) in

response to Browne's (1948) model. This concerned the attempt to describe the behaviour of a single arcing event when many properties may change, by using two models with assumptions which are peculiar to each and which are independent i.e. constant temperature with variable area before current zero and constant area with variable temperature thereafter. It will be shown in chapter 8 that in practice both arc column area and arc temperature may collapse simultaneously during the final few microseconds before current zero. In response to these criticisms Cassie and Mayr (1956) proposed a model which augmented Cassie's (1939) model with a thermal conduction power loss term. Browne (1959) however claimed it was too complex to be used as an efficient arc model. Instead he adapted his composite model to the current zero period and considered imposed square and ramp voltage waveforms as restriking voltages. The use of Cassie's (1939) model enabled Browne (1959) to determine the resistance R_o at current zero when applied in the pre current zero period. By solving Mayr's (1943) equation in the post current zero period using the R_o value as an initial condition and the imposed voltage waveform, this author derived simple relationships for the critical electric field strength in terms of θM, the circuit component values and the steady state arc voltage.

Browne's model, including Slepian's definition of critical electric field strength, was dispelled when measurements showed that arcs could still be quenched despite the post zero conductance initially increasing during the

imposition of the TRV. Thus the importance of incorporating the electrical interaction processes between the arc and the external circuit was realised and dynamic arc models were augmented to include this effect. The first author to achieve a reasonable agreement with the real circuit breaker test results was Kopplin (1962) who used an analog computer to solve a pair of simultaneous non-linear differential equations, one describing the circuit, the other the arc (Browne's (1948) model). He presented his results in the form of two non-dimensionalised quantities representing a time constant and heat dissipation. Kopplin (1962) plotted these two quantities and defined a boundary on the plot which he claimed discriminated between thermal reignition and extinction. The agreement with experimental results was however limited.

Other researchers have attempted to modify Cassie's (1939) and Mayr's (1943) original equations to achieve closer agreement with the experimentally observed phenomena during the current zero period. However these have proved unsuccessful owing to over simplification leading to poor accuracy when compared with experimental measurements or the incurrment of prohibitive mathematical complexity preventing the model from being capable of predicting interruptor behaviour during the current zero period. Clearly only limited success could be obtained by the use of these early models for interruptor behaviour predictions and a superior method of approach would be required if closer agreement with test results was to be obtained.

A convenient method for describing an arc in a flow is to represent it by annular zones at a given axial station which divide the cross-section into two or more segregated regions by clearly defined boundaries. The circuit breaker arc in an axial flow approximates well to this description since the derivatives of properties in the radial direction are greater than those in the axial direction. Under such conditions the arc conservation equations may be formulated using the Boundary layer approximation or analysis.

The first authors to apply this technique to formulate a current zero arc model were Swanson and Roidt (1971, 1972) and Swanson et al (1970, 1971, 1971(a), 1977) in a series of publications describing the basic technique and its application.

In the publication by Swanson and Roidt (1971) their assumed arc energy equation takes the form

thermal storage		radial convection		axial convection	
$\rho\frac{\partial h}{\partial t}$	+	$\rho V\frac{\partial h}{\partial r}$	+	$\rho U\frac{\partial h}{\partial x}$	=

Expansion cooling					
$\left[1 - \rho\left(\frac{\partial h}{\partial P}\right)_T\right] U\frac{dP}{dx}$	-	$W(P,T)$			
+ radial diffusion				+ Joule heating	
$\frac{1}{r}\frac{\partial}{\partial r}\left[r\left(\frac{\mu}{Pr} + \frac{\rho t^{\epsilon}_m}{Pr_t}\right)\cdot\frac{\partial h}{\partial r}\right]$			+	σE^2	2.10

where

ρ is the density

h is the enthalpy

V is the radial velocity

U is the axial velocity

P is the pressure

W is the radiated power per unit volume

ϵ_m is the eddy diffusivity for momentum

Pr_t is the turbulent Prandtl number

Pr is the Prandtl number

σ is the electrical conductivity

E is the voltage gradient

The terms in this equation were integrated across the arc radius R(x,t) and the equation 2.10 transformed in a partial differential form for the dynamic arc radius within an axial range from the tip of the upstream electrode to the nozzle throat. This equation includes two coefficients

$$\upsilon = \frac{\text{excess energy density stored in the arc column}}{\text{rate of energy removal by axial convection}}$$

$$\gamma = \frac{\text{energy loss by radial transfer}}{\text{rate of energy removal by axial convection}}$$

Additionally the following assumptions were made:

(1) The radial integrals which are contained in the coefficients of the radius terms are regarded constant for assumed average radial temperature profiles.

(2) The term accounting for radial energy losses N(x,t,R) is assumed to vary with R only. Consequently the change in thermally stored energy is accounted for by changes in arc radius only. (Eq. 12, Swanson and Roidt (1971)).

Thus with the above two assumptions and taking the arc radius obtained from the quasi-steady state ($^{d}/dt = 0$) solution of the dynamic equation for the arc radius as the initial condition the authors proceed to solve the dynamic equation for a linear current ramp to zero. A value for the current zero arc radius at the nozzle throat was thus obtained. Analytical solutions were obtained for the current zero radius for the case of

(1) The dominant energy removal mechanism being axial convection.

(2) The dominant energy removal mechanism being radial diffusion and radiation.

In both cases the current zero arc diameter is expressed as the quasi-steady value attenuated by certain heat transfer parameters.

The two independently derived expressions for current zero radius are substituted into Frind's (1960) formula for

the thermal time constant of arc dominated by turbulent diffusion. This yields formulae for the current zero arc radius in the nozzle throat for the two cases considered.

The preceeding expressions are used in a comparison paper (Swanson, Roidt and Browne, 1971) where interruption criteria are established for the case of short line faults (Rieder, 1972). In this publication the authors were concerned with the arc at the current zero instant and during the immediate post zero period during which a linear RRRV is imposed.

Swanson et al (1971) make the assumption that during this post arc period energy loss from the narrow column is governed by turbulent and molecular diffusion and that axial convection may be neglected. They also state that energy growth of the arc column is by Joule heating (σE^2) which is proportional to the column conductivity (σ). Above 8000K the variation of electrical conductivity, σ, is taken as linear whereas the variation below 8000K is taken as exponential. Thus Swanson et al (1971) state that above 8000K the arc energy equation can be transformed into a 'Cassie' type integral equation for post arc current whereas below 8000K the same equation can be transformed into a 'Mayr' type equation for post arc resistance. In the former case (with σ proportional to S) the criterion for interr-uption to occur is that the time derivative of the post arc current should reach zero at some instant after current zero. From this condition a critical thermal time constant is established. This is then equated to convection and

diffusion controlled arc time constant obtained by Swanson and Roidt (1971) to determine the value of maximum rrrV which can be imposed without reignition occurring. From the Mayr type solution a criterion is also established whereby interruption must occur. This is that for successful interruption the time derivative the post zero arc resistance must reach zero at some instant. A critical time constant is thus established in a similar manner as indicated above in this case. By further equating this to the arc time constants derived by Swanson and Roidt (1971) another maximum value of rrrV is obtained. Swanson et al (1971) further conclude that from the Cassie and Mayr type equations the maximum rrrV shows the following relationships:

(a) approximately proportional to the gas pressure

(b) proportional to the effective nozzle arc length at current zero and to the number of nozzle arc gaps connected in series

(c) proportional to the coefficients which are functions of the gas properties

(d) inversely proportional to $(^{di}/dt)^{M}$ where $M = {}^{3}/2$ for the Cassie type solution and M = 1 for the Mayr type solution.

Although the authors intend the theory to serve as a limited approximation only for the values of rrrV inadequacies are still inherent in their predictions. These include:

(i) The criterion involving a zero rate of change of post arc current is not in itself a necessary and sufficient condition for interruption. The criterion regarding the zero rate of change of post arc resistance is also erroneous.

(ii) Chapman (1977) in his measurement of localised arc behaviour has shown that the definition of an effective nozzle length to be unrepresentative in the case of real circuit breaker arcs.

(iii) Unrealistic assumptions regarding radial distributions (Bessel functions) of arc properties are made which are mutually inconsistent and not representative of the true physical situation.

(iv) The expression for the dynamic variation of heat flux potential is dependent on the dynamic resistance equation (Swanson and Roidt, 1972). Swanson (1977) proceeds to calculate arc radii and axial temperatures from this pair of equations (Swanson, 1977) which is rigorously invalid.

(v) The time constants used to define the maximum rrrV were derived by the use of different energy transport assumptions and originate from different time periods with respect to current zero.

(vi) It will be shown experimentally in this thesis that to consider the arc temperature constant and allow the arc area to collapse alone is not representative

of the case of a real circuit breaker (chapter 8). This is particularly true close to current zero and one effect of making the constant temperature assumption is to artificially increase the arc thermal time constants (chapter 7).

Another arc model characterising the transient arc behaviour near current zero has been developed by Topham in a series of publications (Topham 1971, 1972(a), 1972(b) and 1973). Topham (1971) formulates a theory on the basis of the following assumptions for a steady state arc in constant pressure axial flow:

(i) Arcs at atmospheric pressure and above can be described by equilibrium thermodynamics and the continuity equations of fluid dynamics.

(ii) Radiation power loss is neglected.

(iii) Self-magnetic effects are neglected (e.g. pinch effects)

(iv) Electrode effects are neglected.

(v) The gas flow is axisymmetric, laminar and unaltered by the presence of the arc.

(vi) Boundary layer approximations are made since the radial derivatives exceed the axial ones.

Topham (1971) proceeded to formulate the integral energy balance equation by invoking Polhausen's integral technique (Schlichting, 1958) and assuming boundary layer conditions. The energy conservation equation was non-dimensionalised by

dividing every parameter within each term of the equation by its value at the 4000K boundary of the arc in pure nitrogen. Due to a lack of experimental data Topham (1971) derived a radial temperature profile from the Elenbaas-Heller equation which the author claims to be only slightly modified by axial convection. This profile is claimed to be a good approximation to the temperature profile of a circuit breaker arc below 100A. This information is then used to evaluate the integral terms of the energy balance equation which is solved to demonstrate that the voltage gradient variation with current is a unique function of the flow conditions.

Topham (1972(a)) extended the original analysis to accommodate arcs subjected to pressure gradients. In this analysis some additional assumptions are made:

(vii) Although the calculations are based on laminar flow, the method can be adapted to include turbulence.

(viii) Viscous forces are considered negligible.

(ix) The kinetic energy of the flow is considered small compared to the thermal energy.

The introduction of a pressure gradient modifies the momentum conservation to yield a solution which is substituted into the enthalpy flow integral. This was then evaluated for an outer thermal layer and the energy balance equation rewritten such that it could be solved analytically for a known pressure gradient.

The same author in a further publication, Topham (1972(b)) attempted to adapt his analysis to the transient case of a circuit breaker arc in the current zero period. In this publication the author incorporated the above assumptions ((i) to (ix)) to quote the dynamic energy equation in an integral form which can be found in standard text books (e.g. Goldstein, 1938). This author (Topham, 1972(b)) further reduced the energy equation for the case of a linear pressure gradient and represented it in non-dimensional form.

Drastic simplifications were then made to obtain the solution of the energy balance. The steady state radial velocity and temperature profiles were used to evaluate the non-dimensional energy integrals which were further assumed to be unique functions of $\overset{*}{G}$, the non-dimensional electrical conductance.

The dynamic arc equation takes the form:

$$\frac{d}{d\overset{*}{t}} \cdot \overset{*}{g}_2 + \overset{*}{g}_1 = \frac{\overset{*}{I}^2}{\overset{*}{G}} \qquad 2.11$$

where

$\overset{*}{I}$ is the non-dimensional current

$\overset{*}{t}$ is the non-dimensional time

$\overset{*}{g}_1$, $\overset{*}{g}_2$ non-dimensional integrals representing heat loss and heat storage functions respectively

$\overset{*}{G}$ is the non-dimensional conductance

Topham (1972(b)) further reduced his energy equation

to the Bernoulli type equation which is true for certain forms of the functions $\overset{*}{g}_1$ and $\overset{*}{g}_2$. Assuming simple power law relationships between $\overset{*}{g}_1$, $\overset{*}{g}_2$ and $\overset{*}{G}$ the arc energy equation becomes

$$\frac{d\overset{*}{G}}{dt} = \frac{1}{a_2 M} \frac{I^2}{(\overset{*}{G})M} - \frac{a_1}{a_2 M} \overset{*}{G} \qquad 2.12$$

where a_1, a_2 and M are constants.

The Cassie and Mayr arc equations may be shown to correspond to equation 2.12 with different power law relationships. The arc circuit interaction may also be described by representing the circuit equation in non-dimensional form.

Using this analysis Topham (1972(b)) describes the current zero period voltage and current waveforms. A criterion is established whereby interruption occurred which led to clearance/failure boundaries being defined for a circuit breaker in a simple busbar test circuit. This analysis showed a qualitative agreement with measurements on a model circuit breaker by Chapman et al (1975) but is unable to provide accurate qualitative predictions.

The lack of experimental data which existed when this model was developed forced the author into making drastic assumptions for the radial property profiles for the dynamic model. The work presented in this thesis (chapter 8) provides such much required data for SF_6 arcs and in particular established the shape of the temperature profile above the

6000K isotherm of an SF_6 gas blast arc during the current zero period. The present work also shows the persistence during the current zero period of copper vapour evolved from the upstream electrode during the high current phase (chapter 6) which has been largely neglected in most arc interruption models.

Topham (1973) has also presented a similar dynamic analysis for the case of a constant pressure flow arc. However this is not considered to be representative of the real aerodynamic conditions present during the current zero period in an interruptor and will not therefore be discussed further.

The Brown-Boveri group produced a series of publications in which they attempted to characterise the transient behaviour of the circuit breaker arc by initially describing the steady state behaviour (Hermann et al, 1974(a), (b)) and then developing a theoretical model in conjunction with experimentally observed phenomena (Hermann et al, 1976 and Hermann and Ragaller, 1977). The authors' experimental observation (Hermann et al, 1976) showed the arc column during the current zero period to have two independent axial sections segregated by the nozzle throat:

(1) The upstream high pressure section which appears uniform and stationary with respect to the axis and whose diameter decays continuously with decaying current.

(2) The downstream (low pressure) region which appears irregular and erratic in cross-section with respect to the axis and whose cross-section oscillates with

decaying current.

The upstream and downstream regions are each characterised respectively by:

(1) laminar flow conditions whereby energy loss is mainly by axial convection

(2) turbulent flow conditions due to the formation of a shear layer between the low density arc column and the high density surrounding hot gas whereby energy loss is principally by radial transport (mainly turbulent mixing)

It is claimed that the two regions dominate the energy balance at different times during the current cycle. During the high current quasi-steady phase the ohmic heating (σE^2) is balanced by convection losses through radiative energy transport, a condition which is well appreciated but difficult to quantify from fundamental considerations (Hermann et al, 1974(a)) thus the upstream region dominates. Paradoxically, as the current approaches zero (within the last 20 μs) energy loss is governed by turbulent mixing and the downstream region is claimed to dominate the energy balance owing to the turbulent energy removal process having a much shorter time scale than the upstream convection process.

Hermann et al (1976) then develop their model by assuming a parabolic axial pressure variation resulting in a linear axial velocity rise in the upstream region. A mean constant velocity is assumed inside the arc column in the

turbulent low pressure region consistent with results in a previous publication (Hermann et al, 1974(b)).

Hermann et al (1976) then develop the model to incorporate all the energy terms (Ohmic heating, energy transport by radiation, turbulent mixing, conduction and convection) in the energy balance, the momentum transport terms (turbulent mixing, convection and friction) in the momentum balance. These processes are considered to be occurring at different times in one cylindrical cross-section whose length is governed by the length of the appropriate dominant axial region (upstream at quasi steady state and downstream at current zero), although they occur physically at different axial regions. Pressure and axial velocity values are inserted according to which process is effective. Near current zero when turbulence is assumed the predominant loss mechanism, the arc cross-section is divided into three regions:

(i) The electrically conducting column which determines the electrical parameters.

(ii) An outer region of cold gas ($T < 1000^{o}K$) which governs the pressure variation along the element and acts as a heat sink.

(iii) An intermediate zone ($1000 < T < 4000K$) which is important for describing the radial processes, principally turbulence i.e. to act as an energy buffer

The energy mass and momentum conservation equations are derived and solved in detail in a further publication (Hermann and Ragaller, 1977). Solution is by radial integration assuming a parabolic temperature profile in the central zone and an exponentially decaying temperature profile in the intermediate zone. Hermann and Ragaller (1977) predict the thermal extinction limiting curves for air and SF_6 for various upstream stagnation processes, and the variation of post arc current with time and different rŗrV for SF_6 at 21 bar and a single peak current.

The authors (Hermann et al, 1976) claim that the model can predict the variation of axial field strength which during the current zero period shows a maximum value near the nozzle throat due to enhanced cooling by turbulence and decays significantly further downstream. Chapman (1977) made the criticism that an increase should be evident further downstream where turbulence is more severe. Hermann et al (1976) explain this phenomenon by a widening of the arc column in this axial region. However the authors claim that an elongated downstream section to the nozzle throat enhances interruption capability. The latter claim is difficult to comprehend in view of the variation of local electric field strength. Indeed such a variation itself implies that the critical area for arc interruption is near the nozzle throat. Experimental results presented in this thesis (chapter 6) show that the arc column is uniform in appearance in the nozzle throat region which is indicative of an arc in a laminar flow. In the same publication

Hermann et al (1976) claim to provide experimental evidence from which they obtain quantitative information regarding the upper limit of the average temperature. The technique used is a side on scanning method with a 1 μs (or greater) scan which exceeds the time constants which characterise their claimed turbulent energy removal mechanism. Indeed the computed temperature variation for an SF_6 arc during the current zero period is of the order of 18,000 to 20,000K 3 μs before current zero (response to discussion on Hermann and Ragaller (1977)) which appears close to the upper limits during the peak current phase and certainly higher than the experimental values presented in this thesis (chapter 6).

A powerful analytical approach to the problem of circuit breaker arc modelling was introduced in a series of papers (Cowley (1974), Cowley and Chan (1974) and Chan et al (1976)) in which the analysis of electrical arcs by integral methods was described. In part I (Cowley, 1974) the overall conservation equations for energy conservation and mass were derived in terms of radial integrals for an arc in longitudinal flow. The equations are formulated such that integral quantities can be characterised by areas relating to specific electrical or thermodynamic properties which are physically meaningful. A standard area is then chosen, namely the thermal area, to which all the area terms defined in the analysis are normalised and the concept of shape factors obtained. The shape factors are thus defined as the ratio of a given area to the thermal area. These depend upon the shape and magnitude of the radial temperature

and velocity profiles but not their radial extent. In order to form a closed set of equations the relationship between the shape factors, in particular the conductance shape factor (δc), and a known characteristic needed to be known. Cowley (1974) relates the shape factors calculated from the full differential solution of the model gas equations to the non-dimensional form of the electrical power input (EI) for a fully developed arc and thus the set of integral equations could be closed.

In part II (Cowley and Chan, 1974) the analysis developed in part I (Cowley, 1974) is tested for two cases, namely the arc in uniform flow and the d.c. arc in accelerated flow. It was shown also in part II that with reference to the free recovery case a rate equation would be required to describe accurately the conductance shape factor variation.

In part III (Chan et al, 1976) it was deduced that a further equation involving axial and timewise differentials was required for satisfactory closure of the integral equations. By limiting the range of radial integration and obtaining an improved method of shape factor prediction the authors derive a useful set of integral equations. One such equation which is of particular use when added to the overall arc equations of Cowley (1974) is the integral energy equation of the arc core. Thus the radial energy transport mechanisms across the core boundary can be considered. If the heat conduction across the core boundary obeys the Fourier law the authors (Chan et al, 1976) state that the

shape factors can be approximated to being dependent only on the Nusselt number for heat conduction at the core boundary. The core energy balance involves the Nusselt number so allowing closure of the set of integral equations.

Walmsley and Jones (1978(ii)) realised the significance of correlating the shape factors with a parameter representing power loss. Curves are presented for conductance shape factor versus Nusselt number Nu and a further parameter χ, the dynamic power loss for different arc types derived from a wide range of operating conditions covered by previous authors. Significantly, a unique set of curves are obtained between δc versus Nu and χ. Thus provided the shape of the temperature profile is known (in order to specify Nu) this correlation curve may be extended to encompass a wide variety of arcing conditions and allow predictive calculations to be made from a limited set of data.

The first current zero arc model to be published utilizing the integral analysis was by Fang and Brannen (1979). This model deals with an arc in an orifice flow of air. The following assumptions were made:

(1) The radial velocity profile is linked to the enthalpy profile by the relationship $\rho\omega^2 = \rho_\infty \omega_\infty^2$ where the subscript ∞ relates to the values of quantities in the external flow. This is equivalent to assuming constant Mach number across the cross-section and makes the momentum equation redundant.

(2) Net radiation is neglected.

(3) The enthalpy area is equivalent to thermal area and the enthalpy flux area is equivalent to the kinetic energy area.

When the above assumptions are incorporated the overall arc energy equation reduces to

$$\frac{\partial}{\partial t}\left(\rho_\infty h_o \theta_\delta\right) + \frac{\partial}{\partial z}\left(\rho_\infty \omega_\infty h_o \delta_h \theta_\delta\right) = \frac{i^2}{\sigma^* \delta_c \theta_\delta} \qquad 2.12$$

where

ρ_∞ is the density of the external flow

h_o is the characteristic value of enthalpy

θ_δ is the thermal area

ω_∞ is the velocity of the external flow

δ_h is the enthalpy flux shape factor

i is the instantaneous current

σ^* is the characteristic value of electrical conductivity

δ_c is the conductance shape factor

In this case radial integration across the thermally influenced arc cross-section has eliminated all the radial diffusion terms.

This equation is then solved for a known δ_h and δ_c which are unique functions of dynamic power loss. The model predicts accurately the axial electric field strength, the arc size, and the $(rrrV)_c$ for a range of current decay rates.

It also predicts correctly the influence of stagnation pressure if correct account is taken of the current waveform distortion and decayed rise of recovery voltage. By this means the model accommodates the imposition of arc - circuit interaction through the distortion of the current waveform.

Unlike the models proposed by Swanson and Roidt and Hermann et al (1976) the energy equation does not need to be altered to account for turbulence. Since the overall energy balance is considered core boundary turbulence is already accounted for in the shape factor relationships.

This model has proved successful in its prediction of arc behaviour in air and orifice flow. It has also been adapted to different nozzle geometries (Shayler and Fang, 1978). However for development of such a model in SF_6 the detailed current zero temperature profile needs to be known so that the shape factors may be calculated and their relationship to the dynamic power loss confirmed.

The models described in this section have involved the use of empiricisms to various extents. Empirical formulae are derived from direct arc property measurement or circuit breaker testing. It is the ultimate aim of theoretical arc modelling to minimise expensive full scale testing so that at least initial feasibility studies of a reliable nature may be made without resorting to the use of industrial test facilities.

2.3 The Evolution of the Circuit Breaker by Empirically Derived Laws

Since many of the present day interruptor design criteria are based upon empirically derived laws, a review of existing literature pertaining to empirical interruptor design criteria with emphasis on thermal performance aspects is in order.

As early as 1946 it was realised that interruptor performance could be optimised by altering such design parameters as the pressure differential across the nozzle throat and the ratio of nozzle diameter to arc length (distance between the electrodes).

Some quantitative analysis were performed by Hudson (1955 and 1964) who considered the effect of nozzle geometry and circuit influences on arc performance. The interrupting capability was characterised in terms of the air mass flow rate through the breaker nozzle when an arc was present (Hudson, 1955). This value was normalised by taking the ratio of mass flow rate with and without an arc present. The mass flow rate ratio M was then empirically expressed as a function of a parameter q where

$$q = \left(\frac{I}{d^{1.5} p^{0.5}} \right) \qquad 2.13$$

where

I is the rms value of the first current loop

d is the throat diameter

p is the initial arc chamber pressure

There apparently exists a band of M values which separate two distinct regions of unity clearance rate and unity failure rate, the centre of which defines the mean critical value of mass flow rate for statistically acceptable clearance and hence an equivalent mean critical value of q. Investigations were made (Hudson, 1955) of the independent effect of varying the upstream distance between electrode tip and nozzle entry plane (the upstream length, Lv) and rrrV upon the critical value for a particular nozzle geometry and circuit condition. It was concluded that the breaker performance deteriorated with an increase in rrrV and Lv. In a further publication, Hudson (1964) investigated the effect of varying the nozzle geometry by introducing a coefficient K to accommodate a newly discovered variation of q(crit)with the values of I, d and p where

$$\left(\frac{1}{K}\right)^2 = \frac{d^{0.6}}{I^{0.5}} pc \qquad 2.14$$

where

pc is the mean critical value of P

From the latter investigations Hudson concluded

(1) The use of a radiused nozzle promotes circuit breaker performance compared with a sharp inlet.

(2) The optimum nozzle length is between ½in. and lin.

(3) No improvement in performance is apparent by using a

divergent nozzle section,

(4) The electrode nozzle gap for optimum performance must be as small as possible, the limit being determined by the voltage insulation between nozzle and electrode.

Conclusion (3) is misleading since other researchers have determined the nozzle divergence semi-angle optimum range to be less than 15^{o}, the minimum value used by Hudson (1964).

Similar work was conducted by Zuckler (1967) where the mass flow rate through the nozzle was related to the current pulse peak value and frequency. This author defined the dynamic back pressure as the pressure required to reduce the mass flow rate to the value when arcing is present. Using high speed photographs Zuckler (1967) showed that improvements in interrupting capability could be achieved by increasing the pressure coupled with a good nozzle design. Zuckler (1969) extended his work to facilitate nozzle blocking by the arc and demonstrated the detrimental effect on interr-uptor performance caused by reducing the cold gas throughput at current zero due to arc nozzle blocking. Mass flow rate alone however is an insufficient means by which to charact-erise circuit breaker performance since, within the arc column and particularly during the high current phase, a decrease in local radial mass density (therefore local axial mass flow) is accompanied by increased axial velocity and thus enthalpy transport.

Following this Kopplin et al (1971) used the peak arc

current as a variable parameter and a fixed rrr^{V} to determine the electrical performance characteristics of a duo flow breaker (bi-directional axial flow) with air and SF_6 as the arcing media. Kopplin et al showed SF_6 to have superior quenching capabilities and an optimum nozzle separation to nozzle radius ratio existed.

Extensive investigations into the effect of the current decay rate and pressure upon the $(rrrV)_c$ were carried out by Frind and Rich (1974). Tests were carried out for a two pressure monoflow interruptor with a laval 12.5mm throat diameter, a 15^{o} semi divergent angle with upstream tank pressures of 100 to 600 p.s.i. for SF_6 and air as quenching gases. The pre-current zero decay rate was varied in the range 5 to 30 A/μs which are representative of peak current values of 10 to 60KA for a 60Hz current pulse (although the frequency used was actually 1200 Hz to enable a sufficiently low value of peak current to be used to avoid nozzle blocking).

Frind and Rich showed that for a fixed value of $^{di}/_{dt}$ (27A/μs) the $(rrrV)_c$ increased with upstream tank pressure linearly for air and to the power 1·4 for SF_6.

The same authors derived the relationship between $(rrrV)_c$ and $^{di}/_{dt}$ as

$$(rrrV)_c \quad \alpha \quad \left(\frac{di}{dt}\right)^{-2} \qquad 2.15$$

for both air and SF_6 at a pressure of 550 p.s.i.a. Although the two curves were parallel, the SF_6 withstood generally

higher (rrrV) values than air for any given $^{di}/_{dt}$.

Although the authors in this case claimed their $^{di}/_{dt}$ to be representative of real arcing conditions the effect of nozzle blocking upon the breaker performance during the peak current phase has not been investigated and is not therefore representative of real circuit breaking conditions.

In a further publication (Frind et al, 1980) the thermal reignition characteristics have been investigated for a gas blast interruptor with a 12.7mm diameter orifice using air and SF_6 as arcing media. The post zero arc current and voltage were measured in order to determine the variation of arc resistance and the electrical power input during the thermal recovery period. The authors also employed high speed photography to evaluate qualitatively which axial arc section responded most rapidly during the transient conditions.

The critical peak post arc current and power loss at that instant were compared with the theoretical calculations of various authors (Swanson, 1977, Hermann and Ragaller, 1977).

Frind et al (1980) drew the following conclusions

(1) The dominant arc section during the thermal reignition period was at the axial location near the nozzle throat, was about 10mm in length and showed a smooth but rapid decay towards current zero.

(2) The erratic and dispersed nature of the downstream arc column during the thermal recovery period made interruption at this axial location unlikely.

(3) The measured post zero current was slightly less than the theoretical values of Hermann and Ragaller (1977).

(4) The critical power loss for arc reignition was considerably less than that predicted assuming turbulent losses to dominate.

(5) Recovery speed was comparable to other nozzle geometries.

Although this experimental investigation forms a significant contribution there are a number of reservations which need to be noted:

(i) The critical time for reignition is determined from the instant at which there is a quasi-steady value of arc resistance. The identification of this instant can only be achieved with limited accuracy.

(ii) The peak arcing current has been restricted to a low value such that nozzle blocking phenomena are precluded.

Briggs (1982) has investigated the influence of various properties of the gas flow upon the thermal interrupting capability of an SF_6 gas blast circuit breaker. The influence of parameters such as upstream pressure and nozzle geometry upon performance have been confirmed and has been claimed to be directly attributable to the size of arc diameter at the

current zero instant. Although most of the work was conducted for reduced power arcing conditions this was supplemented by full power tests. These results are in accordance with the earlier results of Briggs and King (1977) who also identified the important influence upon current zero arc diameter of upstream pressure, upstream geometry coupled with nozzle throat diameter and the need to maintain sonic velocity.

By optimising these parameters the velocity profile (axial and radial components) may be optimised to enhance interruption capability (Briggs, 1982). An investigation of these and other parameters (e.g. arcing medium) upon $(rrrV)_c$ for a wide variety of flow geometries and arcing conditions enabled Briggs (1982) to draw the following conclusions:

(i) For interrupters with modest downstream nozzle lengths, it is the upstream section which governs arc extinction and thus interrupter performance.

(ii) The flow velocity of the quenching gas is the dominant influence upon design.

(iii) The upstream flow profile (i.e. the axial and radial velocity components) determine the characteristic quenching properties of the breaker i.e. breakers utilising a high degree of radial flow component reduce current zero arc time constants while breakers with a high degree of axial velocity component promote good arc transfer to the nozzle throat and low arc duration.

(iv) Optimum performance is predicted to occur in nozzle designs which incorporate a balance between the axial and radial gas velocity components.

Although Briggs (1982) has attempted to quantify the effect of varying the important design parameters upon interruptor performance the following criticism may be made:

Although a wide range of operating conditions have been covered, this has not been undertaken in a rigorously rational manner e.g. the influence of one parameter has been investigated with a throat diameter of 20mm and upstream pressure 6.85 bar whilst another parameter has been investigated with a different nozzle diameter of 45mm and a different upstream pressure of 7.9 bar. Some parameters have been investigated with air as the arcing medium, whereas the performance curves and the time constant variation arc presented with SF_6 as the medium.

The G.E.C. group (Andilewski et al,1984) have derived an empirical equation from a range of test data for predicting the performance of SF_6 circuit breakers. This gives the critical rate of rise of recovery voltage as a function of a number of parameters as follows

$$(rrrV)_c = \frac{a \times p^n \times L \times D_t \times M^q}{(di/dt) \times A} \qquad 2.16$$

where

$(rrrV)_c$ = critical rate of rise of recovery voltage

p = upstream pressure

L = ratio between throat and gap

D_t = throat diameter

M = Mach number

$(^{di}/_{dt})$ = rate of decay of current

A = area of the arc at current zero (cross-section)

a,n,q = constants

The authors also quote an equation for the dynamic arc diameter variation:

$$D_c = \frac{b \times I^{0.63} \times L_u^{0.25}}{p^{0.25} \quad M^{0.25}} \qquad 2.17$$

where

D_c = core diameter in cm

I = instantaneous current in amps

L_u = upstream arc length in cm

p = upstream pressure in bars

M = Mach number

b = constant

which the authors claim to show good agreement with test measurements above a current of 1KA. Clearly equation 2.17 can only be approximate since it implies zero arc diameter at current zero. In practice the authors claim that above a critical current level the measured arc diameter below 1KA increasingly deviate from a monotonic decay. This is a result of the radial inflow being unable to adjust sufficiently

rapidly so that convective effects are limited with the arc column decay retarded.

The same authors also measured the cold flow velocity distribution through the nozzle using a particle tracing technique which the authors claim enable the radial pinch component of the flow to be evaluated.

Finally the authors evolved a method for predicting the dynamic pressure rise with an arc present which they claim to take account of thermal and arc core blocking in a calculation which covers the duration of the contact separation and full current loop. When the current zero is reached equation 2.16 is used to evaluate the performance. The authors then produce a series of performance curves for various values of radial pinch component of the external flow and conclude that a value of 25% radial pinch component shows the best agreement between the calculated and measured performance. This is greater than ideal theory predicts but agrees with cold flow experimental results.

Many difficulties exist in the utilisation of the empirical analysis of Ancilewski et al (1984). Firstly, the empirical equation describing the performance (2.16) has been derived from measurements made on a monoflow interr-uptor. Rigorously it is not clear how the analysis should be applied to calculate the performance of a duoflow interruptor since the physical values of certain variables (e.g. L) is obscure. Secondly, the constants which appear in equation 2.16 (a, n and q) have not been defined nor

values given so inhibiting comparison with test results under different arcing conditions. Thirdly, there are many ways of measuring the optical arc diameter and considerable care is required in relating optical and electrical arc diameters close to current zero. No mention or description of the measurement technique employed has been made so making a meaningful comparison of arc diameters measured by other authors difficult. Finally, although measurements of the cold flow distribution have been made and unexpected flow properties demonstrated no measurements have been made under arcing conditions to confirm the effect, if any, upon the arc column. (Note that no other investigations e.g. dynamic electrical conductance (Chapman, 1977) and laser doppler (Todoronic, 1983) have given any evidence of any unexpected influences under ideal conditions.

An extensive investigation into the current zero electrical arc properties and the thermal performance of a model gas blast circuit breaker has recently been conducted at Liverpool as reported by Taylor et al (1982). Tests were conducted for both reduced power (1.6KA holding current level) and full power (34 to 64KA peak sinusoidal waveform) where a converging-diverging nozzle (12^{o} semi-divergent angle) geometry coupled with an upstream tank pressure of 7.8 bar ensured sonic flow conditions at the nozzle throat (diameter = 35mm). Copper and PTFE were used as nozzle materials and Cu/W and Carbon as upstream electrode materials; the nozzle/electrode geometry remained unchanged throughout

the investigation. The principal arcing medium was SF_6, though some tests were performed with air. Measurements of current and voltage and upstream pressure throughout the arcing cycle and during the current zero period were made for a current decay rate range between 14 to 60A/μs (reduced power) and 14 to 26A/μs (full power). This allowed the detailed interrupting performance to be obtained (plotted in terms of $(rrrV)_c$ versus di/dt), as well as an indication of arc flow interaction (from transient pressure variations). These measurements taken together give an insight into the effect of arc flow interactions upon the interruptor performance.

The authors derived the following empirical relationships for the stated operating conditions:

Reduced power:

$$\left(\frac{dv}{dt}\right)_{crit} = 3.3 \times 10^{3} \left(\frac{di}{dt}\right)^{-2.8} \qquad 2.18$$

Full power:

$$\left(\frac{dv}{dt}\right)_{crit} = 4.6 \times 10^{8} \left(\frac{di}{dt}\right)^{-7.5} \qquad 2.19$$

A comparison of these two equations reflects the more rapid degredation of performance which occurs with full power arcing (exponent of -7.5 compared with -2.8).

In addition to establishing detailed performance trends Taylor et al (1982) calculated the arc conductance and instantaneous power input from which the authors calculated

the Mayr arc time constant as a function of time and di/dt and the critical peak post arc current and power loss for the different operating conditions.

Further empirical analysis was used to derive an expression for the time delay between the current zero instant and the instant of peak critical post arc current as defined by Frind et al (1980) in terms of the conductance decay time constant and the current decay rate.

The results of this investigation led to the following conclusions:

(1) The thermal performance of the test circuit breaker deteriorated with increasing di/dt. The existence of pressure transients for low di/dt values for the full power arcing condition indicated thermal nozzle blocking which did not affect the performance compared with the reduced power level.

(2) The deterioration in performance at the high di/dt values is exaggerated for the full power case (equations 2.18 and 2.19). This corresponds to the existence of severe nozzle ablation in the full power case which results in substantial back-flow. Since the ablation process is different for the two nozzle materials (Cu and PTFE) there exists a slight influence on performance for the full power case due to the nozzle material. This has been shown to be due to differences in the wear of the nozzle throat rather than the direct influence of ablated material or back-flow.

(3) Small changes in arc conductance at current zero can produce relatively large changes in test head performance.

(4) The arc conductance at current zero was found to vary linearly with current decay rate whereas the Mayr time constant was invarient with $^{di}/_{dt}$. Both of these above quantities were found to decrease in sympathy with current during the current zero period and in agreement with the results reported by Briggs (1982).

(5) Post arc currents and critical powers showed reasonable agreement with similar measurements made by Frind et al (1980) and the empirical relationship derived for the time delay for critical thermal reignition showed the correct trend when compared with measured critical thermal reignition data.

(6) The electrical condition of the arc during the current zero period following a full power or reduced power test is the same within the experimental error for a given $^{di}/_{dt}$ value.

Empirical investigations such as the ones described in this section clearly provide useful and directly applicable criteria whereby circuit breakers may be designed. These design parameters may be utilised in order to produce an interruptor design to work at a lower or higher power rating provided the laws governing the scaling of the parameters are known. However such deviations in performance between

reduced power and full power as noted by Taylor et al (1982) imply that fundamental differences in the structure of the current zero arc column are present which do not manifest themselves in the electrical properties (conductance) and therefore warrant investigation by other diagnostic means. The most suitable means for investigating the arc structure is by optical measurements (photographic, total and spectrally resolved radiation or emission). These methods are reviewed in the next chapter.

CHAPTER 3

REVIEW OF OPTICAL DIAGNOSTIC TECHNIQUES

3.1 Introduction

In the previous chapter the theoretical and empirical development of the circuit breaker has been reviewed. The latter involves principally the measurement of overall arc parameters such as current and arc voltage. These measurements enable the performance of a circuit breaker to be evaluated for a particular range of operating conditions. However no information can be derived as to the fundamental thermal properties and structure of the arc column and the physical processes governing arc extinction. To quantify these processes measurement must be made of arc temperature and species concentration, with spatial (radial and axial) and temporal resolution if the arc is in a transient state.

This chapter therefore reviews different techniques which have enabled previous researchers to identify features of arc column structure and in some cases extinction criteria through both qualitative and quantitative analysis of their experimental measurements. Particular sections deal with different types of diagnostic technique each of which enable different fundamental properties to be quantified or at least identified.

3.2 Photographic Techniques

3.2.1 Introduction

Photographic studies of arcs involving usually high speed photography of the luminous arc column have been undertaken by many researchers since it was decided that the appearance of the arc column would play an important part in proving or disproving early theories regarding arc extinction. Biermanns (1932) utilised his high speed photographs to demonstrate the continuity of the arc column at the current zero instant and thus disproved existing theories that the arc may have separated into two independent axial sections to cause circuit interruption.

Whatever photographic technique is employed, care is needed in considering what the luminous cross-section of the arc represents. Clearly this will be affected by the exposure time and type of film or recording surface sensitivity. Where gradual changes in the radial extent of the true luminosity are present e.g. during the current zero period of a circuit breaker arc (particularly downstream of the nozzle throat) this problem becomes acute. For instance, over-exposure can lead to gross over-estimates of the area of the electrically conducting core of the arc. Therefore quantitative analysis using a photographic diagnostic technique must stipulate precisely the photographic operating conditions as well as the optical calibration procedure. Chapter 5 of this thesis describes such an overall calibration procedure conducted during the present investigation.

A major problem with optical diagnosis of circuit

breaker arcs involves gaining optical access through the walls of the flow shaping nozzle. The following section includes a review of significant contributions to date in the field of arc photography in a real circuit breaking environment.

3.2.2 Development of the Technique

A novel method of overcoming the optical access problem was used by Airey (1972) who mounted a camera to view the nozzle throat of a production circuit breaker from a position downstream of the nozzle exit and offset from the axis of symmetry. A framing speed of 8000 fps and a carefully chosen value of neutral density filter enabled the luminous arc diameter at the nozzle throat to be determined for pulsed arc currents of up to 45KA peak in air. Airey (1972) studied the effect of instantaneous arc current and upstream tank pressure on the luminous arc diameter and compared his results with the simplified enthalpy flow model of Frost and Liebermann (1971).

Airey (1972) claims good agreement with the physical model up to an instantaneous current value of 13KA. However once this value is exceeded, the model predicts larger diameters than those measured. The author explains this in terms of the evolution of electrode vapour giving rise to higher electrical conductivity of the plasma. Calculations taking account of the copper vapour plasma gave better agreement with the experimental results. However the model does not take account of radiation loss which is

important at such high current levels and particularly so when the plasma is contaminated with copper vapour (e.g. Strachan et al, 1975(b)).

A more conventional method of gaining optical access to the arc in an interruptor nozzle is to make lateral slots in the nozzle wall which are then sealed so that each slot is gas tight.

Kogelschatz and Schade (1971) used a laval nozzle of 12mm throat diameter with slots as described above with sealed quartz windows. In this way a 2KA, 5ms duration pulsed arc in accelerated flow (23 atm upstream tank pressure) was photographed using a rotating mirror arrangement to give 2μs exposure. Results showed the presence of turbulent perterbations upstream which the authors claim became clear on streak photographs (unfortunately not presented in this publication). No photographic results were presented for the section upstream of the nozzle throat.

In a further publication by the Brown-Boveri group (Hermann et al, 1976) streak photographs for similar arcing conditions to those described by Kogelschatz and Schade (1971) are presented. Hermann et al photographed the arc at four downstream stations and one axial station upstream of the laval nozzle entrance during a period covering 30μs each side of current zero. The results show the arc column to have a turbulent, eratic appearance further downstream throughout most of the current zero period whereas the two

stations furthest upstream showed no signs of turbulence. Based upon these observations it is claimed that turbulence plays an important part in the arc quenching process.

Jones et al (1975) measured the optical radius of an arc in an orifice geometry for triangular arc current pulses up to 17.5KA and 5 to 25ms duration in air using cine photographs (Lidgate, 1973). This enabled the axial (upstream and downstream of the orifice) and temporal variation of the optical arc radius to be measured. Using these measurements, plus others of different arc properties, the terms in the quasi steady state energy balance equation (Swanson and Roidt, 1971) and their relative significance were determined and compared with the instantaneous power input. As a result it was possible to quantify the effects of varying the arcing conditions (e.g. electrode material) upon the peak current phenomena such as arc flow interaction and local and overall arc properties.

Walmsley et al (1976) used a high speed photographic technique to observe in detail the arc diameter variations during the major part of the 3 to 8KA sinusoidal pulse. The authors used a 19mm radiussed orifice, upstream pressures of 50,100 and 150 psig with different upstream electrode geometries and materials. A high speed streak and framing investigation was carried out using an A.W.R.E. 54 camera giving 0.05 to 0.1mm/μs writing speed and a Dynafax 350 camera giving an exposure of 1.6 to 3 μ sec respectively. The authors identified two distinct modes of arc diameter

behaviour, namely normal and oscillatory. When the arc behaved normally the arc diameters were found to correlate well for the range of upstream tank pressure, current and electrode material using parameters deduced from an integrated enthalpy flow analysis. However, under certain circumstances the arc diameter measurements showed distinct axisymmetric oscillations which also appeared simultaneously as oscillations in the arc voltage. Walmsley et al (1976) identified these oscillations with plasma pulsations caused by the interaction of electrode evaporation and flow effects. Furthermore, it was found that the oscillations were most severe for elkonite as the upstream electrode but could be minimised by giving the electrode a rounded or radiussed geometry. The authors further postulated that the existance of such blobs during the current zero period could have a detrimental effect on performance because of their effect on the arc voltage. High speed photographs obtained by Lewis et al (1983) under different arcing conditions, which will be described in chapter 6 of this thesis, have shown similar vericose deformation phenomena so confirming that such oscillations may be anticipated to occur generally rather than for limited, particular conditions.

In a further publication Walmsley et al (1978(i)) extended the previous work on the luminous cross-section of the 19mm orifice arc to the current zero period (100μs before to 9μs after). The techniques in this work included short exposure framing records using both conventional and image converter photography. Streak records were also included.

The image converter photographs were necessary in order to achieve sufficiently short exposure of the low luminosity plasma consistent with the rapid changes which occur in the plasma column properties close to current zero. These image converter photographs were taken using an Imacon 700 camera in conjunction with an image intensifier (3 stage magnetically focussed) at a framing rate of 5×10^5 and 10^6 fps giving exposures of 1μs and 0.2μs respectively. These photographs identified the arc column as having a shallow radial luminosity gradient at its periphery so that care was needed in setting the exposure conditions (such as intensifier bias) in order that the measured luminous area would be physically meaningful and reproducible.

Walmsley et al (1978(i)) presented only a limited amount of luminous area measurements showing the area decay for a 3KA ($^{di}/dt$ = 1.3A/μs at current zero) peak current value at locations upstream and downstream of the orifice over the final 80μs and 14μs of current decay. The trend apparent in these results is for a rapid decay of the downstream area at around the instant of current zero whereas a luminous region persist upstream for a few (at least 6) μs after current zero.

Walmsley and Jones (1978(iii)) have also extended their luminous arc core measurements to currents up to 100KA peak, to a larger diameter (50mm) radiussed orifice and to both air and SF_6 as arcing media. They monitored the luminous diameter over the major part of the current pulse using a

Beckman-Whitley Dynafax 350 framing camera which captured 10,000 to 20,000 fps with exposure times of 1.3 to 2.6μs. Their results confirmed the foundation of a bright inner core with the main luminous arc plasma for currents above 20KA independent of upstream contact material and arcing medium. The diameter of the core was only weakly dependent on the stagnation pressure and instantaneous current. Narrow band filtered photographs around the 515.3nm (Cu line) wavelength showed that the core consisted of electrode material. Severe blocking of the nozzle by the outer plasma column was identified to occur at instantaneous current values of 80KA and above and material ablated off the orifice wall was luminously identifiable downstream where it merged with the arc plasma column. This form of blocking was observed to cease well before current zero.

Plasma oscillations similar to those observed at moderate current values, but ceased at higher current levels.

Although Walmsley and Jones (1978(iii)) did not extend this work to the current zero period a number of peak current effects which could effect interruptor performance at current zero were nonetheless discussed (e.g. electrode vapour entrainment into the column).

Separately identifiable electrode material core had first been identified by Airey et al (1976) downstream of a converging-diverging nozzle (throat diameter 38mm) also at instantaneous current levels above 20KA. The authors also identify oscillatory variations in the core diameter

which were coincident with the voltage oscillations also observed as did Walmsley et al (1976). Airey et al (1976) claim that a high remnant conductivity at the current zero following a 50KA arc in air existed which could have deliterious effects on breaker performance. The need for detailed current zero measurements of arc diameter (and other parameters) is further demonstrated by the latter claim. It is unfortunate however that in this publication all the optical diameter measurements were presented for a section further downstream than the nozzle exit itself whereby such factors as the degree to which the arc filled the nozzle could not be easily established.

Ancilewski et al (1984) present results of arc luminous diameters taken during the current zero period of an arc whose peak current is undefined although the current decay rate is quoted. No indication is given of the optical operating conditions so that unfortunately the diameter measurements quoted cannot meaningfully be compared with the results of other authors. This, of course, is particularly important during the current zero period as indicated by Walmsley et al (1978(i)) since the luminous structure of the arc column during this period is such that variations in exposure etc. can lead to large variations in the recorded optical diameter.

3.2.3 Concluding Statement

Quantitative analysis of photographic measurements has

shown itself to be a useful diagnostic technique whereby for instance certain terms in the energy balance may be evaluated as shown by Jones et al (1975) during the peak current phase. Clearly similar measurements made close to current zero could also be used to elucidate the energy terms during the current zero period in a similar manner. However Walmsley et al (1978(i)) have shown that unlike the peak current regime, during the current zero period the radial profile of the light intensity has shallow wings so that care must be taken in analysing such records. In this thesis measurements of radial relative intensity profile will be presented particularly during the current zero period so that as a result the variation of radial light intensity can be quantified.

3.3 Spectroscopic Techniques

3.3.1 Introduction

A large portion of the work presented in this thesis is based upon information derived from spectroscopic measurements. The branch of spectroscopy with which this thesis is concerned involves atomic spectra since at the temperatures of interest within an arc column most of the species are atomic in nature. The theory and physical principles of atomic spectra are covered in a number of texts (e.g. Herzberg, 1944).

With a knowledge of the physical principles governing atomic spectra, the theory may be applied to the plasma to

derive the localised arc properties of temperature and species density. However, this analysis may be greatly simplified if certain assumptions regarding the thermodynamic state (local thermodynamic equilibrium) and optical depth of the plasma are shown to be valid. These are discussed in detail in chapters 7 and 8. Plasma, and in particular arc, spectroscopy in idealised situations has been used to confirm existing theories and derive fundamental constants of certain materials (e.g. Koch and Richter, 1968 for copper). However the arc column in a circuit breaker departs in many ways from the above mentioned idealised situations, so that care must be taken when making spectroscopic measurement in such situations. As a result it is profitable to review the previously published work on arc spectroscopy.

3.3.2 Development of Arc Spectroscopic Techniques

Much of the early work on arc spectroscopy was conducted on arcs burning in different gases in a wall stabilised environment. As a result of the cylindrical symmetry and well controlled experimental conditions temperature and electron densities could be conveniently and reliably measured. For instance Maecker (1963) measured the radial temperature profiles of nitrogen wall-stabilised arcs for a range of currents between 10 and 250A. Much of the wall stabilised work was conducted for nitrogen, argon and helium plasmas but its relevance to transient circuit breaker arcs at current zero remains to be rigorously demonstrated.

One of the earliest spectroscopic investigations on high current arcs was conducted by Roberts and Prasad (1972) for the quasi steady conditions of a free burning lOKA arc in air. Both streak and shuttered (snapshot) spectra were recorded using a Hilger medium spectrograph type E528 and Ilford HP3 and long range spectral plates. An A.W.R.E. streak camera system (Gabriel, 1960) was used to enable streak records of up to 2ms duration which could be shuttered by a rotating disc to give a 19μs exposure. Measurements were also made using an EMI type 9529/B photo-multiplier. The authors measured radial temperature distributions which were derived from a number of different methods, the most accurate of which were

(i) Relative intensity of the Cu I lines
(ii) Line intensity variation of N I
(iii) Relative intensity of the Cu II lines
(iv) Relative intensity of the N II lines

A similar analytical approach to that of case (i) is used in this thesis and is discussed in chapter 7. Plasma species density were evaluated from existing air plasma equilibrium compositions in those regions of the arc where the equilibrium condition was to be expected. Thus a knowledge of the temperature distribution enabled species concentrations to be evaluated within the copper plasma jet. The electron density, Ne was calculated from the Stark broadening of particular lines, a method which will be further described in chapter 7.

From their streak records Roberts and Prasad (1972)

identified a rotational motion of part of the arc plasma. This plasma column rotated as a distinct entity with a regular frequency of about 22KHz along with a higher frequency irregular fluctuation. The authors also observed the presence of a copper vapour rich core at 10KA which had a lower temperature than the rotating host plasma column owing to increased radiation losses around which the hotter host plasma column rotated.

The authors determined the proportion of the power loss by radiation to be 36% of the total, 90% of this being by copper emission. The remaining energy loss was governed by self generated axial convection, heat conduction being only involved in redistributing energy within the thermally affected region of the arc.

Roberts and Cowley (1973) extended spectroscopic investigations to an arc in an efflux constant pressure flow. It was observed that the efflux flow arc showed less copper radiation but more nitrogen and oxygen emission compared with a corresponding free burning arc. These phenomena were explained by enhanced vapour injection from the cathode and an increase in volume for radiation cooling coupled with a reduction in Nitrogen species concentration. When a flow with Mach number M = 0.7 was imposed, the visible regions at the boundaries became sharper in appearance, implying a steeper radial temperature and electron density gradient at the boundary.

In the above two investigations the authors investigated

high current quasi-steady arcs burning in simple self or constant external imposed flows. They identified the spectral radiation features of the arc column from which they deduced the temperature and species density profiles and the contribution of terms to the steady state energy balance. The need was therefore clear to extend this work to the accelerated flow conditions experienced in real circuit breaker arcs.

This extension to orifice air flow was made by Housby-Smith and Jenkins (1978). The flow was sustained by upstream tank pressures of 50, 100, 150 and 190 psig. A fixed nozzle electrode geometry was used with carbon, steel, copper and elkonite as upstream electrode materials. Peak arc currents of 3 and 8KA were used along with the same spectrometer and rotary shutter system as that used by Roberts and Prasad (1972). Snapshot spectra were obtained for instantaneous current values of 1.9 and 6.8KA during the quasi-steady phase of the respective current pulses. Three axial locations were viewed - 6.5mm upstream, 2mm and 9mm downstream with respect to the orifice edges.

Of the four electrode materials used, copper and especially elkonite gave rise to the most useful spectra showing a high density spectrum both upstream and downstream of intense copper lines and some N II emission downstream. All these lines were found to increase in intensity as the peak current level was raised. The authors selected experimental results for analysis which avoided the inherent problems

caused by a high continuum intensity, spectral line self absorption, overlap effects from intense neighbouring lines and spectral plate over-exposure. The lines chosen were Cu I 330.7nm, 282.4nm, Cu II 276.9nm downstream; Cu I 249.2nm, Cu II 248.9nm upstream; and N II 399.4nm, 444.7nm, 453.Onm and 463.Onm at the downstream station.

Qualitative analysis showed the N II and copper emission species to occupy different radial sections of the arc column, with the hot plasma spectrum oscillating rapidly as in the free burning and efflux flow cases.

Electron temperatures were estimated from the intensity ratio of Cu I and Cu II lines in the copper regions and from different N II lines in the air regions. These calculations assumed local thermodynamic equilibrium and were based upon Abel inverted spectral emissions for the cases when cylindrical assymetry was apparent. Electron densities were derived from Stark broadening effects of selected lines and a method relating the electron density to the continuum intensity, and copper vapour densities from the intensity ratio of Cu II 276.9nm to N II 300.6nm.

Housby-Smith and Jenkins (1978) used the above information (Ne and T) to calculate the local static pressure variation for the peak current levels of 3 and 8KA. The authors found good agreement with earlier pitot probe measurements by Jones et al (1974) only after Stark broadening parameters used to derive Ne were empirically adjusted.

From their analysis Housby-Smith and Jenkins concluded that the arc was similar to the previously investigated free burning and efflux arcs in that there existed two principal emitting species (N and Cu) which were non-coaxial and at different temperatures. The intensity and number of lines of emitting copper was found to be higher in this case implying a higher radiation loss from the copper core, although the vapour concentration was not sufficiently high to effect the transport properties. Also the optical diameter was lower in the orifice flow arc and the electron density higher, which corresponded to a more constricted arc column. These conditions were noted to be advantageous for enhancing current interruption.

Although Housby-Smith and Jenkins (1978) were hampered in their analysis by the assymetric nature of the arc column preventing the use of an Abel inversion procedure, they have presented electron temperature profiles, the majority of which were derived from non-Abel inverted results. Unfortunately no distinction is made by the authors between Abel and non-Abel inverted results. The fact that an inversion procedure was not used makes the electron temperature distribution (shape and absolute value rigorously inaccurate although the magnitude and shape of the profiles are reasonable.

Spectroscopic investigations of the downstream region of SF_6 arcs in a nozzle flow with the direction of flow from anode to cathode presented by Airey (1977). Peak currents

of up to 38KA were investigated with spectra recorded for instantaneous currents as low as 300A using a rapid scanning spectrometer (Monospek 600) arrangement to give good temporal resolution.

Initially, measurements were made of radially integrated at a station 37mm downstream of the anode which was also downstream of the nozzle exit. Photoelectric snapshots of 100μs exposure were used to measure the line intensity and width of Cu I 510.5nm, 529.3nm and 515.3nm from which the average electron temperature and density was calculated.

Further measurements of radially resolved spectra were performed on a section 25mm downstream of the anode which were viewed through a cutaway section of the nozzle. Since at currents below 200A the copper vapour concentration was low in this region it was necessary for Airey (1977) to estimate the radial temperature distribution from the intensity ratio of the F I 624.0nm and S II 545.4nm spectral lines. An Abel inversion procedure was incorporated in this calculation.

Below 20KA (the instantaneous value for the inception of the vapour core) Airey (1977) measured the arc temperature profile to be parabolic with an axis temperature of 20,000K and a radially averaged electron density of 3.2×10^{17} cm^{-3}, which resulted in a predicted pressure of 2.25 bar compared with the 2 bar derived from the flow measurements. At 1KA instantaneous current the temperature profile exhibited a

raised portion confined to a radius of less than 1mm. Large oscillations in the averaged temperature were observed at the peak of a 24.5KA pulse which were attributed to genuine temperature fluctuations (between 17,000 and 31,000K) of the vapour core. These fluctuations existed for currents as low as 10KA but the maximum averaged temperatures had decayed to 19,000K. The author further concluded that conditions of LTE were satisfied for instantaneous current values below 20KA but could break above this value. The copper vapour concentration in the arc was found to increase slowly between 1% and 5% as the peak current value was increased from 7KA to 13KA the values being independent of increasing or decreasing current. However, following a 19KA peak current the Cu concentration increased to 35% at an instantaneous value of 10KA. With a knowledge of the radial distributions of arc temperature and electron density the author formulated a two zone arc model for the high current phase.

Airey (1977) identified globular motions of the copper plasma which appeared to merge into a continuous motion using high speed photographs. This observation was similar to the phenomenon described by Walmsley et al (1976) and could account for the local temperature oscillations. However Airey (1977) did not relate these observations to those of Roberts and Prasad (1972) or Roberts and Cowley (1973) but rather believed them to be associated with temperature fluctuations. Also Airey (1977) did not indicate to what extent the cutaway section of the nozzle effected flow patterns

downstream which could seriously effect local and overall parameters.

Similar measurements were made by Ikeda et al (1982) but in an orifice flow using SF_6 as the quenching medium with an upstream tank pressure of 7 bar. The orifice throat diameter was 50mm and peak current values of 30KA and above were investigated. 0.5ms exposures enabled photographic recording after dispersion through a Hilger-Watts 1000 prism spectrometer. The spectral lines selected for analysis were F I 623.96nm, S II 545.39nm, S II 532.07nm, Cu I 578.31nm, Cu I 529.26nm, Cu I 510.55nm.

Ikeda et al (1982) confirmed the evolution of a copper core above an instantaneous value of 18KA which was in agreement with Airey (1977). However in contrast to Airey (1977) the temperature of the copper core 1mm downstream of the orifice was found to be lower than that of the surrounding plasma, these temperatures being about 15,000K and 20,000K respectively. These authors also determined the electron density from Stark broadening calculations to be 1.5 to 1.8×10^{18} cm^{-3} and a copper vapour concentration of about 70%, 1mm downstream of the orifice exit.

It is unfortunate that, owing to the extreme experimental conditions encountered that the Abel inversion technique could not be employed and a more accurate radial temperature distribution derived. It is also unfortunate that the upstream temperature, electron density etc. could not be calculated owing to reabsorption etc. which would have also

enabled axial gradients of parameters to be determined.

The only spectroscopic investigation made which included the current zero period of an arc similar to that in a circuit breaker was reported by Smith et al (1978). Studies were made during the current zero period of 3KA peak current arc burning in SF_6 and air in a 19mm diameter shaped orifice with an upstream pressure of 100 psig. The upstream and downstream electrode geometries were varied according to which axial region of the arc, 2mm upstream or 1mm downstream was to be viewed. A Hilger and Watts medium quartz spectrograph type E528 was used in conjunction with Ilford HP3 photographic plates for the upstream investigation whereas lower light intensities necessitated the use of an E720 scanning attachment fitted with an IP28 photomultiplier for the downstream investigation. The photographic plates were exposed for 6μs snapshots during the final 200μs before current zero whereas the photoelectric detection system enabled a continuous timewise record of a given spectral line to be obtained during the final 25μs before current zero.

Radially integrated electron temperatures were calculated from Cu I emission spectra at the upstream station by measuring the intensity ratios of the spectral lines 319.4nm and 309.9nm and 319.4nm and 330.7nm and at the downstream station by measuring the intensity ratio of the lines 515.3nm and 510.5nm, 515.3nm and 578.2nm, 521.8nm and 578.2nm and 521.8nm and 570.0nm. Electron density was evaluated at 70μs and 50μs before current zero from the Stark

broadening of the 330.7nm line measured upstream.

The authors used the values of electron density and temperature to confirm the existence of LTE up to 50μs before current zero. In the final 20μs before current zero the downstream air temperature results showed a plateau at about 9,000K up to 10μs before current zero at which instant it rose to about 10,000K before falling steeply over the final 3μs to about 7,000 at current zero. The SF_6 temperatures remained virtually constant (at 8,500K) up to about 5μs before current zero after which a rapid decline occurred to about 6,500K at the current zero instant. Different line pair ratios gave different temperature values throughout the current zero period for both air and SF_6, a phenomenon related to the lower energy levels of the electronic transitions concerned.

It is unfortunate that the authors used different electrode geometries for different measurement locations since this makes comparison of their own results from different axial regions difficult let alone comparison with different authors. No upstream temperature results were presented for SF_6, althouqh the temperatures in this region are similar to those at downstream stations during the current zero period, at which point the authors claim little difference in temperatures for the two gases. No results were presented of the radial temperature distributions which enabled only an overall analysis of the arc column to be made at a given axial position. Furthermore no radial energy distribution

detail could be deduced so that no evaluation of the current zero energy conservation equation could be obtained. An approximate estimated value of current decay rate from the oscillograms of Smith et al (1978) yields a value of 8KA; clearly in order to correspond to real circuit breaking conditions, the current zero spectra of both higher peak current and current decay values need to be investigated.

3.3.3 Concluding Statement

In this section the work of authors using spectroscopic techniques applied to circuit breaker arcs has been reviewed. It has been shown that extensive spectroscopic investigations can be used to calculate local arc parameters which are fundamental for describing the arc column condition and structure. A detailed knowledge of such parameters further enable energy transport terms to be calculated. Much work has been done to calculate the above mentioned parameters for high current arcs in a quasi-steady state for many different operating conditions. However, to obtain a knowledge of such parameters during the current zero period where their effect on current interruption phenomena can be studied directly, a dynamic and extensive spectroscopic investigation during this period is required. Smith et al (1978) studied the overall spectral radiation features of an arc column during the current zero period of 3KA and 8KA arcs in an SF_6 flow. It is the objective of the present experimental investigation to improve on the technique of Smith et al (1978) in order to obtain a detailed spectroscopic

investigation of an SF_6 nozzle flow circuit breaker arc for full power arcing conditions (>34KA peak current).

3.4 Measurement of Radiation Power Loss

3.4.1 Introduction

Photographic and spectroscopic measurements have been reviewed in the previous two sections and it has been shown how they can provide valuable information regarding overall arc as well as detailed local arc column structure. This information is useful for calculating important energy transport terms in the energy balance. Paradoxically neither of these optical measurements can easily provide information about radiative power transfer away from the arc environment on account of the need for detailed absorption information within the thermal volume surrounding the arc plasma. As a result recourse needs to be made to measure this nett radiative loss directly. This is possible if careful consideration is given to arc geometry and overall measurement system calibration. A brief review of some radiation power loss techniques is included since they can provide additional valuable information to that already obtained with spectroscopy and photography.

3.4.2 Development of Radiation Power Loss Measurement

Radiation measurement made for free burning arcs with peak currents in excess of lOKA (up to 23KA) were reported by Strachan (1973, a,b). The arc burned between copper

electrodes which were fixed at a 100mm separation and was viewed at several axial locations using a 3mm width collimating slot laterally situated along the arc diameter. Both thermopiles and flat wavelength response photo-multipliers have been used for such radiation measurements. Adequate time response was obtained with the photomultiplier system whilst the time response of the thermopile could be improved somewhat using a helium atmosphere and suitable deconvolution methods. The author measured radiation loss as a function of time and axial distance and calculated the fraction of local power loss by radiation to local electrical power input using the probe measurements of Barrault et al (1972). Strachan (1973, a,b) showed how the presence of electrode vapour can greatly enhance the radiation power loss in the free burning arc. Similar measurements by Strachan (1974, 1975(a)) showed again that radiation loss provided a major contribution to the total energy loss from the arc column. The increased radiation loss corresponded to the time required for electrode melting (Strachan, 1974, 1975(a)) which is of the order of 2ms and is in agreement with theoretical predictions.

Strachan (1975(b)) and Strachan et al (1977) extended the work on the free burning and efflux flow arcs to the more realistic circuit breaking conditions of the orifice flow geometry. Strachan (1975(b)) and Strachan et al (1977) investigated the effects of varying upstream pressure (4.46 to 14.1 bar), upstream electrode material (copper, carbon, elkonite, tungsten and mild steel) and peak current

(3, 8 and 13KA) upon the radiation power loss. The authors viewed the arc at locations 9mm downstream and 6mm upstream using the same optical system and detector as described by Strachan (1973).

From their measurements Strachan (1975(b)) and Strachan et al (1977(a)) concluded that the upstream electrode material influences the magnitude of the radiation power loss throughout the arcing cycle and along the arc column length. The radiation loss with various electrode materials increased in the order carbon, copper, mild steel, elkonite. The variation in radiation loss with electrode material is reflected by a variation in the measured arc voltage at a given current consistent with energy conservation considerations. The radiation loss when normalized with respect to the electric field and axial pressure distribution was found to correlate with instantaneous current for copper and elkonite upstream electrode materials, but not carbon (which was associated with fusewire material persistence).

From their observations Strachan et al (1977) arrived at the following empirical law:

$$Q = \alpha_r I E \sqrt{p} \qquad 3.1$$

where,

- Q is the total radiation power loss
- I is the instantaneous current
- E is the local electric field strength
- p is the local gas pressure
- α_r is the constant of proportionality whose value is dependent upon the host arcing medium and the upstream electrode material.

Strachan (1975(b)) and Strachan et al (1976) have shown the significance of the radiation loss in terms of the energy balance (up to 30% of the power dissipated is lost radiatively). This may be correlated with instantaneous current if the electric field and pressure distribution are known during the quasi-steady arcing phase according to equation 3.1. However the sensitivity of their detector did not enable the authors to make a similar investigation during the current zero period, thus the significance of radiation loss could not be quantified during this period.

Similar work to that performed by Strachan (1975(b)) and Strachan et al (1977) was reported by Leclerc and Jones (1982) which included radiation power loss measurements for arcs in the peak current range 20 to 100KA burning in a 50mm diameter radiussed orifice. In addition, elkonite and carbon were used as electrode materials, copper and PTFE as nozzle materials and air and SF_6 as arcing gases. The upstream pressure was set at about 7 bar. The arc was viewed at two axial locations, one 1mm upstream of the orifice inlet, the other 1mm downstream of the orifice exit plane, using an RCA 4328 photomultiplier. The validity of the photomultiplier measurements was confirmed by comparison with results obtained during the quasi-steady period using a Hilger-Schwartz thermopile as described in Strachan (1975(a)).

Leclerc and Jones (1982) concluded that, despite the presence of complicating features such as pressure transients

and vapour core formation, similar trends to those observed at lower current levels by Strachan (1975(b)) and Strachan et al (1977) were evident in the high current range. Leclerc and Jones (1982) identified the dominant influence on radiation loss as the arc current followed by the local static pressure. These underlying trends were severely affected by perturbations arising from pressure transients and electrode vapour core formation and the presence of ablated material from the nozzle wall. The latter effected the downstream radiation results in particular. The authors further estimated the radiation power loss from an air arc to be of the order of 10MW from the entire arc length at a current of 90KA.

Jones and Leclerc (1982) identified important effects which occurred during the current peak phase of arcing which could effect interruptor performance during the current zero period. However the authors did not extend their investigations to include the current zero period, therefore again a quantitative statement of the significance of radiation power loss during this period was not possible.

The first measurements of radiation power loss in conditions which were relevant to the current zero period of a real circuit breaker arc were reported by Shammas and Jones (1982). Here reduced power arcing conditions were investigated and the arc current was ramped from a holding level to zero for a current decay rate in the range 12 to 46A/μs. Elkonite and carbon were used as upstream electrode

materials, SF_6 as the host gas with an upstream tank pressure of 8.5 bar. A converging-diverging nozzle with five 2mm width collimating slots was used to view the arc diameter, but in this case only the slot just downstream of the throat was used. A detailed description of this experimental test facility is included in chapter 4 of this thesis. The detector was an RCA 4832 photomultiplier situated sufficiently far (2m) from the arc to validate the inverse square law which was necessary to determine the total radiated power.

Measurements taken during the quasi-steady phase showed the empirical relationship (equation 3.1) to be true down to a current of 300A and was independent of the current decay rate. For instantaneous power levels less than 350KW the radiation loss under transient conditions was greater than that in the steady-state for a given instantaneous power level from which the authors concluded that the percentage of the electrical input power lost by radiation was greater under transient conditions than under steady arcing conditions. The authors also calculated the percentage of the electrical input power lost by radiation during the current zero period and found it to be constant at approximately 20% up to 3.5μs before current zero, after which a rapid increase was observed. Shammas and Jones (1982) associated this phenomenon with a sharp increase in the relative magnitude of the rate of dissipation of the stored energy compared to the electrical power input. This latter

postulation will be further discussed in chapter 8 of this thesis. Measurement of the instantaneous power loss by radiation at the current zero instant for different current decay rates showed a relatively low value (7W/mm arc length) below a $^{di}/_{dt}$ of 24A/μs. However for $^{di}/_{dt}$ values above 24A/μs a sharp increase in the radiated power loss occurred such that the radiative loss for a $^{di}/_{dt}$ of 44A/μs was 80W/mm. The authors concluded that radiation losses in the higher $^{di}/_{dt}$ region assume greater importance and the detection of radiation after the current zero instant (up to 4μs) was regarded as being indicative of the duration of the thermal recovery period. At later times when the arc was made to reignite there appeared a sharp increase in radiation which is indicative of dielectric rather than thermal reignition. This phenomenon was also noticed in the present investigation and is discussed in chapter 8 of this thesis.

From their investigations Shammas and Jones (1982) derived the following empirical relationships between radiation loss and the electrical parameters

(i) During the quasi-steady state the empirical law governing radiation loss corresponded to equation 3.1 with constant pressure and radiation power loss proportional to instantaneous current as

$$L = 0.0143\ (i-300) \text{ for } i>300A \qquad (3.2)$$

where,

L is the equivalent radiative loss in volts
(L = $Q_R/99$, where 99 is the calibration factor)

Q_R is the radiative power loss

i is the instantaneous current

(ii) During the transient current decay period (i<150A)

the following law applied

$$L = A_i^{1.05} + B(i_o)^{1.1} \left(\frac{di}{dt}\right)^{2.37} \quad (3.3)$$

where,

i_o is the holding current level

$\frac{di}{dt}$ is the current decay rate during the final 2μs before current zero

A,B are constants of proportionality

(iii) The decay of radiation during the post current zero

period is described as

$$\tau = 0.174 \left(\frac{di}{dt} - 17\right) \quad (3.4)$$

for $\frac{di}{dt} > 24A/\mu s$ and $i_o = 1.55KA$

where τ is the time for the radiation to decay to a negligibly small value (μs)

Shammas and Jones (1982) have derived, for the first time, empirical laws which describe the total radiation power loss decay for the transient conditions encountered during the current zero period in terms of electrical parameters. This has been performed under reduced power arcing conditions (i.e. steady low level current ramped to zero at different decay rates) which excluded the more complicated effects

encountered when a peak current is passed through the arc (e.g. enhanced electrode vapour entrainment into the column). Shammas (private communication) suggests that under such conditions deviations from this set of empirical laws are likely to exist.

3.4.3 Concluding Statement

Radiation power loss measurements have proved to be reasonably accurate and relatively convenient to make. The measurements at peak current or during the quasi-steady arcing phase have shown consistently that nett radiation power loss does play an important part in the energy balance during this period. However lack of reported experimental data during the current zero period makes such an estimation impossible although some unpublished data by Shammas and Jones does exist and will be used in this thesis (chapter 8) in the quantitative solution of the current zero energy balance.

All the radiative power loss investigations reported in this section have invoked some knowledge obtained from photographic and spectroscopic investigations under equivalent operating conditions. Therefore the use of the three optical techniques (high speed photography, total radiation measurements and spectroscopic measurements) taken in conjunction with each should provide essential information for a better understanding of the current zero period behaviour of arcs in SF_6 circuit breakers.

3.5 Other Techniques

3.5.1 Introduction

Other techniques exist which can provide important information, for example concerning the flow of cooler gas surrounding the arc plasma. It is beyond the scope of this thesis to include an in-depth appraisal of such techniques but it is necessary to include a brief review of work of some authors who have used such techniques to obtain important information which is relevant to the current zero energy balance.

3.5.2 Techniques Description and Review

Non-standard photographic techniques such as Schlieren, interferometry and shadowgraphy, the theoretical background of which is described in Leonard (1965), can provide useful information about the cooler gas flow and thermal regions surrounding an arc plasma.

Bagshaw and Ellis (1969) used a laser Schlieren technique to investigate the air flow during arcing in a model air blast interruptor for peak currents up to 13KA. They demonstrated qualitatively how the presence of the arc disturbs the flow pattern. This was intended as feasability study for the pulsed laser technique, but no quantitative information was derived.

Walmsley et al (1978(i)) employed a laser shadowgraphy method to measure the thermal area fluctuations during the

whole arcing cycle of 3KA and 8KA peak current arcs in an orifice geometry. Particular attention was paid to the current zero period. The electrical and gas flow conditions used in this work have already been described in chapter 3.2.2. Walmsley et al (1978(i)) also used a laser deflection mapping technique to measure gas density variations within the thermal region for a temperature range between ambient and 2000 to 3000K.

From these measurements Walmsley et al (1978(i)) drew the following conclusions:

(a) during the peak current phase

(i) the thermal area - current relationship was linear and took the form

$$\Theta = \Theta_{so} + KI \qquad (3.5)$$

where

θ = instantaneous thermal area
θ_{so} = thermal area at current zero
K = constant of proportionality (dependent on operating conditions)
I = instantaneous current

(ii) hysteresis departures from equation (3.5) were noticable at higher currents and were attributed to electrode vapour effects

(iii) metallic electrodes caused disturbances in the external flow which were attributed to droplet formation

(b) during the current zero period

(i) regular oscillations in θ were observed when the arc reignited and these were attributed to 'plasma blobbing' phenomena

(ii) disturbances to θ persisted for about 150μs upstream and 70μs to a few milliseconds after the gap cleared

(iii) greater disturbances to the thermal region occurred in the case of metallic electrodes than with carbon as the contact material

(iv) the tip of the copper upstream electrodes were molten even several μs after current zero with a similar effect evident with elkonite as the material but to a lesser extent.

From their laser deflection mapping data Walmsley et al (1978(i)) derived radial temperature and mass density results below temperatures of 2 or 3 x 10^3K which aided subsequent work in integral analysis formulations (Walmsley et al, 1978(ii)).

Through their measurements of thermal region characteristics, particularly near current zero, Walmsley et al (1978(i)) identified important factors which could effect the performance of an interruptor (e.g. electrode melting after current zero and 'plasma blobbing').

An alternative method for measuring arc column diameters and average temperatures was proposed by Dhar et al (1978). The authors used radio frequency signals to detect the change in capacitance between a copper ring placed at the throat section of an insulating nozzle and the arc column. The method has the advantage of not requiring optical access through the nozzle. The results from this investigation showed good initial agreement with the work of previous authors who used optical techniques. The work was therefore extended by Dhar et al (1979) to enable the arc diameter and temperature to be measured in a similar fashion at multiple axial locations using a multi-ring electrode arrangement. The nozzle used was profiled, of thoat diameter 19mm, semi-divergent angle of 12^o and made of PTFE. Investigations with

air as the arcing medium during the major part of the 75Hz, 3KA peak current loop and the current zero period were made with carbon and elkonite as upstream electrode materials, nozzle inlet to upstream electrode distances of 2mm and 12mm and an upstream tank pressure of 7.8 bar.

Dhar et al (1979) claimed good agreement with authors using different diagnostic techniques to measure the same parameters i.e. arc diameter and average temperature. Although this claim is justified through good correlation of the diameter results e.g. with Walmsley (1978(i)) it is difficult to envisage a similar agreement between the axial temperatures calculated by these authors (Dhar et al, 1979) and the spectroscopically obtained average temperatures of Smith et al (1978). The radially averaged results of Smith et al (1978) are consistently higher than the axial temperature values of Dhar et al (1979).

3.6 Concluding Statement

In this chapter, diagnostic techniques are mentioned which are both directly and indirectly related to the work reported in this thesis.

It has been shown that with careful calibration procedures photographic techniques can be used to successfully describe the overall arc column diameter and radial intensity profile. If this work is further augmented by application of spectroscopic techniques valuable local temperature and electron density data can be derived. Measurement of the

total radiation power loss from the arc coupled with the information derived from the above two techniques would enable the energy transport terms of the energy balance to be evaluated.

It has been shown that much work using the techniques involved here has been performed during high current or under quasi-steady arcing conditions. However little experimental data obtained from such techniques exists for the current zero period, particularly under full power arcing conditions such as those experienced in a real circuit breaking environment.

This thesis is concerned with presenting time and space resolved high speed photographs and snapshot spectra during the current zero period for both reduced and full power arcing conditions.

CHAPTER 4

EXPERIMENTAL AND TEST FACILITY

4.1 Construction of Test Rig

The test rig used in this investigation was essentially the same as that used by Strachan et al (1977(b)). It consisted of a high pressure upstream reservoir tank which was connected via a blast valve, a honeycombe flow-straightener, the test head and a cylindrical outlet pipe to a low pressure reservoir. The upstream pressure was initially set to 100 psig and the downstream pressure to just below atmospheric for the whole series of investigations.

The test head which was insulated electrically from the remainder to the test rig consisted of a mild steel block into which nozzles of various geometries could be inserted and whose vertical sides could be sealed with glass ports so that optical access was readily available. The schematic overall test rig layout is shown on fig. 4.1.

4.2 Gas Handling System

SF_6 was used as the arcing medium for all the investigations of the present work. In the interests of economy, it was necessary to collect and recycle the spent gas. This was achieved by using a gas recirculation and purification plant which essentially consisted of a compressor, vacuum pump, a refrigeration unit and a number

of strategically placed traps for drying and purifying the gas. The overall layout of the gas handling system is indicated in fig. 4.2. Further details may be found in Strachan et al (1977(b)).

4.3 Pneumatic Initiation Facility

Arc initiation was achieved by striking a low current d.c. arc between the two arcing electrodes. This was achieved by keeping the main arcing electrodes fixed and pneumatically driving an auxilliary electrode (a 6mm diameter rod) through the hollow downstream electrode from its initial rest position in contact with the upstream electrode. The time taken for the rod to fully retract into the electrode was made small compared to the duration of the d.c. initiation arc such that electrical and flow conditions just prior to the main arcing period were quasi-steady. The efficient operation of the pneumatic initiation arrangement was ensured by the use of a vacuum latch and initiator gas supply vessel, the details of which are also reported in Strachan et al (1977(b)).

4.4 Test Head Geometry

The test head geometry including the nozzle used in this investigation is shown in fig. 4.3. The general nozzle geometry consisted of an upstream convergent section connected to a 12^{o} diverging section via a 10mm long parallel sided throat section of 35mm diameter. A specially designed

nozzle with the same flow profile was used for viewing the arc. This carried a number of lateral, sealed slots. One slot was located upstream of the nozzle throat, one at the throat, one near to but slightly downstream of the throat, and a further two were located in the downstream diverging nozzle section. The slots were sealed by a slotted rubber gasket compressed against a 15mm thick glass viewing window so preventing the leakage of gas from the nozzle through the slots. This was an important measure both diagnostically and with regard to electrical performance since leakage of gas could cause image distortion and perturbations or shock waves in the gas flow. Both PTFE and copper were used as nozzle materials. The main arcing electrodes consisted of an upstream contact which was a 32mm diameter cylinder with a hemispherically shaped tip which was situated 17mm upstream of the upstream edge of the nozzle throat, and an identically shaped downstream electrode which carried a hollow bore which housed an auxilliary initiation electrode. The downstream electrode tip was fixed at a distance of 78mm downstream of the downstream edge resulting in an overall gap length of 105mm. The downstream electrode material was 1OW3 elkonite throughout the investigation while the upstream electrode material used was mainly 1OW3, although some tests with graphite were also performed.

4.5 Electrical Power Source

Tests were performed with both reduced and full power

arcing conditions which required the use of two different electric circuits.

4.5.1 Reduced Power Circuit

The circuit used for reduced power testing is shown on fig. 4.4(a). This circuit produced an initial d.c. current level (or holding current) of 1.6KA or 0.7KA and then imposed a negative going ramp to zero at a variable decay rate. The rrrV applied to the arc gap after current zero was determined by the natural restrike of the main capacitor bank. The main current circuit (fig. 4.4(a)) consisted of two separate current loops. The holding current was supplied by a 35.5mF, 6.3KV capacitor bank (C_1) connected in series with a 1.67Ω to 3.5Ω variable limiting resistor (R), inductor (L_1) and the circuit breaker. The supply was switched using an ignitron valve (I_2). The negative going linear ramp was synthesized by discharging an auxilliary capacitor bank (70μF, 20KV) (C_2) through a variable series inductor (L_2, 90 to 330μH) to supply a current in opposition to the holding current through the breaker after switching by ignitron I_4. This circuit allowed independent control of holding current and rrrV. The charging voltage (V_1) and the resistor (R) determine the magnitude of the holding current, while the charging voltage on the auxilliary bank (V_2 on C_2) and the value of the inductance L2 determine the current ramp decay rate. The rrrV was dependent on the value of stray capacitance and resistance in parallel with the breaker. An additional branch in parallel with the

main capacitor bank (C_1) was provided so that excess energy remaining on the capacitor bank following the full arcing sequence was rapidly drained by diverting the current via a low value resistance to earth by means of an ignitron valve (I_3).

The current decay rate range just prior to current zero was 14 to 60 A/μs. The rrrV was in the range 0.1 to 2 KV/μs and could be sustained for durations in the range 2 to 10μs which was dependent upon the holding current and current decay rate values before current zero. The operating conditions are summarised in table 4.I(a) whilst further details of the ramp circuit are available in Taylor et al (1982).

The steady, low level d.c. current required for arc initiation (i.e. whilst the contacts were being separated) was provided by allowing current to flow through a resistor R_1(6Ω), R, L_1, L_2 and the arc column. This produced a steady current of 200A to 300A for approximately 100ms.

4.5.2 Full Power Circuit

The circuit used to produce full power arcing conditions (fig. 4.4(b)) consisted of an L-C (L_1 = 90μH, C_1 = 35.5mF; 6.3KV) ringing arrangement with an auxilliary loop containing a variable damping resistor to supply a quasi steady arc initiation current. The initiation current was switched through the arc by an ignitron valve (I_i) providing a current range of 300A to 800A dependent upon

the value of variable resistor R_1. The main arcing current was switched by triggering the forward biassed ignitron I_2 which effectively shorted out R_1 and gave rise to an independent sinusoidal current waveform with a high peak current value. Smooth commutation of the current through zero was ensured by using a 3rd ignitron (I_3) which was in the opposite sense to I_2. This ignitron was triggered just before current zero and the commutation was ensured by the auxilliary 'holding' anode of I_2. The peak current could be varied by varying the charging voltage on C_1, which resulted in varying current decay rates before zero. The voltage restrike (rrrV) immediately after current zero was provided by the natural circuit response. The rrrV was therefore governed by the charging voltage on C_1 and was again limited by stray-capacitance and leakage across the test head. Again a branch was provided in the circuit for rapid dumping of excess charge on the capacitor bank C_1.

With this arrangement, the current peak value was varied in the range 34 to 65KA resulting in a current zero decay rate ($^{di}/_{dt}$) range of 13 to 30A/μs. A full summary of these operating conditions is given in table 4.I(b). Further details of the full power circuit arc given in Strachen et al (1977(b)).

4.6 Diagnostic Instrumentation

4.6.1 Arc Current and Voltage Measurements

(a) Reduced Power Conditions

The current shunt used for the measurement of arc current was a co-axial type with resistance of 12.35mΩ and an 80ns risetime. This enabled the accurate measurement of arc current during the current zero period. Voltage measurements were made by a differential probe technique, the two probes being situated to measure the voltage directly across the test head (fig. 4.5).

The probes used were tektroniks P6015 high voltage probes which had a bandwidth of 50MHz. The voltage and current were recorded simultaneously on a tektroniks 556 oscilloscope and registered photographically. All the above instrumentation was earthed to a single point located on the 'earth side' of the current shunt (the experimental or signal earth) as shown on fig. 4.5. This was to avoid the occurrence of current loops through the earth connections which could have profound effects on both instrumentation and data for the magnitude of arcing currents in question.

(b) Full Power Conditions

Arc current and voltage measurements (taken in conjunction with photographic measurements) under full power conditions were made in an identical manner to the reduced power measurements. However a different current shunt (1mΩ) was used to avoid excessive power dissipation in the 12.35mΩ shunt and to prevent saturation of the oscilloscope pre-amplifiers by the excessive voltages developed across the

shunt. This was preferred to the fuse protection technique (Taylor et al, 1982) in order to reduce electromagnetic noise problems. Voltage measurement was by an identical technique to that used with the reduced power arcing. Overall calibration of this particular measurement system was performed by Taylor et al (1982).

Arc current and voltage measurements in conjunction with spectroscopic measurements were made using the same measurement system as the arc photography system except that two tektroniks 468 digital storage oscilloscopes were used rather than the tektroniks 556 oscilloscope. The arc voltage and current measurement systems are shown schematically as part of the overall measurement system in fig. 4.5(b).

4.6.2 Optical and Photographic Measurement Systems

The optical system for photographing the arc is shown schematically on fig. 4.6. It consisted of a novel set of collimating mirrors (details on fig. 4.6(b)) which provided a collimated beam for focussing directly onto the image converter camera photocathode by its first lens (6", 152mm, f/2.8 type T32 Taylor Hobson). The camera sensitivity was enhanced by the use of an EMI type 9914, 3 stage image intensifier (Gain $\leq 10^6$) which was optically coupled to the camera thrcugh a relay lens (Oscillac 1:0.42, f/1) which was maintained at its maximum aperture (f/1) throughout the photographic investigations. The image intensifier was

powered off an independent power supply (electrostatic voltage and focus coils current) and the final image on its back screen was photographed with a poleroid camera back attachment which was loaded with a polaroid type 46L film.

The novel collimating mirrors (fig. 4.6(b)) were necessary because it was found that otherwise the collimated light from the nozzle slots was not all collected by the camera lens system. The collimating mirrors gave a 9:2 overall axial image size reduction at the expense of inter-slot separation which did not affect the axial resolution since the image height of each slot remained unchanged after passage through the mirror system. Diametric image sizes were also unaffected for the narrow arc diameters occurring during the current zero period. Aluminised glass plane mirrors were used at each reflecting surface. The mirrors on the exit slot side received collimated light through the entrance slots and were orientated so as to reflect the light onto the five 'output' mirrors bunched closely together on the entrance side and which gave a collimated beam of light through the exit slot. The mirrors were encased in a brass housing box and the two slotted sides were coated with black paint to reduce spurious reflections.

The image converter, a John Hadland Imacon 700, had both streak and framing facilities. The framing speed was set to either 10^6 f.p.s. at 20ns exposure or 2×10^5 f.p.s. at 1μs exposure by the use of different plug in units. Each

photographic sequence consisted of 18 to 20 such frames maximum. The image intensifier was required because the light intensity levels encountered as the arc current decayed to zero required a high sensitivity detection system for such a short exposure. The image intensifier power supply had an electrostatic voltage range of 10KV to 40KV with a focus coils current range of 0 to 15A providing gain in the range 10 to 10^6.

Full Power Arcing Conditions

Owing to the extremely high light intensities (1MW power loss by radiation) which occurred during the current peak of the main arcing pulse, a system of protective shutters was required to safeguard the extremely sensitive photodetector surfaces from saturation or damage. The introduction of these shutters necessitated changes in the optical system configuration (fig. 4.7(a)). The collimating mirrors were retained in the optical system for the same reason as for the reduced power case. However light was brought to a focus by means of a pair of bi-convex f/2, f = 20mm lenses - on the first reflecting surface of the 90^{o} image rotator (fig. 4.7(a)). The image rotator consisted of a mirror/prism arrangement which performed a 90^{o} rotation of an image in the plane normal to the optical axis through it. Further focussing of the rotated image by means of another pair of f/2, f = 20mm lenses allowed the lateral slots of the viewing nozzle to be focussed on a set of vertically orientated slots which formed the back of

the capping shutter (fig. 4.7(b)). The capping shutter allowed light to pass for approximately 1ms. A shorter exposure (200μs) was obtained by using a rotating disc shutter (fig. 4.7(b)). The disc contained 13mm x 10mm slot which, when rotated at a speed of 9,230 r.p.m., yielded a 200μs exposure time. After passing through the shutters the light was collected and focussed by the image converter camera as described above. The image converter and intensifier were used in an identical manner to the reduced power case.

4.6.3 Optical and Spectroscopic Measurement System

The photographic investigations suggested that arc spectra could be profitably recorded through slot 2 (chapter 6 of this thesis). For this reason only one viewing slot was used and so avoided the need for a prohibitively complicated optical system.

The optical system (shown photographically on fig. 4.8 (a) (i) and schematically on fig. 4.8 (a) (ii)) was used to view full power arcs only. It consisted of a focussing arrangement, a shutter (fig. 4.8(b)), a spectral resolving instrument (monochromator) and a detector/analyser system.

Collimated light emerging from slot 2 of the viewing nozzle was focussed by an f/2, f = 20mm biconvex lens onto a first reflecting surface of the same image rotator as described in section 4.5.2. After the subsequent 90^{o} image

rotation the light was focussed onto the entrance slit of the monochromator such that the whole of the internal collimating mirror of this instrument was illuminated.

A single action capping shutter (fig. 4.8(b)) was incorporated in the light path and situated close to the monochromator entrance slit. This prevented light from being incident on the entrance slit for up to 100μs before current zero. The monochromator was a Hilger Watts mononspek 1000 grating (1200 line/mm) spectrometer type D400-352 fitted with an F1497 slit on the entrance plane. The slit width was set to 28μm resulting in a dispersion of about 0.7nm/mm at about 500nm. The detector camera was a vidicon SIT 500 which enabled spatial resolution in two dimensions by virtue of its multi-element diode array photo detector surface or target (fig. 4.8(c)). One dimension in this case was occupied by wavelength due to dispersion by the monochromator. The other dimension represented image dimensions across the entrance slit which in this case corresponded to the diameter of the arc. The camera operation was such that the diode array could be split into five lateral segments. These segments therefore corresponded to five segments along the arc diameter (fig. 4.8(d)). After intensification (fig. 4.8(c)) and resolution, the information stored on the diode surface (target) was synchronously scanned off the target by an electron beam which took 32ms to scan the whole target and 1.2ms to 'flyback' and restart. The information collected off the target in this manner was

instantaneously converted into an analogue signal and transferred to the parent OSA 500 system to be digitally processed. For the entire spectroscopic investigation the SIT 500 camera was operated in 'gated' mode. This meant that an internal electronic shutter allowed light to be incident on the vidicon target for a preset exposure time (1.6μs). The operational limitations of the camera were such that this exposure time had to coincide with the scan flyback period. The gate pulse (-1KV) for the shutter was provided by an external unit. After the information was recorded on the camera target in this manner the scanning electron beam required three full scans to fully transfer the information into the OSA 500 memory. This meant that some background (dark current) noise would be accumulated with each scan which could subsequently be removed using one of the OSA 500 control (or call programs) (appendix 7). In addition, the OSA 500 controlled the scanning sequence and other operational parameters of the camera. A summary of these is given in appendix 7.

Using this system,1.6μs snapshots of arc spectra at selected wavelengths could be taken with radial resolution at different instants during the decay of arc current to zero.

4.7 Timing Sequences

During the operation of the model circuit breaker many events were required to occur in a precise sequence.

It is clear therefore that the timing of such events was important to ensure reliable and reproducible arcing conditions. It is convenient to split the timing sequences into two categories.

(i) The overall timing of the breaker mechanism and the arcing pulse.

(ii) The precision (microsecond or submicrosecond) timing during the current zero period of all the associated diagnostic instrumentation.

4.7.1 Overall Timing of the Breaker Mechanism and Arcing Pulse

(a) Reduced Power Conditions

The flow of gas from the upstream pressure vessel through the test head was controlled by operating three magnetic valves which prohibited or allowed gas to flow through certain vessels at specified times.

Essentially the gas blast was generated by triggering (opening) an electro-magnetic blast valve which sealed the upstream high pressure vessel prior to opening. This was further aided by the operation of the vacuum latch and actuator vessels which were also connected to the main test rig through electro-magnetically actuated valves. The pulses required to operate these valves were provided in the correct sequence by a rotary cam-timer device which gave sufficiently accurate and reproducible timing for these purposes. The steady flow of gas through the test head could

be sustained for hundreds of milliseconds in this manner which provided sufficient time for the arcing events to occur. Further details of the timing of the gas flow are given in Strachan et al (1977(b)).

The timing of the arcing events required greater accuracy than the gas flow sequence but a knowledge of the latter remained essential to ensure reproducible arcing conditions.

It was essential to ensure the inception of flow of arc initiation current before the initiation rod was pneumatically lifted off the upstream electrode and electrical contact lost. The initiation ignitron (fig. 4.4) was fired by an auxilliary pulse unit which was triggered initially from the 200V output of a Culham delay unit at the instant t_i (fig. 4.9). Sufficient time elapsed for the initiation rod to wholly retract into the hollow downstream electrode before the main arc current pulse was triggered to ensure reproducible arc length. Thus at the instant t_1 (fig. 4.9(a)) the first main ignitron was triggered via an auxilliary pulse unit which was in turn triggered by a 200V Culham delay unit pulse, and the main arcing sequence started. A holding current of up to 1.6KA was allowed to flow for about 5ms (t_1 to t_2, fig. 4.9(a)) before the second main ignitron was triggered (in the same manner to the first ignitron) and the current was subsequently ramped to zero at a decay rate determined by the parameters discussed in section 4.5.1 above. The dump ignitrons were triggered at some preset

time after current zero (usually 2 or 3 milliseconds). Using this configuration all the arcing events could be timed to an accuracy of about 1% or better.

(b) Full Power Conditions

The sequence of gas flow conditions remained unchanged from the cold flow conditions of the reduced power circuit so that the timing sequences were identical for the magnetic valve triggering.

For reasons explained later in this section (4.7.2) the initiation arc was sustained for variable durations. The first main ignitron (fig. 4.10(b)) was fired by an auxilliary unit and the 200 volt output from a Culham delay unit. The main current pulse was generated from the LC ringing circuit as described in section 4.5.2 above (and fig. 4.4(b)) and had a half period of 6.45ms (fig. 4.10(a)). About 300μs before current zero the 2nd main ignitron was fired in a similar manner which would facilitate a smooth commutation of current through zero in the event of arc reignition. At some time after current zero the remnant charge on the capacitor bank was dumped electronically by firing the dump ignitrons. Again the timing of the ignitron firing etc. was performed to an accuracy of 1% or better by use of the Culham delay units.

4.7.2 Timing of the Diagnostic Instrumentation Particularly Near Current Zero

Microsecond or sub-microsecond time resolution was

required for an accurate investigation of the current zero period plasma processes. For this reason, the timing of the diagnostic instrumentation recording sequences etc. needed to be of microsecond accuracy or better.

(a) Diagnostics with Reduced Power Arcing

In the case of reduced power arcing, sufficient accuracy of timing was obtained by triggering the image converter camera and current zero arc voltage and current recording oscilloscopes from a delay unit (fig. 4.9(b)) which was set on a scale of 0 to 100μs, thus providing the microsecond accuracy. This delay unit was triggered at the same instant as the start of the current ramp (t_2 on fig. 4.9(a)) and provided a means by which the camera and oscilloscopes could be tuned to the current zero period.

(b) Diagnostics with Full Power Arcing

A more sophisticated method of timing was required in the full power case. The reason for this was that once the first ignitron valve was triggered the resulting half cycle of arcing had a duration of 6.45ms $\pm$ 0.05ms regardless of the instant at which the second ignitron was triggered (fig. 4.10). This $\pm$ 50μs fluctuation in the half period clearly did not meet the required current zero timing specifications. Thus it was more convenient to trigger the diagnostic instrumentation off the falling current waveform as it approached zero (fig. 4.11).

An additional complication to the timing problem arose due to the nature of the shutter system. The rotating disc shutter could not be synchronised to the experiment without

the use of unnecessarily complicated control electronics which might have failed in the harsh environment experienced in close proximity of the full power arcing test head. It was therefore more convenient to synchronise the experiment and in particular the current zero instant to the fully open period of the rotating shutter.

The precise period and the position of the slot in the disc with respect to the optical axis could be monitored using a laser and a photodetector unit (fig. 4.11(a)), circuit diagram in appendix 6). The laser light was passed through a hole in the disc situated on an axis on the plane of the disc which ran through the disc centre and the centre of the slot, and at a marginally greater diameter than the outermost edge of the slot (fig. 4.7(b)). Thus the detection of a light pulse from the laser coincided with the instant of the shutter slot being fully open with respect to the optical axis. The disc was rotated at a speed such that the time for a full revolution of the disc was identical to the half period of the arcing pulse i.e. 6.45ms. This time was measured using the photodetector in conjunction with an electronic pulse shaping unit (appendix 6) and a Gould TC 320 timer/counter (fig. 4.11(a)) which was capable of measuring to an accuracy of $\pm$ 1μs in 1000μs. The maximum deviation between a number of successive periods of rotation of the disc was 5μs which was insignificant since the radial extent of the slot on the disc allowed for a timing error of $\pm$ 10μs.

The object of using this timing system was to achieve a timewise coincidence of the current zero instant and camera exposure. This was achieved by matching the beginning of the main arcing pulse to the fully open position of the rotating shutter (fig. 4.11(b)). At this instant the capping shutter was shut and no light was incident on the camera. Since the period of rotation of the rotating disc was matched to the half period of the arc current pulse the current zero instant coincided with the shutter being fully open following a further full rotation at t_o (fig. 4.11(b)). At this instant the capping shutter was in its fully open position and the camera was exposed to light from the arc column.

The image converter recording sequence was triggered by the falling current waveform (fig. 4.11(a)). This was achieved by deriving a fast rising-edge pulse from the time base sweep (A gate) pulse of the current measuring oscilloscope (fig. 4.11(a)). The oscilloscope could be set to trigger off any required instantaneous current during the linear decay to zero, consequently the camera was able to record for a range of durations within the current zero period.

Because the current recording oscilloscope was triggered off the falling arc current,simultaneous arc current, voltage and photographic records were obtained.

The timing requirements for the spectroscopic diagnostic system were similar to those of the photographic system for

the full power arcing case. Similar principles were employed in the electronic timing technique for the measurement system and shutter. However, owing to differences in the mode of operation of the OSA 500 system, the techniques were applied in a different manner.

The continuous scanning operation of the SIT 500 as described in section 4.6.3 above meant that the timing sequence of the rest of the experiment would have to be synchronised to the scanning period of the camera. Also it was no longer possible to use the rotating shutter since this could not be synchronised with the continuous camera scanning.

As described in section 4.6.3 above, the time taken for the camera to complete one scan of the diode matrix (scanning period) was 33ms which was followed by a 1.2ms flyback interval. It was necessary to record the required information on the camera target during the 1.2ms flyback period so that the current zero period was to coincide with this flyback period. The camera could then be gated (section 4.6.3) during this time. The same electronic coincidence unit as used in the photographic investigation was used to achieve this timewise coincidence (fig. 4.12(a), circuit diagram in appendix 6). Pulses of 1.2ms duration (corresponding to the flyback period) with a period of 33ms were provided by an electronic pulse shaping unit (circuit diagram in appendix 6). The pulses were input to the coincidence unit which was externally triggered from a Culham delay unit

(fig. 4.12(a)) so enabling the unit for a duration of 33ms (fig. 4.12(b)). A pulse appeared on the output immediately after receiving the first pulse at the camera input when the unit was enabled (fig. 4.12(b)). The output pulse was then used to trigger the ignitron valves with the correct delay settings to ensure that the current zero instant coincided with the next pulse at the camera input of the coincidence unit i.e. during the camera flyback period (fig. 4.12(b)).

The vidicon camera was gated (exposed) by a -1KV pulse applied to the cathode of the tube whose duration corresponded to the exposure time and which was supplied by an external vidicon gate pulse generator (circuit diagram in appendix 6) (fig. 4.12(a)). The gate pulse was generated at different instances during the arc current decay by using the gate output of the current measuring oscilloscope as was used in the photographic investigation. The gate out pulse was further shaped and delayed by variable amounts (0 to 10μs) by an auxilliary delay unit which ultimately triggered the vidicon gate pulse generator (fig. 4.12(a)).

The shutter, whose physical characteristics were discussed in section 4.6.3 above (fig. 4.8(b)) was triggered following the output pulse from the coincidence unit (fig. 4.12(a)). The delays were set so that the shutter would expose the camera fully at about 20 or 30μs before current zero (fig. 4.12(b)).

With this experimental configuration,consistent simultaneous records of arc voltage, current and spectra during the current zero period were obtained.

LIST OF TABLES

Parameter	Range, Material etc.	Units
Upstream Tank Pressure	110	p.s.i.
$\frac{di}{dt}$	11.5 to 49	A/μs
$\frac{dv}{dt}$ or RRRV	0.07 to 2	KV/μs
Nozzle Material	Copper	
Electrode Materials	Carbon, Elkonite (10W3)	
Holding Current	1.6 and 0.7	KA

(a)

Parameter	Range, Material etc.	Units
Upstream Tank Pressure	110	p.s.i.
$\frac{di}{dt}$	13 to 30	A/μs
$\frac{dv}{dt}$ or RRRV	0.2 to 2.5	KV/μs
Nozzle Material	Copper (Photography only) PTFE	
Electrode Material	Elkonite (10W3)	
Peak Current	34 to 65	KA

(b)

Table 4.I Summary of Arcing Conditions

(a) Reduced Power
(b) Full Power

(i) Image Converter Characteristics

Framing Unit	Characteristics	Quantity
2×10^5	Number of Frames Framing Interval Exposure No. of Frames per Record	2×10^5 f.p.sec. 5μs 1μs 18 to 20
1×10^6	Number of Frames Framing Interval Exposure No. of Frames per Record	1×10^6 f.p.sec. 1μs 200ns 18 to 20

(ii) Intensifier Characteristics

Effective Gain : 10^2 to 2×10^3

(iii) Recording Film Characteristics

Type : 46L (Polaroid)

Speed : ASA 800

(iv) Additional Information

Optical Filters Used:

521 $\pm$ 4.5nm Interference

515 $\pm$ 0.5nm Interference

Table 4.II Summary of Photographic Optical System Characteristics

(i) Spectrometer Characteristics

Type	:	Monospek 1000
Mount	:	Czerny - Turner
Grating	:	1200 lines/mm
Slit Width	:	28μm
Dispersion	:	0.7nm/mm at 500nm
Aperture	:	f/8
Focal Length	:	1m

(ii) Camera Characteristics

Sensitivity	:	12 photons/count (maximum
Exposure	:	1.6μs

Table 4.III Summary of Spectroscopic Optical System Characteristics

LIST OF FIGURES

4.10 General timing and triggering of the experimental system used for the full power investigation

(a) Arc current waveform and important timing points
(b) Schematic representation of the delay unit timing sequence

4.11 Timing system for current zero full power arc photography

(a) Schematic diagram
(b) Timing diagram

4.12 Timing system for current zero full power arc spectroscopy

(a) Schematic diagram
(b) Timing diagram

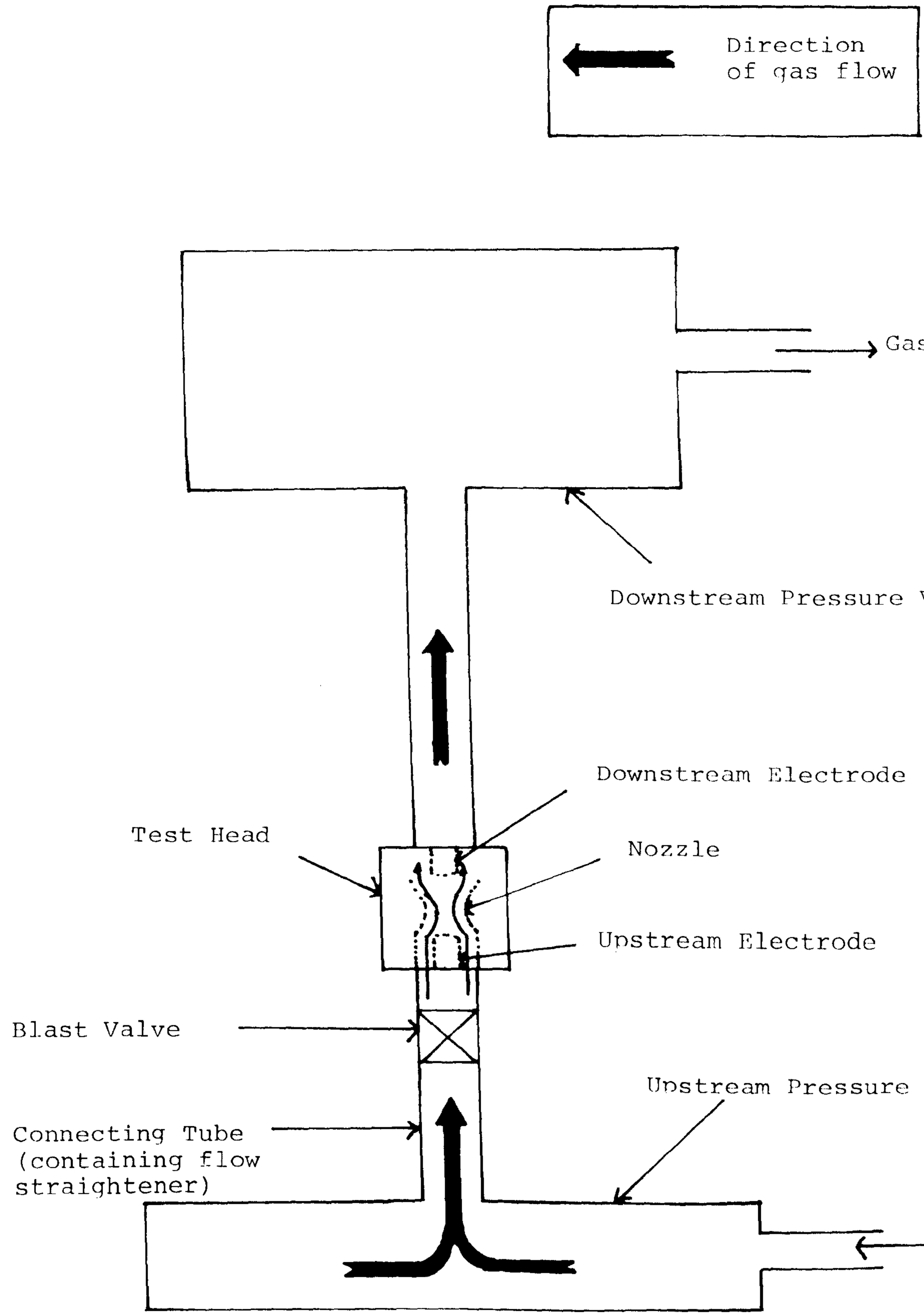

Fig. 4.1 Schematic Diagram of the SF_6 Test Rig

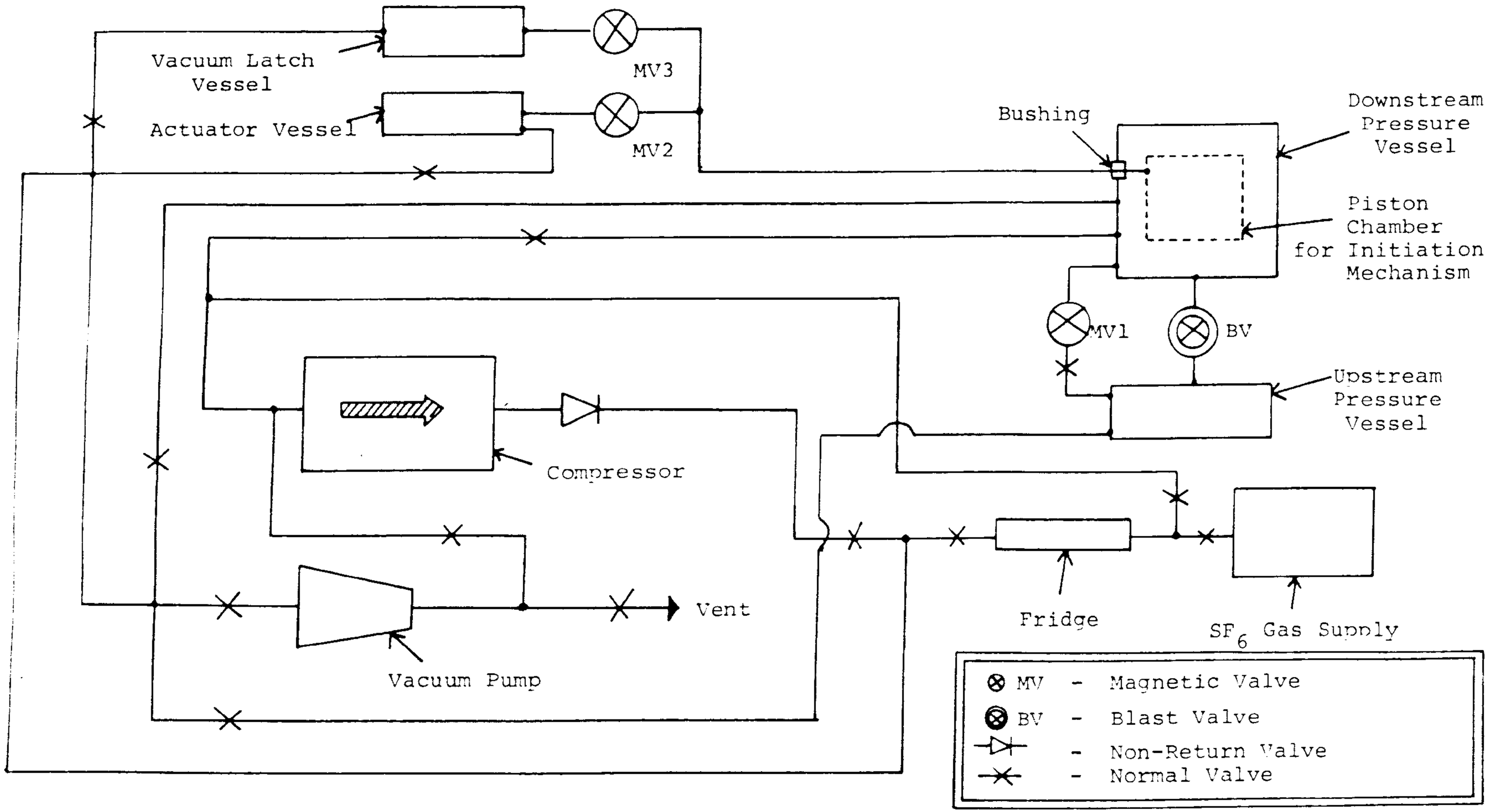

Fig. 4.2 Schematic Diagram of the SF_6 Gas Handling System

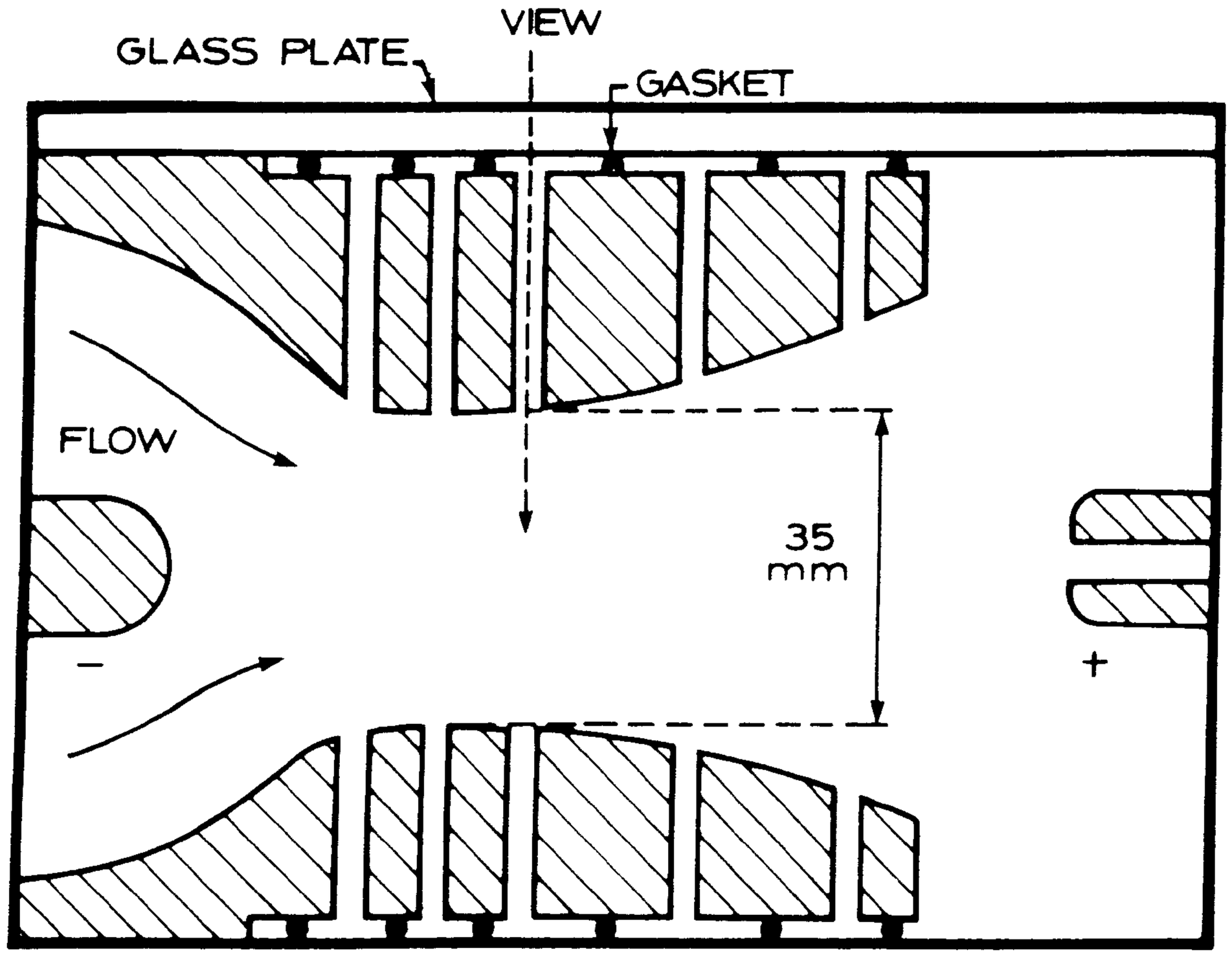

(a)

Fig. 4.3 The Test Head Geometry

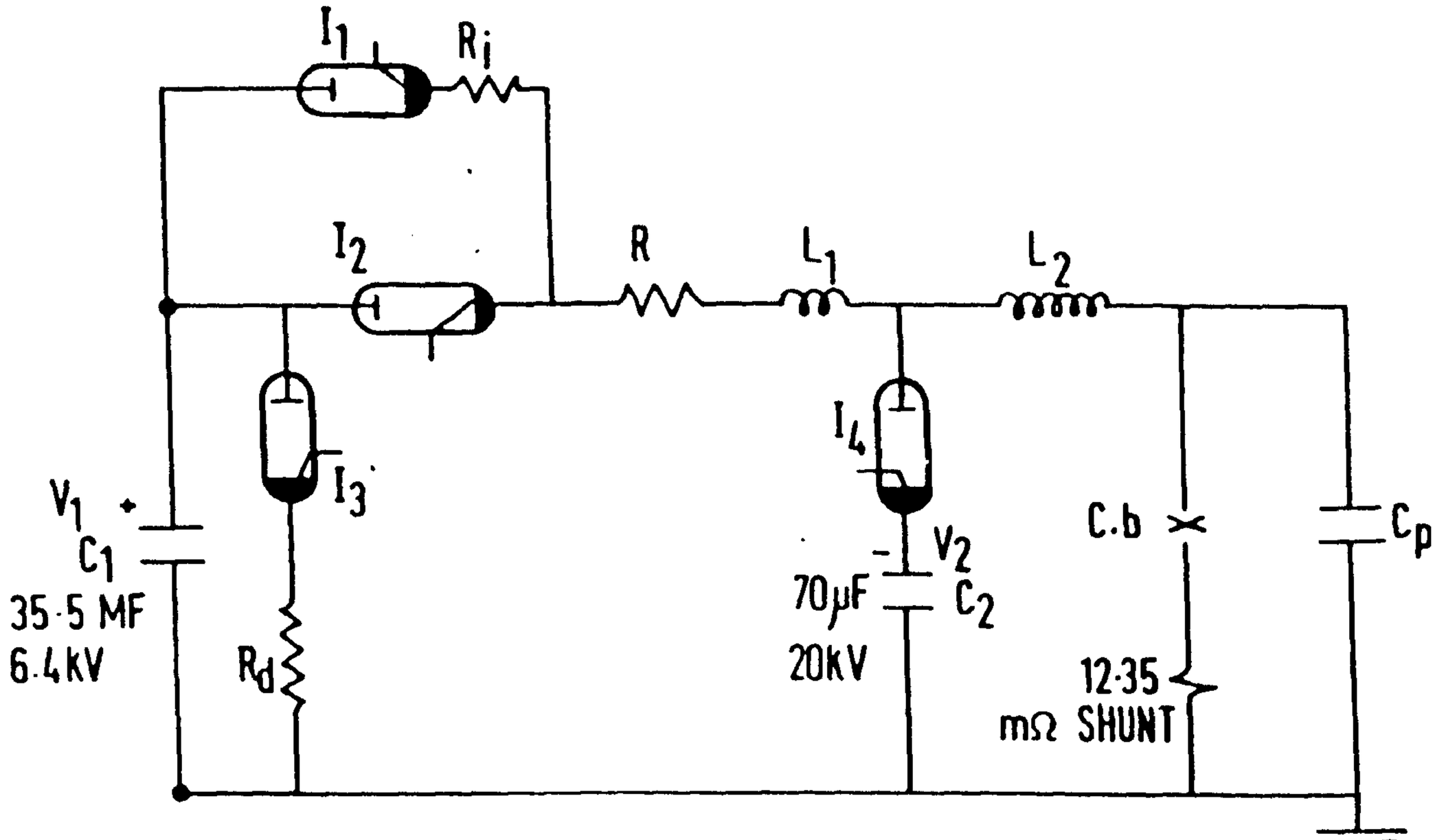

I_1 Low current initiation ignitron

I_2 High current ignitron

I_3 High current dump ignitron

I_4 High reverse current injection ignitron

L_1 = 366 μH

L_2 = 90 - 300μH

R_1 = 6Ω

R_d = 0.0475Ω

R = 1.67 - 3.5Ω

C_p = 6.37 nF - 3μF

Fig. 4.4 The Electrical Test Circuit

(a) Reduced Power

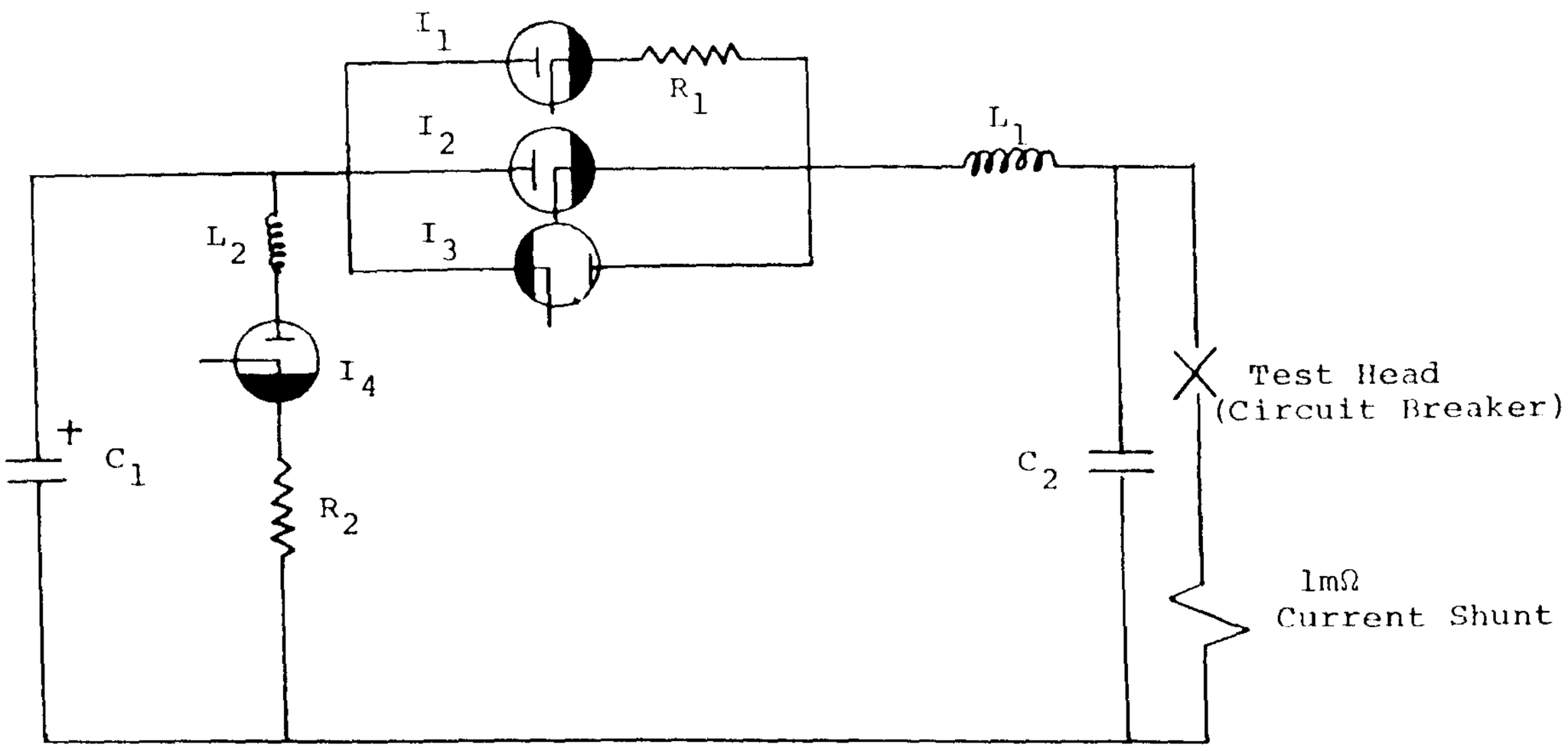

R_1 = 4 to 8 Ω

R_2 = 0.36Ω

C_1 = 35.5mF, 6.3KV

C_2 = stray capacitance >1000pF

L_1 = 90μH (for 78Hz operation)

L_2 = 24μH

I_1 low current forward ignitron BK488

I_2 high current forward ignitron BK488

I_3 high current reverse ignitron BK488

I_4 high current dump ignitron BK488

(b) The Full Power Circuit

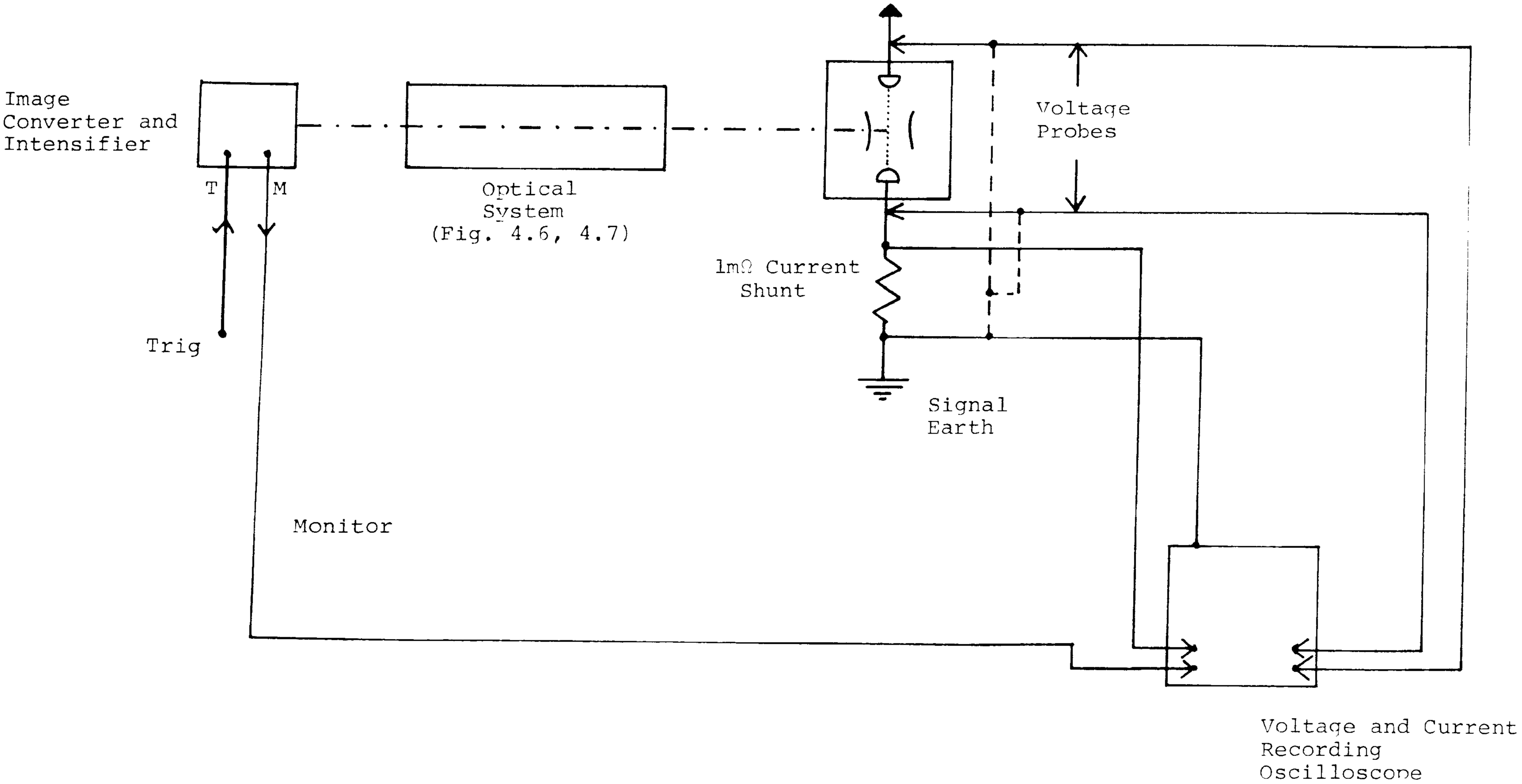

Fig. 4.5 Schematic Diagram of the General Measurement System
(a) Photographic System

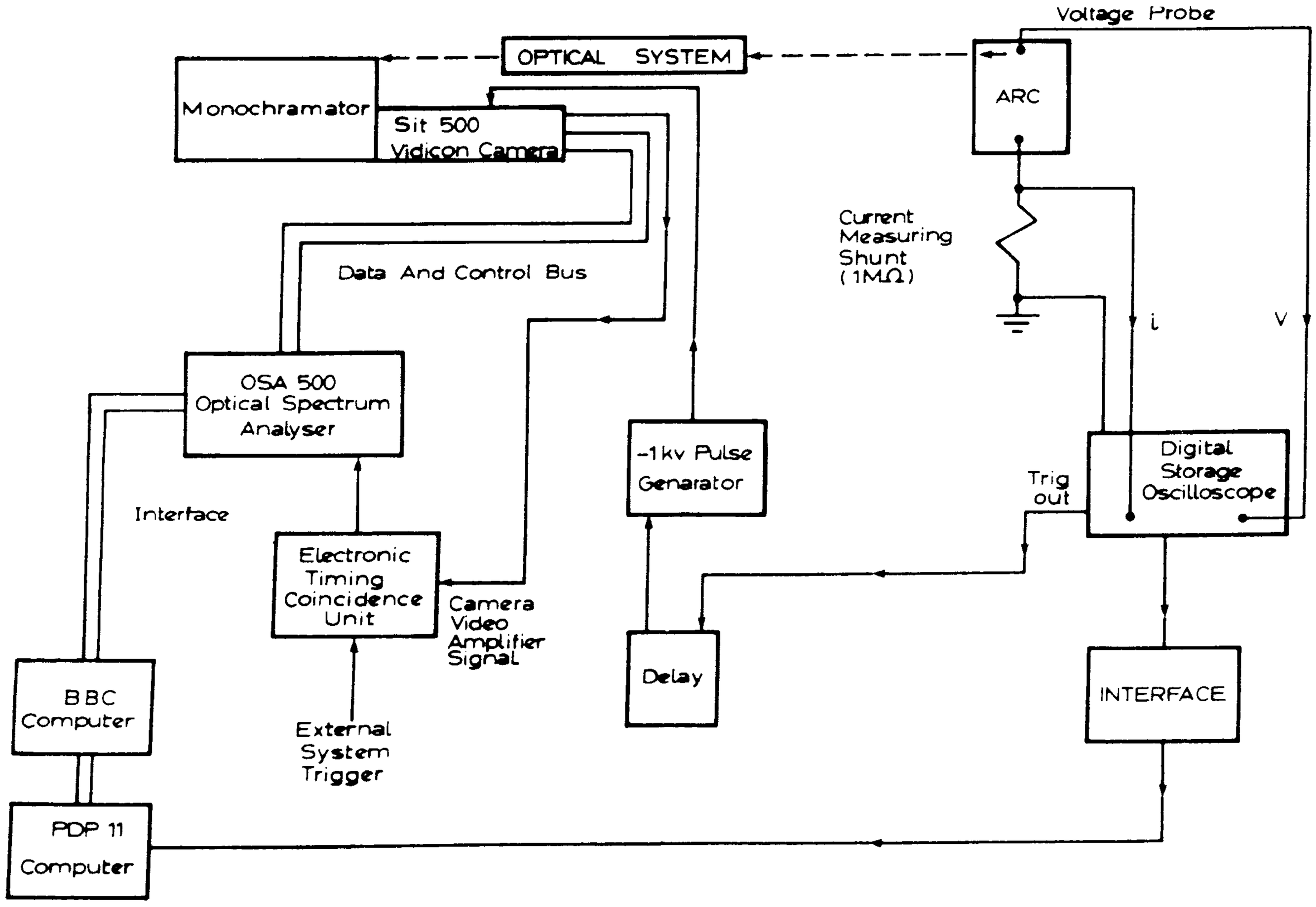

(b) Spectroscopic System

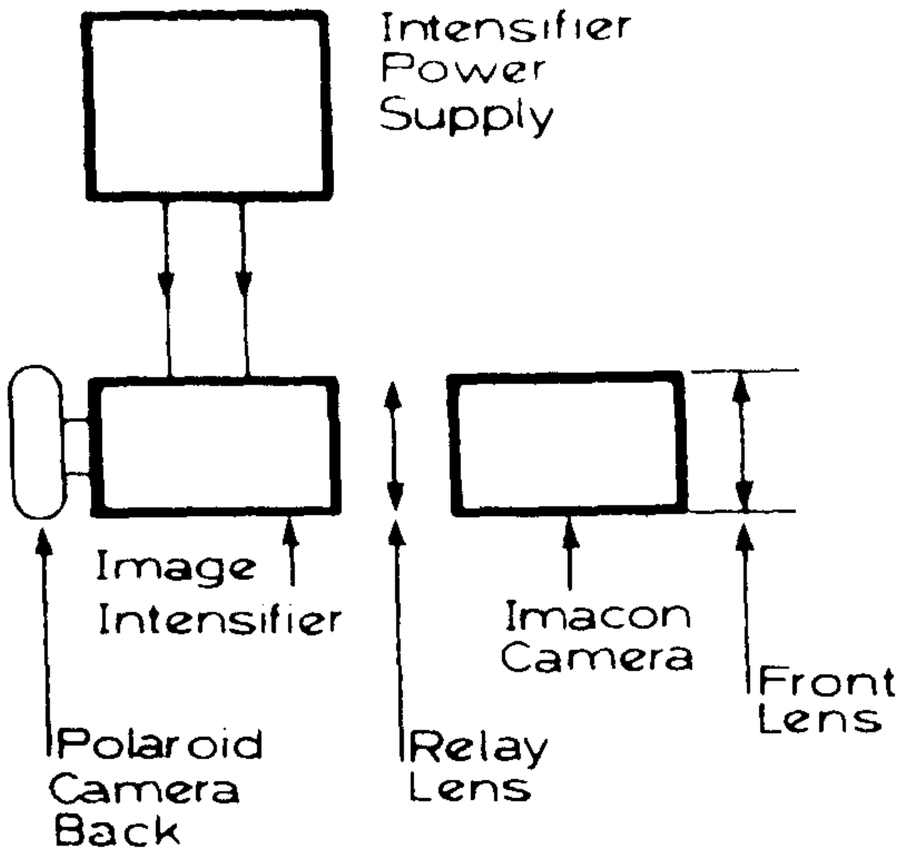

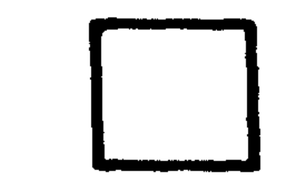

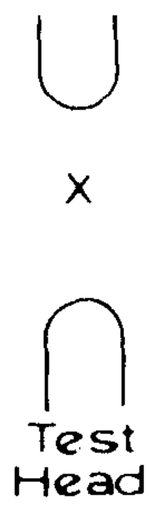

Imacon Framing Units : 1×10^6 And 2×10^5 Frames 1sec
Imacon Front Lens : 6", 152mm f/2·8 T32
Relay Lens : Oscillac, Mag – 1:0·42 f/1
Polaroid Camera Lens : Normal Oscilloscope Type Lens
Polaroid Film : Type 46 L

(a)

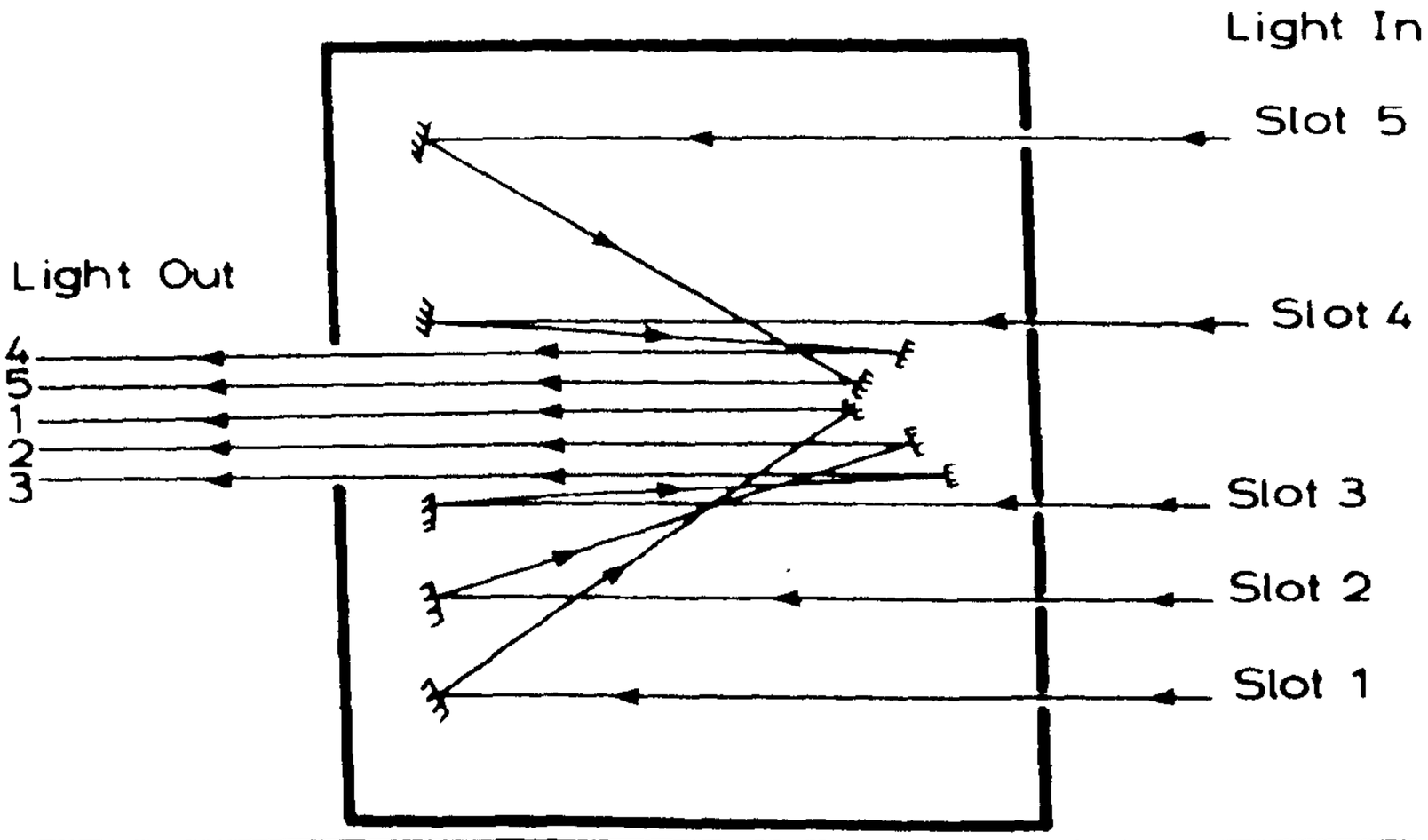

Scale 1:1
Mirror System Gives 9:2 Demagnification In
Axial Direction; 1:1 Demagnification Diametrically

(b)

Fig. 4.6 Optical System used for Arc Photography

(a) Overall
(b) Construction of the Collimating Mirror System

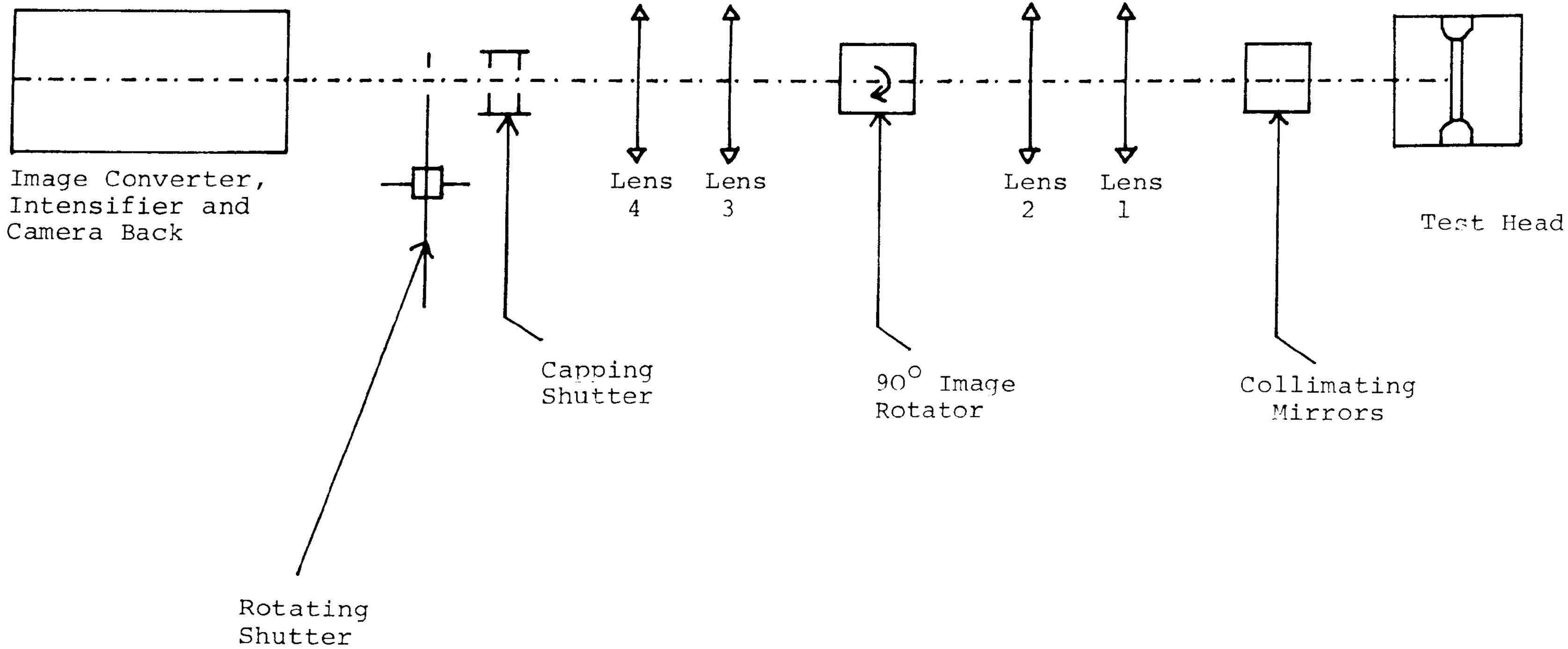

(a) Overall System

Fig. 4.7 Optical System used for Full Power Arc Photography

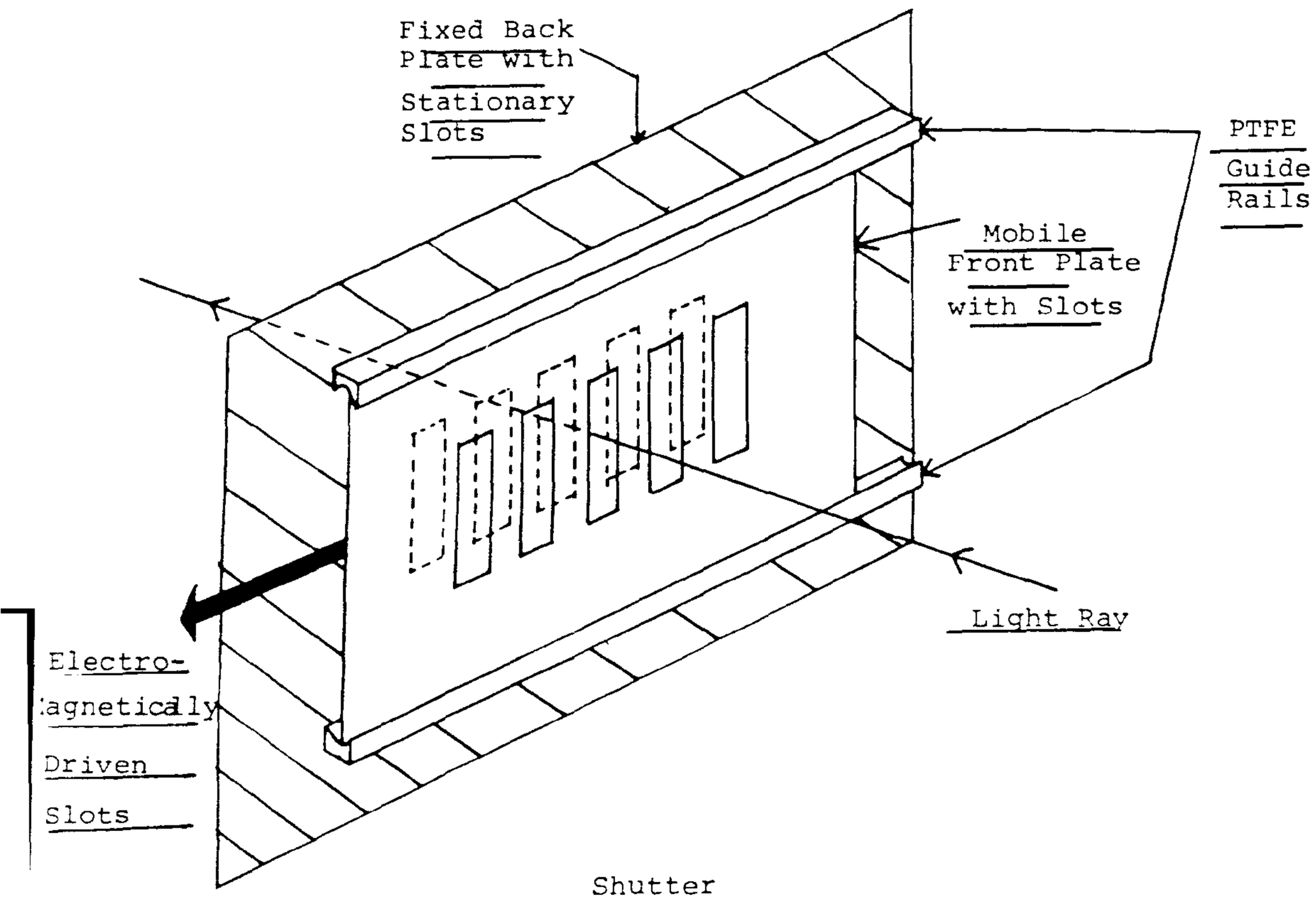

Shutter Design

(i) Capping Shutter

(b) Shutter Details

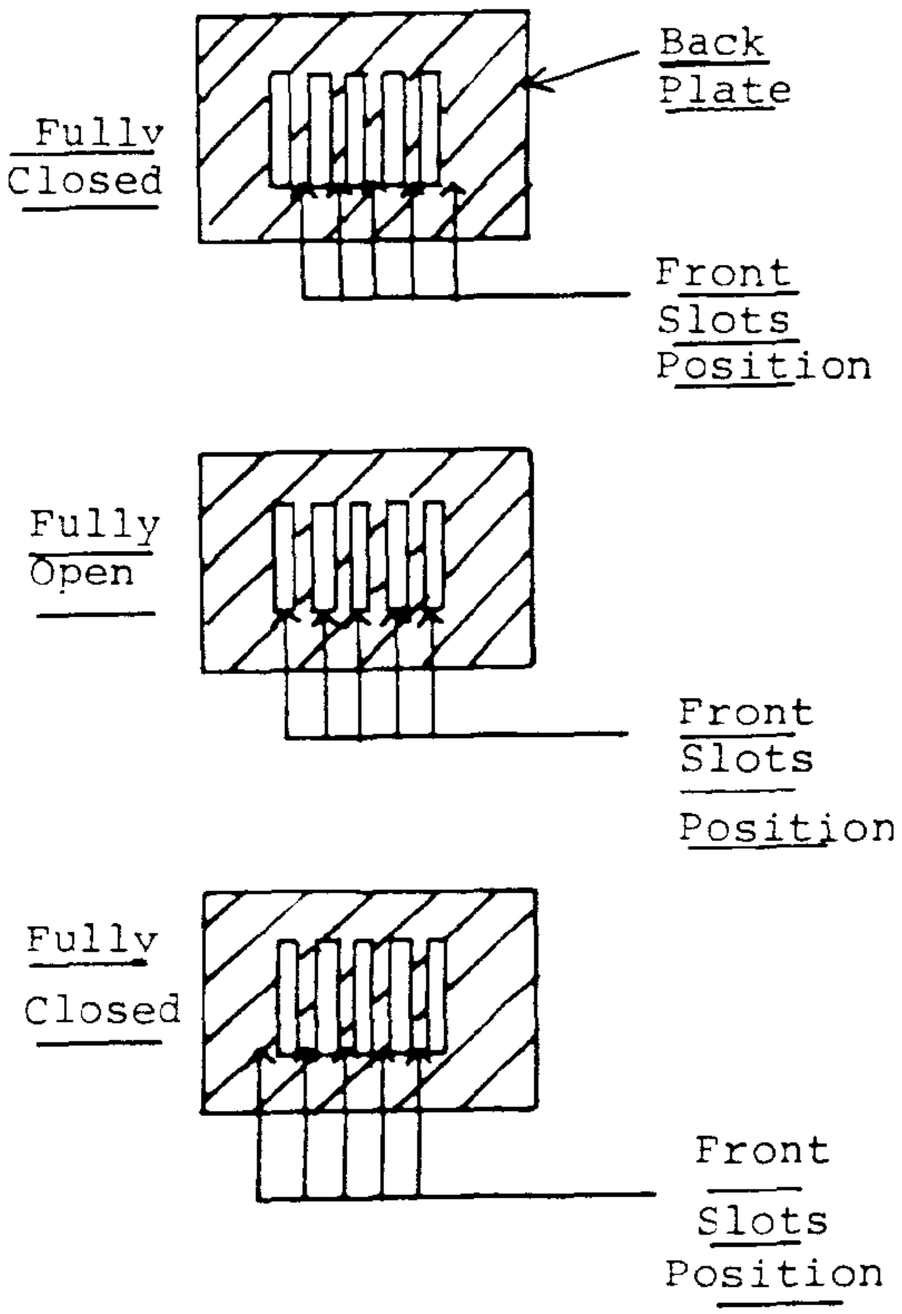

Shutter Action

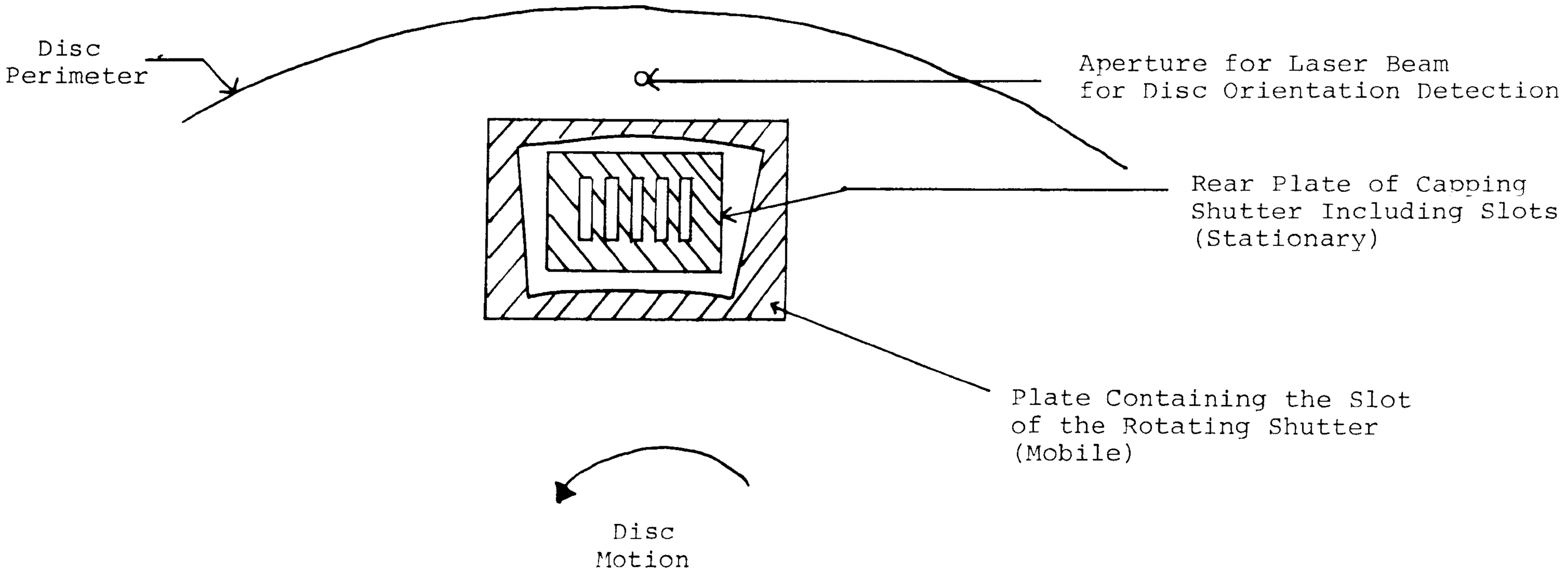

(ii) Rotating Shutter

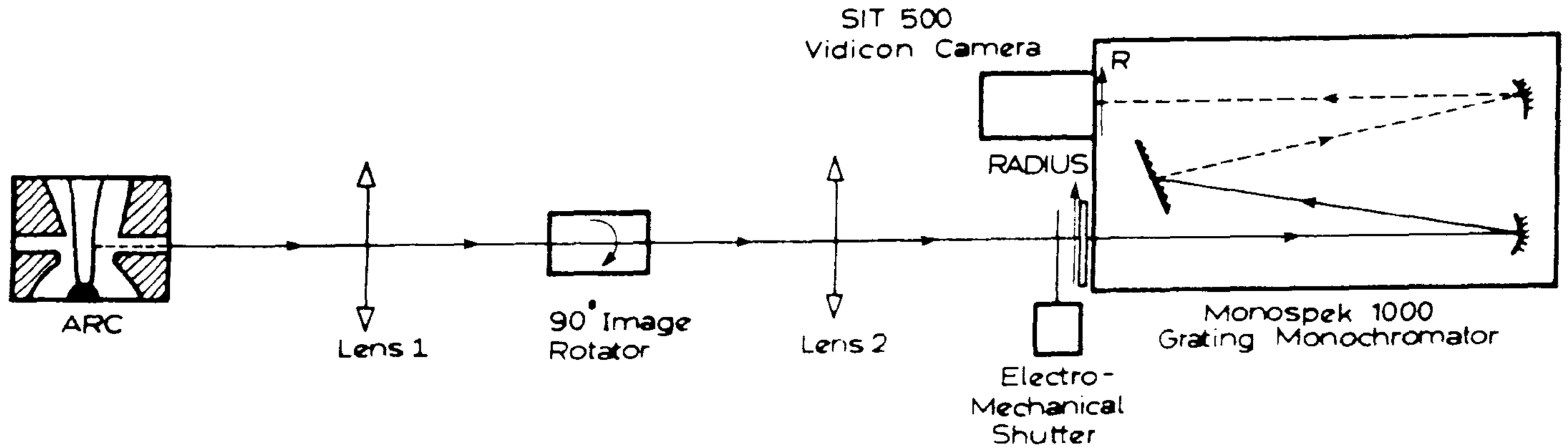

(a)

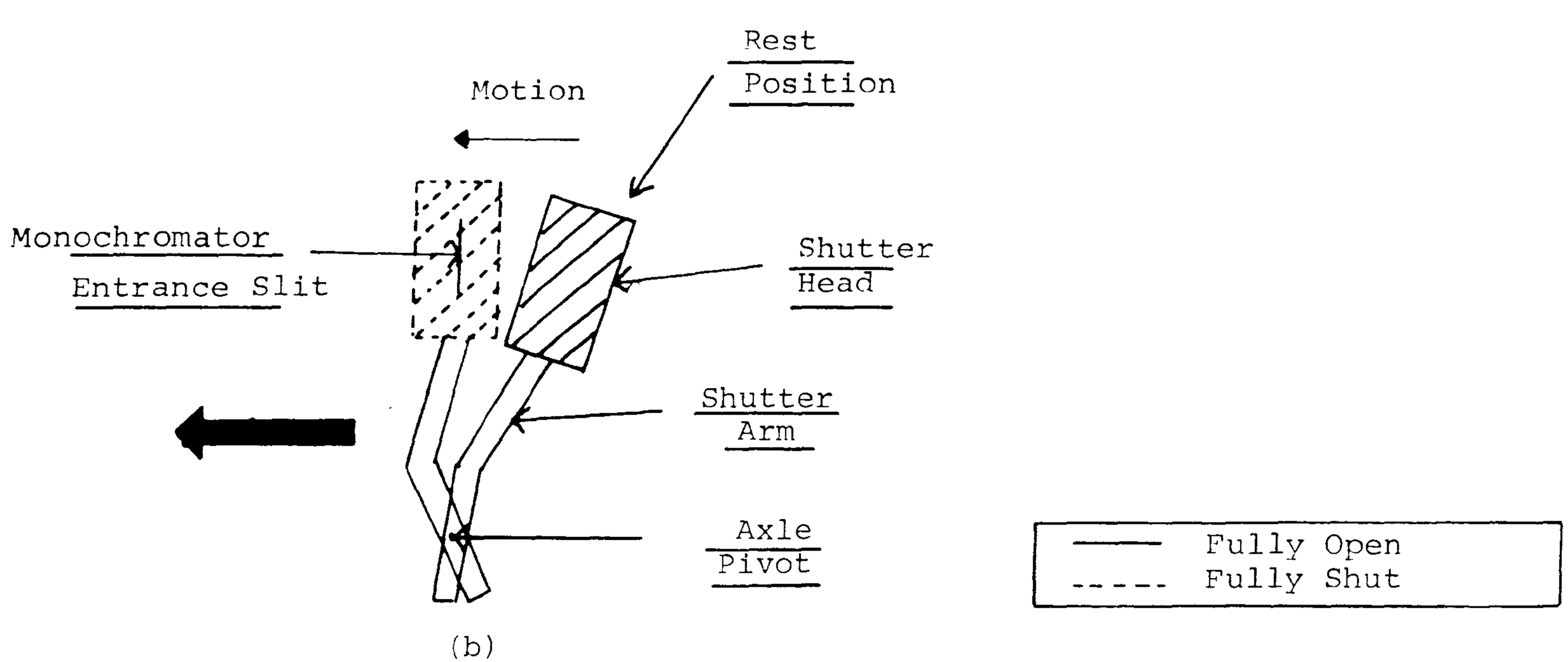

(b)

Fig. 4.8 Optical System used for Arc Spectroscopy - (a) Schematic Diagram
(b) Capping Shutter Operation

VOLUME CONTAINS CLEAR OVERLAYS

OVERLAYS SCANNED SEPERATELY AND OVER THE RELEVANT PAGE.

a(i) Photograph

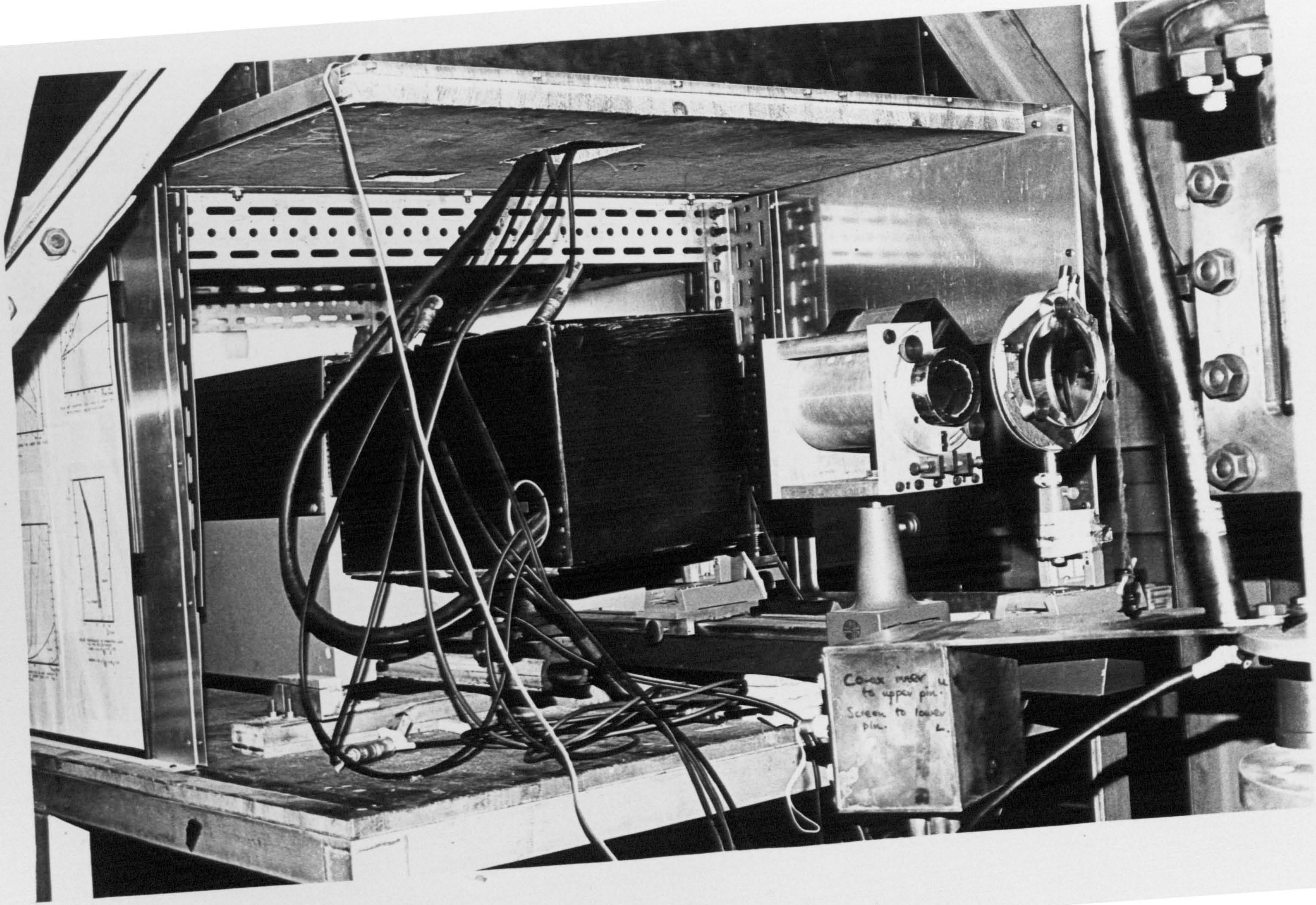
Coax mark. u
to upper pin.
Screen to lower
pin. L.

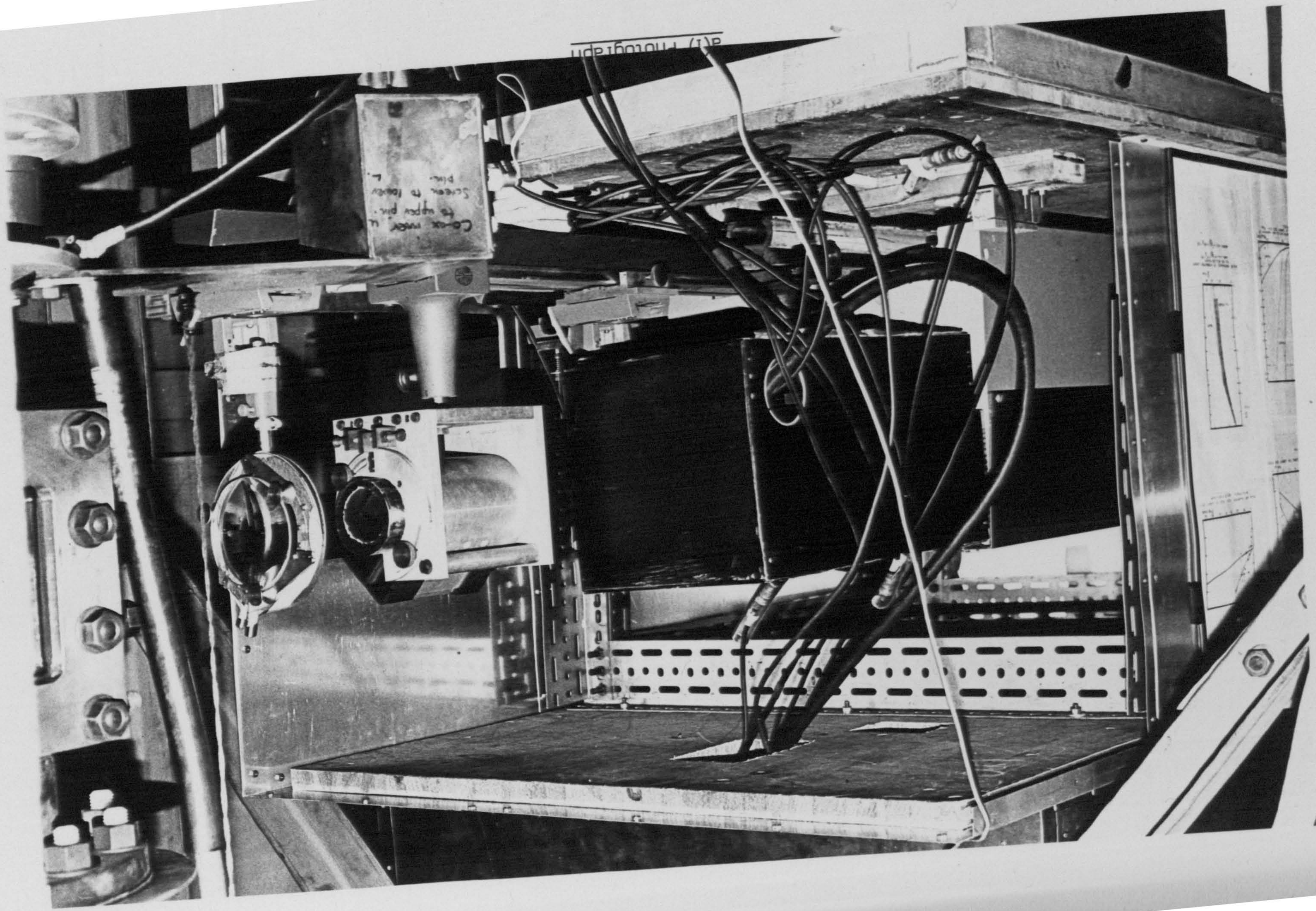

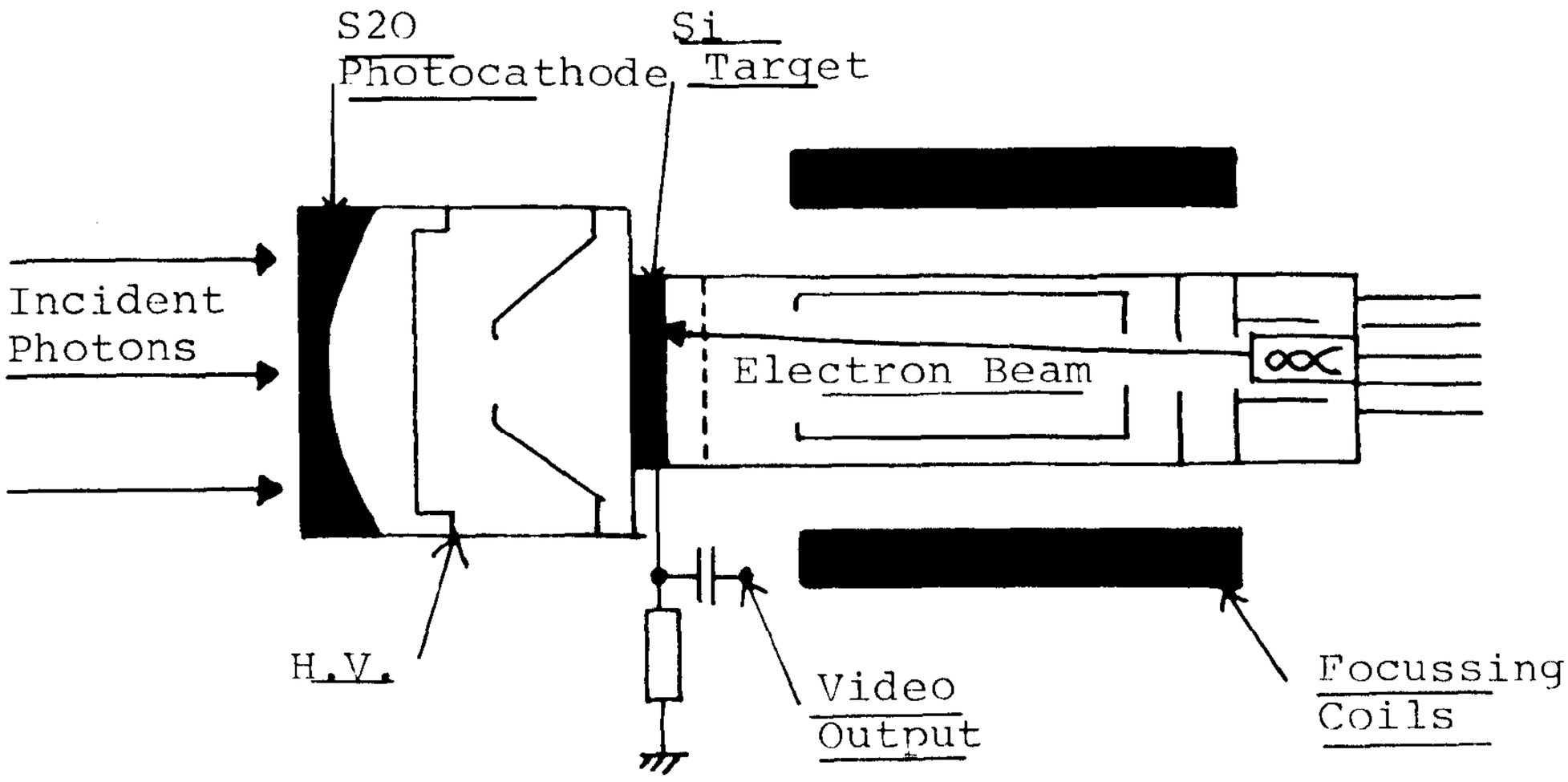

(c)

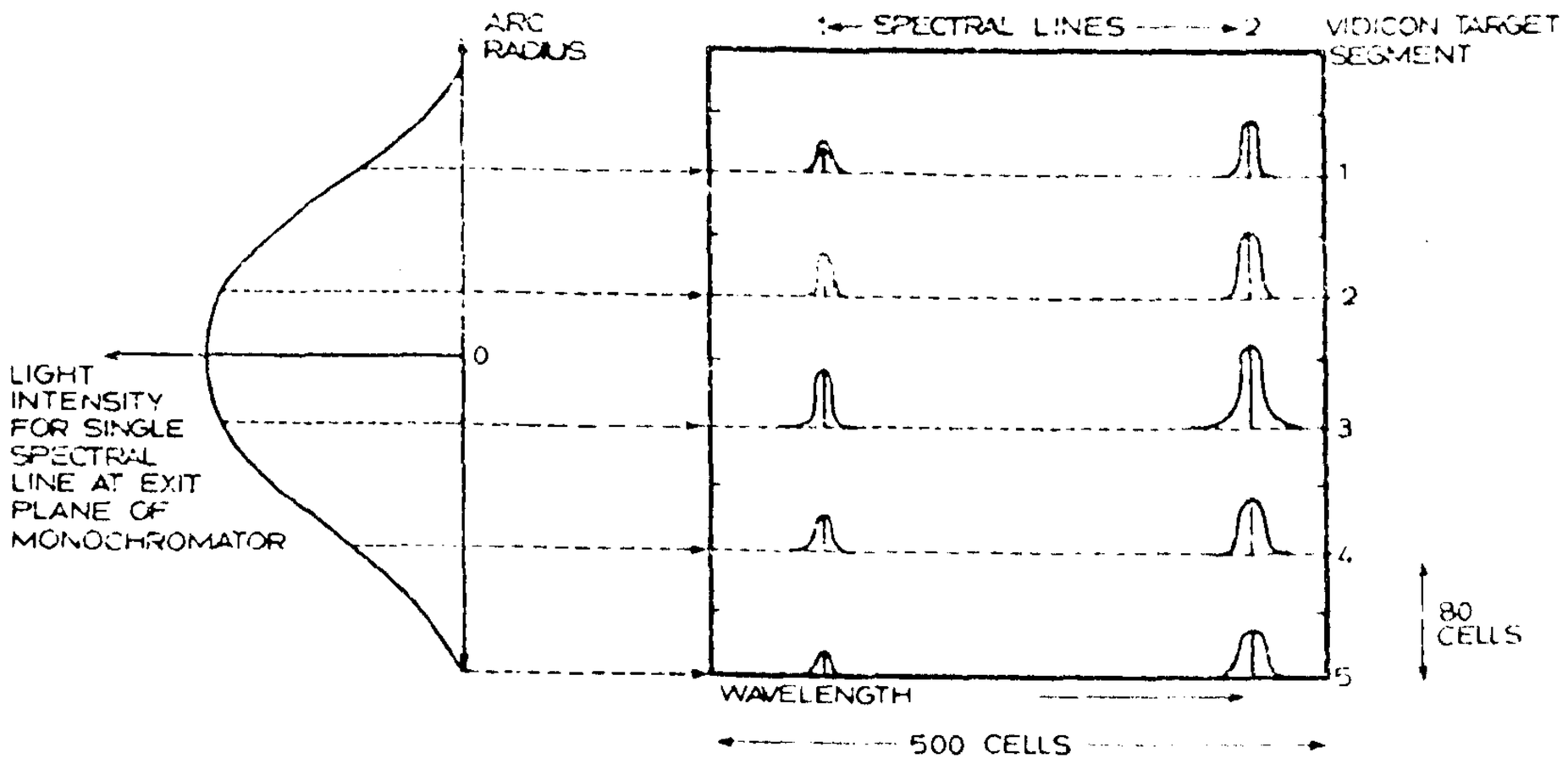

(d)

Fig. 4.8 (c) Vidicon Camera Details

(d) 2-dimensional Scanning Facility

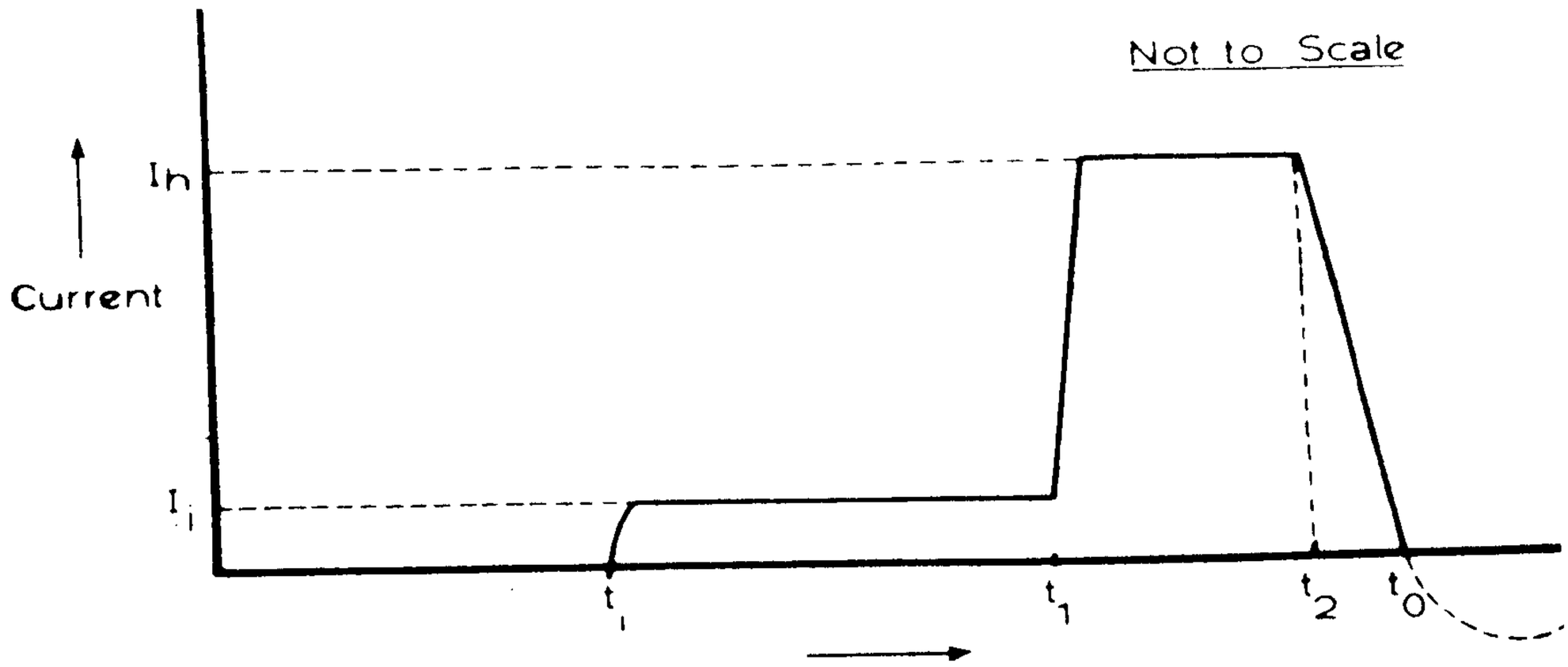

I_h – Holding Current = 0·36 — 1·6kA; I_i – Initialion Current ≃ 50A.
t_i = Position of Firing Initiation Ignitron.
t_1 = Position of Firing First Ignitron.
t_2 = Position of Firing Second Ignitron.
t_0 = Position of Current Zero.
$t_1 - t_i \simeq 60ms$, $t_2 - t_1 \simeq 5ms$
Current Zero Recording Oscilliscopes And Imacon Triggered At Times Between (t_o-15μs) And (t_o 5μs)

(a)

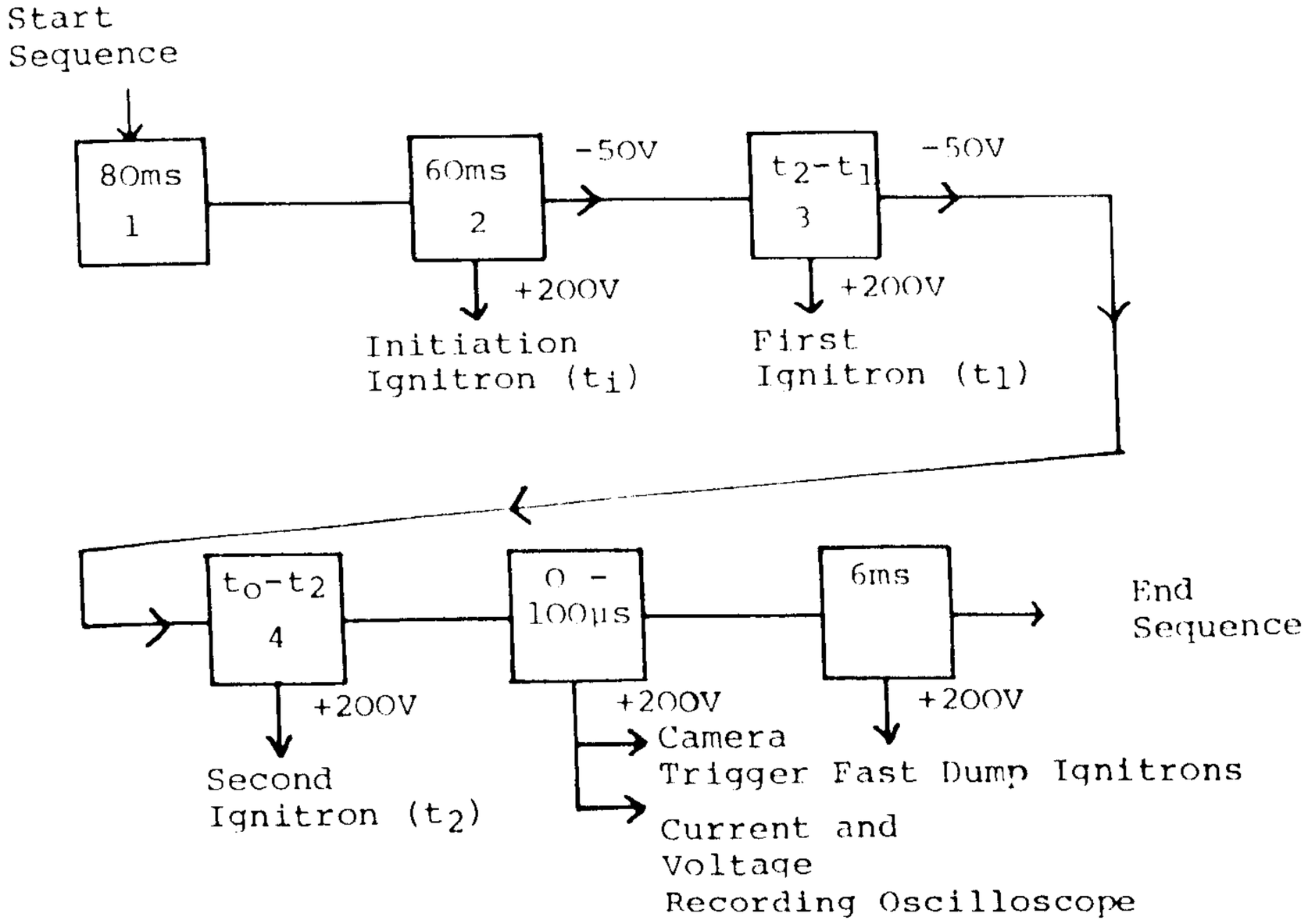

(b)

Fig. 4.9 General timing and triggering of the experimental system used for the reduced power investigation

(a) Arc current waveform and important timing points

(b) Schematic representation of the delay unit timing sequence

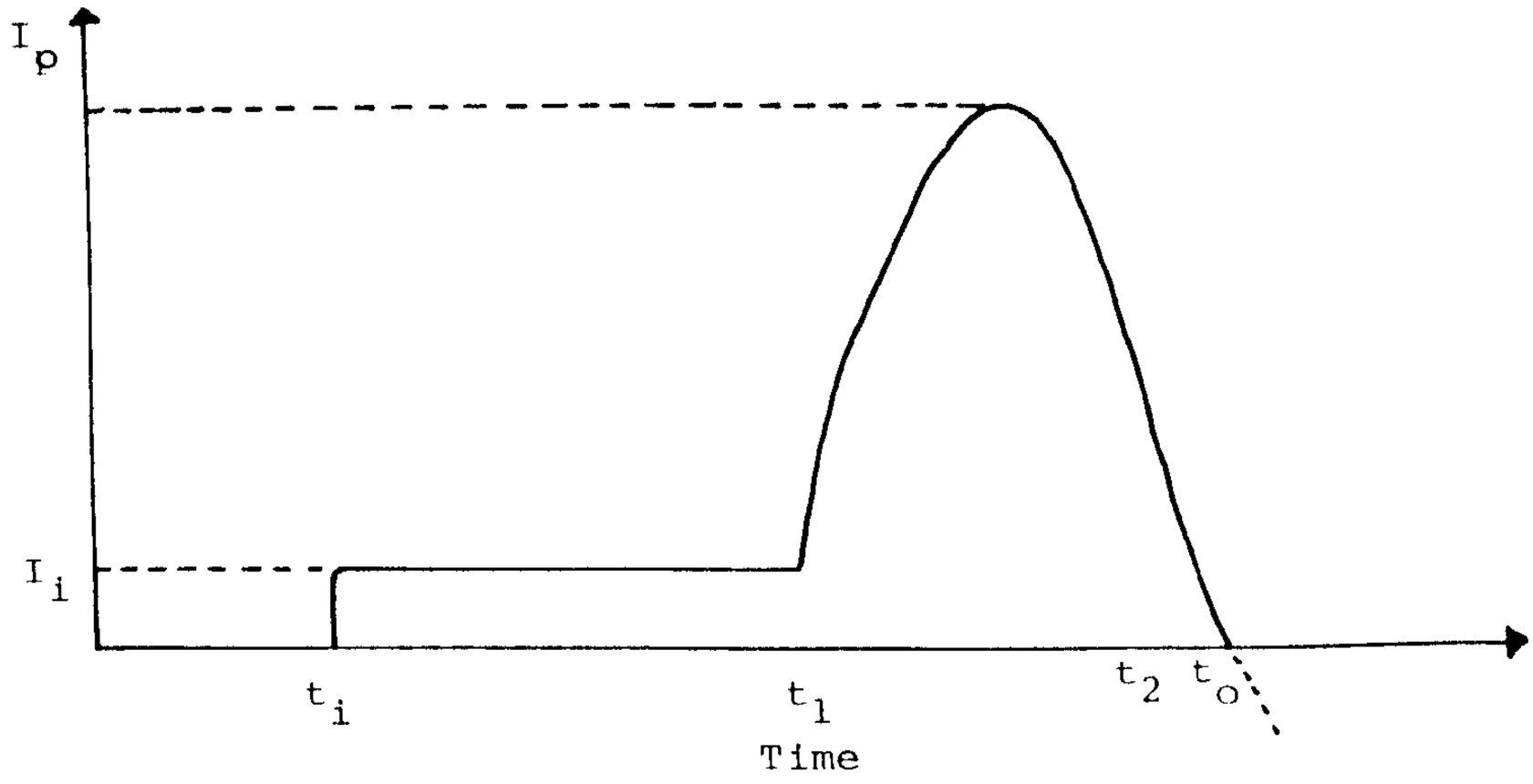

I_p = Peak Current = 30 to 65KA ; I_i = Initiation Current = 300–800A

t_i = Instant of Firing Initiation Ignitron

t_1 = Instant of Firing First Ignitron

t_2 = Instant of Firing Second Ignitron

t_o = Current Zero Instant

$t_1 - t_i$ 60ms (Photography) $t_o - t_i$ 50 to 100ms (Spectroscopy)

Current Zero Scopes and Image Converter or Vidicon Cameras Triggered off the Falling Current Waveform

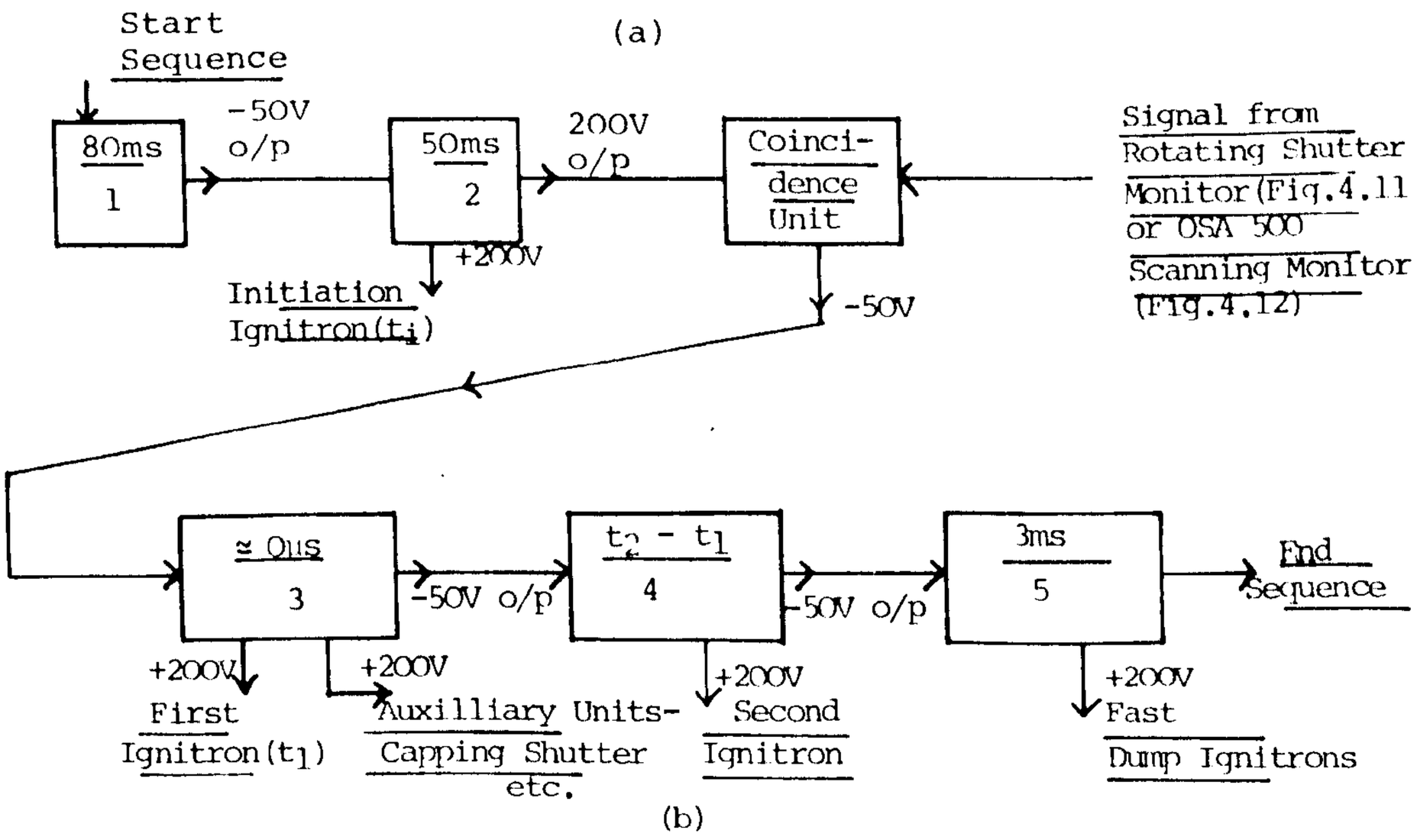

Fig. 4.10 General Timing and Triggering of the Experimental System used for the Full Power Investigation
(a) Arc Current Waveform and Important Timing Points
(b) Schematic Representation of the Delay Unit Timing Sequence

Fig. 4.11 Timing System for Current Zero Arc Photography

(a) Schematic Diagram

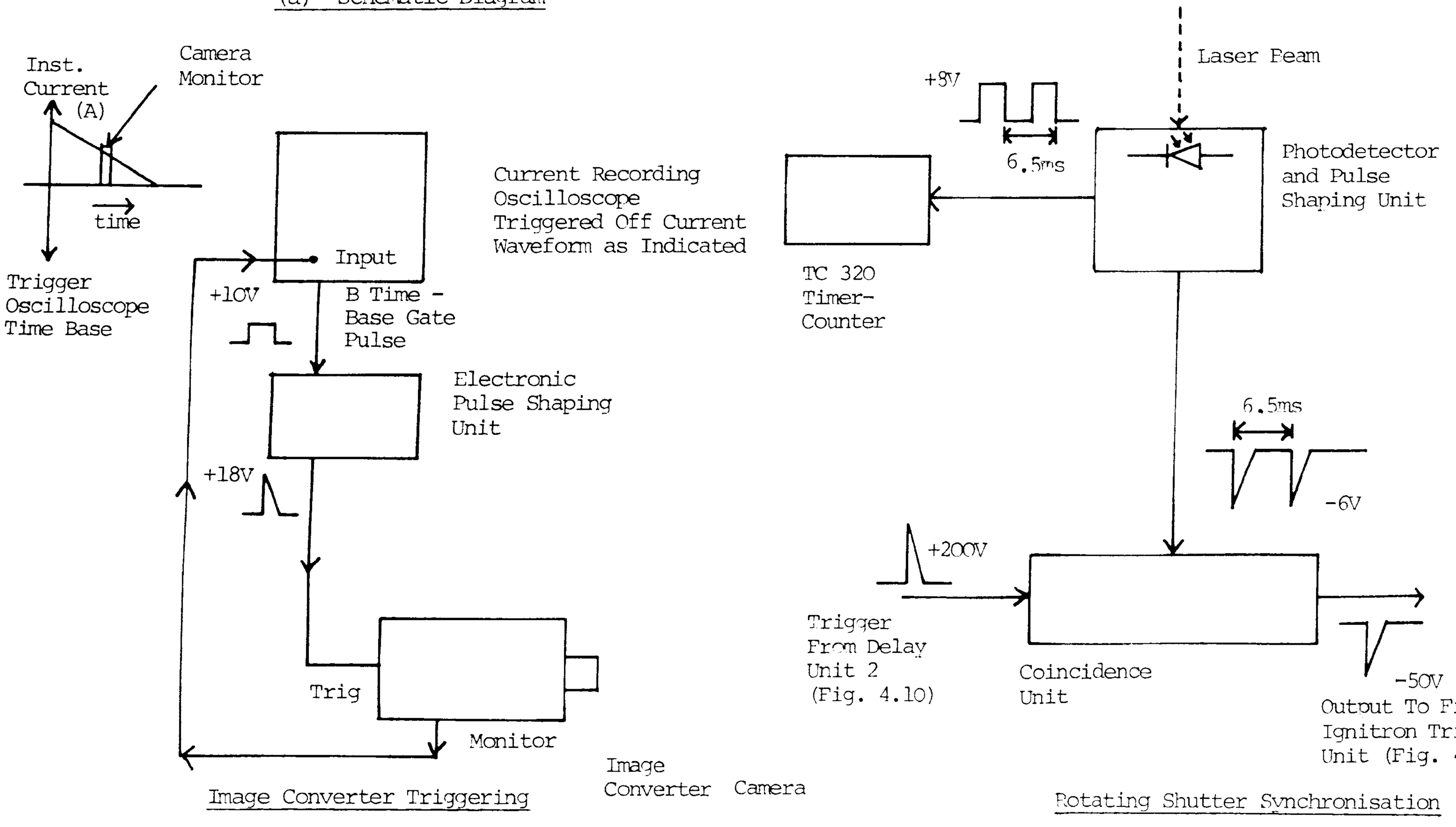

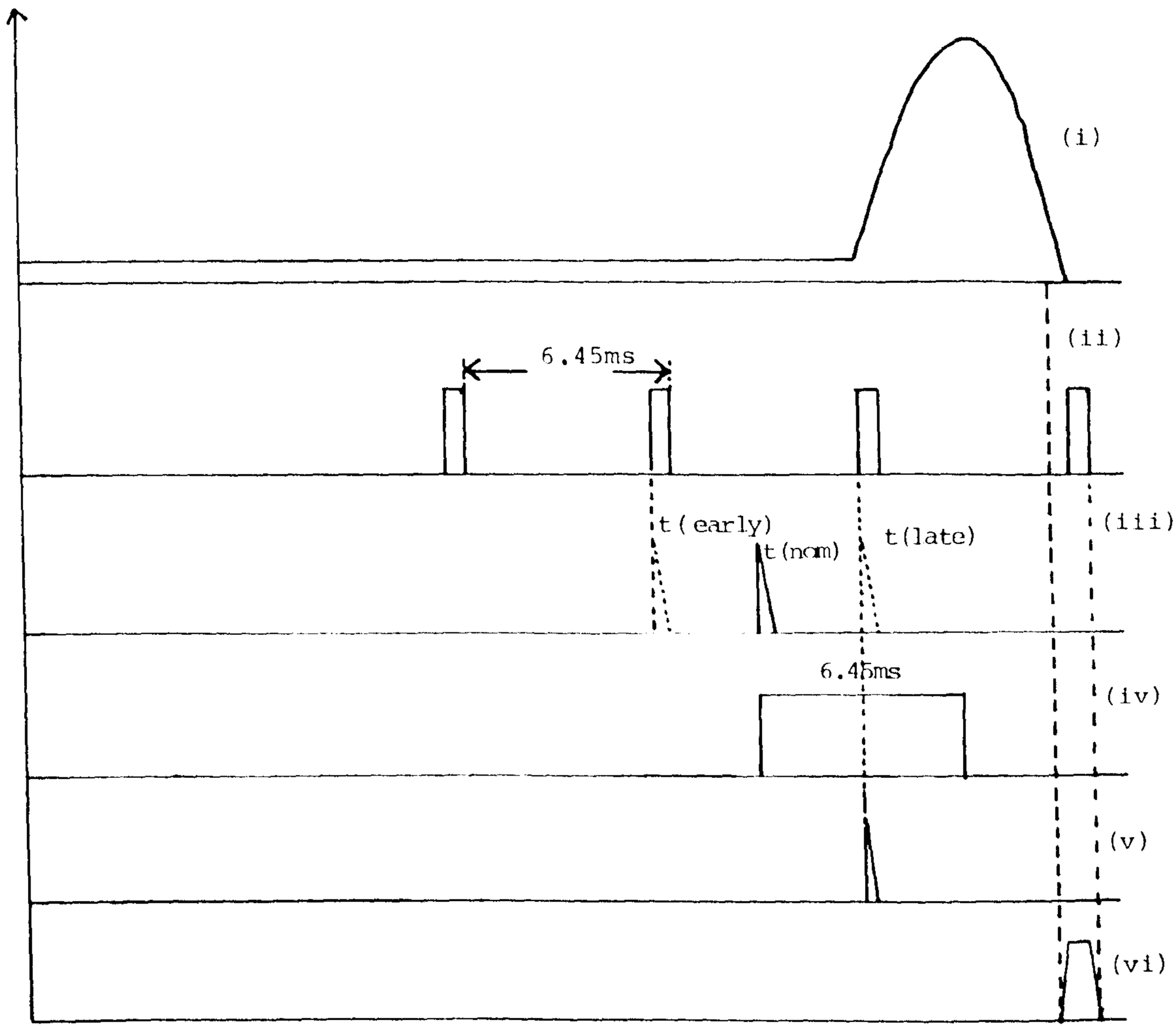

Key

(i) Arc Current Waveform

(ii) Rotating Shutter Monitor Signal (Rising Edge of Pulse when Shutter is Fully Open)

(iii) Pulse from Delay Unit 2 to Trigger Coincidence Unit (fig.4.10) - Instant of Occurrence of this Pulse was Variable wrt waveform (ii)

t(early) - Earliest Possible Instant of Occurrence wrt waveform (ii)
t(late) - Latest Possible Instant of Occurrence wrt waveform (ii)
t(nom) - Nominal Occurrence Instant

(iv) Gate Pulse of Coincidence Unit - for which duration the Coincidence Unit is Enabled (6.45ms)

(v) Trigger out of Coincidence Unit - Triggers 1st Ignitron and the Main Arcing Sequence

(vi) Capping Shutter Exposure Characteristic

(b) Timing Diagram

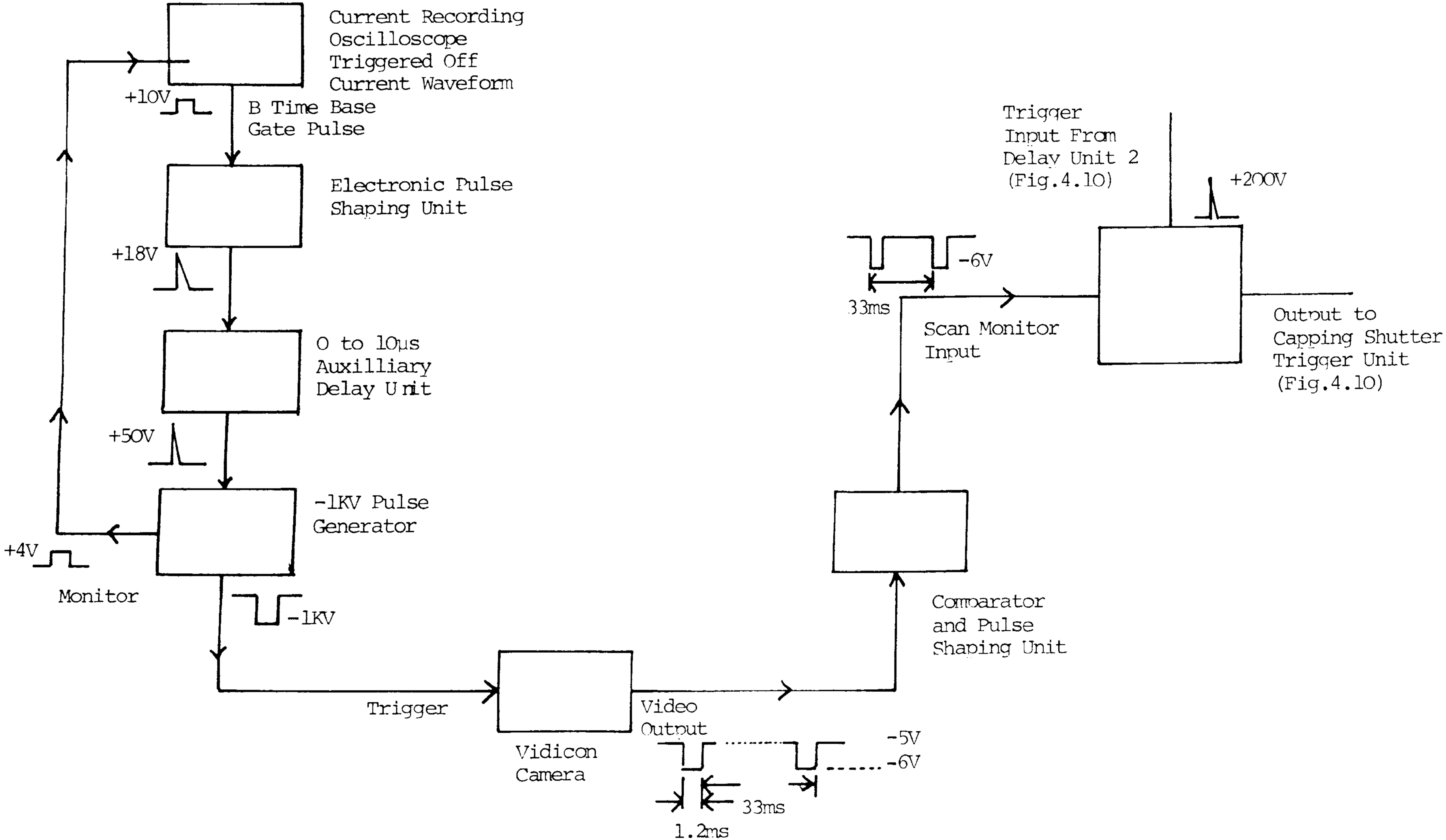

Fig. 4.12 Timing System for Current Zero Full Power Arc Spectroscopy (a) Schematic Diagram

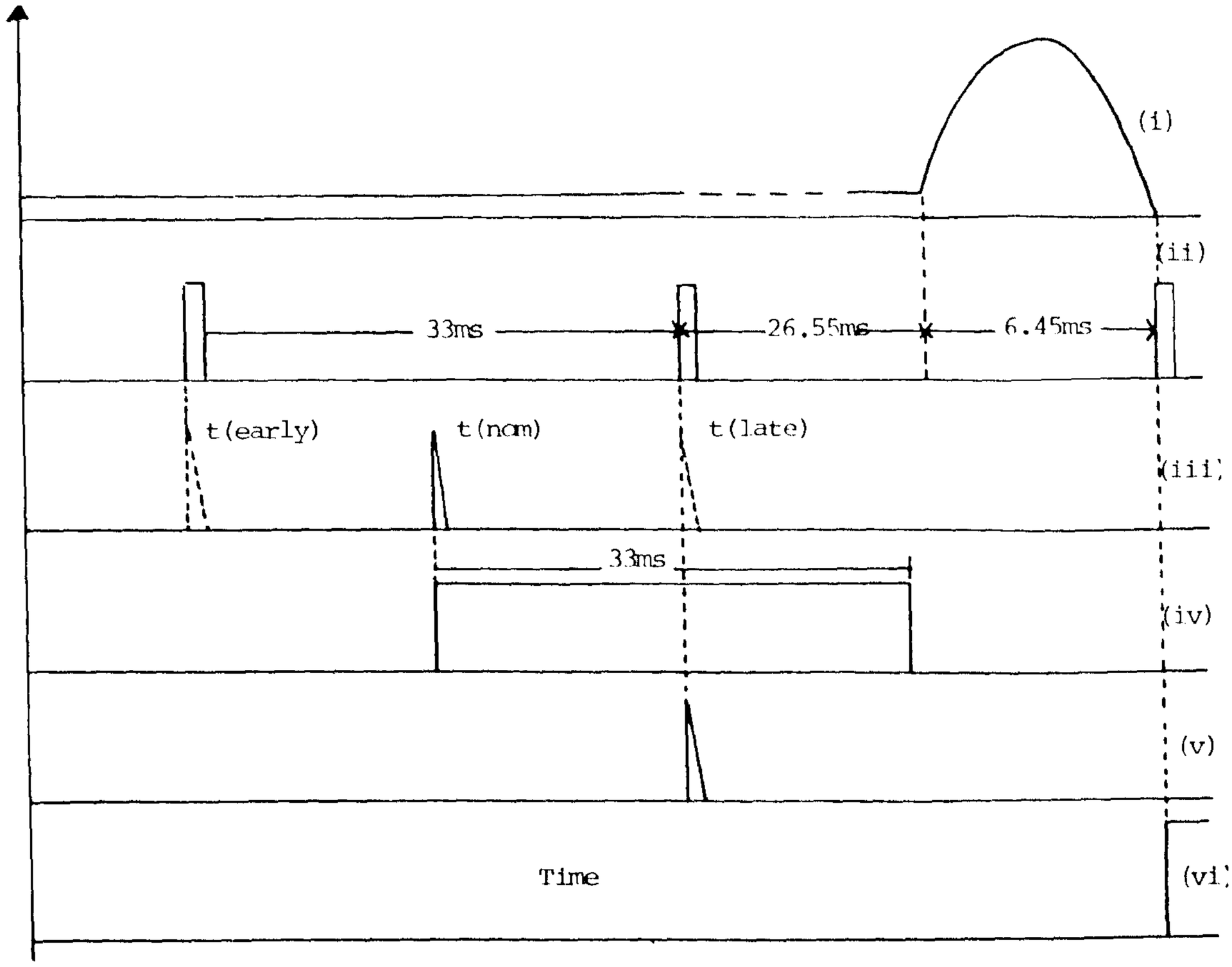

Key

(i) Arc Current Waveform

(ii) Vidicon Video Output Scanning Monitor Signal

(iii) Pulse from Delay Unit 2 to Trigger Coincidence Unit (Fig.4.10) - Instant of Occurrence was Variable wrt waveform (ii)

t(early) - Earliest Possible Instant of Occurrence wrt (ii)
t(late) - Latest Possible Instant of Occurrence wrt (ii)
t(nom) - Nominal Occurrence Instant

(iv) Gate Pulse of Coincidence Unit - for which duration the Coincidence Unit is Enabled (33ms)

(v) Trigger out of Coincidence Unit - Triggers the Capping Shutter Trigger Unit and later the 1st Ignitron

(vi) Capping Shutter Exposure Characteristic

(b) Timing Diagram

CHAPTER 5

CHARACTERISTICS OF THE PHOTOGRAPHIC AND SPECTROSCOPIC SYSTEMS

5.1 Introduction

The optical systems for both the photographic and spectroscopic measurement consisted of a complicated geometric focussing system with a detector whose response characteristics are highly non-linear. Although it is possible in principle to consider each element of the optical system individually and then combine the individual characteristics to obtain an overall response, the complexity of the overall system made such an approach difficult.

It was more convenient and more accurate to consider the overall system using a suitable known standard or calibration source to simulate the arc.

The choice of source was made according to the following requirements:

(i) Its spectral emission characteristic needed to cover approximately the same range as the arc emission to be investigated i.e. between 400 and 500nm.

(ii) The source needed to be of sufficient intensity to allow detection by the snapshot photography (1μs and 200ns exposures) and spectroscopy (1.6μs exposure) in addition to being sufficiently short duration (pulsed operation) so as not to damage the

exposed photosensitive detector surfaces.

(iii) The radiation power emitted from the pulsed source needed to be sufficiently constant for the duration of the pulse and sufficiently reproducible over a number of successive operations.

(iv) The source needed to be capable of operation on a test bench as well as in situe in the circuit breaker test head.

A suitable source which met all the above requirements was a flashgun (Sunpak autozoom 2400).

The parameters requiring calibration were image dimensions, intensity and the spectral composition. The effect of varying certain parameters of the optical system also required investigation, as well. The influence of electromagnetic interference produced by the circuit breaker arc upon the diagnostic instrumentation particularly the spectroscopic detection and recording instruments.

5.2 Calibration Technique and Procedure

5.2.1 The Photographic System

The simplest form of calibration performed with this system was to determine the magnification factor i.e. the ratio of the final image size (corresponding to arc radius) to object size.

This was performed directly in the case of the reduced

power arc by mounting two thin parallel tungsten wires 5mm apart and coaxial with the arc column between the outer nozzle wall and the sealing gasket (fig. 4.6). The arc could be viewed directly through the wires thus providing a scale on the final image (the photographic record) from which the luminous arc diameter was directly reduced.

This method was not feasible in the full power case since the higher power dissipation from the arc during the peak current phase of arcing caused the destruction of the wires through severe ablation. Also the cone of focus of this optical system (fig. 4.7) was much steeper and would have resulted in large errors.

In this case,the method adopted for overall system magnification calibration consisted of focussing the flash-gun on the plane of focus of the optical system shown on fig. 4.7 (i.e. normally the central arc axis) where 3, 5mm width vertical (in the axial direction) slots at 5mm spacing (in the radial direction) were located. This was used as a test object, the luminous regions of which were taken to correspond to 5mm of luminous arc diameter. An identical procedure was followed with the optical system used for the reduced power arcing investigation and good agreements with the 'wire' method was obtained.

A detailed investigation was conducted into the effect of individually varying the optical system parameters upon

the final image. The optical systems used for both full and reduced power arc photography (figs. 4.6 and 4.7) were studied independently.

In order to obtain a continuous final image the flashgun source was placed in the plane of focus of the optical system in question i.e. the arc axis. Collimation of the light was achieved by viewing the flashgun through a single slot of the arc viewing nozzle which was displaced towards the optical system, thus acting as a single long collimating slot. Image converter records were taken during the flashgun light pulse and the radial intensity variation of the image analysed on a Hilger type microphotodensitometer.

5.2.2 The Spectroscopic System

The magnification factors of the optical system and the resulting image geometry on the camera target when operated in the 2 dimensional (and gated) mode (chapter 4) were investigated.

The flashgun light pulse was triggered simultaneously to the vidicon gate pulse (approximately 10μs duration) to enable detection of a clear spectral line in the flash-light spectrum (centred on 529.1nm). The camera target in this case was split into 30 segments in order to give a good radial resolution so that the radial extent of the image could be accurately identified. To split the target into so many segments and scan them all would not be feasible for viewing the arc since the total scanning time would be

longer than the decay time of the image on the photo-sensitive target, thus giving erroneous intensity profiles. However the intensity of the spectral line of the flash was not important and its detection was sufficient to identify the image geometry.

From the previous spectroscopic investigations (Housby-Smith and Jenkins, 1978) it is clear that many of the diagnostic spectral lines, and in particular copper lines, occupy a narrow spectral range and in addition may be accompanied by satellite or neighbouring lines for which little data exists. For this reason it was imperative that the accuracy of the monochromator in indicating the correct wavelength was confirmed. This was achieved by using a low pressure mercury 'pen ray' lamp as a spectral calibration source. The lamp was situated at the same location as the arc axis in the vacant test head and a continuous image of the lamp was formed. The monochromator was adjusted to cover a wide range of wavelengths (365.0nm to 546.0nm) and the wavelengths of the detected peaks were compared with the lamp manufacturers specifications.

A tungsten light source (filament temperature 2000K) was used to provide a continuous emission radiation spectrum. This continuous spectrum was used to evaluate the overall system spectral response. The tungsten source was operated to give a constant light intensity and the monochromator again was adjusted to cover a wide spectral range (300nm to 700nm). The spectral output of the lamp was known but

was adjusted by correction factors to take account of the spectral response of the individual components of the optical system e.g. the neutral density filters, the vidicon camera and the blaze of the monochromator grating (blaze = 500nm). Thus the adjusted specified output of the lamp could be compared with the measured spectral response.

The above procedures (with the exception of the geometry calibration) were used to evaluate the steady state response of the system. However in the experiments during arcing the vidicon camera was used in the gated mode as described in chapter 4. Thus it was important to evaluate the system response when used in this manner. Further calibration tests were performed which necessitated using the arc as the light source. These were used to ascertain the effect of electro-magnetically induced noise from the arc and the general image quality of selected diagnostic lines.

5.3 Calibration Results

5.3.1 The Photographic System

A summary of the magnification factors calculated for the optical systems used for photographing both the reduced and full power arcs are presented in table 5.1. These magnification parameters were used throughout the photographic investigation.

The flashgun source was photographed as described in section 5.2.1 and microphotometer measurements were made of

the diametric intensity distribution on the recording film. This allowed a study of the effects of the following operating conditions upon the image properties to be made:

(i) The effect of varying the NDF (neutral density filter) transmission value upon the image diameter (fig. 5.1(a)) and the exposure of the film (inverse of opacity) which is hitherto referred to as the recorded intensity (fig. 5.1(b)).

(ii) The effect of varying the image intensifier bias upon the image diameter (fig. 5.2(a)) and recorded intensity (fig. 5.2(b)).

The diameter values in fig. 5.1(a) and the four central values of fig. 5.2(a) were selected from exposures where the film emulsion was known not to have been saturated. The luminous diameter shows no significant variation throughout the range of NDF values. On fig. 5.1(b) it appears that the recorded intensity increases with the use of less opaque NDF. This result alone may not appear significant. However, if more parameters are known then the increase in recorded intensity when the NDF value or intensifier bias are varied can be predicted.

One such important parameter which was considered in this analysis was the film characteristic curve (the specified response of the film emulsion opacity to changes in incident intensity) which is shown on fig. 5.3. The effect of introducing the film response is included in the predicted variation

of recorded intensity with intensifier bias for a NDF nominal transmission value of 0.44 (fig. 5.2(b)). This adjustment is only valid if the intensifier bias setting is the same for a given reduction by an NDF. If the value of NDF was such that a higher value of intensifier gain was required to make the image visible (such as the case of the 0.05 (nominal) transmission NDF) then a knowledge of the intensifier gain versus applied bias was required. The specified gain characteristic as supplied by EMI is shown on fig. 5.4. Also shown on fig. 5.2(b) is the predicted intensifier bias setting (calculated from the gain characteristic) to achieve the same recorded intensity when the 0.05 (nominal) transmission coefficient NDF is introduced. Since the image converter and intensifier both have a type S20 photocathode then the peak sensitivity lies at about 400nm (EMI, 1972). This being so the transmission coefficient of the neutral density filter in question in that particular wavelength range needed to be considered. This was found to be about 0.03 (Ilford, data sheet F26.1).

Thus the measured variation of the luminous structure of the image when different parameters in the optical system were varied has shown good agreement (fig. 5.2(b)) with the expected variation when the response of certain system elements were considered.

The diameter versus intensifier bias characteristic (fig. 5.2(a)) indicates that there exists a range of bias for which the luminous diameter shows little or no change.

However on either side of this plateau the variation of the luminous diameter with intensifier gain is steep. For the low intensifier gain the steepness is due to the intensifier just detecting the peak of the image intensity profile, thus giving rise to an artificially low diameter. For the higher intensifier gain values the intensity of the image on the intensifier phosphor is so high that helation effects were becoming apparent both on the film and the intensifier, thus giving rise to an artificially high diameter value. Additionally, the diameter value within the plateau region is independent of the value of NDF used (fig. 5.1(a)), indicating that the use of an NDF has no effects such as clipping of the 'wings' of the intensity profile which would give rise to a smaller diameter. A useful criterion from which the film exposure limits could be obtained was available when the luminous diameter was plotted against the peak recorded intensity for several cases over the whole recorded intensity range (fig. 5.5). On fig. 5.5 there are four main regions of interest. The first is the range of diameters for intensity values less than 0.01. The diameters measured in this range were sometimes as low as half the diameters measured for mid-range intensity values. The second range of interest is the mid-range, for intensities between 0.01 and 0.5 in which case the diameter values are virtually constant within the experimental scatter of 10%. This range coincides with the linear region of the film characteristic (fig. 5.3) in which case there is only a slight departure from linearity above 0.3 up to 0.5. Another region exists

where the luminous diameter increases gradually for intensities of 0.5 up to about 0.95 where the film characteristic reaches another saturation limit (fig. 5.3). Beyond this value of intensity the diameters (fig. 5.5) increase assymptotically which corresponds to the fourth region of interest. The assymptotic increase can be explained by the fact that as the intensity of the image on the rear screen of the intensifier increases, the film emulsion which is already in saturation cannot respond to further increases in intensity and the increase in luminous diameter is due to helation effects. Thus the criterion for the film exposure is that the film should not be exposed to an extent that an optical density greater than 2 (transmission factor 0.01) or less than 0.02 (transmission factor 0.95) should be recorded. If this is the case the luminous diameters can be recorded to an accuracy of about 20% or better. An improved accuracy is obtained if the maximum of the exposure is limited to give an optical density of 0.3 (transmission factor 0.5).

5.3.2 The Spectroscopic System

The diameter of the arc which each segment represents was calculated after illumination of the vidicon target using the flashgun source as described in section 5.2.2. The results of section 5.3.1 were used as the object (the flash source) luminous diameter. The dimension of arc diameter which each segments represents is summarised in table 5.2 which shows the segment to be representative of 1mm of arc

diameter.

The accuracy of the monochromator wavelength calibration was tested as described in section 5.2.2 using the low pressure mercury source. The results of this investigation are summarised in table 5.3. They show generally good agreement with the lamp manufacturers specifications thus indicating that the monochromator wavelength calibration is indeed accurate.

The results of the investigations of the system spectral response characteristics are presented in fig. 5.6 where a comparison is made between specified spectral output of the lamp (for a colour temperature of 2,000K) and the observed response which was corrected by taking into account the individual spectral responses of the optical system components. These components included the camera response, the neutral density spectral characteristic, the blaze characteristic of the monochromator grating and the cut-off due to the glass windows. This calibration was performed over a wavelength range of 300 to 700nm. No results were obtained below a wavelength of 400nm since insufficient light was detected by the vidicon camera and the normalised spectral radiance value using glass optics is of the order of 10^{-15} at 350nm. There seems to be poor agreement between the two curves at a wavelength of 400nm but this is due to the fact that both sets of radiance values are very low in this range. Better agreement (within 25%) is evident over the rest of the wavelength range which is good when the cumulative errors

due to uncertainties in manufacturers specification of individual components (e.g. NDF's) are considered. Thus the system spectral response was by no means linear but was significantly accurate over the wavelength range required for testing purposes.

A detailed investigation was undertaken to examine any deliterious effects upon the camera response when it was operated in the gated mode. Although intense electrical interference was detected on the video output of the vidicon camera at the instant of application of the gate pulse, this was not found to be significant provided the gate pulse was applied during the camera fly-back period (chapter 4.6.3). The camera operation necessitated the application of the gate pulse during this period and it could not be applied at any time during the scan since interference of the nature shown in fig. 5.7(a) would be present. No noise from the peripheral electronic units was present in either continuous or gated modes.

Some noise was present on all records and was due to the operation of the electro-mechanical shutter which caused microphonic pick-up by vibrating the electron gun of the vidicon tube. This manifested itself in regular low amplitude oscillations on the baseline of the video signal. A typical record including this noise is shown in fig. 5.7(b) which represents a typical Cu I arc spectrum (λ_c = 521.8nm).

On most experimental test records this noise was found

to contribute less than 10% to the true signal.

The arc itself proved to be an additional source of interference. This manifested itself on the video output signal by distorting the baseline as shown in fig. 5.8(a). This shows two regions of distortion, the first being on the left hand side of the record where, in the presence of the arc the baseline level is lowered gradually as the left extreme is approached. The second region of interest is a more severe dip in the baseline which occurred at the right extreme of the records. Fig. 5.8(b) shows a typical arc spectrum which was subjected to the interference described above. The intensities (height) of the spectral lines in this case was unaffected by the distortion of the baseline described above. The spectrum of figure 5.8(b) was corrected by superposition of the correction spectrum (fig. 5.8(c)) and the result is shown in fig. 5.8(d). For the purpose of experimental tests, the wavelength setting was thus selected so that the spectral lines occupy a spectral range outside the influence of the above mentioned distortion.

5.4 Conclusions

The magnification factors for both the spectroscopic and photographic optical system were carefully deduced and were sufficiently accurate for the measurement of the small luminous arc diameters which occur close to current zero.

Measurement of the luminous diameter and recorded intensity of the flashgun source on the type 46L film showed

that little or no effects from such factors as film emulsion saturation occurred, provided the exposure required to give a peak recorded intensity on the film between 0.01 and 0.95. Thus system parameters such as image intensifier bias and NDF value could be varied and provided the range of film exposure was ensured any intensity or diameter variations observed could be attributed to variations due to the source alone.

In addition to the useful intensity-diameter criterion, the required gain setting for the image intensifier could be predicted for a known attenuation or amplification in light intensity.

The wavelength calibration of the spectroscopic optical system and in particular the monochromator showed the optical system to be accurate in wavelength determination for the range in question (365nm to 546nm). The optical system had a measured spectral response which was consistent with that expected from specifications of the individual system components in the wavelength range 300 to 700nm.

Interference from the arc or any other source was not present on any operating conditions. Some microphonic pick-up was present on the spectroscopic records but this could be eliminated by averaging (e.g. in the continuum estimation of the 'OSPLT3' program of appendix 2) and was of insufficient amplitude to seriously effect the spectral data. Interference caused by the arc was present but could

be compensated for by superposition techniques. Furthermore this type of interference did not affect the intensity level of a given recorded spectral line above the continuum level, and therefore caused no additional errors in the subsequent temperature estimation.

Thus, a detailed calibration procedure has enabled the limitations and overall response characteristic of the two principal optical systems employed in the arc diagnostics described in this thesis to be determined. As a result a high degree of confidence may be placed on the results obtained with both the photographic and spectroscopic systems.

LIST OF TABLES

Measured Separation of Calibration Wires = 5mm

Separation Measured on Microphotometer = 35mm

Magnification of Microphotometer = 15mm

Optical Magnification = $5 \times \frac{15}{35}$ = 2.15

Table 5.1(a) Optical Calibration of Arc Diameter Measurements in the Reduced Power Arcing Case

Measured Width of Calibration Slot = 5mm

Luminous Width (On Microphotometer) = 21.8

Optical Magnification = $5 \times \frac{21.8}{35}$ = 3.11

Table 5.1(b) Optical Calibration of Arc Diameter Measurements using a Test Slot and the Flashgun for the Full Power Arcing Case

Luminous Diameter of the Flash Tube = 11mm
(Section 5.3.1)

Number of Segments into which the Vidicon target was divided = 30

Number of Segments Illuminated = 20

Proportion of the Diameter of the Test Object (the Flashgun) Viewed by each Segment= $\frac{11}{20}$ = 0.55mm

($\pm$ 0.05mm

Number of Segments into which the Vidicon target was divided for Viewing the Arc = 15

Proportion of the Arc Diameter Viewed by each Segment = 0.55 x 2

= $\underline{1.1\text{mm}}$
$\pm$ 0.1mm

Table 5.2 Optical Calibration of Arc Diameter to Enable Radial Resolution of Arc Spectra

Specified Wavelength (nm)	Observed * (Y or N)
3650	Y
3654	Y
3663	Y
4047	Y
4358	Y
5460	Y

* Line was observed in region close to the centre of the screen of the WPI.

Source of Specified Wavelengths:

Data Sheet For Mercury Source

Table 5.3 Calibration of the Monochromator using the Mercury Source

LIST OF FIGURES

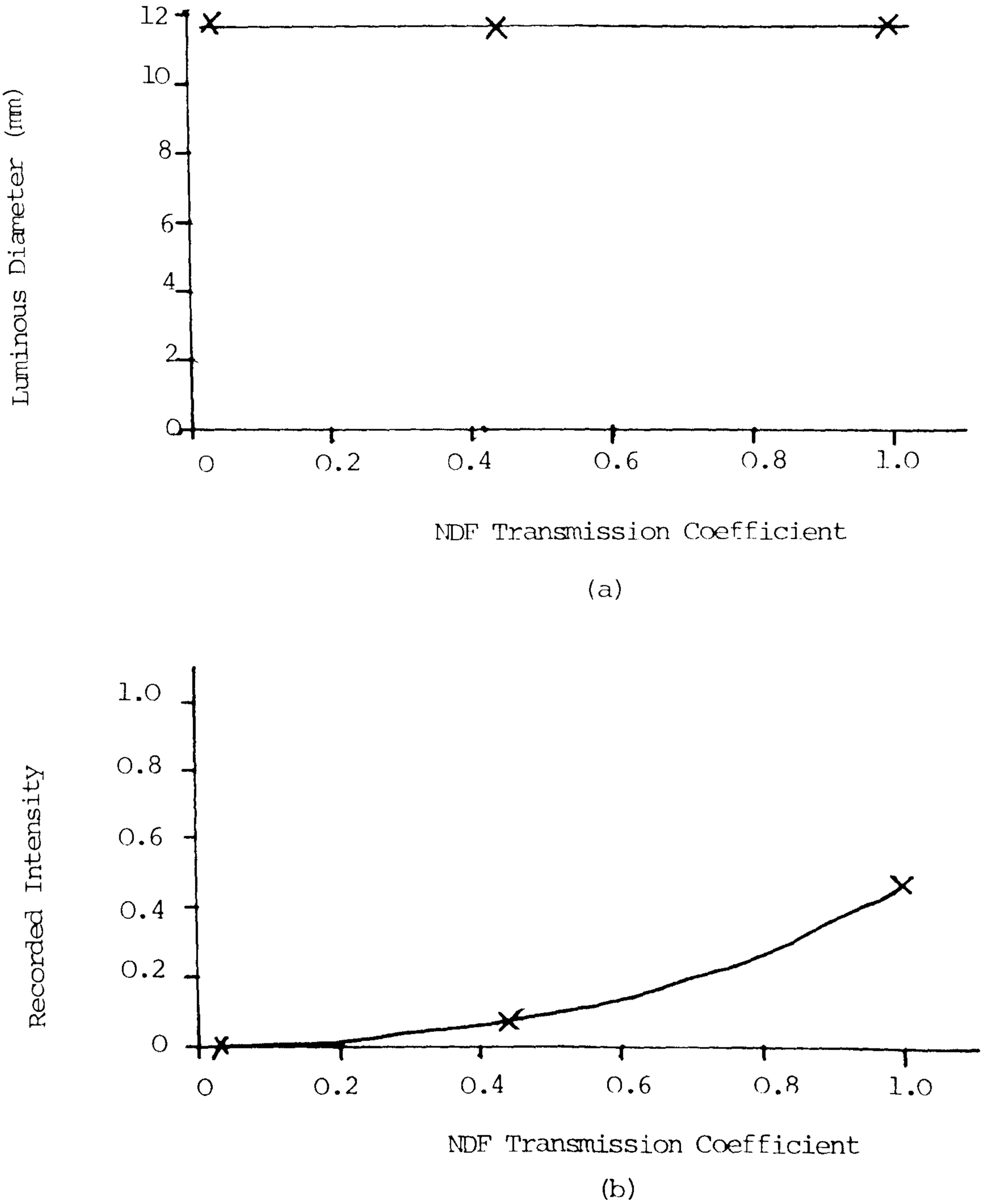

Fig. 5.1 The Effect of Using Different Valued Neutral Density Filters upon the Final Image Characteristics:

(a) Luminous Diameter
(b) Recorded Intensity

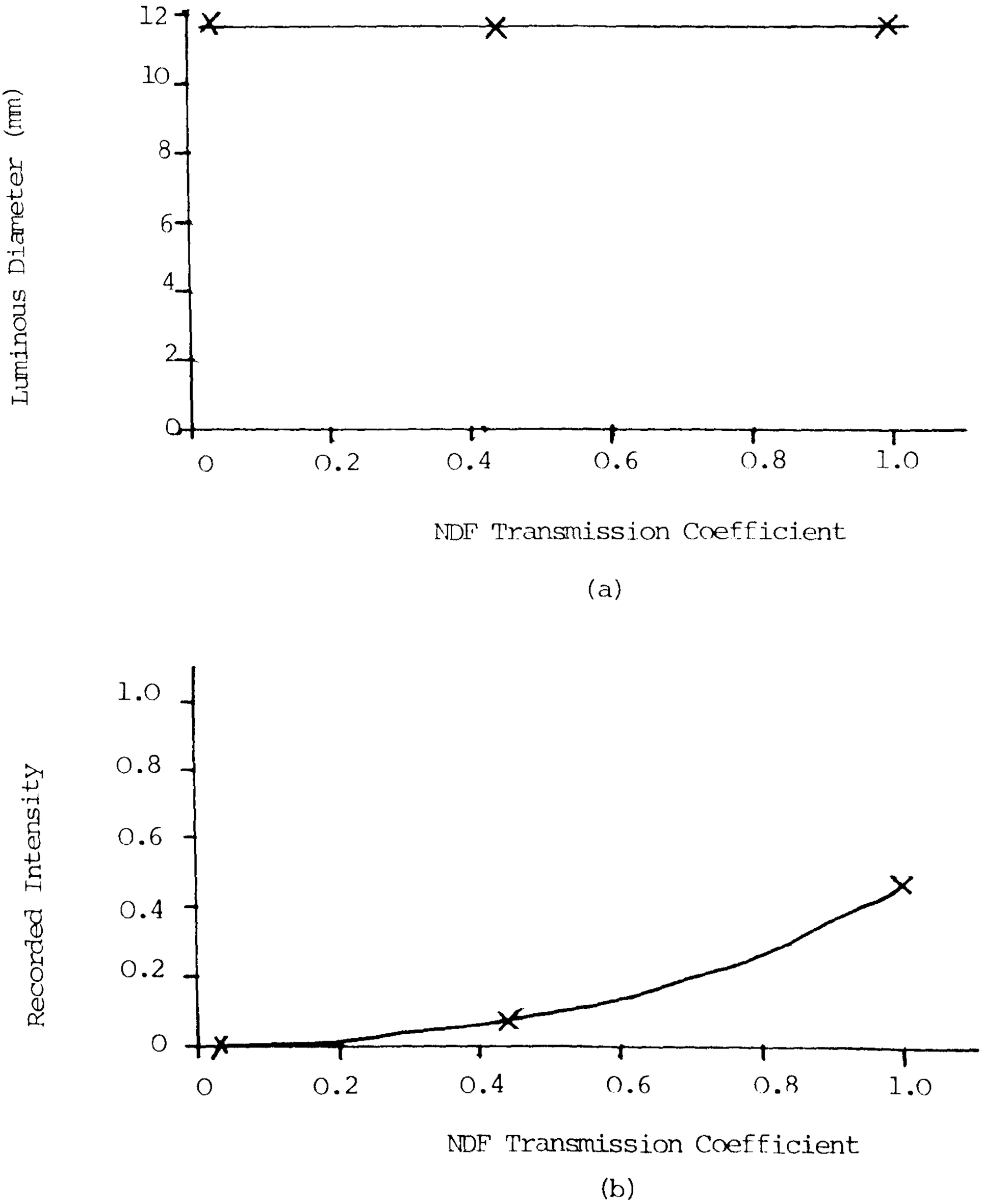

Fig. 5.1 The Effect of Using Different Valued Neutral Density Filters upon the Final Image Characteristics:

(a) Luminous Diameter
(b) Recorded Intensity

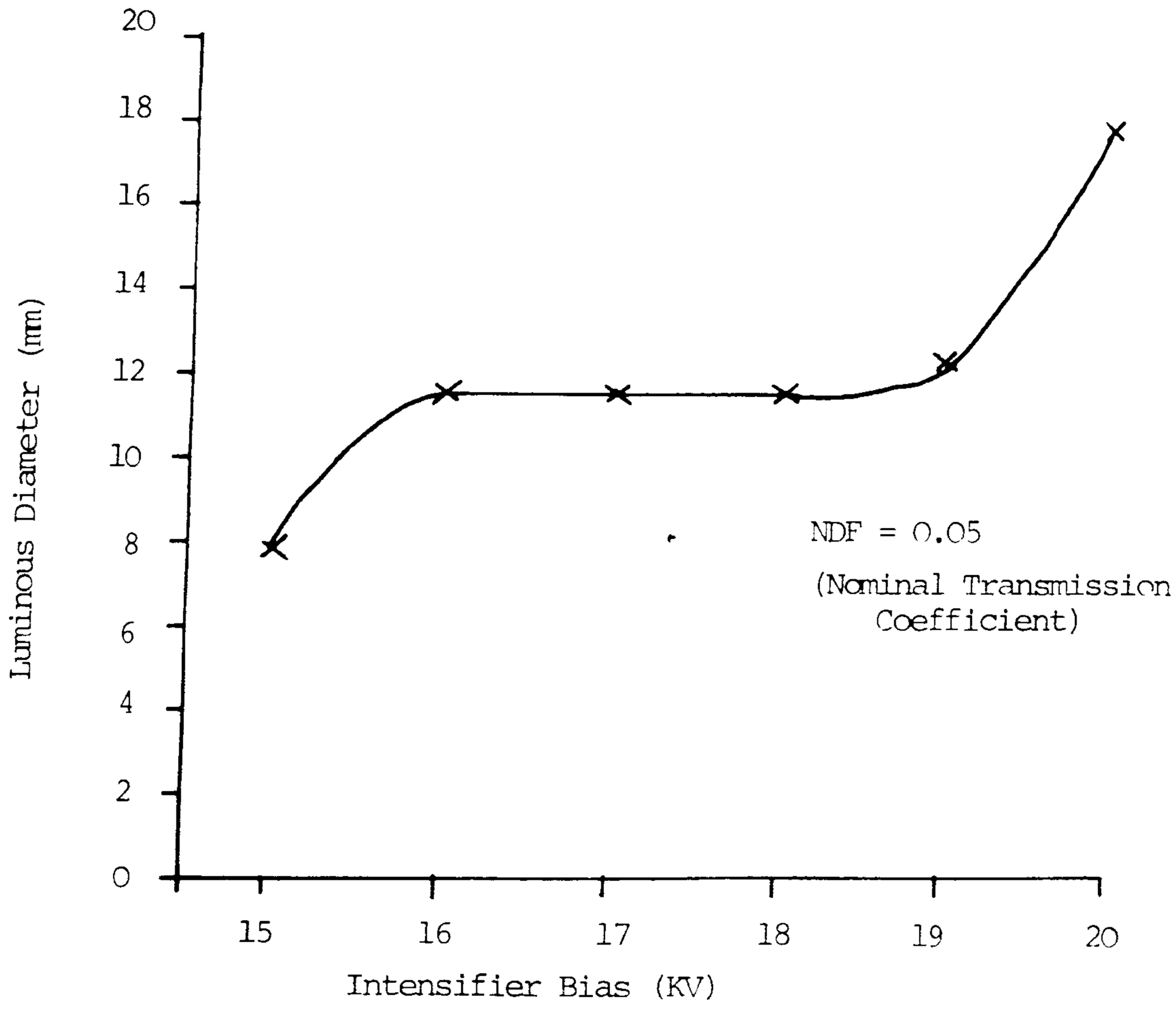

Fig. 5.2 (a) The Flash Source Luminous Diameter Variation with Image Intensifier Gain

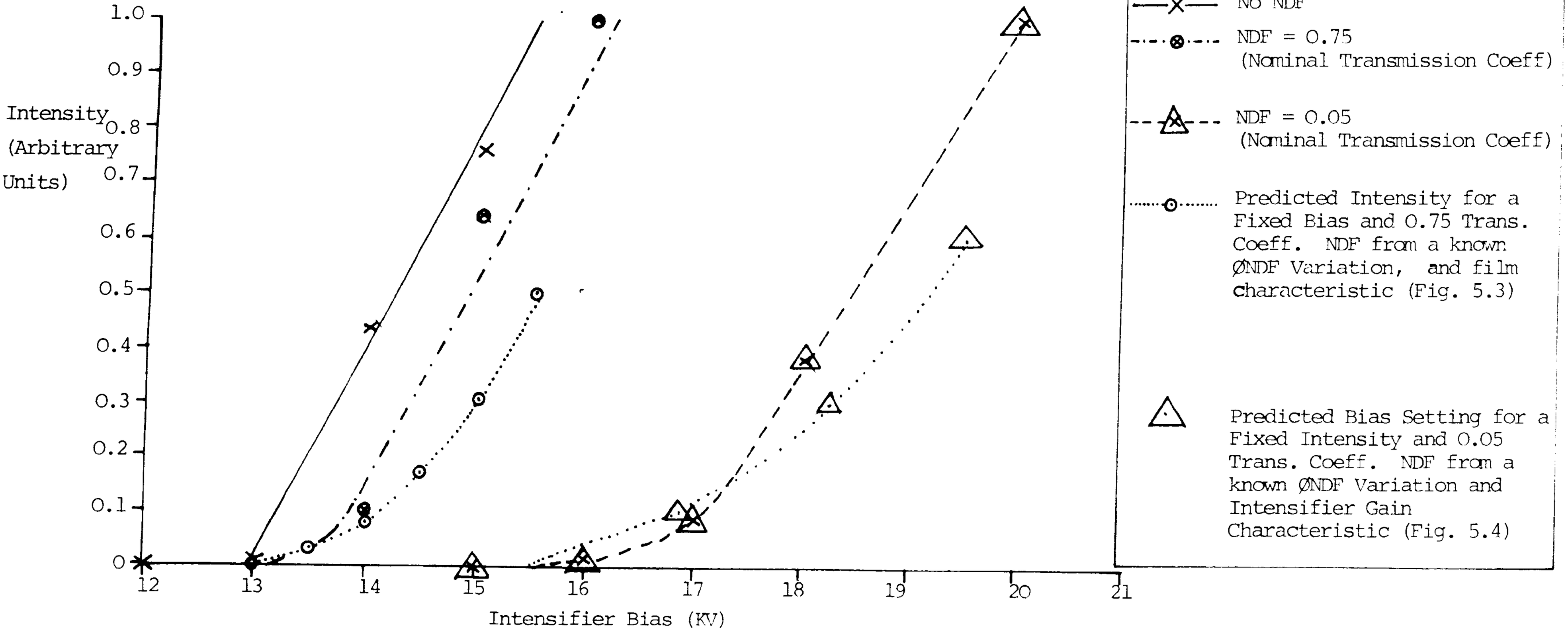

Fig. 5.2 (b) The Recorded Intensity Variation with Image Intensifier Gains for Different NDF Valves

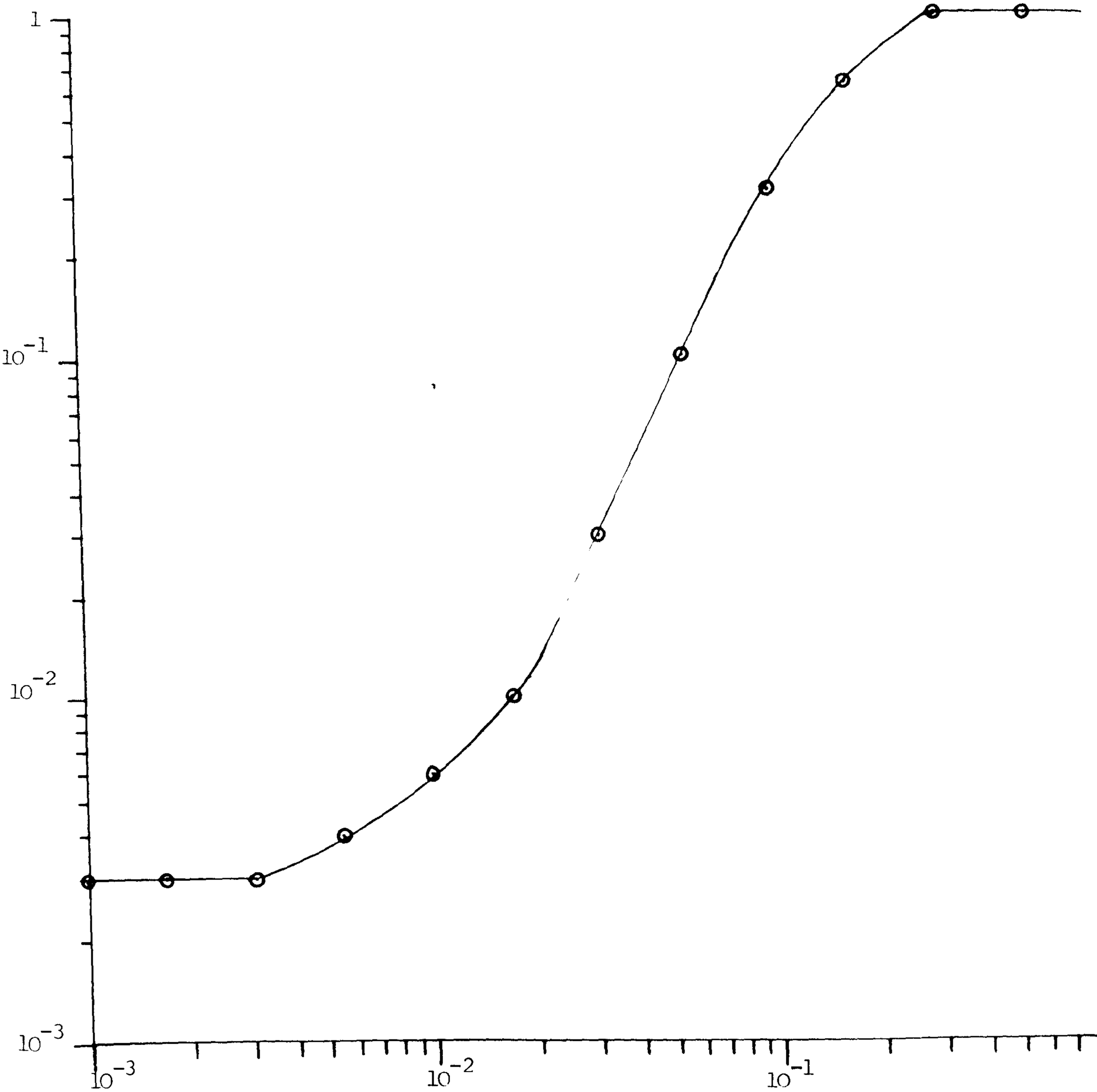

Fig. 5.3 Characteristic Curve of the Polaroid Type 46L Film

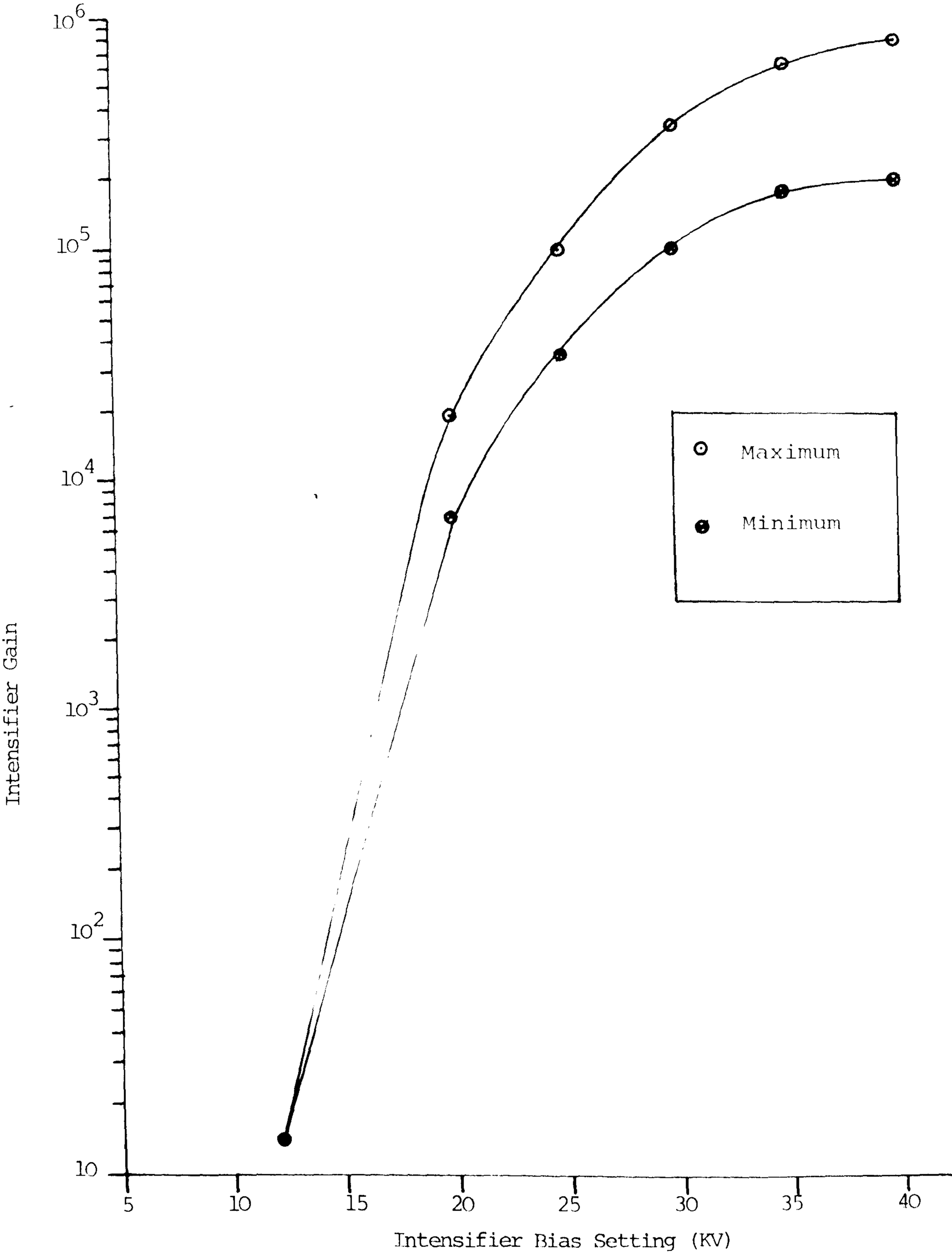

Fig. 5.4 The EMI Type 9914 Image Intensifier Gain Characteristic

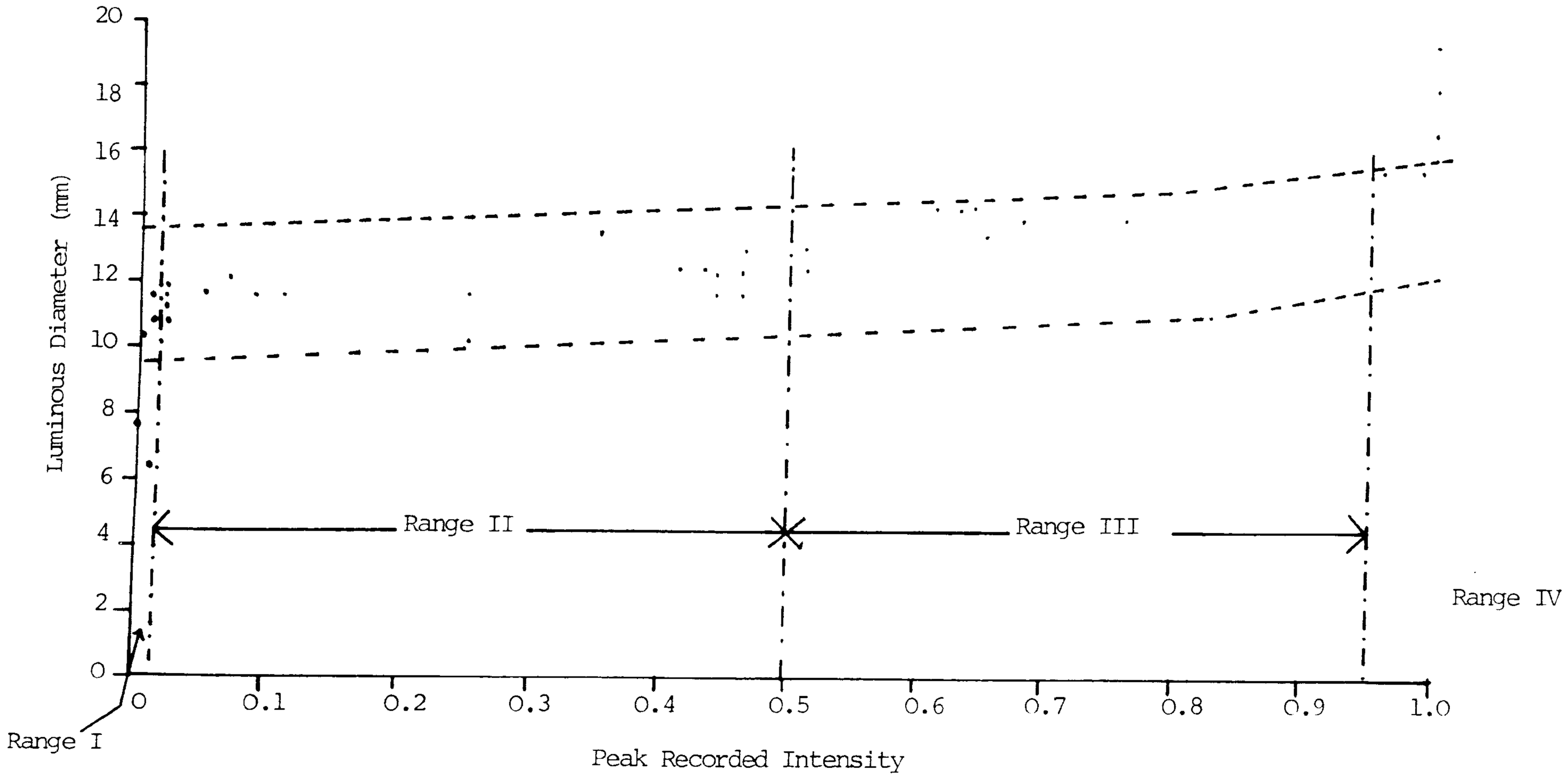

Fig. 5.5 Correlation of Luminous Diameter with the Peak Recorded Intensity

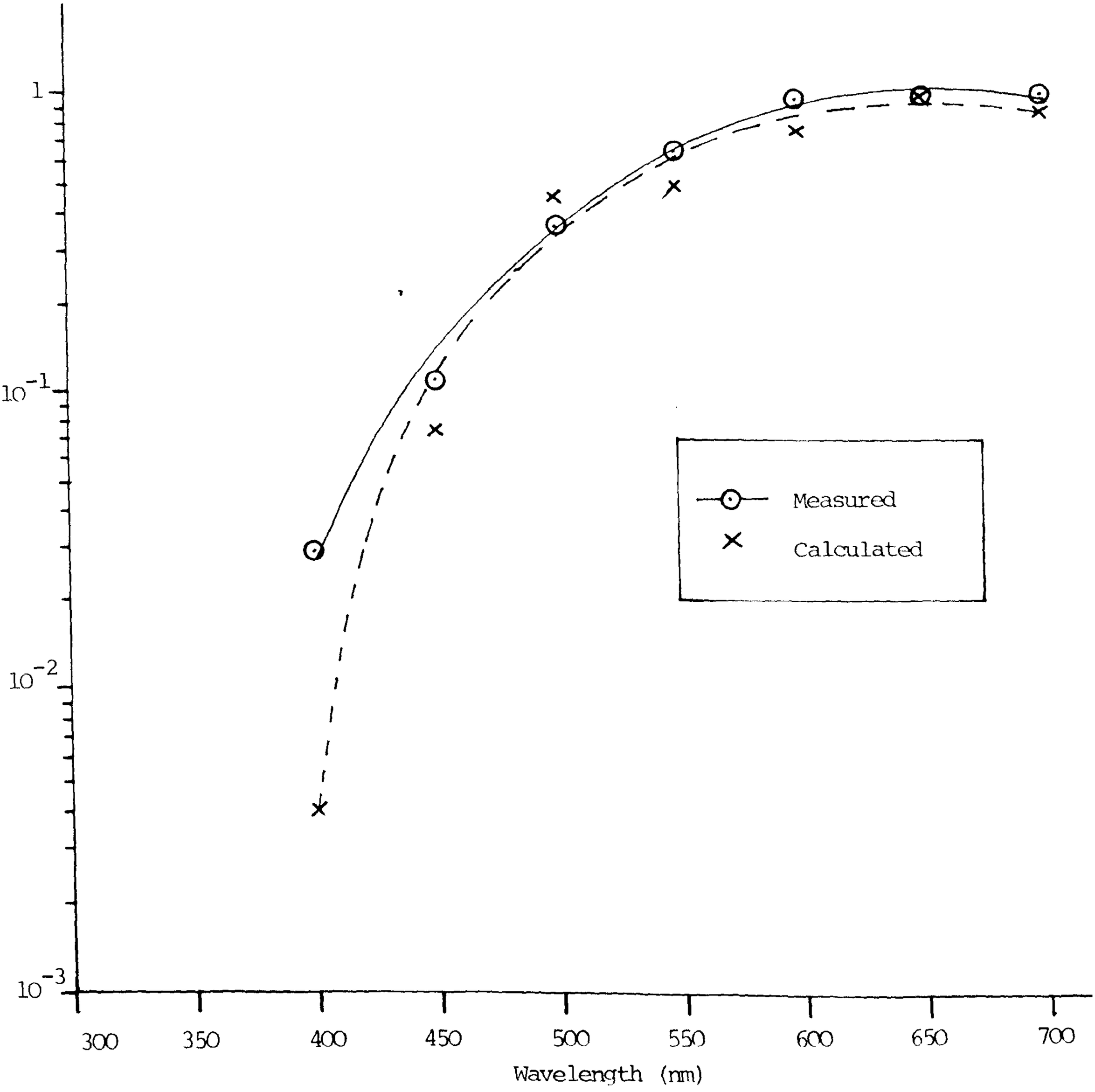

Fig. 5.6 Comparison of the Measured and Calculated Spectral Response of the Spectroscopic Optical System using a Tungsten Lamp Source

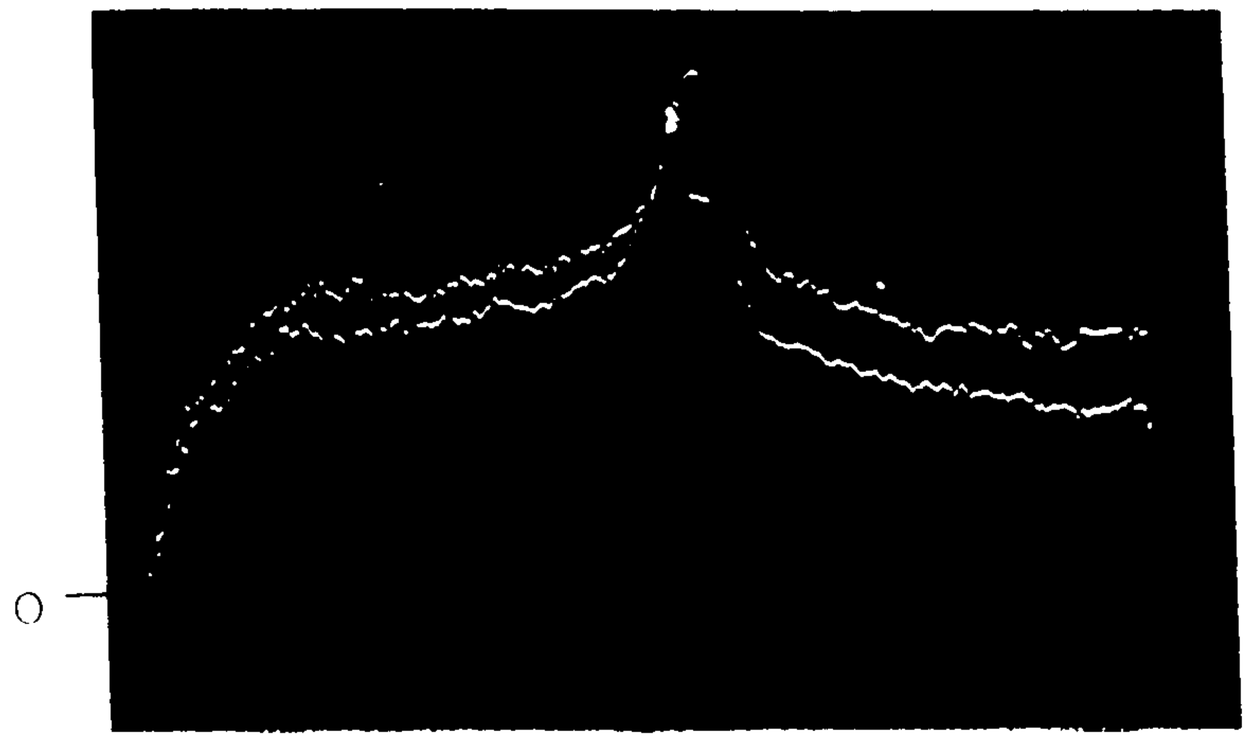

(a) Interference Caused by Incorrect Timing of Vidicon Gate Pulse

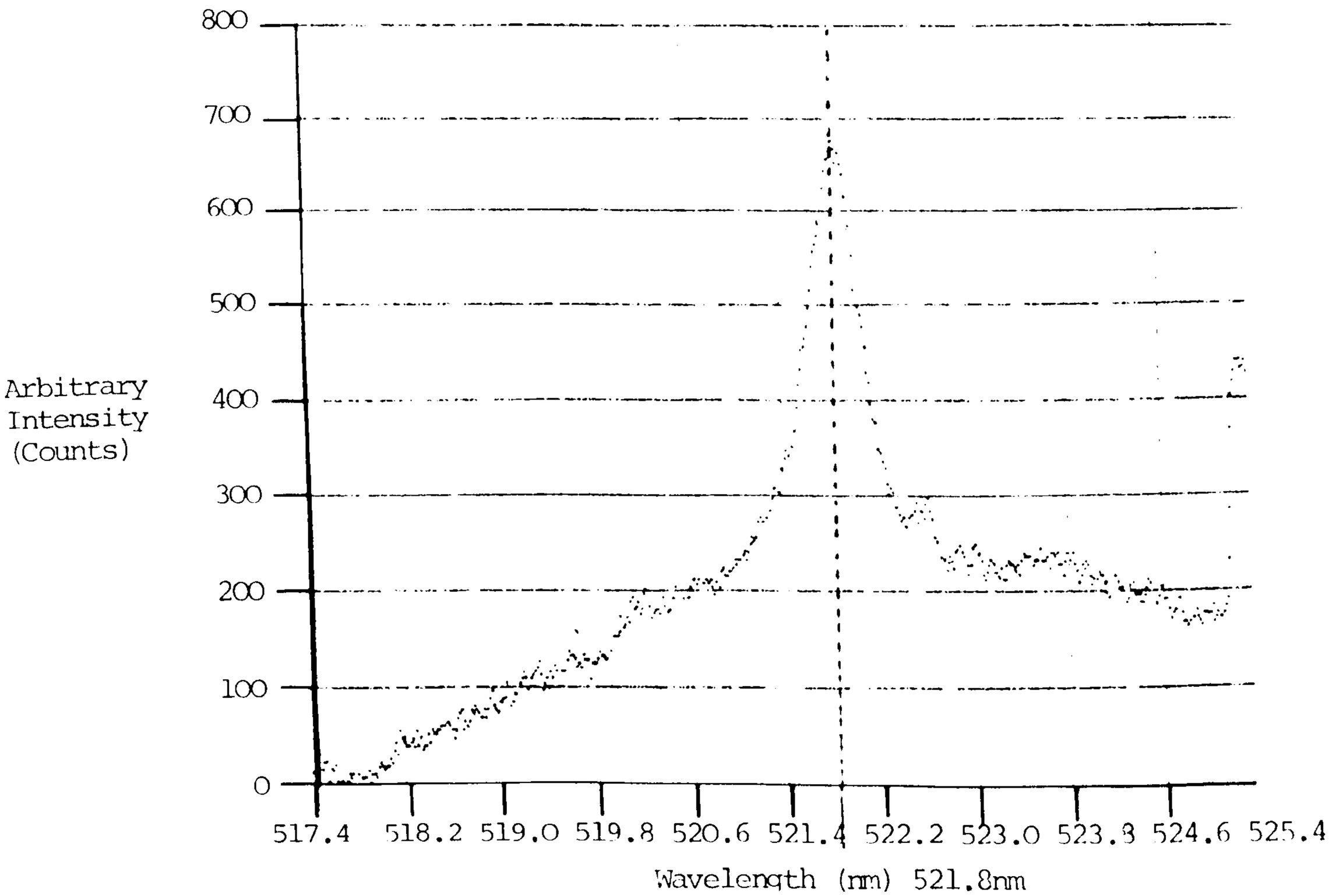

(b) Microphonic Pickup Caused by Operation of Mechanical Shutter

Fig. 5.7 The Effect of Sources of Interference within the Optical System upon the Vidicon Output

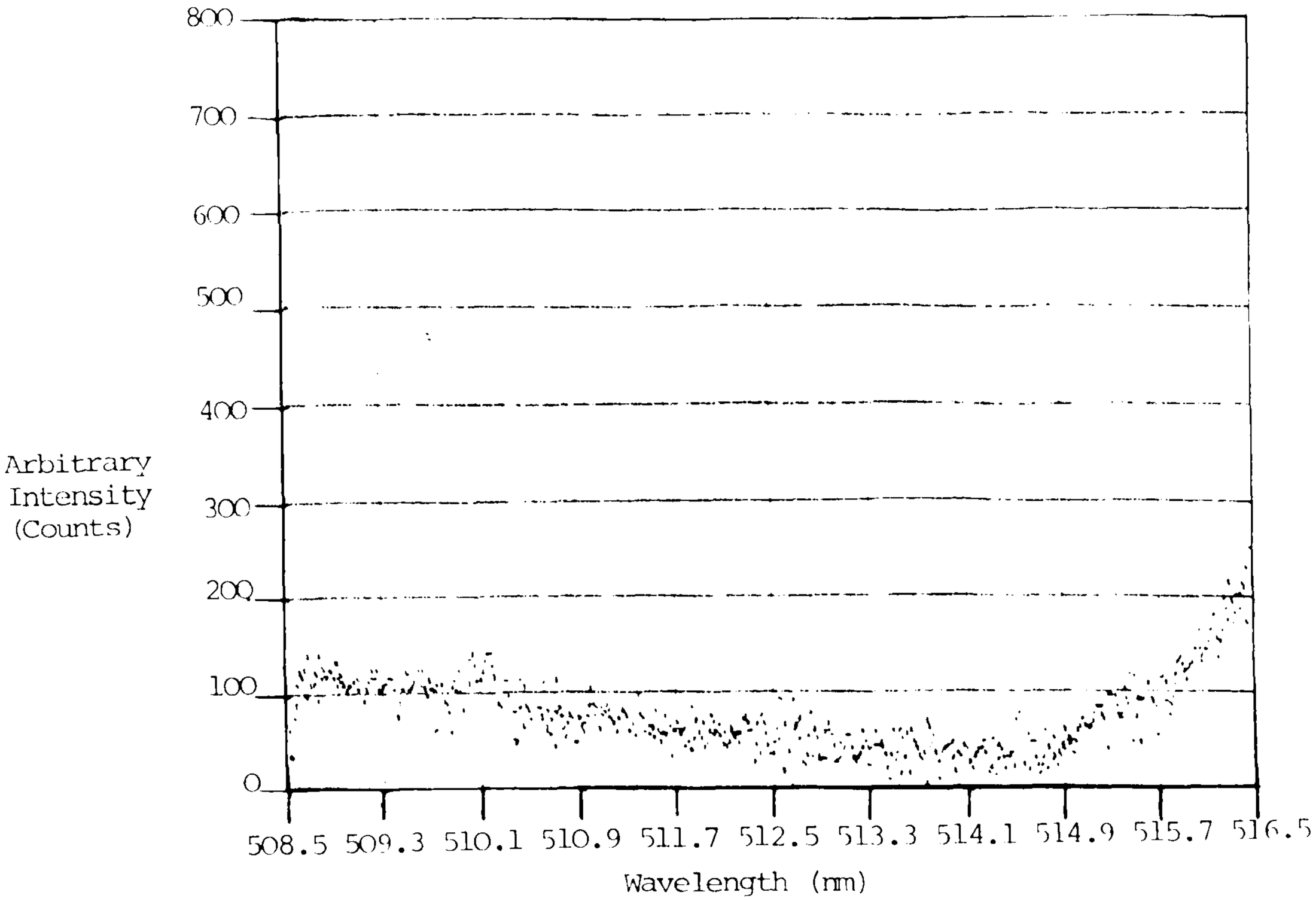

(a) A Noisy Low Intensity Spectrum

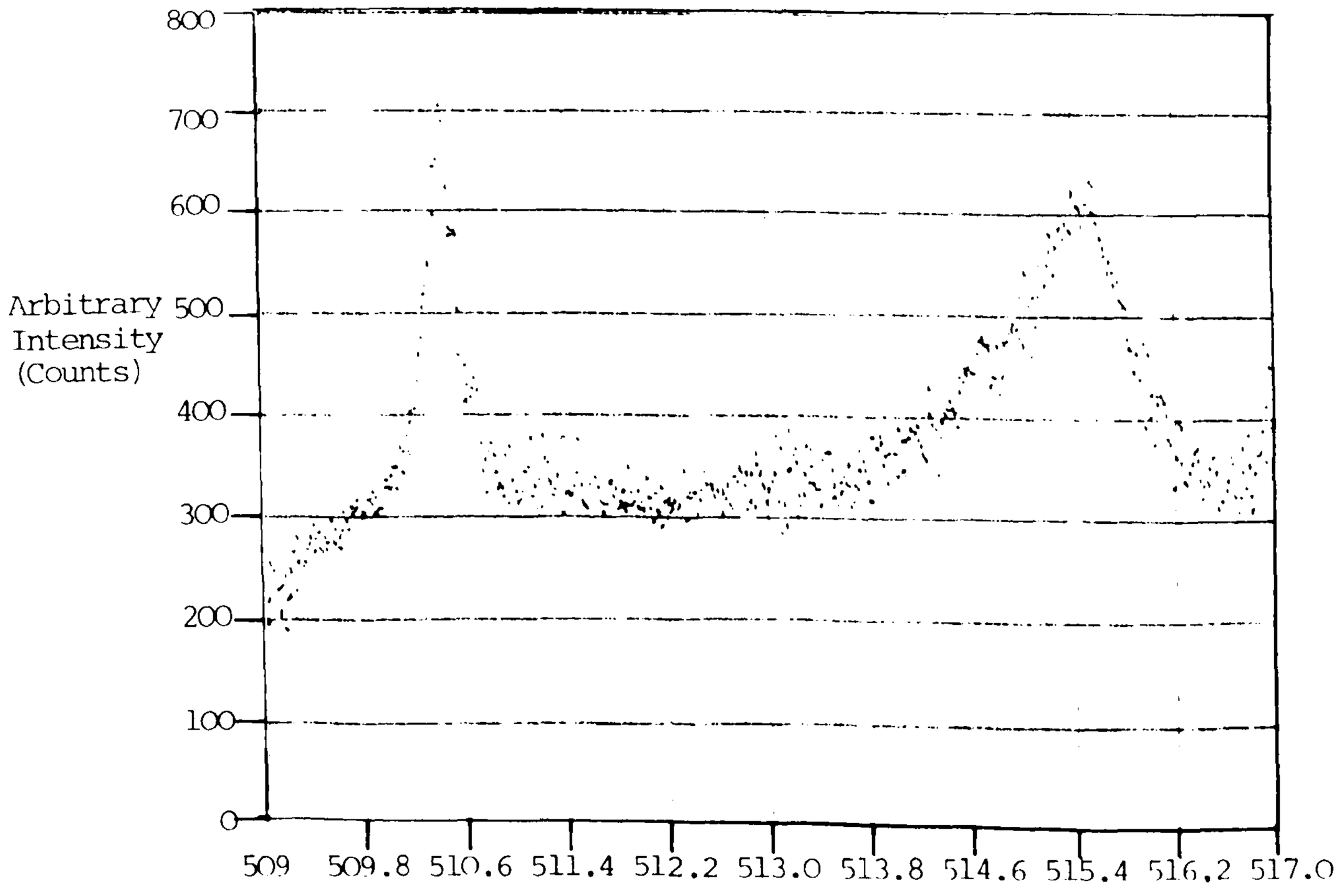

(b) A Noisy High Intensity Spectrum

Fig. 5.8 The Effect of Noise Caused by the Arc upon the Vidicon Output

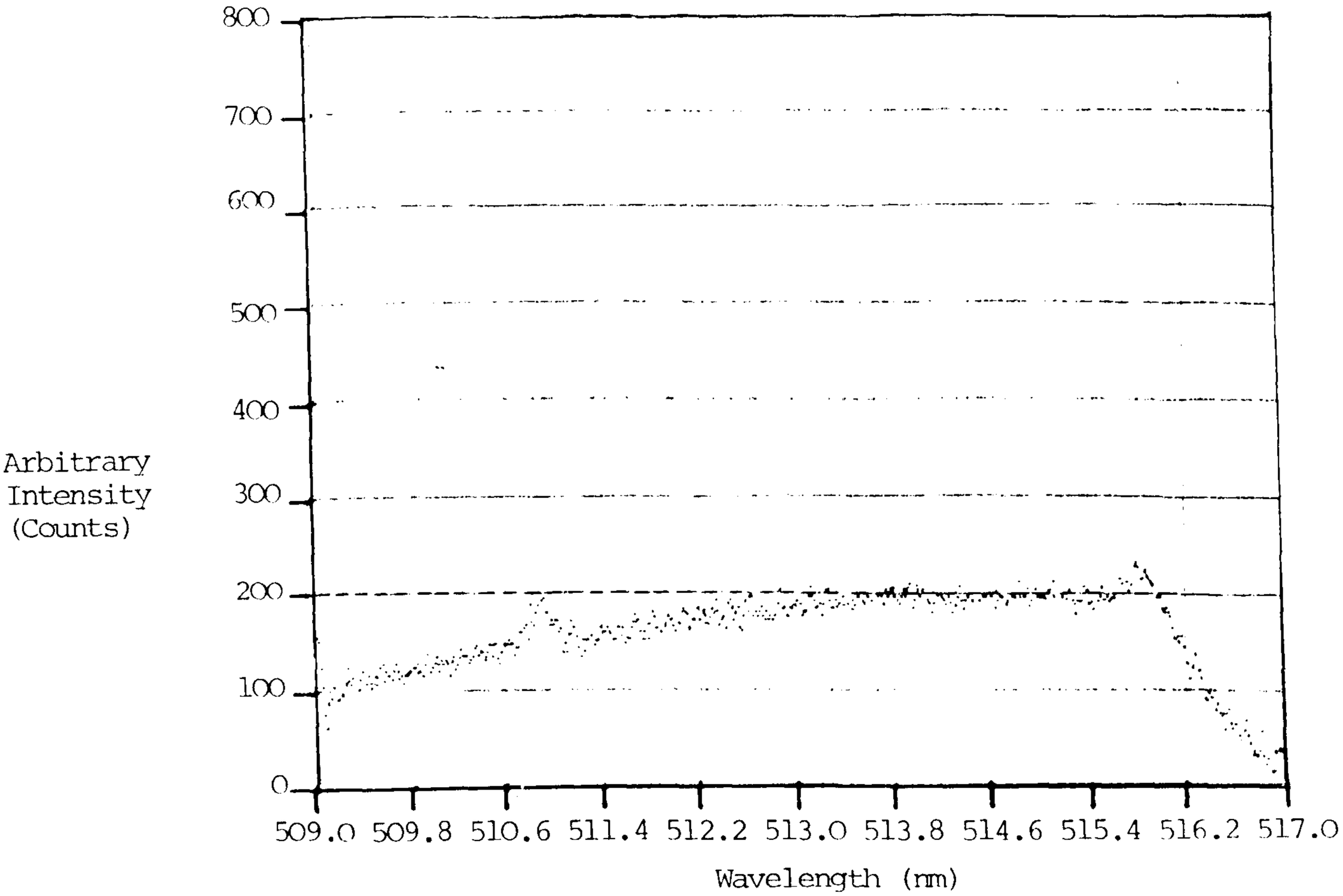

(c) The Correction for Arc Induced Noise

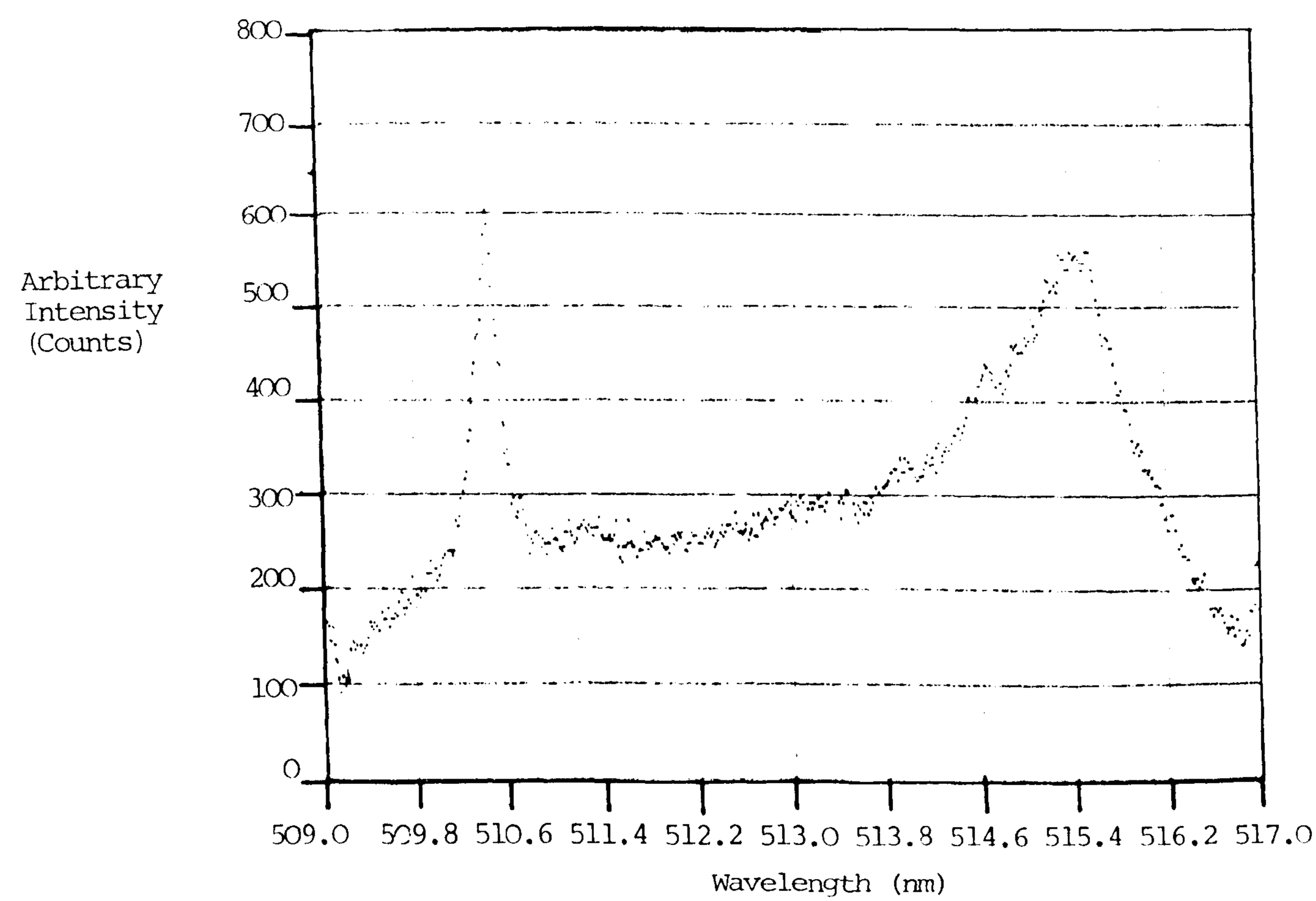

(d) Spectrum (b) Corrected Using (c)

CHAPTER 6

ARC COLUMN PHENOMENA OBSERVED EXPERIMENTALLY DURING THE CURRENT ZERO PERIOD

6.1 Photographic Results

6.1.1 Introduction

High speed photographs of the decaying luminous arc column during the current zero period are presented. Observations were made of the variations in diameter and radial intensity distributions throughout the current zero period of both the full and reduced power arcs. In some cases problems were encountered in observing the entire arc length simultaneously since for some conditions the light levels from the upstream portion of the arc could be at least one order of magnitude greater than from downstream. In these cases the arc photograph was slightly over exposed at the portion of the image corresponding to upstream before and after current zero (in the case of reignition) so that the correct exposure conditions were obtained close to the current zero instant.

Experimental results are reported for a wide range of operating conditions which are summarised in table 4.I. Simultaneous records of current and voltage are also presented in some cases.

6.1.2 Observations made with the Reduced Power Arcing Facility

(i) The Temporal Variation of the Luminous Arc Cross-Sectional Area, Peak Light Intensity, Arc Current and Voltage over the Major Part of the Current Ramp

The time variations of the arc voltage and current are shown on fig. 6.1(a) together with the high speed photograph corresponding to that particular test (fig. 6.1(b). The arc column cross-section and relative axial light intensity measured from fig. 6.1(b) for a 60μs interval encompassing the instant of current zero are shown on fig. 6.1(c) and (d) respectively. The condition shown corresponds to a holding current of 1.6KA, a current decay rate of 40A/μs and with an elkonite upstream electrode. The rate of rise of recovery voltage after current zero was sufficient to ensure efficient arc reignition.

Fig. 6.1(c) shows that substantial fluctuations occur in the arc diameter during the current decay. The period of these oscillations is typically 20 to 30μs which is similar to that reported by Walmsley et al (1978(i)) during the current zero period of an 8KA arc in air. This phenomenon will be further discussed in chapter 8. Corresponding fluctuations in the light intensity (fig. 6.1(d)) were also consistent with the simultaneous total radiation loss measurements of Shammas and Jones (1982). The amplitude of these oscillations varies with axial position but no phase difference is apparent between the occurrence of the oscillations at the various axial positions.

These oscillations of arc cross-section are superimposed upon a general decrease as the arc sustaining current decays to zero. The decay is gradual until about 5 to 10μs before current zero when a more substantial collapse occurs. Note also that before current zero the arc diameter at slot 3

is somewhat less than the diameter at slot 2, both being significantly less than the diameter at slots 4 and 5. Furthermore, the diameters at slots 3 and 4 increase more slowly after current zero (particularly at slot 4 at which there is a pause before a rapid rise occurs after about 15μs.

The light intensity from the arc column segment also decays with current and shows oscillations of the same period as the arc diameter oscillations (fig. 6.1(d)). Slot 3 appears to be the least intense during the current zero period in the case of an Elkonite electrode and exhibits a similar variation to the other downstream slots during the current decay. Slot 2 which is located nearest the nozzle throat exhibits very low intensity close to the current zero instant but prior to that the intensity is high and comparable to that at slot 1. The rapid intensity decay occurs over the final 5 or 10μs before current zero.

During reignition the light intensity at all slots recovers more rapidly than their respective diameters. This effect is important in describing the reignition behaviour of switchgear arcs and will be discussed in detail in chapter 8.

Whereas the mean arc areas at the axial positions corresponding to slots 2, 4 and 5 vary proportionally with current, the arc area at slot 1 merely fluctuates about a mean value except perhaps within a few microseconds of current zero. This reflects the extent to which a plasma

volume is sustained in front of the upstream electrode.

(ii) <u>The Temporal Variation of the Luminous Arc Area, Peak Light Intensity, Arc Current and Voltage During the Current Zero Period</u>

The timewise variation of the current and voltage close to current zero is shown in fig. 6.2(a). The high speed photograph corresponding to the oscillogram of 6.2(a) was taken with an exposure of 200ns and a framing speed of 1×10^6 f.p.s. and is shown in fig. 6.2(b). The operating conditions for this photograph correspond to a $^{di}/_{dt}$ of 13A/μs, a $^{dv}/_{dt}$ of 0.5 KV/μs, a holding current of 1.6KA and with an elkonite upstream electrode.

Fig. 6.3(a) to (d) show the variation of cross-sectional area, light intensity and current with time close to current zero for a holding current of 1.6KA, an elkonite upstream electrode and $^{di}/_{dt}$ in the range 32 to 36A/μs. Optical results are shown for slots 1, 2, 4 and 5 and the influence of restrike voltages after current zero of 0.07 to 0.31KV/μs is shown.

Figs. 6.3(a) and (b) show results under clear and fail conditions respectively when no optical filter was incorporated in the system. These results are indicative of the shot to shot variation which can occur during the pre-current zero period, as well as the fluctuations which can occur in the luminous arc area and axis intensity during the 10μs or so of observation. The latter fluctuations are of an oscillatory nature and have a period which varies between 2 and 4 μs. The cause of these fluctuations is most

likely to be associated with plasma pulsation effects which will be discussed in further detail in chapter 8.

The 2 to 4 μs oscillations could only be detected when the 1 x 10^6 framing unit was used which enabled 1 frame per microsecond and a 200ns exposure to be achieved over a 10μs interval. The statistical variations in arc diameter which result from these oscillations produce a substantial uncertainty in the estimated mean diameter. This was found to be particularly acute at slot 5, the furthest downstream.

The results of fig. 6.3(c) show that when a significant post arc current flows the arc diameters respond vigorously. For the case depicted in fig. 6.3(c) a narrow band optical filter with a centre wavelength of 521 nm (table 4.II). Although the spectral range of the filter meant that only a very narrow proportion of the light spectrum was viewed the spectral content of the light emitted from the arc suggests that to view the arc diameter at this wavelength (521 nm) was representative of the total radiation emission spectrum. Therefore it is equally feasible to state that the diameter measured in this way is representative of the arc luminous diameter provided the exposures etc. are arranged to be equivalent.

The results of fig. 6.3(a) to (d) show that the oscillations in arc diameter are more pronounced downstream of the nozzle throat. This variation in the oscillatory nature of the arc cross-sectional area with axial position

is consistent with that measured by Dhar et al (1980), although these oscillations were measured over a longer time scale (they had a period of approximately 50μs). If the oscillations are regarded as occurring about a mean line drawn through a set of points then it can be seen from fig. 6.3(a) to (d) that the arc diameter before current zero generally decreases as the current decays. This result is in good agreement with Dhar et al (1980) and Walmsley et al (1978(i)). Generally before current zero the arc diameter nearest the throat region (slot 2) is the smallest of the visible locations. At slot 1 the diameters are generally more stable throughout the pre-current zero period and for a relatively long time afterwards. The pronounced oscillations in luminous area at slots 4 and particularly 5 make it difficult to identify underlying trends but from fig. 6.3(a) to (d) clearly the tendency is for the arc area to collapse during the current zero period. No light was detected in the region corresponding to slot 3 for the results in fig. 6.3(a) to (d). This was most likely to be due to obstructions (e.g. ablated material) in the viewing slot or slight misalignment of the optical system.

Trends are apparent in fig. 6.3(a) to (d) during the post current zero period, particularly when reignition occurs. It is noticeable that when the arc diameters begin to expand following arc reignition they do so at the downstream locations first and also most rapidly. This is particularly true for the case of the results of fig. 6.3(b). In all these cases a luminous region persists after current zero at the region nearest the upstream electrode (slot 1).

Also shown in fig. 6.3(a) to (d) are the temporal variations of the peak relative axis intensity for slots 1, 2, 4 and 5 and the respective operating conditions. Slots 4 and 5 exhibit a generally lower intensity value than slot 2. Taken in conjunction with the diameter measurements this is indicative of a more diffuse arc column in the former locations whereas a brighter, more sharply defined column exists at slot 2. The axial intensity at slot 1 remained consistently high throughout the current zero period in fig. 6.3(a) to (d). Such behaviour is consistent with the observation made from the diameter measurements that a volume of plasma survives in front of the upstream electrode after current zero.

(iii) Radial Light Intensity Distribution During the Current Zero Period

The evaluation of meaningful arc column cross-sections from photographic records requires a steep intensity gradient at the luminous periphery which accurately defines the extent of the arc column. If such a situation does not exist then the alternatives are

(a) to maintain an unchanged optical recording system so that relative values of arc diameters are obtained for comparison of different operating conditions,

and

(b) wherever changes in the optical system operating conditions (e.g. intensifier gain) are made necessary (e.g. an excessive change in the arc luminous intensity) these changes may be correctly compensated such that the same relative standard of arc diameters is obtained. This is possible with the knowledge of the system calibration discussed in the previous chapter.

The latter two conditions (a) and (b) have been satisfied throughout the present investigations but it is also necessary to examine how well the initial criterion (i.e. the profile gradient) is satisfied under the most difficult experimental situation so that absolute, rather than relative, arc diameters can be determined and the general applicability of the diameter values quoted here is established.

Fig. 6.4(a) shows typical radial intensity profiles measured at slots 1, 2, 4 and 5, 2μs before, at and 2μs after the current zero instant for a case in which the arc has reignited. The peripheral intensity gradients at slots 1, 2 and 4 are sufficiently steep for meaningful absolute diameters to be derived, but at slot 5 this criterion is only satisfied to a limited degree. Note that the intensity at slot 5 is less than at slot 4 although the slot 5 diameters are greater than those at slot 4. This is consistent with the deduced diffuse nature of the arc column in this downstream region.

No results for slot 3 are shown on fig. 6.4(a) since no light intensity was recorded photographically. To investigate the intensity profile at slot 3 a record for which the $^{di}/_{dt}$ value corresponded closely to that of fig. 6.4(a) was chosen. The $^{di}/_{dt}$ for the case presented in fig. 6.4(b) is 33.5A/μs and the variation of the radial intensity profile is shown throughout the current zero period at 2μs intervals. Fig. 6.4(b) shows that for the frames in which the arc was visible the peripheral intensity gradients

at slot 3 are sufficient to enable a meaningful arc column diameter to be identified.

Figs. 6.4(a) and (b) also extend into the post current zero period. In the case of 6.4(a) the arc eventually cleared following a passage of some post arc current (fig. 6.3(a)) and the intensity profiles eventually collapse after current zero. However, in the case of 6.4(b) arc reignition occurred. The evolution of arc column reformation is of particular interest. In this case the intensity profile immediately after current zero appears steeper than it was prior to current zero. Furthermore, on the onset of reignition it is the axis intensity which grows very quickly rather than the luminous diameter (fig. 6.4(c)). This rapid growth in axis intensity is followed by a more gradual increase in luminous diameter. This growth pattern provides vital information as regards to arc reignition which will be further discussed in chapter 8.

(iv) <u>The Influence of Different Operating Conditions upon the Collapse of Arc Cross-Sectional Area during the Current Zero Period</u>

Results for various operating conditions are shown in fig. 6.5(a) and (b). Fig. 6.5(a) shows the influence of the initial holding current (1.6 and 0.35 KA) and the current decay rate (35A/μs and 15A/μs) for an elkonite upstream electrode whilst fig. 6.5(b) shows the influence of the same parameters for a carbon electrode.

Despite shot to shot variations and diameter oscillations the results shown on fig. 6.5(a) and (b) indicate little

effect of holding current but a distinct effect due to the current decay rate. No substantial overall effect due to the upstream electrode material is evident although the arc at slot 3 was visible with the carbon electrode but not in the case of the elkonite electrode. As stated previously the lack of visibility of the arc column at slot 3 was probably due to a slot obstruction or partial misalignment of the optical system.

Fig. 6.5(a) (i) and (iii) allow the influence of a 0.3 optical density (= 0.52 transmission factor) neutral density filter to be observed. These results show that within the large experimental scatter, the measured arc diameters are not drastically affected when the incident light intensity is attenuated.

Fig. 6.5(a) (i) and (ii) and 6.5(b) (i) and (iii) correspond to conditions of critical reignition and in all cases the delayed response of the arc cross-section is apparent.

(v) <u>The Variation of Arc Cross-Sectional Area and Peak Light Intensity at the Current Zero Instant with $^{di}/_{dt}$</u>

The influence of $^{di}/_{dt}$ upon the arc column at the current zero instant may be examined through the luminous diameter and the peak light intensity. The results shown in fig. 6.6 give the variation of current zero arc diameters at various axial positions with $^{di}/_{dt}$ for both carbon and elkonite electrodes. These results represent mean values and so exclude the substantial oscillations which can produce shot to shot variations. As a result clear behavioural

trends are apparent.

For an elkonite upstream electrode the detailed variation with $^{di}/_{dt}$ of arc diameter at current zero depends upon axial position. At the downstream locations corresponding to slots 4 and 5 the arc diameter is relatively insensitive to $^{di}/_{dt}$ within the experimental uncertainty. The slot 5 diameters are in the range 3 to 5mm and the slot 4 diameters are virtually constant at about 3mm. At slot 3 no current zero diameters were detected below a value of $^{di}/_{dt}$ between 29 and 34A/μs. Above this range the arc column becomes visible and increases with $^{di}/_{dt}$.

The arc diameter at slot 2 increases with $^{di}/_{dt}$ throughout the whole range of observation and increases in value from 2 to 3mm. The arc diameter at slot 1 shows a similar increasing trend between 2.8 and 4.5mm.

The variation of current zero arc diameters with $^{di}/_{dt}$ and with carbon as the upstream electrode material is similar to the elkonite electrode case throughout the current decay rate range at slots 1 and 2. However, at slot 3 with carbon, the arc column was detected at low $^{di}/_{dt}$ and increases from about 2 to 3mm over the $^{di}/_{dt}$ range. The arc diameters at slots 4 and 5 are similar for carbon and elkonite electrodes at the higher $^{di}/_{dt}$ values, but the arc column with the carbon electrode was not detected at the lower $^{di}/_{dt}$.

Thus, the only substantial difference between the carbon and elkonite electrode results arises from the invisibility

of the arc column for some different conditions for the two electrode materials. This strongly suggests that the absence of a visible column is associated with an eclipse of the arc light due to an external agency rather than a genuine arc column effect.

The variation of axial light intensity at current zero with $^{di}/_{dt}$ is shown in fig. 6.6(b) for the case of an elkonite upstream electrode. These results show a substantial increase in light intensity at slots 1, 2, 4 and 5 over the $^{di}/_{dt}$ range investigated. This result is consistent with the simultaneously measured total radiation power loss (Shammas and Jones, 1982) which showed similar changes in the total radiation loss at slot 3 over the same $^{di}/_{dt}$ range.

(vi) Results Summary

The results presented above constitute a study of the transient variation of the luminous arc diameter during the current zero period. The effect of various operating conditions such as current decay rate and upstream electrode material has also been studied. All the results were gathered for the case of reduced power arcing where the arc current has been held at a relatively low steady value (up to 2KA) before being ramped to zero to simulate the current zero period of full power arcing.

The purpose of the reduced power investigation was to establish the general trends concerning performance and arc column features without including some of the complicating

factors incurred by full power arcing e.g. nozzle blocking. Therefore having conducted a detailed photographic investigation into the reduced power arc a description of the application of the technique to full power arcing is made so that a comparison of results becomes possible.

6.1.3 Observations for the Full Power Arcing Facility

(i) The Arc Column during the Quasi-Steady Peak Current Period

The arc current and voltage for 100μs during the peak current range are shown on fig. 6.7(a) together with the corresponding high speed photograph (fig.6.7(b)). The operating conditions for fig. 6.7(a) and (b) correspond to a peak current of 34KA, elkonite electrodes and a PTFE nozzle. The overall arc conductance can be measured from fig. 6.7(a) and in this case is 42.5S which compares well with corresponding values measured by Taylor et al (1982) who used identical operating conditions.

Fig. 6.8 shows the variation with peak current value over a range of 32 to 56KA of the luminous arc area measured at the current peak. Values of area are presented for axial positions corresponding to slot 2 (nearest the throat) and slot 3 (about 10mm downstream) and for both PTFE and copper as nozzle materials. The copper nozzle areas show a marked increase over the peak current range while the PTFE values are generally lower and show a much more gradual increase, if any, over the corresponding current range.

Also shown in fig. 6.8 are luminous arc areas measured

by Walmsley et al (1978(iii)) for an SF_6 arc burning in a 50mm copper orifice. Reasonably good agreement is evident with the copper nozzle results of the present investigation.

(ii) The Temporal Variation of the Luminous Arc Diameter, Peak Light Intensity, Arc Current and Voltage over the Final 50μs of Current Decay

A current and voltage oscillogram together with the corresponding high speed photograph are shown following a peak current of 46KA in fig. 6.9. These were captured over the final 50μs before current zero. The operating conditions for this case corresponded to a current zero di/dt of 19.5A/μs with elkonite electrodes and PTFE as the nozzle material.

Fig. 6.10 shows the variation of arc luminous area, peak axis intensity and current measured over a similar time scale to that of fig. 6.9 for a wide range of di/dt values. Fig. 6.10(a) to (c) indicate that the oscillations in column area which were present in the reduced power case are still present at full power but have a somewhat reduced amplitude in comparison. However the period of these oscillations remain unchanged from the reduced power arcing case.

Underlying trends can be identified in fig. 6.10(a) to (c) if the oscillations are ignored and a more general view of the arc collapse is adopted. It is clear that the areas (where detected, in some cases e.g. slot 1 fig. 6.10(b) the viewing slot was obstructed) throughout the current zero

period generally increase with $^{di}/_{dt}$. Also, significantly as the $^{di}/_{dt}$ value is increased the rate of collapse of area close to current zero increases particularly at those slots situated upstream and around the throat (1, 2 and 3).

Mild (if any) oscillations are present on the intensity results presented on fig. 6.10(a) to (c). These intensity results show two different modes of behaviour corresponding to the upstream and downstream locations. Upstream (slots 1 and 2) the intensity is quite high at a time greater than 20μs before current zero before a more rapid decline occurs. Also as the $^{di}/_{dt}$ increases the period for which the intensity remains high approaches the current zero instant more closely until as in the case of $^{di}/_{dt}$ = 29.3A/μs the intensity persists at a high level even after current zero when significant post arc current flows. The corresponding results for the two slots furthest downstream, 4 and 5 (when visible) show a generally lower intensity value which is similar to the trend observed with the reduced power arcing and the decay is a more linear one throughout the observation period. At slot 3 the intensity with the low $^{di}/_{dt}$ value (fig. 6.10(a)) is comparable to that further downstream (slot 4), although the decay is of the same nature as in the upstream regions. In fig. 6.10(b) ($^{di}/_{dt}$ = 22A/μs) the decay at slot 3 is more oscillatory in nature but the intensity values are generally slightly higher than in fig. 6.10(a). When the current decay rate is high ($^{di}/_{dt}$ = 29.3A/μs) as in the case of fig. 6.10(c) the slot 3 intensity is generally very high throughout the current zero period and follows the trend

of slots 1 and 2. Therefore a large increase in the observed luminous intensity on the arc axis is evident above a $^{di}/_{dt}$ of about 22A/μs which is consistent with a similar sharp rise observed in the simultaneously measured total radiation power loss (Shammas, private comm.) above this current decay level.

(iii) The Radial Light Intensity Distribution during the Final 20μs of Current Decay

The radial light intensity distribution at slot 3 captured at 10μs intervals during the final 20μs before current zero is shown in fig. 6.11. The steepness of the peripheral regions of the profile is sufficiently steep to indicate an accurate diameter measurement in each of the three cases shown. However a region exists at the extremities of the profiles, particularly the one measured 14.2μs before current zero, which corresponds to a uniform annulus of constant luminous intensity. This was attributed to hot gas of relatively low luminous intensity which also caused reflection of the arc column light into the optical path. For these reasons this annular region was discarded for the purpose of diameter measurement and was considered to artificially superimpose wings onto an otherwise steep-sided intensity profile.

(iv) The Influence of Different Operating Conditions upon the Luminous Arc Area Collapse during the Final 50μs of Current Decay

Fig. 6.12(a) shows the timewise arc cross-section area variation at similarly low current decay rates (18.2 and 16.2A/μs) where PTFE and copper were used as nozzle materials.

The optical experimental conditions were maintained as similar as possible in these two cases, the only difference being an image intensifier bias change from 14KV to 15KV when PTFE and copper were used as the respective nozzle materials (i.e. the copper nozzle image was less intense). According to the film emulsion calibration of chapter 5 this change in bias has an insignificant effect on the recorded luminous diameter provided the exposure limits stipulated in chapter 5 were not exceeded. In this case this condition was satisfied. However the increased gain of the intensifier meant that an image was detected at slot 5 in the copper nozzle case which was just visible. The luminous intensity of the arc column in this axial region is low compared to the regions further upstream, and the PTFE slot 5 luminous intensity is probably just below the light detection threshold of the optical system for an intensifier gain bias setting of 14KV. Comparison is also difficult in the case of the slot 3 areas in the copper nozzle case, a 'blob' of luminous material has artificially dilated the arc cross-section at times well before current zero. Ablated material then appears to eclipse the arc column at this viewing slot close to current zero resulting in an apparent premature area collapse. This masking of the arc column at slot 3 is a feature which occurs regularly with the copper nozzle and is associated with the ablation characteristics of the nozzle in the throat region (just upstream of slot 3) (Taylor et al, 1982).

A direct comparison can be made between the two cases

shown on fig. 6.12 at slots 1, 2 and 4 which are axial regions that cover a large proportion of the arc length. If these are compared, the previously discussed oscillations are disregarded and the area collapse is regarded as an average decay, then similarities are evident in the two cases. For instance, the slot 2 diameters are similar during the final 20μs but the PTFE are lower prior to that time. This could be associated with the globular nature of the arc column particularly in view of the similar behaviour of the neighbouring slot 3 diameters.

At slots 1 and 4 the decay trends are similar throughout the current zero period, the magnitude of the areas also being similar.

The slot 3 arc areas in the PTFE nozzle case show a temporal decay trend which is similar to the one observed by Walmsley et al (1978(i)) for an axial location 2mm downstream of the nozzle (orifice) throat. Although the absolute magnitude may not be the same, which is understandable in view of the different arcing conditions employed (nozzle geometry, 3 to 8KA peak currents and air as the host gas), the trends are similar.

Fig. 6.12(b) shows the corresponding temporal variation of arc areas in PTFE and copper nozzles but at higher $^{di}/_{dt}$ values (22 and 23.7A/μs). Again slot 5 areas are absent in the PTFE nozzle case and can be attributed to a lower luminous intensity. Also absent in the PTFE nozzle case is the slot 1 areas. This was due to severe obstruction of the viewing

window by carbon deposits which were generated during the peak current phase and subsequently deposited on the window. The same is true for the slot 3 areas in the copper nozzle case where the deposits were solidified copper.

However, when a comparison is made between the slot 2 and 4 areas striking similarities exist once again over the recording interval (the final 30μs before current zero).

(v) The Temporal Variation of the Luminous Arc Cross-Sectional Area, Peak Light Intensity and Arc Current During the Final 10μs before Current Zero

A typical arc current and voltage oscillogram and the corresponding high speed photograph taken during the final 10μs of current decay are shown in fig. 6.13. The photographic record was made at a framing rate of 1×10^6 f.p.s. and an exposure of 200ns per frame. The operating conditions in this case correspond to a peak arc current of 34KA resulting in a current zero decay rate of 15A/μs between elkonite electrodes and in a PTFE nozzle.

Fig. 6.14(a) to (c) shows the timewise variation of the luminous arc cross-sectional area, current and column axis intensity for three values of $^{di}/_{dt}$ between 15 and 27.1A/μs in a PTFE nozzle over the final 10μs or so of the current decay. It is clear from these figures that the area collapse over the final 5 or 10μs generally corresponds to the area collapse of fig. 6.10(a) to (c). The only severe departure from this appears between the slot 2 areas in the high $^{di}/_{dt}$ case which could be explained by the

appearance of a plasma blob causing the higher areas in the long time scale case.

The oscillations observed in the reduced power case are again present throughout the recording interval and are of similar frequency and amplitude except downstream (slots 4 and 5) where the amplitude of the full power case oscillations is surpressed compared to the reduced power case.

In the case of low $^{di}/dt$ (fig. 6.14(a)) the areas of the arc at the upstream slots 1 and 2 are generally larger than those at slots 3 and 4 throughout the current zero period, the arc not being visible at slot 5. The axial intensity measurements (fig. 6.14(a)) show a similar trend which also indicate the intensity values dropping to a very low value just prior to current zero (1μs before at slot 1, 3μs before at slots 2, 3 and 4). In the case of the higher $^{di}/dt$ values (fig. 6.14(b) and (c)) the arc area at slot 1 remains the largest but the slot 3 areas are comparable to the slot 2 areas and larger than those measured at slots 4 and 5. The axis intensity at slot 3 also becomes comparable to the slot 1 and 2 intensities at the high $^{di}/dt$ values. However there is some evidence of partial light obstruction at slot 3 in fig. 6.14(c) which was probably caused by ablated material fragments. In general the cross-sectional areas at all the slots increase as the $^{di}/dt$ value increases. This trend is consistent with that observed over a longer time scale (fig. 6.10(a) to (c)). A departure from this trend is

apparent at slots 3 and 4 in the high $^{di}/_{dt}$ case (fig. 6.14 (c)) but this can be explained by the partial light obstruction caused by ablated material fragments which also cause a dip in the luminous intensity just before current zero.

The rate of decay of the arc cross-sectional areas at the upstream slots (visible until the current zero instant) is approximately the same being slightly higher at slot 1 than at slots 2 or 3. Also the area decay rate generally increases with current decay rate for the cases where an arc image was detected.

(vi) <u>The Radial Light Intensity Distribution Close to Current Zero</u>

Fig. 6.15 shows the radial and timewise variation of the photographically measured light intensity during the final few microseconds before and the few microseconds immediately after current zero at slots 2 and 3. The operating conditions in this case correspond to a current decay rate of 27.1A/μs (a peak current of 64KA) for an arc burning between elkonite electrodes in a PTFE nozzle i.e. the same as fig. 6.14(c). Sufficient evidence exists in fig. 6.15(a) and (b) to show that the photographic intensity profile is sufficiently steep at the column periphery at slots 3 and 2 respectively to enable accurate measurement of luminous arc diameters to be made. This was an observation made with both the reduced power (section 6.12(iii)) and with the longer recording interval under full power (section 6.1.3(iii)).

Fig. 6.15(a) shows the arc intensity profile collapsing at slot 3 as the current decays to zero, which is consistent with trends established from similar measurements presented above. The arc intensity profile at the instant closest to current zero in fig. 6.15(a) (0.4μs after current zero) appears to be generally very much attenuated with respect to the profiles at all other times. However as discussed in 6.1.3(iv) this was probably due to partial eclipsing of the radiated light. The reduction in intensity by the partial eclipsing in this case does not make it possible to determine whether a true reduction in the axial column intensity occurred. However during the reignition the next frame on fig. 6.15(a) (2.4μs after current zero) shows a well formed arc column with an axial intensity value which is somewhat higher than the arc column before current zero at a corresponding instantaneous current value (fig. 6.14(c)) with little or no change in the extent of the profile (extreme of the luminous diameter). Further evidence of the arc column reignition process is available on fig. 6.15(b) which shows the arc intensity profile over the same period at slot 2 for the same test as fig. 6.15(a). The arc column intensity growth occurs at a slightly later time in this case (the +4.4μs frame) and is not as exaggerated as in fig. 6.15(a). However this provides ample evidence of the arc column reignition behaviour under full power arcing conditions and is consistent with the same reignition behaviour observed under reduced power arcing conditions (section 6.1.2(iii)).

(vii) The Influence of Different Operating Conditions Upon the Luminous Arc Area Collapse during the Final 10μs of Current Decay

The influence of different nozzle materials (PTFE and copper) upon the arc cross-section decay over the last 10μs before current zero for two values of $^{di}/_{dt}$ is shown on fig. 6.16(a) and (b). Similar experimental photographic operating parameters were maintained in each case so that direct comparisons could be made.

Fig. 6.16(a) shows the cross-sectional area variation for values of $^{di}/_{dt}$ of 15 and 17.5A/μs corresponding to PTFE and copper as the respective nozzle materials. In this case differences are apparent in the case of the area variation at slot 1, the area being generally larger in the copper nozzle case. The somewhat higher values in the latter case are attributable to local plasma blobing. These values are also higher than the corresponding ones in fig. 6.12(a) (taken over a longer time scale) which is further evidence of a spontaneously high area value in this case.

The cross-sectional area variations at slots 3, 4 and 5 compare well if the oscillations present on some records are disregarded.

No areas were recorded at slot 2 in the copper nozzle case. This was due to severe obstruction of the viewing window as described in part (iv) of this section. Comparison is not therefore possible in this case although the results of fig. 6.12(a) indicate a reasonably good comparison at

slot 2 under similar operating conditions.

Fig. 6.16(b) represents the temporal area variations for PTFE and copper nozzles at a higher $^{di}/_{dt}$ value. Clearly, the slot 1 area variation corresponds well for the two nozzle materials.

The slot 2 areas appear to be generally lower in the copper nozzle case. However this is not a genuine effect since comparison with fig. 6.12(b) over the final 10μs indicates slot 2 copper nozzle areas of similar magnitude to the PTFE nozzle areas during that time interval. Furthermore the lack of slot 3 information for the copper nozzle case indicates that there could be some eclipsing or obstruction of the arc column in this axial region.

The slot 4 cross-sectional areas in the copper nozzle case are somewhat lower than the corresponding PTFE areas. However the general lack of reproducibility of the arc appearance at this axial station makes comparison difficult. The same hypothesis applies to the arc column at slot 5. However the arc column here does appear luminous up to and beyond the current zero instant in the copper nozzle case (fig. 6.16(b)). The presence of a luminous arc column at current zero with the copper nozzle but not the PTFE nozzle is also a feature of fig.6.12(a) and (b). Thus the trend appears to be consistent with similar results taken with different exposure times and could be associated with the ablation characteristics of the nozzle.

The effect of different current decay rates upon the

arc column cross-section at the current zero instant is shown on fig. 6.17 for both PTFE (fig. 6.17(a)) and copper (fig. 6.17(b)).

The results of fig. 6.17(a) show that the upstream (slots 1 and 2) cross-sectional areas increase gradually with increasing $^{di}/_{dt}$. A similar trend is evident at slot 3 where the areas are generally smaller than at slots 1 and 2. A corresponding trend at slots 4 and 5 is difficult to ascertain since the lack of luminous intensity at these downstream locations did not make an area measurement possible. The limited measurements available only at high $^{di}/_{dt}$ values (fig. 6.17(a)) show the cross-sectional areas at these axial locations to be smaller again.

Similar measurements for a copper nozzle are presented in fig. 6.17(b). It is clear from this figure that a large experimental scatter is present in the case of slots 1 and 2. This could be due to enhanced plasma blobbing effects at these axial stations.

The cross-sectional areas at slot 3 (fig. 6.17(b)) follow a more clearly defined trend which shows them to be increasing slightly with $^{di}/_{dt}$. They also correspond closely to the slot 3 areas of fig. 6.17(a) (PTFE nozzle).

Since the luminosity of the arc column downstream of the nozzle (slots 4 and 5) is higher at the current zero instant with copper than PTFE it is possible to establish a current zero area - $^{di}/_{dt}$ trend. Fig. 6.17(b) shows that the arc areas at these axial locations again increase with

$^{di}/_{dt}$ which is slightly more pronounced than the corresponding variation at slot 3. The arc areas at the high $^{di}/_{dt}$ values are also somewhat higher (particularly slot 4) than the corresponding PTFE values (fig. 6.17(a)). Thus the arc column downstream of the throat in a copper nozzle at the current zero instant is relatively large but photographic optical density measurements indicate the luminosity to be rather low in comparison to that at the upstream stations (1, 2 and 3). Thus the arc column here has a diffuse appearance. Such an appearance is consistent with an arc column in a slightly turbulent or disturbed flow. Further consideration to these effects is given in chapter 8.

Also shown on fig. 6.17(a) is the corresponding current zero area - $^{di}/_{dt}$ characteristic for the reduced power arcing conditions. The arc areas at slot 1 under the full power conditions are generally higher than the corresponding reduced power arc areas. Slot 1 is the furthest upstream and is located nearest to the upstream electrode. The apparent anomaly could be associated with more severe contact evaporation following full power arcing. The arc column areas at slot 2 correspond satisfactorily between full and reduced power arcing conditions for the lower values of $^{di}/_{dt}$. However for the raised $^{di}/_{dt}$ values (>20A/μs) agreement breaks down and the full power arc areas exceed the correspondin reduced power areas. The same trend is evident at slot 3 which is located just downstream of the nozzle throat. The difference in arc column dimensions near the nozzle throat is indicative of fundamental differences in the overall arc

column structure. The difference and its significance with respect to the thermal performance of the circuit breaker is further discussed in chapter 8.

The comparison of the full and reduced power arc areas at slots 4 and 5 was difficult for two reasons. Firstly, no luminous arc column was detected at the current zero instant when a low rate of current decay was used. Secondly, the temporal oscillatory behaviour of the reduced power arc column area close to current zero (fig. 6.1 (c)) introduces a large uncertainty on the current zero arc column area at the current zero instant.

(viii) <u>The Variation of the Axial Light Intensity at the Current Zero Instant with $^{di}/_{dt}$</u>

The variation of the axial light intensity at slot 3 for the full power arcing conditions is shown on fig. 6.18. The most striking feature of this characteristic is a sharp rise in intensity above a value of $^{di}/_{dt}$ of about 20A/μs. This is in agreement with the total radiation power loss results of Shammas (private comm.) which are also shown on fig. 6.18 (solid line).

The corresponding slot 3 results for the reduced power case is also shown on fig. 6.18. This characteristic also exhibits an accelerated rise above a certain $^{di}/_{dt}$ value. However in this case the rise is more gradual than in the full power case and takes place above a $^{di}/_{dt}$ level of about 30A/μs.

6.1.4 Concluding Statement

A number of photographic results have been presented for a wide range of operating conditions which have enabled the interpretation of a luminous arc diameter and measurement of the photographic radial intensity profile to be made. By employing a careful analysis procedure the relevant information can be obtained from these results and when coupled with further simultaneous radiation measurements (Shammas and Jones, 1981, Shammas private comm.) can be used to formulate a relationship between the overall circuit breaker performance and particular arcing parameters (including arc cross-sectional area).

The measurement of the photographic intensity profile has proved a useful indicator for the validity of the assumption that the luminous arc area is representative of a meaningful conducting column area.

The photographic intensity profile when corrected for line of sight effects provides a basis for the correlation of radial spectral data (chapter 7) such as those presented in the next section below.

6.2 Spectroscopic Results

6.2.1 Introduction

In this section,time and space resolved spectra of the decaying arc column during the current zero period of a full power arc are presented. The arc was observed at a

single axial location near the nozzle throat (slot 2) which was considered to represent a suitable location at which important parameters governing arc extinction/reignition could be identified. The spatial resolution of the arc spectra corresponds to the arc diameter at the single axial location and was limited only by the resolution of the optical system and the vidicon camera scan capability as explained in chapter 4 (section 4.6.3). The temporal resolution for all the results is 1.6μs (exposure time) which was governed by the camera gate time (chapter 4) and limited by the amount of light incident to the camera. A wide range of operating conditions were investigated following an inaugural feasibility study or spectral survey (6.2.2), using PTFE as the nozzle material.

Snapshot spectra (1.6μs exposure) are presented at different instants during the final 10μs of current decay for a given set of operating conditions where current, voltage and pressure conditions were for successive tests to ensure good reproducibility of the arc column under observation. Simultaneous arc current and voltage measurements were also made for all the results in this section.

6.2.2 Spectral Survey

To obtain meaningful temperature results during the transient arc column decay conditions occurring during the current zero period, two fundamental conditions must be satisfied:

(1) The spectral lines under observation must satisfy many constraints applied by the physical nature of the source.

(2) Adequate time resolution must be achieved to identify important transient current zero arc processes.

The first of these conditions will be dealt with in depth later in this section (6.2.2(ii)). The second of the conditions in question is wholly a function of the overall system sensitivity. Therefore it is vitally important that adequate light intensity exists during the current zero period to enable short duration exposures. The demands imposed by arc conditions within the investigated time period are that the exposure should be as short as possible to freeze changes associated with the short arc time constants (1 to 2μs, chapter 8) but sufficient to ensure adequate light intensity for detection. The intensity requirement is made more severe by the requirement for radial resolution. Therefore there was a need to identify an axial region of the arc column where all the above requirements were satisfied for all the operating conditions prior to any serious spectral investigation.

(i) <u>Evaluation of a Suitable Nozzle Material and Axial Viewing Station for Current Zero Spectroscopy</u>

Many investigations were conducted where the arc was viewed at slot 3 through a copper nozzle. However this was found to be unprofitable since insufficient light intensity was present during the current zero period and particularly in the case of the lower current decay rates.

This light intensity defficiency was believed to be associated with the absorbent nature of copper vapour ablated from the

nozzle wall during the high current phase and already identified through the total radiation results of Shammas et al (private comm.). This being the case, the optical system was then aligned with slot 2 which is actually located nearer to the nozzle throat than slot 3. Sufficient light was detected but only on an irregular basis. The reason for this was the coating of the viewing window by copper vapour 'spluttering' prior to current zero as discussed above (6.1.2). The effect was particularly acute when the arc column during the peak current phase could burn asymetrically to one side of the nozzle. This condition gave rise to intermittent gathering of results when light was collected from the entire arc diameter (radially averaged) and locally degraded results in the radially resolved case since the coating could be denser at certain radial localities. Such a situation was tolerable in the case of the photographic measurements since all of the slots were viewed simultaneously and to lose the information at one (or even two) slots on a single record could be tolerated. However with the single slot viewing implemented in the spectroscopic investigation intermittent loss of information was no longer tolerable.

Consequently, it was more profitable to utilise the PTFE nozzle for the preliminary investigations. The result of these investigations was that arc spectroscopy was possible with both satisfactory time and space resolution throughout the current zero period. Fig. 6.19 shows a typical radially resolved arc spectrum with an exposure of 1.6μs. The operating conditions corresponding to these

records were $^{di}/_{dt}$ = 14 to 18A/μs, captured 4.8 to 9.6μs before current zero viewing the copper I line emissions in the wavelength range 459-529nm.

The broadening of the spectral lines due to the influence of the viewing slit of the monochromator was known to be negligible when compared with the spectral line widths of typically a few angstroms (1 angstrom = 0.1nm). This was confirmed by Ibuki (Ph.D. thesis, 1978) who used the same monochromator.

(ii) The Evaluation of Suitable Spectral Lines

There are many requirements which a spectral line must satisfy before it may be used for diagnostic purposes owing to physical processes present in the source rather than purely due to measurement limitations.

The first of these requirements concerns the broadening of the spectral line in question by various physical processes. Since the switchgear arc plasmas have relatively high particle densities (Ne $>10^{15}$ cm^{-3}) it is reasonable to assume that the only broadening mechanism which could have a measurable effect on a diagnostic line is Stark Broadening (Griem,1964) (Further consideration of the line broadening mechanisms is made in chapter 7). The spectral line should maintain a consistent line profile over the range of pressure variations within the plasma for the scope of the operating conditions studied. Also, important parameters linking line width and particle (electron) densities should be known. If a line satisfies these two constraints then it is possible to make

spectroscopic measurements of electron density and thus compare this electron density with a theoretical value for a given plasma pressure (chapter 8).

A second but equally important requirement for a good diagnostic line is that the line in question satisfies the optical density criteria (chapter 7) and shows no signs of self reversal.

A third constraint which must be satisfied is that the line profile is not impeded by satellite emissions in the close neighbouring spectral range to the extent that the line profile is distorted to give a false line width.

Fig. 6.19 shows a typical Cu I line emission at 521.8nm with the operating conditions as indicated. This shows that this particular spectral line is free from any of the deliterious effects outlined above. A small satellite emission (Cu I, 522.2nm) is present but does not seriously impede the line profile and the instrument's spectral resolution is sufficient to resolve the two line peaks.

Further suitable diagnostic lines included the Cu I emissions at 510.5nm, 515.3nm, 529.1nm, 459nm and 465nm, examples of which are presented in fig. 6.19(b) (i) to (iii) with the corresponding operating conditions.

The parameters governing an accurate spectroscopic investigation have been identified and satisfied for a wide range of arcing conditions. Thus a comprehensive and meaningful investigation during the current zero period is

possible provided that the limits of the constraints established in this section are satisfied.

6.2.3 Spectroscopic Measurements of the Arc During the Current Zero Period

(i) Radially Averaged Spectra Captured During the Final 10μs of Current Decay

The radially averaged, time resolved spectra of the decaying arc column are shown on fig. 6.20(a), (b) and (c) for different peak current values between 34 and 50KA (corresponding to current zero $^{di}/_{dt}$ values of 15A/μs and 23A/μs). Spectra are shown for the two major wavelength domains investigated here, namely those centred on 521.8nm and about 512nm.

Fig. 6.21(a) represents the intensity decay of the three principal diagnostic lines used in this investigation (515.3nm, 510.5nm and 521.8nm) during the current zero period. These values were derived from the results of fig. 6.20(a) by a computational analysis of the respective spectrograms. Two distinct regions may be identified corresponding to different decay rates, period A and period B (fig. 6.21(a)). Period A corresponds to the period 10μs to 2.5μs prior to current zero, during which the decay of the 521.8nm intensity is slow or non-existent as in the case of the other two lines. Period B corresponds to the period 2.5μs to 0μs during which the line intensities have decayed to a level which is below the threshold of detection of the Vidicon camera. The decay rate during this interval is

characteristically high and is indicative of an arc column in a highly transient state. Further consideration to these phenomena will be given in chapter 8.

The radially averaged intensity decay of the arc column during the current zero period of a 46KA peak current arc is shown on fig. 6.21(b). The intensity variation was recorded for two Cu I spectral lines at 510.5nm and 515.3nm. The 521.8nm emission was excluded in this case in order to economise on the number of heavy current tests. Sufficient information is available from the two lines investigated to allow extensive temperature and electron density information to be extracted.

Again two distinct time intervals exist which relate to different characteristic intensity decay rates as was the case with the lower peak current value. However, in this case, there is a slight intensity decay rate during period A which is not the case for the same two spectral lines on fig. 6.21(a). Also period A extends closer to current zero before the rapid intensity decay occurs. It is difficult to judge whether the intensity decay rate is greater in the case during period B due to the lack of data during this time interval on account of the low intensities. The intensities of these lines are similar in magnitude to the 34KA peak case throughout the current zero period except within the final two microseconds before current zero where a higher intensity is evident in the 46KA case.

The corresponding intensity variation with a peak current

of 53KA is plotted on fig. 6.21(c). The two distinct periods of intensity decay rates are apparent once more. Period A is again characterised by a steady intensity decline similar to that of the 46KA case. However, a considerably higher rate of intensity decay is evident during period B. Also in this case the threshold between the two periods is even closer to current zero than the 46KA case (fig. 6.21(b)). It is clear from comparing fig. 6.21(c) and fig. 6.21(a) and (b) that the intensities of both the spectral lines are greater during the final two microseconds before current zero. In fact light was detected 1.2μs before current zero which means the camera exposure time (1.6μs) actually overlapped the current zero instant in this case. It is also worth noting that the intensity of the 515.3nm line is generally higher in the 53KA case throughout the current zero period, whilst the 510.5nm line intensity is not vastly different. The significance of this phenomenon will emerge in the following section concerning arc temperature deductions from this data.

Arc spectra during the current zero period have been captured for a wide range of arcing conditions and their resulting temporal intensity variations presented. However timewise intensity variations of spectral lines in this manner can be misleading owing to their unique intensity: temperature characteristics (chapter 7). A more meaningful physical representation of the arc column would be a timewise variation of temperature rather than intensity.

(ii) Time Variations of Radially Averaged Arc Temperatures

Radially averaged arc temperatures have been calculated from the data presented in section (i) above. The method of calculation is described fully in chapter 7 of this thesis. Essentially, the temperature was deduced from the ratio of two Cu I line intensities as insufficient information existed for the radially resolved spectra.

Fig. 6.22 shows the temporal variation of the radially averaged arc temperature at the nozzle throat during the current zero period for the two extreme cases of peak arcing currents used in the present investigation. There are two sources of uncertainty involved in these temperature measurements. The first is the scatter produced by experimental test to test variation, the second, and equally important, is the uncertainty in atomic data values e.g. transition probabilities which can be as high as 20% in some cases. The relevant atomic data will be presented in chapter 7 of this thesis. These uncertainties represent a total uncertainty of about $\pm$ 500K which is shown in fig. 6.22 as an error bar.

Two clear trends emerge from fig. 6.22. Firstly, the temperatures relating to the 34KA case occupy a range generally lower than the corresponding 53KA values throughout the current zero period. Secondly, the temperature values in the 53KA case appear to rise at a time between one and two microseconds before current zero to a value above 10,000K and then fall sharply as current zero itself is approached.

Insufficient intensity made such a temperature measurement impossible closer to current zero. However certain criteria are developed in chapter 8 whereby upper and lower limits of radially averaged temperatures so close to current zero can be defined.

(iii) The Radially Averaged Arc Temperature Variation with Current Decay Rate

Owing to the lack of intensity of the spectral lines at the current zero instant in the lower peak current case a plot of radially averaged arc temperature at the current zero instant would be of limited value. However results are available at times within the final 10μs before current zero (fig. 6.22) which enable comparisons to be made between the different operating conditions and this is shown on fig. 6.23. The most striking feature of these results is the sharp rise in current zero period temperature above a $^{di}/_{dt}$ value of about 20A/μs. For example, at the 15A/μs value the radially averaged temperatures lies in the range 7.5×10^3K to 8.5×10^3K whereas at 22A/μs the range of temperature values is 8.5×10^3K to above 1.05×10^4K.

It is notable that the value of $^{di}/_{dt}$ at which the radially averaged temperatures rise sharply is 20A/μs which corresponds to the $^{di}/_{dt}$ values at which the arc column axis intensity (measured photographically) and the total radiation power loss show a similar increase.

The nature of these radially integrated results clearly can only provide an approximate insight into arc temperature

changes. More detailed and reliable information can be derived from radially resolved measurements.

(iv) Radially Resolved Arc Spectra Captured During the Final 10μs of Current Decay

Radial resolution of the spectral lines was obtained by dividing the photosensitive area of the camera into five equally proportioned strips as described in chapter 4. Each of these strips represents 1mm of the arc column diameter (chapter 5).

Fig. 6.24(a) represents the radially resolved arc spectra of 3 cases of peak current in the range 34 to 53KA at the viewing position near the nozzle throat (slot 2). Two Cu I spectral lines are presented per record, centred on about 513nm (to include the 510.5nm and 515.3nm Cu I emission). A further two records centred on about 521nm (to include the 521.8nm Cu I emission) is presented on fig. 6.24(b) which corresponded to peak currents of 34 and 46KA. These spectra were recorded at different instants during the current zero period and were representative of similar records taken at different times before current zero for each case of peak current.

The radially resolved spectra presented in fig. 6.24 provide useful information regarding the arc radial intensity variation even before temperatures are calculated. Comparing figures 6.24(a)(i) and (a)(ii) reveals that the luminous diameter of the arc has increased from between 2 and 3mm to between 3 and 4mm with an increase in peak current from

34 to 53KA. A similar comparison between fig. 6.24(b)(i) and (a)(ii) shows that although no apparent increase in radial extent has occurred between the two cases (which correspond to a given time instant before current zero but different peak currents, b(i) corresponding to 34KA, a(ii) to 46KA) the intensity of the arc in a(ii) is higher at the extreme of the radial profile. This is indicative of either a slightly wider arc in the latter case whose image is still contained within the same viewing area, or the latter has a higher temperature value at its periphery. It is worth noting in this case that the emissions in the centre viewing portion of 6.24(a)(ii) (Ip = 46KA) is also somewhat higher than 6.24(b)(i) (Ip = 34KA) which is indicative of a higher temperature existing in the centre portion of the latter arc column. This is further reinforced by the fact that the 515.3nm and 521.8nm Cu I emissions share a proportional temperature dependence (chapter 7 fig. 7.4), the 521.8nm emission being the most intense for a given temperature.

The radial extent of the line intensities provides an indication of the arc luminous area. Thus fig. 6.24(a)(i) and (b)(i) indicate that following a peak current of 34KA the luminous diameter lies between 3mm and 4mm 7.4μs before current zero and about 3mm 2μs before current zero. If these diameters are converted into areas and a comparison made with fig. 6.14(a) (which is the photographically recorded luminous area variation under similar operating conditions) then the two values of area correlate well.

Fig. 6.24(a)(iii) represents the spectrogram centred at a wavelength of 513.5nm captured 7.9μs before the current zero of a 53KA arc. The data is limited to this particular wavelength in this case because of the limited data available at this high value of peak current caused by excessive wear on components (nozzles, electrodes). Comparison of fig. 6.24(a)(iii) (Ip = 53KA) with fig. 6.24(a)(i) (Ip = 34KA) and fig. 6.24(b)(ii) (Ip = 46KA) shows that no great differences in line intensities (above the continuum) exist over the whole extent of the arc diameter. This result is in good agreement with the radially averaged results obtained at corresponding peak current values and instants before current zero. It is difficult to compare the radial extent of this arc with the others since not all the arc was captured within the viewing aperture in this case. It is somewhat more complicated to make comparisons of the luminous extent of the arc with the photographic records at the higher $\frac{di}{dt}$ values than may at first appear. This is due to the fact that with rising $\frac{di}{dt}$ the continuum level also rises. At the low $\frac{di}{dt}$ values (15A/μs) the contribution of the continuum, particularly near the periphery was very low. However as the $\frac{di}{dt}$ value increases a significant amount of continuum was detected near the periphery where no spectral line emissions may be present. This becomes clear when fig. 6.24(a)(i) and (b)(ii) and (a)(iii) are compared (which correspond to different cases of $\frac{di}{dt}$ for similar instants before current zero). The increase in continuum may give rise to a luminous region near the periphery of an arc photograph. Therefore the photographically

measured luminous diameter may not correspond to the diameter at which no further spectral line emissions occur in the case of high $^{di}/_{dt}$ values. Comparison of figs. 6.24 (b)(ii) and 6.14(b) shows that the photographically measured diameter at corresponding instants prior to current zero (d = 6mm) is indeed larger than the diameter covered by spectral line emissions alone.

Radially resolved arc spectra have been presented which have enabled a comparison to be made with the radially averaged spectra and the photographic measurements presented in section 6.1.3(v). Also certain qualitative features regarding the radial profile of spectral light intensity have been identified. However the radial distribution of the spectral intensity of the arc enables the calculation of the arc temperature profile. The calculation of this profile further enables the physical properties of the arc column to be determined in a quantitative manner.

(v) Arc Temperature Profiles Calculated from the Radially Resolved Arc Spectra

The arc temperature profiles calculated from the radially resolved spectra of fig. 6.24 (except the case of the 34KA peak in which case another spectrum was used) are presented on fig. 6.25. A temperature profile is presented for three different peak current (current zero $^{di}/_{dt}$) cases at various times during the current zero period. The arc spectra were 1.6μs snapshots captured at 10μs, 2.3μs and 7.9μs before current zero for current decay rates of 14, 17 and 21A/μs respectively.

The temperature profile of fig. 6.25(i) shows the arc to have a central axis temperature of about 8,800K and to have a 6,000K isotherm at a radius of about 2.2mm. The radially averaged temperature results of fig. 6.22 show reasonable correlation with the temperature profile at the corresponding current level. The radial position of the 6,000K isotherm also shows reasonable correlation with the photographic luminous area measurements of fig. 6.14 (a) which indicates a luminous radius of 2.52mm at the same axial viewing station.

Fig. 6.25(ii) represents the profile captured at 2.3μs before current zero for a current decay rate of 17A/μs. The profile in this case indicates an arc with a slightly higher axis temperature but with a significantly reduced 6,000K isotherm radius (about 0.75mm).

The temperature profile at 7.9μs before current zero for a peak current of 53KA is shown on fig. 6.25(iii). It is again indicative of a narrow arc column with a 6,000K isotherm radius of about 1mm and an axis temperature of 10,000K. This temperature profile is again consistent with the radially averaged measurements of fig. 6.22 for equivalent arcing conditions.

In the case of fig. 6.25(ii) (46KA) and (iii) (53KA) comparisons have not been made with the photographic luminous area results of fig. 6.14 for the same reasons as stated earlier (i.e. visible continuum). In such an event the photographic records might be expected to yield a larger

diameter for corresponding arcing conditions, which indeed is the case (fig. 6.14(b)). Such interpretation of the data has a significant influence upon the calculations of arc energy loss processes and will be discussed in detail in chapter 8.

The temperature profiles presented on fig. 6.25 have a steep temperature gradient at the 6,000K isothermal boundary which plays an important role in the justification of the boundary layer approximation of the integral analysis (chapter 7).

A final observation on the radially resolved arc spectra of fig. 6.24 is that the spectral lines do not appear in the same set of viewing tracks from test to test. This indicates that the arc column moves from test to test by as much as a column diameter. Apart from making such spectra difficult to capture in successive tests, this indicates an arc which is prone to eccentric movement about a central axis. Although the spectral records show that this may occur between different tests, no such pronounced eccentric movement was detected on the framing photographs for a given single current zero arcing sequence.

(vi) Electron Density Measurements

The electron density in the arc plasma was calculated using a formula which describes the Stark broadening of a particular spectral line (chapter 7, section 7.2.2.1). Use was made of Stark broadening coefficients (Jenkins, private comm.) for the diagnostic spectral lines in this formula.

Fig. 6.26 shows the variation of the radially averaged electron density during the current zero period following the three different peak arc currents investigated. These electron density values were derived from the same spectra as the temperature results of fig. 6.22.

The results of fig. 6.26 show that the average electron density of the arc column at this particular axial location lies in the range 1.5 x $10^{17}cm^{-3}$ to 4.5 x $10^{17}cm^{-3}$ over the whole range of operating conditions during the current zero period.

In the case of the 34KA peak current no significant change in electron density was evident during the current zero period. However insufficient light was available to give spectral line widths closer to current zero than 3μs. The higher peak current cases showed a gradual decline of electron density during the current zero period which is particularly evident in the 46KA case.

(vii) Summary of the Spectroscopic Measurements

Arc spectra captured during the current zero period of a full power arc have been presented. The spectra were both time and space resolved (along the arc diameter). Furthermore these spectra have enabled both the radially averaged arc temperature and electron density to be calculated. The spatially resolved spectra have also allowed detailed arc temperature profiles to be measured under full power arcing conditions for the first time.

6.3 Concluding Statement

The experimental results presented in this chapter have been classified into two major categories, namely the photographic and spectroscopic results. The photographic results allowed not only the luminous arc diameter to be determined but also detailed intensity profiles. Photographic measurements were made at 5 strategically located axial viewing stations. The spectroscopic results included time and space resolved arc spectra during the current zero period. Radially averaged spectra were also presented with the same time resolution. These spectra further allowed radially resolved and radially averaged arc temperatures and radially averaged electron densities to be calculated.

The significance of the two categories of results analysed collectively is realised in chapter 8 which includes an evaluation of the current zero power balance using the results of this chapter. However it is important to present the theoretical background from which such considerations as the power balance as well as other important calculations can be made. This is considered in chapter 7.

LIST OF FIGURES

(b) Variation of the photographic intensity of the arc column at different axial stations for elkonite electrodes with di/dt.

6.7 Typical arc current and voltage record with the corresponding high speed photograph taken during the peak current period.

(a) Arc current and voltage oscillogram
(b) The high speed photograph corresponding to fig. 6.7(a)

6.8 Variation of luminous arc area at the current peak with peak current value.

6.9 Typical arc current and voltage record with the corresponding high speed photograph taken during the last 50μs of the current decay.

(a) Arc voltage and current oscillogram
(b) High speed photograph corresponding to (a)

6.10 Variation of arc cross-sectional area, axis light intensity and arc current over the final 50μs of the current decay.

(a) Low di/dt
(b) Medium di/dt
(c) High di/dt

6.11 Measured radial intensity distribution at 10μs intervals on the approach to and after current zero at slot 3.

6.12 The influence of the nozzle material on the arc area on the approach to current zero.

(a) Low di/dt
(b) High di/dt

6.13 Typical arc current and voltage record with the corresponding high speed photograph taken during the final 20μs of the current decay.
Peak current = 34KA

(a) Arc voltage and current
(b) High speed photograph corresponding to (a)

6.14 The variation of arc cross-sectional area, axis light intensity and arc current over the final 10μs of the current decay.

(a) Low di/dt
(b) Medium di/dt
(c) High di/dt

6.15 Measured radial intensity distribution at 2μs intervals (200ns exposure) on the approach to and after current zero at slot 3.

(a) Slot 3
(b) Slot 2

6.16 The influence of the nozzle material on the arc areas very close to current zero.

(a) Low di/dt
(b) Medium di/dt

6.17 The influence of di/dt upon the arc areas measured at the current zero instant.

(a) PTFE
(b) Copper

6.18 Variation of the total radiation loss and maximum of the radial photographic intensity profile at the current zero instant with di/dt.

6.19 Typical arc spectra at various wavelengths

(a) λ_C = 521.8nm
(b) (i) λ_C = 510.5nm and λ_C = 515.3nm
(ii) λ_C = 529.1nm
(iii) λ_C = 459nm and λ_C = 465nm

6.20 Examples of radially averaged spectra for different instants during the current decay.

(a) (i) Low di/dt, 515.3nm and 510.5nm spectral lines

(ii) Low $\frac{di}{dt}$, 521.8nm spectral line

(b) Medium $\frac{di}{dt}$, 515.3nm and 510.5nm spectral lines

(c) High $\frac{di}{dt}$, 515.3nm and 510.5nm spectral lines

6.21 Decay of various spectral line intensities during the current zero period.

(a) 34KA Peak Current
(b) 46KA Peak Current
(c) 53KA Peak Current

6.22 Variation of the radially averaged temperature under different arcing conditions.

6.23 Variation of the radially averaged temperature during the current zero period with the current decay rate.

6.24 Radially resolved arc spectra during the current zero period.

(a) λ_c (centre wavelength setting of monochromator 512nm

(i) Low $\frac{di}{dt}$
(ii) Medium $\frac{di}{dt}$
(iii) High $\frac{di}{dt}$

(b) λ_c 521nm

(i) Low $\frac{di}{dt}$
(ii) High $\frac{di}{dt}$

6.25 Arc temperature profiles during the current zero period.

(i) Ip = 34KA
(ii) Ip = 46KA
(iii) Ip = 53KA

6.26 The radially averaged electron density versus time, for different peak currents, during the current zero period.

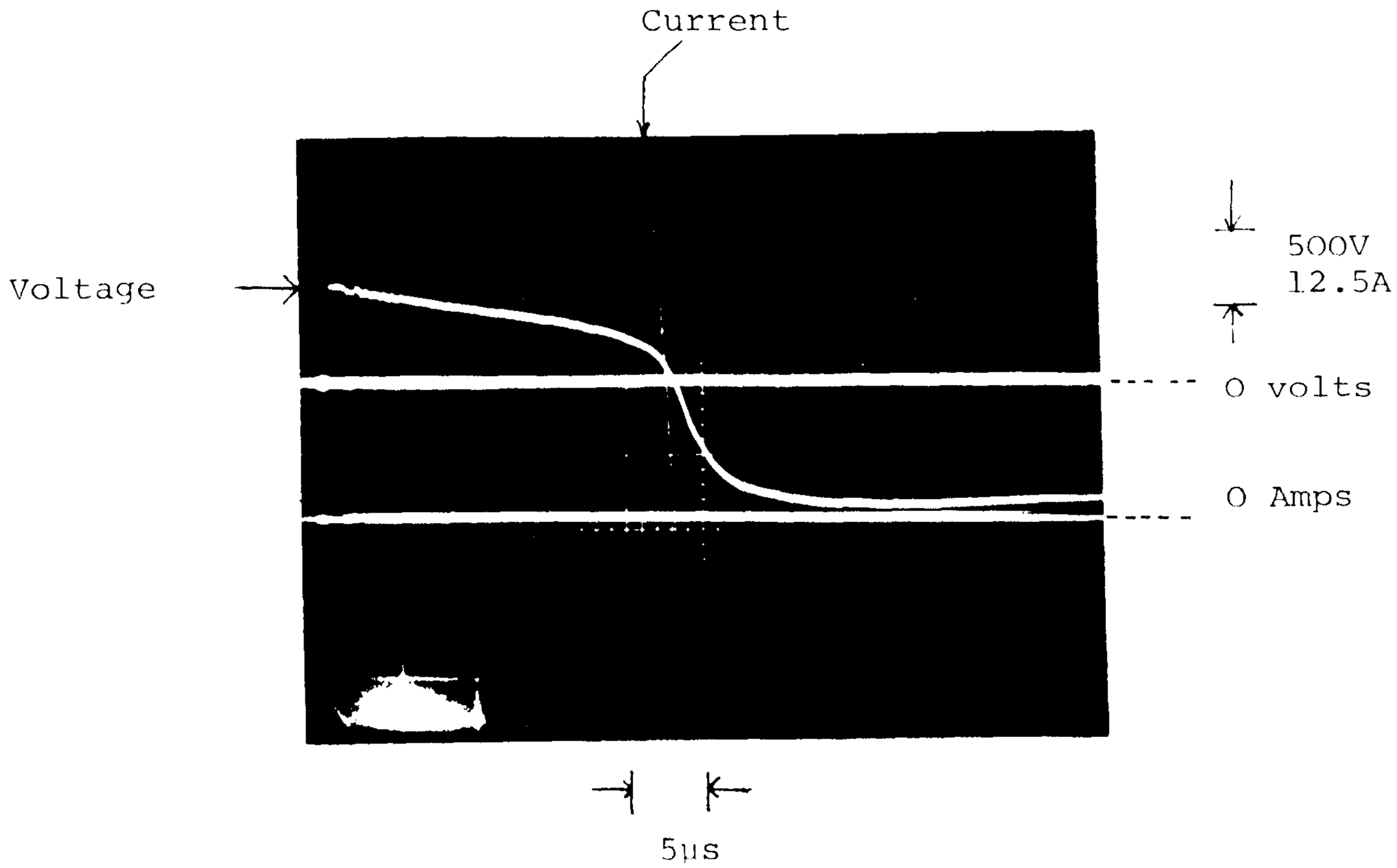

(a) Arc Current and Voltage

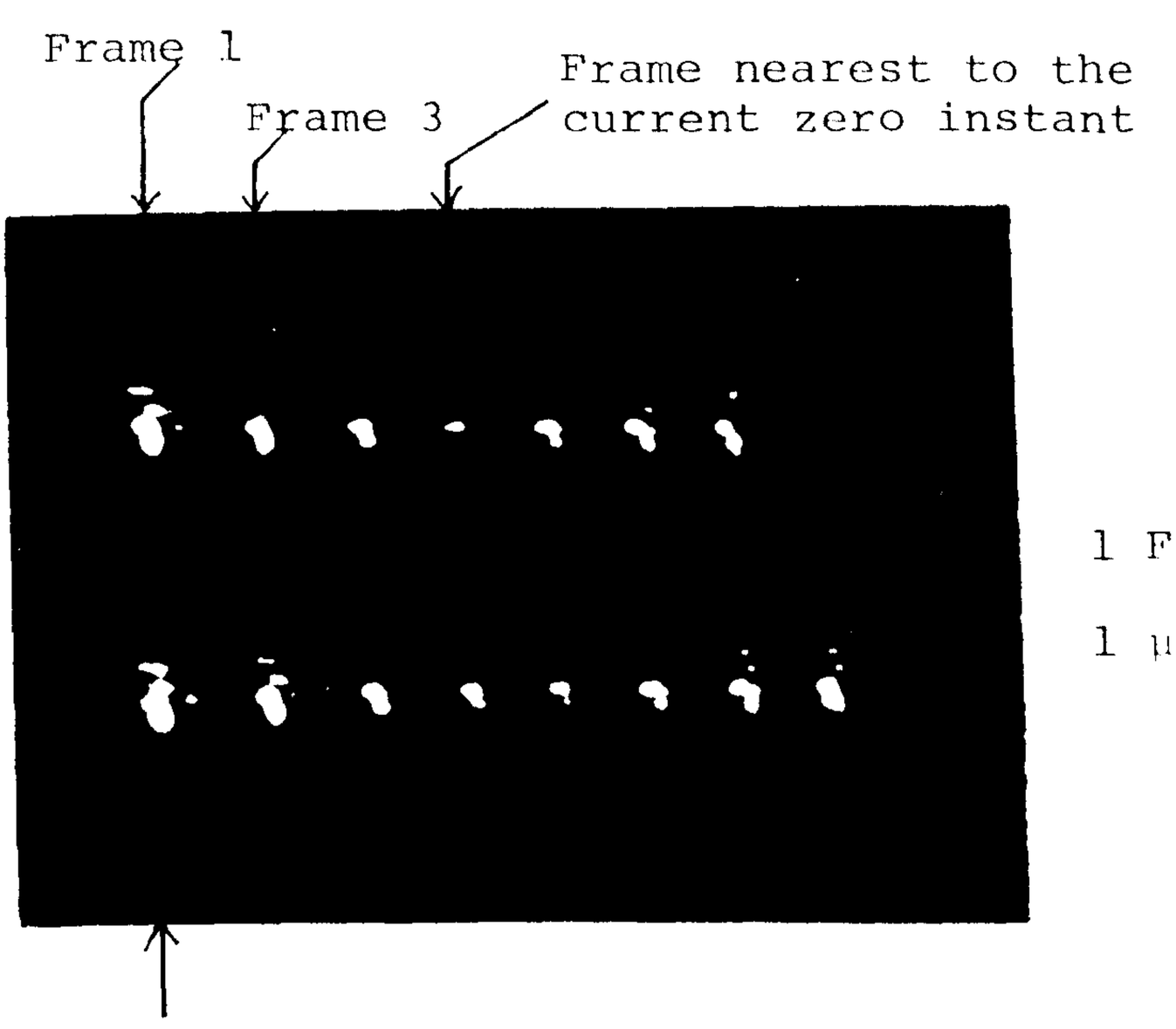

(b) The High Speed Photograph

Fig. 6.1 Typical Arc Current, Voltage, Luminous Cross-section and Peak Light Intensity Variation over the Major Part of the Current Ramp

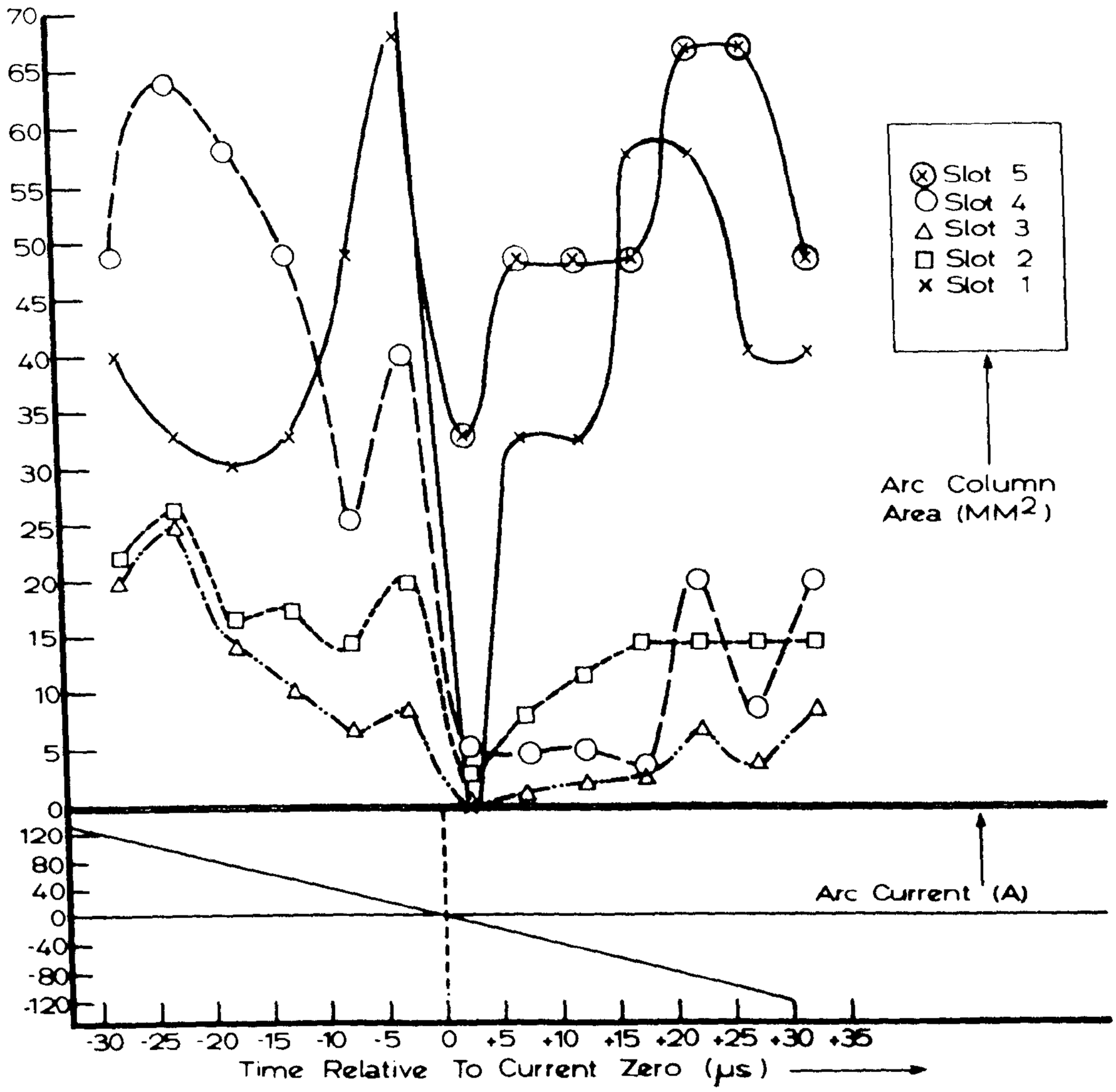

Operating conditions

Electrode material: Elkonite ; Holding current : 1·6KA

di/dt = 40 A/μs

1μs Exposure at 5μs framing interval; intensifier bias : 14KV

Fig. 6.1(c) Luminous Cross-section

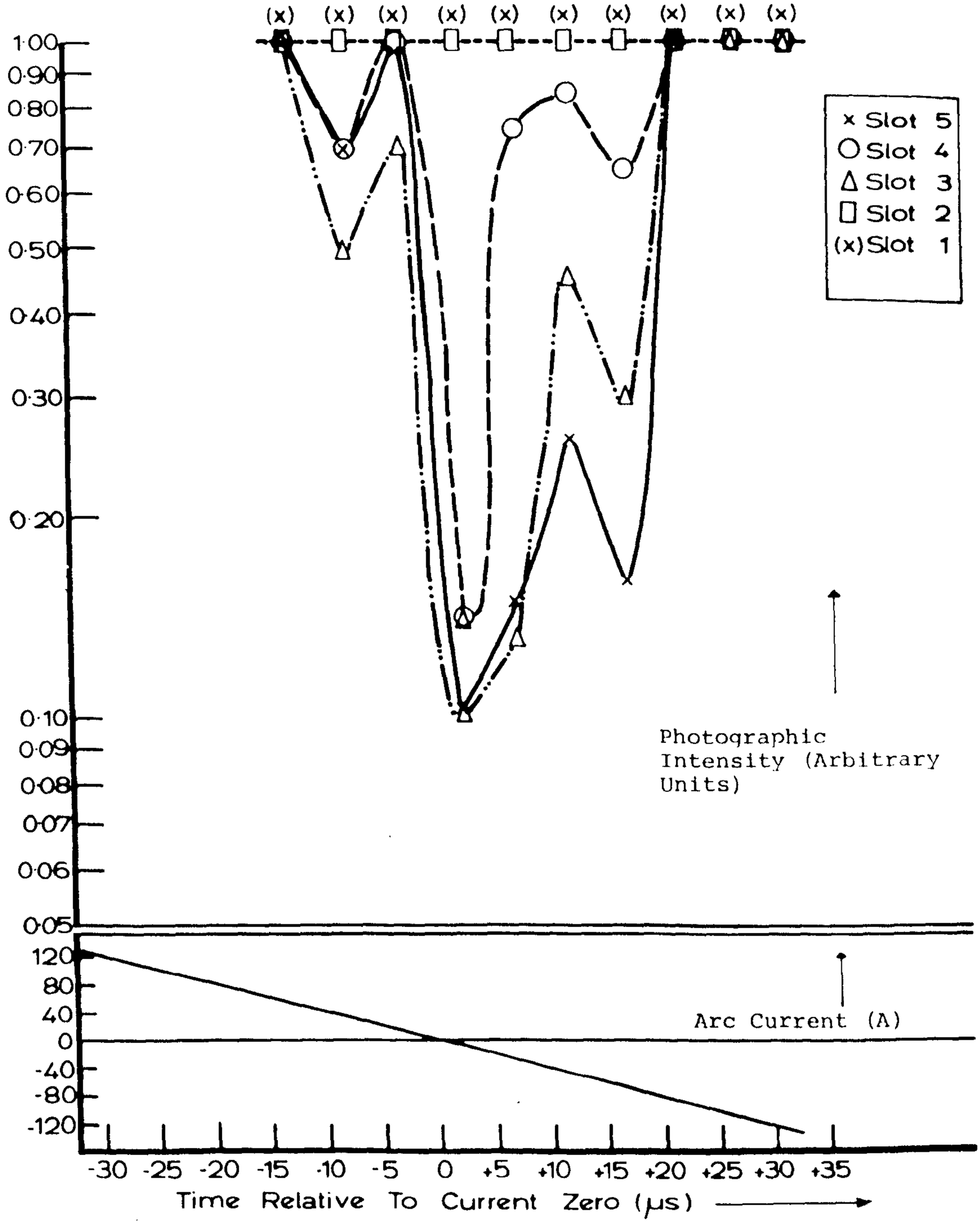

Operating conditions as for figure 6.1(c)

Fig. 6.1(d) Photographic Intensity

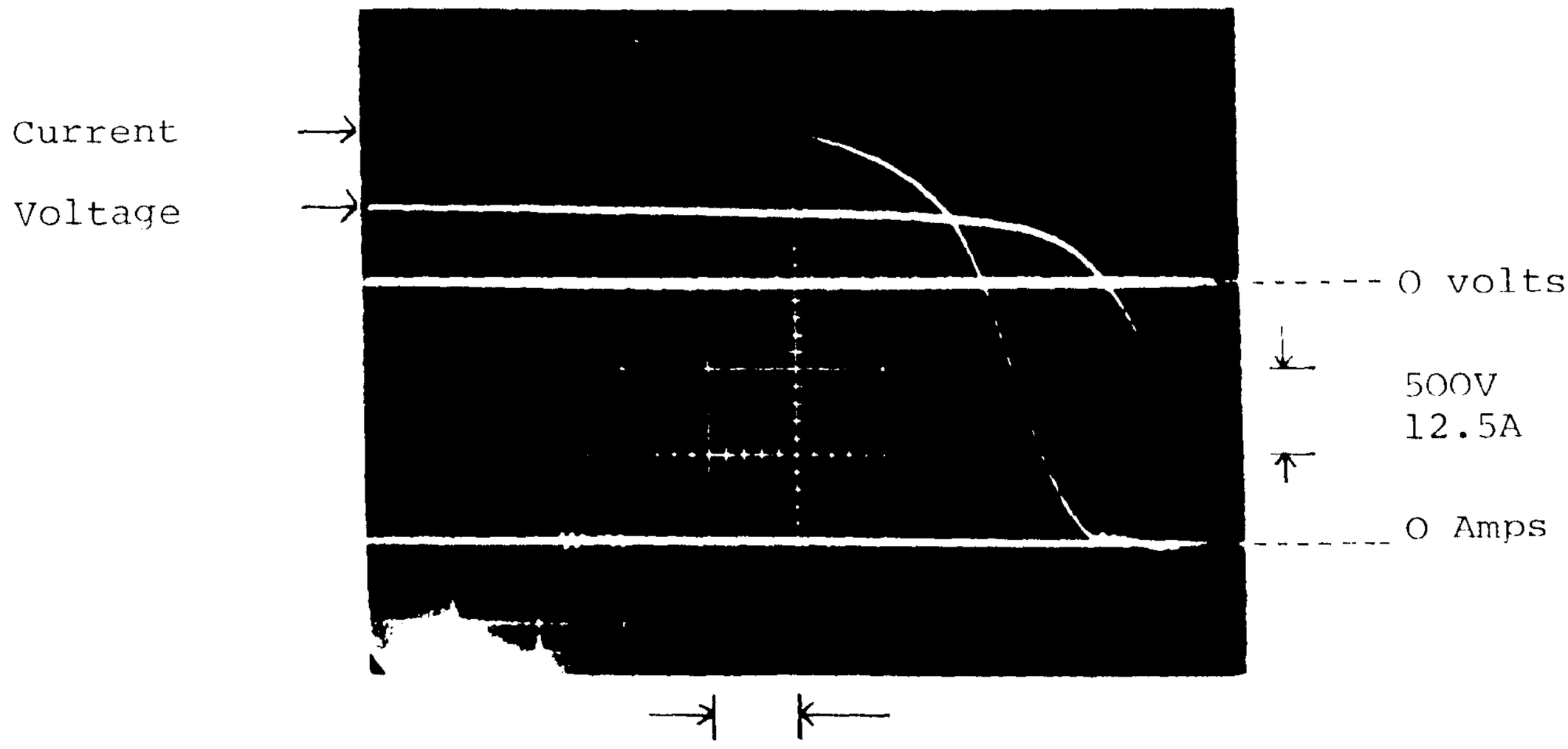

(a) Arc Current and Voltage

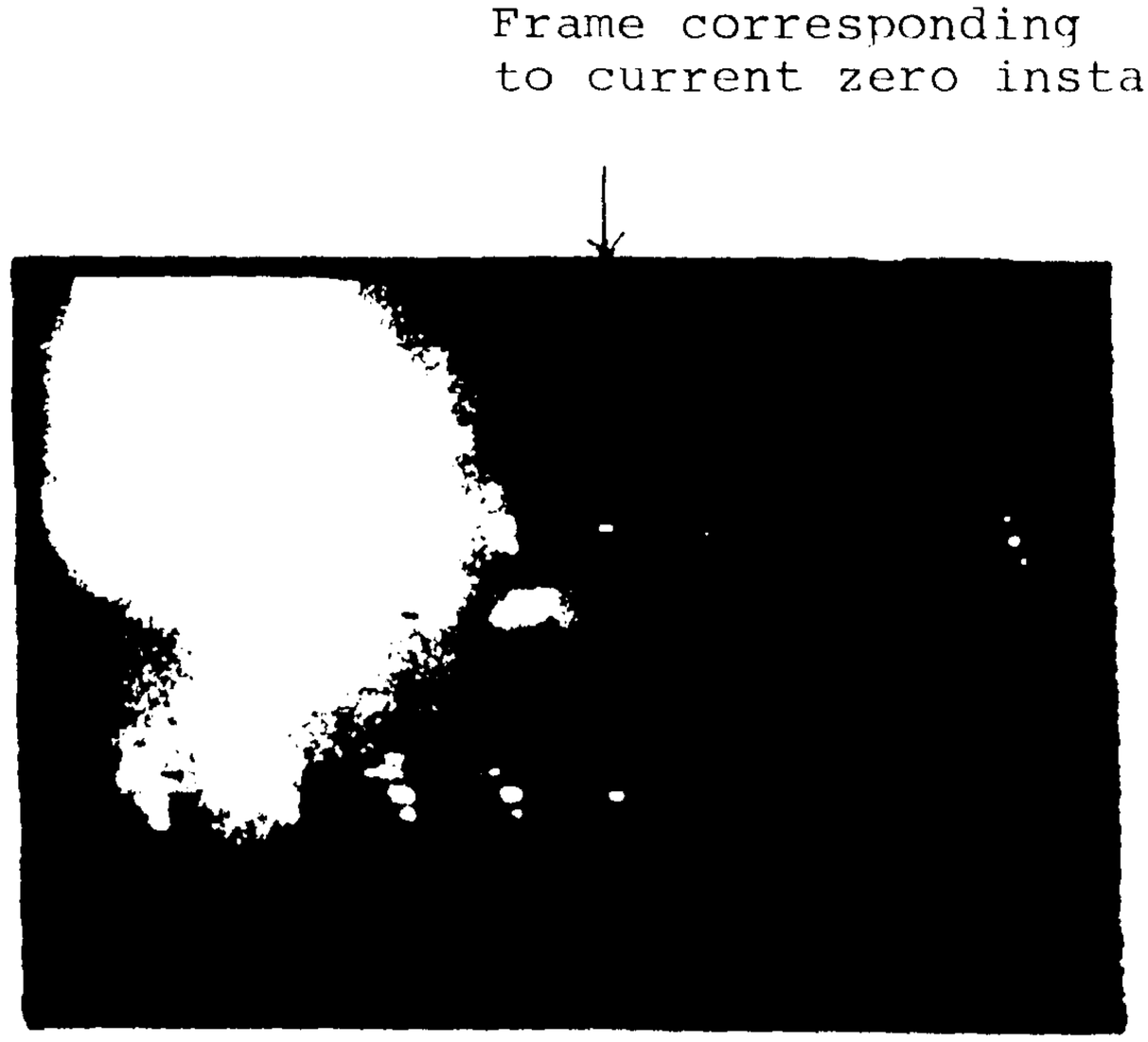

(b) A High Speed Photograph

Fig. 6.2 Current Zero Oscillogram and High Speed Photograph

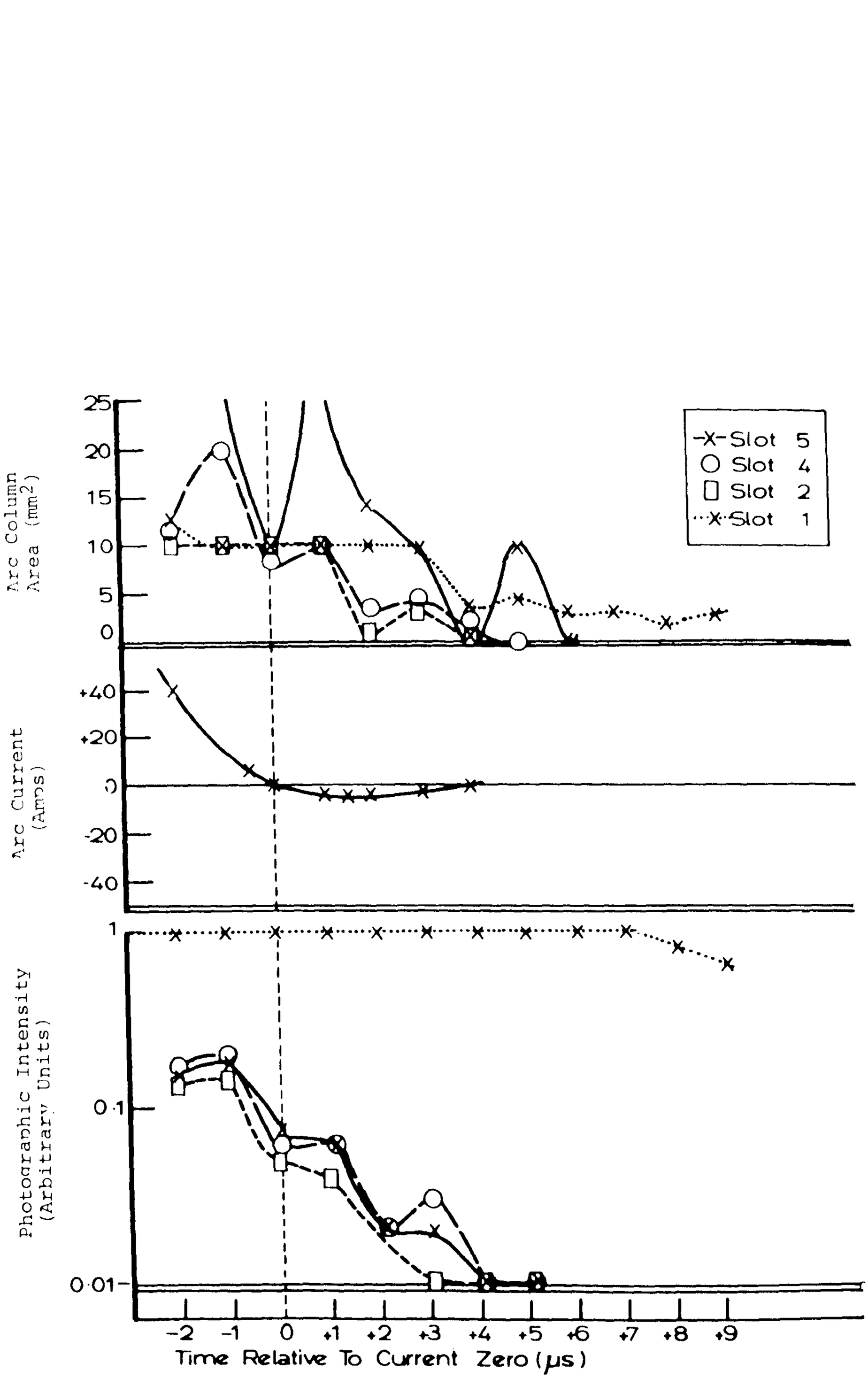

Clearance – no optical filters.
dI/dt = 36·0 A/μs ; dV/dt = 0·07 KV/μs
I holding = 1·6KA ; Upstream electrode – elkonite.

Fig. 6.3 Variation of Arc Area, Photographic Intensity and Current During the Current Zero Period

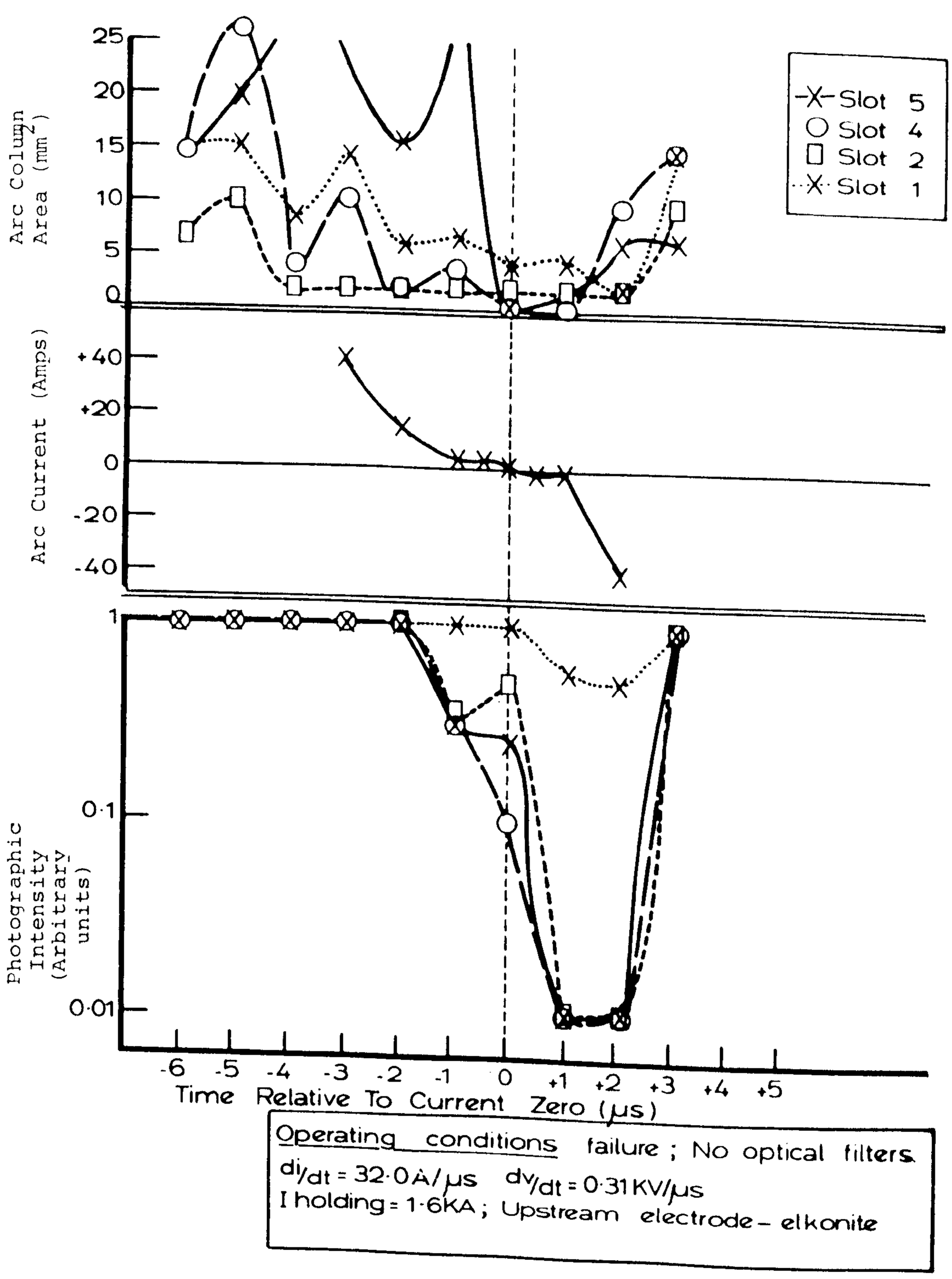
Arc Column Area (mm^2)
25
20
15
10
5
0
Slot 5
Slot 4
Slot 2
Slot 1
Arc Current (Amps)
+40
+20
0
-20
-40
Photographic Intensity (Arbitrary units)
1
0·1
0·01
-6 -5 -4 -3 -2 -1 0 +1 +2 +3 +4 +5
Time Relative To Current Zero (μs)
Operating conditions failure ; No optical filters
di/dt = 32·0A/μs dv/dt = 0·31KV/μs
I holding = 1·6KA ; Upstream electrode – elkonite

Fig. 6.3(b)

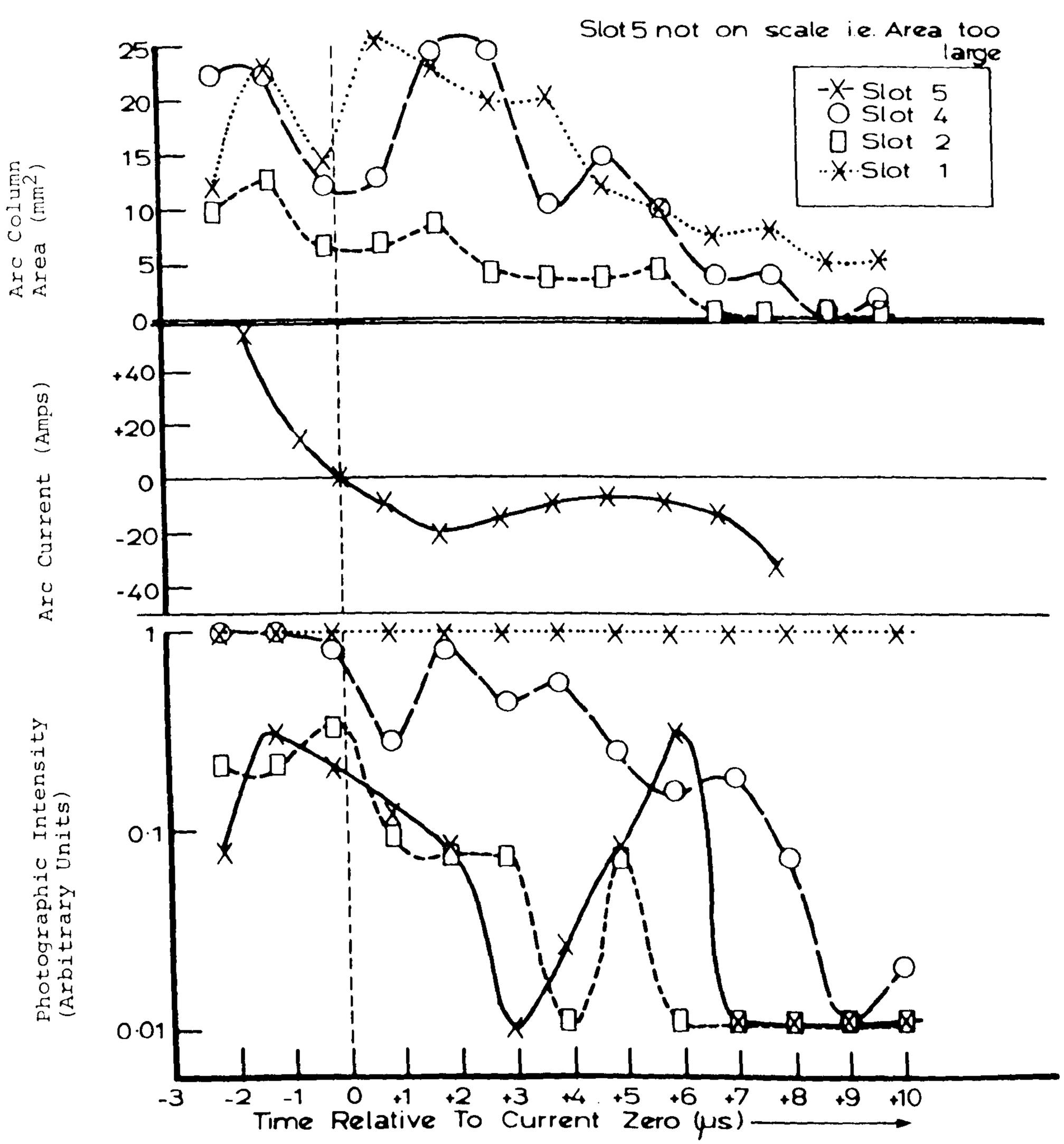
Slot 5 not on scale i.e. Area too large
Slot 5
Slot 4
Slot 2
Slot 1
Arc Column Area (mm^2)
25
20
15
10
5
0
Arc Current (Amps)
+40
+20
0
-20
-40
Photographic Intensity (Arbitrary Units)
1
0·1
0·01
-3 -2 -1 0 +1 +2 +3 +4 +5 +6 +7 +8 +9 +10
Time Relative To Current Zero (μs)
Operating Conditions
Clearance; Optical filter - Cu band 517 ± 4·5nm
48% transmission di/dt = 33·0A/μs ; dv/dt 0·07KV/μs
I holding = 1·6KA ; Upstream electrode - elkonite.

Fig. 6.3(c)

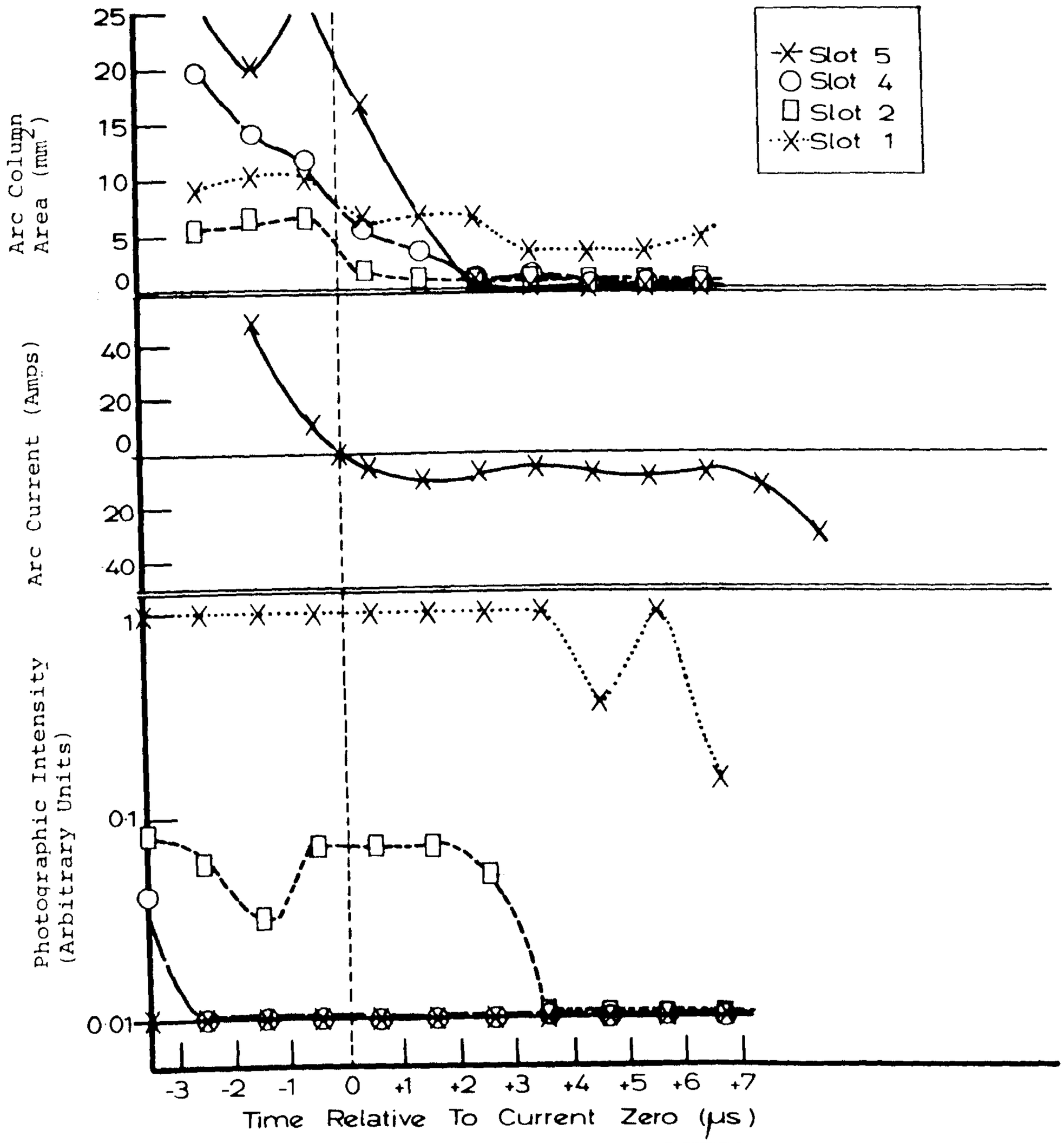

Operating conditions: Failure: optical filter – Cu band 517 ± 4·5nm 48% transmisson $di/dt = 35{\cdot}5A/\mu s$; $dv/dt = 0{\cdot}1KV/\mu s$; I holding = 1·6KA; Upstream electrode – elkonite.

Fig. 6.3(d)

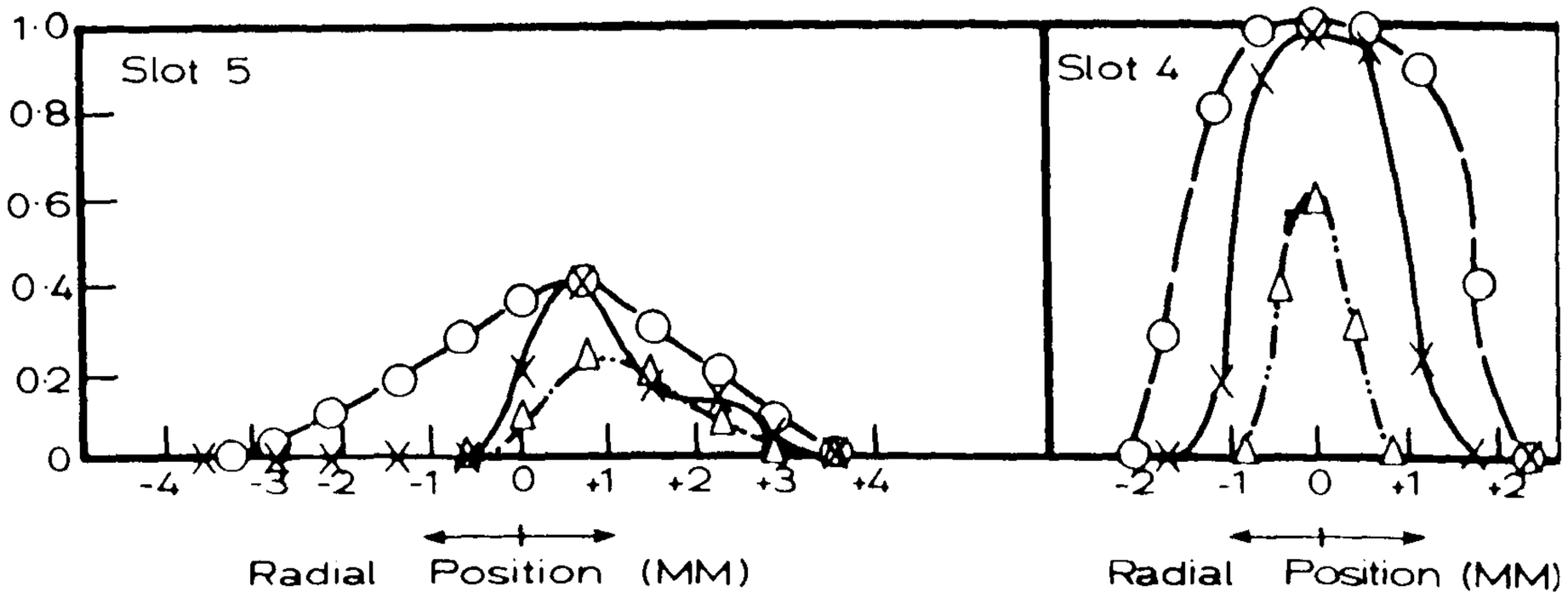

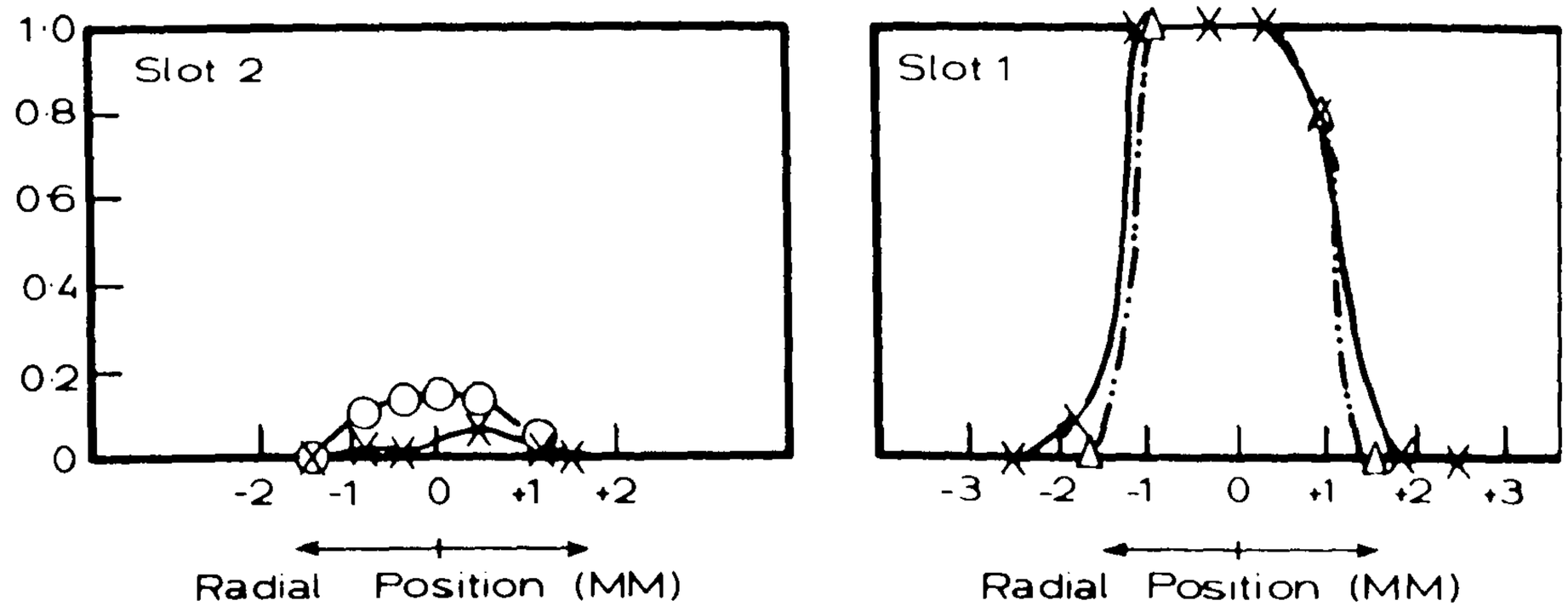

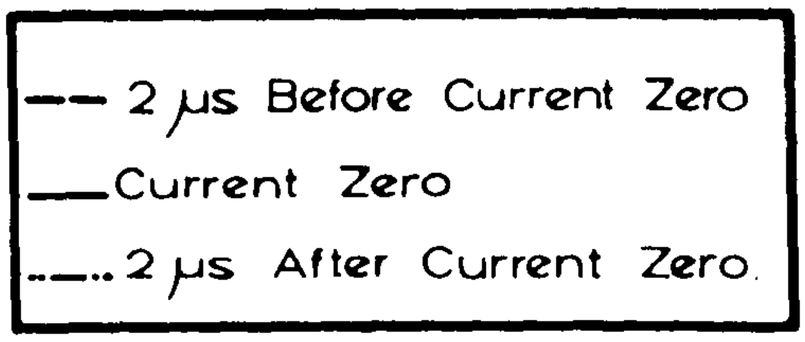

Figure. 6.4a Measured Radial Intensity Distributions At Different Slots (1,2,4,5,) For The Times 2μs Before, At And 2μs After Current Zero.

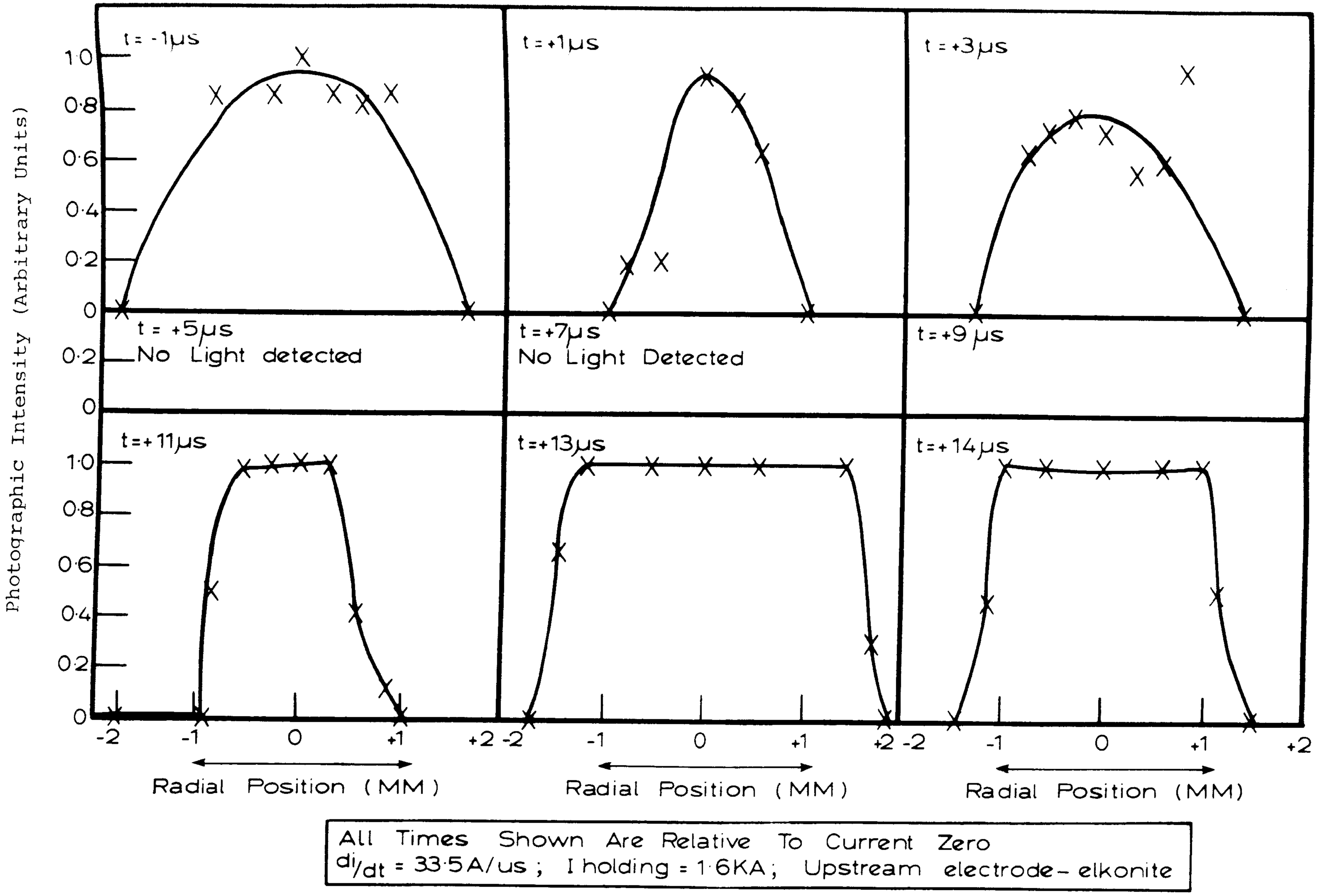

Fig. 6.4(b) Measured Radial Intensity Distributions for Slot 3 during the Current Zero Period

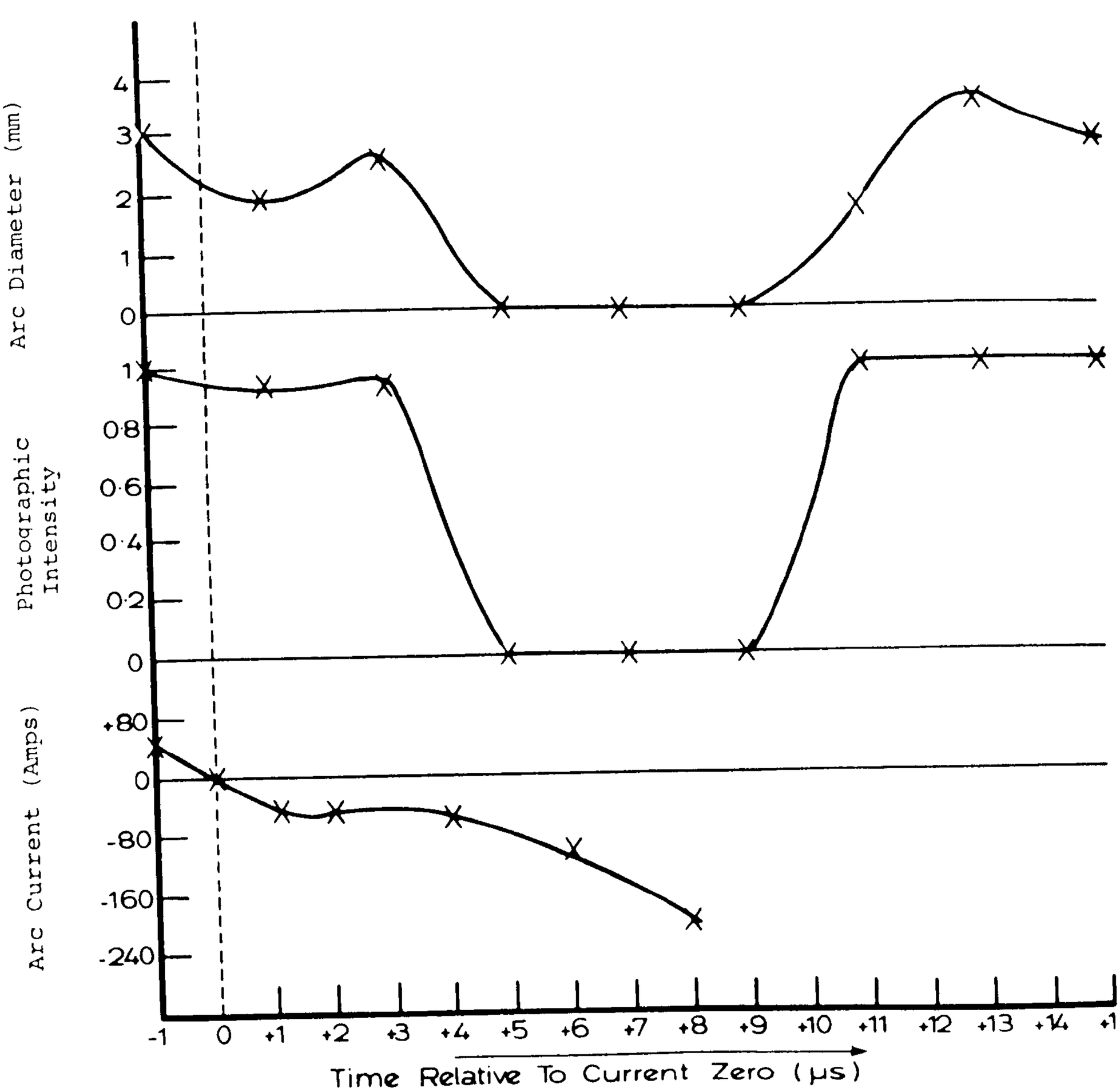

Operating Conditions

di/dt = 33.5A/μs — Holding Current = 1.6KA

dv/dt = 0.2KV/μs — Upstream Electrode Material - Elkonite

Fig. 6.4(c) Variation of the Slot 3 Luminous Arc Diameter, Photographic Intensity and Current With Time

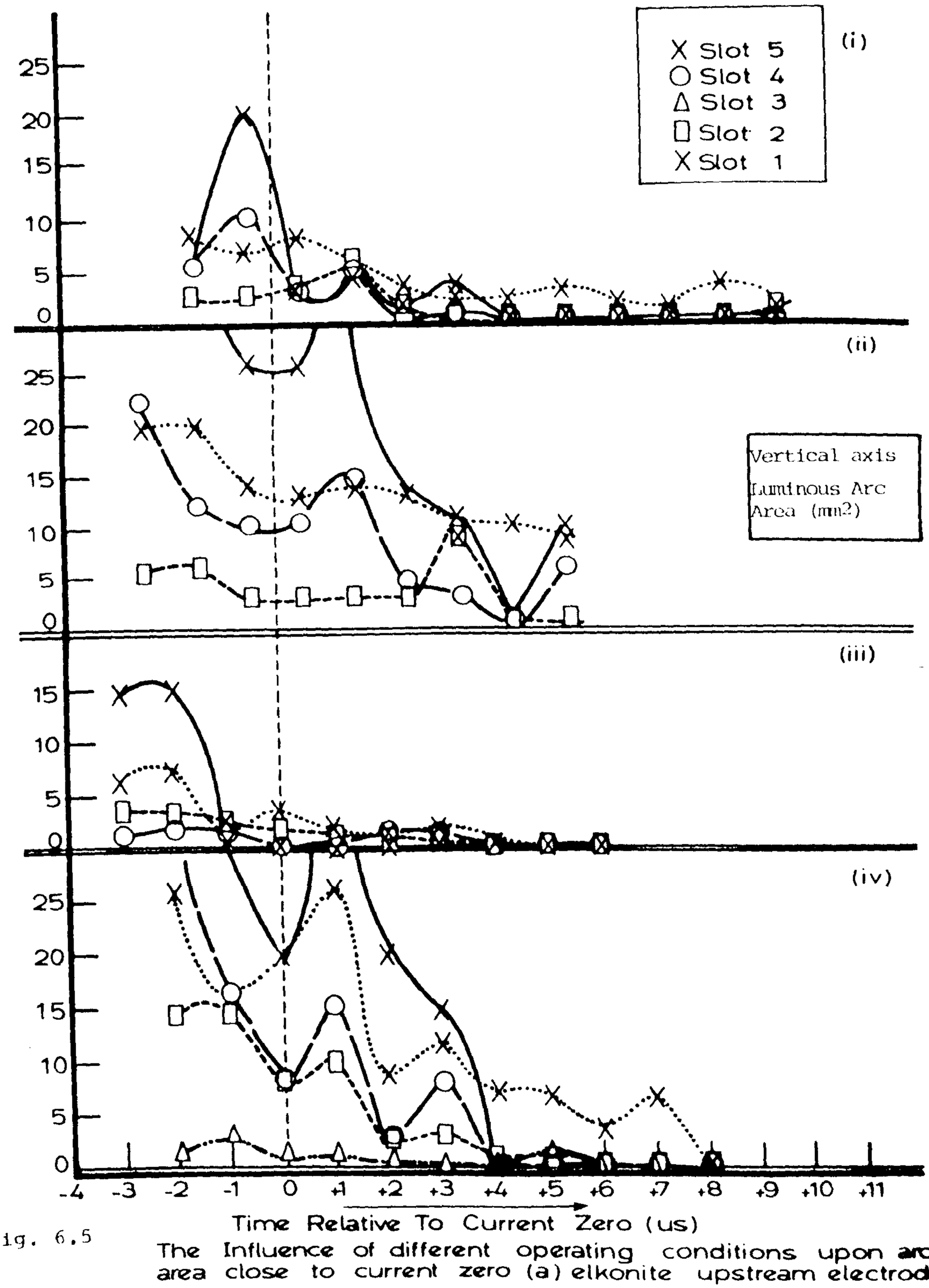

Fig. 6.5 The Influence of different operating conditions upon arc area close to current zero (a) elkonite upstream electrode

	I holding	di/dt	dv/dt	optical filters
(i)	1·6 KA	18A/μs	KV/μs	None
(iii)	0·36 KA	15A/μs	KV/μs	Neutral Density 0·3

	I holding	di/dt	dv/dt	optical filters
(ii)	1·6 KA	365A/μs	0·1KV/μs	None
(iv)	0·36KA	35A/us	KV/us	None

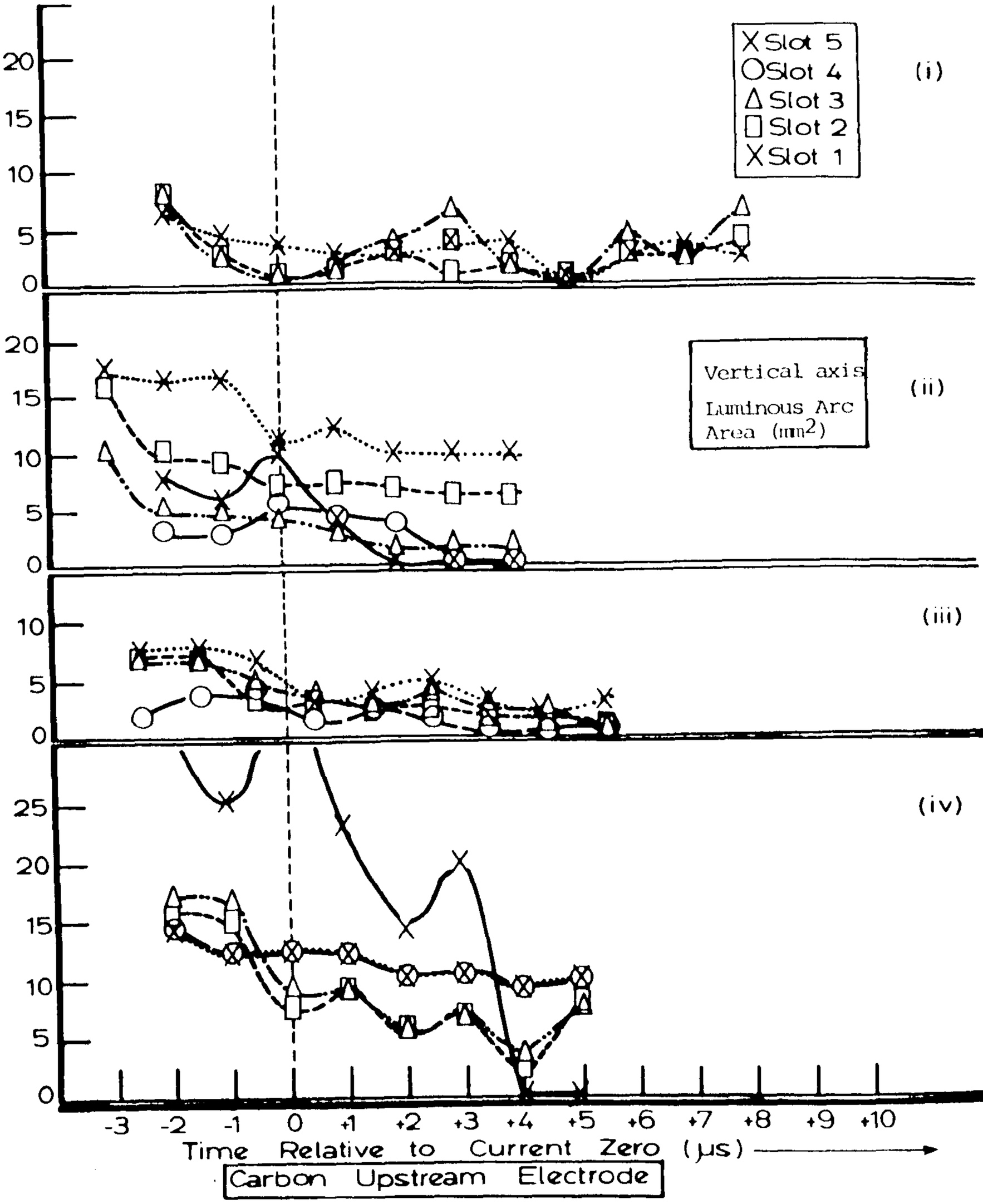

	I holding	di/dt	dv/dt	optical filters
(i)	1·6KA	165A/μs	2·5KV/μs	None
(iii)	0·7KA	189A/μs	1·7KV/μs	None

	I holding	di/dt	dv/dt	optical filters
(ii)	1·6KA	39A/μs	0·23 KV/μs	Copper 517±45nm
(iv)	0·7KA	37·5A/μs	0·27 KV/μs	None

Fig. 6.5(b) Carbon Upstream Electrode

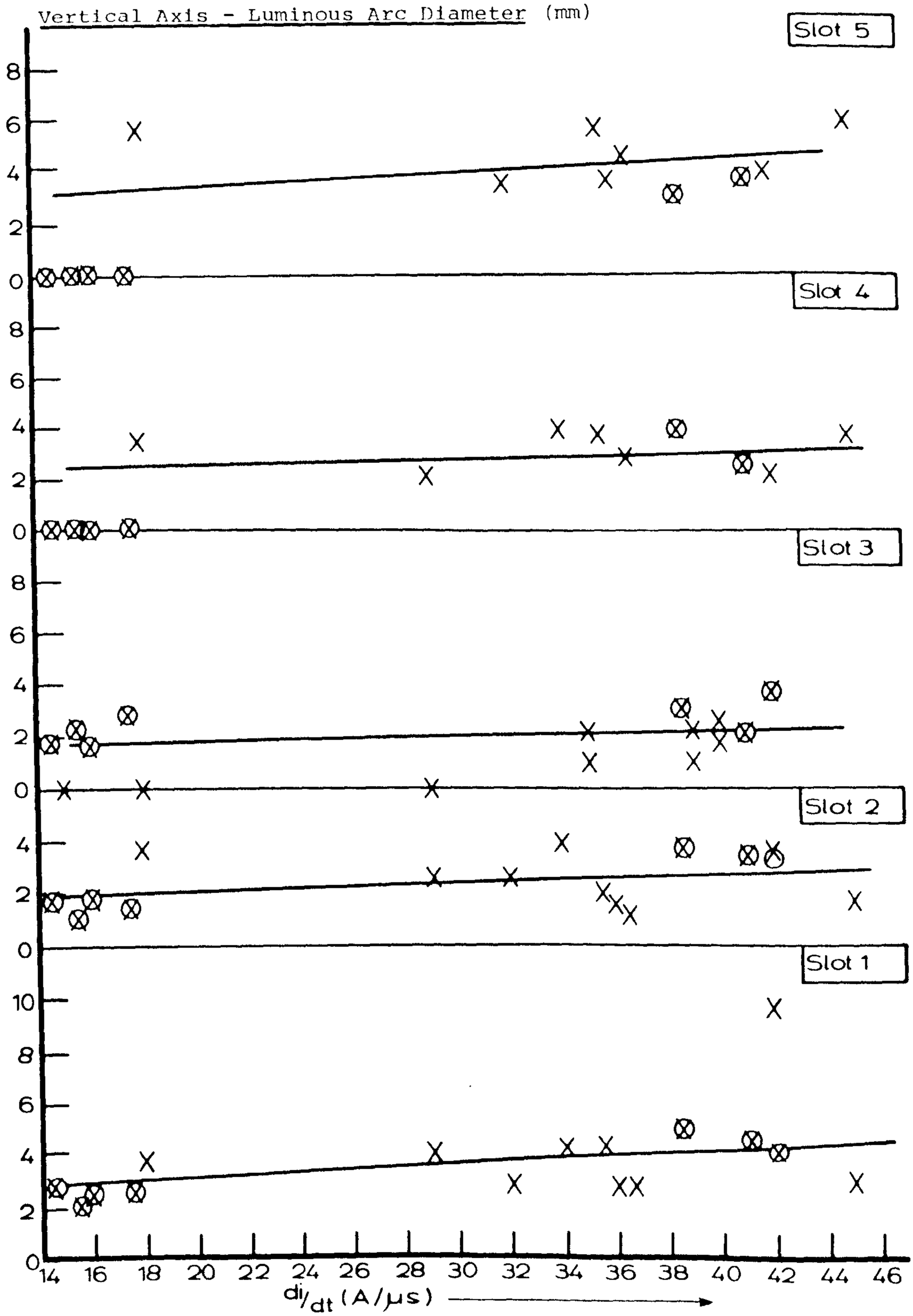

Figure. 6.6a Variation of Arc Diameter at Current Zero With di/dt For Carbon and Elkonite Electrode Arcs

⊗ - Carbon X - Elkonite

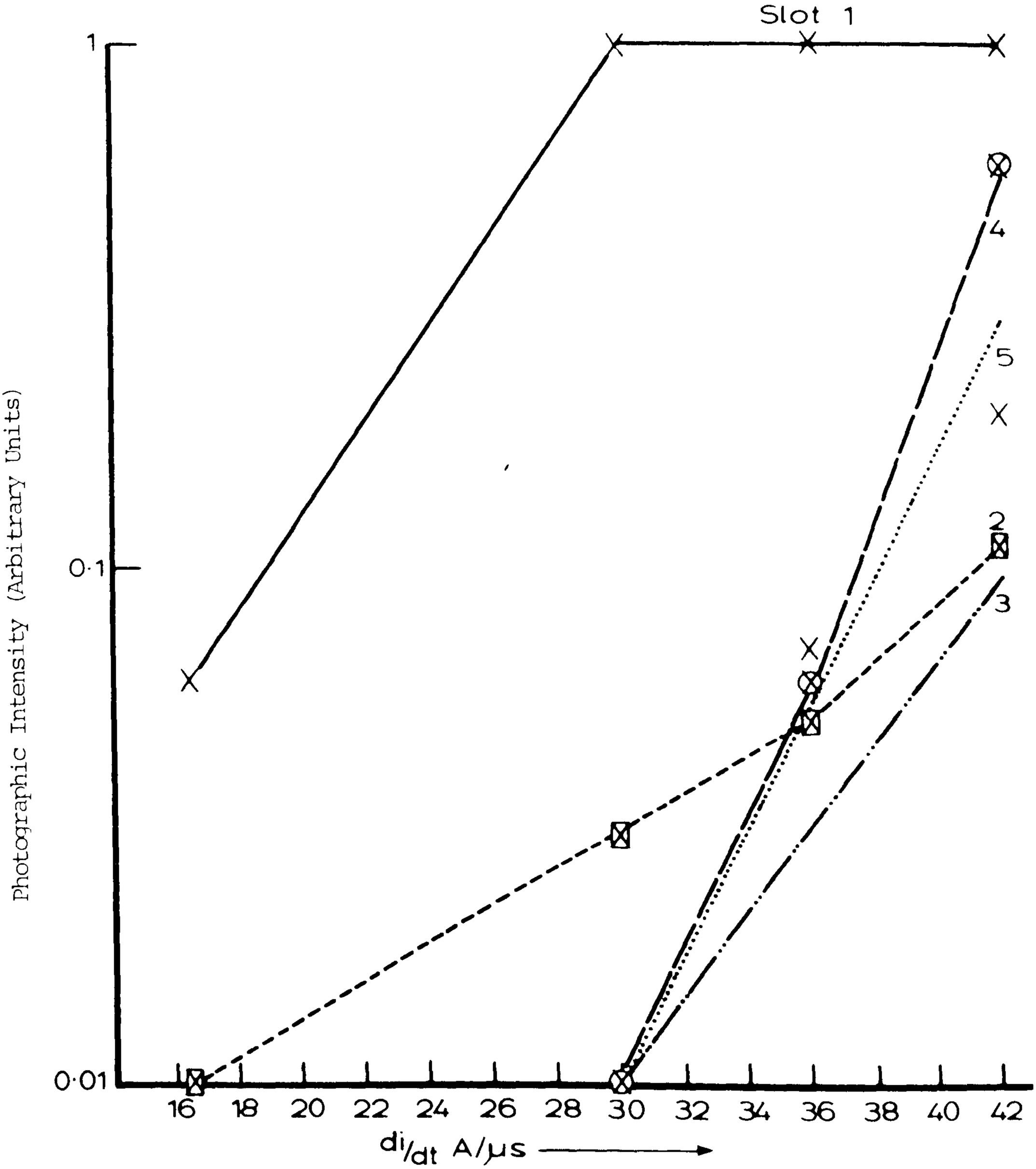

Fig. 6.6(b) Variation of the Photographic Intensity of the Arc Column at Different Axial Stations for Elkonite Electrodes with di/dt. (3 from Shammas and Jones, ULAP T70)

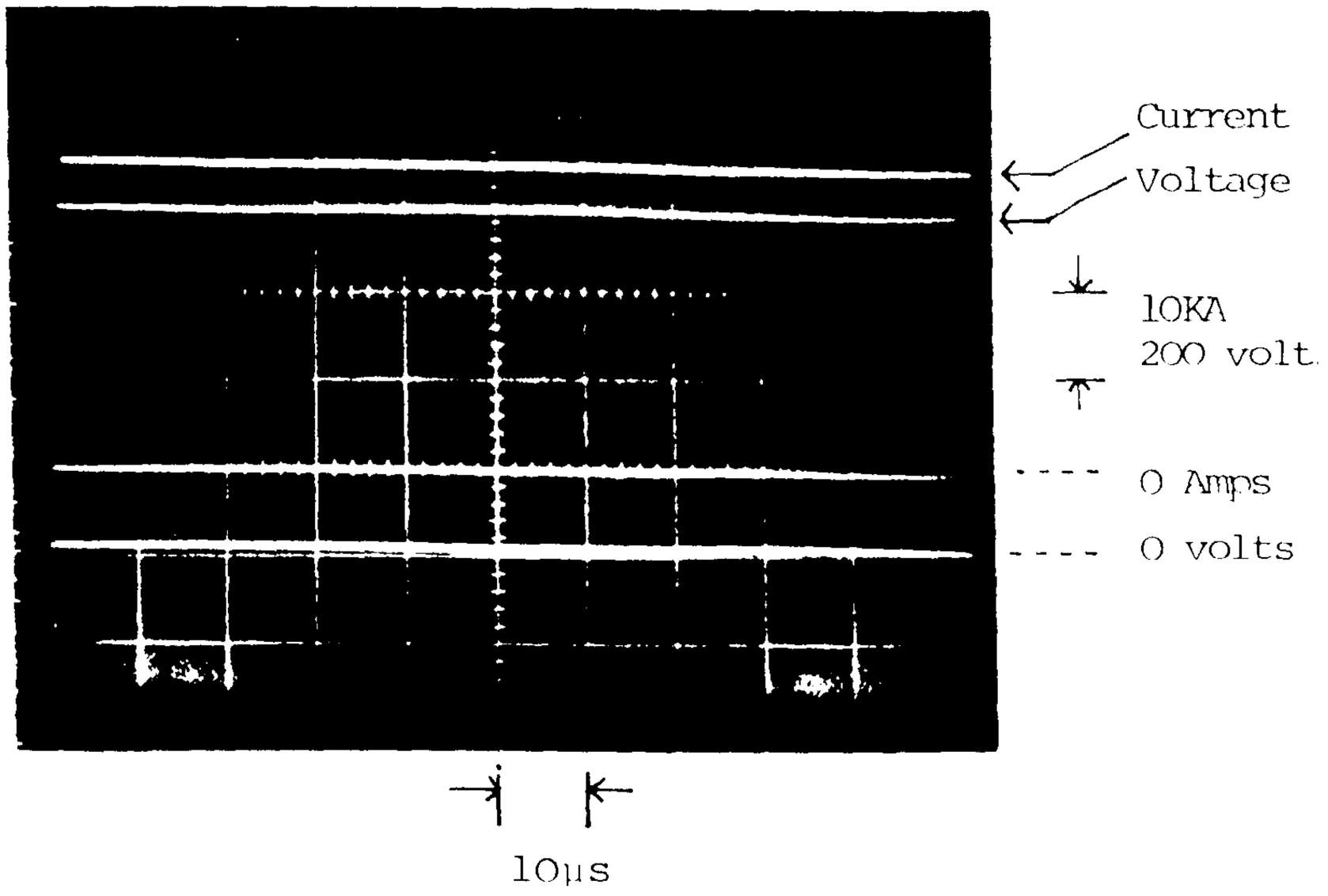

(a) Arc Current and Voltage Oscillogram

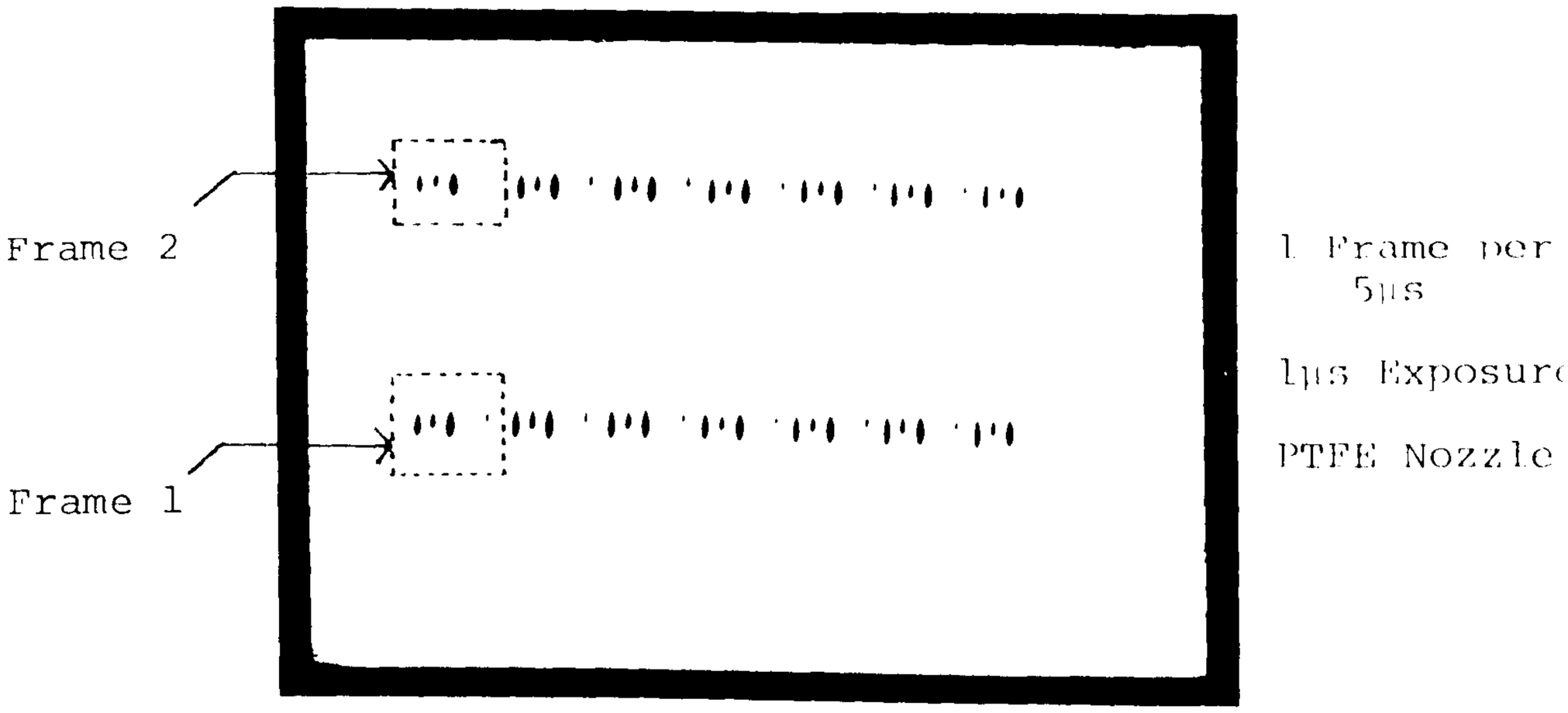

(b) The High Speed Photograph Corresponding to Fig. 6.7(a)

Fig. 6.7 Typical Arc Current and Voltage Record with the Corresponding High Speed Photograph taken during the Peak Current Period

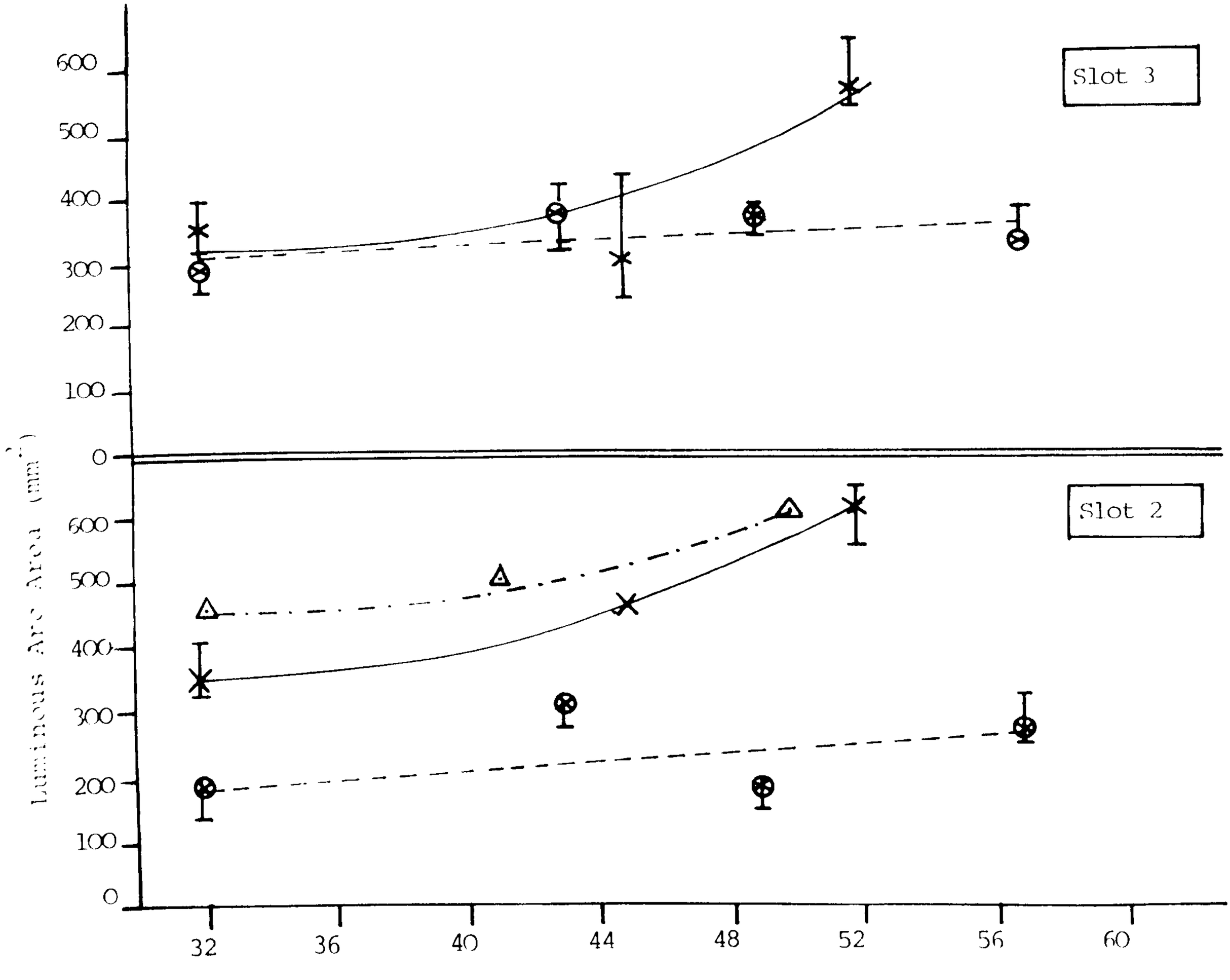

Fig. 6.8 Variation of Luminous Arc Area at the Current Peak with Peak Current Value

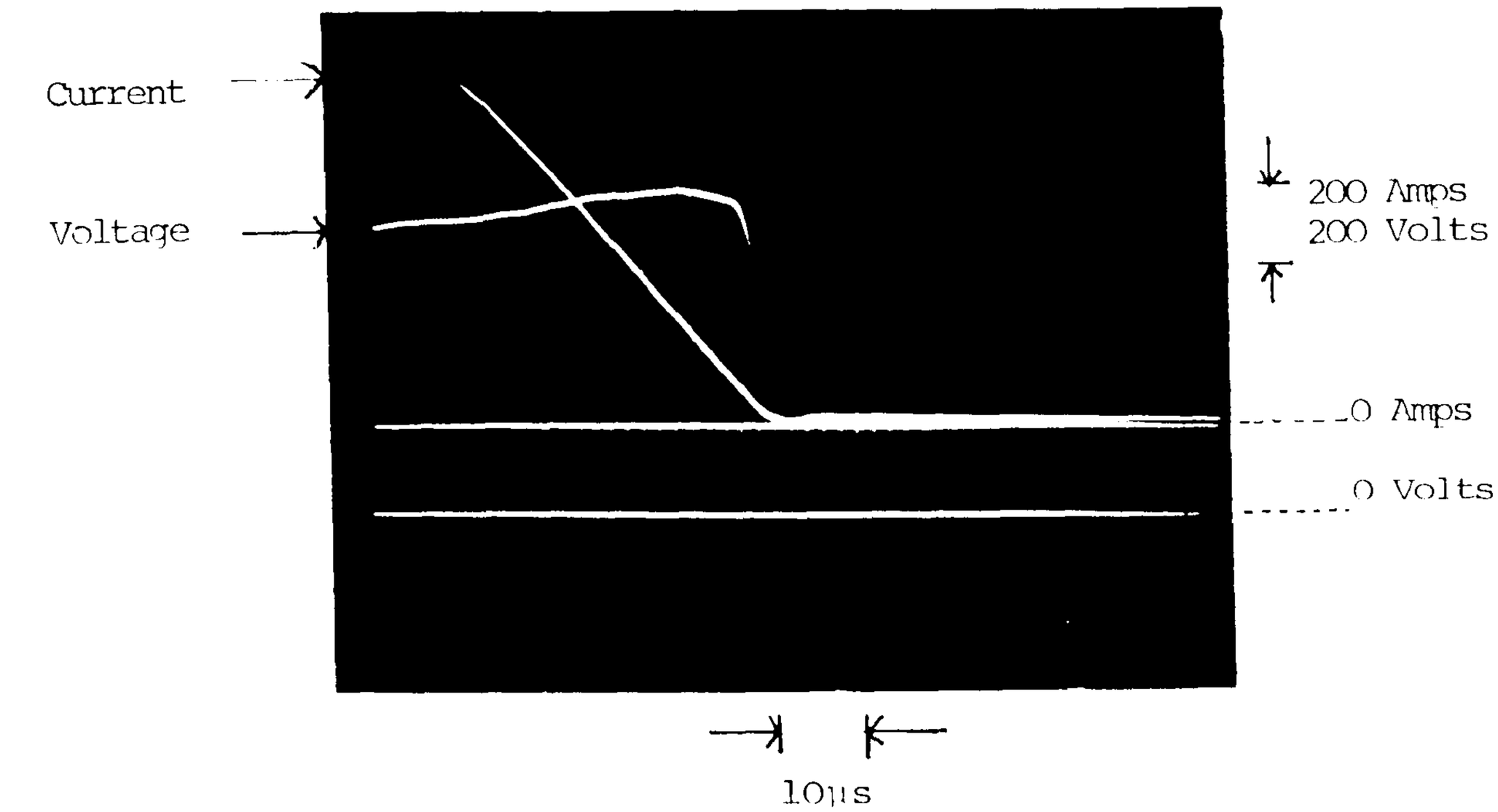

(a) Arc Voltage and Current Oscillogram

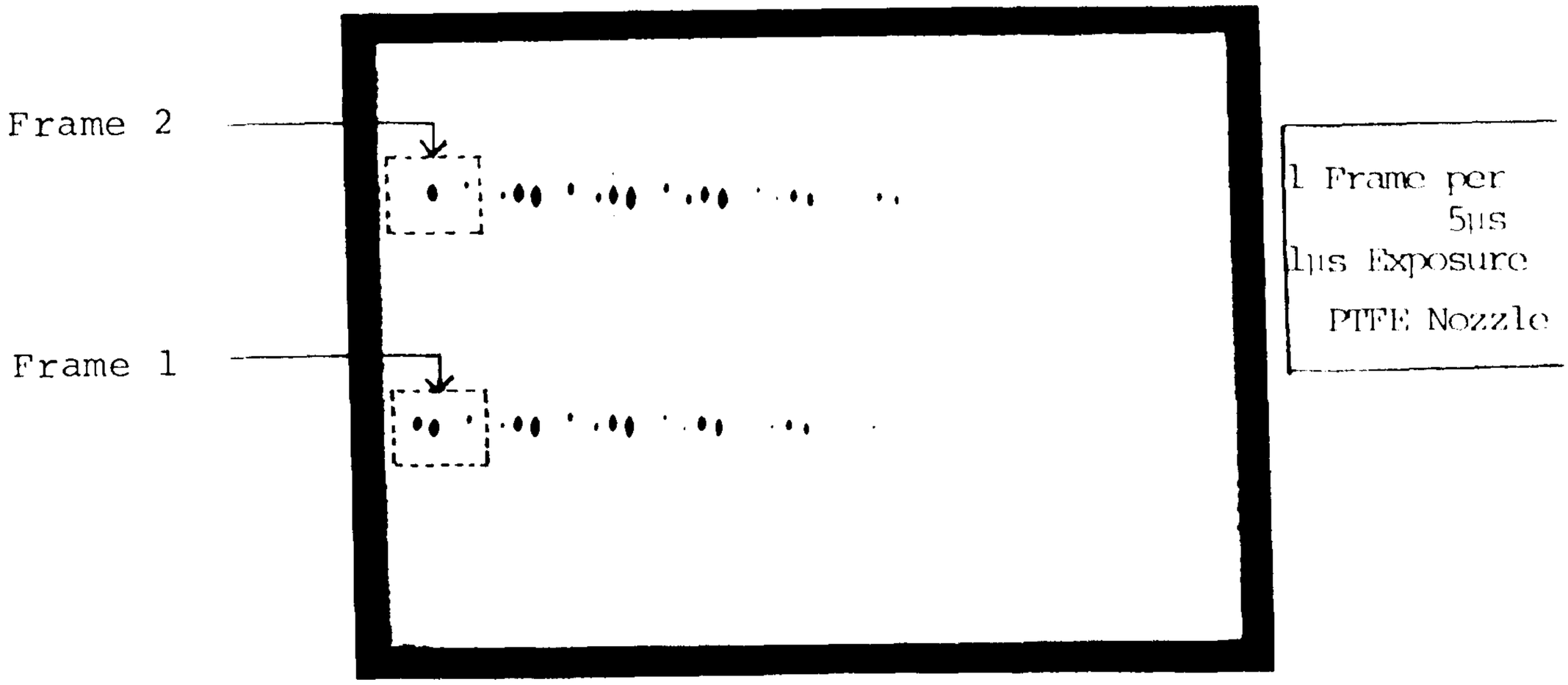

(b) High Speed Photograph Corresponding to (a)

Fig. 6.9 Typical Arc Current and Voltage Record with the Corresponding High Speed Photograph Taken During the last 50μs of the Current Decay. Peak Current = 46KA

Figure Number	di/dt (A/us)	Nozzle Material	Electrodes Material	Peak Current	Intensities Bias (KV)	NDF Value
(a)	18.2	PTFE	Elkonite	36	14	0
(b)	22.0	PTFE	Elkonite	53	14	0
(c)	26.0	PTFE	Elkonite	62	14	0

Summary of Operating Conditions

Fig. 6.10 Variation of Arc Cross-sectional Area, Axis Light Intensity and Arc Current Over the Final 50us of the Current Decay

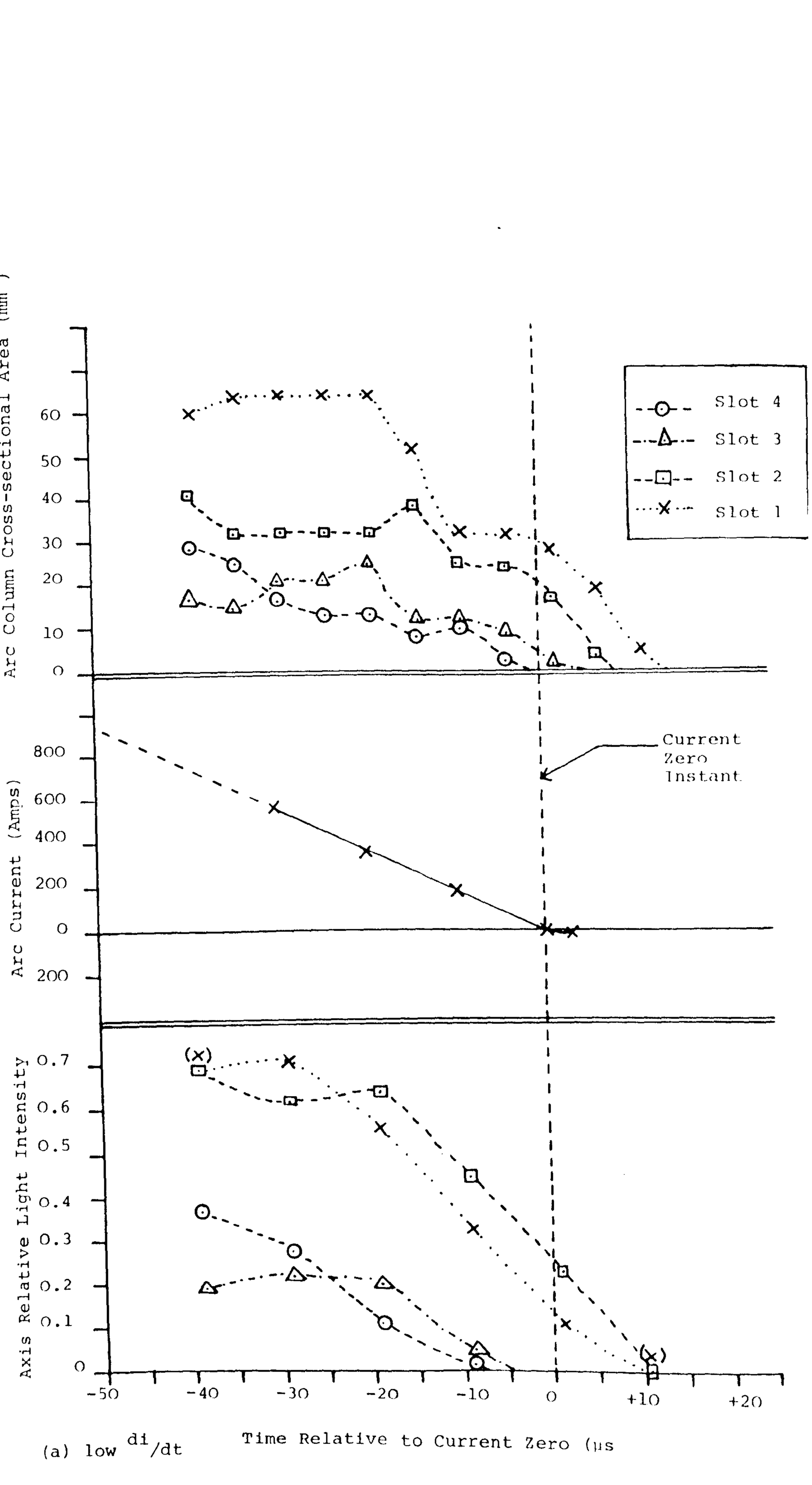
Arc Column Cross-sectional Area (mm²)
60
50
40
30
20
10
0
Slot 4
Slot 3
Slot 2
Slot 1
Current Zero Instant
Arc Current (Amps)
800
600
400
200
0
200
Axis Relative Light Intensity
0.7
0.6
0.5
0.4
0.3
0.2
0.1
0
(X)
-50
-40
-30
-20
-10
0
+10
+20
Time Relative to Current Zero (μs

(a) low di/dt

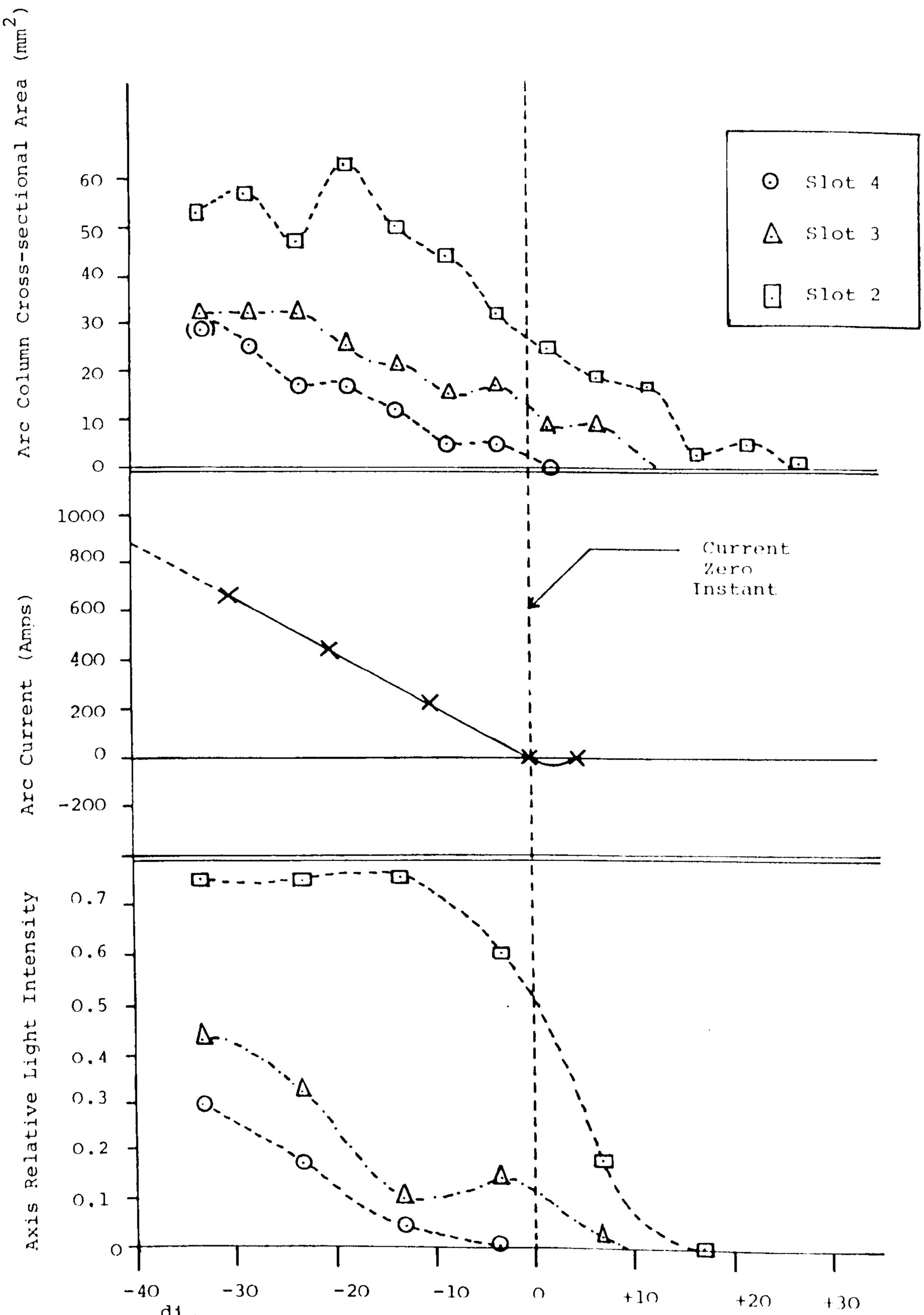
Arc Column Cross-sectional Area (mm^2)
60
50
40
30
20
10
0
Slot 4
Slot 3
Slot 2
1000
800
600
400
200
0
-200
Arc Current (Amps)
Current Zero Instant
0.7
0.6
0.5
0.4
0.3
0.2
0.1
0
Axis Relative Light Intensity
-40
-30
-20
-10
0
+10
+20
+30
(b) Medium di/dt
Time Relative to Current Zero (μs)

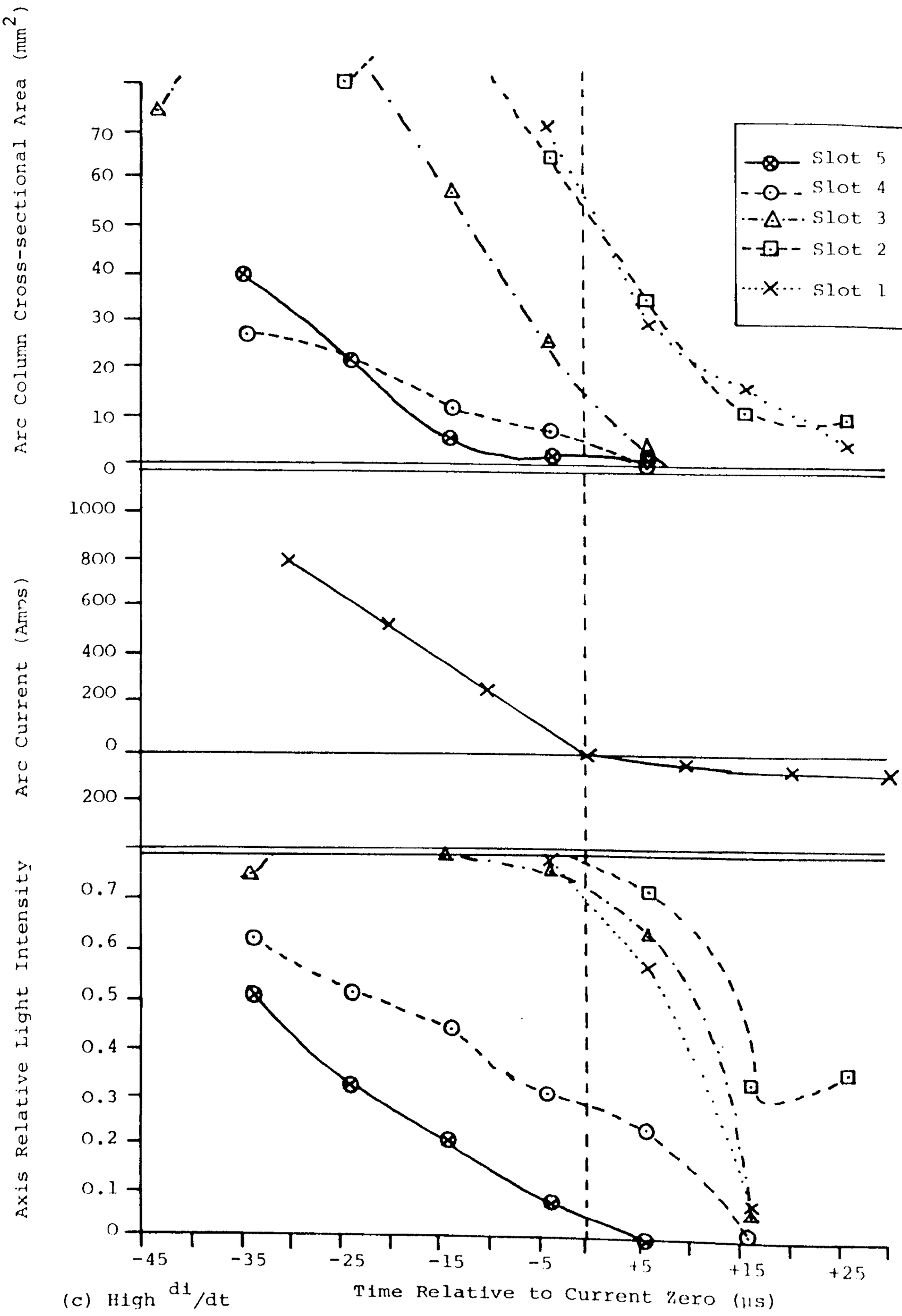

(c) High $\frac{di}{dt}$

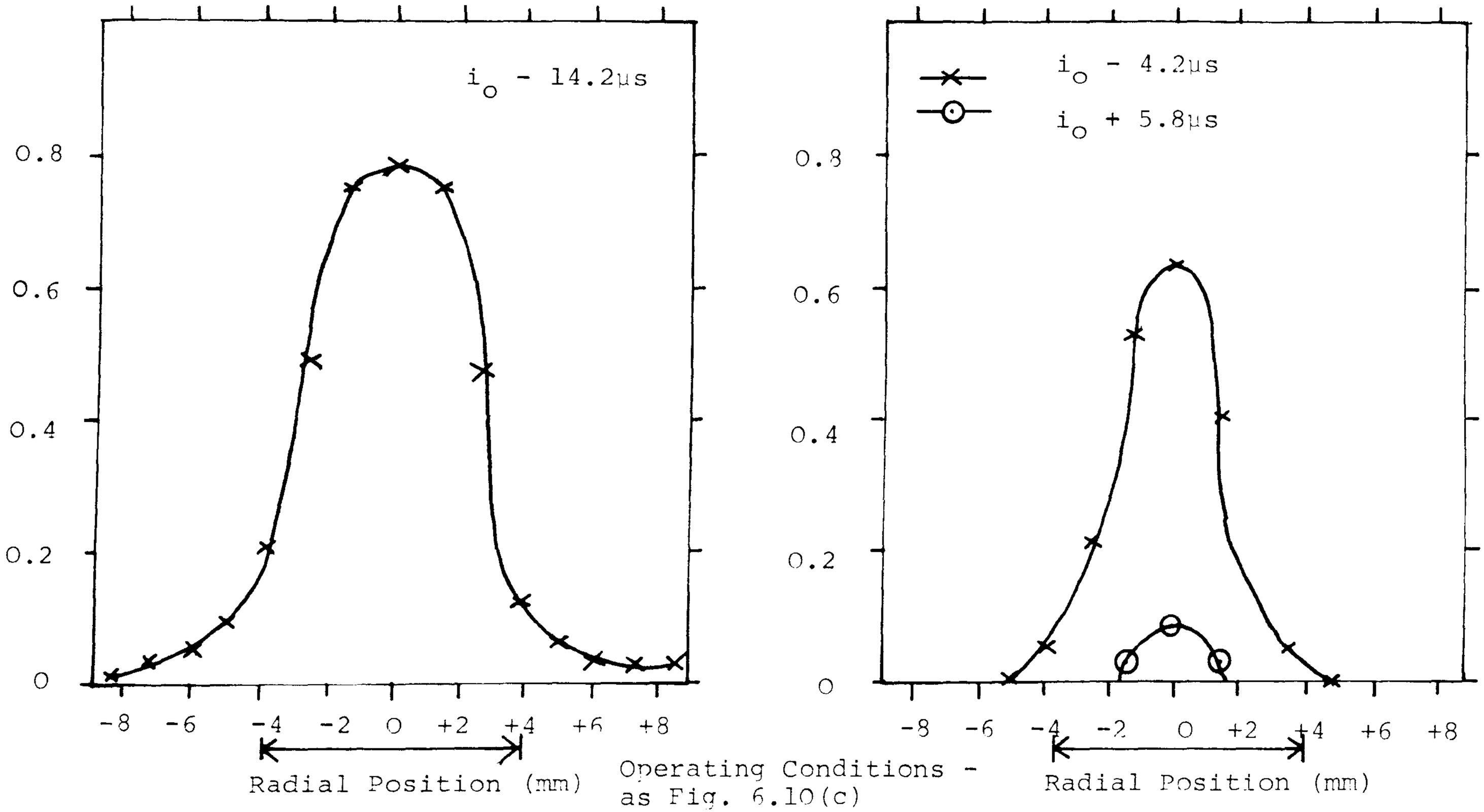

Fig. 6.11 Measured Radial Intensity Distribution at 10μs Intervals on the Approach To and After Current Zero at Slot 3

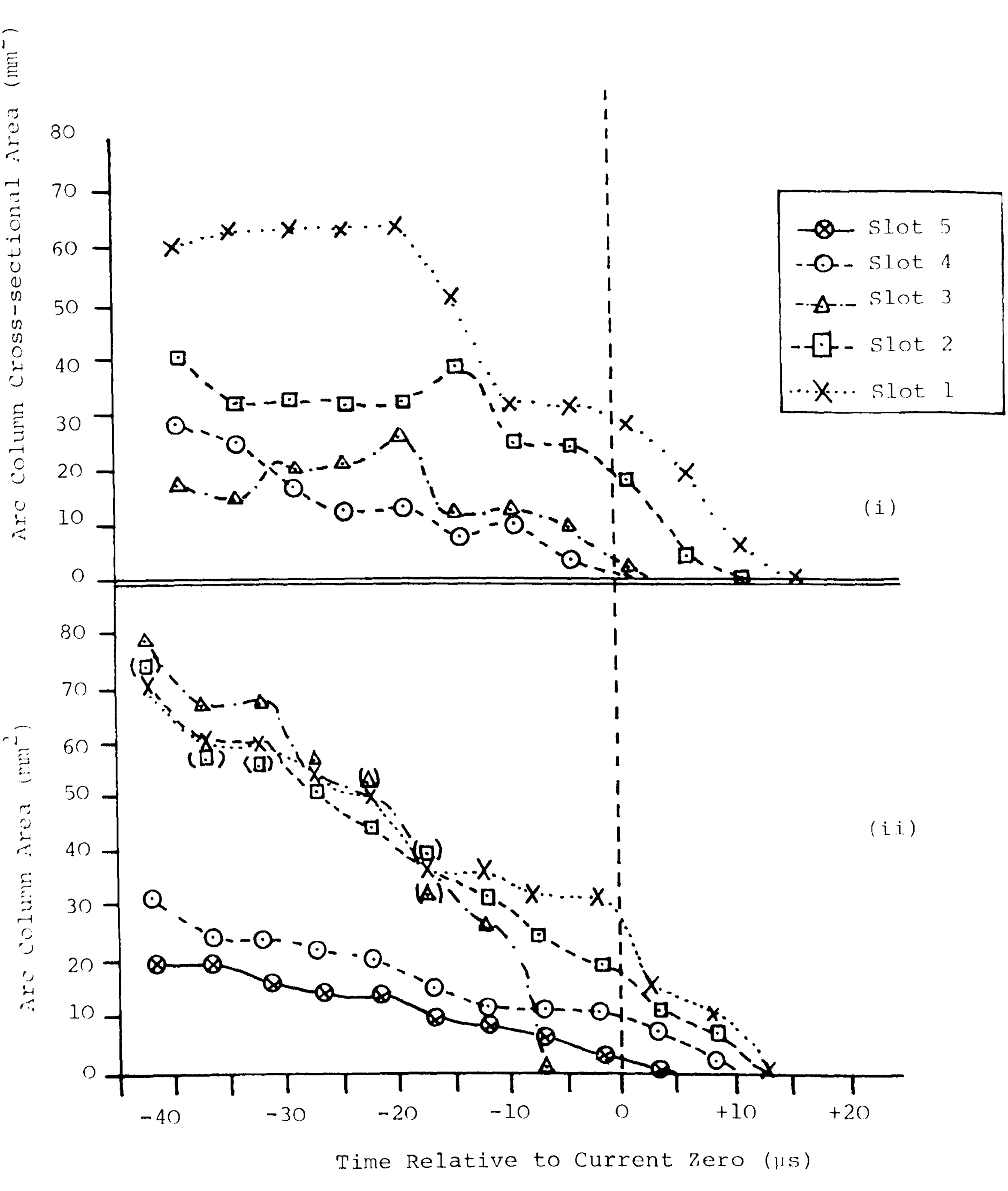

Operating Condition	Nozzle Material	di/dt (A/μs)	Electrodes Material	Intensifier Bias (KV)	Optical Filters
(i)	PTFE	18.2	Elkonite	14	None
(ii)	Copper	16.2	Elkonite	15	None

(a) Low di/dt

Fig. 6.12 The Influence of the Nozzle Material on the Arc Area on the Approach to Current Zero

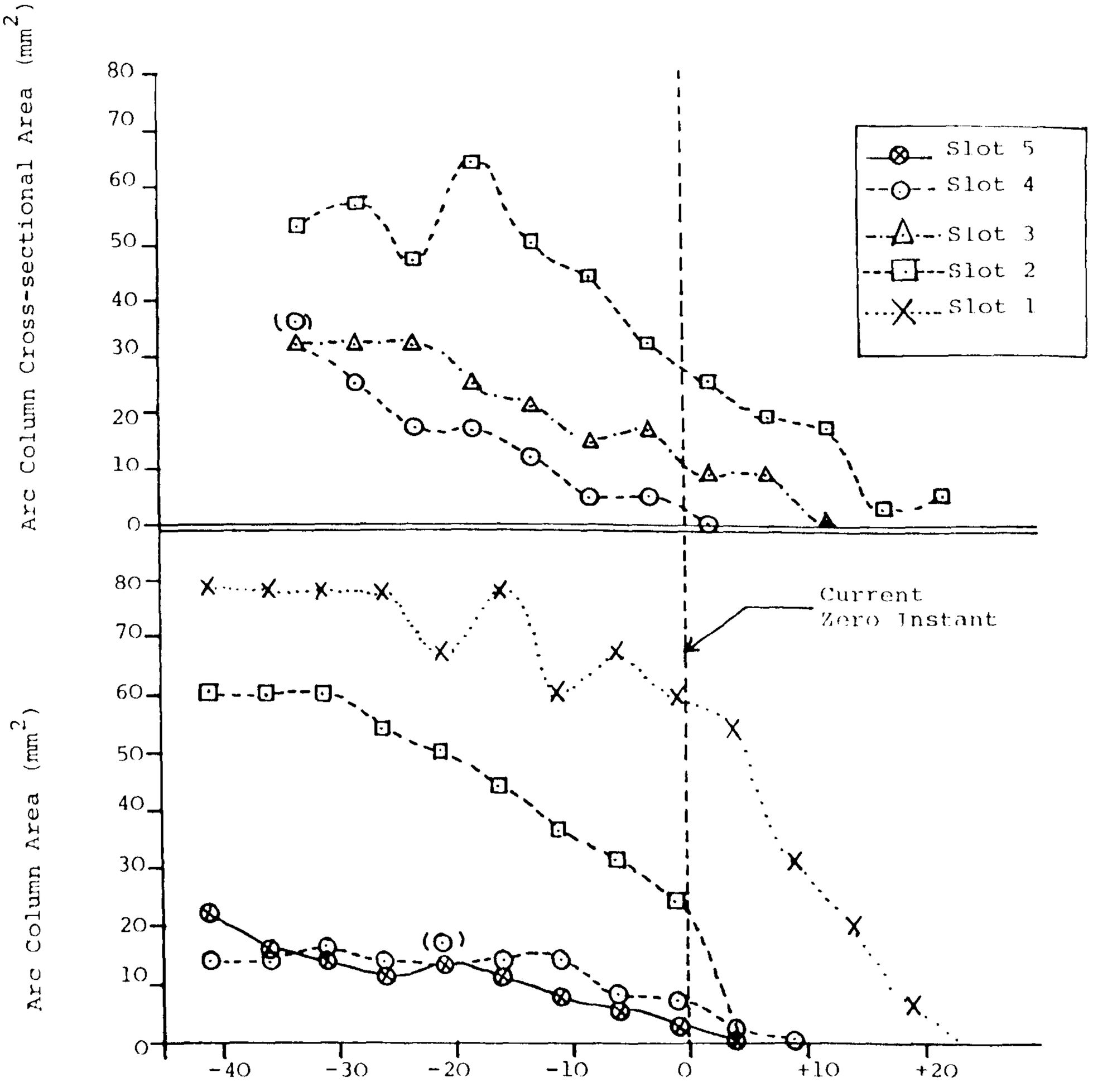

Operating Condition	Nozzle Material	di/dt (A/μs)	Electrodes Material	Intensifier Bias(KV)	Optical Filters
(i)	PTFE	22.0	Elkonite	14	None
(ii)	Copper	23.7	Elkonite	14	None

(b) High $^{di}/_{dt}$

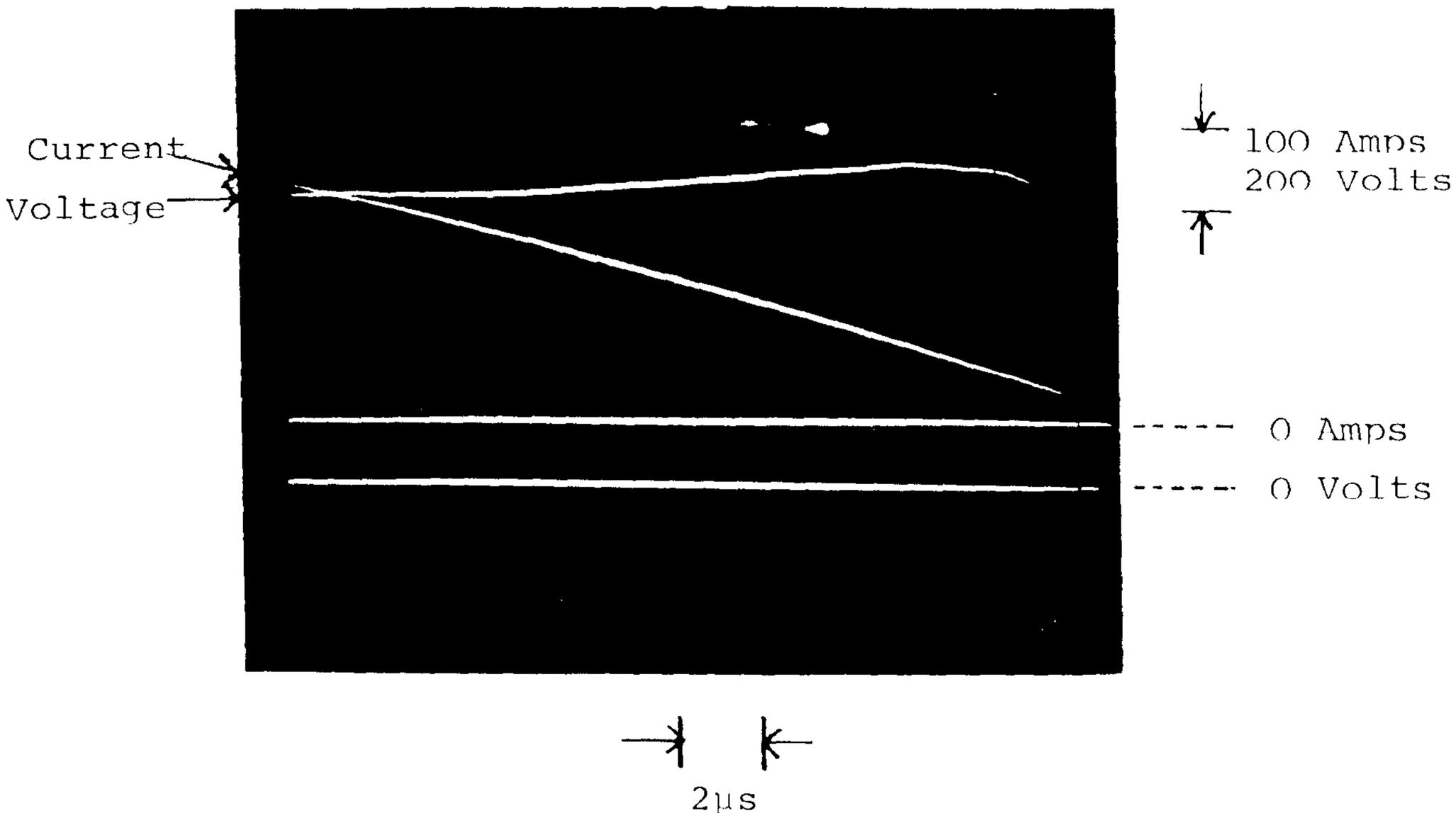

(a) Arc Voltage and Current

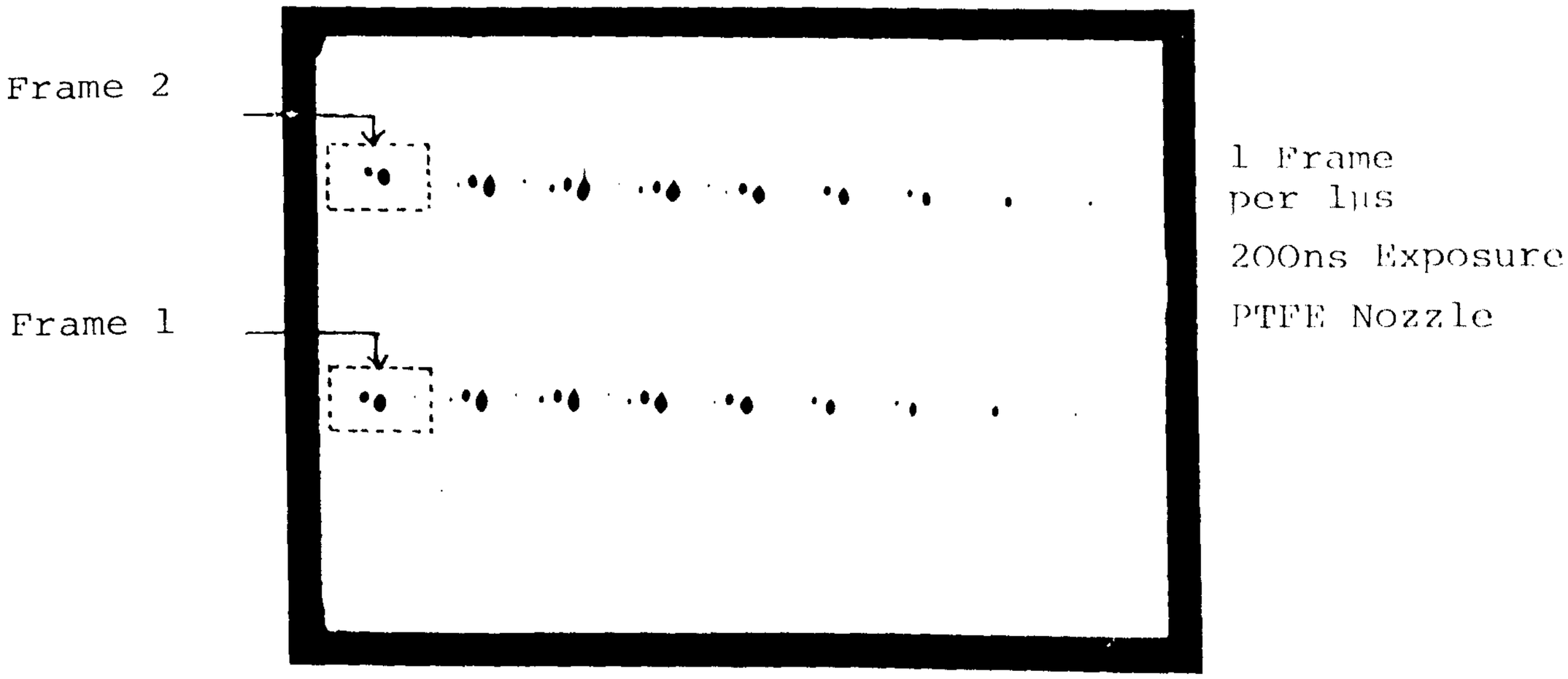

(b) High Speed Photograph Corresponding to (a)

Fig. 6.13 Typical Arc Current and Voltage Record with the Corresponding High Speed Photograph Taken During the Final 20μs of the Current Decay.
Peak Current = 34KA

Figure Number	di/dt (A/μs	Nozzle Material	Electrodes Material	Peak Current (KA)	Intensifier Bias (KV)	NDF Value
(a)	15.0	PTFE	Elkonite	34	18	O
(b)	21.3	PTFE	Elkonite	53	18	O
(c)	27.1	PTFE	Elkonite	64	18	O

Summary of Operating Conditions

Fig. 6.14 The Variation of Arc Cross-sectional Area, Axis Light Intensity and Arc Current over the Final 10μs of the Current Decay

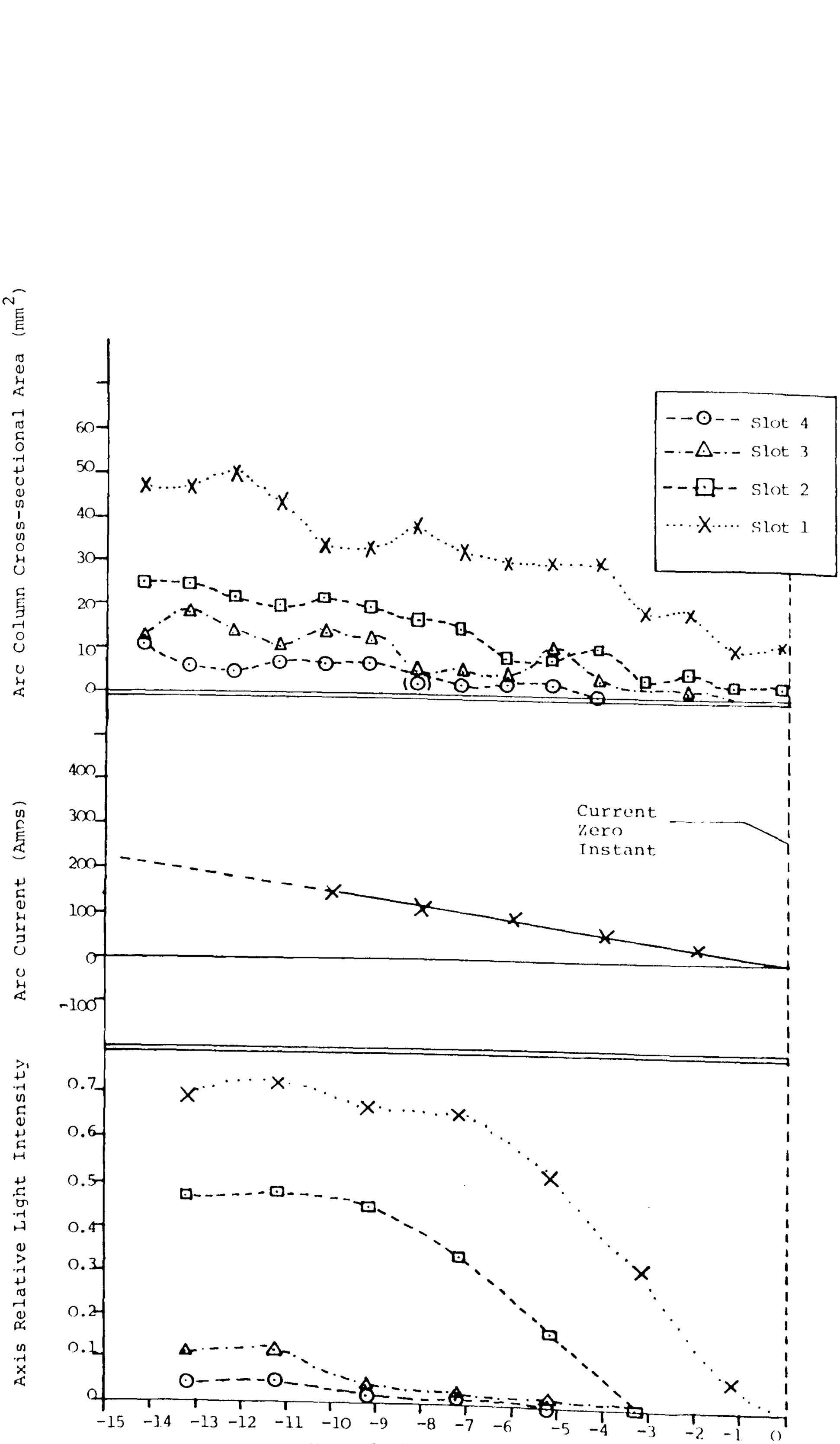
Arc Column Cross-sectional Area (mm²)
60
50
40
30
20
10
0
Slot 4
Slot 3
Slot 2
Slot 1
Arc Current (Amps)
400
300
200
100
0
-100
Current Zero Instant
Axis Relative Light Intensity
0.7
0.6
0.5
0.4
0.3
0.2
0.1
0
-15 -14 -13 -12 -11 -10 -9 -8 -7 -6 -5 -4 -3 -2 -1 0
Time Relative to Current Zero (μs)

(a) Low di/dt

Slot 5
Slot 4
Slot 3
Slot 2
Slot 1

Arc Column Cross-sectional Area (mm^2)

60
50
40
30
20
10
0

Arc Current (Amps)

400
300
200
100
0
-100

Current Zero Instant

Axis Relative Light Intensity

0.7
0.6
0.5
0.4
0.3
0.2
0.1
0

-7 -6 -5 -4 -3 -2 -1 0 +1 +2 +3 +4 +5 +6 +7

Time Relative to Current Zero (μs)

(b) Medium di/dt

Slot 5
Slot 4
Slot 3
Slot 2

Arc Column Cross-sectional Area (mm^2)

60
50
40
30
20
10
0

Arc Current (Amps)

400
300
200
100
0
-100

Current Zero Instant

Axis Relative Intensity

0.7
0.6
0.5
0.4
0.3
0.2
0.1
0

-6 -5 -4 -3 -2 -1 0 +1 +2 +3 +4 +5 +6 +7 +8

Time Relative to Current Zero (μs)

(c) High di/dt

Operating Conditions:

As Fig. 6.14(c)

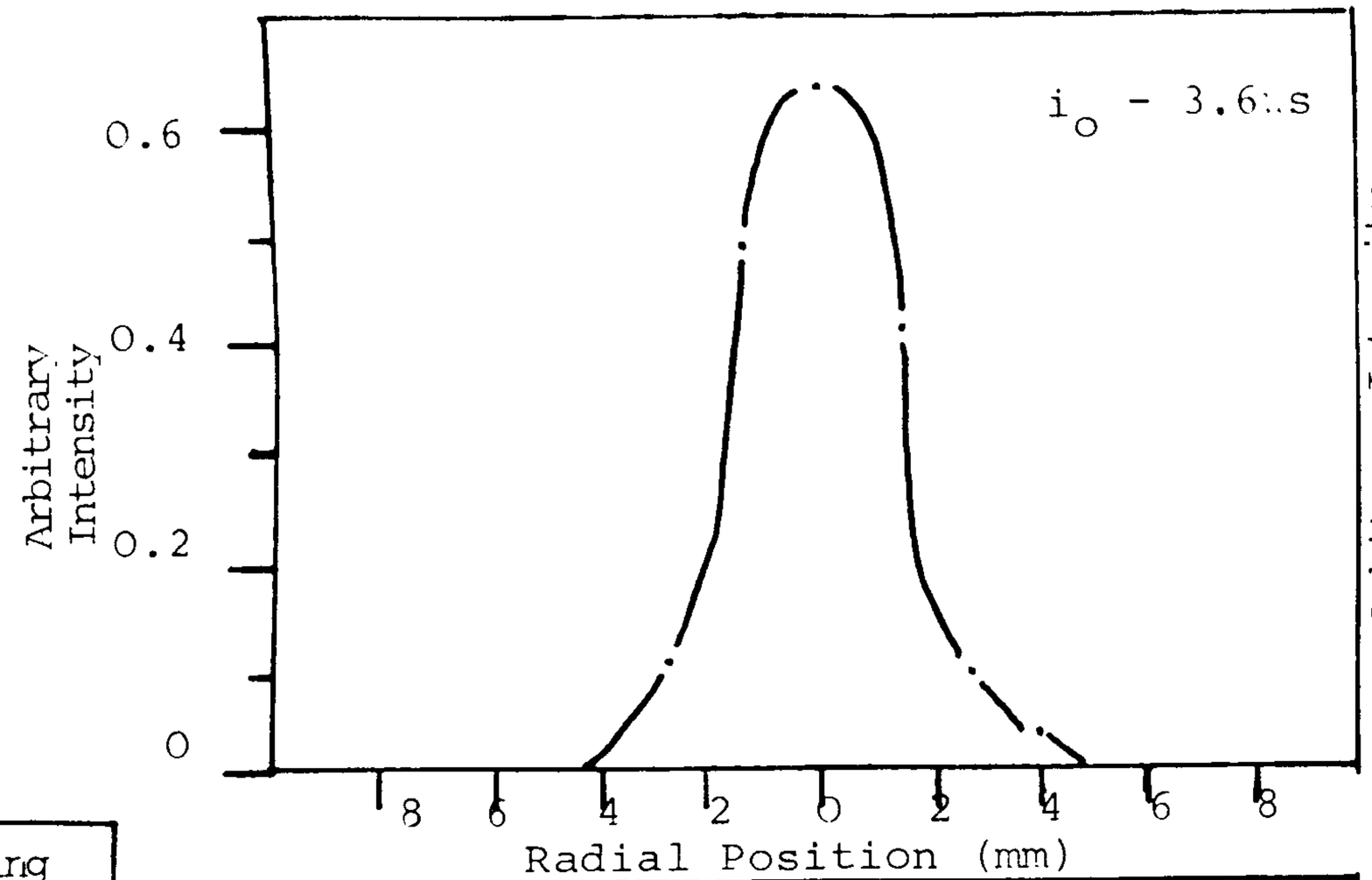

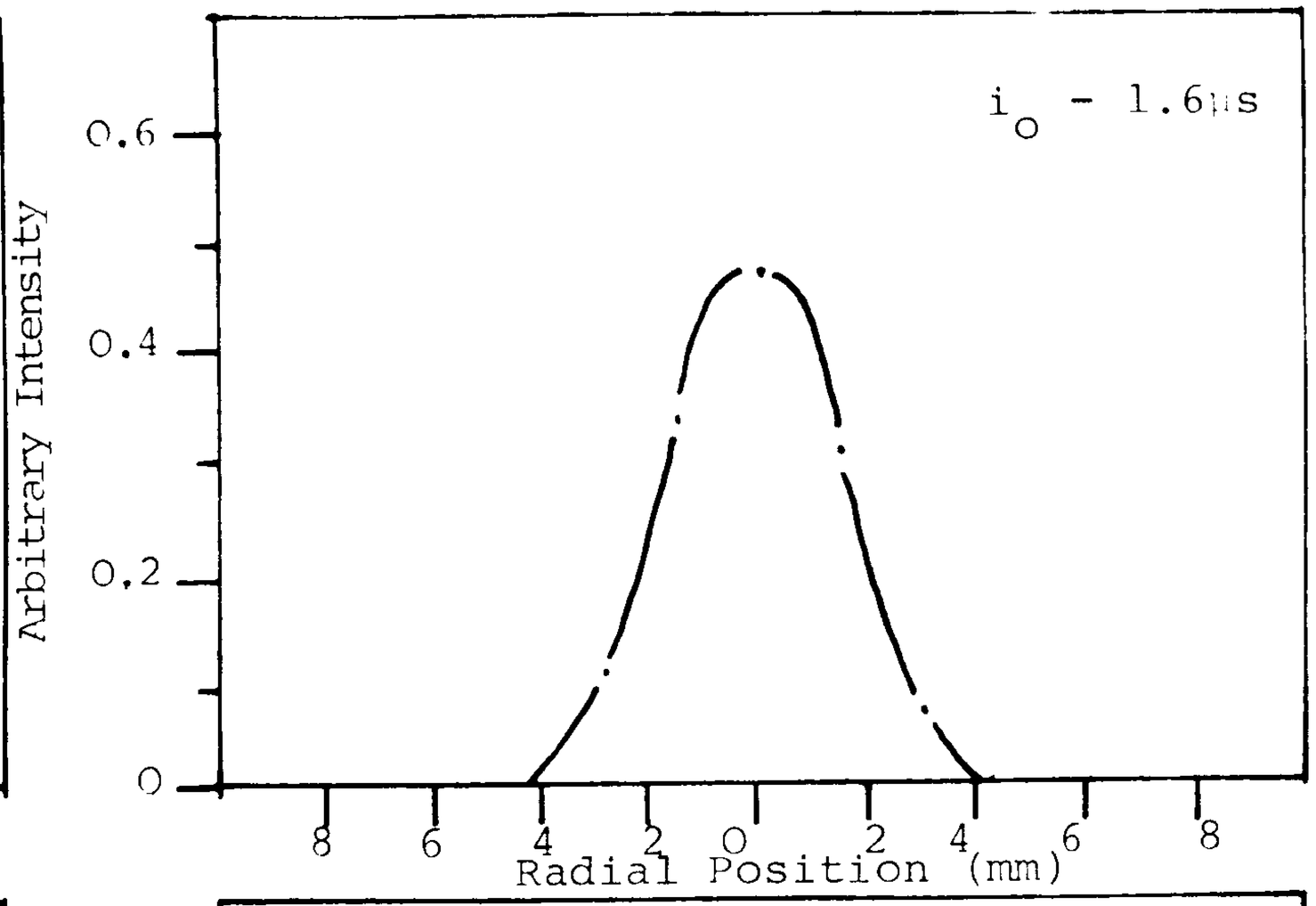

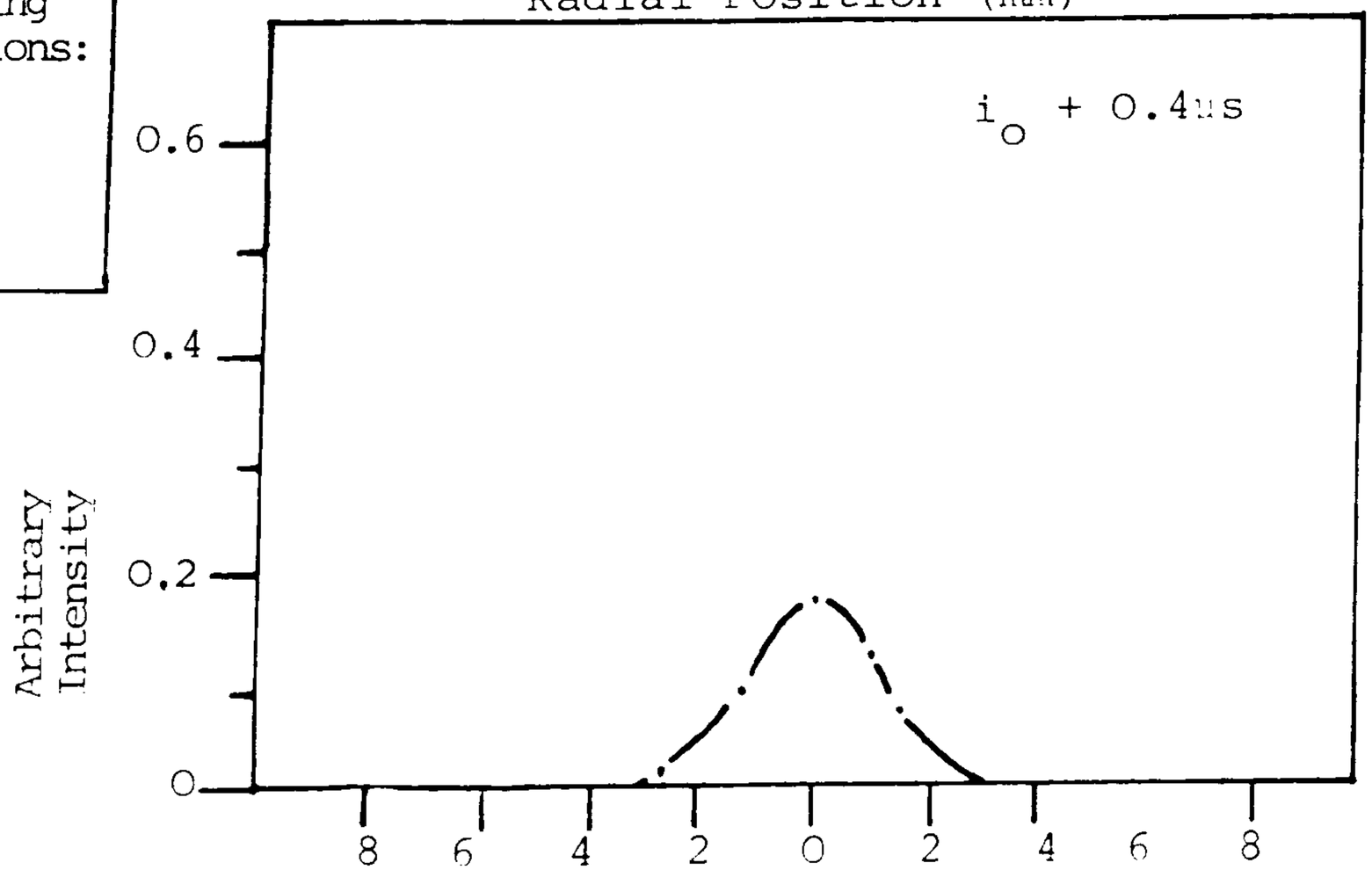

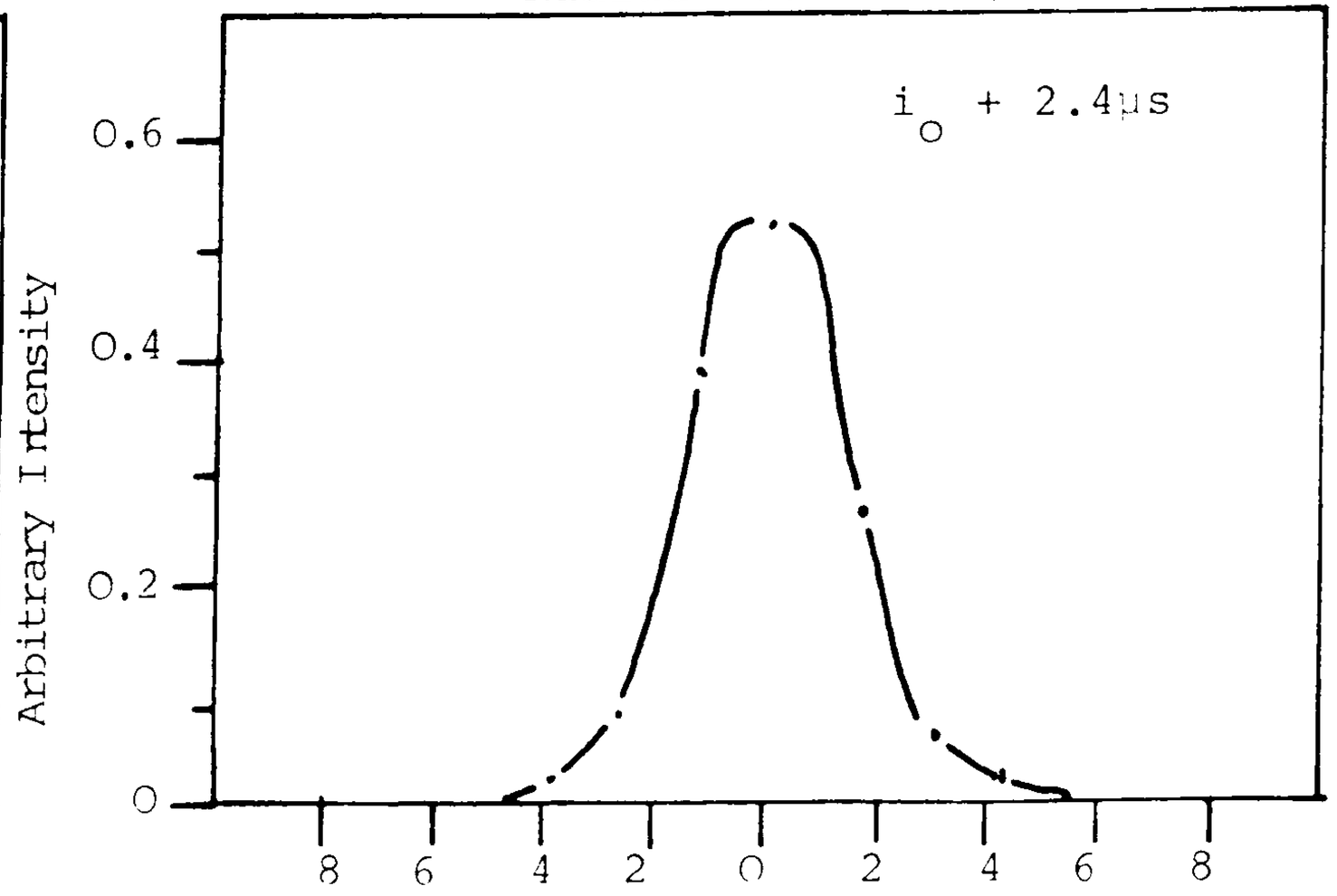

Fig. 6.15 (a) Slot 3 Measured Radial Intensity Distribution at 2µs Intervals (200ns Exposure) on the Approach To and After Current Zero

Fig. 6.15 (b) Slot 2 Measured Radial Intensity Distribution at 2µs Intervals (200ns Exposure) on the Approach to and After Current Zero

Operating Conditions

As Fig. 6.14(c)

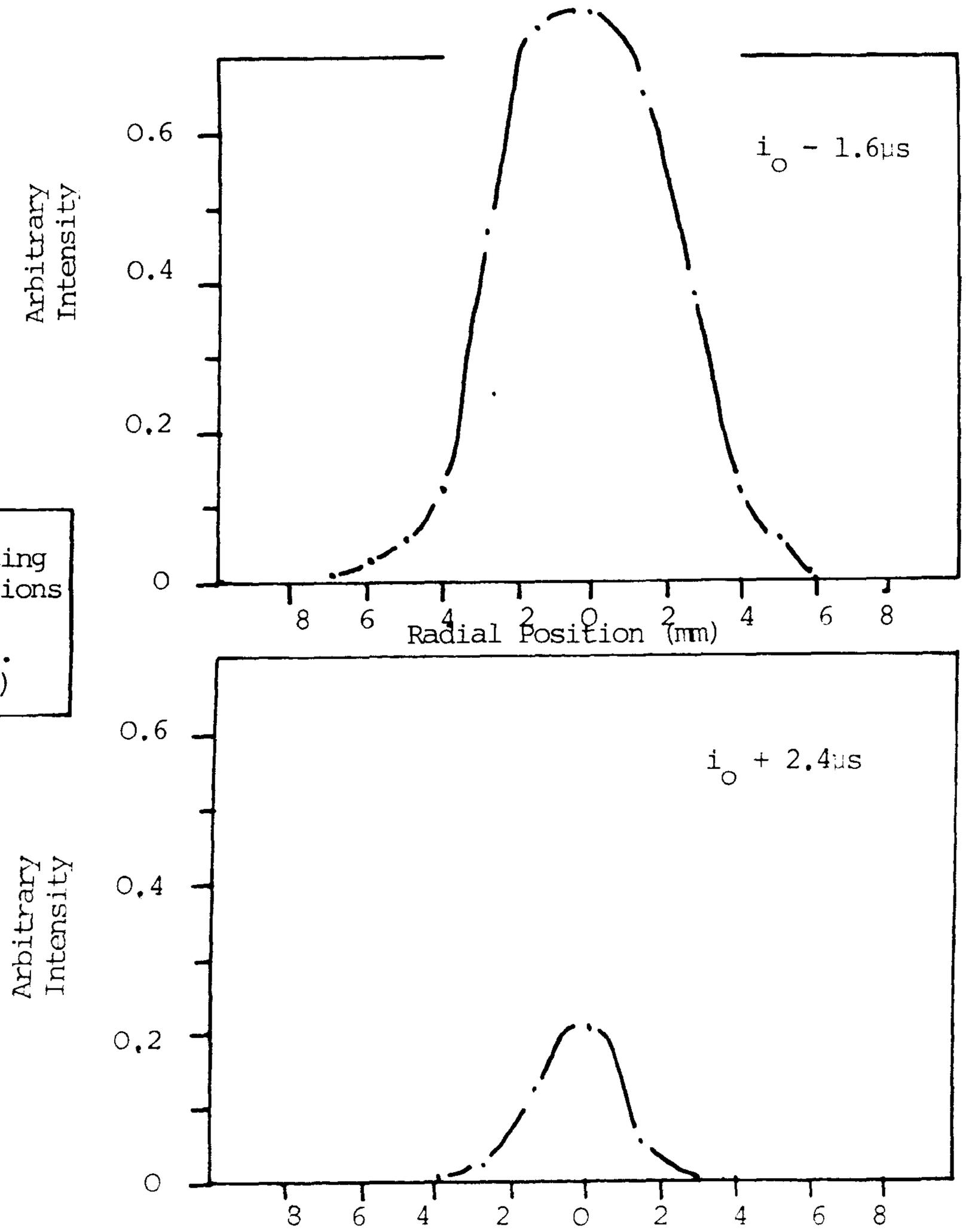

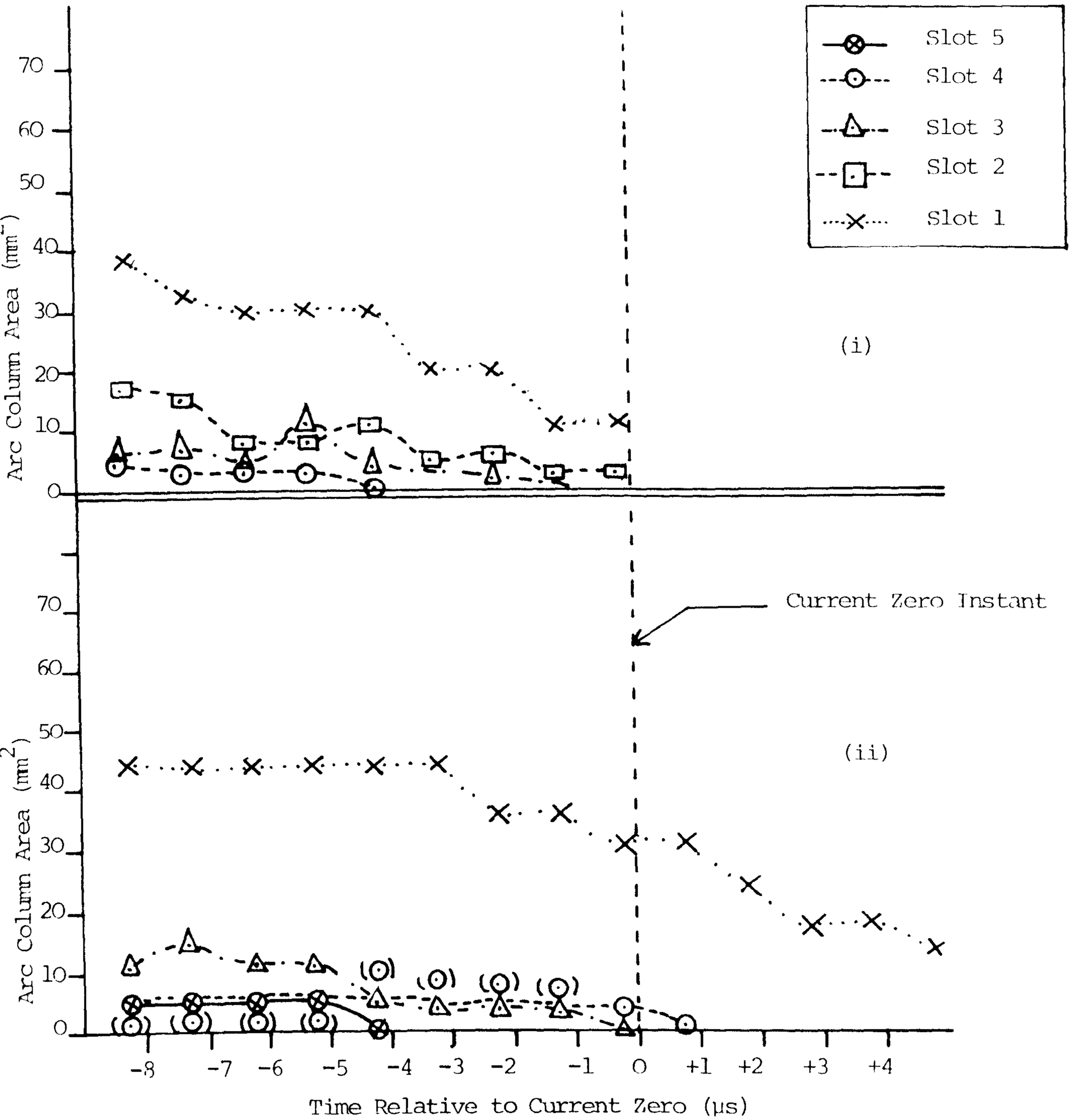

Operating Condition	Nozzle Material	di/dt (A/μs)	Electrodes Material	Intensifier Bias (KV)	Optical Filters
(i)	PTFE	15	Elkonite	18	None
(ii)	Copper		Elkonite	18	None

(a) Low $^{di}/_{dt}$

Fig. 6.16 The Influence of the Nozzle Material on the Arc Areas Very Close to Current Zero

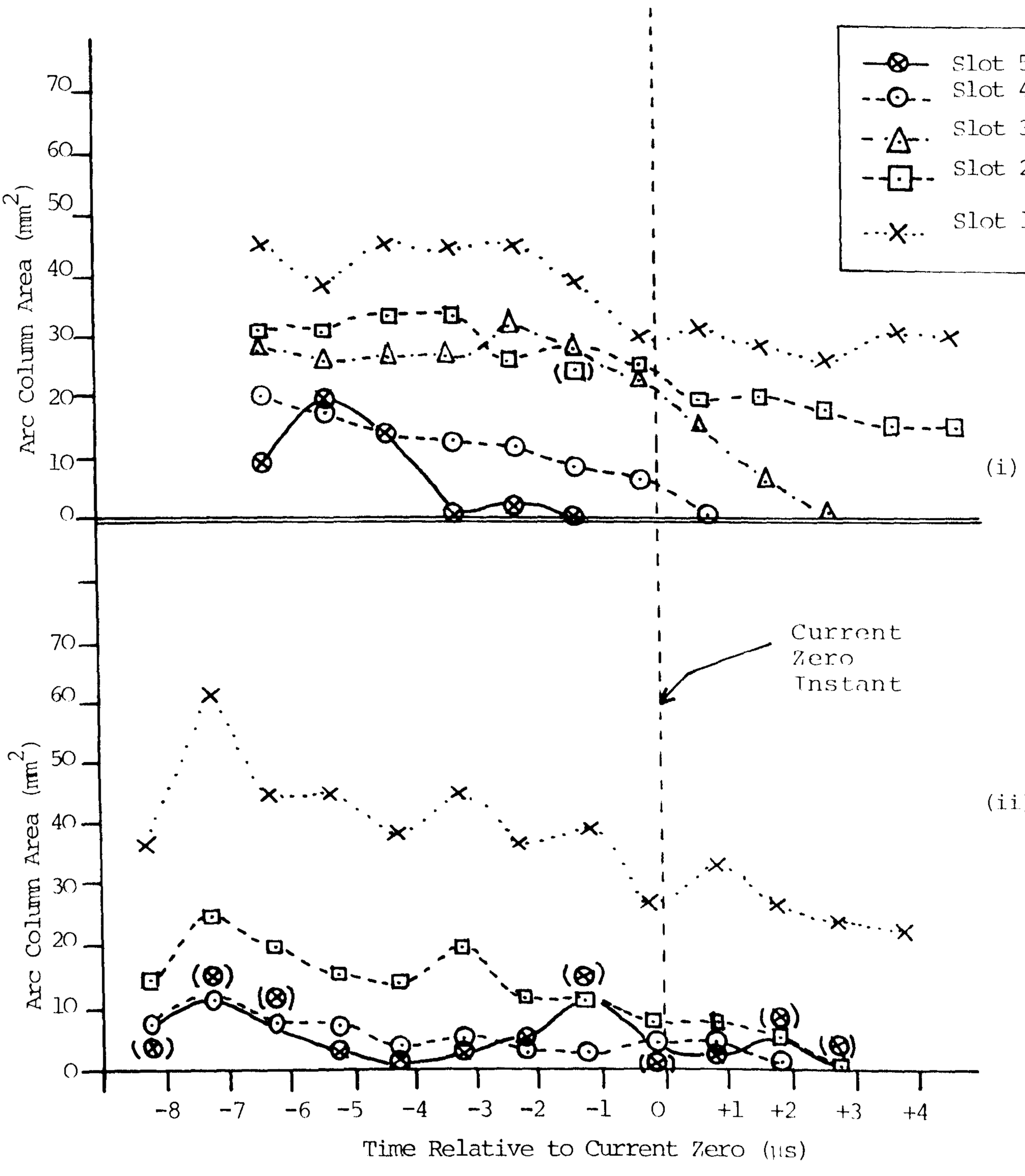

Operating Condition	Nozzle Material	di/dt (A/μs)	Electrodes Material	Intensifier Bias (KV)	Optical Filters
(i)	PTFE	21.3	Elkonite	18	None
(ii)	Copper	23.3	Elkonite	18	None

(b) Medium di/dt

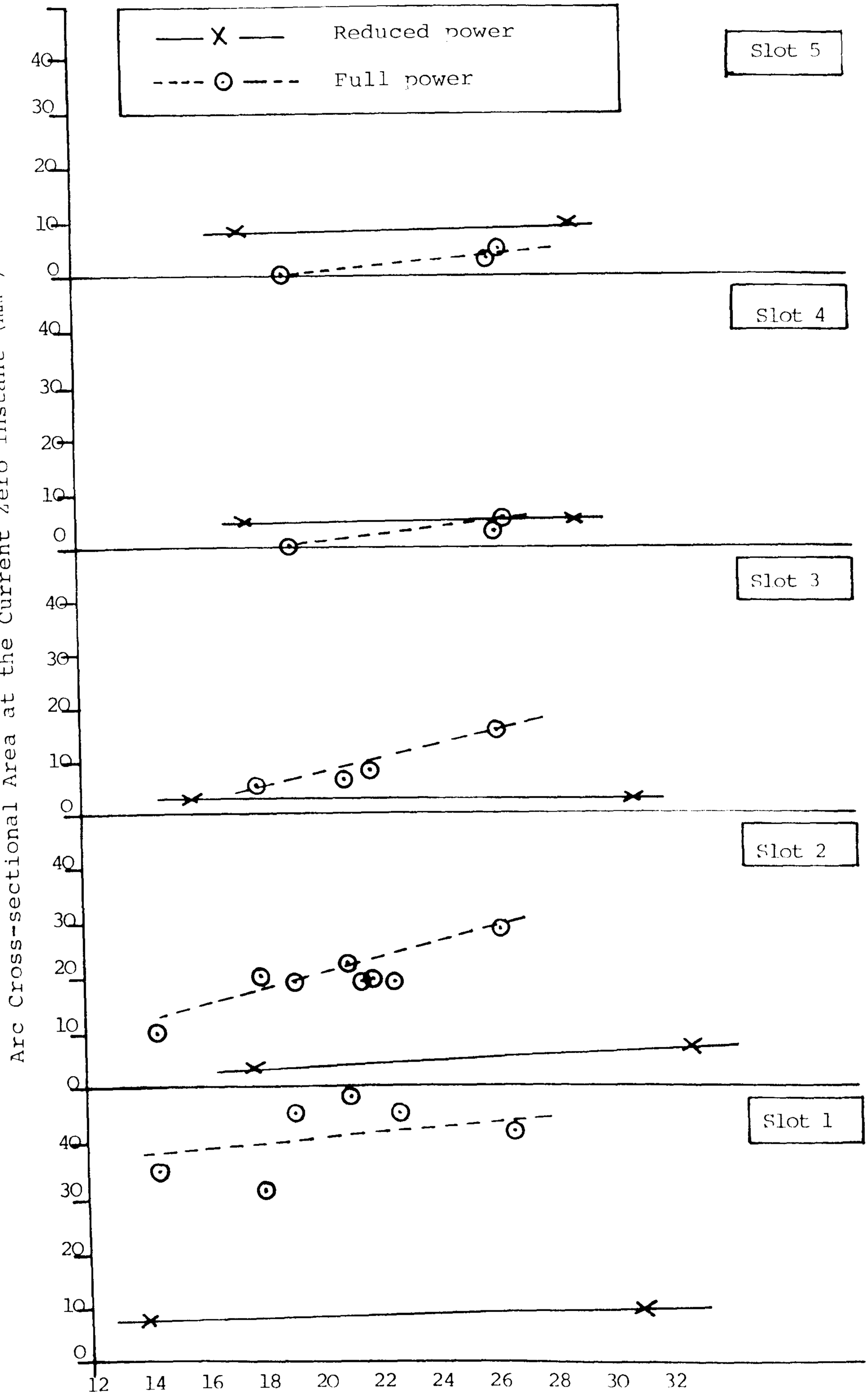

(a) PTFE

Fig. 6.17 The Influence of $^{di}/_{dt}$ Upon the Arc Areas Measured at the Current Zero Instant

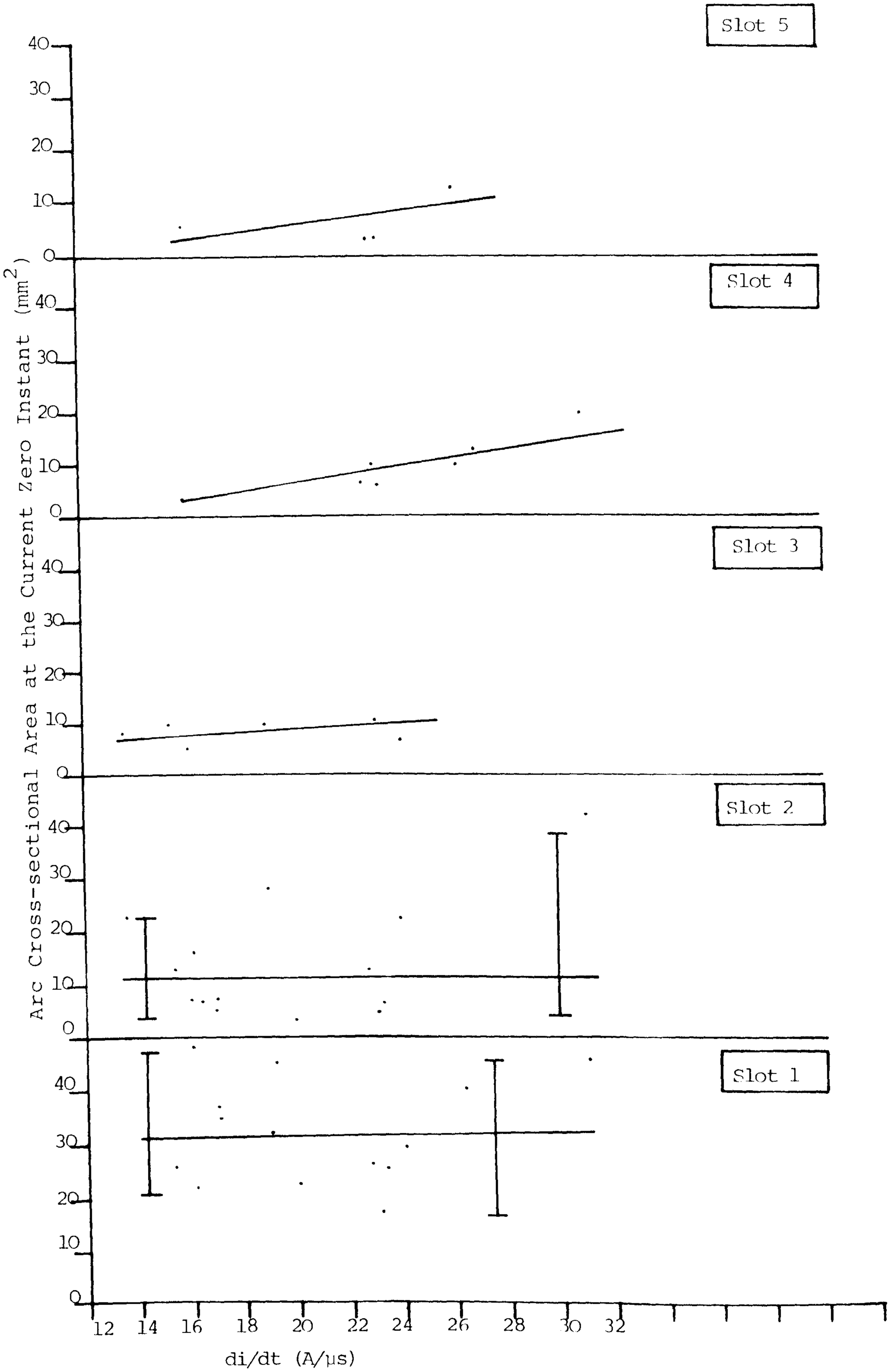
Slot 5
Slot 4
Slot 3
Slot 2
Slot 1
Arc Cross-sectional Area at the Current Zero Instant (mm²)
40
30
20
10
0
40
30
20
10
0
40
30
20
10
0
40
30
20
10
0
40
30
20
10
0
12
14
16
18
20
22
24
26
28
30
32
di/dt (A/μs)

(b) Copper

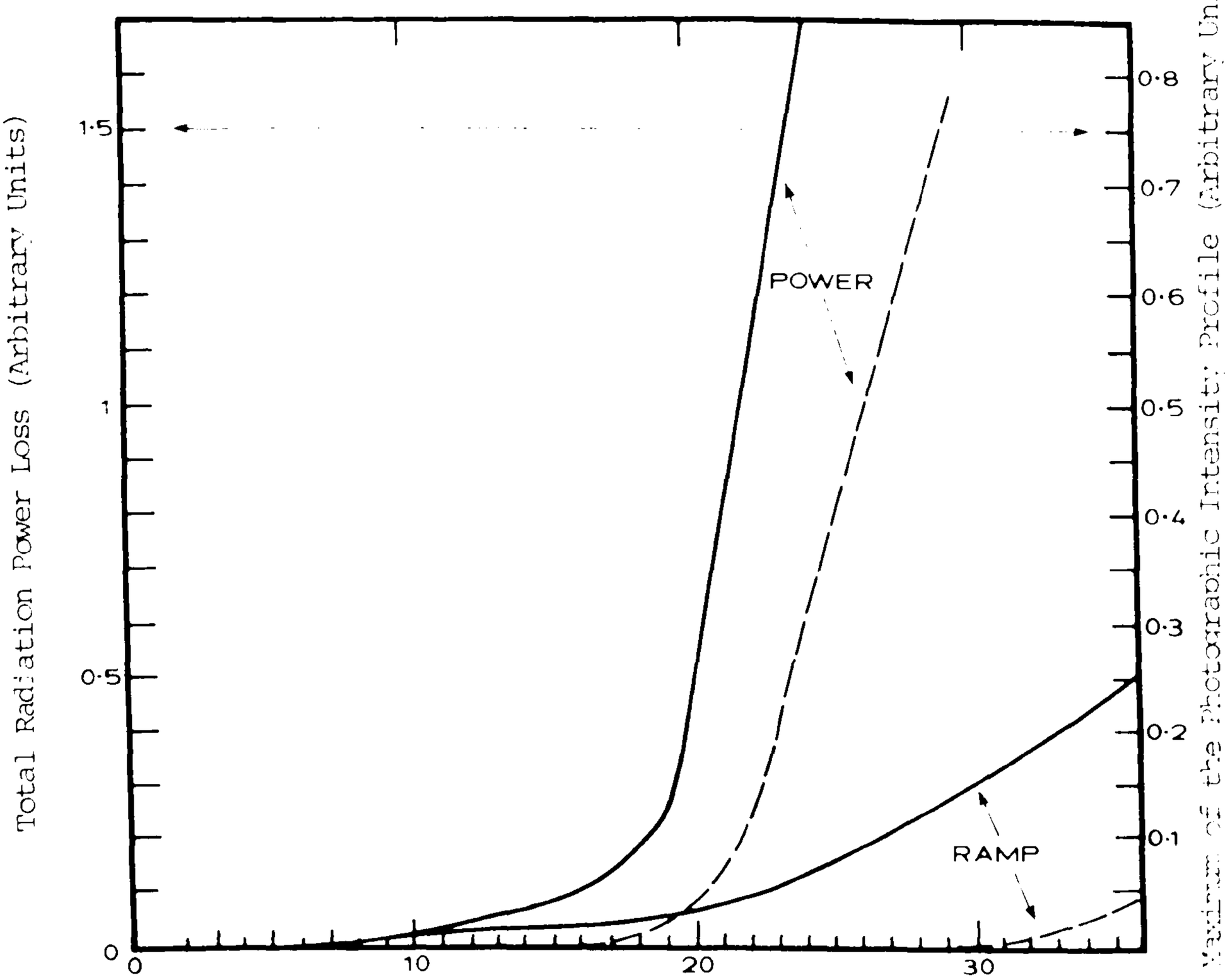

Fig. 6.18 Variation of Total Radiation Loss and the Maximum of the Radial Photographic Intensity Profile at the Current Zero Instant with di/dt

Fig. 6.19 Typical Arc Spectra at Various Wavelengths

(a) λ_c = 521.8nm

(b) (i) λ_c = 510.5nm and λ_c = 515.3nm

(ii) λ_c = 529.1nm

(iii) λ_c = 459nm and λ_c = 465nm

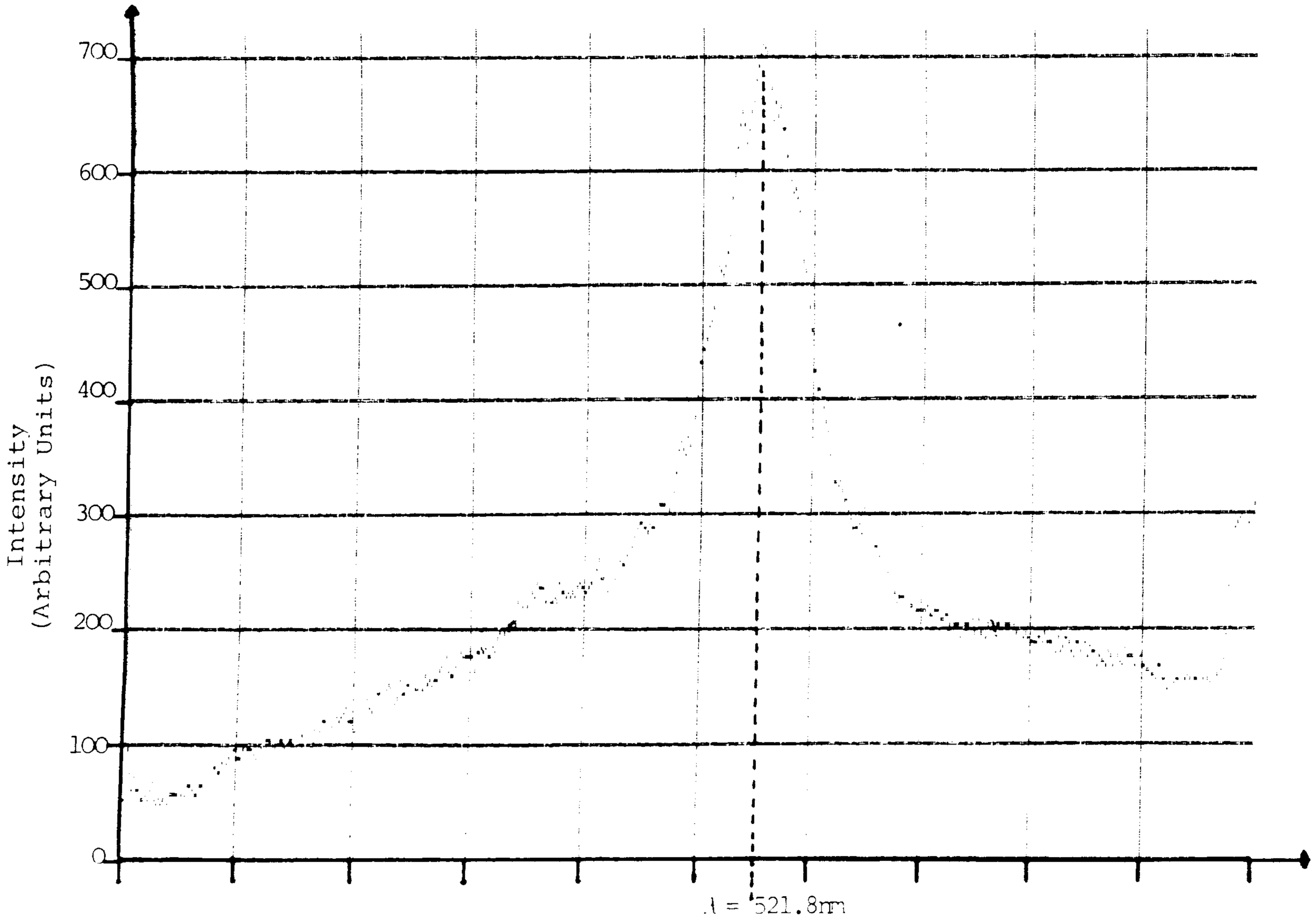

Fig. 6.19(a) λ_c = 521.8nm

Operating Conditions
Time Before Current Zero = 6μs
Exposure time = 1.6μs
di/dt = 15A/μs

Horizontal Scale

λ = 0.76nm

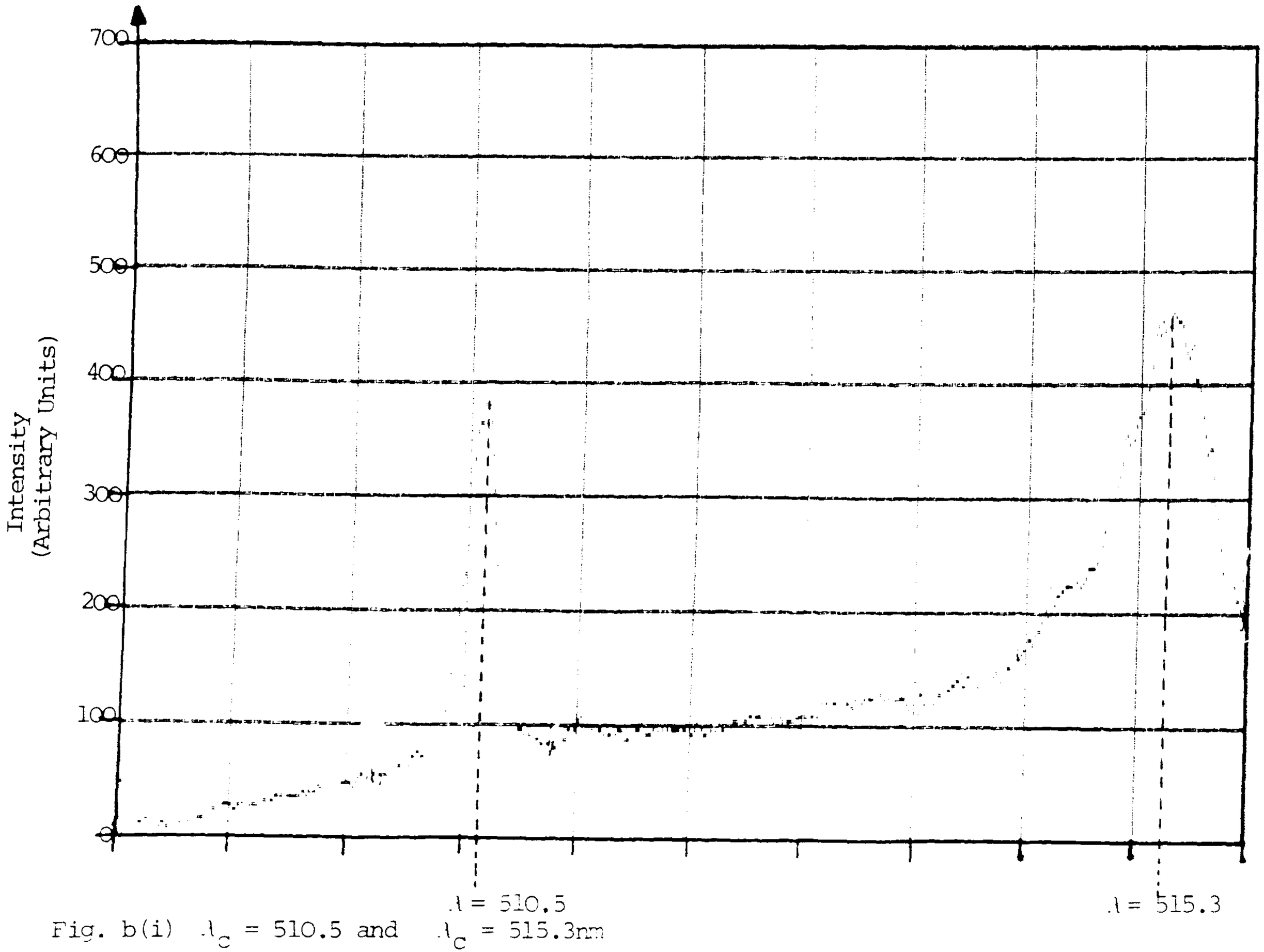

Fig. b(i) λ_c = 510.5 and λ_c = 515.3nm

Operating Conditions
Time Before Current Zero = 4.8μs
Exposure time = 1.6μs
di/dt = 14A/μs

Horizontal Scale

0.76nm

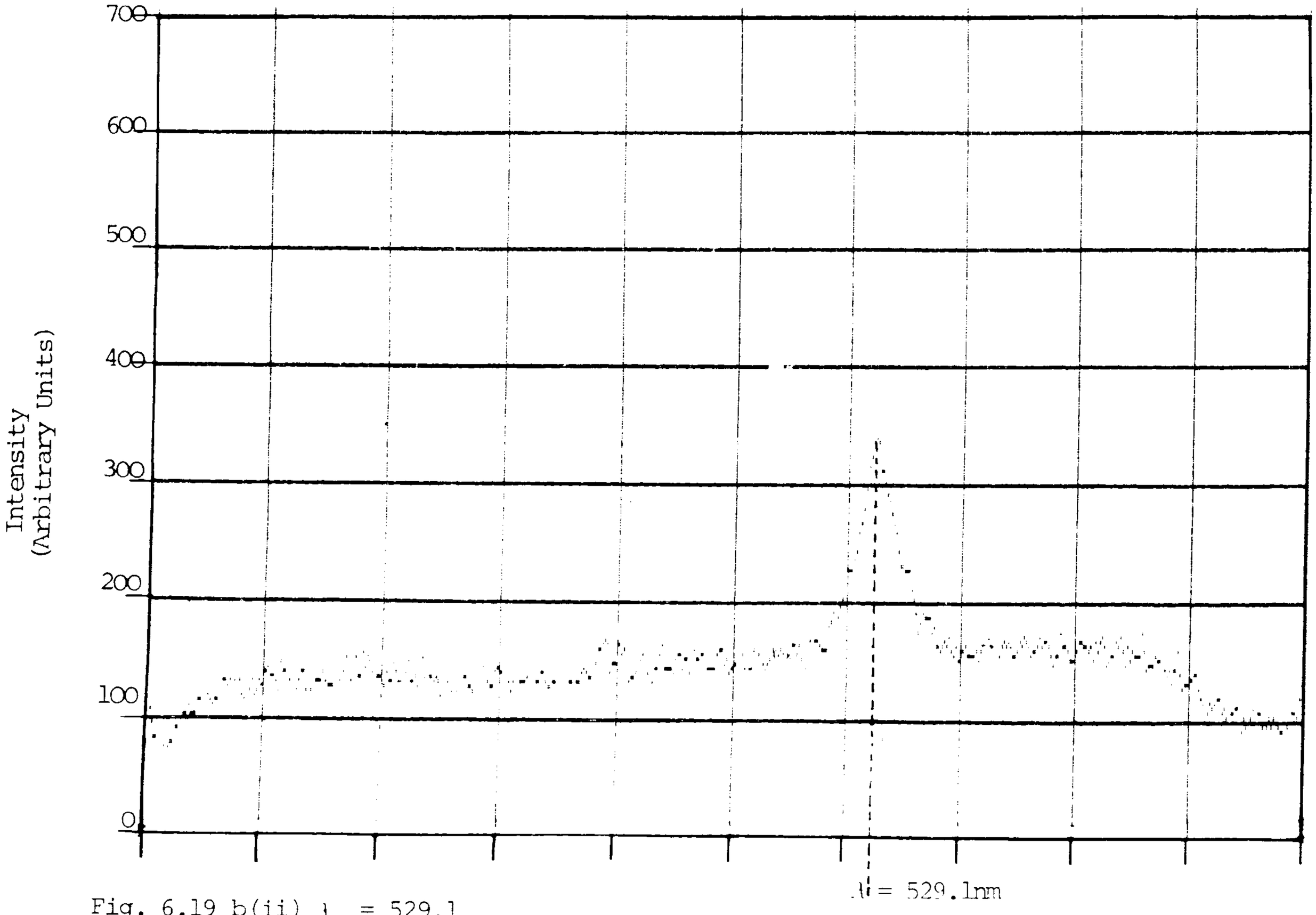

Operating Conditions
Time Before Current Zero = 9.6μs
Exposure time = 1.6μs
di/dt = 18A/μs

Horizontal Scale

0.76nm

Fig. 6.19 b(ii) λ_c = 529.1

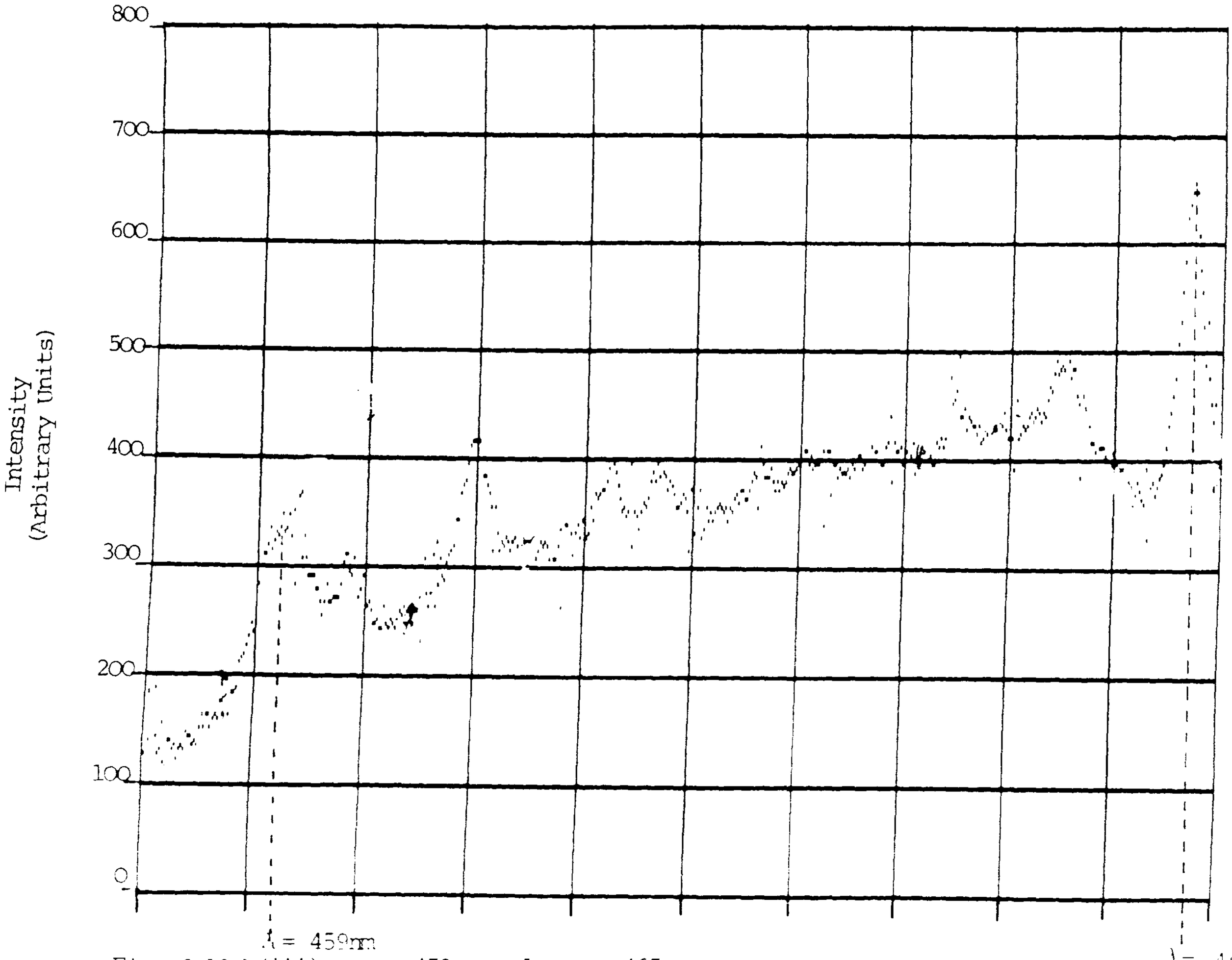

Operating Conditions
Time Before Current Zero = 7.2μs
Exposure time = 1.6μs
di/dt = 14A/μs

Horizontal Scale

0.67nm

Fig. 6.19 b(iii) λ_c = 459nm and λ_c = 465nm

Fig. 6.20 Examples of Radially Averaged Spectra for Different Instants During the Current Decay

(a) (i) Low $\frac{di}{dt}$, 515.3nm and 510.5nm Spectral Lines

(ii) Low $\frac{di}{dt}$, 521.8nm Spectral Line

(b) Medium $\frac{di}{dt}$, 515.3nm and 510.5nm Spectral Lines

(c) High $\frac{di}{dt}$, 515.3nm and 510.5nm Spectral Lines

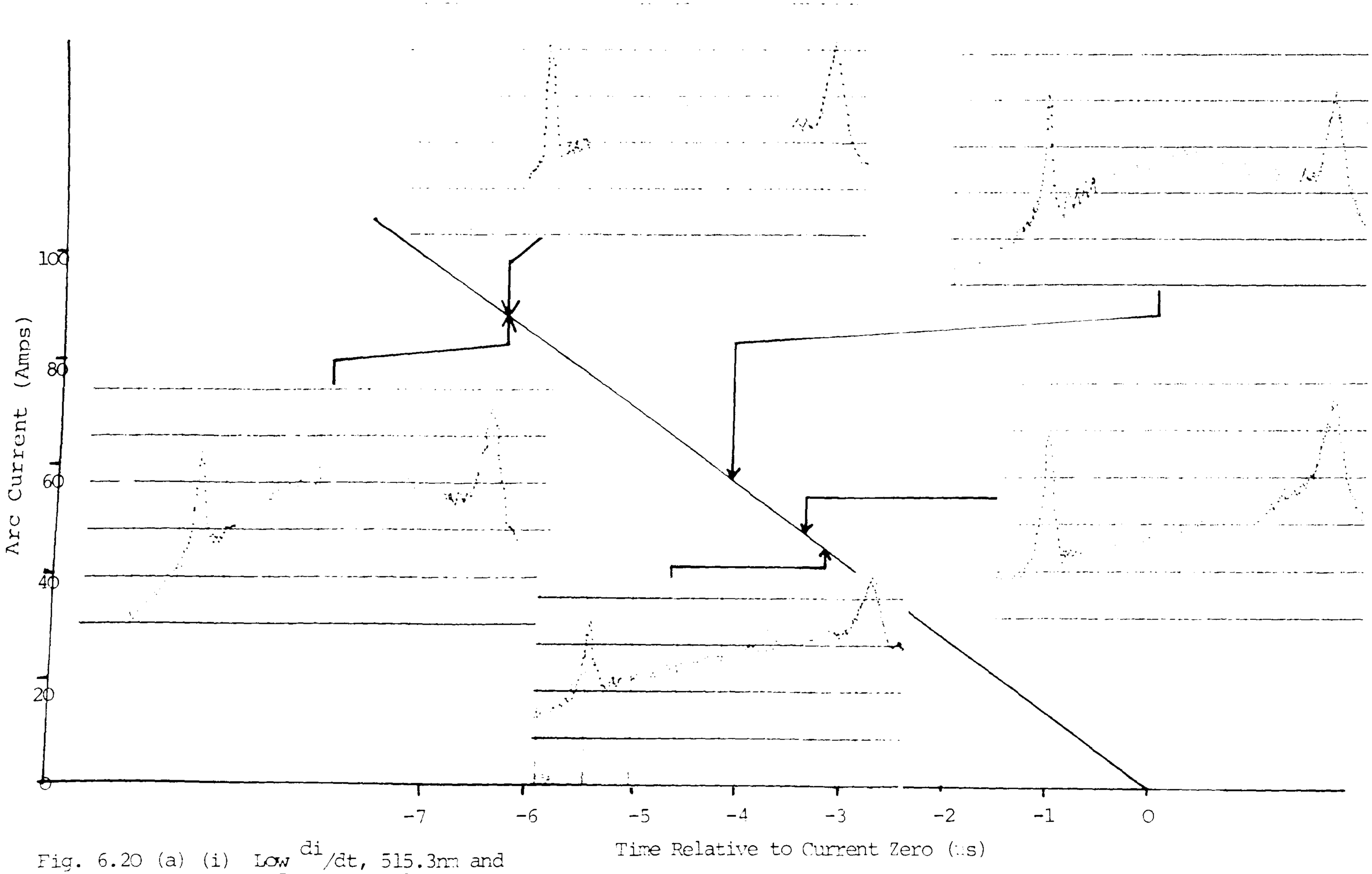

Fig. 6.20 (a) (i) Low di/dt, 515.3nm and 515nm Spectral Lines

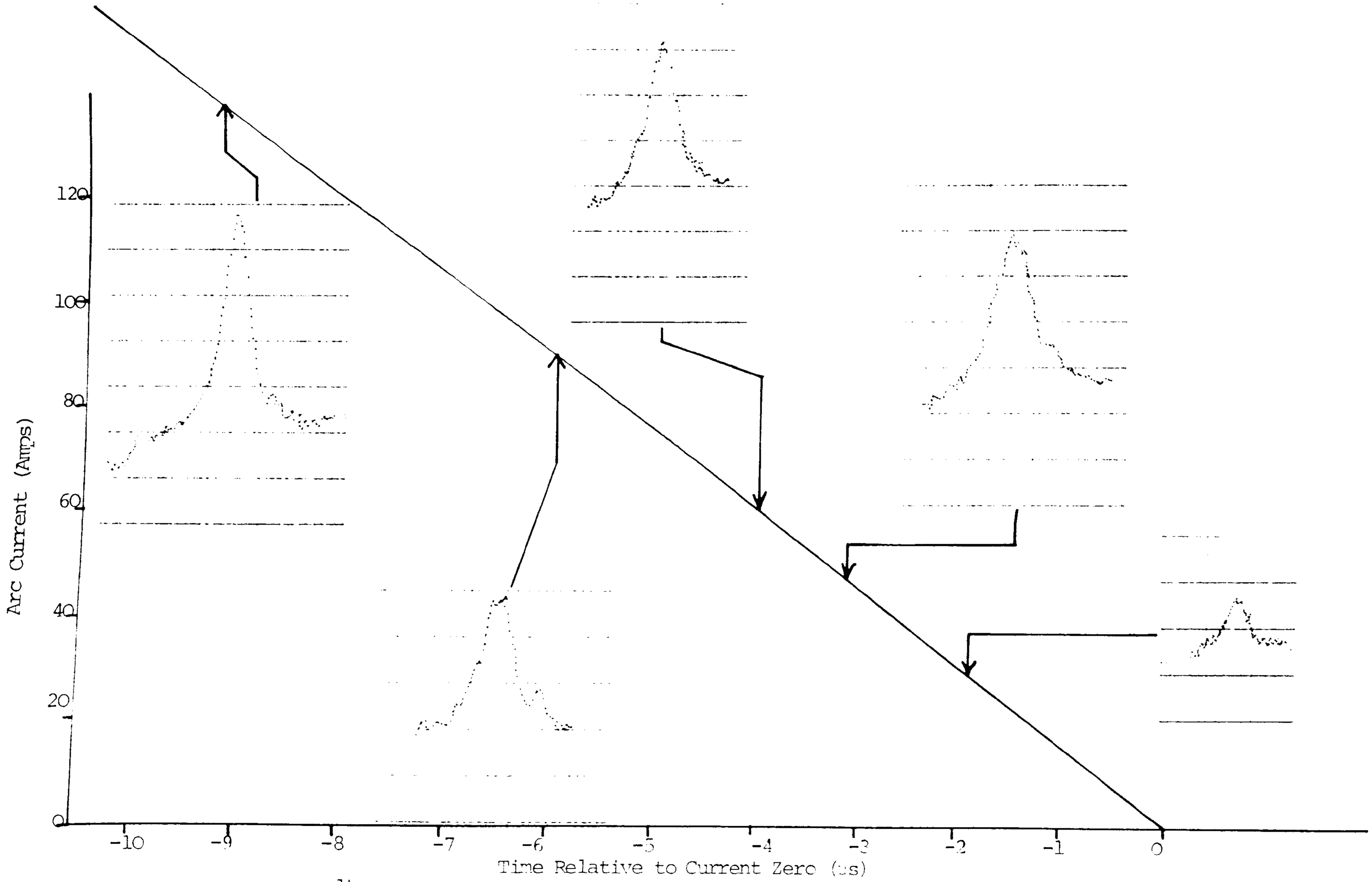

Fig. 6.20 (a) (ii) Low $\frac{di}{dt}$, 521.8nm Spectral Line

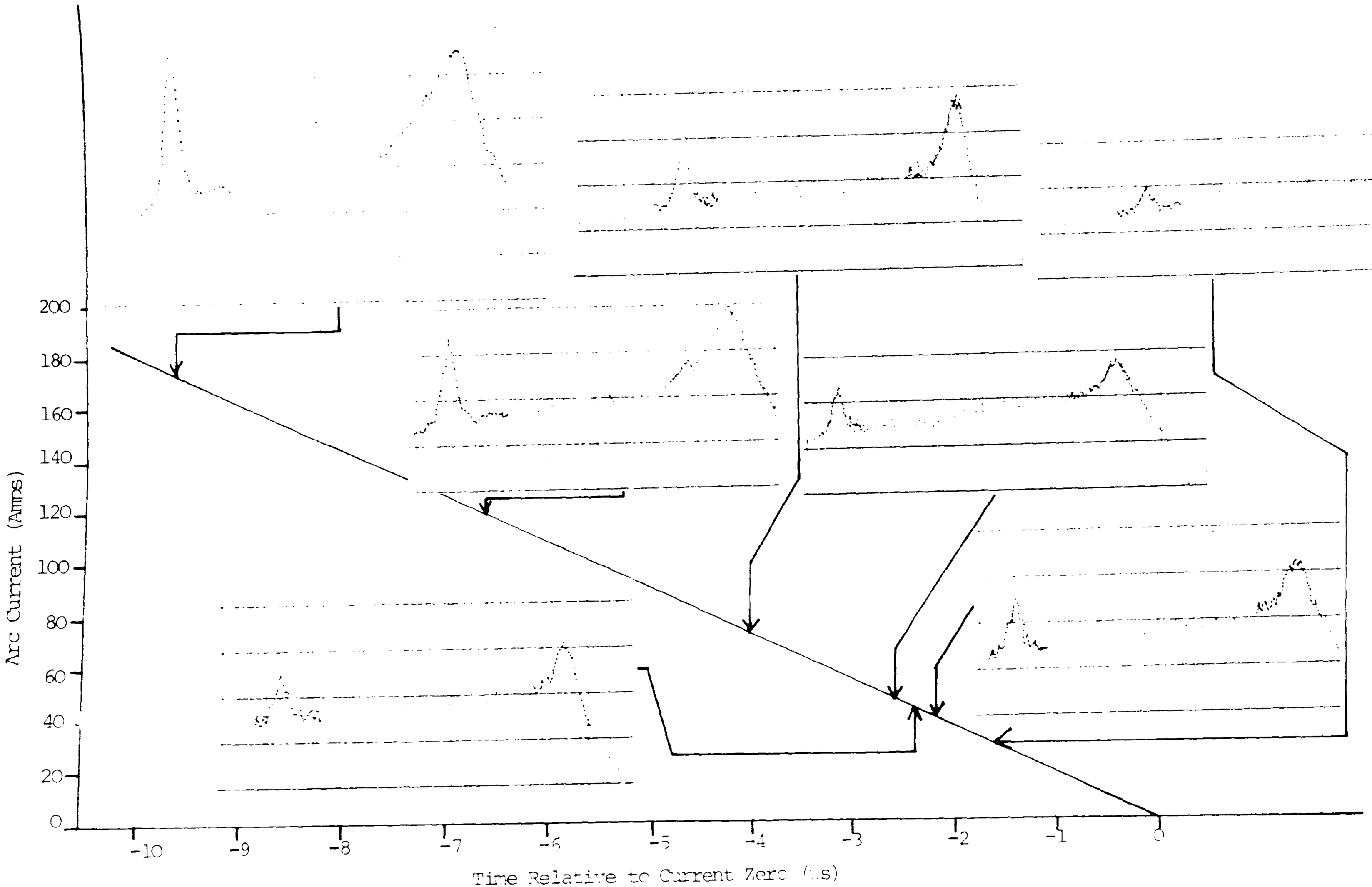

Fig. 6.20 (b) Medium $\frac{di}{dt}$ 515.3nm and 510.5nm Spectral Line

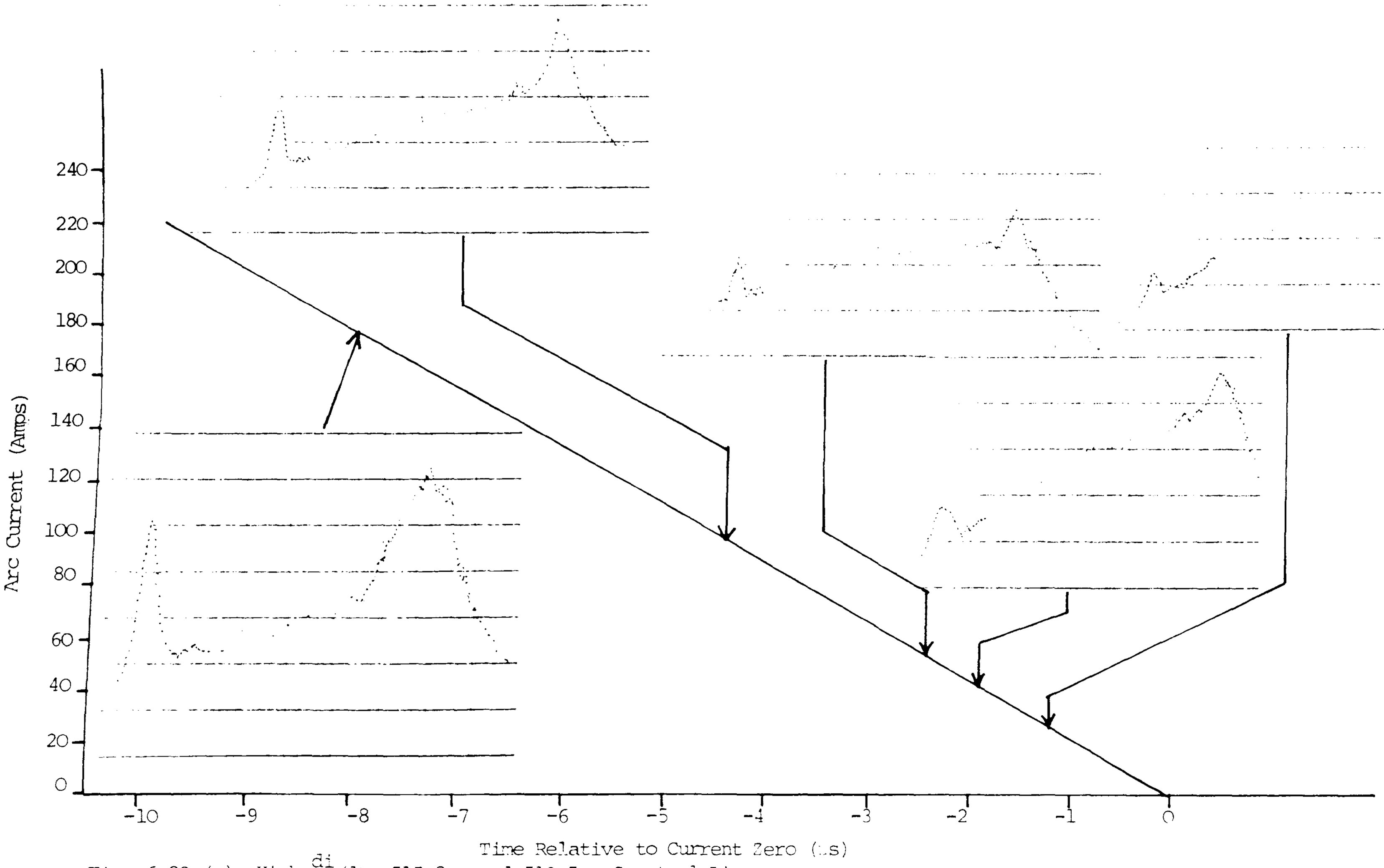

Fig. 6.20 (c) High $\frac{di}{dt}$, 515.3nm and 510.5nm Spectral Lines

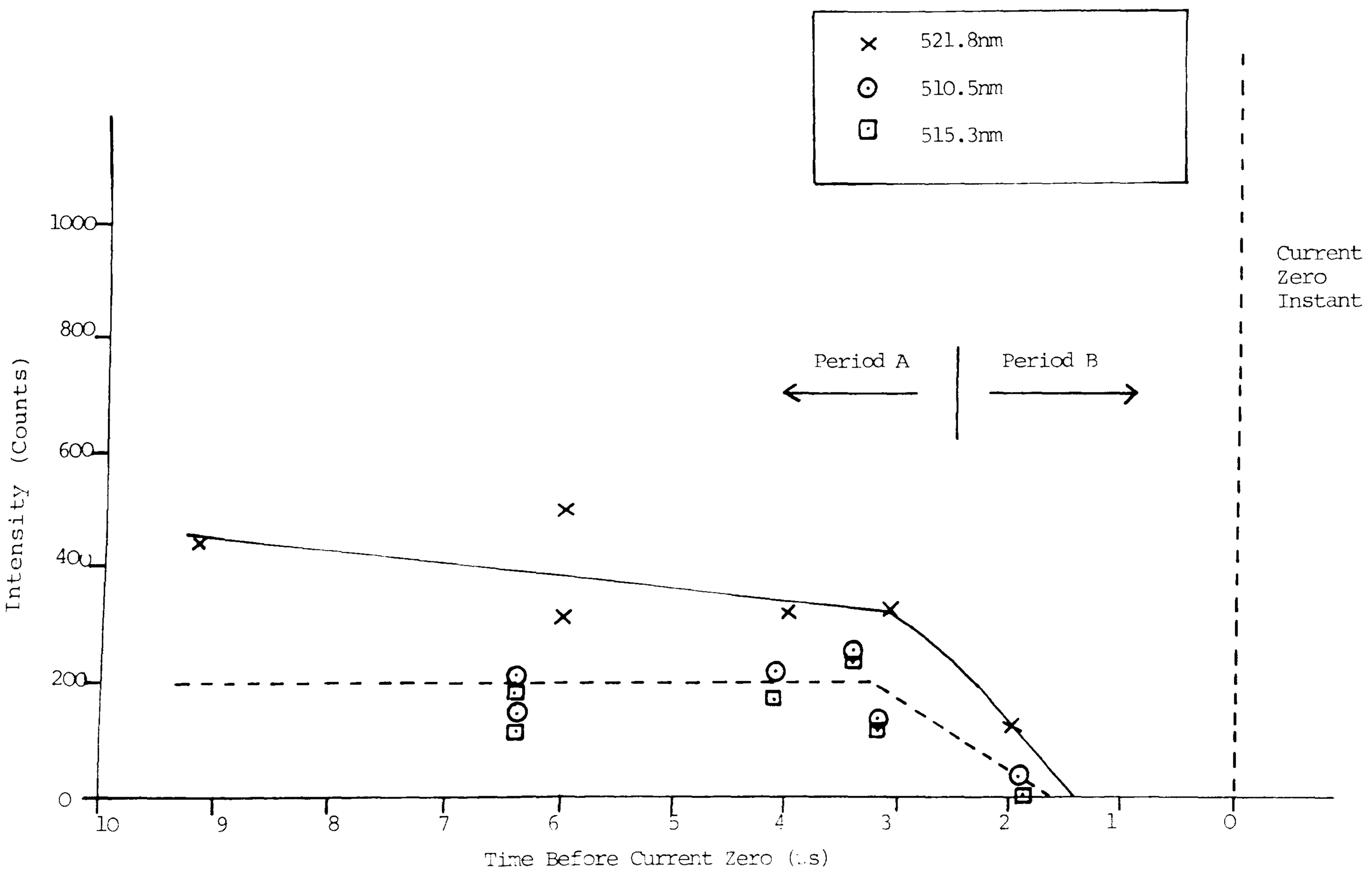

Fig. 6.21 Decay of Various Spectral Line Intensities During the Current Zero Period (a) 34KA Peak Current

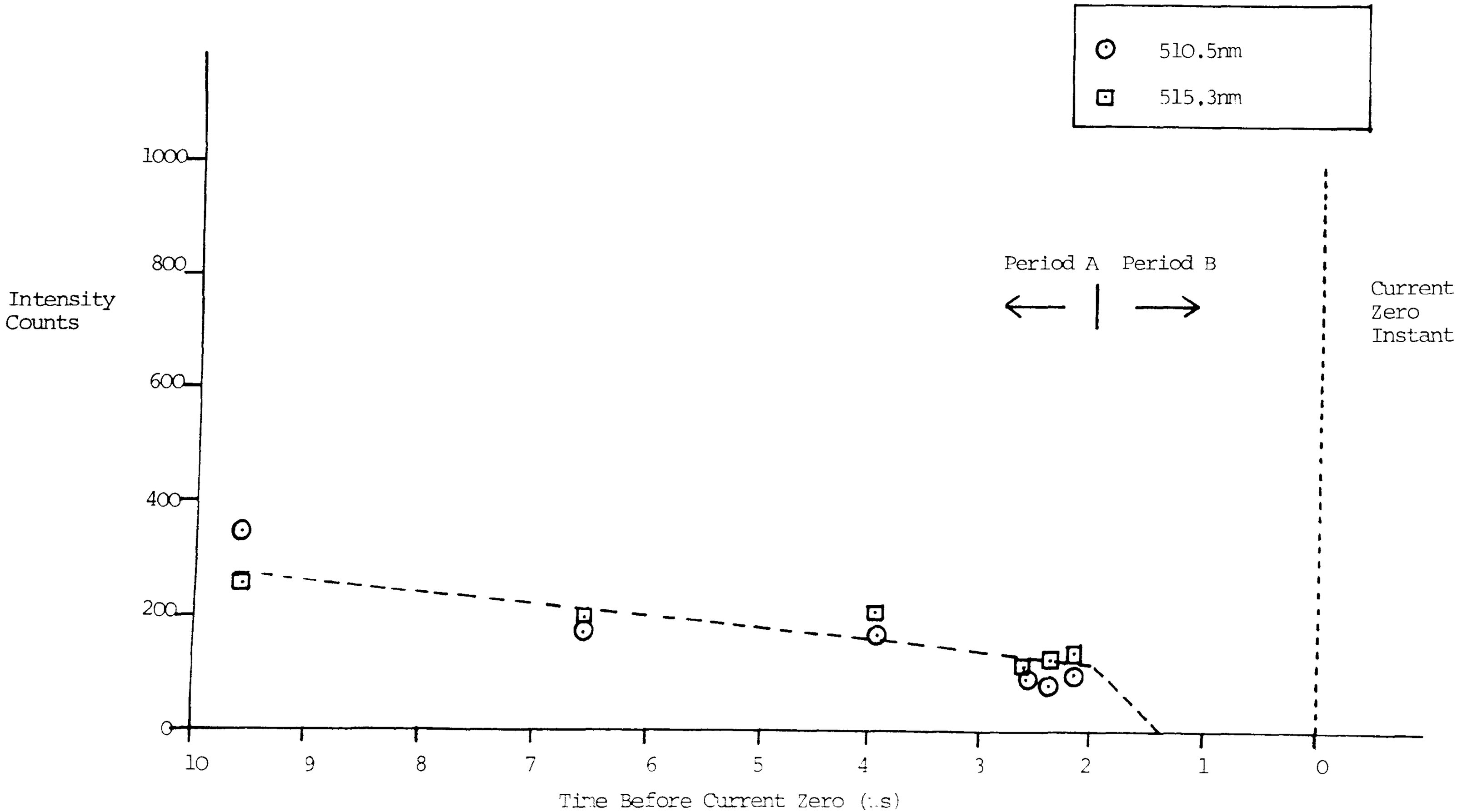

(b) 46KA Peak Current

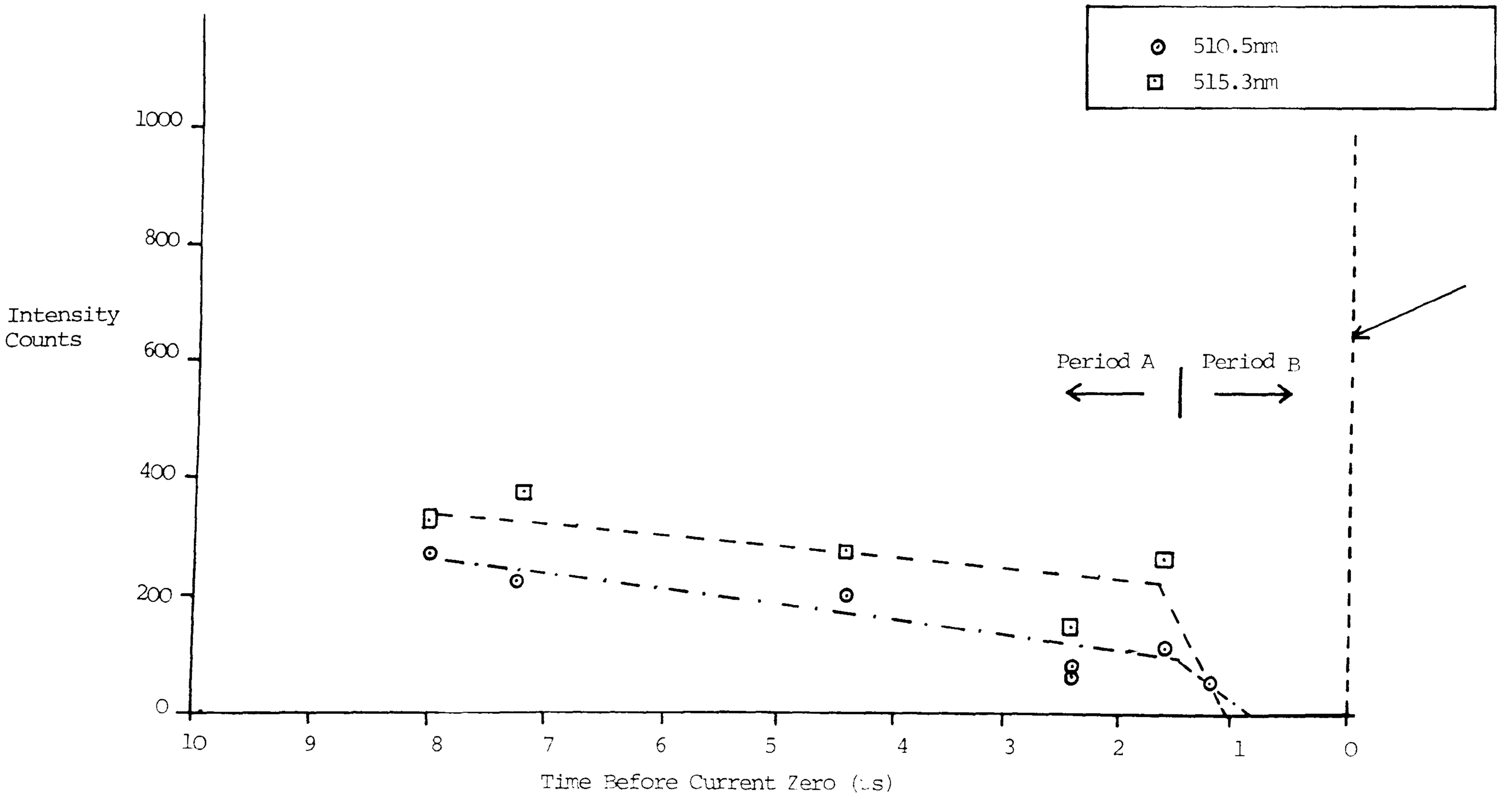

(c) 53KA Peak Current

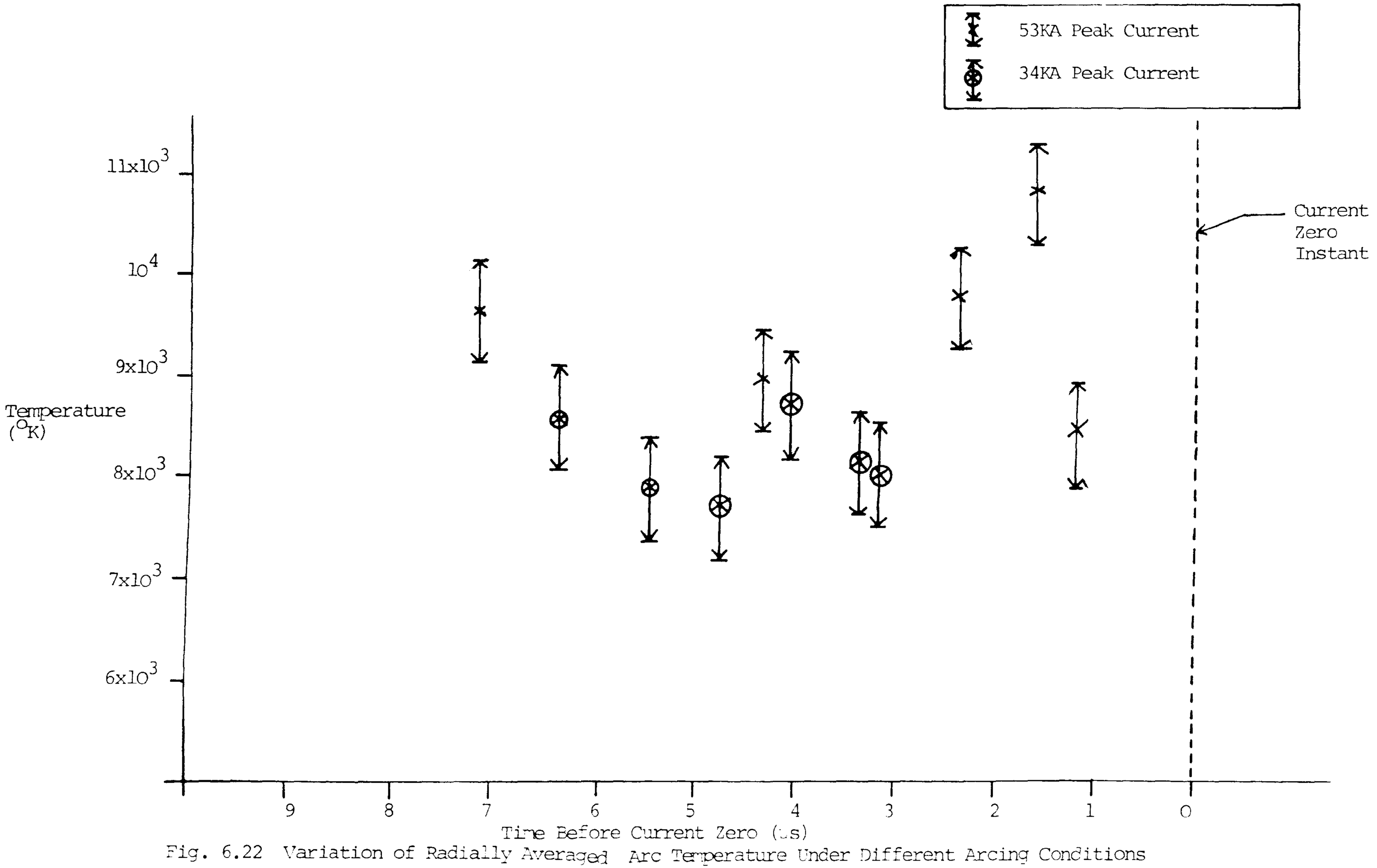

Fig. 6.22 Variation of Radially Averaged Arc Temperature Under Different Arcing Conditions

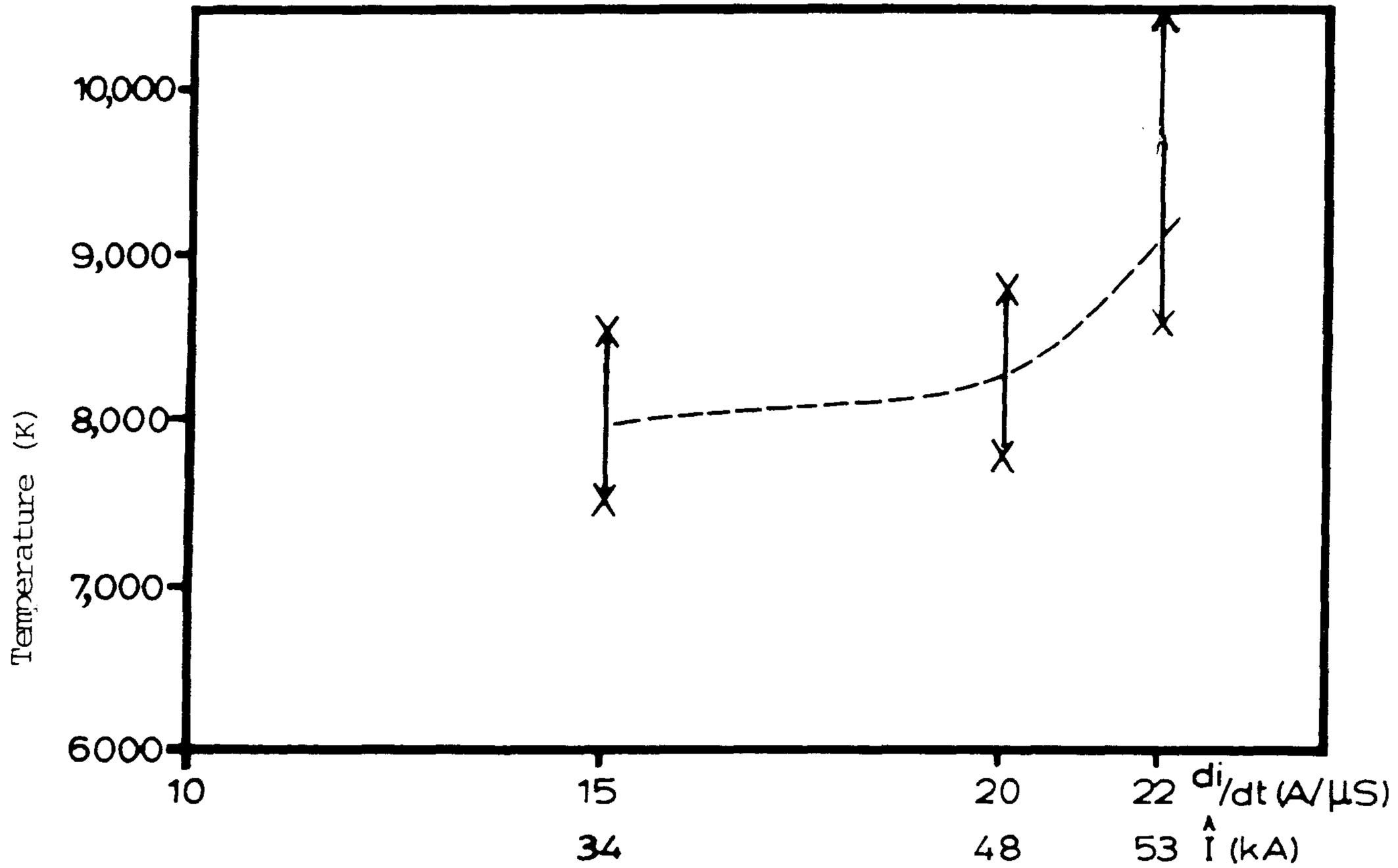

Fig. 6.23 The Variation of the Radially Averaged Temperature During the Current Zero Period with the Current Decay Rate

(a) λ_c = (Centre Wavelength Setting of Monochromator) = 512nm

(i) Low di/dt

(ii) Medium di/dt

(iii) High di/dt

(b) λ_c = 521nm

(i) Low di/dt

(ii) High di/dt

Fig. 6.24 Radially Resolved Arc Spectra During the Current Zero Period

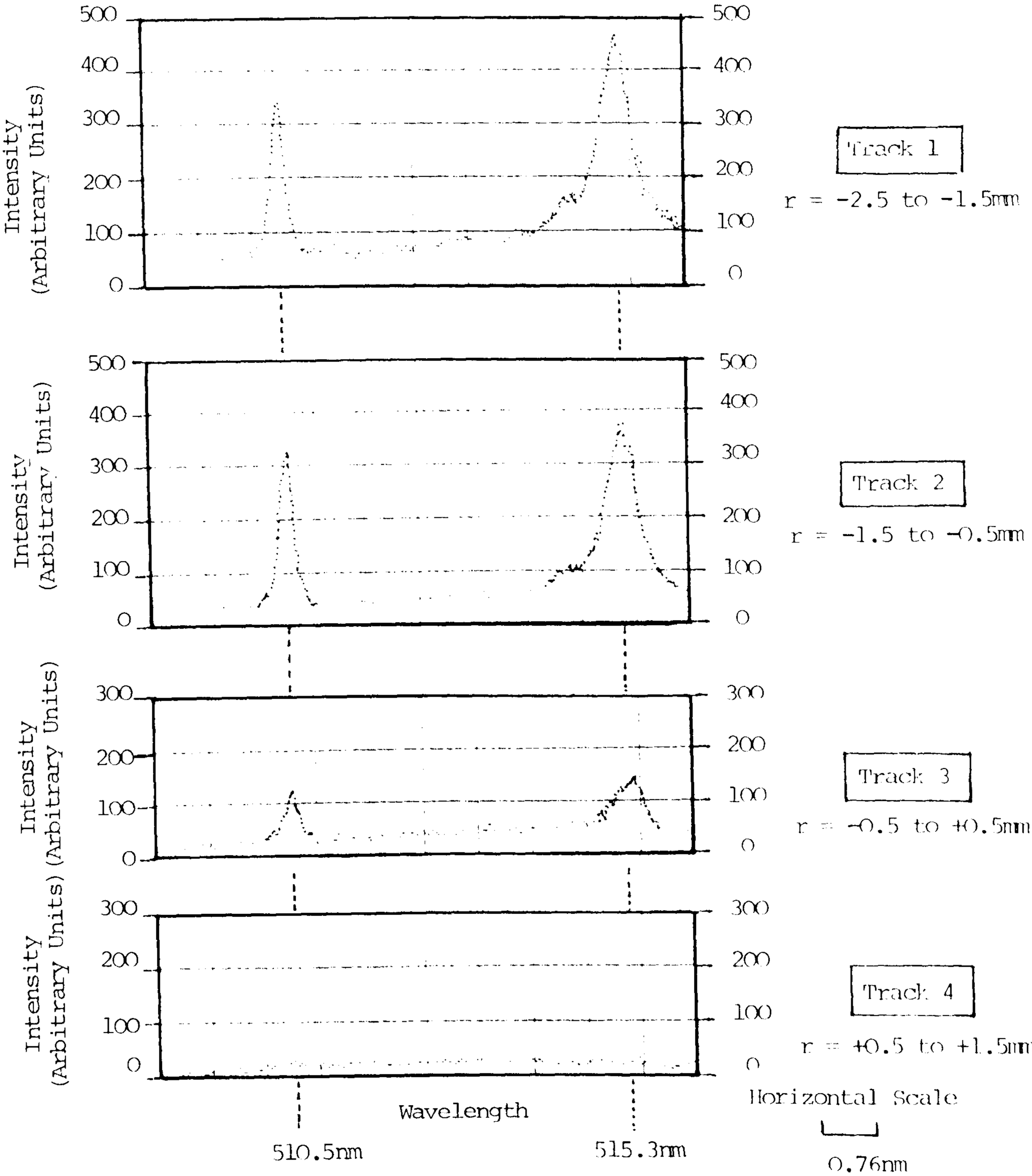

Operating Conditions	
Peak Current = 34KA	Time Before Current Zero = 7.4μs
di/dt = 15A/μs	Exposure Time = 1.6μs

Fig. 6.24 (a) (i) λ_c = 512nm ; Low di/dt

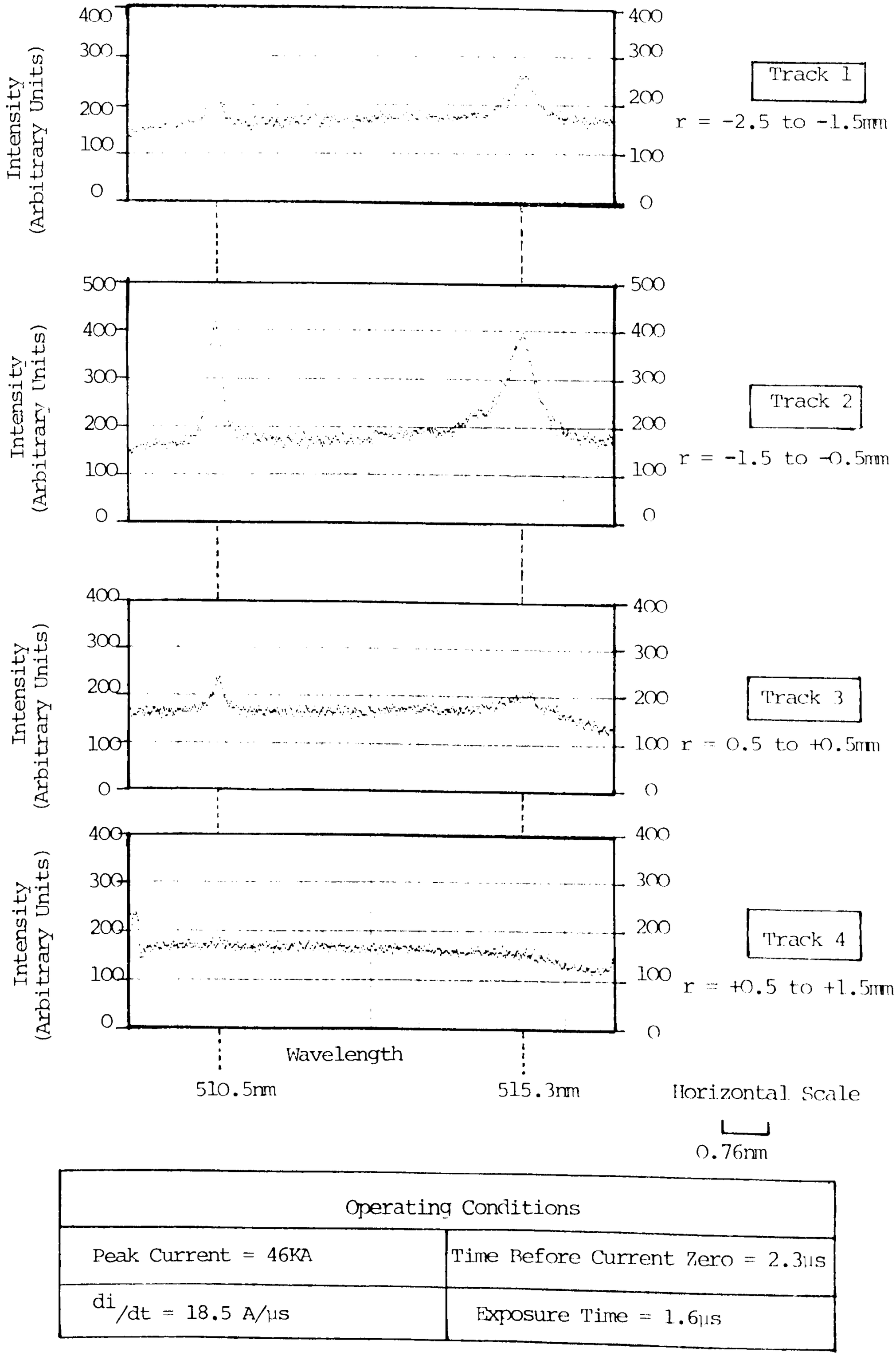

Operating Conditions	
Peak Current = 46KA	Time Before Current Zero = 2.3μs
di/dt = 18.5 A/μs	Exposure Time = 1.6μs

Fig. 6.24 (a) (ii) λ_c = 512nm ; Medium di/dt

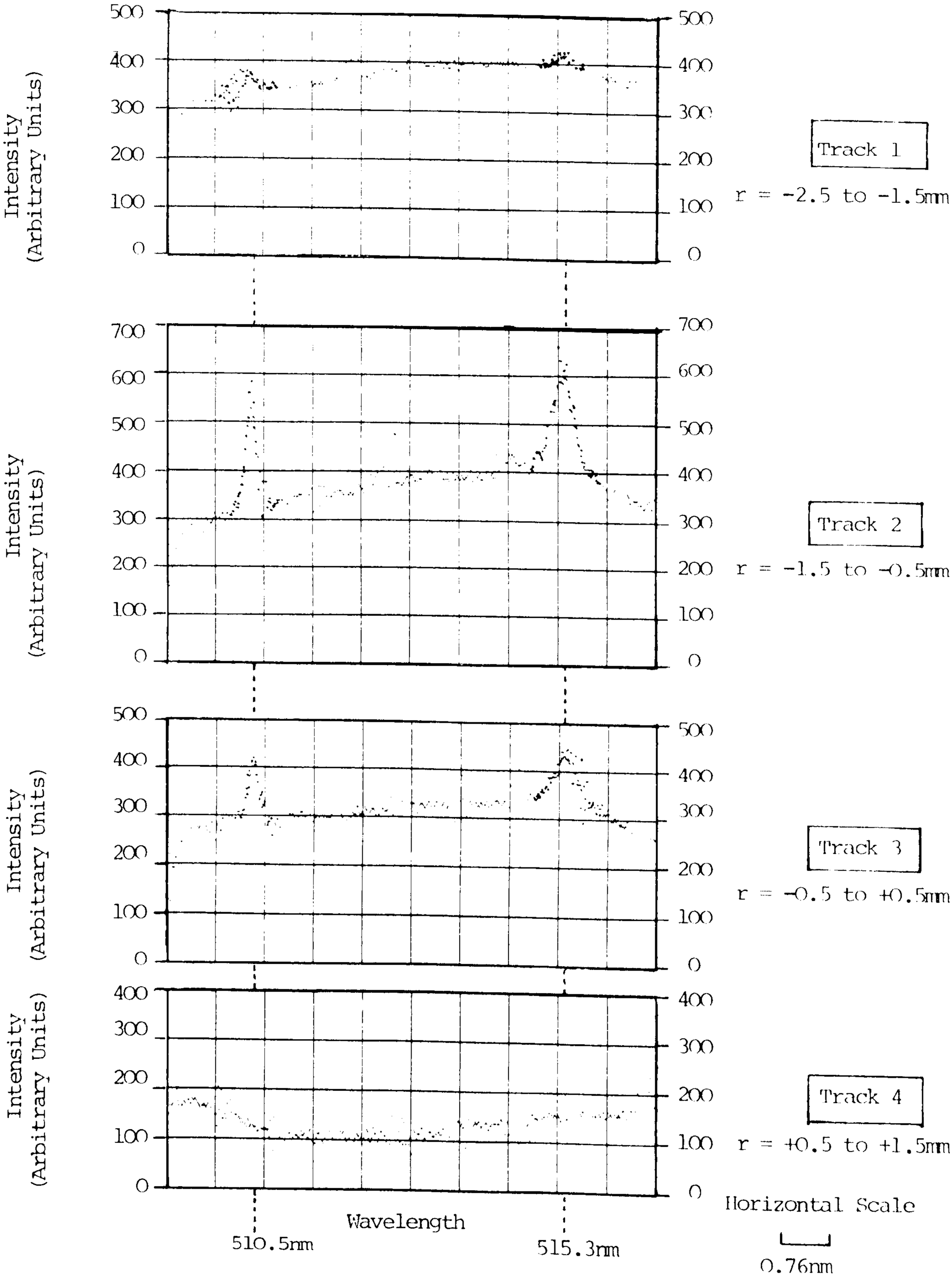

Operating Conditions	
Peak Current = 53KA	Time Before Current Zero = 7.9μs
di/dt = 21 A/μs	Exposure time = 1.6μs

Fig. 6,24 (a) (iii) λ_c = 512nm ; High di/dt

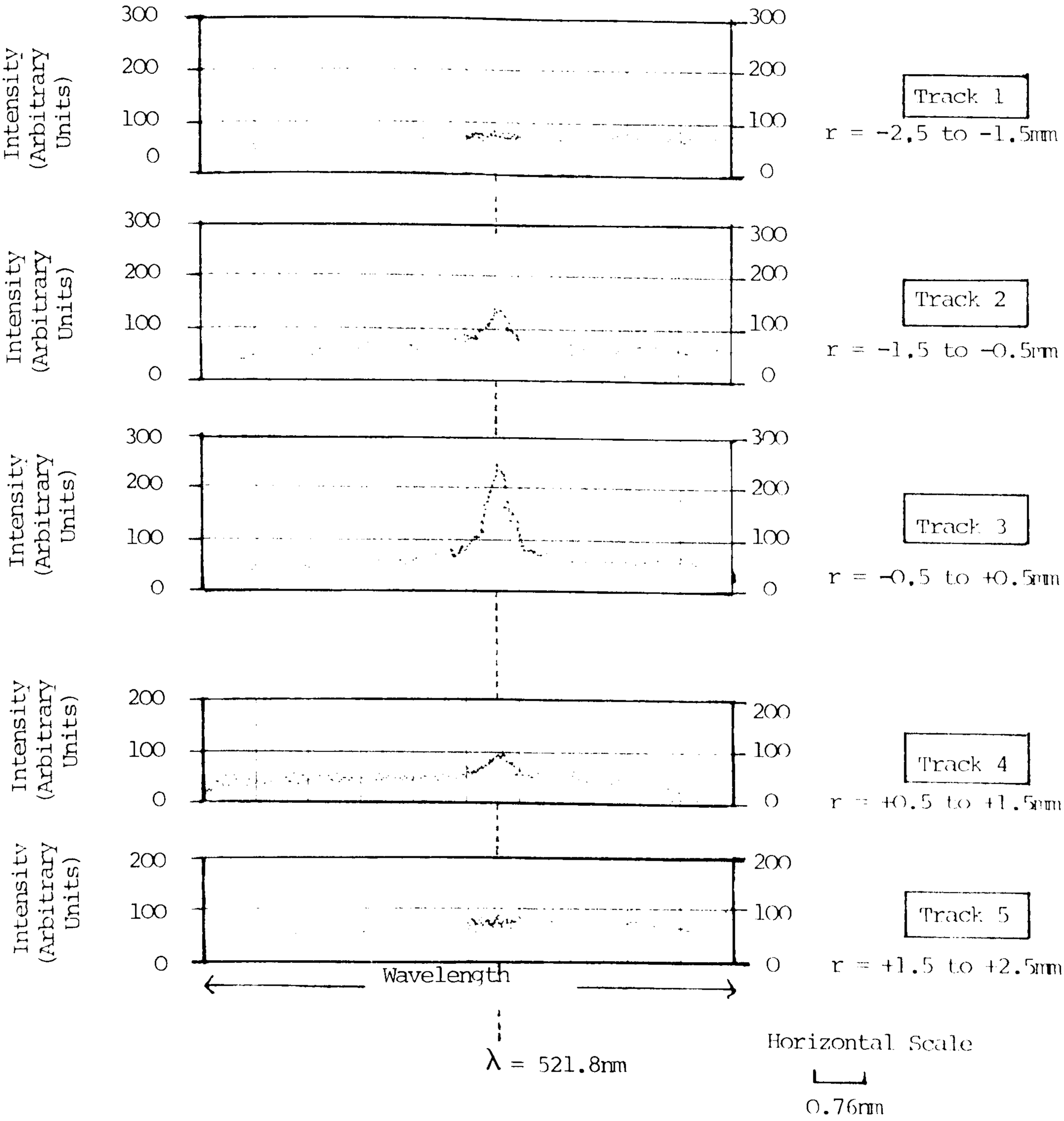

Operating Conditions	
Peak Current = 34KA	Time Before Current Zero = 2μs
di/dt = 15 A/μs	Exposure time = 1.6μs

Fig. 6.24 (b) (i) λ_c = 521nm ; Low di/dt

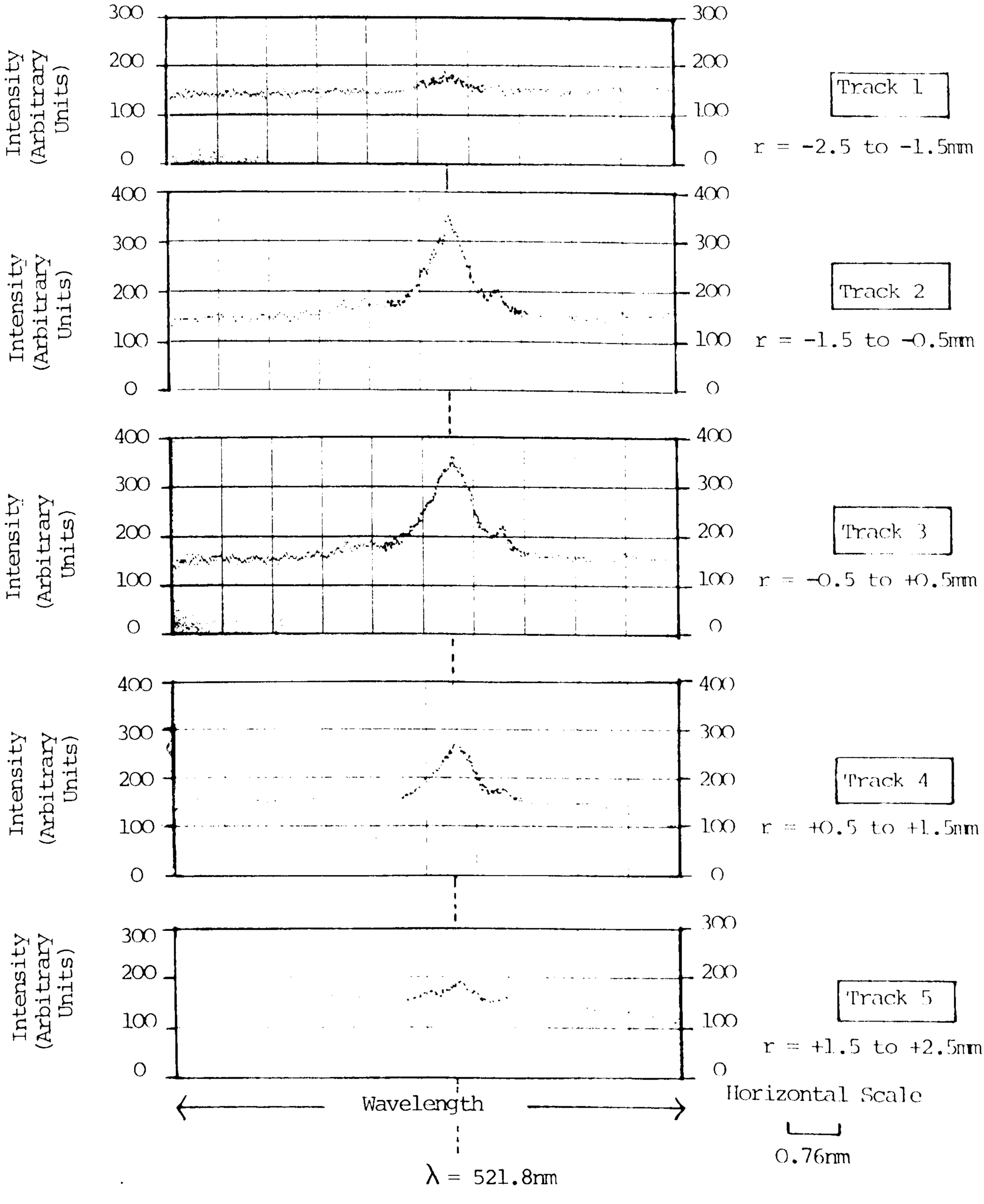

Operating Conditions	
Peak Current = 46KA	Time Before Current Zero = 5.3μs
$^{di}/_{dt}$ = 17.5 A/μs	Exposure time = 1.6μs

Fig. 6.24 (b) (ii) λ_c = 521nm ; Medium $^{di}/_{dt}$

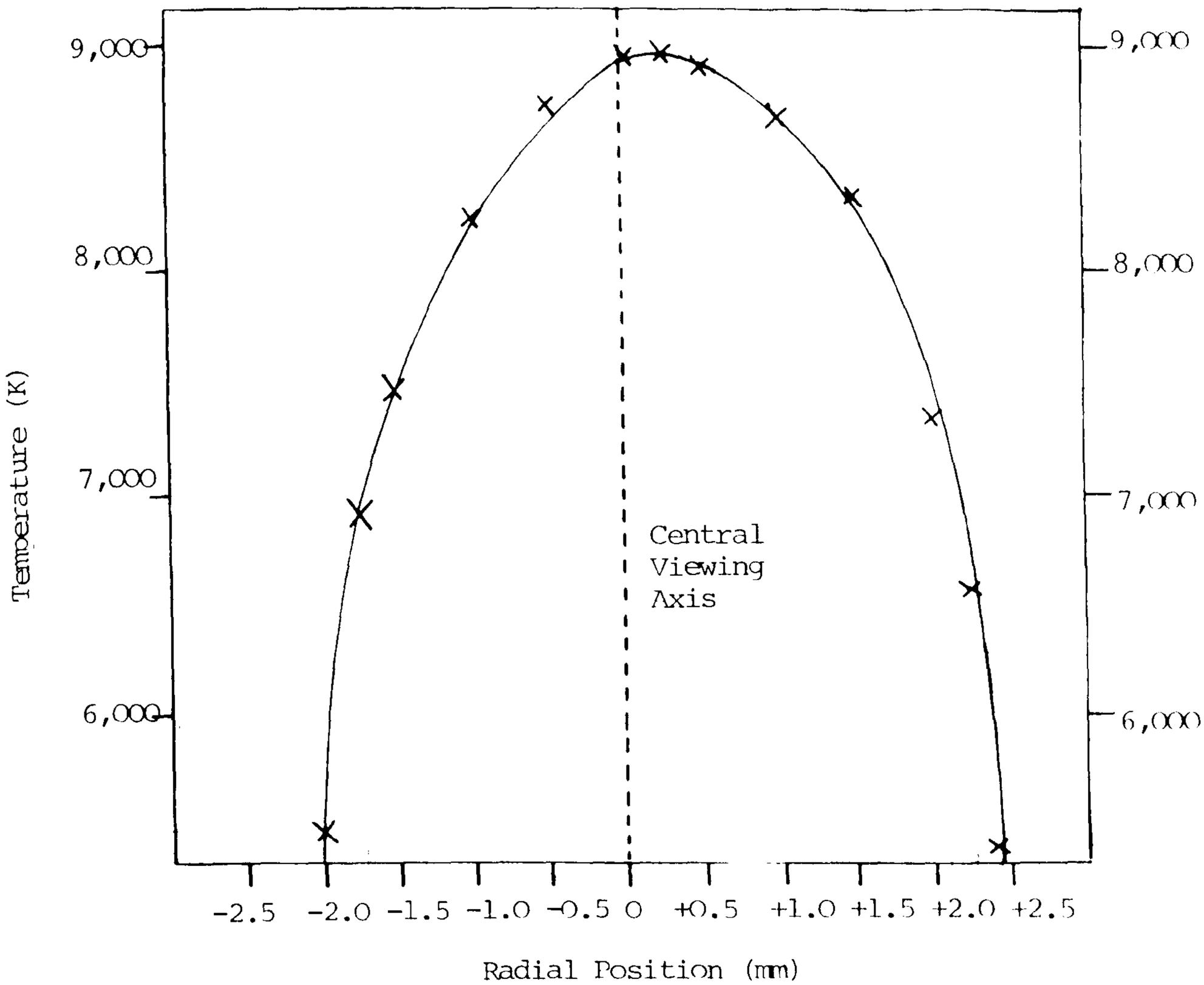

Operating Conditions:

Time Before Current Zero = 10μs

Exposure = 1.6μs

di/dt = 14.2 A/μs

Fig. 6.25 Arc Temperature Profiles During the Current Zero Period

(i) Ip = 34KA

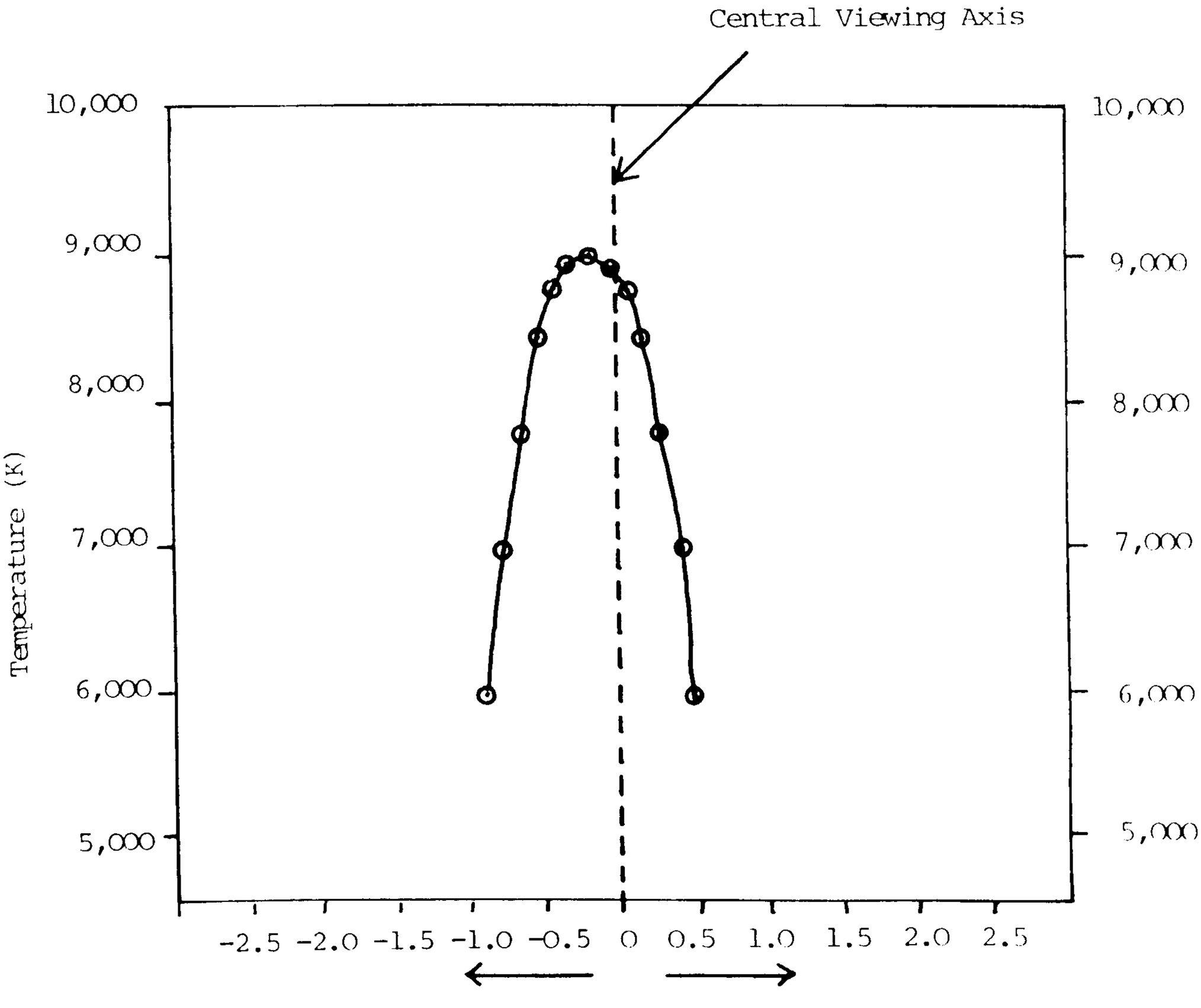

Operating Conditions:

Time Before Current Zero = 2.2μs

Exposure = 1.6μs

di/dt = 21 A/μs

(ii) Ip = 46KA

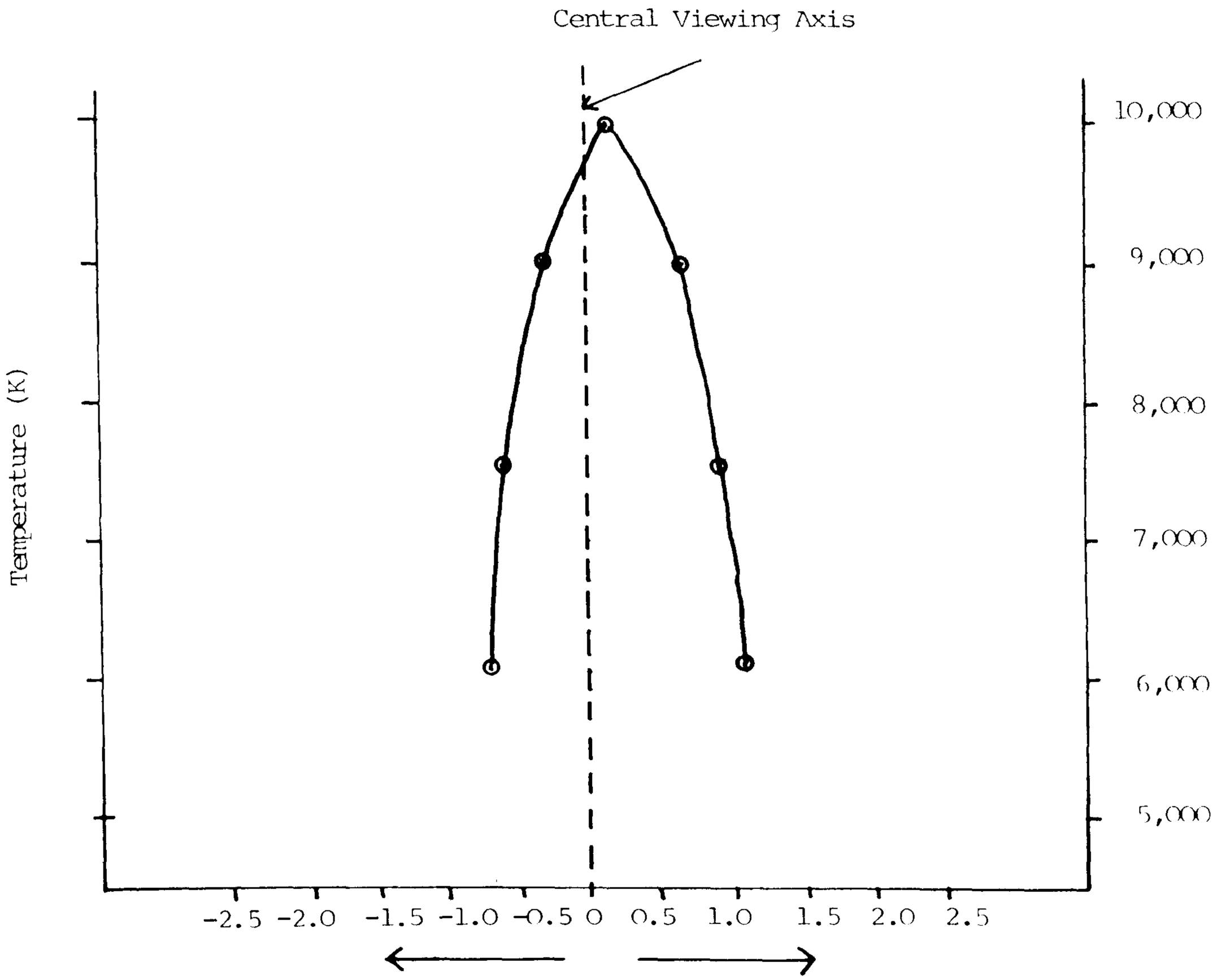

Operating Conditions:

Time Before Current Zero = 7.9μs

Exposure = 1.6μs

di/dt = 21 A/μs

(iii) Ip = 53KA

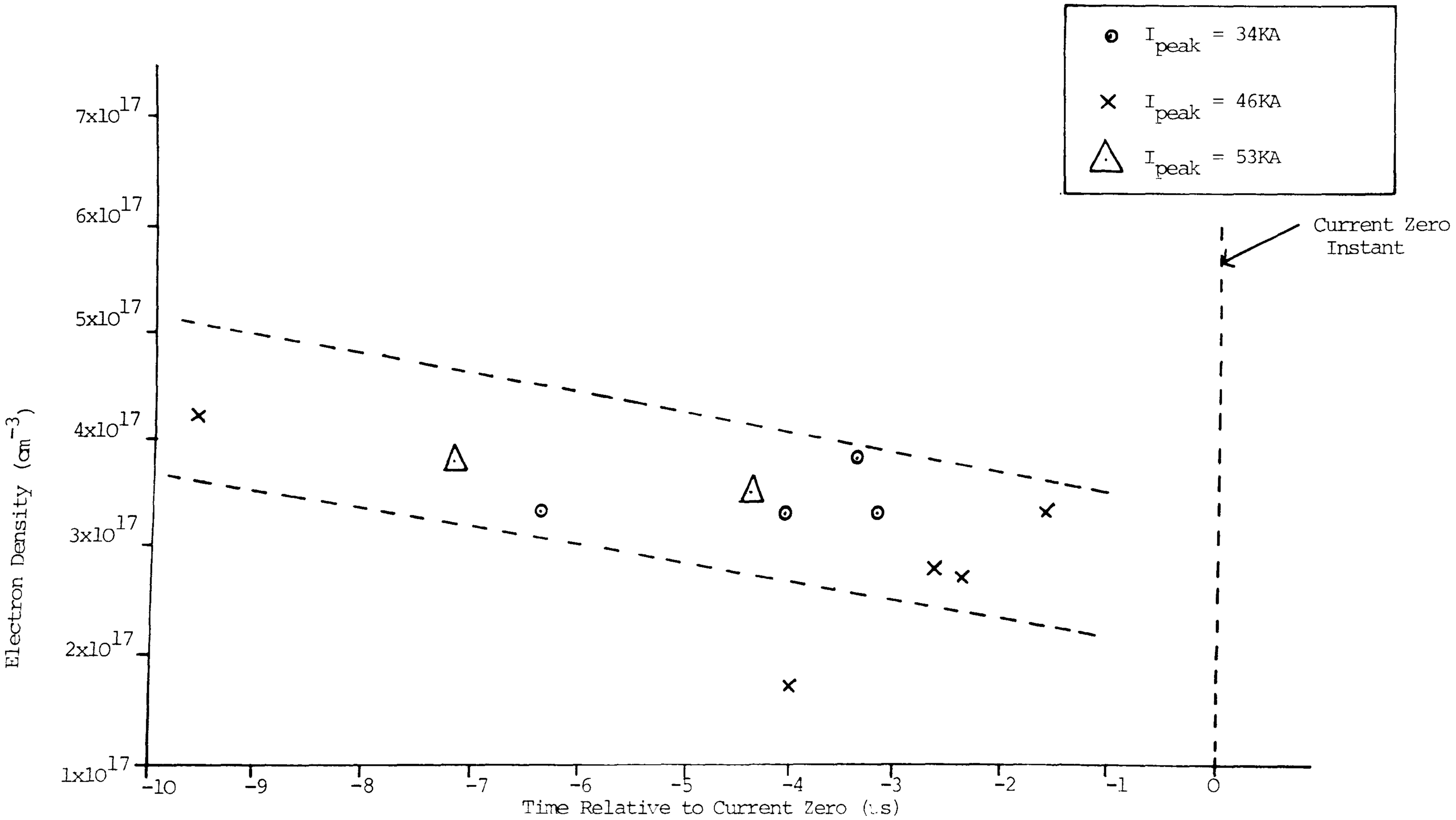

Fig. 6.26 The Radially Averaged Electron Density Versus Time, for Different Peak Currents, During the Current Zero Period

CHAPTER 7

THEORETICAL BACKGROUND TO PHOTOGRAPHIC AND SPECTROSCOPIC CALCULATIONS

7.1 Introduction

This chapter is concerned with a discussion of the theoretical aspects of arc spectroscopy and photography relevant to this investigation. Particular attention is paid to formulations which allow the results of chapter 6 to be analysed and interpreted in both a qualitative and quantitative manner. The interpretation of the results is dealt with in the next chapter of this thesis.

The first section of this chapter deals with background spectroscopic formulations, their physical origins and application to a circuit breaker arc. Such a theoretical approach was not considered necessary in the case of the photographic investigation since the arc photographs could be interpreted directly with a knowledge of the calibration discussed in chapter 5. Special attention is given at the end of this section to the interpretation of the spectroscopic data from which the temperature profiles in chapter 6 were derived.

The second section of this chapter is concerned with the definition of important parameters in terms of measurable quantities. Particular attention is paid to the arc thermal (Mayr) time constant, the shape factors of the integral

analysis, and definition of the terms in the dynamic arc energy conservation equations. Again the implications of the above formulations coupled with the experimental data will be discussed in chapter 8.

7.2 Basic Plasma Spectroscopic Theory and its Application to the Current Zero Arc Column

7.2.1 Introduction

This section is concerned with the basic development of plasma spectroscopic theory and its application to the specialised measurement technique of the present investigation.

The concept of an arc in complete thermodynamic equilibrium is introduced which is then extended to the more realistic case of an arc in local thermodynamic equilibrium (LTE). Basic spectroscopic formulations are then introduced (assuming LTE) from which local plasma temperatures and electron densities can be derived from measurable quantities.

The existence of LTE in the circuit breaker arc at the nozzle throat is then assessed by the application of a suitable criterion which can be evaluated from experimental data. This is undertaken in chapter 8.

Even with the existence of LTE in the current zero circuit breaker arc the validity of the calculation of plasma temperature and electron density is still dependent on the

assumption that the plasma is optically thin. Hence consideration is given to establishing the concept of the plasma optical depth.

Two further criteria are developed to test whether the plasma optical depth is sufficiently small (ie. optically thin) to validate the above temperature calculations. Results obtained from the second of these criteria involve a plasma diameter which may be compared with the luminous arc diameter and temperature profile measurements of chapter 6.

7.2.2 LTE and Optical Depth Criteria and the Determination of Temperature and Electron Density

This section is concerned with the development of formulae which allow the temperature and electron density of a plasma in LTE to be calculated from measurable quantities. All formulae developed depend upon the plasma being in LTE. If the concept of LTE is to be understood then it is necessary to describe briefly the properties of a plasma in complete thermodynamic equilibrium (CTE).

7.2.2.1 Thermal Equilibrium and the Calculation of Electron Temperature and Density

A plasma in complete thermodynamic equilibrium has totally homogenous values of mass density, temperature and chemical composition. In such a case the electrons obey a Boltzmann distribution in occupying various energy states and the free electron velocities follow a Maxwellian

distribution. The radiation emission from a CTE plasma is 'black-body' in nature. A further important property of a plasma in CTE is that all the plasma particles exist at the same temperature so that a single plasma temperature may be defined which corresponds to the same temperature. Clearly in many dense plasmas where many electron-atom collisions occur the tendency is towards such a thermodynamic equilibrium. However where radiative mechanisms become comparable to or dominate over the collision mechanisms account needs to be taken of such effects through a coupling of the appropriate terms in the governing rate equations (Griem, 1964). This coupling complicates any subsequent equilibrium relations. Fortunately, most high pressure arc plasmas are collision dominated and in the case of low current arcs the plasma is generally optically thin. However, the existence of CTE is rarely experienced in many laboratory plasmas let alone in a circuit breaker arc. Thus it is convenient to identify regions of a plasma which may have the same properties as a CTE plasma. A plasma with such localised regions in which thermodynamic properties persist is said to be in local thermodynamic equilibrium.

The concept of LTE may be applied to a circuit breaker arc whereby certain key regions of the arc plasma can be tested for LTE and the LTE equations applied. The nozzle throat of the circuit breaker is such a key region since the photographic results of chapter 6 have already shown it to be a region in which the arc is sensitive to changes in operating conditions etc.

The equations to determine the electron (plasma) temperature and density can thus be applied initially assuming LTE and the existence of LTE itself is later confirmed using established criteria.

The first formulation which is necessary is one whereby the plasma temperature can be calculated from spectroscopically measurable values.

The absolute intensity of the radiation from a spectral line from an 'optically thin' plasma (a concept that is dealt with later in this chapter) is described by

$$I_{mn} = \frac{1}{4\pi} A_{mn} g_m N_{(T)} \frac{hc}{\lambda_{mn}} \cdot \frac{1}{Z(T)} \text{Exp} \left| \frac{-E_M}{KT} \right| \qquad -7.1$$

where,

the subscripts m and n refer to two bound energy levels

A_{mn} = transition probability for m to n transition

$N_{(T)}$ = species density

h = Planck's constant

c = velocity of light

λ_{mn} = wavelength

Z(T) = Partition function

gm = statistical weight of the upper energy level

E_m = Energy of bound level m (upper level)

K = Boltzmann's constant

T = temperature

Clearly it is possible to calculate temperature from

equation 7.1 from a knowledge of the atomic data and the absolute line intensity I_{mn}. However it is difficult to measure the absolute line intensity in practice since source and optical system geometry as well as absolute instrument detection threshold are factors which need to be taken into account. It is more reliable to calculate the temperature from intensity ratio of two lines. Furthermore, if the intensity ratio of two spectral lines emitted by the same atomic species is used then the temperature dependent variables N(T) and Z(T) in equation 7.1 may be also eliminated.

The ratio of two such spectral lines is given by

$$\frac{I_{mn}}{I_{mn}^{1}} = \frac{A_{mn}g_m}{A_{mn}^{1}g_m^{1}} \cdot \frac{\lambda_{mn}^{1}}{\lambda_{mn}} \text{ Exp } \frac{E_m^{1}-E_m}{KT} \qquad -7.2$$

Thus if the intensities of two spectral lines of the same atomic species are known then with a knowledge of the relevant atomic data the temperature of the plasma may be calculated. It is clear from equation 7.2 that in order to establish the temperature in such a manner spectral lines must be chosen whose upper energy level value (E_m) must be different. If this condition is not satisfied then I_{mn} and I_{mn}^{1} differ only by a constant factor so that their ratio is independent of temperature. However this fact may be used for assessing the optical depth of the plasma as considered below.

A program was developed to calculate the plasma temperature from the measured line intensity ratio and atomic

data for a pair of spectral lines (details in appendix 2). The relevant atomic data for Cu I (A_{mn}, E_m, g_m) was obtained from Koch and Richter (1968). Thus the plasma temperature could be determined from the interpretation of raw spectral data to which formulae for plasmas in LTE have been applied. The temperatures derived in this manner need to be further assessed in terms of source and system geometry etc. in order to obtain radially resolved arc temperature profiles. This latter interpretive exercise is not related to fundamental spectroscopic theory and so is considered later.

Another parameter of importance in the present investigation is the electron density. The electron density of the arc was determined from the broadening of the spectral lines due to increases in the electrostatic forces due in turn to an increased electron density. The broadening of spectral lines can be caused by several processes which include pressure and doppler effects. However in the case of a collision dominated high pressure arc plasma as is the case in the present work, the principal broadening mechanism is Stark broadening. The theoretical description of other broadening mechanisms can be found in the literature (e.g. Griem, 1974) and their relative importance in a similar arc plasma has been reviewed by Airey (1977). Another broadening mechanism which needs to be considered is that associated with the measuring instrument (instrument broadening). The slit width of the monochromator was maintained at 28.5μm for the entire investigation of the

present work resulted in an instrument broadening of 0.03nm. This value was obtained from the calibration of the same instrument (Ibuki, 1978) which is shown in appendix 7.

The broadening of the spectral line due to the Stark effect is given by Griem (1964) as

$$W_{TOTAL} = \left[1 + 1.75\alpha(1-0.75r)\right] w \qquad 7.3$$

where

W_{TOTAL} is the total half width due to Stark broadening

W is the electron impact width in angular frequencies

r is a correlation parameter defined by

$$r = \frac{\text{mean distance between ions}}{\text{Debye radius}} = 6^{1/3}\ \pi^{1/6} \left(\frac{e^2}{4\pi\epsilon_o KT}\right)^{\frac{1}{2}}\ N^{1/6}$$

N is the number density of perturbing ions (Ne)

$$\alpha = \left(\frac{C_\alpha F_o^{\,2}}{\omega}\right)^{3/4}$$

F_o is the normal field strength

$$F_o = \frac{2.61}{4\pi\epsilon_o}\ Ne^{2/3}$$

C_α is the quadratic Stark coefficient

Jenkins (private communication) has evaluated equation 7.3 using values of α, r and ω calculated by himself for different spectral lines of Cu I and a range of Ne and temperature values. The results of these calculations of selected spectral lines of interest are shown in table 7.1.

The first of the two criteria which needs to be considered is McWhirter's criterion (Huddlestone and Leonard, 1965). McWhirter defines the collision transition rate τ_C as:

$$\tau_C = n_e\, n_p X(T_e,p,q) \qquad 7.4$$

where

n_e is the electron density (cm^{-3})

$n_{(p)}$ is the population density of energy level p

$X(T_e,p,q)$ is the de-excitation coefficient

Subscripts p and q refer to bound energy levels

It is further postulated that for radiative decay rates to cause less than 10% departures from LTE, the collisional rates must be at least an order of magnitude greater than the radiative rates. Thus for energy levels p and q,

$$n_e\, n_{(p)}\, X(T_e,p,q) \geq 10\, n_{(p)}\, A_{(p,q)} \qquad 7.5$$

where $A_{(p,q)}$ is the atomic transition probability

In the case of high temperature plasmas which McWhirter has defined as including temperatures of the order 10^4K where plasmas are mostly ionic rather than atomic he uses the threshold excitation of ions (Seaton, 1962) as

$$X(T_e,q,p) = \frac{6.5 \times 10^{-4}}{X(p,q)T_e^{\frac{1}{2}}}\, f(q,p)\,\mathrm{Exp}\left[\frac{-X(p,q)}{KT_e}\right]$$

where

$X(p,q)$ = Excitation potential of level p from q (eV)

$f(q,p)$ = absorption oscillator strength

McWhirter further relates this to the de-excitation coefficient by

$$X(T_e,p,q) = \frac{g(q)}{g(p)} X(T_e,q,p) \text{ Exp } \left[\frac{X(p,q)}{KT_e}\right]$$

where g(q) and g(p) are statistical weights of levels q and p.

The equation relating the spontaneous transition probability to absorption oscillator strength is then invoked

$$A(p,q) = \frac{1}{1.5} \cdot \frac{g(q)}{g(p)} \cdot \lambda^2 f(q,p)$$

and the McWhirter criterion becomes

$$n_e \geq 1.6 \times 10^{12} (T_e)^{\frac{1}{2}} \left[X(p,q)\right]^3 \qquad 7.6$$

Equation 7.6 is least likely to be satisfied for $X(p,q)$ being equivalent to the largest energy gap in the term scheme of the ions present. This then represents the most severe LTE test on the basis of the McWhirter criterion.

A still more severe test is provided by the Griem formulation (Lochte-Holtgreven, Ed. Lochte-Holtgreven, 1964). This is based upon the hypothesis that the collisional excitation rate should exceed the radiative decay rate by an order of magnitude. An expression is developed for each

transition rate, one of which contains N_e, the electron density. An inequality is formed on the basis of the above hypothesis and the Boltzmann equation is invoked to close the set of equations. The final formulation becomes

$$N_e \geq 9 \times 10^{17} \left\{ E_2 \frac{z-1,a}{E_H} \right\} \left\{ \frac{KT}{E_H} \right\}^{\frac{1}{2}} \qquad 7.7$$

where

N_e is the electron density (cm^{-3})

$E_2^{z-1,a}$ is the first excited level (upper resonance level (eV)

E_H is the ionization energy (eV)

The values of $E_2^{z-1,a}$ and E_H for Cu I are 3.82eV and 7.724eV respectively. As an illustrative example, if the electron temperature is 10,000K then according to equation 7.7 N_e must be greater than 3.64×10^{16} for LTE to exist. If similar values are inserted into McWhirter's criterion (equation 7.6) with X(p,q) = 2.73eV for Cu then N_e must exceed 3.26×10^{15} cm^{-3} for LTE existence. Clearly, of the two criteria, Griem's (1964) represents the most severe test. The two criteria will be applied carefully using the results of chapter 6 and discussed further in chapter 8. Initial indications are that the LTE criterion of Griem (1964) is satisfied by about an order of magnitude according to the electron density measurements of chapter 6 (fig. 6.26) for a temperature of 10,000K.

7.2.2.2 Optical Depth of a Plasma

As already indicated, it is necessary to establish, in addition to the existence of LTE, whether the plasma is sufficiently 'optically thin'. A plasma is optically thin if its radius is sufficiently small so as to cause little or no re-absorption of the radiation escaping from the central axis by the cooler outer radial regions. Thus all the radiation from each individual atom is transmitted away from the plasma.

Three methods of determining whether the current zero arc plasma is optically thin are available.

The first method involves an inspection of the shape of particular spectral lines. If the plasma departs from being optically thin then re-absorption of the radiation at a wavelength corresponding to the line centre occurs. The effect of this is to give the line an increasingly flattened appearance and, in the extreme, self reversal occurs whereby the line profile shows a dip at the centre wavelength. It was beyond the capability of the present optical system to detect the Cu I resonance lines (which are centred in the u.v. part of the spectrum), so that it was not possible to detect whether self reversal occurred for these lines. However inspection of the profile of the lines centred on 521.8nm (fig. 7.2(a)) shows no indication of flattening at the centre wavelengths. The line centred on 521.8nm in this case is accompanied by a satellite emission centred on 522.0nm (this is a weaker Cu I emission).

The second method for testing for optical depth involves taking the ratio of two peaks of a multiplot (Lochte Holtgreven, in Lochte-Holtgreven, 1968) or a pair of independent lines which share the same upper energy level. In the latter case no variation in their ratio should occur with temperature change since the term (Em^1-Em) in equation 7.2 tends to zero.

Equation 7.2 thus reduces to

$$\frac{I_{mn_1}}{I_{mn}} = \frac{A_{mn}g_{m}\lambda^1_{mn}}{A_{mn}{}^1 g_{m}{}^1 \lambda_{mn}} \qquad 7.8$$

If the atomic parameters Amn, gmn are known (these are included on table 7.2 for a number of visible spectral lines of Cu I) then a purely theoretical value of the intensity ratio can be calculated. If the measured line profile is not affected by optical depth and LTE exists then the measured ratio of two such lines should correspond to this theoretical value within the error margins. The emissions at 521.8nm and 522nm have a common upper energy level value (E_m in table 7.2). Therefore if these two lines can be resolved by the monochromator, an intensity ratio can be measured. Since the two lines shown on fig. 7.2(a) can be resolved their intensity ratio may be determined. This ($I_{521.8}:I_{522.0}$) was measured as 5.5:1 for the case of fig. 7.2(a) when the mean continuum level (the centre dotted line on fig. 7.2(a)) was used as the reference level. The intensity ratio according to equation 7.8 and the values in table 7.2 is 7.5:1. This represents an error of about

26% between the measured and theoretical values. However the errors in the atomic data of table 7.2 are as much as $\pm$ 12% (Kock and Richter, 1968) per parameter so that the difference between the measured and deduced ratios is within the total error (including a 10% contribution from experimental sources).

The two spectral lines involved in this calculation were recorded simultaneously on the same record so that shot to shot variations were eliminated. Similar comparisons have been made between the 521.8nm line and the 515.3nm line which, however, could not be captured simultaneously (Lewis et al, 1985(ii)). In this case two records corresponding to well matched operating conditions were selected. Agreement between measured and theoretical values in this case was found to be particularly good. This quantitative method has been used to confirm that the arc plasma is optically thin during the current zero period of a 34KA arc (15A/μs, 9μs before current zero).

Airey (1977) postulated an alternative quantitative approach to optical depth determination. With this method the spectral line intensity from a sphere is equated to the 'black body' radiation from the same sphere at the wavelength of interest. The value of the black body radiation power in this case forms the limit at which the spectral line radiation would begin to show a flattening at the centre wavelength. The two radiation functions (black body and spectral line) were integrated over a volume (black body)

and area x wavelength (line emission). Thus the subsequent equality enables the determination of a value of 2r (r = radius of sphere) which corresponds to the critical optical depth at which self absorption begins to occur.

The black body radiation function is

$$B(\lambda,T) = \frac{C_1}{\lambda_{mn}^5}\left[\left|\mathrm{Exp}\left(\frac{C_2}{\lambda_{mn}T}\right)\right| - 1\right]^{-1} \qquad 7.9$$

where,

λ_{mn} is the wavelength (cm)

T is the electron temperature (K)

C_1, C_2 are constants (Pivovonsky and Nagel, 1961)

$C_1 = 1.91 \times 10^{-12}$ W $cm^2 sr^{-1}$

$C_2 = 1.438$ cmK

The spectral line intensity was defined in equation 7.1 as

$$I_{mn} = \frac{1}{4\pi} N(T) \frac{g_m A_{mn}}{Z(T)} \cdot \left(\frac{hc}{\lambda_{mn}}\right) \mathrm{Exp}\left[-\frac{Em}{KT}\right]$$

Multiplying equation 7.9 by surface area and d_{mn} (the wavelength interval of interest gives the total black-body radiation escaping from the sphere of radius r, and the wavelength concerned. Thus

$$B(\lambda,T).4\pi r^2\, d\lambda_{mn} = 4\pi r^2\, d\lambda_{mn} \frac{C_1}{\lambda^5_{mn}}\left(\mathrm{Exp}\left[\left(\frac{C_2}{\lambda_{mn}T}\right) - 1\right]\right) \qquad 7.10$$

Multiplying equation 7.1 by the volume of the sphere of radius r gives

$$I_{mn} \cdot \frac{4}{3}\pi r^3 = \frac{1}{4\pi} \cdot \frac{4}{3}\pi r^3 \cdot N_{(T)} \frac{g_m A_{mn}}{Z(T)} \left(\frac{hc}{\lambda_{mn}}\right) Exp\left[-\frac{Em}{KT}\right] \qquad 7.11$$

Thus when the expressions for radiation power of equation 7.10 and 7.11 are equated a value of r is obtained which when multiplied by 2 represents the optical depth at which self absorption effects begin to occur i.e.

$$2r = \frac{24\pi Z_{(T)}\ d\lambda_{mn} \left(\frac{C_1}{\lambda^5\ (Exp(C_2/T) - 1)}\right)}{Nz(T)\ A_{mn}\ g_m\ \Delta\ Emn\ Exp\left[-\frac{Em}{KT}\right]} \qquad 7.12$$

where $\Delta Emn = \frac{hc}{\lambda_{mn}}$

and h is in Js if C_1 is in $W_{cm}2\ S_r-1$

The value of the partition function Z(T) was obtained from Drawin and Felenbok (1965) in the temperature range 6,000 to 12,000K. The population density of Cu I, $N_z(T)$ was obtained from unpublished data of Kinsinger (Airey, private comm.) for a 10% Cu : 90% SF_6 plasma mixture. The value of 2r was then calculated from equation 7.12 for some of the Cu I diagnostic lines over a temperature range 6,000 to 12,000K and is shown on fig. 7.2(b). The program for this calculation is listed in appendix 2. For example, the line at 515.3nm at a temperature of 9,000K yields a value

of 2.45mm. For the temperature profiles of figs. 6.25(ii) and (iii) the 6,000K isotherm lies within the boundary described by 2r in this case. Furthermore since no self absorption effects are evident in the line profiles from which the temperature profiles of fig. 6.25 were calculated then any cooler Cu I species at a radius greater than r must have little or no self absorption effect. Thus the concentration of Cu I in these regions must be low. Although in the case of the temperature profile for the lower $^{di}/_{dt}$ case (fig. 6.25(i)) the 6,000K isotherm diameter exceeds 2r the spectral lines again showed no indication of self absorption effects.

Airey's (1977) method of optical depth determination provides the most severe test for optical thickness in the plasma since it represents the conditions under which self absorption may first be observed.

In summary, three tests have been developed which allow the optical depth of the plasma to be determined. Various degrees of severity were evident for the different methods but comparison with the temperature profiles and the spectral data of chapter 6 have shown the current zero arc plasma to be generally optically thin. One result from chapter 6 failed the most severe test (Airey's method, 1977) but no evidence of self absorption was present in the spectral line shapes even in this case. Consequently it is considered that the arc plasma may be considered to be optically thin.

7.3 The Evaluation of Radial Temperature Profiles from Line of Sight Considerations

Although methods for determining temperature and electron density have been established, the optical thickness of the arc plasma has been determined and the existence of LTE established it still remains to provide radial resolution of the arc plasma temperatures.

Since the arc plasma column is essentially a cylindrical source the recorded spectrum needs to be corrected for its line of sight nature. A standard technique for making such a correction is the Abel inversion (Lochte-Holtgreven in Lochte Holtgreven, pp.184, 1968). Fig. 7.3(a) represents the cross-section of a cylindrical arc source. The received intensity profile at a given displacement on the y axis from the centre (fig. 7.3(a)) will be due to emissions from a number of microscopic sources along the line of sight such as AA^1 in fig. 7.3(a). In order to derive a true radial intensity profile (along the y axis of fig. 7.3(a)) it is necessary to be able to analyse a continuous received radial intensity profile. Such a received profile was available in the form of the measured photographic intensity profiles. Fig. 7.3(b) represents such a measured profile when an interference filter centred on a wavelength of 521.8nm was used (this was of wide enough bandwidth to include the whole Cu I line emission centred on $\lambda = 521.8$nm).

The received intensity profile was subjected to the

above mentioned Abel inversion for which it was assumed that the cylinder (or its cross-section) could be sub-divided into 5 concentric shells (or rings). Lines of sight were drawn (such as AA^1 in fig. 7.3(a)) at five equi-spaced radial positions for the received intensity profile of fig. 7.3(b) which corresponded to the radius of the innermost shell with the innermost line of sight being at a 'y' displacement of $^{rl}/2$ (fig. 7.3(a)). Also shown on fig. 7.3(b) is the Abel inverted intensity profile derived from the measured (or received) intensity profile discussed above. The computer program relating to the method of calculation of the inverted profile ('ABEL') is described in appendix 2. The Abel inverted profile of fig. 7.3(b) corresponds closely to a parabolic shape. This profile is referred to hereafter as the emissivity profile and forms the basis for the interpretation of the radially resolved arc spectra (from which the radial temperature profiles are determined.

In chapter 4 the mode of operation of the OSA which resulted in radially resolved arc spectra was discussed. This radial resolution corresponds to a splitting of the arc diameter into 5 viewing strips of equal width (i.e. radial dimension). Five strips across the diameter would give insufficient resolution to perform a proper Abel inversion for obtaining an emissivity profile directly. Also since these viewing strips are fixed with respect to the nozzle central axis small radial arc movements could

further complicate such a direct interpretation so resulting in major errors.

A more convenient and more accurate method of obtaining the temperature profile could be implemented if the emissivity profile was known and the inverse of the Abel inversion performed in order to predict the received line intensity. This method would be particularly attractive in the case where two spectral lines are captured simultaneously which is the case in the spectra of fig. 6.24(a) in chapter 6. The emissivity profile obtained by the Abel inversion of the photographic intensity profile shown on fig. 7.3(b) was centred on λ= 521.8nm for the Cu I line. The two lines on fig. 6.24(a) are centred on 510.5nm and 515.3nm. The theoretical line intensity variation with temperature for each of the above mentioned spectral lines calculated from equation 7.1 is shown on fig. 7.4. It is clear from fig. 7.4 that throughout the temperature range 6,000K to 12,000K the intensity values of the 521.8nm and 515.3nm emissions differ only by a constant factor. Consequently the ratio of intensities of the two lines will remain constant within this region and be independent of temperature. In other words these two lines cannot be used to derive a radial temperature profile on account of their identical temperature variation dependence. Consequently the radial emissivity profile of the 515.3nm spectral line intensity is identical in shape to that of the 521.8nm case (fig. 7.3(b)). Also shown on fig. 7.3(b) is a theoretical

parabolic distribution for comparison.

With the known parabolic emissivity profile of the 515.3nm line the arc was divided into three concentric rings with the outermost ring forming the 6,000K boundary as shown on fig. 7.5. Also shown on fig. 7.5 are the 5 lines of view along which the arc diameter is observed by the optical spectrum analyser. The situation for an arc diameter of 6mm is shown although the same would apply to any arc diameter. It is of significance however that, regardless of this diameter, the width of the viewing strips remains constant. In the case of fig. 7.5 areas are produced by the intersection of the rings with the lines of view. The area enclosed by two rings represents an area of homogeneous emissivity. This is representative of an average value of emissivity over the radius interval in question. Also shown on fig. 7.5 is a typical arc emissivity profile (shown in arbitrary units).

It is possible for the emissivity profile extent (radius) to change with changing arc radius as well as the position of the profile centre with respect to the fixed line of sight due to arc movement.

A program has been developed which predicts the effect of the above changes on the recorded intensity. In this program the areas described above are calculated according to a given arc radius and displacement from the central viewing axis. The recorded intensities are calculated

according to a similar fixed emissivity profile of the arc column to that described above. Thus a number of predicted recorded intensities are generated for a single arc emissivity profile (515.3nm line) which correspond to different arc radii and displacement from the central axis. These recorded intensities are in the form of radially resolved histograms and the program which calculates these is called 'IDISP2' and is described in detail in appendix 2.

The radially resolved arc spectra centred at the 515.3nm wavelength captured by the OSA are normalised to the largest line intensity value and an experimentally measured radial histogram is obtained. The experimentally obtained histogram is then compared with the family of histograms calculated by the above method. A best fit of the experimental data is then obtained which enables the radial shift of the arc axis and the arc radius to be determined. The method also enables assymetry about the central axis to be incorporated in the calculations. For instance parabolas of different radii on opposite sides of a common central axis may occur in some cases.

The experimental data of chapter 6 often included not only the line emission at 515.3nm but also the 510.5nm spectral peak on the same record. The temperature variations of the intensity of these lines calculated from equation 7.1 is shown in fig. 7.4. It is clear from this figure that the temperature variation for the 510.5nm spectral line intensity is different from that of the 515.3nm line. Thus

for a given temperature profile a unique emissivity profile will exist for the 510.5nm line.

El Kholy (unpublished) has calculated a series of similar intensity histograms for different axis temperature values and further normalised these intensity histograms to the corresponding histogram for the 515.3nm line for a given arc shift and radius. Comparison of the experimentally derived 510.5nm histogram with the above calculation of El Kholy's enables the full continuous temperature profile to be determined. This was the procedure used in chapter 6 to determine the temperature profiles of fig. 6.25.

Thus a method has been developed whereby the raw spectral data captured by the OSA 500 can be subjected to computational analysis and converted to a continuous radial temperature profile.

7.4 Summary

Formulae have been developed from which the current zero arc temperature and electron density can be determined from the relative intensities of two spectral lines and spectral line widths. Also two criteria have been discussed from which the existence of LTE conditions in the plasma can be investigated using the values of electron density and temperature presented in chapter 6. Initial indications have shown that LTE does exist near the nozzle throat during the current zero period of the circuit breaker arc of the present investigation.

A further investigation has also been conducted into the optical thickness of the arc plasma. Three criteria for the optical depth determination have been discussed. These have been used in conjunction with the results of chapter 6 to confirm that the arc plasma near current zero is generally optically thin.

A method has also been developed which utilises the radially resolved spectral data of chapter 6 and the photographically measured Cu I line intensity profile (fig. 7.3(b)) in conjunction with some of the background theory above to calculate a continuous radial temperature profile.

Having obtained a method for calculating the temperature profile of the arc column it is equally important to make use of the temperature profiles by application to the energy equation of the current zero arc column.

7.5 Theoretical Consideration of the Current Zero Energy Conservation

7.5.1 Introduction

This section is concerned with the development of theoretical arc formulae which are applied to the results of chapter 6, the implications of which are discussed in chapter 8.

The section deals initially with a brief discussion of the development of the terms in the dynamic current zero energy conservation equation applied to the arc core.

Attention is then given to the development of the shape factors of the integral analysis of Chan et al (1976). Particular attention is also given to important arc time constants. An equation relating the Mayr arc time constant to the luminous area and the local arc conductivity is developed. An alternative means of evaluating the thermal time constant is also considered which is derived from the terms of the current zero energy conservation.

7.5.2 Definition of the Energy Conservation Terms

In their paper on the formulation of integral methods for analysing arcs, Chan et al (1976) derived an expression for the energy conservation of the arc core. They applied the boundary layer assumptions to the core energy equation, which included radial diffusive transport terms (i.e. radiation and heat conduction). By substituting for the mass flow rate crossing the arc boundary (which was derived from the mass flow continuity equation) into the above core energy equation and then introducing the energy equation for the external flow, the authors were able to write the complete energy equation for the arc core (equation 5 in this reference). For the boundary layer analysis applied in this case, the author is able to set $p_I = p_\infty$ (where p_I is the pressure at the core boundary, p_∞ the cold flow pressure) i.e. pressure balance is assumed.

The core energy equation of Chan et al (1976) can be written in the following form:

Electrical Power Input to the Core + Rate Of Decay Of The Stored Energy In The Core = Radial Heat Conduction from the Core + Axial Heat Convection from the Core + Nett Power loss due to Radiation Loss from the Core + Radial Heat Convection From The Core

7.13

Equation 7.13 corresponds to

$$Ei + \frac{d}{dt}\int_{o}^{r_{arc}} \rho(r).h(r).2\pi r dr = \int_{o}^{r_{arc}} \frac{1}{r}.\frac{\partial}{\partial r}.\left(Kr\frac{\partial T}{\partial r}\right)\ 2\pi r dr + \frac{\partial}{\partial x}\int_{o}^{r_{arc}} (\rho(r).h(r).C)\ 2\pi r dr + Q_R - M_e h_I \qquad 7.14$$

for which the following assumptions have been made:

1. The enthalpy at the core edge is much greater than the square of the local axial flow velocity. Thus

$$h_{rarc} >> W^2_{rarc}$$

2. Radial pressure balance exists.

3. The radial heat conduction occurs according to the Fourier Law.

4. The work done against shear stress is discarded.

Thus with a knowledge of the temperature profile the

terms in equation 7.13 can be individually evaluated (except for Q_R). A full discussion of the quantitative aspects of the core energy balance during the current zero period is presented in chapter 8.

Chan et al (1976) further introduce core areas which correspond to integrals which in turn correspond to physical processes e.g. momentum, Kinetic energy. These integrals were first introduced in the initial work on integral methods for the overall arc equations (Cowley, 1974). The integrals for the conductance of the arc column are as follows:

(i) Overall conductance

$$\Theta_c = \int_0^\infty \left(\frac{\sigma(r)}{\sigma^*}\right) 2\pi r dr \qquad 7.15$$

(ii) Core conductance

$$\Theta_c = \int_0^{r_{arc}} \left(\frac{\sigma(r)}{\sigma^*}\right) 2\pi r dr \qquad 7.16$$

$\sigma(r)$ is the local electrical conductivity and σ^* is a characteristic value which is arbitrarily chosen.

Cowley (1974) and Chan et al (1976) further referred these values to the thermal areas which are defined as:

(i) Overall thermal

$$\Theta_\delta = \int_0^\infty \left(1 - \frac{\rho(r)}{\rho_\infty}\right) 2\pi r dr \qquad 7.17$$

(ii) Core thermal

$$\phi_{\delta} = \int_{o}^{r_{arc}} \left(1 - \frac{\rho(r)}{\rho_c}\right) 2\pi r dr \qquad 7.18$$

where $\rho(r)$ is the local gas density ρ_∞ the value in the surrounding flow and ρ_c the value at the core edge.

The ratios of the conductance areas to the corresponding thermal areas were then used to define the overall and core conductance shape factors as

$$\delta_c = \frac{\theta_c}{\theta\delta} \quad - \quad \text{overall} \qquad 7.19$$

$$\lambda_c = \frac{\phi_c}{\phi\delta} \quad - \quad \text{core} \qquad 7.20$$

Using the results of chapter 6 the variation of these overall shape factors for the cases of low and high di/dt are investigated in chapter 8 using a universal correlation parameter.

The thermal time constant of a circuit breaker arc close to current zero should provide useful information to the circuit breaker designer. For commercial circuit breakers it is desirable to have these time constants as small as possible. One such time constant which may be conveniently evaluated is the Mayr time constant. This is derived from the Mayr equation which was reviewed in chapter 2. Lee (1975) describes a method by which the Mayr time constant can be evaluated from a plot of $\frac{1}{G} \cdot \frac{dG}{dt}$ versus V.I where

G is the instantaneous arc conductance. The Mayr equation is

$$\frac{1}{G}\frac{dG}{dt} = \frac{1}{\tau}\left\{ V\frac{I}{No} - 1\right\} \qquad 7.21$$

where,

G is the instantaneous conductance
τ is the Mayr time constant
I is the instantaneous current
V is the instantaneous arc voltage
No is the rate of loss of energy per unit length

The intercepts to the tangent to the characteristic on the $\frac{1}{G}\frac{dG}{dt}$ axis corresponds to the reciprocal of the Mayr time constant, τ, for that instant. Taylor et al (1982) have evaluated this time constant using their measurement of arc current and voltage during the current zero period. It is also possible to estimate the Mayr time constant using values of area and conductivity which can be derived from the arc photographs and temperature profiles of chapter 6.

If an average value of temperature is considered to represent the radial variation in temperature then a corresponding value of conductivity can be allocated to this temperature according to fig. 7.6. Fig. 7.6(a) shows the values of electrical conductivity for a temperature range between 7,000K and 10,000K according to the calculations of various authors. Clearly the conductivity values for a pure copper plasma (Shayler and Fang, 1976) and those corresponding to a pure SF_6 plasma (Frost and

Liebermann, 1971) converge near the lower end of the temperature range, whereas good agreement with the calculations of Kinsinger (unpublished) only occurs in the high temperature range. Clearly if the time constants are to be evaluated for instants close to current zero then it is the lower end of the temperature range that is of interest. Fig. 7.6(b) shows the variation of the electrical conductivity in the range 5,000K to 7,000K according to Shayler and Fang (1976) (pure Cu plasma) and Frost and Liebermann (1971) (pure SF_6 plasma).

Equation 7.21 can be written in terms of the electrical conductivity, σ , and the area, A, as

$$\frac{1}{G} \cdot \frac{dG}{dt} = \frac{1}{\sigma A} \cdot \frac{d}{dt} (\sigma A) = \frac{1}{\sigma A} \left(A \frac{\partial \sigma}{\partial t} + \sigma \frac{\partial A}{\partial t} \right) \qquad 7.22$$

Thus the term $\frac{1}{G} \frac{dG}{dt}$ can be evaluated using the arc photographs and temperature profiles of chapter 6. This method is applied and discussed in chapter 8 for different times before current zero and different $^{di}/_{dt}$ values.

Another time constant which can be evaluated during the current zero period arises from a comparison of the instantaneous stored energy and the total power loss per unit length. It is assumed that the total power loss remains constant during the current zero period,then the ratio of the instantaneous stored energy to the power loss at a given instant with EI (the electrical power input) set to zero represents the decay time to affect complete recovery. It

is unlikely that the power loss remains constant throughout the current zero period, a fact which is bourne out in the energy balance discussion of chapter 8 but such an evaluation does provide the lower limit for the thermal time constant.

Again the results of chapter 6 are used in chapter 8 to evaluate the latter time constant and a comparison is made with the Mayr time constant.

7.5.3 Summary

Equations have been developed which can be used to evaluate the current zero energy conservation and the electrical conductance shape factor of the integral analysis formulations of Cowley (1974) and Chan et al (1976). Two means of identifying the arc thermal time constant during the current zero period have also been described. All the above formulations allow the corresponding arc parameters to be evaluated using the arc photographs and temperature profiles of chapter 6.

7.6 Chapter Summary

The work presented in this chapter has dealt with many of the theoretical aspects of plasma spectroscopy and the formulation of the integral analysis as applied to a real circuit breaker in practice.

Formulae have been developed in the section on plasma spectroscopy which allow the electron temperature and density

to be calculated for a plasma in LTE. Also two criteria developed to test for the existence of LTE were discussed.

In addition to this the concept of optical depth of a plasma was introduced and the optical 'thickness' of the present circuit breaker arc was tested using three independent criteria. In almost every case the plasma was found to be optically thin. This implies that no self absorption of the visible spectral lines occurs which would invalidate the calculations of electron temperature and density.

The method of calculation of the arc temperature profile was described which enables continuous arc temperature profiles to be derived from the radially resolved spectral data of chapter 6.

The basic formulations of the integral analysis (Cowley, 1974 and Chan et al, 1976) have been introduced and used to formulate a dynamic core energy balance for the current zero period. The form of the energy balance is such that the results of chapter 6 can be used to investigate the influences of individual energy transport terms upon the current zero arc column.

The Mayr time constant has been defined in such a way that the results of chapter 6 can be used directly for its evaluation. Another thermal time constant has also been defined which can be evaluated using energy terms already defined in the energy conservation equation.

λ_c Centre Wavelength (nm)	Amn Transition Probability (S^{-1})	Gm Statistical Weight of Upper Energy Level	Em Energy Value of Upper Energy Level (eV)	Emn Energy Difference Between Levels m and n (eV)
521.8	7.5×10^7	6	6.19	2.37
515.3	6.04×10^7	4	6.19	2.40
510.5	0.2×10^7	4	3.82	2.43
578.2	0.17×10^7	2	3.79	2.15
570.0	0.02×10^7	4	3.82	2.18
529.2	1.09×10^7	8	7.74	2.35
465.1	3.8×10^7	8	7.74	2.67

Source : Kock and Richter (1968)

Table 7.2 Atomic Data for the Spectral Lines of Cu I

Centre Wavelength (nm)	Temperature (^{o}K)	Ne (cm^{-3}) =	Half Width at Half Height (nm)		
			10^{16}	10^{17}	10^{18}
521.8	5,000		1.22×10^{-2}	1.22×10^{-1}	9.08×10^{-1}
	10,000		1.33×10^{-2}	1.36×10^{-1}	1.19
	20,000		1.39×10^{-2}	1.44×10^{-1}	1.37

Centre Wavelength (nm)	Temperature (^{o}K)	Ne (cm^{-3}) =	Half Width at Half Height (nm)		
			10^{16}	10^{17}	10^{18}
515.3	5,000		1.19×10^{-2}	1.19×10^{-1}	8.86×10^{-1}
	10,000		1.29×10^{-2}	1.32×10^{-1}	1.16
	20,000		1.36×10^{-2}	1.40×10^{-1}	1.34

Table 7.1 Stark Broadening of Cu I Lines

LIST OF FIGURES

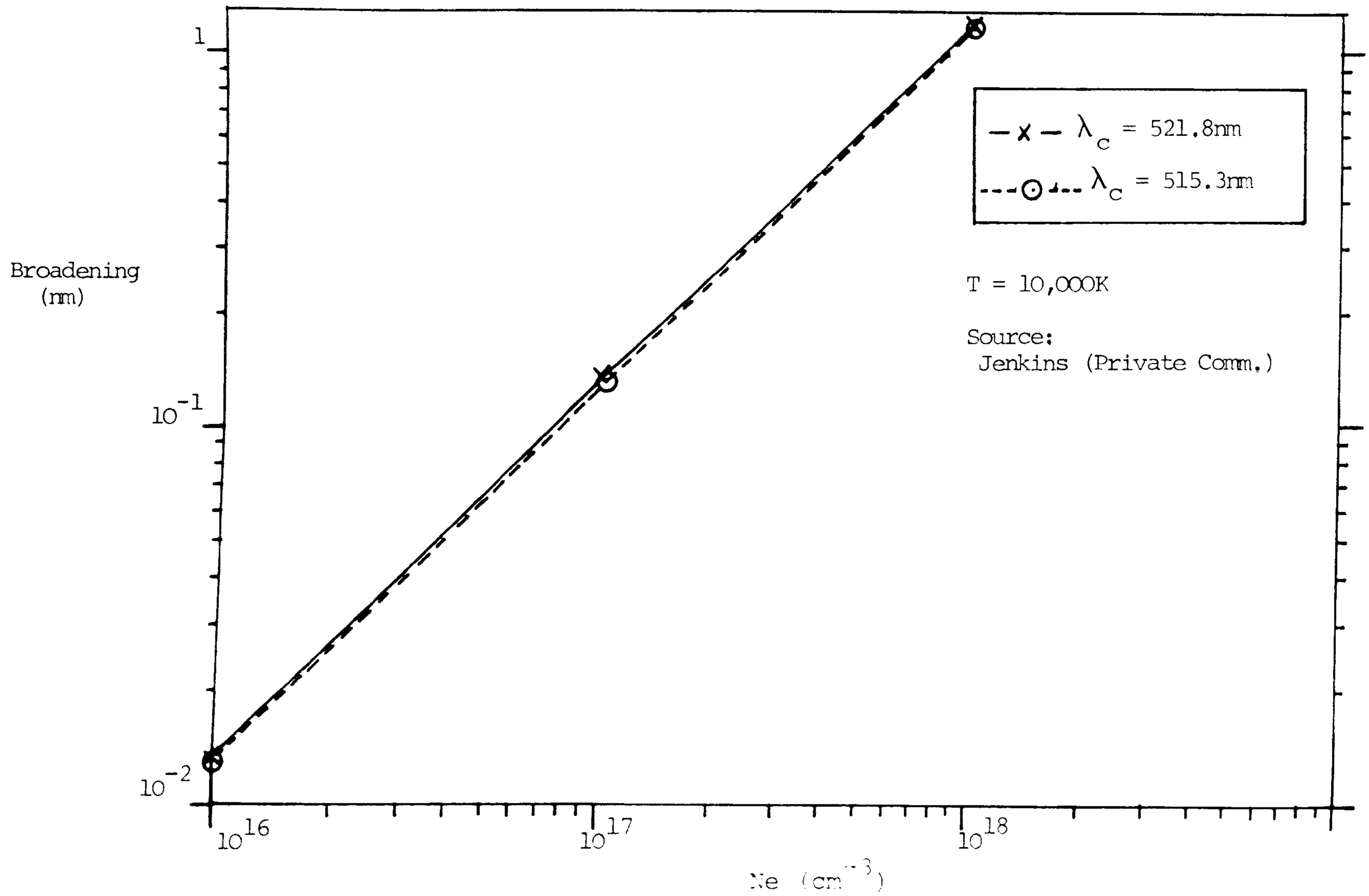

Fig. 7.1 The Stark Broadening of Cu I Lines

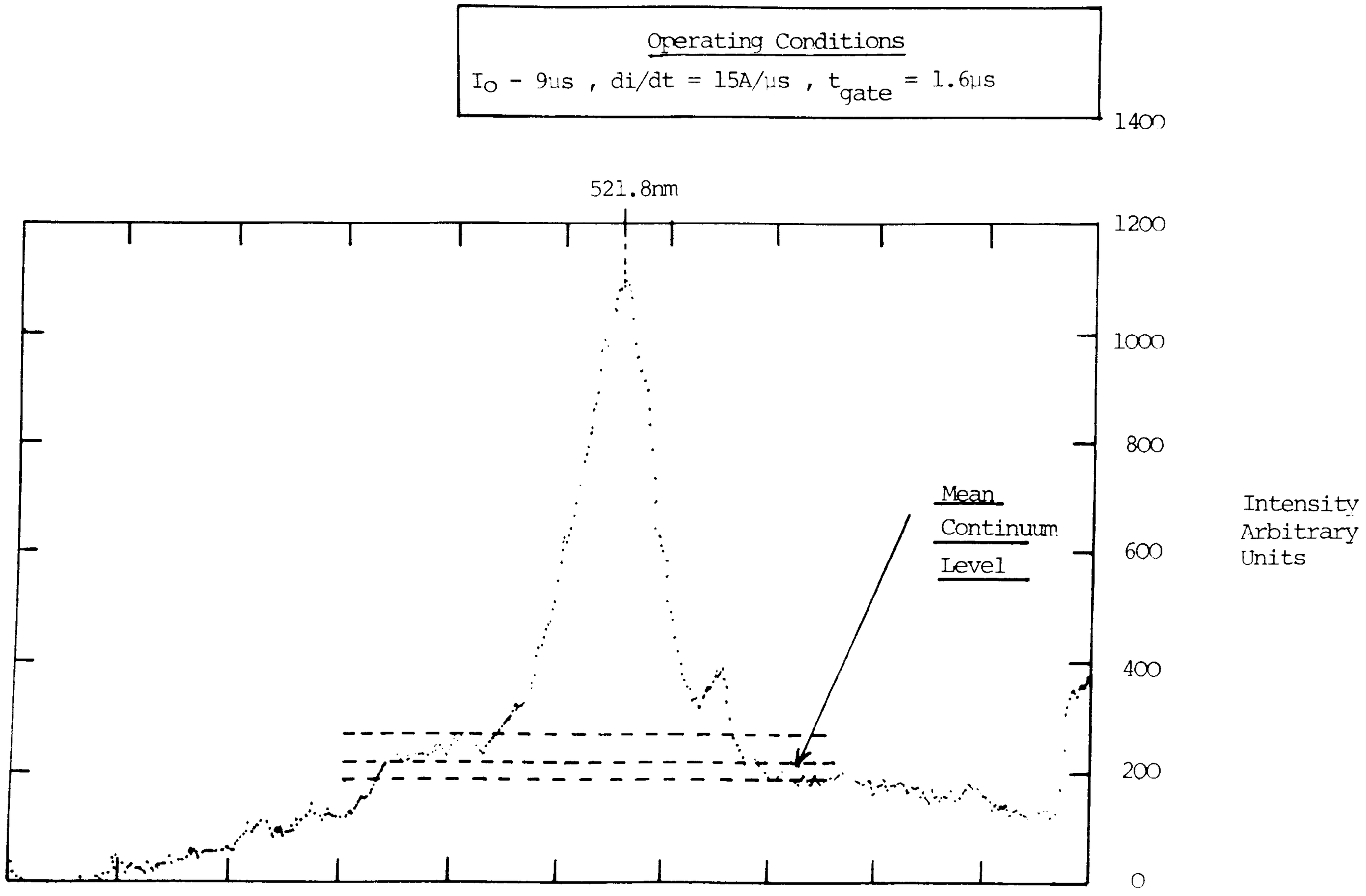

Fig. 7.2(a) Optical Depth of the Plasma by Inspection of the Diagnostic Lines

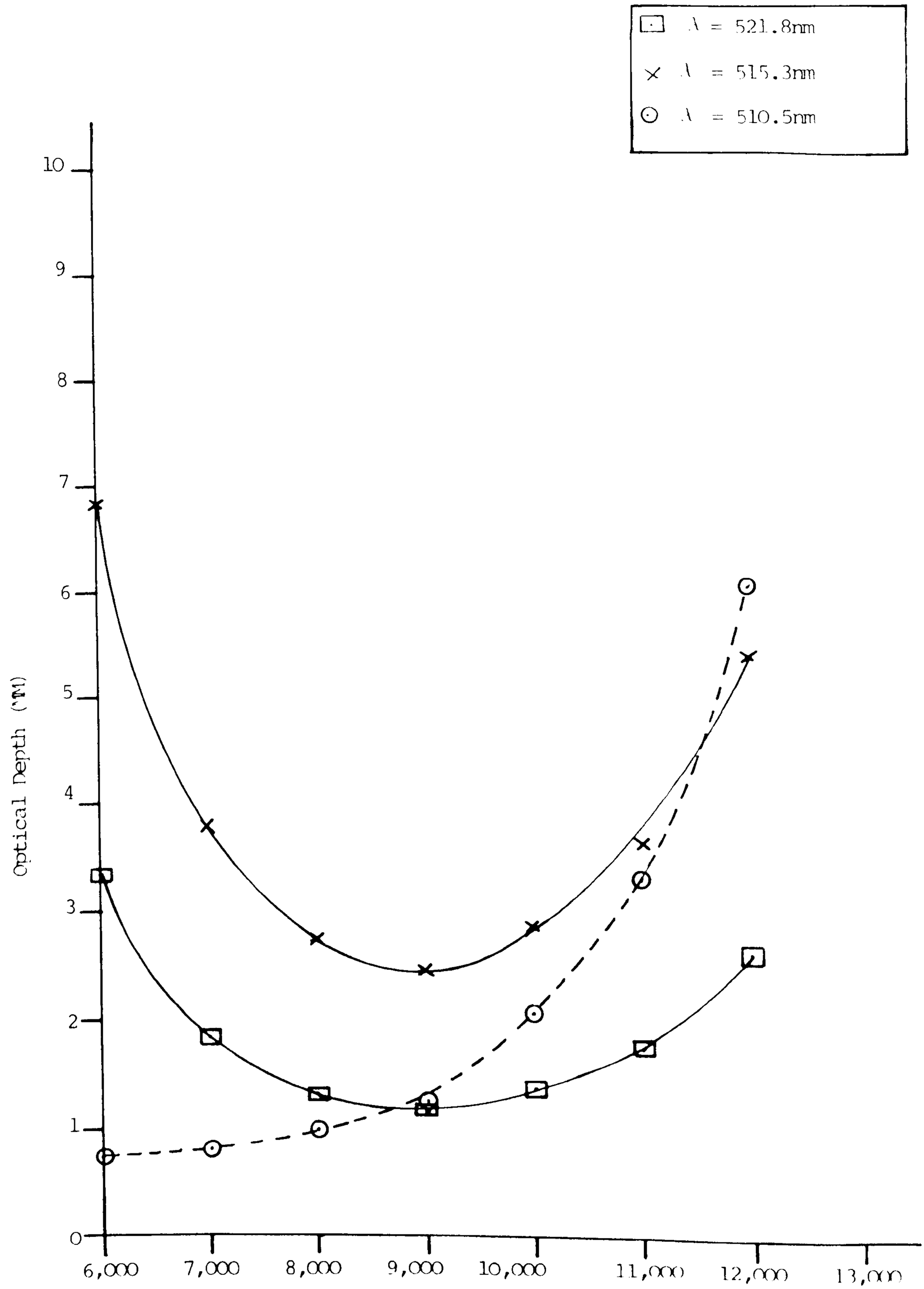

Fig. 7.2(b) Optical Depth of the Plasma by Comparison of the Black Body Limit with Theoretical Line Intensity

7.3(a) Representation of the Cross-section of the Plasma

Fig. 7.3(b) Measured and Abel Inverted Intensity Profiles

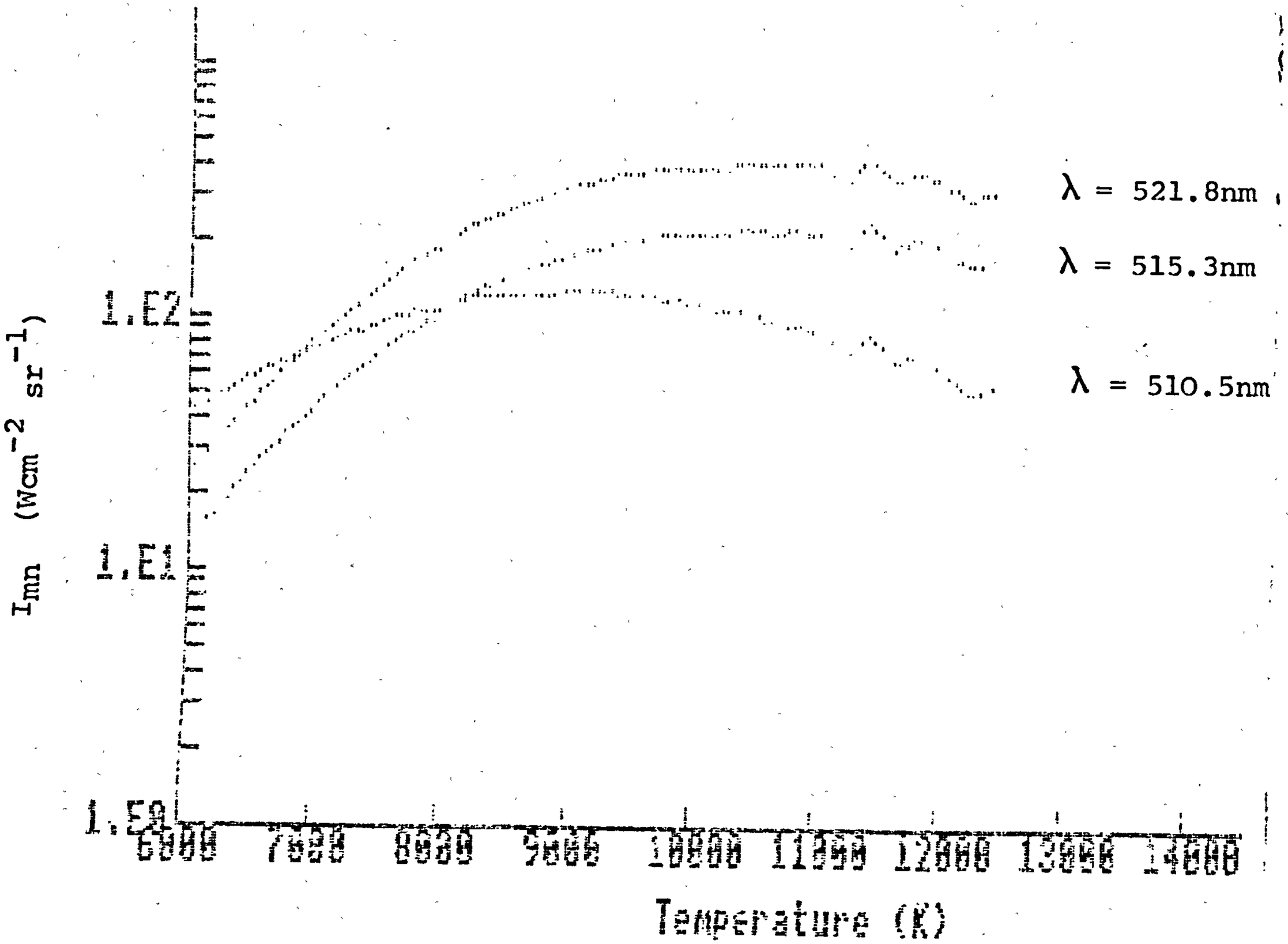

Fig. 7.4 The Theoretical Intensity Variation of the Principal Diagnostic Spectral Lines with Temperature

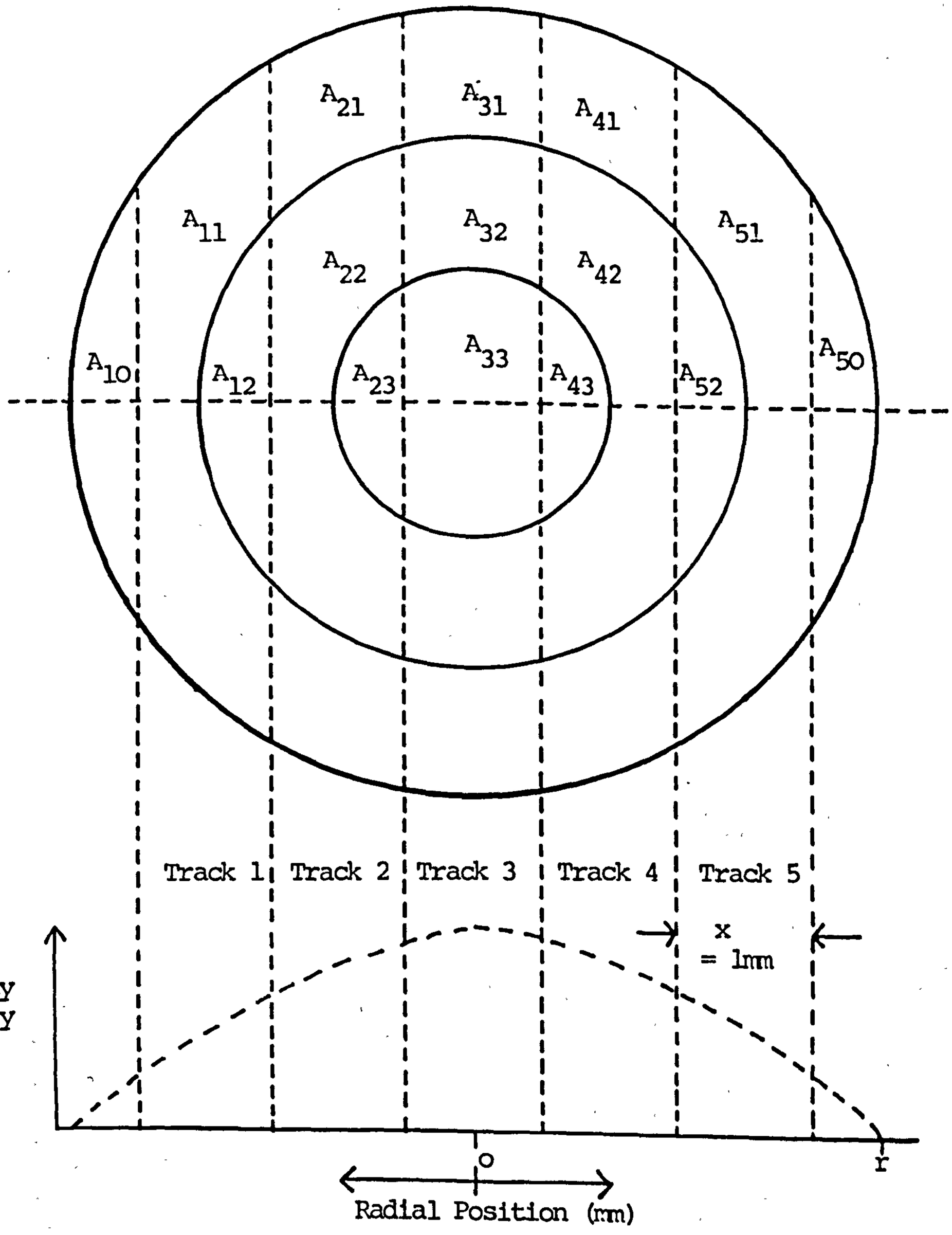

Fig. 7.5 Conversion of the Emissivity Profile into a Radial Intensity Histogram

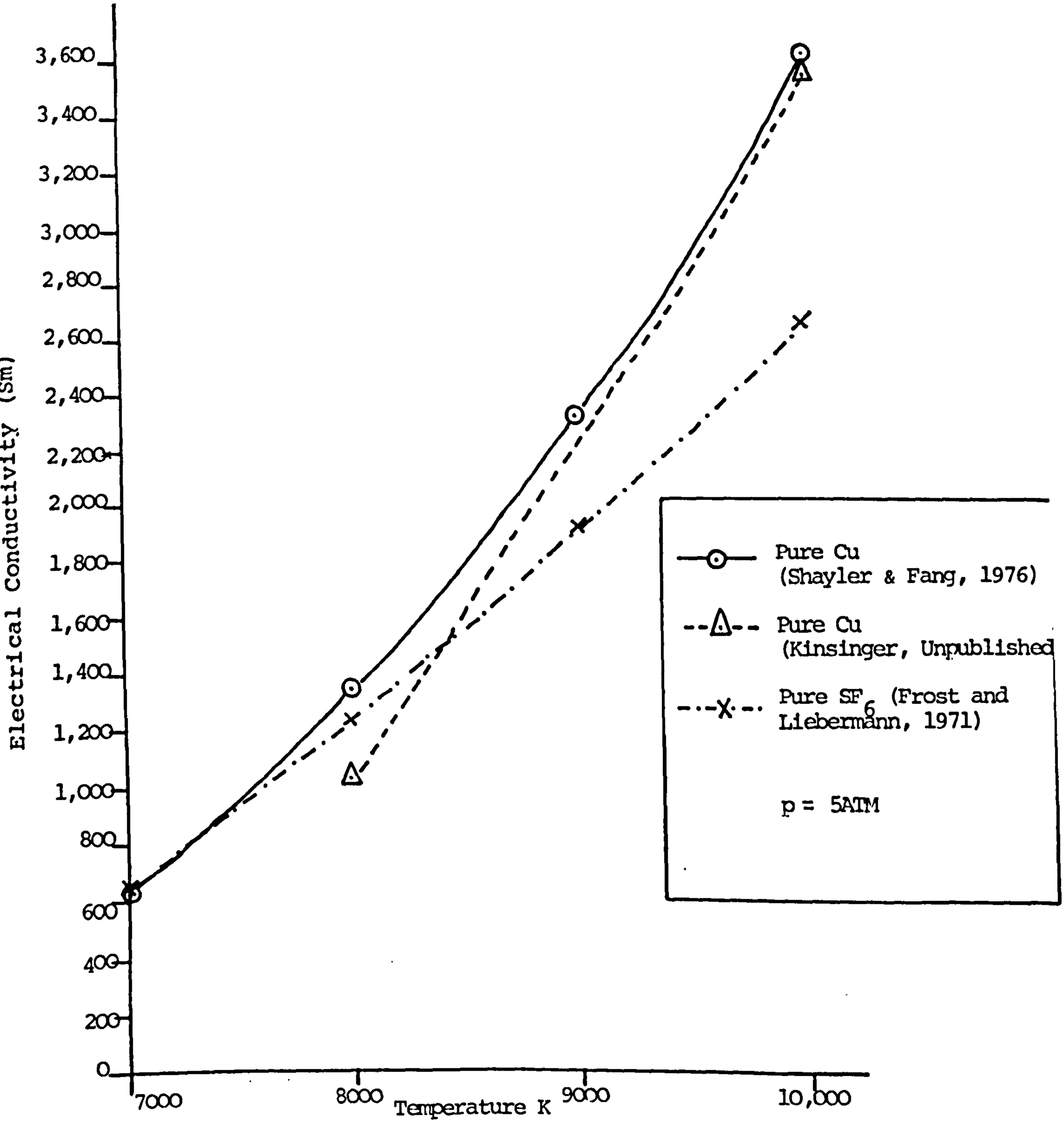

Fig. 7.6 Variation of Electrical Conductivity with Temperature
(a) In the Range 7,000 to 10,000K

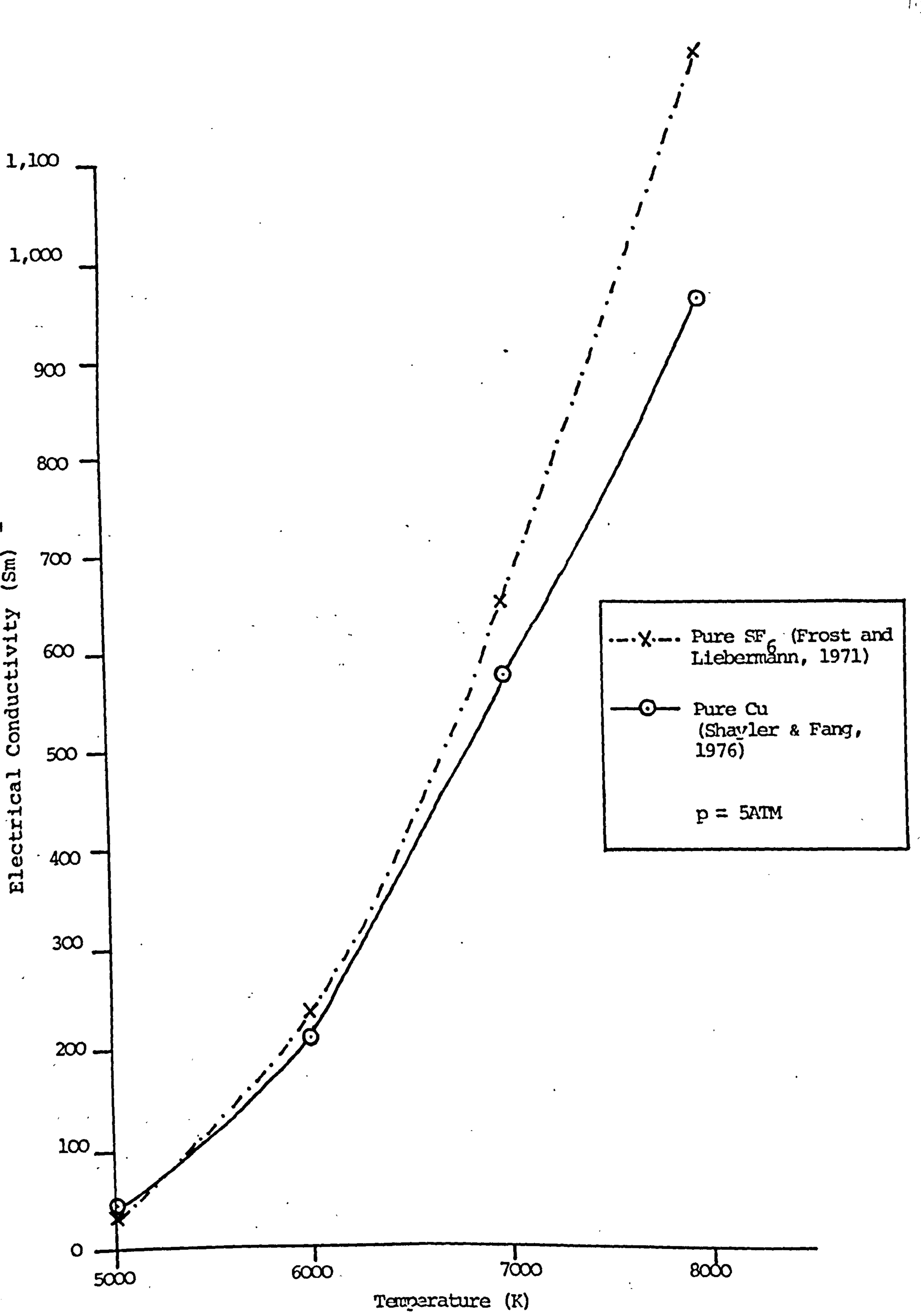

(b) In the Range 5,000 to 8,000K

CHAPTER 8

CURRENT ZERO PHENOMENA AND THEIR INFLUENCE ON ARC COLUMN PROPERTIES AND STRUCTURE

8.1 Introduction

The experimental results presented in chapter 6 fell into two major categories, namely photographic and spectroscopic. It is the aim of this chapter to provide a quantitative insight into the processes governing arc thermal reignition. That aim may only be achieved through careful analysis of the results of chapter 6 in conjunction with the theoretical arc considerations dealt with in chapter 7. Furthermore, in order to gain an overall knowledge of the thermal behaviour of the arc column near current zero, it is necessary to invoke results from both the major categories stated above as well as some theoretical considerations. Therefore in this chapter no attempt is made to identify these categories, the photographic and spectroscopic information of chapter 6 being often used simultaneously. However, it is convenient to divide the thermal arc processes into those occurring before and after the current zero instant so that these two time intervals may be dealt with independently. Subsequently individual descriptions of the processes governing arc extinction are combined in an overall empirical relationship which predicts the performance of a circuit breaker.

8.2 The Arc During the Pre Current Zero Period

8.2.1 The Appearance of the Arc Column

The physical appearance of the photographic image of the arc column during the current zero period gives an important insight into which energy transfer processes may dominate at different axial locations.

It was established in chapter 6 that in the case of both reduced and full power arcing, although the luminous arc diameter exhibited some oscillatory characteristics, no arc column splitting or swirling was evident (particularly upstream of and near the nozzle throat). Arc column splitting probably indicates turbulent flow conditions. The arc photographs of chapter 6 also indicated that the arc column downstream of the nozzle throat was generally more diffuse in nature than the upstream column during the current zero period for both full and reduced power arcing conditions. It is therefore clear that upstream of and in the nozzle throat vicinity the arc appears to be surrounded by laminar flow conditions whereas further downstream turbulent conditions may exist in some cases.

It is of importance that no arc splitting or prominent turbulent effects are in evidence at the localities at which the arc temperature profile is measured so that energy flow calculations may be applied radially and axially without complication and complies with the boundary layer approximations described in chapter 7. Also the continuous nature of the radial arc intensity profile allows the above mentioned

boundary layer formulations to be applied to the dynamic arc equations.

The oscillations observed in the arc diameter are similar to those observed at higher currents (Walmsley et al 1978(iii)) which were due to plasma aerodynamic and magnetic pumping effects. However the current level during the current zero period is too low to produce oscillations of that nature but also the frequency was somewhat less than in the present investigation. Another explanation for this phenomenon is that molten copper is ejected from the electrode and propagates axially through the plasma as a pulsation. These pulsations interact with the surrounding flow to maintain the oscillations. This type of oscillation has also been observed at higher current values (Walmsley et al, 1978(iii)).

In chapter 6 photographic results were presented which recorded with a Cu I line filter (λ_c = 521.8nm) included in the optical system. It was also stated in chapter 6 that such records were representative of a true arc luminous diameter. Careful examination of fig. 6.24(b)(ii) shows that significant radiation (enough to give rise to a spectral peak) was detected at 4 if not 5 of the radial viewing locations. Comparison between the area derived from this case (17.5A/μs) and one photographically measured under similar operating conditions (15A/μs) e.g. fig. 6.14(b) show a close correspondence of photographic luminous area (about 15mm^2 in this case). Therefore the use of a copper line filter record to describe the arc column appearance is justified

provided similar exposure conditions are used. This was the case in this investigation. The importance of justifying this hypothesis is realised in the fact that it was a copper line filter record which provided the experimental evidence for the basis of the Abel inversion calculation of chapter 7 (which in turn allowed the continuous intensity profile at this wavelength to be identified as parabolic).

8.2.2 Behavioural Trends of the Arc on the Approach to Current Zero

Important trends in the current zero arc behaviour have emerged from the photographic and spectroscopic investigations of chapter 6.

Firstly, it is evident from chapter 6 (sections 6.1.2(iv) and 6.1.3(iv) that no apparent effect due to nozzle material exists upon the upstream current zero arc column diameter and luminous intensity in the case of both full and reduced power arcing. This result is of particular interest in the latter case since it seems to suggest that effects due to nozzle material entrainment into the arc column have ceased to exist before the current zero period at that upstream region. The performance data of Taylor et al (1982) suggests that there is a difference in circuit breaker performance between the two nozzle materials. However the same authors have identified this to be an effect solely associated with ablation processes which occur during the peak current period. Indeed the conductance measurement of the same authors show differences at the higher peak current between the two nozzle materials but in each case the subsequent conductance decay

towards current zero are similar. Thus no differences in upstream arc column properties are anticipated beyond the statistical shot to shot variations which the results mentioned above indicate. However, some subtle differences were detected in the arc column further downstream of the nozzle throat (slots 4 and 5). In some cases (fig. 6.12(b), 6.16(b)) some luminous areas were detected when a copper nozzle was used and although much less intense than the upstream luminosities they were not visible in the case of a PTFE nozzle. The source of the downstream luminous areas could be luminous copper particles initially trapped upstream by the existing backflow (Taylor et al, 1982) where they were heated before being released downstream by the relief from nozzle blocking. As stated previously, the regions further downstream of the nozzle throat are occupied by turbulent flow conditions. Thus some particles released in this manner could be caught in the turbulence. Of course, the same applies for PTFE but the spectral radiation produced by PTFE arcing products is several orders of magnitude less intense than copper for temperatures lower than 10,000K. Thus the PTFE particles are not expected to be luminous.

However the appearance of the luminous material downstream is not necessarily accompanied by changes in the arc diameter or luminous intensity in the upstream regions close to current zero. It is shown later in this chapter that changes which occur in the arc column in the upstream regions and in particular near the nozzle throat play a more dominant role in determining arc extinction/reignition.

The oscillations in luminous arc diameter commented on above are superimposed upon more general trends of diameter and luminous intensity decay variations. Two common forms of arc column collapse are evident. Fig. 8.1 shows the arc intensity, area and radially averaged temperature for slots 2 and 3 for 2 different $^{di}/_{dt}$ cases under full power arcing and a selected (high) value of $^{di}/_{dt}$ in the reduced power case (slot 2 area shown only) for comparison. In the low $^{di}/_{dt}$ case (fig. 8.1(i)) the tendency is for a linear area decay with the more gradual decay occurring at slot 3. The intensity collapses at slots 2 and 3 in fig. 8.1 (i) are somewhat deceptive in that some general masking of the light has occurred in this case. The effect has been to prematurely reduce the axis intensity at slot 2 so that as the material moves further downstream, the intensities at slot 3 have similarly been curtailed which would otherwise show a gradual decay towards zero throughout the current zero period. This is reinforced by the fact that a luminous diameter was detected and measured in this case (at slots 2 and 3) but the intensity was so low that a reliable optical density measurement was impossible (on the microphotometer). Further evidence of the gradual diameter decay at slots 2 and 3 at similar $^{di}/_{dt}$ levels is visible in fig. 6.16(a) for both copper and PTFE nozzles.

Also shown on fig. 8.1(i) is the radially averaged temperature decay during the current zero period of an arc subject to similar operating conditions to the one selected for the area and intensity variation. It is seen here that

the radially averaged arc temperature fluctuates about a mean value of about 8,000K up to 3μs before current zero. Temperatures closer to current zero than this instant could not be measured in the conventional manner (comparison of two line intensities, chapter 7) owing to a lack of optical intensity from at least one of the spectral lines. Clearly, an alternative means of temperature calculation would be necessary to evaluate the temperature during this critical period. An alternative method was described in Appendix 1 whereby upper and lower limits of radially averaged temperature were derived. This hypothesis was applied to two real cases of arcs close to current zero (1.9 and 1.6μs before) whose spectra are shown on fig. 8.2. The temperatures derived from this sample spectrum of fig. A1.1 of Appendix 1 was about 6,000K at the arc column edge. This figure of 6,000K represents the minimum arc temperature at which both the 510.5nm and the 515.3nm Cu I spectral lines can be simultaneously detected. If a single line at 510.5nm is detected with the 515.3nm absent, then according to the temperature/emission characteristics of these lines (fig. 7.4) the temperature in such cases must be lower than 6,000K. This is the case in fig. 8.2(i) and (ii), therefore 6,000K represents the maximum temperature in this case. The minimum temperature can be determined from a comparison of the intensity of 510.5nm emission with the corresponding spectral line of fig. A1.1. This drop in intensity corresponds to a decrease in temperature of about 500K. Thus the lower limit of the radially averaged temperature of the arc where the single 510.5nm line is detected, lies at about

5,500K. This is shown on fig. 8.1.

The temperature results of fig. 8.1 indicate a rapid collapse of arc temperatures during the final two or three microseconds prior to current zero for both $\frac{di}{dt}$ values shown. However differences exist in the temperature trends for the two $\frac{di}{dt}$ values:

(i) In the low $\frac{di}{dt}$ case temperatures fall from a quasi steady value of about 8,000K to a value between 5,500K and 6,000K within the final 3μs before current zero.

(ii) In the high $\frac{di}{dt}$ case the temperature decay is from a somewhat higher level (about 9,000K) to a value of 8,000K in the final 2μs before current zero.

The temperature profiles measured during the current zero period are shown in chapter 6 (fig. 6.24) for three cases of current decay rates. In addition to the observations already made in chapter 6 the following comments are noteworthy:

(i) The temperature at the profile centre increases with increasing $\frac{di}{dt}$ value.

(ii) The shape of the temperature profile above the 6,000K isotherm is continuous i.e. there is no evidence of dips for example. However the profile may not necessarily be symmetric about the centre (i.e. the line defining the temperature maximum.

(iii) The radial temperature gradient at 6,000K is particularly steep. For instance in the case of fig. 6.24(iii) it has a value of 17,800K/mm. However, owing to the assymetry of the profile this may not necessarily be equal on opposite sides of the arc column.

The above observations regarding the radially averaged temperatures and the temperature profiles both have important implications on the calculation of arc energy transfer terms

during the current zero period as discussed in greater detail later in this chapter.

8.2.3 Behavioural Trends of the Arc Close to Current Zero A. A Function of $^{di}/_{dt}$.

Trends of the current zero radially averaged temperature (fig. 6.22) at slot 2, the luminous arc areas at all slots (fig. 6.17) and the photographic axis intensity at slots 2 and 3 coupled with the total radiation loss at slot 3 (fig. 6.18) with changing $^{di}/_{dt}$ were all established in chapter 6. These trends are summarised on fig. 8.3.

The results of fig. 8.3(i) show that the arc luminous areas at the current zero instant after full power arcing follow a different trend to the ones following reduced power arcing. In the case of the slot 3 areas (just downstream of the nozzle throat) there exists no difference in their magnitudes within the experimental scatter (40% in the case of areas) when the current decay rate is less than 20A/μs. However at higher $^{di}/_{dt}$ values this is not the case and the current zero areas at this axial station are greater in the case of the full power arcs than the reduced power arcs. Thus the rate of increase of current zero area just downstream of the nozzle throat with $^{di}/_{dt}$ is greater in the case of full power arcing than reduced power arcing. The trend at slot 2 (just upstream of the nozzle throat) is similar to that of slot 3 for both full power arcing cases, however the absolute magnitudes of the slot 2 areas are generally higher throughout the $^{di}/_{dt}$ range in both cases.

It is clear from fig. 8.3(i) that at both the axial stations investigated the areas for the full power cases increase steadily with increasing $^{di}/_{dt}$ and that no rapid increases in areas occur.

The intensity and total radiation results of fig. 8.3 (iii) show a quite different trend. The total radiation and luminous intensity results at slot 3 were captured simultaneously in the case of both full and reduced power arcs and therefore offer a means by which the two parameters can be directly compared. The trends for both quantities in the reduced power case show both parameters to rise slowly up to a value of about 25A/μs above which a more rapid increase occurs. In the case of the full power arcs the intensity and radiation trends follow a similar pattern. However the $^{di}/_{dt}$ value at which the more rapid increase occurs is about 18 to 20A/μs in this case. Also the magnitude of the radiation losses and luminous intensities are generally higher for the full power arcs. The increase in total radiation loss for the high $^{di}/_{dt}$ case (22A/μs) between reduced and full power cases is more than an order of magnitude.

Also shown on fig. 8.3(iii) is the luminous intensity at the current zero instant measured at slot 2. In the case of the low power arcs the slot 2 intensities are generally higher on the arc axis than slot 3 only by a nominal amount (which is more clearly indicated in fig. 6.6(b)) However in the case of full power the luminous intensity is

generally higher at slot 2 than slot 3 throughout the di/dt range, being about double the value at a di/dt of 22A/μs. For di/dt values higher than 22A/μs the relative difference between the slot 2 and 3 intensities (the ratio of $I_{slot\ 2}$ to $I_{slot\ 3}$) decreases. This was a trend also reflected in the timewise variation of the respective intensities first noted in section 6.13(ii) (in chapter 6). In this case the intensity variation during the current zero period at slot 3 approached that of slot 2 as the di/dt value increased. These trends are strongly indicative of an increasing energy loss by radiation which grows from upstream to further downstream as the di/dt value is increased.

Fig. 8.3(ii) represents the radially averaged temperature at slot 2 captured within the final 1.6μs before current zero as a function of di/dt. The increase in temperature over the di/dt range in question is less vigorous than the intensity changes of fig. 8.3 (iii) over the di/dt range in question. However there is a greater increase in the radially averaged temperature above a di/dt value of 18 to 20A/μs. Such changes in temperature can give rise to significant changes in arc column properties. For instance, a change between 6,000K and 8,000K can cause an increase in the electrical conductivity of an SF_6/Cu arc by a factor 5 (fig. 7.4). Furthermore such increases in temperature can cause substantial increases in spectral line emission intensities of the predominant Cu I lines (fig. 7.4).

The arc area, peak intensity and total radiation results for the current zero arc column all show significant differences between full and reduced power in the range $^{di}/_{dt}$ >20A/μs. These results taken together suggest the important result that the different total radiation emission between full and reduced arcing conditions is mainly due to differences in the emission intensity rather than to geometry changes as reflected by arc diameter differences. Consequently the implication is that the current zero arc column properties and radial structure following full power arcing differ from those following reduced power arcing at high values of $^{di}/_{dt}$.

The discussion thus far has been qualitative in nature. In order to ascertain the effects of influences of the operating conditions on the circuit breaker performance as well as gaining a greater knowledge of the fundamental processes governing arc thermal behaviour a more quantitative approach is of course necessary. The following section is therefore devoted to a quantitative study of the arc column decay processes during the current zero period.

8.2.4 Quantitative Implications of Results

(i) Local Thermodynamic Equilibrium (LTE) in the Current Zero Arc Column

In chapter 7 two criteria were established which allowed the existence (or not) of LTE to be confirmed in the current zero arc column. The results of chapter 6 were used to evaluate both of these criteria in turn, the implications

of which are discussed in this section.

Firstly, equation 7.6 is a statement of McWhirter's criterion:

$$Ne > 1.6 \times 10^{12} (T)^{\frac{1}{2}} x^3 \qquad 8.1(a)$$

where all the symbols were defined in chapter 7 (and x = X(p,q))

Fig. 8.4 shows the variation of the product on the right hand side of equation 8.1(a) for the different arcing conditions investigated in this thesis. Also shown in fig. 8.4 are the values of electron densities obtained experimentally from Stark broadening calculations based upon the spectroscopic data of chapter 6. The temperature value (T) required for the right hand side of equation 8.1(a) was taken as the experimentally measured radially averaged arc temperature. Using this data it is clear that the McWhirter criterion for the existence of LTE is satisfied by more than an order of magnitude. Also shown in fig. 8.4 are values based on a similar calculation but with T equal to 6,000K. This calculation was made to test the existence of LTE at the 6,000K radial isotherm. In each of the above calculations the value of x for a Cu I line is taken as $2.73_e V$.

The second criterion which was discussed in chapter 7 was Griem's criterion which was stated as follows:

$$Ne > 9 \times 10^{17} \left(\frac{E_2}{X_H}\right)^3 \left(\frac{KT}{X_H}\right)^{\frac{1}{2}} \qquad 8.1(b)$$

where all the symbols have been defined in chapter 7 and X_H and E_2 take the values 7.72eV and 3.82eV respectively for Cu I.

A similar calculation to the one for the McWhirter criterion was made for each $^{di}/_{dt}$ case and the results are shown on fig. 8.4. These results show that the Griem criterion is a more severe test of LTE existence. Despite this the same results also show that this criterion is also comfortably satisfied (in the worst case by a factor 7). Also shown on fig. 8.4 is the calculation according to Griem's criterion for the 6,000K isotherm. This also shows that LTE also exists for this temperature.

Thus the two criteria for testing LTE existence derived in chapter 7 have been evaluated using the experimental data of chapter 6. Comparison with measured values of electron density (also from chapter 6) shows that LTE exists in the circuit breaker arc throughout the current zero period over the whole $^{di}/_{dt}$ range investigated. Furthermore a comparison of the same formulae using a value of temperature of 6,000K with the measured electron densities shows that LTE exists within the confines of the 6,000K isotherm i.e. the conducting radius. However the degree to which LTE is satisfied may not be as high in the latter case as is initially apparent. This is because the above values of Ne (measured) are all radially averaged and to make a completely rigorous test the local value of Ne should be considered. However although it was not possible to measure the radial electron density profile

in this case it is unlikely that Ne should be an order of magnitude less at the 6,000K isotherm than the radially averaged value. Thus it is therefore likely that LTE does indeed exist at the 6,000K isotherm radius.

(ii) Pressure Balance in the Current Zero Arc Column

In many arc models including the integral analysis or boundary layer models of Cowley (1974) and Chan et al (1976) radial pressure balance has been assumed i.e. $\delta P/\delta r = 0$.

The results of this investigation provide a means by which this assumption can be tested. If the plasma composition during the current zero period is assumed to be 90% SF_6 : 10% Cu as was assumed by Smith et al (1978) then the value of Ne measured from Stark broadening calculations (Jenkins private comm.) can be compared with theoretical plasma composition data of Kinsinger (unpublished, shown in appendix 5). For a pressure of 5 atm, a temperature of 10,000K and 90% SF_6 : 10% Cu mixture the value of electron density (Kinsinger) is 2.26×10^{17} cm^{-3}. The corresponding value for a pressure of 4 atm would be about 2×10^{17} cm^{-3}. The values of Ne derived from Stark broadening calculations are shown in fig. 8.4. These values lie between 2.3×10^{17} cm^{-3} and 3.0×10^{17} cm^{-3} for most of the current zero period and are subject to an overall error of at least 20%. Thus the latter Ne values show at least reasonably good agreement with the theoretical values for an axis temperature of about 10,000K. Therefore a pressure of about 4atm would appear to exist in the locality of the arc axis at slot 2. When

compared with the value of 4atm measured in the cold flow and at the same axial location by Taylor (1982) good agreement exists between the two.

Thus radial pressure balance does appear to exist in the case of the current zero circuit breaker arc column.

(iii) Experimental Evaluation of the Thermal Time Constants

The Mayr time constant (chapter 7) at a given instant prior to current zero is the intercept of the $\frac{1}{g}\frac{dg}{dt}$: electrical input power characteristic on the $\frac{1}{g}\frac{dg}{dt}$ axis (e.g. Taylor et al, 1982).

In order to determine the term $\frac{1}{g}\frac{dg}{dt}$ it was necessary to define the conductance g from the measured values of the electrical conductivity (σ) and the electrical column cross-section (A) i.e. assuming a radially averaged

$$\frac{1}{g}\frac{dg}{dt} = \frac{1}{(\sigma A)}\frac{d}{dt}(\sigma A) = \frac{1}{\sigma A}\left(A\frac{\partial \sigma}{\partial t} + \sigma\frac{\partial A}{\partial t}\right) \qquad 8.2$$

The following assumptions are required:

(i) A corresponds to the photographic luminous areas measured in chapter 6 and shown in fig. 8.1 for different di/dt values.

(ii) The radial conductance profile integral over the conducting arc radius can be replaced by a single radially averaged value. In this case the radially averaged conductance value was assumed to correspond to the radially averaged arc temperature which was also measured in chapter 6 and is shown for different di/dt values in fig. 8.1.

(iii) The radial temperature profile (hence conductivity profile) does not alter drastically during the current zero period. This has been shown to be the case on fig. 6.25 of chapter 6.

Thus equation 8.2 may be evaluated using electrical conductivity values for SF_6 (Frost and Liebermann, 1971) and the experimental results of chapter 6 which are also presented in fig. 8.1. The variation of the quantity $\frac{1}{(\sigma A)} \frac{d}{dt} (\sigma A)$ versus electrical power input is shown in fig. 8.5(a) for two cases of $^{di}/_{dt}$. The corresponding calculations of Taylor et al (1982) who obtained the conductance directly from the voltage and current are also shown in fig. 8.5(a) for comparison.

The results of fig. 8.5(a) were thus used in the determination of the arc time constants as indicated above. The time constants are shown on fig. 8.5(b) and (c) for times close to current zero. The time constants derived in a similar way by Taylor et al (1982) and Briggs (1982) are also shown on fig. 8.5(a).

Close agreement between the present work and these other authors is clearly evident for times within 1μs of current zero for both $^{di}/_{dt}$ cases. The agreement at 2μs before current zero between the present work (low $^{di}/_{dt}$) and Taylor et al (1982) is poorer but this can be accounted for by experimental errors in both cases. These errors can be as much as 40% in the present calculations and a similar figure applies to the work of Taylor et al (1982) for times so close to current zero.

The arc time constants evaluated in the present work show a dependence upon $^{di}/_{dt}$ which is greater for the higher $^{di}/_{dt}$ case. This was not the case in the work of Taylor et al

(1982) but it was so in the work of Briggs (1982). The values of the time constant for different $^{di}/_{dt}$ values do however converge as current zero is approached. However it is anticipated that some difference in the current zero values of these constants should exist since the thermal performances of the two arc types are different.

In conclusion it may be stated that:

(a) The time constants calculated from the present results are in agreement with those of other workers for the critical period 2μs before current zero.

(b) An increase in the thermal arc time constant is co-incident with an increase with $^{di}/_{dt}$.

(c) This is also accompanied by a deterioration of the same circuit breaker thermal performance which was measured by Taylor et al (1982).

Although the analysis this far has been based upon the radially integrated arc properties, a knowledge of the detailed temperature profiles (chapter 6) allows the shape factors of the integral analysis (chapter 7) to be calculated.

(iv) <u>The Electrical Conductance Shape Factor</u>

In chapter 7 of this thesis the concept of boundary layer integrals associated with different annular arc regions were introduced. These integrals have units of area and were thus called characteristic areas. One of these integrals is the conductance area, θc. According to the integral analysis of Cowley (1974) the conductance area is represented by:

$$\theta c = 2\pi \int_0^\infty \frac{\sigma(r)}{\sigma *} \, r dr \qquad 8.3$$

where $\sigma(r)$ = the local radial electrical conductivity (s/m)

r = radial position (m)

σ^* = the characteristic electrical conductivity (s/m)

In this thesis the characteristic value of electrical conductivity was chosen to be that value corresponding to a temperature of 7,000K in SF_6 which is equal to 650s/m at 4atm pressure. This value was chosen on the basis of a comparison with other authors who used a similar characteristic value in nitrogen. Walmsley et al (1978(ii)) gave a value of σ^* = 366s/m for nitrogen. For their working pressure this corresponds to a temperature of about 5,500K (Shayler and Fang, 1976). The conducting radius for nitrogen is defined according to many authors working on both theoretical and empirical arc models (e.g. Topham, 1971) as being at a radius defined by an isotherm whose value usually lies between 4,000K and 5,000K. The value of 5,500K deduced from Walmsley et al's (1978(ii)) work therefore lies above the normal temperature of the conducting boundary. Therefore if a similar hypothesis is applied to the present investigation then a temperature value of 7,000K (the 6,000K isotherm represents the conducting radius) seems reasonable. Shimmin (private comm.) has also confirmed the present value of to be a reasonable one for SF_6.

All the transport properties of SF_6 used in this chapter are summarised in table 8.1.

The conductance area θc may be evaluated using the

measured temperature profiles (fig. 6.25) and equation 8.3. These calculations have been made for $^{di}/_{dt}$ values of 14.2A/μs and 21A/μs at instants of 10μs and 7.9μs before current zero in the case of full power arcing. For the purpose of these calculations the core boundary (Rc) was defined as the 6,000K isotherm. Using the above data the following values of θc were obtained

(i) for $^{di}/_{dt}$ = 14.2A/μs and at 10μs before current zero
θc = 26.3mm^2

(ii) for $^{di}/_{dt}$ = 21A/μs and at 7.6μs before current zero
θc = 5.85mm^2

The two values carry only limited significance unless referred to another integral to form a shape factor. The area chosen for such normalising purposes is usually the thermal area which then yields the primary shape factor δ_c of Chan et al (1974), where:

$$\delta_c = \frac{\theta c}{\theta \delta} \qquad 8.4$$

and
$$\Theta\delta = \int_0^\infty \left(1 - \frac{\rho(r)}{\rho_\infty}\right) 2\pi r dr \qquad 8.5$$

$\rho(r)$ = local gas density

ρ_∞ = cold flow density

$\theta\delta$ = thermal area

To a first approximation the thermal area may be equated to the area which would be obtained from a shadowgraph measurement θ_s. Unfortunately little experimental data for this area exists for SF_6 arcs during the current zero period.

Some limited theoretical data for temperature profiles of arcs down to under 1,000K is given by Mitchell et al, 1985. However, the operating conditions are somewhat different to the ones used in the present investigation.

Owing to this lack of available data it is only possible to make an approximate estimate of the overall conductance shape factor. An approximate estimate of the lower limit to the shadow area may be made from the observation (fig. 6.15(b)) that the luminous column had wings at each extremity which extended to radii of about 6 or 7 mm. This was attributed to weakly emitting hot gas or scattering of the arc light into the optical path by particles present in these regions. In the analysis of the arc photographs to determine the conducting area this annular region was discarded.

However, its presence alone suggests that the local gas temperature is sufficient for it to form at least a part of the thermal area. The temperature in such a region would be typically less than 5,000K causing a very weak emission over the whole spectrum. Thus the radius of such a region forms the lower limit for a thermal area.

Work published by Graf et al (1984) concerning interferometric methods to determine the temperature profiles at the extremities of SF_6 puffer arcs for different arcing currents indicates that the radial temperature profile is steep sided from ambient up to at least 1,500K. It is possible that because of this steep gradient the weakly

luminous region may also correspond approximately to the shadow area for the present investigations.

Thus the thermal area may be estimated as

$$\theta_s = \pi(6.5)^2 = 133mm^2 \qquad 8.6$$

giving with equation 8.4:

$$\delta_c = \frac{26.3}{133} = \underline{0.198} \qquad 8.7$$

for $^{di}/_{dt}$ = 14.2A/μs, and

$$\delta_c = \frac{5.85}{133} = \underline{0.04} \qquad 8.8$$

for $^{di}/_{dt}$ = 21A/μs

These values of δ_c may be correlated to the results of other authors with different operating conditions through a universal correlation parameter. Such a parameter is the Nusselt number which represents the non-dimensional heat loss by conduction across the arc core boundary. Calculation of this parameter requires a knowledge of the temperature gradient at the core boundary which the temperature profiles of fig. 6.25 provide. The Nusselt number is defined as (Walmsley, 1978(ii))

$$Nu = \frac{Cp^*}{K^*_{h^*}} \cdot \frac{Kc}{Cpc} \cdot Rc \left(\frac{dh}{dr}\right)_{r=Rc} \qquad 8.9$$

where

Cp^* = specific heat capacity (characteristic value)

K^* = thermal conductivity (characteristic value)

h^* = specific enthalpy (characteristic value)

K_C = thermal conductivity (at core edge)

Cpc = specific heat capacity (at core edge)

R_C = radius of core edge

All the above values are given in table 8.1. The Nusselt number was then computed using the values of table 8.1 and $^{dh}/dr\ r=R_C$ obtained from the temperature profiles of fig. 6.25 for $^{di}/dt$ values of 14.2A/μs and 21A/μs. The values obtained were:

$$Nu/\frac{di}{dt} = 14.2A/\mu s = 0.55$$

$$Nu/\frac{di}{dt} = 21A/\mu s = 1.72$$

The values of δ_C corresponding to these values of Nu are shown in fig. 8.6 and compared with results for other operating conditions.

The low $^{di}/dt$ result clearly correlates well with previously reported results but not so the higher $^{di}/dt$ results. In the case of the high $^{di}/dt$ the radial temperature profile and thus the electrical conductivity profile was narrower with a higher axial value than the low $^{di}/dt$ case.

To examine the credibility of this difference between low and high $^{di}/dt$ results further a comparison may be made for the core (λ_C) rather than overall (δ_C) shape factors. The core shape factors are determined as ratios involving

integration not to infinity but rather to the core boundary (Chan et al, 1976).

Thus the core thermal area is defined as

$$\phi_s = \int_0^{R_C} \left(1-\frac{\rho}{\rho_C}\right) 2\pi r dr \qquad 8.11$$

which is analogous to equation 8.5.

Walmsley et al (1978(ii)) also defined the equivalent shadow area referred to the core as

$$\phi_s = \int_0^{R_C} 2\pi r dr = \pi R_C^2 \qquad 8.12$$

Thus by restricting the integration to the core both ϕ_C (equivalent to θ_C) and ϕ_s may be determined more accurately from the present results. Also by making the Cowley (1974) approximation that ϕ_s and ϕ_s are equivalent the conductance shape factor referred to the core boundary is then:

$$\lambda_C = \frac{\phi_C}{\phi_s} = \frac{\theta_C}{\pi R_C^2} \qquad 8.13$$

Equation 8.13 may be evaluated for both low and high di/dt conditions giving for the low di/dt case (14.2A/μs)

$$\lambda_C = \frac{26.3}{\pi(4.35/2)^2} = 1.77, \quad Nu = 0.55$$

and for the high di/dt case (21A/μs)

$$\lambda_C = \frac{5.85}{\pi(1.8/2)^2} = 2.30, \quad Nu = 1.72$$

Fig. 8.7 shows these values of λ_c plotted against the Nusselt number along with other values of λ_c obtained from different arcing conditions (Walmsley and Jones, 1978(ii)). Again a good correlation exists in the low di/dt case but not so in the high di/dt case. However the agreement is within the uncertainty of the previously determined values.

(v) The Current Zero Energy Balance

The dynamic core energy balance of an axially blown arc during the current zero period may be written:

$$\begin{array}{l}\text{Electrical Power Input} = \text{Losses Due to Thermal Convection From Core} - \text{Losses Due to Radial Heat Conduction From Core} + \text{Losses Due to Radiation From Core} \\ + \text{Power Dissipated by Thermally Stored Energy Changes in the Arc Core}\end{array} \qquad 8.14$$

In equation 8.14 it is assumed that the following energy transfer terms are negligible and can therefore be ignored:

(a) turbulence (b) axial heat conduction

Both of these energy transport terms are eliminated by the Boundary layer approximation (chapter 7) of the integral analysis formulations.

In this section the terms in equation 8.14 are individually for the current zero period using the experimental

data of chapter 6 and their relative significance determined. Each term will be evaluated for the instants of 10μs and 7.9μs before current zero for the $^{di}/_{dt}$ values of 14.2A/μs and 21A/μs respectively. In these two cases detailed temperature profiles (Fig. 6.25) have already been measured.

The Electrical Power Input

$$Q_E = E\,i = \frac{Varc}{\alpha_z} \qquad 8.15$$

where

i = instantaneous current (A)

E = overall arc electric field strength (V/m)

Varc = instantaneous arc voltage (volts)

α_z = overall gap length = 100mm

In this case the value of E is taken as the arc voltage divided by the overall gap length. This is representative of an average value of E for the whole arc column.

For $(^{di}/_{dt})$ = 14.2A/μs and t = -10μs

$$Q_E = \frac{800}{0.1}\,(142) = \underline{1.14\text{x}10^6\ \text{W/m}}$$

For $(^{di}/_{dt})$ = 21A/μs and t = -7.9μs

$$Q_E = \frac{780}{0.1}\,(165.9) = \underline{1.29\text{x}10^6\ \text{W/m}}$$

The Change in Thermal Energy Stored in the Arc Column (Core)

The rate of dissipation of stored energy in the core is defined as

$$Q_s = \frac{d}{dt} \int_0^{r_{arc}} \rho(r)\, h(r) \cdot 2\pi r dr \qquad 8.16$$

where

$\rho(r)$ = local radial value of gas density

$h(r)$ = local radial value of enthalpy

r = radial position

With a knowledge of the radial temperature profile (chapter 6) the integral in equation 8.16 can be evaluated for both $^{di}/_{dt}$ values in question, for the respective times before current zero.

To evaluate the time derivative term in equation 8.16 a further assumption must be made. This is that the shape of the temperature profile of the luminous arc does not change drastically about the instant in question and that only the peak temperature and core radius may change. This assumption is justified to a large extent by the fact that the core shape factors discussed in the previous section only changed from 1.77 to 2.30 with a $^{di}/_{dt}$ variation between 14.2A/μs and 21A/μs. Thus a knowledge of a single temperature profile coupled with a timewise variation of arc temperature and radius would enable the time derivative to be evaluated. The latter two quantities can be evaluated

from the temperature and area variations of fig. 8.1.

For $^{di}/_{dt}$ = 14.2A/μs and t = -10μs.

The values of ρ and h for different temperatures at a pressure of 4atm were obtained from Frost and Liebermann (1971) and the product $\rho(r)$ x h(r) x r was computed for the radial temperature profile corresponding to this case (fig. 6.25(i)).

Fig. 8.1 shows that up to 3μs before current zero little or no temperature change occurs. Thus the arc area is the only remaining variable which can effect the integral in equation 8.16 up to 3μs before current zero. Therefore with a constant radially averaged temperature the $\rho(r)$ h(r) radial profile has at least a nearly constant maximum value and a radius which changes with time. The mathematical meaning of this is that the radius of integration is altered by the change in arc radius up to the 3μs instant. In this way the energy storage term was evaluated by performing two integrals at times of 10μs and 3μs before current zero and thus obtaining the time derivative. Hence

$$Q_s = \pi \frac{(12.875-7.8)}{(10-3) \times 10^{-6}} = \underline{2.28 \times 10^6 \text{ W/m}}$$

For $^{di}/_{dt}$ = 21A/μs and t = -7.9μs

It was observed in chapter 6 (section 6.2.3 (iii)) that due to an increase in continuum emission at the periphery of the arc spectral radial profile with increasing $^{di}/_{dt}$ it was difficult to compare the photographic and spectroscopic

areas at the high $^{di}/_{dt}$ value. For this reason it would not be reasonable to compare the luminous areas of fig. 8.1(ii) with the radial extent of the temperature profile of fig. 6.25(iii). However, in the same way as described in the low $^{di}/_{dt}$ case trends may be observed which give an indication of the temperature profile behaviour about the instant in question. It is clear from fig. 8.1 that temperature decay rate about the 7.9μs instant is low so that the assumption made for the low $^{di}/_{dt}$ case applies up to 3μs before current zero. However it would not be reasonable to compare absolute magnitudes of diameter in this case for the reasons stated above. Therefore it would be more meaningful if changes in the luminous arc area on fig. 8.1 can be related to the changes in profile extent and expressed as a percentage change thereof during this time period.

The percentage change in the luminous diameter of the arc viewed at slot 2 on fig. 8.1 is 2.2% in the time interval 8 to 3.5μs before current zero (the instant before which the area decay rate changes dramatically). This percentage diameter change can thus be translated into an equivalent diameter change of the 6,000K isotherm of fig. 6.25(iii). Since the temperature profile of fig.6.25(iii) is steep-sided then the change of 2.2% in diameter corresponds to 4.4% change in area if no significant changes in peak temperature occur. This latter condition has already been satisfied for times greater than 3.5μs before current zero in the radially averaged temperature results of fig. 8.1. Thus it

is also to be expected that this 2.2% change in the temperature profile extent will be reflected by a 4.4% change in the integral of equation 8.16.

Thus the energy storage term of the arc core may be evaluated for a $^{di}/_{dt}$ of 21A/μs at an instant 7.9μs before current zero as

$$Q_s = \frac{(1.55 \times 0.04)}{3.5 \times 10^{-6}} = \underline{1.77 \times 10^4 \text{ W/m}}$$

where 1.55 is the value $\int_0^{r_c} 2\pi\rho hr dr$ at t = -7.9μs

The power dissipated due to the change of thermal stored energy (this is effectively a power input since the arc is contracting) has been calculated for two cases of current decay rate and found to remain constant up to a time before current zero after which the temperature decay rate accelerates (fig. 8.1).

Power Loss due to Radial Thermal Heat Conduction Across the Core Boundary

The power loss by radial thermal conduction is defined as

$$Q_{co} = \int_0^{r_{arc}} \frac{1}{r} \cdot \frac{\partial}{\partial r}\left(Xr \frac{\partial T}{\partial r}\right) 2\pi r dr \qquad 8.17$$

With a knowledge of the temperature profiles (fig. 6.25) the above integral may be solved for both $^{di}/_{dt}$ cases of interest.

For $^{di}/_{dt}$ = 14.2A/μs, t = -10μs

The temperature profile of fig. 6.25(a) with the transport properties data of Frost and Liebermann (1971) were used to evaluate the integral of equation 8.17 over the arc diameter. Care was taken to measure the $^{dT}/_{dr}$ value at the core boundary since this formed the most significant contribution to the integral value.

The loss due to radial thermal conduction was evaluated in this manner as

$$\underline{Q_{co} = 4.6 \times 10^4 \text{ W/m}}$$

$\underline{\text{For } {}^{di}/_{dt} = 21\text{A}/\mu\text{s}, \quad t = -7.9\mu\text{s}}$

The value of radial thermal conduction for the core in this case was determined in a similar manner to the above using the temperature profile of fig. 6.25(iii).

The value of the term in this case is

$$\underline{Q_{co} = 2.97 \times 10^4 \text{ W/m}}$$

The Power Loss due to Axial Heat Convection

This power loss term is defined by the equation:

$$Q_{cA} = \frac{\partial}{\partial x} \int_0^{R_c} (\rho(r)\ h(r)\ C(r))2\pi r dr \qquad 8.18$$

where $\rho(r)$, $h(r)$ and r have their usual meanings

and $C(r)$-local axial gas velocity

Since the DPIS nozzle is designed to give sonic flow velocity (under non-arcing conditions) at the throat

(Taylor 1983), the gas velocities were also assumed to be sonic for a given local radial temperature value even during the current zero period.

The integral in equation 8.18 was evaluated for the axial viewing stations of both slots 2 and 3. This was a simple task in the case of slot 2 since the radial temperature profiles have been measured for this axial locality (fig. 6.25). However to evaluate the integral for the case of slot 3 the following assumptions were made:

(a) In the case of the low $^{di}/_{dt}$, according to the results of fig. 8.1 a transition from slot 2 to 3 at an instant of 10μs before current zero results in a reduction of luminous area to 12mm^2 (from the value of 19mm^2 in the slot 2 case) and an order of magnitude reduction in light intensity on the axis. The change in area (for the low $^{di}/_{dt}$ case only) was interpreted as a direct change in radius of the 6,000K isotherm. The change in light intensity was interpreted as a drop in axis temperature of about 1,000K.

(b) In the case of the high $^{di}/_{dt}$, again according to the results of fig. 8.1 a transition from slot 2 to 3 represents an area change of 10% which as discussed in the section above on thermal heat storage can be translated to a proportional change in the 6,000K isotherm. However it should be noted from fig. 8.1 that the temperature change cannot be substantial since little difference exists in the peak axis intensity between slots 2 and 3.

The measurements of local axial gas pressure of Taylor (1983) have provided the knowledge of the axial pressure distribution which is necessary to evaluate the local values of the transport properties for a given arc temperature profile for both $^{di}/_{dt}$ values. In this case it is necessary that radial pressure balance exists at the axial location of interest. This was verified earlier in this chapter for slot 2. Departure from pressure balance at slot 3 is also unlikely.

The axial separation of slots 2 and 3 is 10mm. The axial pressure profile in this region is close to linear (Taylor, 1983). Thus the axial derivative in equation 8.18 is calculated as the difference between two integrals (one for each slot) divided by the interslot separation (10mm).

Thus the axial convection term was calculated for each $^{di}/_{dt}$ case to give

for $^{di}/_{dt}$ = 14.2A/μs, t = -10μs

$\underline{Q_{CA} = 3.36 \times 10^{6} \text{ W/m}}$

for $^{di}/_{dt}$ = 21A/μs, t = -7.9μs

$\underline{Q_{CA} = 6.32 \times 10^{5} \text{ W/m}}$

Power Loss due to Radiation

The radiative loss at the arc core boundary is difficult to calculate in detail since the radiative emission and absorption characteristics of the arc plasma and surrounding

heated gas are complicated functions of wavelength and temperature. However it is possible to establish a lower limit to the radiative transfer by measuring the total radiation remote from the arc. (The radiative loss at the arc core boundary is of course given by the sum of this radiation remote from the arc and that absorbed by the surrounding heated gas).

The decay of the visible total radiation power loss (400nm to 900nm) was measured simultaneously (Shammas, unpublished) with the photographic records presented in this thesis. Thus instantaneous radiation power loss was measured throughout the current zero period for a number of $^{di}/_{dt}$ levels corresponding exactly to the operating conditions of the investigation of this thesis. The results of Shammas (unpublished) have been used to evaluate the net radiation loss from the arc for the two cases in question.

The lower limit for power loss by visible radiation was thus calculated as follows

For $^{di}/_{dt}$ = 14.2A/μs, t = -10μs

$$Q_{R/\text{slot } 3} = 0.9 \times 99 = 89.1 \text{ W/mm}$$

where the figure 99 represents the calibration factor of Shammas and Jones (1982). The figure Q_R in this case represents the radiation power loss per mm length of arc in the axial region corresponding to slot 3. However, from the results of fig. 8.1 it is clear that the radiation emitted from the slot 3 region is less than that from the

slot 2 region for the case of the low $^{di}/_{dt}$. The difference between these two quantities could be as high as an order of magnitude. If this is so then

$$Q_{R/slot\ 2} = 8.91 \times 10^2 \text{ W/mm}$$

Thus in this axial position

$$\underline{Q_R = 8.91 \times 10^5 \text{ W/m}}$$

For $^{di}/_{dt} = 21A/\mu s$, $t = -7.9\mu s$

The radiation power loss from the data of Shammas is:

$$Q_{R/slot\ 3} = 0.75 \times 10 \times 99$$
$$= 7.43 \times 10^2 \text{ W/mm}$$

For these operating conditions the results of fig. 8.1 are indicative of an arc which has a similar photographic luminous intensity as well as luminous area at both the axial stations of slots 2 and 3. In this case it can be assumed that

$$Q_{R/slot\ 3} = Q_{R/slot\ 2}$$

$$\therefore \quad \underline{Q_R = 7.43 \times 10^5 \text{ W/m}}$$

The radiation power loss measurements of Shammas which are referred to in this section are shown in Appendix 4.

The Core Power Balance

The major terms in the arc core energy conservation

equation (8.14) have thus been evaluated at two instants during the current zero period for two different current decay rates. The energy conservation (power) terms are summarised on table 8.2.

For both $^{di}/_{dt}$ cases the input and output power terms are equal to within 10%. This agreement is well within the experimental scatter and measurement accuracy which is at least 20%.

The power dissipated due to stored energy release is greater in the lower $^{di}/_{dt}$ case since the rate of change of arc area is greater than that in the high $^{di}/_{dt}$ case. The implication of this result is that the change in area in the low $^{di}/_{dt}$ case has a greater influence on this energy transport term than the change in temperature in the high $^{di}/_{dt}$ case.

The radial heat conduction term is small compared with the axial convection term in both $^{di}/_{dt}$ cases. However the ratio Q_{CO} : Q_{CA} is higher in the high $^{di}/_{dt}$ case. This is indicative of a narrower arc with a higher axis temperature and thus a more steep sided temperature profile at the 6,000K isotherm. However as current zero is approached and the arc contracts more rapidly whilst the axis temperature remains above 8,000K (as in the high $^{di}/_{dt}$ case) the above ratio should increase further.

The axial heat convection term forms a significant power loss term in both cases, the greatest contribution occurring in the case of the low $^{di}/_{dt}$. This result is to

be expected since the arc in this case is wider thus providing extra cross-section for energy removal. The arc in the low $^{di}/_{dt}$ case had a greater proportional axial change in radius as well as temperature than the one in the high $^{di}/_{dt}$ case. Therefore both these effects contribute to a greater convection power loss in the low $^{di}/_{dt}$ case but the change in core area remains the predominant contributor to this.

The most interesting change in power loss terms between the two $^{di}/_{dt}$ cases occurs in the power loss due to radiation. For the low $^{di}/_{dt}$ case the power loss by radiation at the axial region corresponding to slot 2 forms a reasonably small percentage of the total power input terms (20%), the dominant energy removal mechanism being axial heat convection. However in the case of the high $^{di}/_{dt}$ the radiation power loss in this axial region corresponds to the greatest energy removal mechanism. The percentage of total power input in this case is greater than 50% for the case of slot 2. A similar power loss by radiation also occurs at slot 3. Thus the arc in the high $^{di}/_{dt}$ case relies increasingly on radiation as a means of energy removal.

In the case of the low $^{di}/_{dt}$ the total electrical power input for an arc length of 100mm is 114KW. In this case the corresponding radiation loss is 0.89KW/mm (Table 8.2), with the radiation power loss at slot 3 being an order of magnitude less. Thus the greatest contribution of radiated

power comes from the upstream region. The length of the arc up to slot 2 is 25mm (the distance from the electrode tip to slot 2). Thus since the bulk of the radiation loss occurs in this region it may be reasonable to deduce that the total arc radiation power loss in the low $^{di}/_{dt}$ case corresponds to (25 x 0.891 =) 22.3KW. Thus the total radiation power loss as a percentage of electrical power input is 19.5%. This closely corresponds to the figure of total radiation power loss as the percentage of electrical power input presented by Shammas et al (1982) for reduced power arcing.

In the case of the high $^{di}/_{dt}$ the radiation levels extend to slot 3 (fig. 8.1). Thus if a similar effective length hypothesis is to be applied in this case then the effective arc length must be increased to at least 35mm (the distance of slot 3 above the upstream electrode tip). A similar calculation results in a total radiation power loss : electrical power input percentage of 20.2%. A similar result was obtained by Shammas et al (1982) for similar instants prior to current zero.

The work of Shammas and Jones (1982) showed also that as current zero is approached the value of the ratio of power loss by radiation to the electrical power input rose sharply, particularly within the final three microseconds. This was attributed to an increase in power input due to the energy storage changes in the arc. Clearly, from the results of fig. 8.1 the thermal storage power term does

increase as current zero is approached since the rate of change of temperature and luminous area in the high $^{di}/_{dt}$ case increase significantly during this time. It would therefore be of interest to make a similar evaluation of the arc energy balance in this highly transient period.

(vi) Arc Core Energy Conservation within the Final 3μs before Current Zero

A study is presented of the energy conservation equation (involving the five principal energy removal mechanisms discussed in the previous section (v)) during the final 3μs of current decay when conditions are highly transient in nature.

The case considered is for a full power arc in which a peak current of approximately 40KA flowed resulting in a current zero $^{di}/_{dt}$ of 18.5A/μs. The radially resolved arc spectra for this condition were captured 2.3μs before current zero and the corresponding temperature profile was presented on fig.6.25(ii) in chapter 6.

The individual terms of the energy conservation of the arc core for this condition are considered in the same manner as the cases discussed above.

Electrical Power Input

According to equation 8.15 above the electrical power input is

$$Q_E = (8 \times 10^3) \times (18.5) \times 2.2$$

$$= \underline{3.26 \times 10^5 \text{ W/m}}$$

Change in Thermal Stored Energy

Equation 8.16 was again evaluated using the radial temperature profile of fig.6.25(b) and making a similar assumption to evaluate the time derivative as was made in section (v) above.

The temperature profile shape does not alter drastically for the time interval considered, i.e. the 2.2μs immediately prior to current zero.

The radially averaged temperature at the current zero instant for a $^{di}/_{dt}$ of 18.5A/μs is just below 7,000K (fig. 8.3). Thus it is reasonable to assume the axis temperature to be 7,000K.

The diameter of the 6,000K isotherm in this case was obtained by examining the spectrum of an arc captured close to current zero. Such a spectrum is given on fig. 8.8 which shows the Cu I line emission at the 521.8nm wavelength, and a time 1.2μs before current zero for the same $^{di}/_{dt}$. In this case two low intensity (51 counts) spectral peaks were detected. This is indicative of an arc with a 6,000K isotherm at a maximum diameter of 1.5mm. By the instant of current zero this diameter will reduce further, probably to be 1mm.

The energy storage of equation 8.16 was evaluated at each instant and the time derivative calculated to give:

$$Q_s = 6.57 \times 10^5 \text{ W/m}$$

Power Loss due to Radial Thermal Conduction

Equation 8.17 was evaluated for the temperature profile of fig. 6.25(b). The value of the power loss due to radial thermal conduction was calculated as

$$Q_{co} = 4.02 \times 10^4 \text{ W/m}$$

Power Loss due to Axial Heat Convection

The axial gas velocity in the throat region was again assumed to be sonic.

The results of fig. 8.1 show the decaying arc areas for slots 3 and 2 about the instant 2.2μs before current zero for the case of $^{di}/_{dt}$ = 15A/μs.

Since the thermal structure of the arc column at the current zero instant for a $^{di}/_{dt}$ of 18.5A/μs resembles the lower $^{di}/_{dt}$ more than the higher $^{di}/_{dt}$ case (fig. 8.3), the following may be assumed:

(a) The arc core area at slot 3 2.2μs before current zero is approximately half the value of the slot 2 area as in the 15A/μs case in fig. 8.1. Therefore the 6,000K isotherm radius of the arc column at slot 3 is less than at slot 2 by a factor of $\sqrt{2}$

(b) As in the previous section concerning thermal convection loss calculation the axis temperature may be assumed to be as much as 1,000K less at slot 3 than slot 2.

The same axial pressure variation exists between slot 2

and 3 as stated in the previous section about the axial convection power loss. That is the pressure in the slot 2 region is 4 bar and that in the slot 3 region is 3 bar.

With the above information the integral of equation 8.18 was evaluated for the slot 2 temperature profile and subsequently for slot 3. The axial derivative was then evaluated as in the previous section concerning the axial convection power loss. Thus,

$$\underline{Q_{CA} = 7.80 \times 10^5 \text{ W/m}}$$

Power Loss due to Radiation

The results of Shammas (appendix 4) were used to evaluate the radiation power loss at slot 2 in a similar manner as in the previous section on radiation power loss. The radiation power loss at slot 3 according to the results of Shammas (appendix 4) is

$$Q_{R/\text{slot } 3} = 0.26 \times 99 = 25.74 \text{ W/mm}$$

Again since the arc in this case resembles the low di/dt arc more than at high di/dt, the equivalent radiation loss at slot 2 could be as much as an order of magnitude higher than the above figure for slot 3. Thus,

$$Q_{R/\text{slot } 2} = 257.4 \text{ W/mm}$$

$$= \underline{2.57 \times 10^5 \text{ W/m}}$$

Summary

The power terms corresponding to the energy transport mechanism of the dynamic energy balance for the arc core are presented on table 8.3.

The power input term due to the thermally stored energy term forms $^{2}/3$ of the total power input i.e. it is twice as high as the electrical power input term.

The radial heat conduction term (Q_{co}) still only forms quite a small contribution to the energy balance. However it does form a higher proportion of the total power loss than either of the two cases in the previous section (table 8.2).

The power loss due to axial convection remains the dominant power loss term in the $^{di}/dt$ case in question (18.5A/μs), but does form a slightly lower proportion of the total power loss than the previously discussed low $^{di}/dt$ case (table 8.2).

The proportion of radiation power loss in the total power loss in this case is also slightly higher than in the low $^{di}/dt$ case shown on table 8.2. The total electrical power input for a 100mm arc length is 32.6KW. Also, if the effective length hypothesis of the previous section is applied in this case the effective total radiation power loss of the arc column is 6.43KW. Thus the proportion of radiative power loss in this case is 19.7%. This again corresponds to the radiation power by proportion calculations

of Shammas et al (1982) for an intermediate $^{di}/_{dt}$ 2.2μs before current zero.

In this section it has been shown that dynamic energy balance for the core of the circuit breaker arc in an axial flow has been satisfied (to within 10%) for an intermediate $^{di}/_{dt}$ value (18.5A/μs) at an instant 2.2μs before current zero.

(vii) Time for Complete Recovery (τ_s)

The terms in the current zero energy balance of the arc core can be used to define an alternative thermal time constant to the Mayr time constant which has already been discussed in section (iii) above.

If there was no electrical power input then the instantaneous rate of change of the thermally stored energy must be dissipated by the total power loss at that instant. If it is assumed that this value of power loss stays constant (which is unlikely but is sufficient to provide an order of magnitude comparison with the Mayr time constant) then the time for complete recovery is

$$\tau_s = \frac{\text{Energy Stored}}{\text{Total Power Dissipated}}$$

This ratio was evaluated for the three $^{di}/_{dt}$ cases (at the respective instants before current zero) considered in the energy balance calculations of sections (v) and (vi) above. These results are shown on fig. 8.5(c) for direct comparison with the Mayr time constants.

These results show a reasonable correlation with the previously calculated Mayr time constants (fig. 8.5(c)) throughout the current zero period.

8.3 The Arc during the Post Current Zero Period

8.3.1 Introduction

The performance of the circuit breaker investigated in this thesis is represented by a band region on the $^{di}/_{dt}$: $^{dv}/_{dt}$ characteristic which segregates the positive clearance and failure regimes (Taylor et al, 1982). In this band the circuit breaker may clear or fail in successive tests under identical operating conditions. When a circuit breaker fails under such conditions the type of reignition is referred to as a critical arc reignition. The high speed photography of this investigation has enabled arc growth phenomena to be investigated in such cases of critical reignition for both full and reduced power arcing.

It is the aim of this section therefore to ascertain the nature of the post zero arc growth phenomena under realistic circuit breaking conditions from the photographic results presented in chapter 6.

8.3.2 Growth Phenomena of the Circuit Breaker Arc under Critical Reignition Conditions

In the case of the reduced power arcs photographs were analysed in such a critical reignition case and the results of this analysis are presented on fig. 6.4(a) to (c). Fig. 6.4(c) which represents the dynamic variation of the arc luminous

diameter and intensity for times from 1μs prior to until several microseconds after current zero shows some important critical reignition features of the circuit breaker arc. The arc intensity and diameter decay up to 3μs after current zero whereupon arc growth occurs after a further pause of about 6μs. As initially observed in chapter 6, two important trends are of particular interest:

(a) The arc intensity profile 1μs after current zero is steeper sided and narrower than at the corresponding time before current zero.

(b) When the arc begins to reform at the +11μs instant (fig. 6.4(b)) it is the axis intensity which increases rapidly whilst the arc diameter increases more slowly.

The implication of (a) is that the arc column immediately following current zero has a different thermal structure to the arc immediately before current zero. This means that the arc column which has undergone the transition through current zero has contracted but its axis intensity (and temperature) is sustained. The criterion which determines whether reignition is sustained relates to whether sufficient power transport is produced by the axial temperature increase, to overcome the column cross-section decrease. This type of reignition is dependent upon the thermal state of the arc channel (thermal reignition) and for SF_6 usually occurs within 3 or 4μs of the current zero. This is not the case in fig. 6.4(c) where a 3μs pause has occurred 4μs after current zero. The reason for this pause is not totally

clear but is likely to be due to a partial obliteration of the arc column.

The more pronounced increase in intensity during reignition, compared with arc diameter, is consistent with the experimental results of Jones et al (1973). This latter investigation was for a lower (holding) current wall stabilised arc where the arcing current was reduced to zero in a similar manner to the reduced power method used in the present work. The results of Jones et al (1973) show that on application of a step voltage to a decaying arc column, the axial temperature responds first by showing a pronounced increase, whilst the electrical cross-section of the arc column may continue to decrease. Thus the criterion governing reignition described above needs to be satisfied during this critical period. The results of the present work indicate that a similar process governs reignition occurrance in the case of a real circuit breaker in the case of reduced power arcing.

The photographic results of the present work enable the reignition growth of an arc to be determined following full power arcing. The results of fig. 6.15 show the measured intensity profiles of the arc column at the axial locations corresponding to slots 2 and 3 for times immediately before and after current zero. Although the reignition is not as critical as the one shown for the reduced power conditions, the trends of post zero arc column growth are still in evidence.

In the case of slot 2 the arc column immediately after current zero is narrower than the one captured 1.6μs before current zero with the axis intensity being similar in both cases. This was a trend also in evidence in the reduced power case. The arc column intensity and diameter then both decay in the case of both slots 2 and 3. On the onset of strong reignition it is again the axis intensity which grows more rapidly than the arc diameter. The latter trend is more pronounced in the case of slot 3 and occurs at an instant closer to current zero than the slot 2 case. It is clear from these results that the region in the immediate vicinity of the nozzle throat has an important role to play in arc reignition.

8.3.3 Summary

The growth pattern of the arc column for the case of a critical reignition has been established under real circuit breaking conditions for both the reduced and full power arcing cases.

The results of chapter 6 have shown that it is the intensity of the arc column axis which responds most rapidly to the increase in the reigniting arc current followed later by an increase in luminous diameter. This was the case for both full and reduced power arcing. The good correlation of the present results with those of Jones et al (1973) shows that the same criterion for reignition is observed for the real circuit breaking conditions as was the case with the wall stabilised arcs investigated by these authors.

The observation of the reignition trends at the axial station, slots 2 and 3 shows that the arc in the nozzle throat plays an important part in reignition.

8.4 Formulation of an Empirical Relationship for the Thermal Performance

8.4.1 Introduction

Arc photographs and spectra coupled with the total radiation loss results of Shammas et al (1982) and private comm. (appendix 4) for a wide range of operating conditions have enabled an empirical relationship predicting the thermal performance of the test circuit breaker to be formulated.

Many attempts have been made in the past to formulate such empirical relationships some of which were reviewed in chapter 2 of this thesis. However, many, if not all, of these attempts have proved inadequate for application to real circuit breaking conditions since either experimental conditions in such cases differed significantly from the real ones or inadequate experimental data was available and such values would have to be assumed.

It is the aim of the work presented in this section not only to develop the empirical performance relationship for the particular model interruptor of this investigation but to form a basis from which the results may be applied to commercial interrupter design.

8.4.2 Thermal Performance and Arcing Parameters

The temporal decay of the arc areas represented on fig. 8.1 are characteristic of similar trends reported previously for identical arcing conditions (Lewis et al, 1985). Other measurements have been reported by Ancilewski et al (1984) which are claimed to include a temporal luminous diameter variation during the current zero period. The absolute magnitude of the diameters presented by Ancilewski et al (1984) differ somewhat from the diameters of the present work. The former are about factor of 3 less than the latter over the $^{di}/_{dt}$ range 15 to 24 A/μs. The reasons for this apparent discrepancy are not known since Ancilewski et al (1984) have not indicated their experimental technique nor details of their operating conditions. The most likely reason for the discrepancy is a different measurement technique involving a different photographic sensitivity. Also the authors in this case have employed different pressures and nozzle/contact geometries, which may well result in entirely different flow conditions.

Despite the differences in operating conditions and absolute magnitudes of luminous diameter consistencies are present in trends of diameter decay. For instance the diameter collapses in sympathy with the arcing current over the final 10μs for current decay rates of 15A/μs or less. Also Ancilewski et al (1984) reported a pre-current zero plateau in their diameter: time characteristic which occurred within the final 10μs in the case of higher $^{di}/_{dt}$'s. However,

the present results (fig. 8.1 and Lewis et al (1985)) show the luminous areas (and diameters) to decay more rapidly for times less than 4μs before current zero. Unfortunately the results of Ancilewski et al (1984) do not include luminous diameter measurements during this critical time domain.

The photographic results of this investigation have enabled the luminous diameter at (or within 1μs framing accuracy) the current zero instant to be captured on a 200ns exposure. The variation of the luminous diameter for slots 2 and 3 at the current zero instant over the full range of $^{di}/_{dt}$ for both full and reduced power is shown in fig. 8.3. These results show that the arc luminous area (and diameter) increases with $^{di}/_{dt}$, the increase being sharper in the case of the full power than in the reduced power case. For the low values of $^{di}/_{dt}$ the areas (and diameters) overlap for both arcing power levels within the experimental scatter. The trends of arc diameter, photographic axis intensity and total radiation power loss at the current zero instant with $^{di}/_{dt}$ have been discussed in section 8.2.3 of this chapter. Collectively they indicate that the difference in total radiation power loss between full and reduced power arcing conditions is due mainly to differences in the emission intensity which is in turn due to a raised axis temperature rather than differences in the luminous diameter.

The thermal reignition performance under both full and reduced power arcing conditions for the circuit breaker used

in the present work has been measured by Taylor et al (1982) and is represented on fig. 8.9 (labelled power and ramp).

Ancilewski et al (1984) produced an empirical relationship which related the $(rrrV)_c$ to many variables e.g. upstream pressure, throat diameter. In the present work only $^{di}/_{dt}$ was varied as an operating condition. This being so, it is possible to write

$$(rrrV)_c = aA_o^{-m} (^{di}/_{dt})^{-1} \qquad 8.19$$

where $(rrrV)_c$ = critical rate of rise of recovery voltage

A_o = luminous area at the current zero instant

$(^{di}/_{dt})$ = current decay rate

a, m = constants

The geometrical variables and pressure in the formula of Ancilewski et al are of course constant for the present investigation and thus were absorbed into the constant of proportionality a.

When a rigorous empirical analysis is made of the experimental results for the reduced power current zero arc diameter at slot 3 as a function of $^{di}/_{dt}$ (fig. 6.6(a)) the following relationship may be derived:

$$A_o \quad \alpha \quad \frac{di}{dt}^{1.6} \qquad 8.20$$

It is also possible to derive similar relationships between A_o and $^{di}/dt$ for the case of the full power arcs. In this case the empirical relationship needs to be divided into two domains since, as already identified, the full power arc behaviour and thermal structure differ significantly for different $^{di}/dt$ ranges. Thus

for I peak < 40KA ($^{di}/dt$ < 20A/μs)

$$A_o \propto \left(\frac{di}{dt}\right)^{1.6} \qquad 8.21$$

and for I peak > 40KA ($^{di}/dt$ > 20A/μs)

$$A_o \propto \left(\frac{di}{dt}\right)^{2.5} \qquad 8.22$$

These results may be compared with the implications of the performance results of Taylor et al (1982) which were also expressed in an empirical manner. These expressions were

(a) for the reduced power

$$\left(\frac{dV}{dt}\right)_{crit} = (rrrV)_c \simeq a \left(\frac{di}{dt}\right)^{-2.1} \qquad 8.23$$

(b) for the full power

$$(rrrV)_c \simeq a \left(\frac{di}{dt}\right)^{-2.1} \qquad 8.24$$

for I peak < 40KA ($^{di}/dt$ < 20A/μs)

$$\text{and } (rrrV)_c \simeq a' \left(\frac{di}{dt}\right)^{-6.75} \qquad 8.25$$

for I peak > 40KA ($^{di}/dt$ > 20A/μs)

Note that equations 8.23, 8.24 and 8.25 are all approximate equalities since the performance trends of Taylor et al (1982) could only be represented by regions of finite bandwidth on the $^{dv}/_{dt}$:$^{di}/_{dt}$ characteristic (fig. 8.9).

These results may be compared with values computed from the following empirical relationships which were derived solely from the photographic results of chapter 6 and fig.8.1 (and which are independent of the results of Taylor et al (1982))

$$(rrrV)_c = 4.34 \times 10^2 \left(\frac{di}{dt}\right)^{-1.47} A_o^{-1.25} \qquad 8.26$$

in the case of reduced power arcing, and

$$(rrrV)_c = 1.27 \times 10^7 \left(\frac{di}{dt}\right)^{-4.66} A_o^{-1.25} \qquad 8.27$$

in the case of full power arcing

The agreement between the points computed from equation 8.26 with the reduced power and low $^{di}/_{dt}$ full power characteristic of Taylor et al (1982) is good (fig. 8.9). The broken line on fig. 8.9, corresponding to equation 8.27 also shows good agreement with the interruptor performance in the case of higher $^{di}/_{dt}$ values for the full power arcs.

By combining equations 8.21 and 8.22 with 8.24 (= 8.23) and 8.25 respectively, it is possible to arrive at equations describing the $^{di}/_{dt}$ and A_o variation with $(rrrV)_c$ from the performance curves of Taylor et al (1982). These take the following form

(a) $(rrrV)_c \cong aA_o^{-1.3}$ 8.28

for the reduced power case

(b) $(rrrV)_c \cong aA_o^{-1.3}$ 8.29

in the case of full power arcs for which $^{di}/_{dt} < 20A/\mu s$

(c) $(rrrV)_c \cong a^1 A_o^{-1.5} (^{di}/_{dt})^{-3}$ 8.30

in the case of full power arcs for which $^{di}/_{dt} > 20A/\mu s$

In these equations it is assumed that the dependence upon A_o should be identical regardless of operating conditions. Thus equations 8.28 and 8.29 are identical and reflect the similar performance between the reduced and full power results at lower peak currents (<40KA). However, the high current part (>40KA) of equation 8.30 depends upon $^{di}/_{dt}$ in addition to its dependence upon A_o. This implies that the differences in the performance trends between low and high $^{di}/_{dt}$ under full power conditions are due, not only to arc cross-section differences, but more dominantly due to changes in the arc column thermal structure as reflected in the substantial increase in the radiative loss during the current zero period (fig. 8.2) and particularly at the current zero instant (fig. 8.3). This means that the changes in thermal structure of the arc column close to current zero are reflected in a stronger dependence upon $^{di}/_{dt}$ than could be expected solely due to the area influences in equations 8.21 and 8.22. The exaggerated $^{di}/_{dt}$ dependence is also reflected in the empirical equations derived from luminous area

considerations (equations 8.26 and 8.27) although the indeces in these cases are not identical to the former case.

Since the exaggerated $^{di}/_{dt}$ effects only occur in the case of full power arcing and in the case of high $^{di}/_{dt}$ only then equation 8.19 must be modified accordingly. Thus in the case of full power arcing, equation 8.19 needs to be rewritten as

$$(rrrV)_c = \underbrace{aA_o^{-1.3}}_{\text{Factor 1}} \quad \underbrace{\left[1+1.2x10^{-14}I_p^{3}\right]^{-1}}_{\text{Factor 2}} \qquad 8.31$$

where,

Factor 1 is the term which describes the normal interruptor performance under reduced arcing conditions and full power conditions for the case of low $^{di}/_{dt}$ (< 20A/μs) only.

Factor 2 is the term included to define the interruptor performance for the case of high $^{di}/_{dt}$ values (> 20A/μs). In this the $^{di}/_{dt}$ has been replaced by the peak current value I_p where

$$I_p = \frac{di}{dt} \cdot \omega^{-1} \qquad 8.32$$

where $\omega = 2\pi$ x current waveform frequency.

Consequently the threshold for the onset of peak current effects may be identified from equation 8.31 according to the equality

$$1 = 1.2x10^{-14}\ I_p^{3} \qquad 8.33$$

as

$$I_{p_{crit}} = 4 \times 10^{4} A = 40KA \qquad 8.34$$

This threshold value may of course depend upon other parameters such as contact geometry and upstream tank pressure. This originates from the influence of these parameters as indicated in Ancilewski et al's (1984) original equation.

The peak current factor (equation 8.31) is incorporated to take account of effects which are peculiar to arcs subject to a high $^{di}/_{dt}$ under full power conditions. Such effects may include the entrainment of material from the nozzle wall or contact into the arc column which the relationship of Ancilewski et al does not cater for. The performance measurements of Taylor et al (1982) also suggest that effects may occur due to increased nozzle wall ablation processes.

8.4.3 Conclusions

The photographic luminous area results of chapter 6 coupled with the detailed performance measurements of Taylor et al (1982) have been used to derive an empirical relationship predicting the performance of a test circuit breaker. The resulting equation requires a knowledge of the circuit breaker geometry, the current zero arc area and the range of current zero $^{di}/_{dt}$. The equation indicates that changes in arc structure leads to changes in circuit breaker performance

which occur for high $^{di}/dt$ values (> 20A/μs) under full power arcing conditions. These performance changes have been related to structure which have been confirmed from the measurements of chapter 6 where changes in the axis temperature of the arc column were observed with changing $^{di}/dt$.

8.5 Conclusions

The results of chapter 6 have been used to make a quantitative evaluation of many important aspects of the current zero arc column.

The results have shown that the time constants of the decaying arc column are submicrosecond in the case of current decay rates of 15A/μs close to current zero. However the time constant values at corresponding times were somewhat higher for $^{di}/dt$ values in excess of 20A/μs.

The shape factors (overall and core) of the integral analysis have been evaluated for the current zero period in two cases of current decay rate (15A/μs and 21.3A/μs). They have been correlated to the work of others which have used widely different operating conditions through a universal correlation parameter, the Nusselt number. The correlation with the work of Walmsley et al (1978(ii)) is in good agreement at lower $^{di}/dt$ values. Some departure for universal agreement is apparent at higher values of $^{di}/dt$ but the trends still remain within the uncertainty boundaries of previous estimates.

An evaluation of each term appearing in the core energy

conservation equation has been made using experimentally measured core temperature profiles. The results of table 8.2 and 8.3 are plotted on figs. 8.10 and 8.11 respectively. These results show a number of important trends:

(i) The total power loss decreases with increasing $^{di}/_{dt}$ (fig. 8.10). This is due to the fact that the arc column in the higher $^{di}/_{dt}$ case is thinner and this reduction in area has a profound effect on the axial convection loss term.

(ii) The axial convection power loss from the arc core is the dominant power loss mechanism in the case of the low $^{di}/_{dt}$.

(iii) The axial convection power loss (arc core) decreases more rapidly with $^{di}/_{dt}$ than radiation so that in the higher $^{di}/_{dt}$ case radiation loss dominates. The decrease in the convection is due to the reduction in arc area as stated in (i) above. The increase in radiation power loss is associated with the higher core temperature in the case of the higher $^{di}/_{dt}$. It is also of significance that the increase in the core temperature was not sufficient to offset the decrease in convection power loss caused by the decrease in core area. Thus the change in area is the dominant effect upon the axial convection power loss for the arc core.

(iv) The results of fig. 8.11 show that although the

contribution to the energy loss by radial heat conduction remains small as a proportion of the total loss, this proportion does grow significantly as current zero is approached. In the limit, with a narrow arc core as is the case at the current zero instant with a low $^{di}/_{dt}$ it is likely that radial heat conduction and radiation from the core could form the dominant energy transport mechanisms. However the verification of this requires further investigation.

The arc reignition has been considered with particular emphasis on the case of critical reignition. Here the photographic evidence of post current zero arc growth has confirmed trends which were also identified by Jones et al (1973). The initial increase in axis intensity at the onset of severe reignition observed in the present work is consistent with the energy from the restrike voltage primarily influencing the column axis temperature rather than the arc column diameter. In the case of critical reignition, Jones et al (1973) defined the growth of this axis temperature to be just sufficient to cause the arc to reignite. In addition to the critical reignition case the work presented in this chapter and chapter 6 have shown that this trend is also in evidence for cases of less critical reignition.

Finally, an empirical relationship has been derived which relates the thermal performance of the test breaker to the arc area at current zero. There is also a factor in the relationship which takes account of the effects present

due to the arc current passing through an excessively high value (> 46KA) prior to current zero. It was necessary to incorporate such a factor into the relationship since it has been shown earlier that the thermal structures of full power arcs at current zero following such a major current peak and lower values are different.

LIST OF TABLES

Quantity	Symbol	Characteristic Value at p = 4ATM
Electrical Conductivity	σ^*	650 $(Sm)^{-1}$
Enthalpy	h^*	20.31×10^6 (J/Kg)
Thermal Conductivity	K^*	0.48^* (W/m^oK)
Specific Heat Capacity	C_p^*	10^3 (J/Kg^oK)

(i) Characteristic Values

Quantity	Symbol	Value at Conducting Core Edge
Thermal Conductivity	K_c	0.35 (W/m^oK)
Specific Heat Capacity	C_{pc}	10^3 (J/Kg^oK)

(ii) Values at Core Edge

Table 8.1 Summary of the Thermal Transport Properties used in this Chapter

Power Input Terms	Value	Power Loss Terms	Value
Electrical Power Input (Q_E)	1.14×10^6	Radial Heat Conduction (Q_{CO})	4.6×10^4
		Axial Heat Convection (Q_{CA})	3.36×10^6
Change in Thermally Stored Energy (Q_S)	2.28×10^6	Radiation Power Loss (Q_R)	8.91×10^5
Total =	4.42×10^6 W/m	Total =	4.30×10^6 W/m

(i) $di/dt = 14.2A/\mu s$, $t = -10\mu s$

Power Input Terms	Value	Power Loss Terms	Value
Electrical Power Input (Q_E)	1.29×10^6	Radial Heat Conduction (Q_{CO})	2.97×10^4
		Axial Heat Convection (Q_{CA})	6.32×10^5
Change in Thermally Stored Energy (Q_S)	1.77×10^4	Radiation Power Loss (Q_R)	7.43×10^5
Total =	1.31×10^6 W/m	Total =	1.41×10^6 W/m

(ii) $di/dt = 21A/\mu s$, $t = -7.9\mu s$

Table 8.2 Summary of the Power Terms in the Current Zero Energy Balance for Different Operating Conditions

Power Input Terms	Value	Power Loss Terms	Value
Electrical Power Input (Q_E)	3.26×10^5	Radial Heat Conduction (Q_{CO})	0.40×10^5
		Axial Heat Convection (Q_{CA})	7.80×10^5
Thermally Stored Energy Change (Q_S)	6.57×10^5	Radiation Power Loss (Q_R)	2.57×10^5
Total =	9.83×10^5 W/m	Total =	1.08×10^6 W/m

$$di/dt = 18.5A/\mu s$$

Table 8.3 Summary of Power Terms in the Energy Balance Close to Current Zero

LIST OF FIGURES

Fig. 8.1 Summary of temporal arc area, temperature and intensity decay during the current zero period

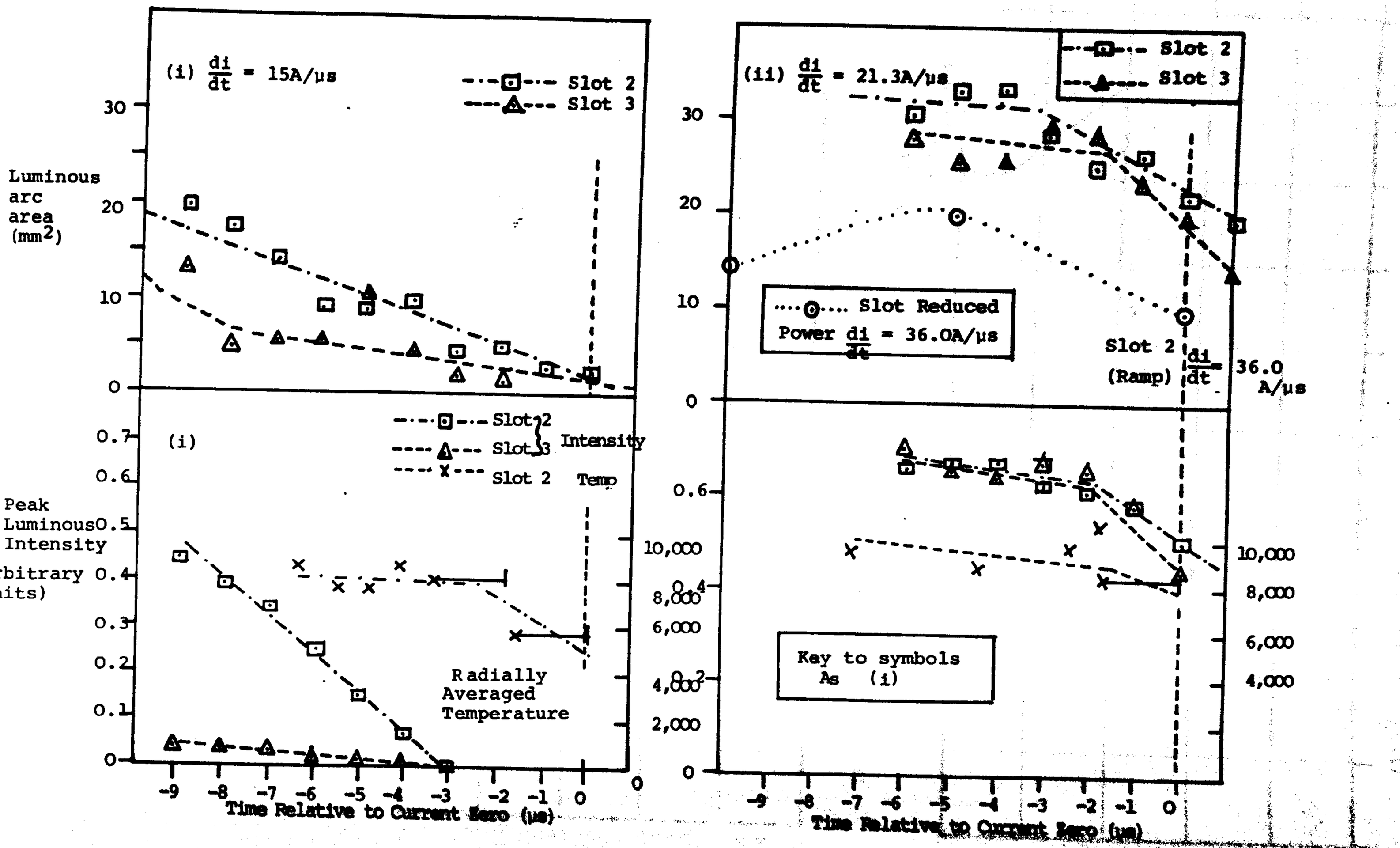

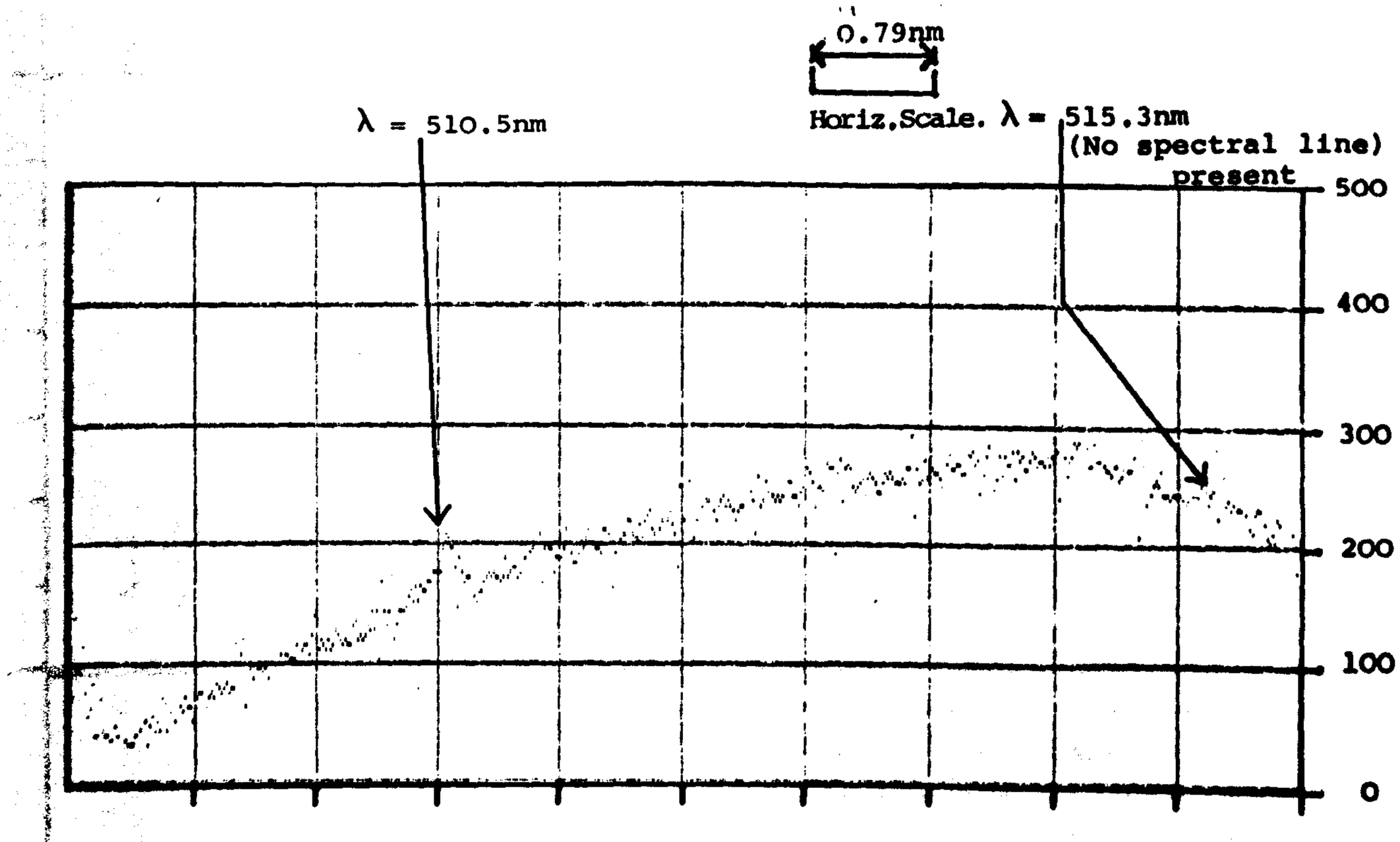

(i) 1.9μs Before Current Zero

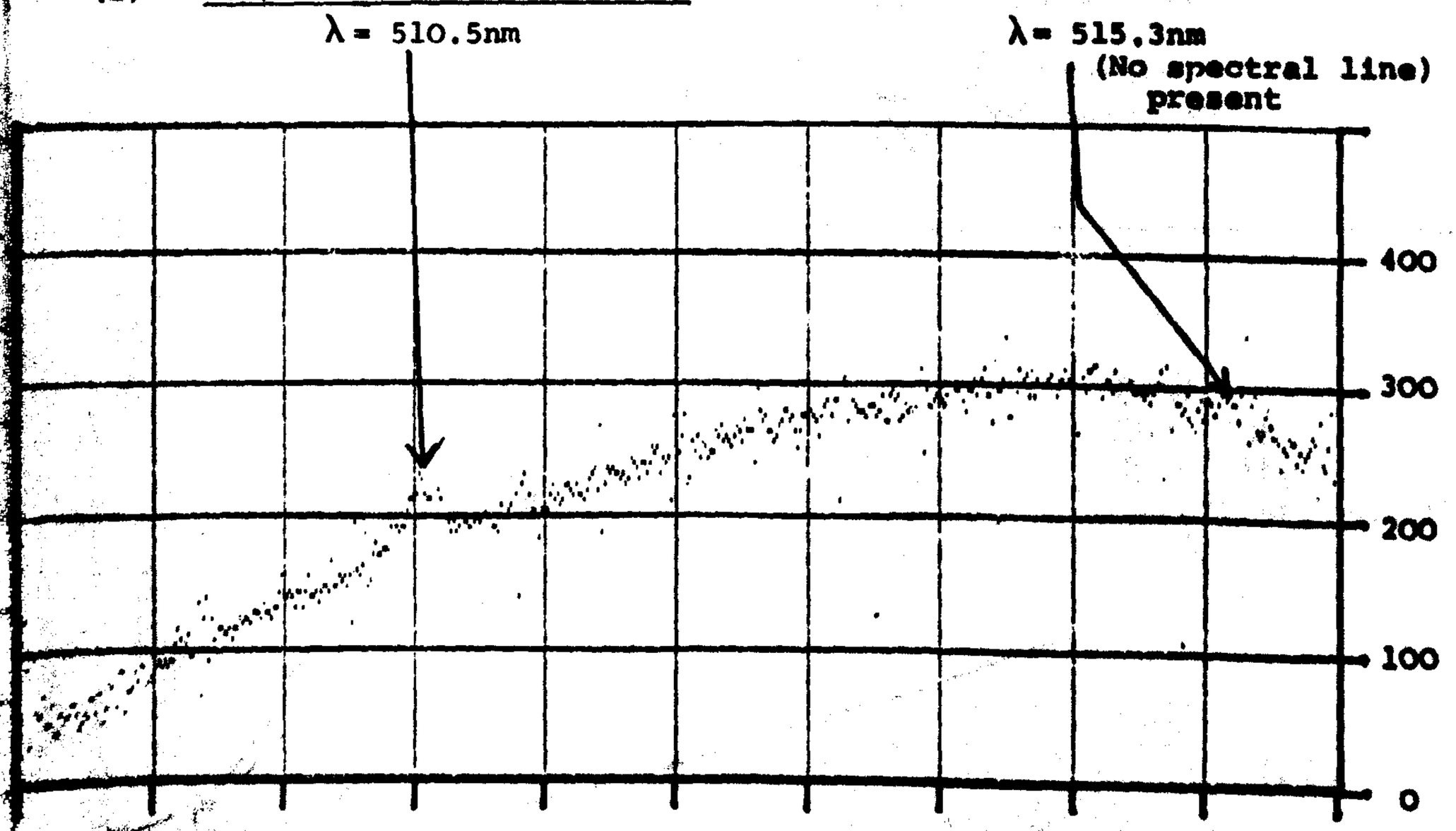

(ii) 1.6μs Before Current Zero

Operating Conditions: $\frac{di}{dt}$ = 14A/μs ; Exposure time = 1.6μs

In both cases

8.2 The Spectra of Arcs Close to Current Zero in the case of Low $\frac{di}{dt}$

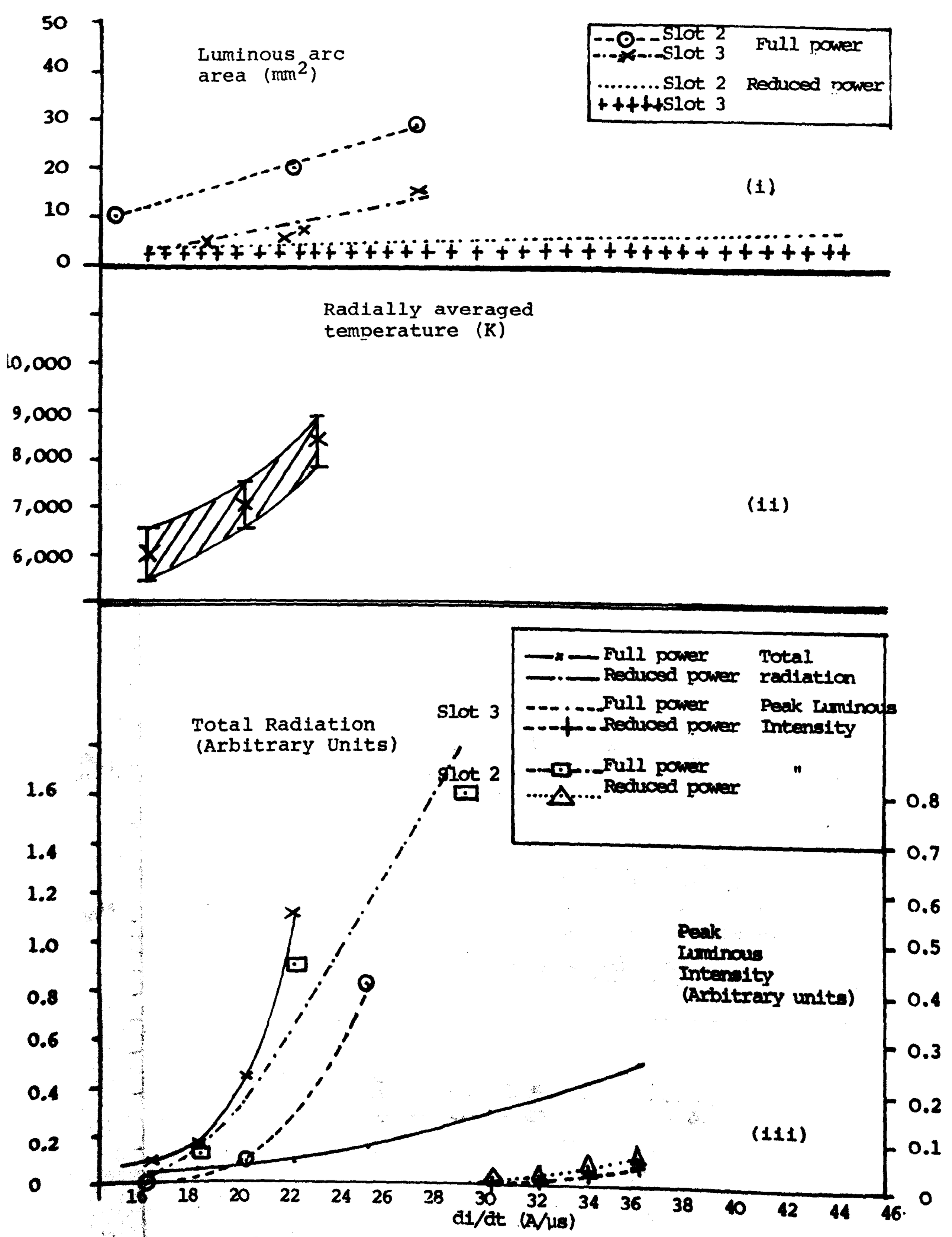

Fig. 5.3 Summary of Current Zero Arc Area, Temperature (Radially Averaged) and Intensity Variation with di/dt

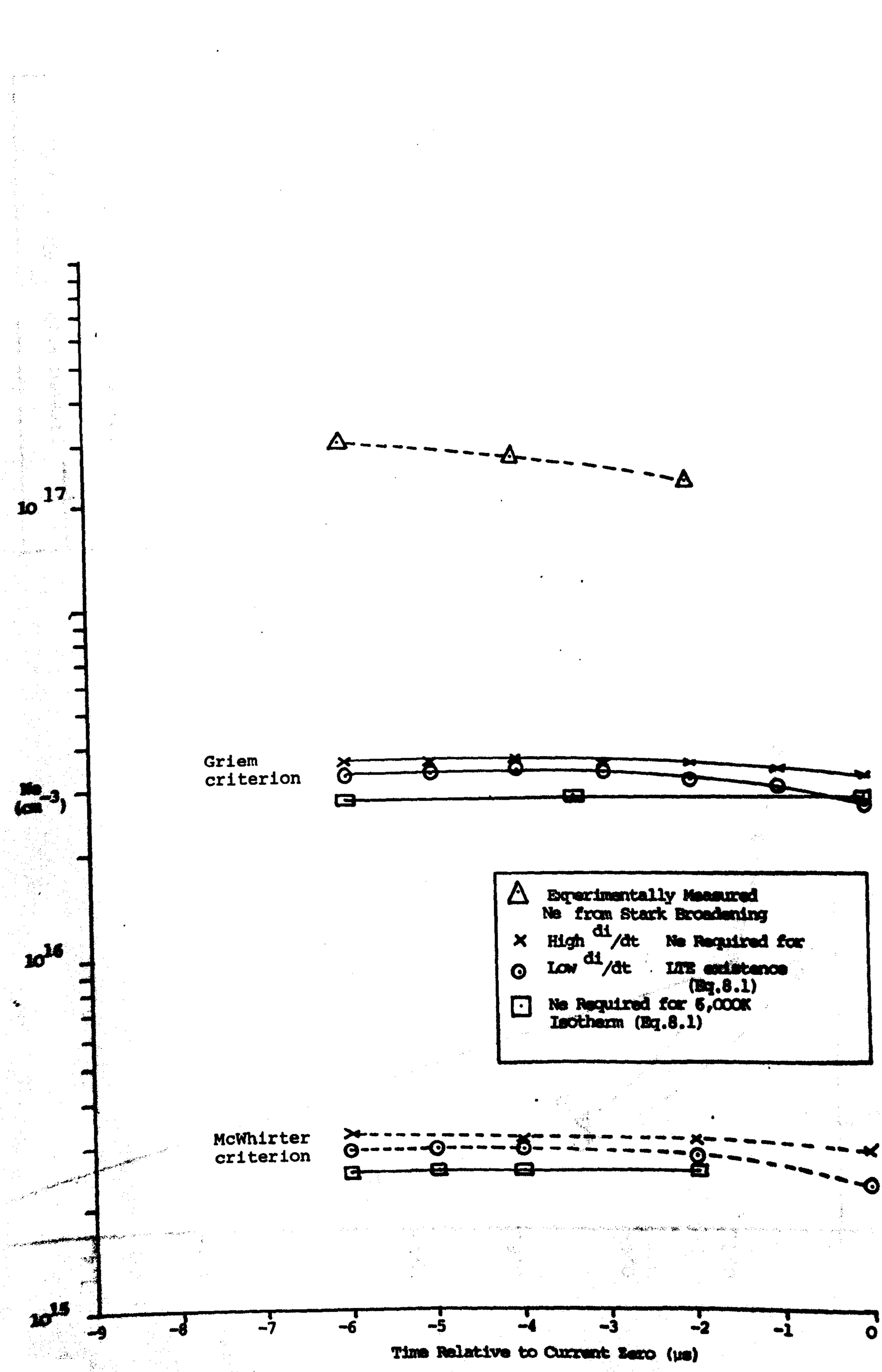

Fig. 8.4 Justification of Existence of LTE

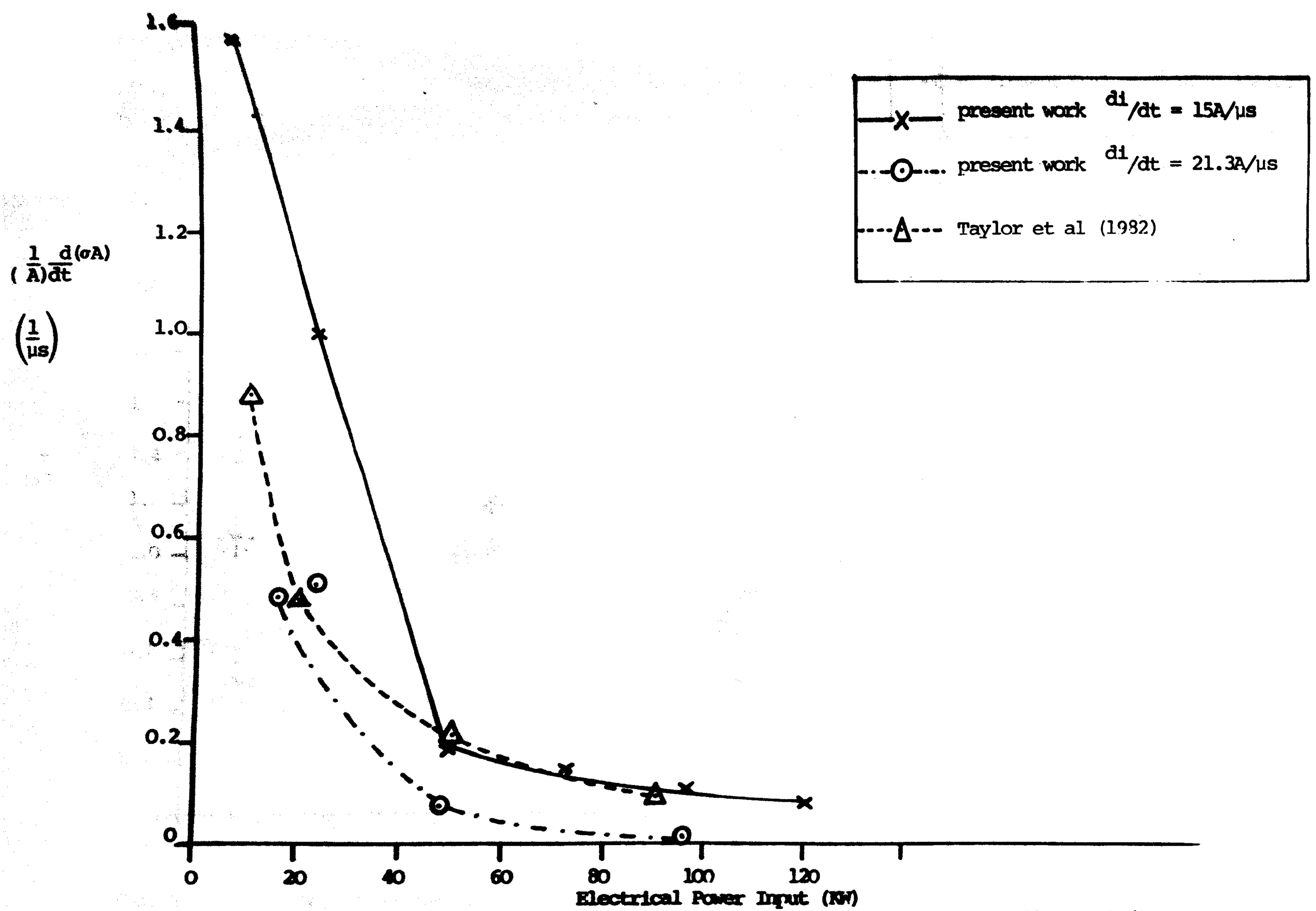

Fig. 8.5 (a) The Determination of the Mayr Time Constants for a Full Power Arc and Different di/dt Values

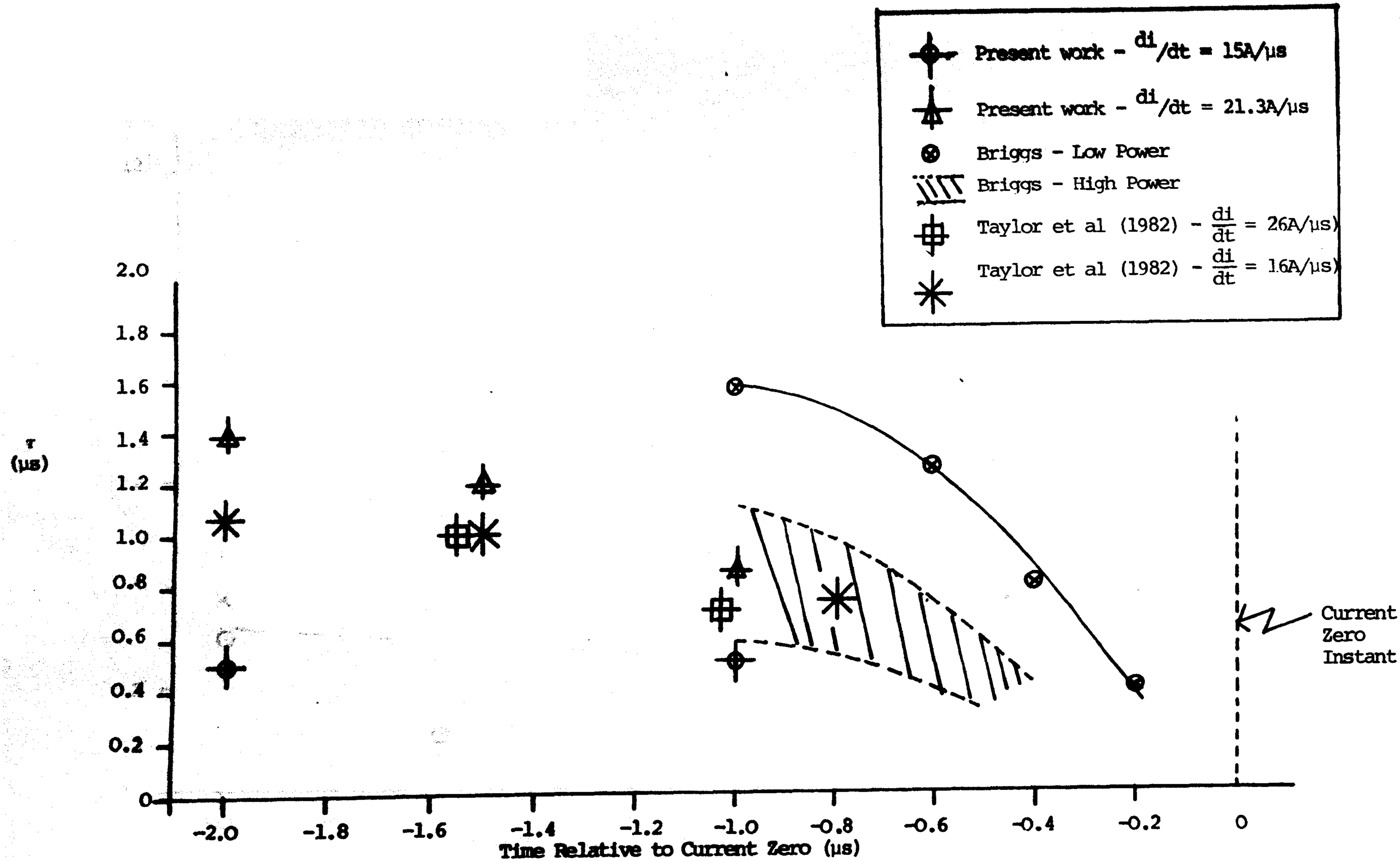

Fig. 8.5(b) The Mayr Time Constant Variation Within the Final Two Microseconds of Current Delay

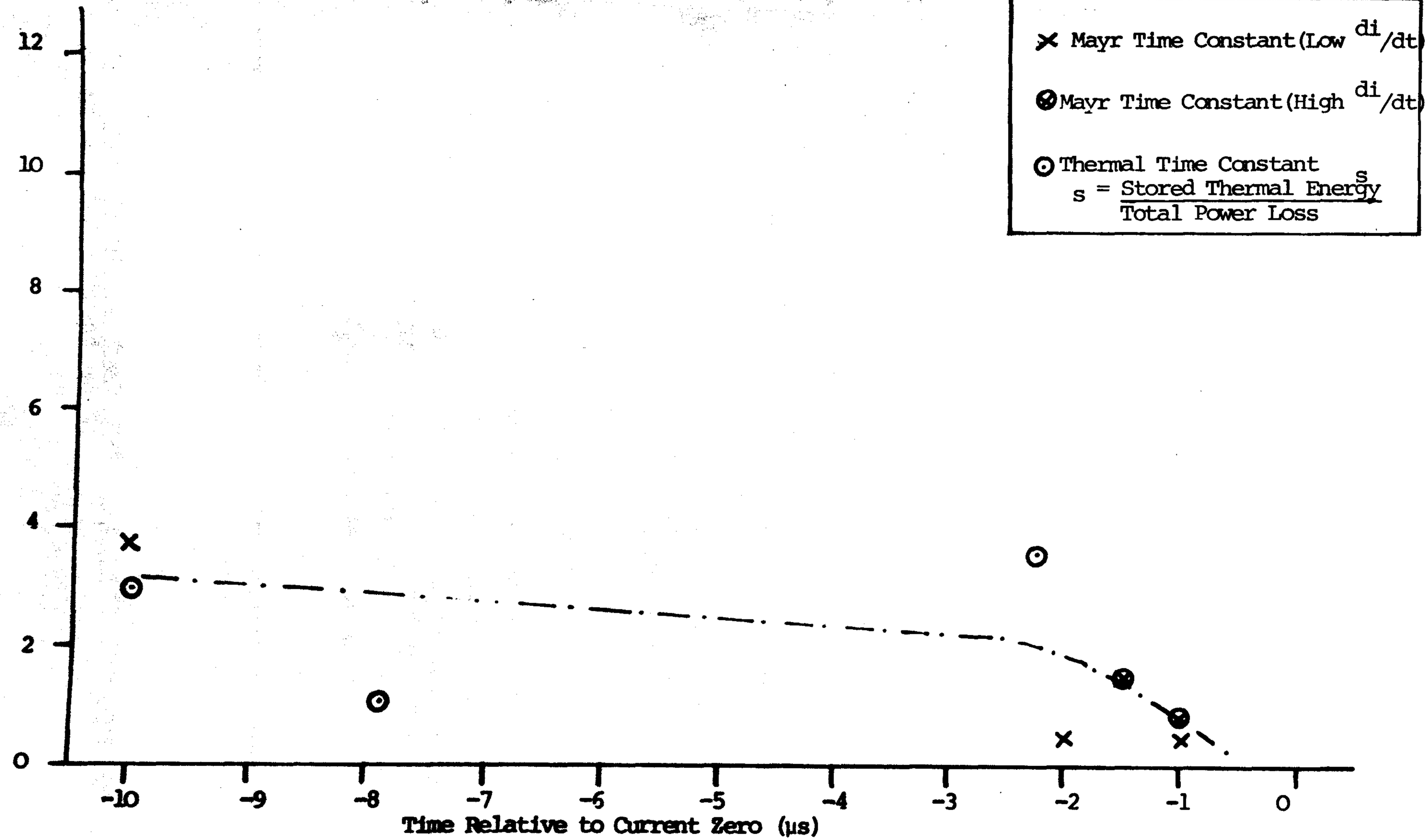

Fig. 8.5(c) The Mayr and Thermal Time Constant Variation over the Final 10μs of Current Decay

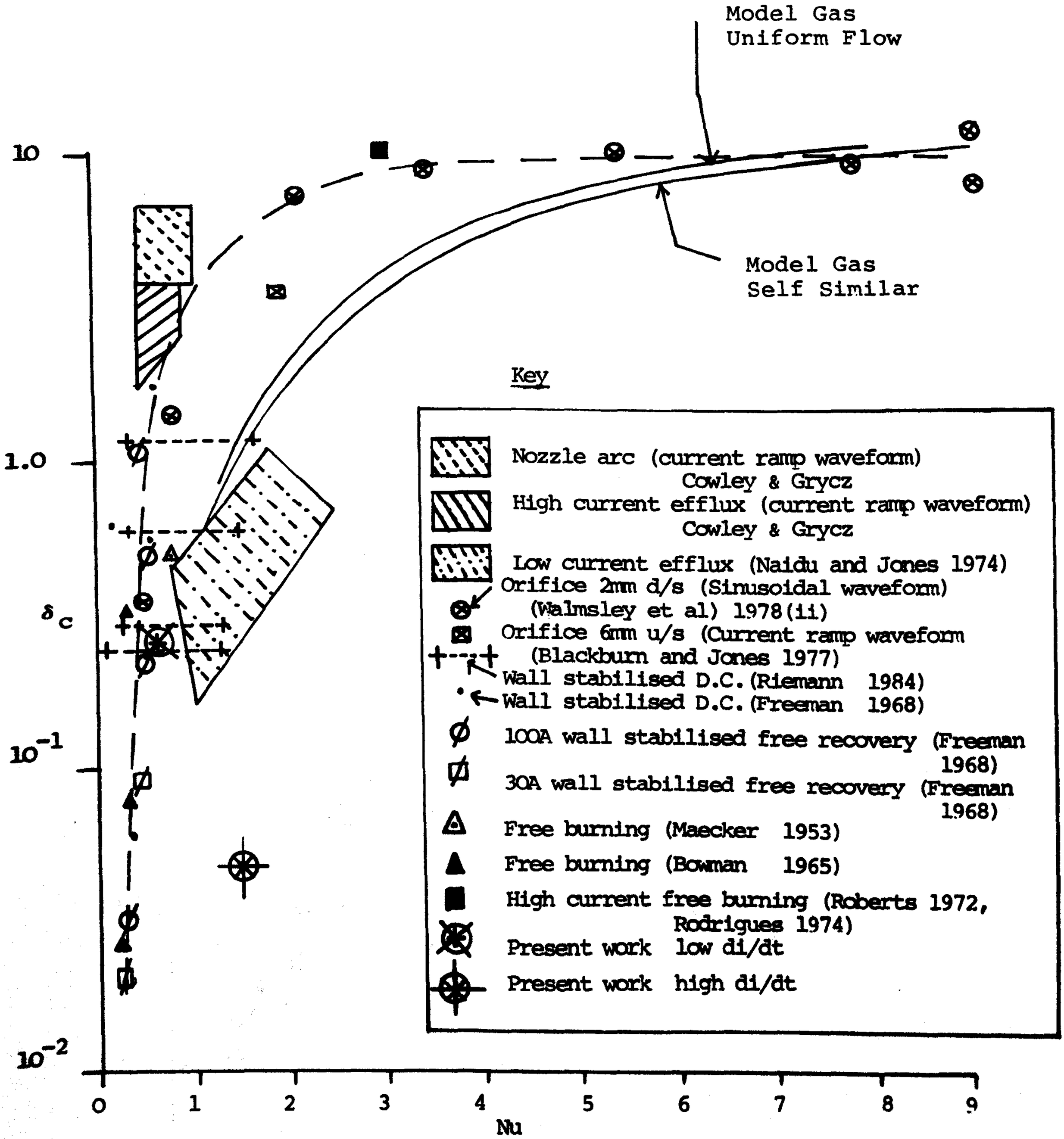

Fig. 8.6 The Overall Conductance Shape Factor (δ_c) Variation with Nusselt Number (Nu) for Different Arc Types

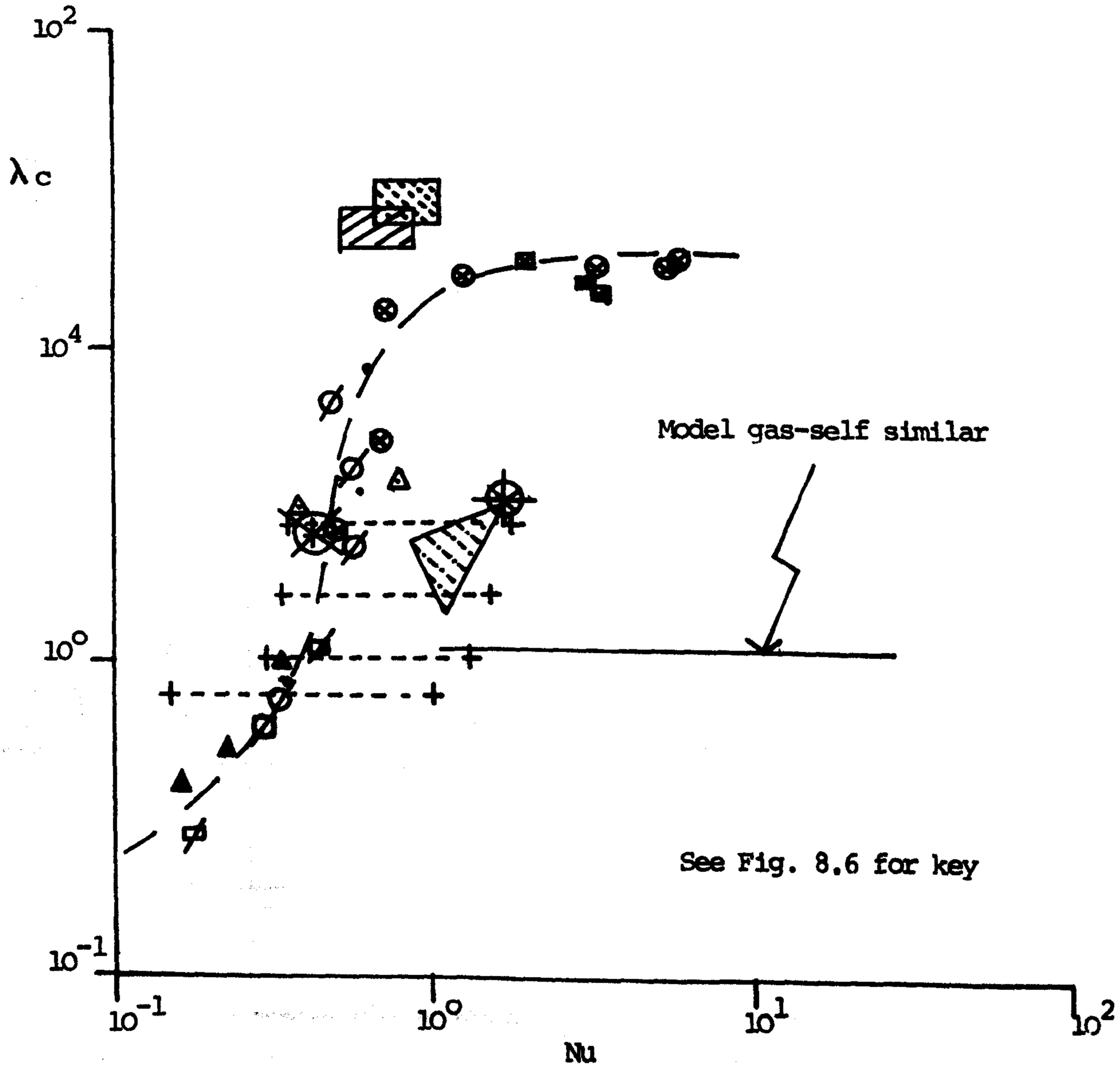

Fig. 8.7 The Core Conductance Shape Factor (λ_c) Variation with Nusselt Number (Nu) for Different Arc Types

Operating Conditions		
Time Before Current Zero	Exposure Time	di/dt
1.2μs	1.6μs	18A/μs

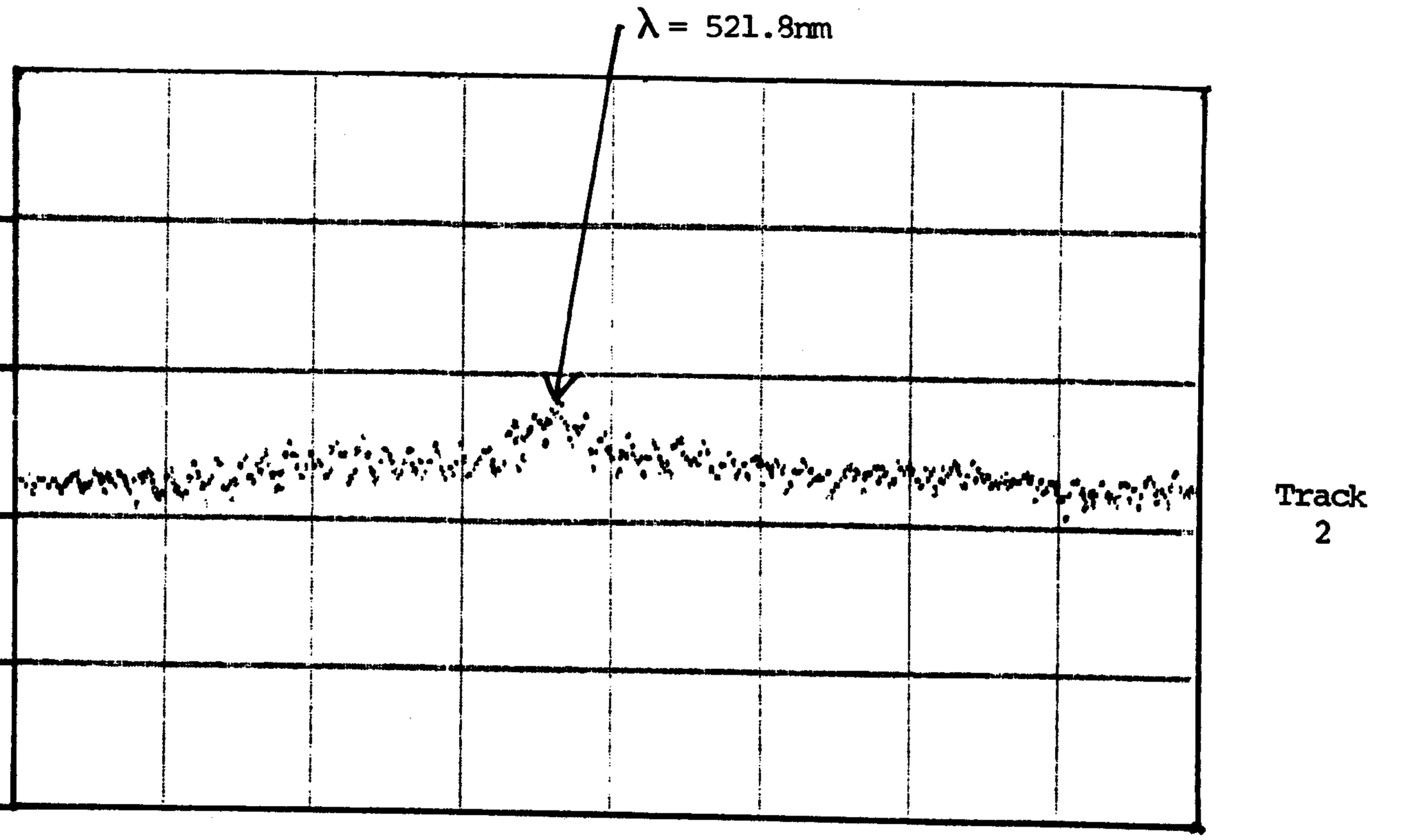

Fig. 8.8 The Radially Resolved Spectrum of the Arc Close to Current Zero

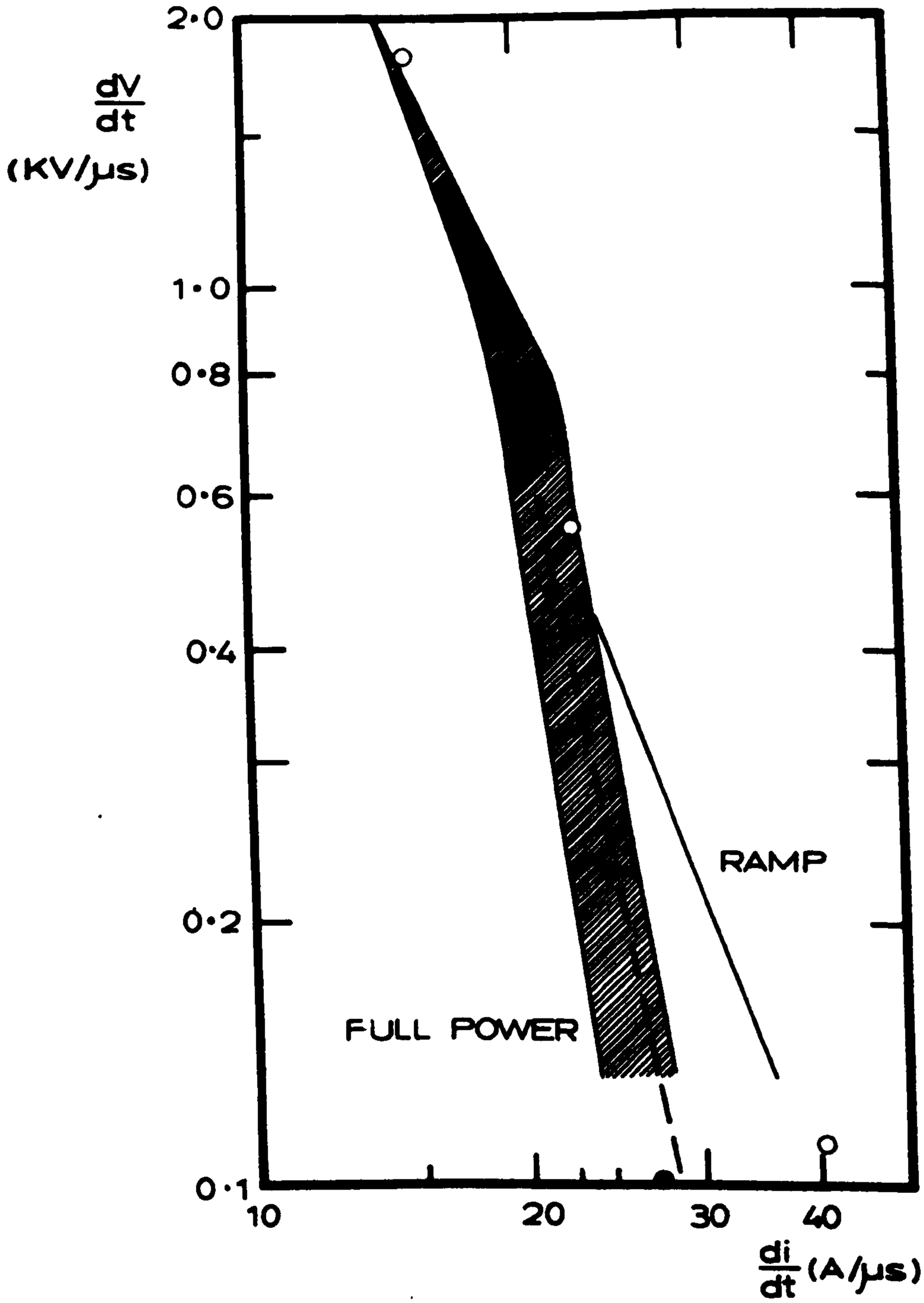

Fig. 8.9 PERFORMANCE OF INTERRUPTER UNDER FULL AND REDUCED POWER.

○ $RRRV = 4{\cdot}34 \times 10^{2} \left(\frac{di}{dt}\right)^{-1{\cdot}47} A_o^{-1{\cdot}25}$

● $RRRV = 1{\cdot}27 \times 10^{7} \left(\frac{di}{dt}\right)^{-4{\cdot}66} A_o^{-1{\cdot}25}$

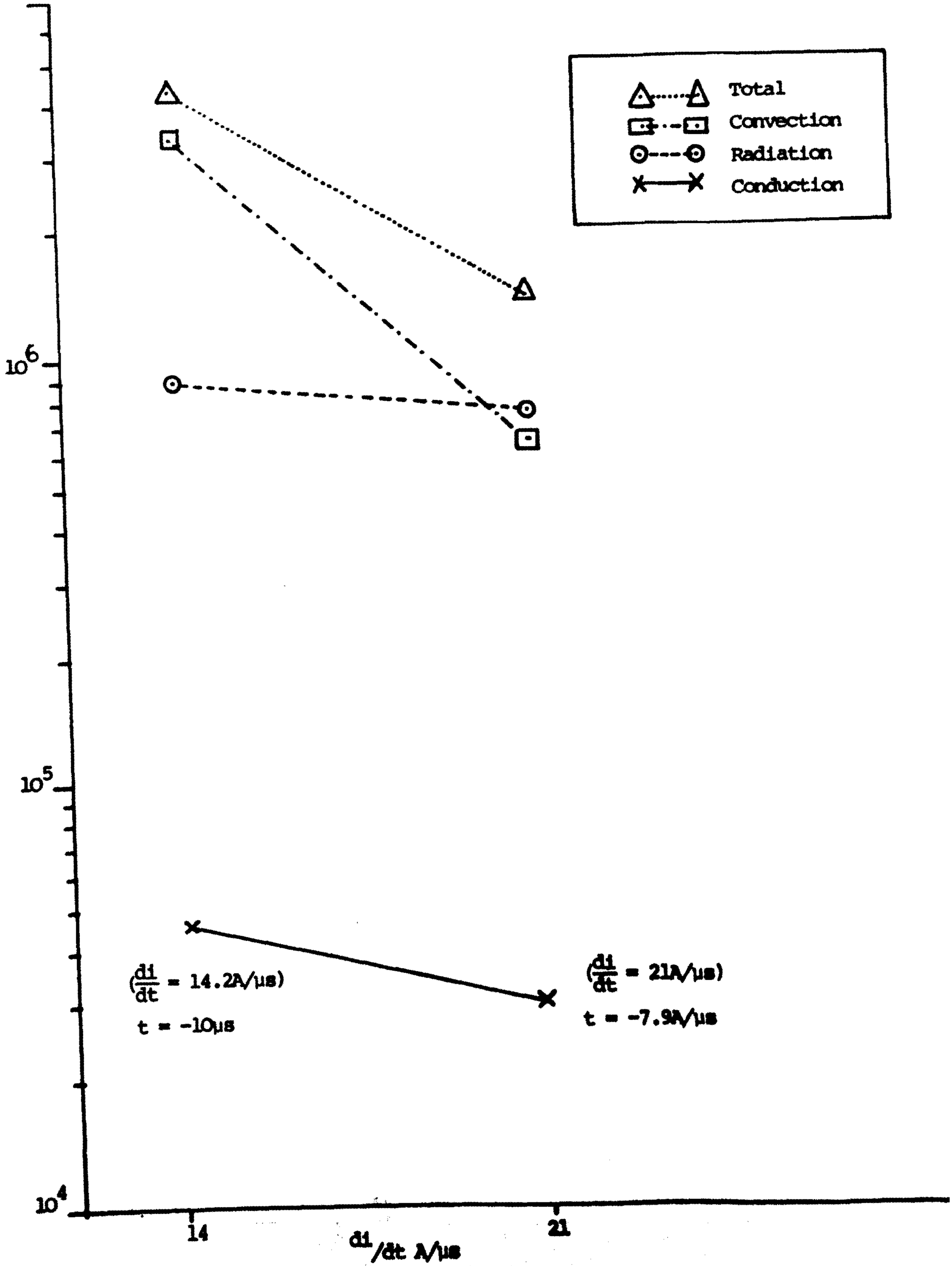

Fig. 8.10 Variation of the Power Loss Terms in the Core Power Balance with di/dt

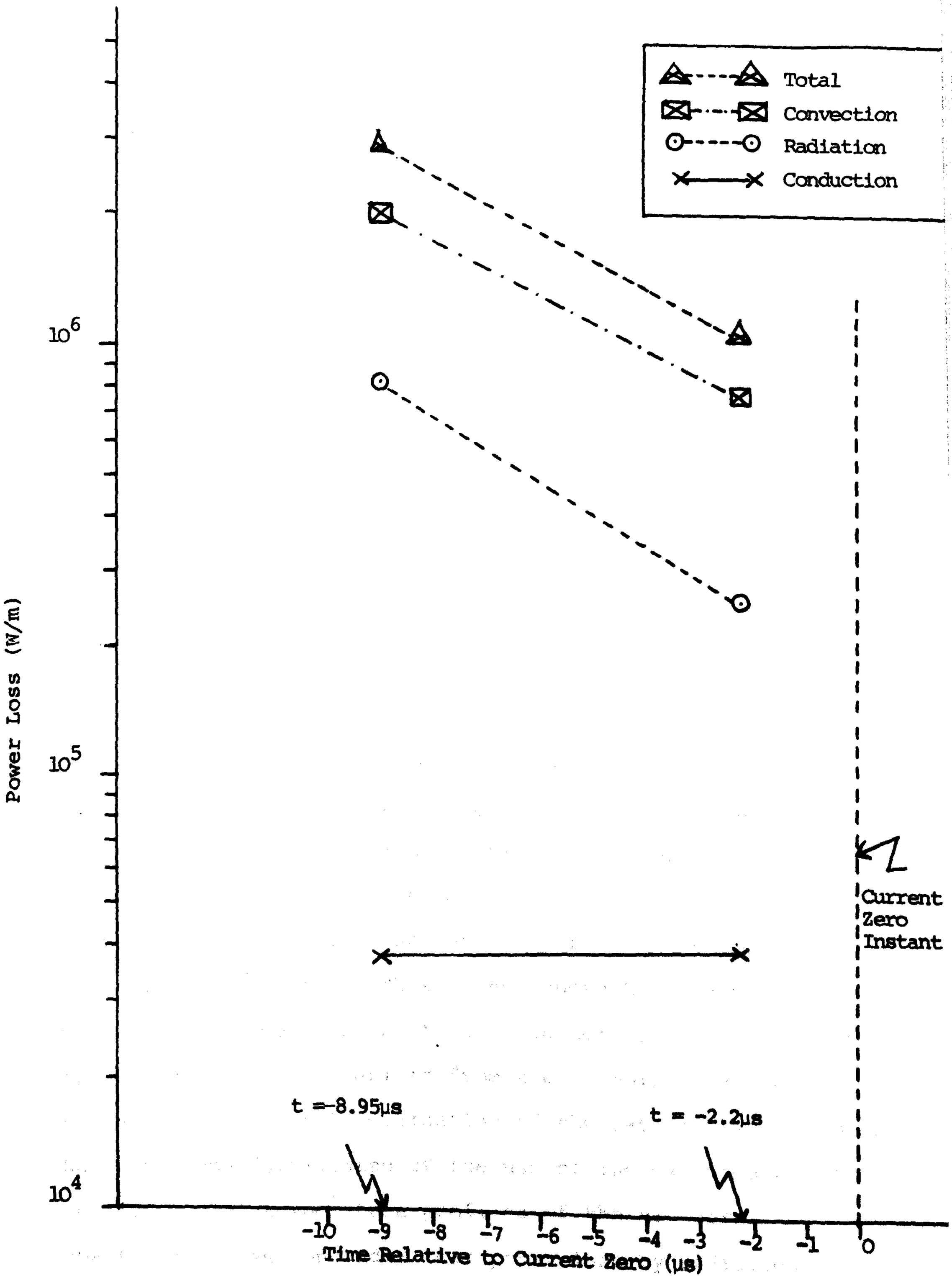

Fig. 8.11 Variation of the Power Loss Terms in the Core Power Balance with Time

CHAPTER 9

CONCLUDING DISCUSSION

The work presented is based primarily upon two fundamental optical diagnostic techniques but relies also upon simultaneous current, voltage and radiation power loss measurements. The two main diagnostic techniques, namely arc photography and spectroscopy have formed the basis of an investigation in which not only the thermal structure of the arc was observed, but also the establishment of criteria from which the thermal performance of a test circuit breaker could be predicted for a wide range of operating conditions.

The calculation of radial temperature profiles from the radially resolved spectra has allowed many quantitative aspects of the properties of the arc core during the current zero period of a full power arc to be investigated. These include an accurate evaluation of the Mayr arc time constants even within the highly transient one or two microseconds prior to current zero. These time constants have been compared with the results of other authors as well as thermal time constant values derived from the dynamic core power balance. The accurate evaluation of the latter power balance has also been facilitated by the use of the experimentally derived radial temperature profiles of the arc core. In chapter 8 it was concluded that power loss by radiation becomes increasingly significant with increasing $^{di}/_{dt}$

(fig. 8.10). This is consistent with an arc column whose thermal structure is different in the case of the higher current zero current decay rates. Also it has been shown that as current zero is approached, the power loss by conduction forms a proportionally more significant part of the total power loss than the other energy removal processes (convection, radiation) (fig. 8.11). This is indicative of an arc column which becomes progressively thinner as current zero is approached, the reduction in area having a profound effect on the convection power loss.

The experimental radial temperature profiles have also led to an accurate evaluation of the core conductance shape factors and an estimate of the overall conductance shape factors of the integral analysis. The above mentioned shape factors have also been correlated with the work of others and good agreement was observed, particularly in the case of the low $^{di}/_{dt}$ arcs.

A knowledge of the photographically measured arc column cross-sectional area during the current zero period has led to an empirical formula describing the thermal performance of the test circuit breaker, which distinguishes between the influence of various other factors. The results of the present investigation showed that in the case of the higher $^{di}/_{dt}$, under full power arcing conditions only, the thermal performance was characterised by an enhanced dependence upon influences other than the current zero instant cross-sectional area which was represented as an enhanced dependence upon

di/dt.

Thus the physical properties of a circuit breaker arc column during the crucial final few microseconds of current decay have been experimentally measured. Their influences upon the thermal structure, the dynamic power balance and interruptor performance have been accurately identified for a wide range of operating conditions.

The utilisation of the measurement techniques for investigating the post zero thermal and dielectric recovery regimes could further elucidate the performance limitations of power circuit breakers.

APPENDIX A1

THE TEMPERATURE LIMITS FOR LOW INTENSITY SPECTRA

In chapter 8 the temporal variation of the radially averaged arc temperatures during the current zero period was discussed. Conventional spectroscopic formulae could be applied to the cases where two spectral lines were simultaneously visible on the same record in order to determine the temperature. However in the cases where one or both spectral lines disappeared, which was evident for the records close to the current zero instant, particularly for low $^{di}/_{dt}$ values, these formulae were not applicable. In such cases the temperature was insufficiently high to record a spectral line. However special cases exist for which only one spectral line (namely the 510.5nm emission) remains visible whilst the 515.3nm is not. In such cases it is also not possible to apply the conventional spectroscopic formulations described in chapter 7. However it is possible to apply certain criteria which enable upper and lower limits of the radially averaged temperature to be determined.

When the 510.5nm emission is visible and 515.3nm is not, then the upper limit of the radially averaged arc temperature is determined by the ratio of the 510.5nm intensity to the value of noise on the record. This ratio, when substituted into equation 7.2, yields a maximum value of the radially averaged temperature. However a more accurate value of the maximum value of the average temperature would be obtained if a record was available on which both the 515.3nm and the 510.5nm were visible, and the 510.5nm intensity was reasonably high but the 515.3nm emission was just visible above the noise.

This was so in the case of fig. A.1.1 (iii). The two line intensities were measured and processed using the software of appendix 2. The temperature in this case was found to be about 6,000K. This therefore corresponds to a maximum temperature below which at least one spectral line would disappear from view.

A minimum value of temperature can be determined from the observation of the particular record in question. If the 510.5nm line only is visible in such a case, then the temperature must be lower than 6,000K. If the intensity of the 510.5nm line forms some fraction of the intensity of the case of the corresponding 510.5nm line on fig. A.1.1 (iii), then one of the following extreme cases has occurred:

(i) The temperature on that record is the same as that of fig. A.1.1 (iii) and that the spectral light intensity is generally lower for some reason

or

(ii) The change in intensity of the 510.5nm spectral line is entirely due to a temperature change and the 515.3nm emission has consequently disappeared (fig. 7.4).

The temperature obtained from the latter case corresponds to the minimum.

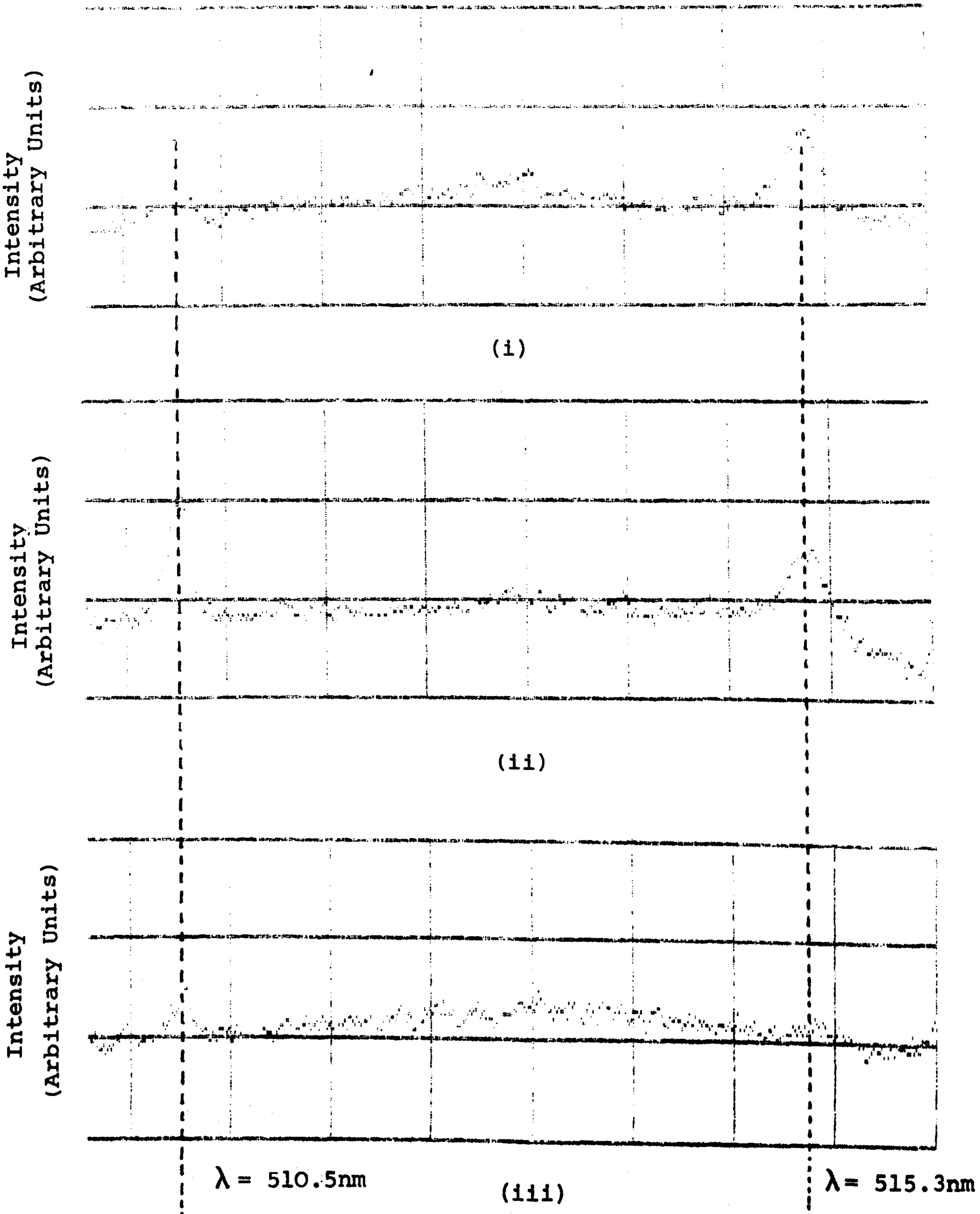

Operating Conditions
Time Before Current Zero =1.6μs
di/dt = 20 A/μs
Exposure Time =1.6 μs

Horizontal scale 0.76nm

Fig. A.1.1 Sample Spectrum for Determination of the Maximum Arc Temperature Close to Current Zero

APPENDIX A.2

COMPUTER PROGRAMS

In this section it is intended to present some of the software which has been developed and used to interpret the spectral test data. The programs uses have been divided into two categories. Firstly, the software designed to convert the spectral data into radially averaged temperature and half-line widths (for electron density measurement) is presented. Also additional software is presented which deals with the calculation of theoretical spectral line intensities. A second category includes the software which was used to interpret the radially resolved data and convert it to a deconvoluted radial intensity profile which can be used to calculate the radial temperature profiles (chapter 7).

Fig. A.2.1 shows the overall program structure for the interpretation of data into radially averaged temperatures and further calculation of the theoretical line intensity and optical depth. The following programs were developed to implement the above task.

(1) OSPLT 3

The spectral data was input from the OSA 500 in the form of data files, one per arc test. The software in this program is designed to log the above data onto disc and display it on the VDU for dumping onto a printer etc.

(2) OSADAT 2

This program was developed so that the above files may

be interrogated. The program calculates the spectral line intensity above the continuum level between two specified wavelength limits. The width of the spectral line at half intensity is also calculated. This task can be performed a number of times per file to facilitate the possibility of a record containing more than one spectral line.

(3) TEMPEST

This program was used to calculate the radially averaged arc temperature using the data from DATA INT and the formula of equation 7 .

(4) DEPTH 2

This program uses the data from DATA INT as well as theoretical data from another program (LOADER) to calculate the theoretical spectral line intensity and the critical optical depth (equation 7.12) for a range of temperatures between 6,000K and 12,000K. This data is shown in figures 7.4 and 7.2 respectively.

Interpretation of the Radially Resolved Spectrum

The listing of the program to calculate the Abel inverted intensity profile from the continuous (photographic) image is shown at the end of this appendix and is labelled 'ABEL'.

A program has been developed which generates a set of predicted radial intensity histograms for a known (parabolic) radial emissivity profile. These intensity histograms are designed to coincide with those measured on the OSA 500 system. The program which performs this task is called 'IDISP 2' whose flow diagram is shown on fig. A.2.2.

In 'IDISP 2' two arrays are formed initially, namely Iy and AM; a further array A is also formed. The array Iy corresponds to a number of individual integrated emissivity values along a given line of sight at a radial displacement y from the arc centre (fig. 7.3(a)). Thus each y displacement has its corresponding value of Iy. The values of Iy are calculated in 'Proc icalc' in the program at an interval of dY per batch of 10 x dY. The latter batch of 10dY are then radially integrated in 'Proc simp' (Simpson's rule) and a value A(M) is assigned to the corresponding integral. The program can generate up to 25 such values of A(M), therefore the step length dy can form $^{1}/_{250}$ of R, the radius.

Having obtained a number of radial values of the integrated intensity (A(M)) the arc diameter is divided into five strips corresponding to the viewing tracks (chapter 4). Thus the integrated intensity values (A(M)) are allocated to the corresponding strip and superimposed within that strip to give rise to an integrated value of intensity for the strip (AM(N)). 'IDISP 2' also has the facility of calculating such radial histograms for a number of different arc displacements with respect to the central viewing axis through the procedure 'proc disp'.

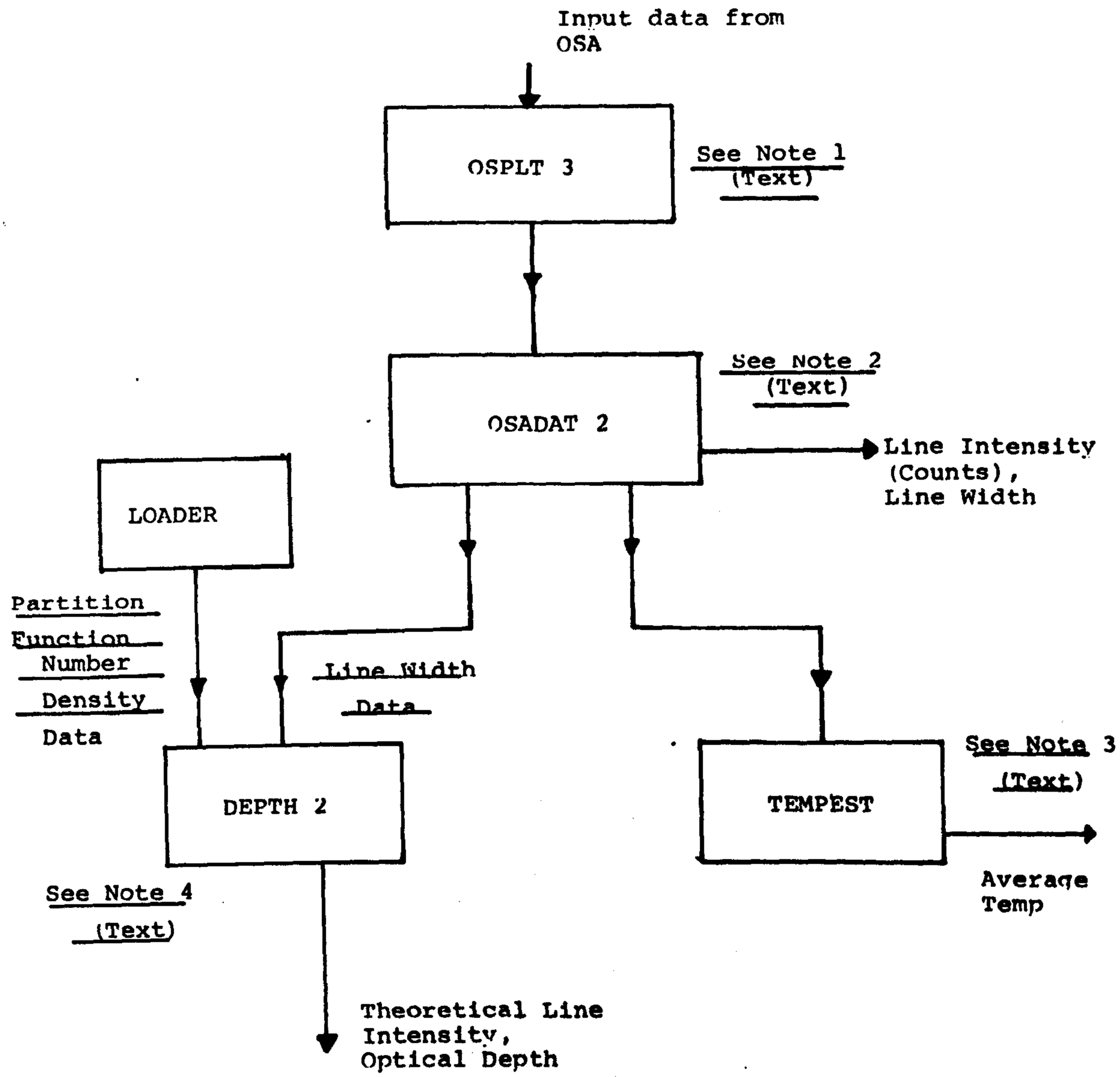

Fig. A.2.1 Program Structure for Interpretation of Data into Radially Averaged Temperature and Evaluation of Theoretical Line Intensity and Optical Depth

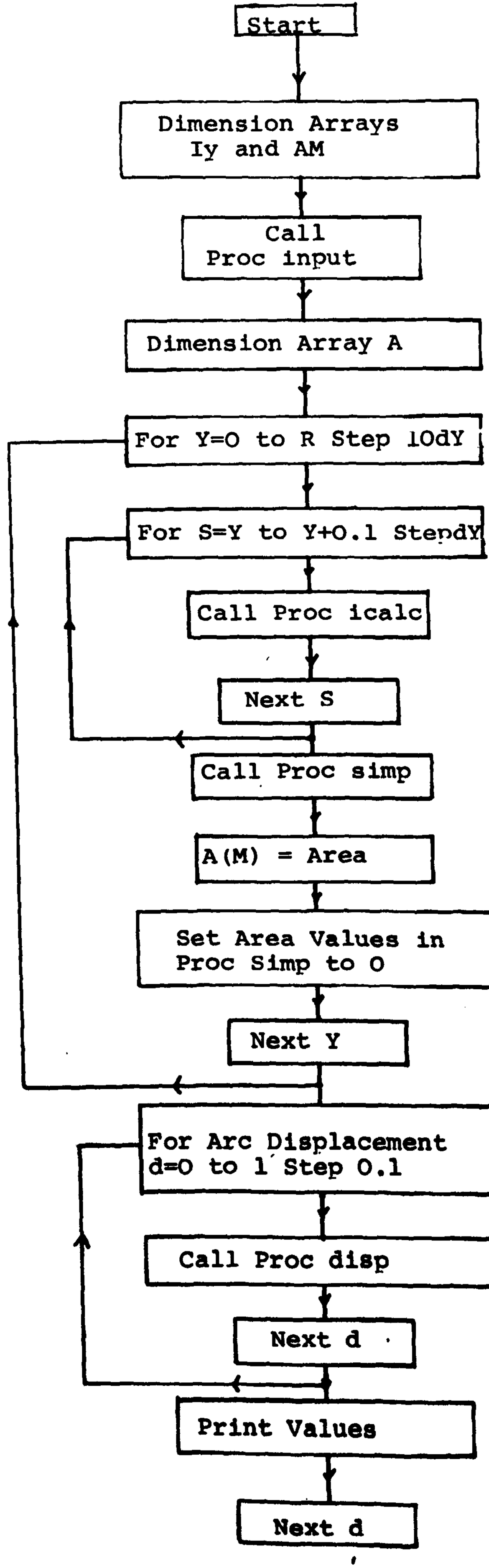

Fig. A.2.2 The Flow Diagram of the Program 'IDISP 2'

OSPLT 3

```
 10 REM PLOT ROUTINE FOR OSA Data   23-Feb-84
 20
 30 MODE0
 40 PROCline(0.0,1023,0)        :REM draw X axis
 50 PROCline(25,0,25,825)        :REM draw Y axis
 70
 90
 91 label$ = "counts"
 92 PROCvertlabel(78,15,label$)
100 label$ ="wavelength (nm)"
101 PROChorizlabel(25,4,label$)
110   VDU30                :REM cursor home
120   PROCerase line
125 PROCplot
130 PROCinput
135 PROCgrid
140
150 PROCprint
180 END
190
200 DEF PROCplot
210   LOCAL I,X%,Y%
220   INPUT "Filename ? " file$
230   F% = OPENIN (file$)
240   PROCerase line
250   REPEAT
260      PTR# F% = 0
270      VDU 31,22,0                              :REM move text cursor
280      INPUT "Scale Factor = " S
290      FOR I=1 TO 499
300         INPUT# F%,Y%
310         Y%=Y%*S
320         X%=I*2+25
330         PLOT 69,X%,Y%
340      NEXT I
350      PROCerase line
355 CLOSE#F%
370
380 ENDPROC
400 DEF PROCline(Sx,Sy,Fx,Fy)
410   MOVE Sx,Sy
420   DRAW Fx,Fy
430 ENDPROC
440
450 DEF PROCgrid
460   LOCAL I
470   FOR I = 25 TO 1050 STEP 100
480      PROCline(I,0,I,850)
485      PROChorizcal(I,L)
487      L=L+.7 : REM INCREMENT L FOR PROC horizcal
490   NEXT I
500
510   FOR I = 0 TO 825 STEP 100
520      PROCline(25,I,1023,I)
525      PROCcal (I)
530   NEXT I
540 ENDPROC
550
560 DEF PROCvertlabel(x%,y%,label$)
```

```
570    LOCAL i%,line%
580    line%=42
590    FOR i% = 1 TO LEN(label$)
600       IF i%+y% <= line% THEN PRINT TAB(x%,i%+y%-1);MID$(label$,i%,1)
610    NEXT i%
620 ENDPROC
630
640 DEF PROChorizlabel(x%,y%,label$)
650    PRINT TAB(x%,y%);label$
660 ENDPROC
670
680 DEF PROCerase line
690    VDU 31,60,0
700    FOR I=60 TO 1 STEP -1:VDU 127:NEXT I
710 ENDPROC
720
730 DEF PROCprint
731 VDU30
740IF ANS$="Y" THEN CHAIN"DUMP0"
750 ENDPROC
770 DEF PROCcal(I)
790 X=I/S
800 MOVE 1100,I+25
805 VDU 5
810 PRINT;X
830 ENDPROC
850 DEF PROChorizcal(I,L)
860 MOVE I-25,850
870 VDU5
880 PRINT;L-3.5
890ENDPROC
950 DEF PROCinput
960 VDU 31,22,0
970 INPUT "Centre Wavelenth = " L
980 PROCerase line
990 INPUT "Do you want a printout at the end of this program ?" ANS$
1000 PROCerase line
1010 VDU 30
1110 INPUT "Io - "t0
1120 PROCerase line
1130 INPUT "  dI/dt = "D
1140 PROCerase line
1150 INPUT"  Tgate ="Tg
1155 PROCerase line
1160 PRINT TAB(2,2);"Io - ";t0;" micS","  dI/dt = ";D;"A/micS","  Igate =";Ig;"
micS"
1165 PRINT TAB(2,1);"filename$ ";file$
1170 VDU30
1180 ENDPROC
>
```

OSADAT 2

```
  50 MODE7
 100 DIM I%(500)    :      DIM A%(500)
 110 CLS
 150 PRINT"FIRST CHOOSE VALUES OF INTENSITY BELOW AND ABOVE WHICH ANY OTHER REC
ORDED VALUES WILL BE IGNORED"
 200 INPUT"THE CHOSEN UPPER THRESHOLD VALUE IS  "Q1%
 250 INPUT"THE CHOSEN LOWER THRESHOLD VALUE IS  "Q0%
 300 PRINT"NOW CHOOSE THE INITIAL CHANNEL (WAVELENTH) LIMITS FOR THE INITIAL RE
GIUN OF INTEREST . NOTE OTHER REGIONS MAY BE SELECTED LATER "
 350 INPUT"THE CHOSEN LOWER WAVELENTH LIMIT  "L0%
 400 INPUT"THE CHOSEN UPPER WAVELENTH LIMIT  "L1%
 420 INPUT"THE CHOSEN LOWER CHANNEL LIMIT FOR CONTINUUM LEVEL ESTIMATION "X0%
 440 INPUT"THE CHOSEN UPPER CHANNEL LIMIT FOR CONTINUUM LEVEL ESTIMATION "X1%
 445 INPUT"THE CENTRE WAVELENGTH "LAMBDA
 450 INPUT"TIME BEFORE CURRENT ZERO "I0
 460 INPUT"dI/dT"DI
 470 INPUT"Tgate"Tgate
 480 INPUT"filename  "file$
 490 PRINT''''''
 500 MODE7:VDU 14
 520 PROCdatain
 850 C1%=1       : REM SET INITIAL VALUE OF Q
 855 J = 0  : J1 = 0  : REM J AND J1          ARE ARBITRARY COUNTERS
 860 IL = 0 :IR = 0
 870    PROCcontinuum
 900 FOR I = L0% TO L1%
 950   PROCpeakdetect
1000 NEXT I
1010 FOR I = L0% TO L1%
1020   PROClinewidth
1030 NEXT I
1050 PROCprint
1060 W = (INT(LAVR)-INT(LAVL))*4.8/310
1100 END
1150 DEFPROCpeakdetect
1200   C%=A%(I)
1300   IF C%<Q0% OR C%>Q1% THEN GOTO1450    : REM SPECIFY RANGE
1350     IF C% > C1% THEN CMAX% = C%     :     LC%=I%(I)
1400    C1%  = CMAX%
1450 ENDPROC
2000 DEFPROCdatain
2010 F%=OPENIN (file$)
2020 FOR I = 1 TO 499
2030 INPUT# F%,A%
2040 I%(I) = I    :     A%(I) = A%
2050 NEXT I
2060 CLOSE# F%
2070 ENDPROC
3000 DEFPROCcontinuum
3005 SUM = 0
3010 FOR I = X0% TO X1%
3020   SUM% = SUM% + A%(I)
3030 NEXT I
3040 CONT% = SUM%/(X1%-X0%)
3050 ENDPROC
3500 DEFPROClinewidth
3510 Y = A%(I) - CONT%
3520 IF(Y-(CMAX%-CONT%)/2) > 20 OR (Y-(CMAX%-CONT%)/2) < -20 THEN GOTO 3600
3540 PROClhs
```

```
3550 PROCrhs
3600 ENDPROC
4000 DEFPROClhs
4005 IF I > LC% THEN GOTO 4040
4020 J = J + 1  :    IL = IL + I
4030 LAVL = IL/J
4040 ENDPROC
4500 DEFPROCrhs
4505 IF I < LC% THEN GOTO 4540
4520 J1 = J1 + 1  :  IR = IR + I
4530 LAVR = IR/J1
4540 ENDPROC
5000 DEFPROCprint
5005 VDU2
5010 PRINT"filename = ";file$
5015PRINT
5020 PRINT"TIME BEFORE CURRENT ZERO = ";I0;" micS"
5025 PRINT
5030 PRINT"dI/dt =";DI;" Amps/micS"
5035 PRINT
5040 PRINT"Tgate =";Tgate;" micS"
5045 PRINT
5060 PRINT"CENTRE WAVELENGTH = ";LAMBDA;" nm"
5065 PRINT''
5070 W = (INT(LAVR)-INT(LAVL))*4.8/310
5080 @% = &00310
5090 PRINT"PEAK LINE INTENSITY = ";(CMAX%-CONT%);" COUNTS"
5095 PRINT
5100 PRINT"LINE WIDTH = ";W;" nm"
5150 PRINT ''''''''
5170 VDU3
5200 ENDPROC
>
```

TEMPEST

```
 10 INPUT"UPPER ENERGY LEVEL FOR I1 IN eV    " E1
 20 INPUT"UPPER ENERGY LEVEL FOR I2 IN eV    " E2
 30 INPUT"LINE INTENSITY 1   "I1
 40 INPUT"LINE INTENSITY 2   "I2
 50 INPUT"LINE CENTRE WAVELENGTH 1   "L1
 60 INPUT"LINE CENTRE WAVELENGTH 2   "L2
 70 INPUT"STATISTICAL WEIGHT OF UPPER ENERGY LEVEL OF LINE 1   "GM1
 80 INPUT"STATISTICAL WEIGHT OF UPPER ENERGY LEVEL OF LINE 2   "GM2
 90 INPUT"TRANSITION PROBABILITY FOR LINE 1   "AMN1
100 INPUT"TRANSITION PROBABILITY FOR LINE 2   "AMN2
110 K = 1.38E-23
200 REM NOW CALCULATE THE ARC TEMPERATURE USING THE FOLLOWING EQUATION
210    T = ((E2-E1)/K)*1.6E-19/LN((I1/I2)*(L1/L2)*(GM2*AMN2)/(GM1*AMN1))
220 PRINT T
>
```

DEPTH 2

```
L.
    5 MODE7  :    @% = &10410
   10 REM PROGRAM TO CALCULATE THE THEORETICAL LINE INTENSITY AND CRITICAL
      OPTICAL DEPTH FOR A KNOWN TEMPERATURE AND PARTICLE DENSITY
   20 REM FIRST INPUT NECASSARY SPECTRAL DATA
   30 PROCinput
   40 PROCcalc
   50 PROCoutput
 1000 END
 2000 DEFPROCinput
 2010  DIM A(7) : DIM G(7) : DIM EM(7) : DIM EMN(7) : DIM L(7) : DIM DL(7)
 2015  DIM T(128) : DIM Imn(128) : DIM D(128)
 2020     FOR N = 0 TO 6
 2030       READ A(N)
 2080     NEXT N
 2100     FOR N = 0 TO 6
 2110       READ G(N)
 2120     NEXT N
 2150     FOR N = 0 TO 6
 2160       READ EM(N)
 2170     NEXT N
 2200     FOR N = 0 TO 6
 2210       READ EMN(N)
 2220     NEXTN
 2250     FOR N = 0 TO 6
 2260       READ L(N)
 2270     NEXT N
 2280     FOR N = 0 TO 6
 2290       READ DL(N)
 2295     NEXT N
 2300 REM INPUT THE RELEVANT CONSTANTS
 2310    C1 = 1.1909E-12 : C2 = 1.4380          : C = 2.998E10
 2320 Ne = 6E17  : REM THE AVERAGE                              ELECTRON DENSITY
 2330 h = 4.136E-15 * 1.602E-19      :    K = 8.617E-5
 2340 CLS
 2350 INPUT" INPUT THE ARRAY INDEX NUMBER "X
 2500  DATA 7.5E7,6.04E7,0.20E7,0.165E7,0.024E7,1.07E7,3.8E7
 2510  DATA 6,4,4,2,4,8,8
 2520  DATA 6.19,6.19,3.82,3.79,3.82,7.74,7.74
 2530  DATA 2.37,2.40,2.43,2.15,2.18,2.35,2.67
 2540  DATA 521.8,515.3,510.5,578.2,570.0,529.2,465.1
 2550  DATA 0.415,0.458,0.166,0.217,0.217,0.759,0.217
 2600 ENDPROC
 3000 DEFPROCcalc
 3010 LOCAL I
 3020 CLS
 3030 INPUT"THE FILENAME FOR THE PARTITION FUNCTION DATA"file$
 3040 F = OPENIN(file$)
 3050 FOR I = 0 TO 128
 3060 INPUT# F,T,ZT,ST,NZ
 3065 PRINT T; ZT; ST; NZ
 3070 PROCformulae
 3075 T(I)=T : Imn(I)=Imn : D(I)=D
 3200 NEXT I
 3210 CLOSE# F
 3250 ENDPROC
 4000 DEFPROCformulae
 4050 IC = ((1/(4*PI))*NZ*G(X)*A(X)*(1/ZT)*h*C*(1/(L(X)*1E-7)))
 4060 Imn = (IC)*(EXP(-EM(X)/(K*T)))
 4100 B = (C1/(L(X)*1E-7)^5)/(EXP(C2/(L(X)*T*1E-7))-1)
```

```
4200 A = A(X)*G(X)*(EMN(X)*1.6E-19)*EXP(-(EM(X))/(K*T))
4300 D = 24*PI*ZT*(DL(X)*1E-7)*B/(NZ*A)
4400 ENDPROC
5000 DEFPROCoutput
5100 LOCAL I
5200 INPUT"THE OUTPUT FILENAME "file1$
5300 A = OPENOUT(file1$)
5350 VDU2
5400 FOR I = 0 TO 128
5500 PRINT# A,T(I),Imn(I),D(I)
5600 PRINT;  T(I);  Imn(I);  D(I)
5700 NEXT I
5720 PRINT# A,L(X)
5725 PRINT'
5730 PRINT"LAMBDA = ";L(X)
5800 CLOSE# A
5850 VDU3
5900 ENDPROC
>
```

LOADER

```
  50 @% = &10410
 100 MODE3
 200 DIM N(33)
 300 DIM T(15)
 400 DIM Z(15)
 500 EI = 7.724      :         K =  8.617E-5
 600 INPUT "EXI, THE REDUCTION IN IONIZATION POTENTIAL = "EXI
 700 EX = EI - EXI
 800 @% = &10410
 900 A = OPENOUT ("ZSNDATA")
1000 FOR J = 0 TO 15
1100 READ T(J)
1200 NEXT J
1300 J = 0
1400 FOR J = 0 TO 15
1500 READ Z(J)
1600 NEXTJ
1700 J = 0
1800 FOR J = 0 TO 15
1900 NEXT J
2000 J = 0
2010 FOR J = 0 TO 33
2020 READ N(J)
2030 NEXT J
2040 PROCncalc
2100 N=15   :    X=0
2200 DIM M(N) : DIM C(N)
2300 FOR J= 0 TO 14
2400 M(J) = ( Z(J+1) - Z(J) ) / ( T(J+1) - T(J) )
2500 C(J) = 0.5*(Z(J) + Z(J+1) - M(J)*(T(J) + T(J+1)))
2600 PROCzcalc
2700 NEXT J
2800 CLOSE# A
2900 END
3000 DEFPROCzcalc
3100 TI = (INT(T(J)/50))*50 + 50
3200 FOR T1 = TI TO (T(J+1)) STEP 50
3300    ZT = M(J)*T1 + C(J)
3400 ST = 2.4125E15 * T1^1.5 * (EXP(-EX/(K*T1)))
3500 PROCdataout
3550 X = X+1
3600 NEXT T1
3700 ENDPROC
3800 DEFPROCdataout
3900 PRINT# A,T1,ZT,ST,NT(X)
4000 PRINT T1,ZT,ST,NT(X)
4100 ENDPROC
4200 DEFPROCdatain
4300 INPUT# A,T1,ZT
4400 PRINT T1,ZT
4500 ENDPROC
5000 DEFPROCncalc
5010 LOCAL T,J
5011 RESTORE 9000
5012 FOR J = 0 TO 33
5014 READ N(J)
5015 NEXT J
5020 DIM MN(33) : DIM CN(33) :  DIM NT(128)   : T = 6000
5030 FOR J = 0 TO 32
```

```
5040 MN(J) = (N(J+1) - N(J))/(200)
5050 CN(J) = 0.5*(N(J) + N(J+1) - MN(J)*(2*T +200))
5060 T = T + 200
5070 NEXT J
5080 T = 6000  :  X = 0
5090 FOR J = 0 TO 31
5100 FOR Q = 1 TO 4
5110 NT(X) = (MN(J)*T + CN(J))*1E18
5120 T = T + 50  :  X = X+1
5130 NEXT Q
5140 NEXT J
5141 NT(X) = (MN(J)*T + CN(J))*1E18
5150 ENDPROC
8000 DATA 5986,6285,6599,6929,7276,7640,8022,8423,8844,9286,9750,10238,10750,
          11287,11852,12444
8500 DATA 2.579,2.665,2.761,2.866,2.981,3.108,3.248,3.401,3.570,3.757,3.963,
          4.193,4.449,4.733,5.051,5.406
9000 DATA 1.6,1.55,1.48,1.4,1.3,1.25,1.2,1.13,1.08,1.0,0.96,0.90,0.85,0.8,0.75,
0.7,0.65,0.58,0.54,0.50,0.45,0.41,0.38,0.34,0.30,0.27,0.24,0.22,0.19,0.17,0.15,0
.13,0.115,0.10
>
```

Loop 2

L.

```
   10 REM PROGRAM TO CALCULATE THE OBSERVED INTENSITY FROM A KNOWN RADIAL EMISSI
VITY PROFILE
   30 MODE3
   40   DIM Iv(10)   :   DIM AM(4)
  110 PROCinput
  120  DIM A(25)
  210 M = 0
  410 FOR Y = 0 TO (R - 0.0001) STEP 10*dY
  420 M = ((Y+0.0001)*10) DIV 1
  425 U = Y
  430 FOR S = U  TO M/10 + 0.1001 STEP dY
  440  PROCicalc(Y,Y+10*dY,S)
  450 NEXT S
  460  PROCsimp(Y,Y+10*dY)
  470 A(M) = AREA
  478 AREA1 = 0    :     AREA2 = 0    :    AREA3 = 0
  480 NEXT Y
  482 FOR d = 0 TO 1.0 STEP 0.1
  485 PROCdisp
  490 NEXT d
  905 VDU7
  910 VDU3      :     VDU30
 1010 END
 1110 DEF PROCinput
 1210 INPUT" THE LINE SEPARATION IN mm dY = "dY
 1310 INPUT" THE ARC RADIUS R = "R
 1610 INPUT" THE MAXIMUM EMISSIVITY e0 = "e0
 1710 PRINT''''
 1750 AREA1 = 0    :     AREA2 = 0    :    AREA3 = 0
 1810 ENDPROC
 1910 DEF PROCicalc(Y1,Y2,Y)
 1920 L = (100*(S-U+0.001)) DIV 1
 1940 IF Y = 0 THEN GOTO 2650
 1950 IF Y = R OR Y > R THEN GOTO 2650
 2010  I1 = FNRY
 2110  I3 = (R^2*FNRY/2 + (R*Y^2)*FNCOSH/2)
 2210  I4 = (Y^2*R*FNCOSH - Y^2*FNRY)/2
 2310  I5 = (FNRY)^3/3
 2320  Iy = 2*e0*I1 - (e0*2/R^2)*(I3 - (I4 - I5))
 2330  Iy(L) = Iy
 2510 DEF FNRY = (R^2 - Y^2)^0.5
 2610 DEF FNCOSH = (LN((R/Y) + ((R/Y)^2 - 1)^.5))
 2650 ENDPROC
 2700 DEFPROCsimp(Y1,Y2)
 2705 N = (Y2-Y1)/dY
 2710 IF Y = 0 THEN Iy(0) = Iy(1)
 2720 AREA1 = ((Y2 -Y1)/(3*N))*(Iy(0) + Iy(10))
 2730 AREA2 = ((Y2 -Y1)/(3*N))*2*(Iy(2) + Iy(4) + Iy(6) + Iy(8))
 2740 AREA3 = ((Y2 -Y1)/(3*N))*4*(Iy(1) + Iy(3) + Iy(5) + Iy(7) + Iy(9))
 2850  AREA = AREA1 + AREA2 + AREA3
 2860 ENDPROC
 3000 DEF PROCdisp
 3010  ON (d*10 + 1) GOTO 3050,3150,3250,3350,3450,3550,3650,3750,3850,3950,4050
 3050     AM(0) = 2*(A(0)+A(1)+A(2)+A(3)+A(4))
 3060     AM(1) = (A(5)+A(6)+A(7)+A(8)+A(9)+A(10)+A(11)+A(12)+A(13)+A(14))
 3070     AM(2) = (A(15)+A(16)+A(17)+A(18)+A(19)+A(20)+A(21)+A(22)+A(23)+A(24))
 3080     AM(3) = AM(1)
 3090      AM(4) = AM(2)
 3100    GOTO 5000
```

```
3150      AM(0) = A(5) + 2*(A(3)+A(2)+A(1)+A(0)) + A(4)
3160      AM(1) = (A(6)+A(7)+A(8)+A(9)+A(10)+A(11)+A(12)+A(13)+A(14)+A(15))
3170      AM(2) = (A(16)+A(17)+A(18)+A(19)+A(20)+A(21)+A(22)+A(23)+A(24))
3180      AM(3) = (A(4)+A(5)+A(6)+A(7)+A(8)+A(9)+A(10)+A(11)+A(12)+A(13))
3190      AM(4) = (A(14)+A(15)+A(16)+A(17)+A(18)+A(19)+A(20)+A(21)+A(22)+A(23))
3200     GOTO 5000
3250      AM(0) = A(6)+A(5)+A(4)+A(3) + 2*(A(2)+A(1)+A(0))
3260      AM(1) = (A(7)+A(8)+A(9)+A(10)+A(11)+A(12)+A(13)+A(14)+A(15)+A(16))
3270      AM(2) = (A(17)+A(18)+A(19)+A(20)+A(21)+A(22)+A(23)+A(24))
3280      AM(3) = (A(3)+A(4)+A(5)+A(6)+A(7)+A(8)+A(9)+A(10)+A(11)+A(12))
3290      AM(4) = (A(13)+A(14)+A(15)+A(16)+A(17)+A(18)+A(19)+A(20)+A(21)+A(22))
3300     GOTO 5000
3350      AM(0) = A(7)+A(6)+A(5)+A(4)+A(3)+A(2) + 2*(A(1)+A(0))
3360      AM(1) = (A(8)+A(9)+A(10)+A(11)+A(12)+A(13)+A(14)+A(15)+A(16)+A(17))
3370      AM(2) = (A(18)+A(19)+A(20)+A(21)+A(22)+A(23)+A(24))
3380      AM(3) = (A(2)+A(3)+A(4)+A(5)+A(6)+A(7)+A(8)+A(9)+A(10)+A(11))
3390      AM(4) = (A(12)+A(13)+A(14)+A(15)+A(16)+A(17)+A(18)+A(19)+A(20)+A(21))
3400     GOTO 5000
3450      AM(0) = A(8)+A(7)+A(6)+A(5)+A(4)+A(3)+A(2)+A(1) + 2*(A(0))
3460      AM(1) = (A(9)+A(10)+A(11)+A(12)+A(13)+A(14)+A(15)+A(16)+A(17)+A(18))
3470      AM(2) = (A(19)+A(20)+A(21)+A(22)+A(23)+A(24))
3480      AM(3) = (A(1)+A(2)+A(3)+A(4)+A(5)+A(6)+A(7)+A(8)+A(9)+A(10))
3490      AM(4) = (A(11)+A(12)+A(13)+A(14)+A(15)+A(16)+A(17)+A(18)+A(19)+A(20))
3500     GOTO 5000
3550      AM(0) = A(9)+A(8)+A(7)+A(6)+A(5)+A(4)+A(3)+A(2)+A(1)+A(0)
3560      AM(1) = (A(10)+A(11)+A(12)+A(13)+A(14)+A(15)+A(16)+A(17)+A(18)+A(19))
3570      AM(2) = (A(20)+A(21)+A(22)+A(23)+A(24))
3580      AM(3) = (A(0)+A(1)+A(2)+A(3)+A(4)+A(5)+A(6)+A(7)+A(8)+A(9))
3590      AM(4) = (A(10)+A(11)+A(12)+A(13)+A(14)+A(15)+A(16)+A(17)+A(18)+A(19))
3600     GOTO 5000
3650      AM(0) = A(10)+A(9)+A(8)+A(7)+A(6)+A(5)+A(4)+A(3)+A(2)+A(1)
3660      AM(1) = A(11)+A(12)+A(13)+A(14)+A(15)+A(16)+A(17)+A(18)+A(19)+A(20)
3670      AM(2) = A(21)+A(22)+A(23)+A(24)
3680      AM(3) = A(0)+A(0)+A(1)+A(2)+A(3)+A(4)+A(5)+A(6)+A(7)+A(8)
3690      AM(4) = A(9)+A(10)+A(11)+A(12)+A(13)+A(14)+A(15)+A(16)+A(17)+A(18)
3700     GOTO 5000
3750      AM(0) = A(11)+A(10)+A(9)+A(8)+A(7)+A(6)+A(5)+A(4)+A(3)+A(2)
3760      AM(1) = A(12)+A(13)+A(14)+A(15)+A(16)+A(17)+A(18)+A(19)+A(20)+A(21)
3770      AM(2) = A(22)+A(23)+A(24)
3780      AM(3) = A(1)+A(0)+A(0)+A(1)+A(2)+A(3)+A(4)+A(5)+A(6)+A(7)
3790      AM(4) = A(8)+A(9)+A(10)+A(11)+A(12)+A(13)+A(14)+A(15)+A(16)+A(17)
3800     GOTO 5000
3850      AM(0) = A(12)+A(11)+A(10)+A(9)+A(8)+A(7)+A(6)+A(5)+A(4)+A(3)
3860      AM(1) = A(13)+A(14)+A(15)+A(16)+A(17)+A(18)+A(19)+A(20)+A(21)+A(22)
3870      AM(2) = A(23)+A(24)
3880      AM(3) = A(2)+A(1)+A(0)+A(0)+A(1)+A(2)+A(3)+A(4)+A(5)+A(6)
3890      AM(4) = A(7)+A(8)+A(9)+A(10)+A(11)+A(12)+A(13)+A(14)+A(15)+A(16)
3900     GOTO 5000
3950      AM(0) = A(13)+A(12)+A(11)+A(10)+A(9)+A(8)+A(7)+A(6)+A(5)+A(4)
3960      AM(1) = A(14)+A(15)+A(16)+A(17)+A(18)+A(19)+A(20)+A(21)+A(22)+A(23)
3970      AM(2) = A(24)
3980      AM(3) = A(3)+A(2)+A(1)+A(0)+A(0)+A(1)+A(2)+A(3)+A(4)+A(5)
3990      AM(4) = A(6)+A(7)+A(8)+A(9)+A(10)+A(11)+A(12)+A(13)+A(14)+A(15)
4000     GOTO 5000
4050      AM(0) = A(14)+A(13)+A(12)+A(11)+A(10)+A(9)+A(8)+A(7)+A(6)+A(5)
4060      AM(1) = A(15)+A(16)+A(17)+A(18)+A(19)+A(20)+A(21)+A(22)+A(23)+A(24)
4070      AM(2) = 0
4080      AM(3) = A(4)+A(3)+A(2)+A(1)+A(0)+A(0)+A(1)+A(2)+A(3)+A(4)
4090       AM(4) = AM(0)
4100     GOTO 5000
```

```
 5000     PRINT "ARC DISPLACEMENT d = "d
 5100     PRINT'
 5200    FOR W = 0 TO 4
 5300     PRINT "THE TOTAL INTENSITY AT TRACK ";W;" = ";(AM(W)/AM(0))
 5400     NEXT W
 5500     PRINT''
 5600   ENDPROC
>
```

APPENDIX A.3

RADIAL PROFILES OF THE THERMODYNAMIC PROPERTIES USED IN THE ARC CORE ENERGY CONSERVATION

Included in this section are the radial profiles of thermodynamic quantities used in the evaluation of the arc core energy equation of chapter 8. Also included are profiles of the electrical conductivity which were used in the evaluation of the shape factors of the integral analysis formulations (chapter 8).

(i) The Quantity $\partial/\partial r \left[rK \partial T/\partial r \right]$ Used in the Evaluation of the Thermal Conduction Loss

The radial profiles of this quantity corresponding to the radial temperature profiles of fig. 6.25 (i) and (iii) are shown in fig. A.3.1. The value of K for corresponding T was obtained from Frost and Liebermann (1971).

(ii) The Quantity (ρhr) Used in the Evaluation of the Thermal Storage Change Term

The radial profiles of the quantity (ρhr) was calculated for radial temperature profiles at different instants during the current decay as described in chapter 8. Fig. A.3.2 (i) shows the (ρhr) profiles at instants of 10μs and 3μs before current zero for the low di/dt case. Fig. A.3.2 (ii) shows the (ρhr) profile for the heat storage term calculation as outlined in chapter 8 for an instant 7.9μs before current zero and a di/dt value of 21A/μs.

(iii) The Quantity (ρhrc) Used in the Evaluation of the Convection Loss Term

The variation of sonic velocity, c for SF_6 and a pressure

of 4 bar with temperature (Frost and Liebermann, 1971) is shown on Fig. A.5 (appendix 5). These values coupled with the values of ρ, h, r (Frost and Liebermann, 1971) were used to calculate the quantity (ρhcr) for various radial temperature values. The radial profiles of (hcr) at slots 2 and 3 (as discussed in chapter 8) for the cases of low and high $^{di}/dt$ are shown in fig. A.3.3 (i) and (ii) respectively.

(iv) <u>The Radial Profiles of the Three Thermodynamic Quantities Very Close to Current Zero</u>

Included on fig. A.3.4 are the radial profiles of the quantities (ρhr), (ρhcr) and $^{\partial}/\partial t$ (rK $^{\partial T}/\partial r$) for the radial temperature profile of fig. 6.25 (ii) which corresponds to a $^{di}/dt$ of 15A/μs and an instant 2.2μs before current zero. The temperature profiles corresponding to instants of 2.2μs and 1.2μs (at slot 2) before current zero and slot 3 at 2.2μs before current zero are also shown on fig. A.3.4.

(v) <u>The Radial Electrical Conductivity Profiles</u>

The radial electrical conductivity (σ) profiles were calculated from the temperature profiles of fig. 6.25 (i) and (iii) and the data of Frost and Liebermann (1971). The radial profiles of σ and the product σ x r for values of $^{di}/dt$ of 14.2A/μs and 21A/μs are presented in figs. A.3.5 (i) and (ii) respectively.

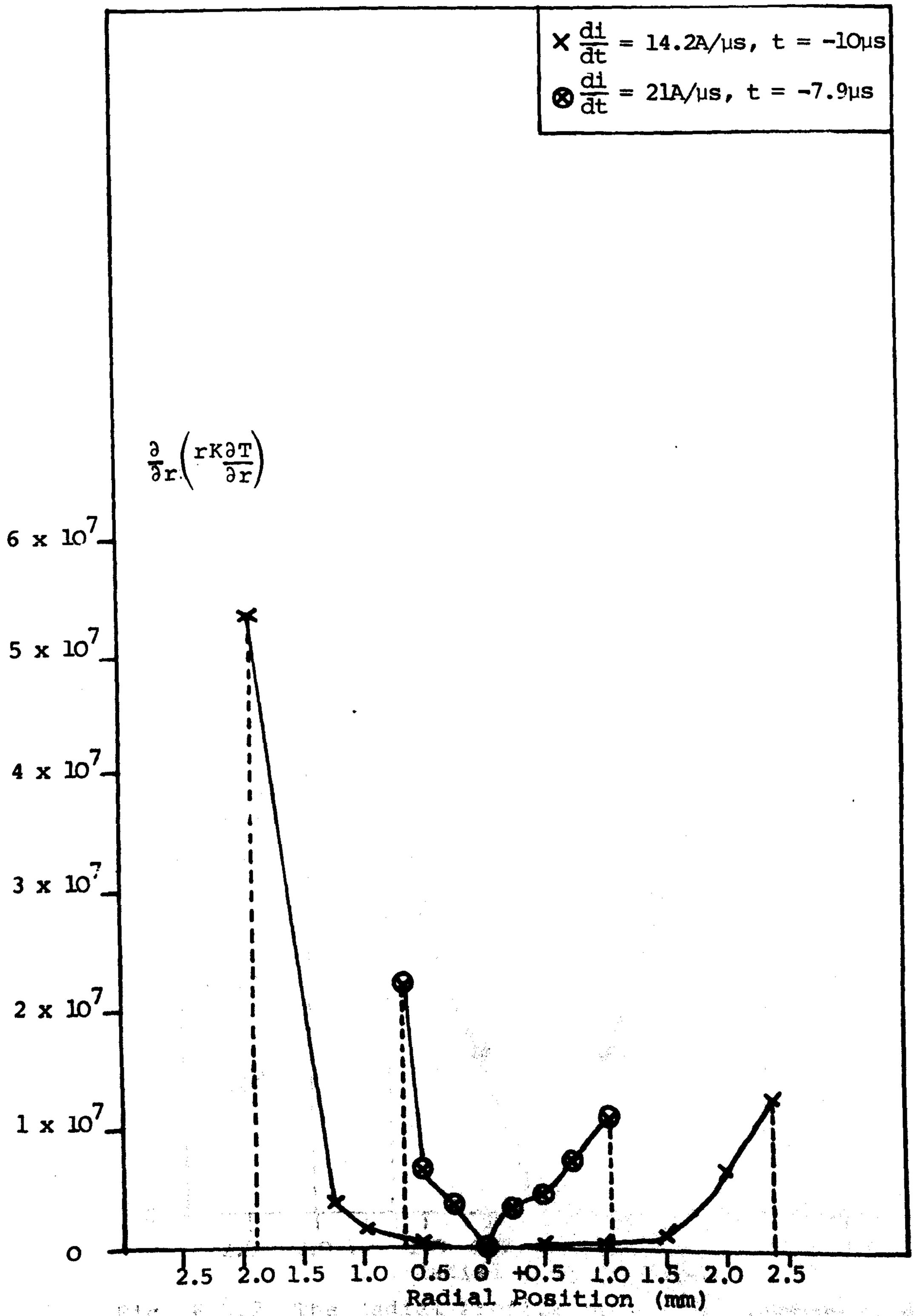

Fig. A.3.1 The Radial Profile of the Thermodynamic Quantity $\frac{\partial}{\partial t}\left(rK\frac{\partial T}{\partial r}\right)$ Used in the Core Energy Conservation

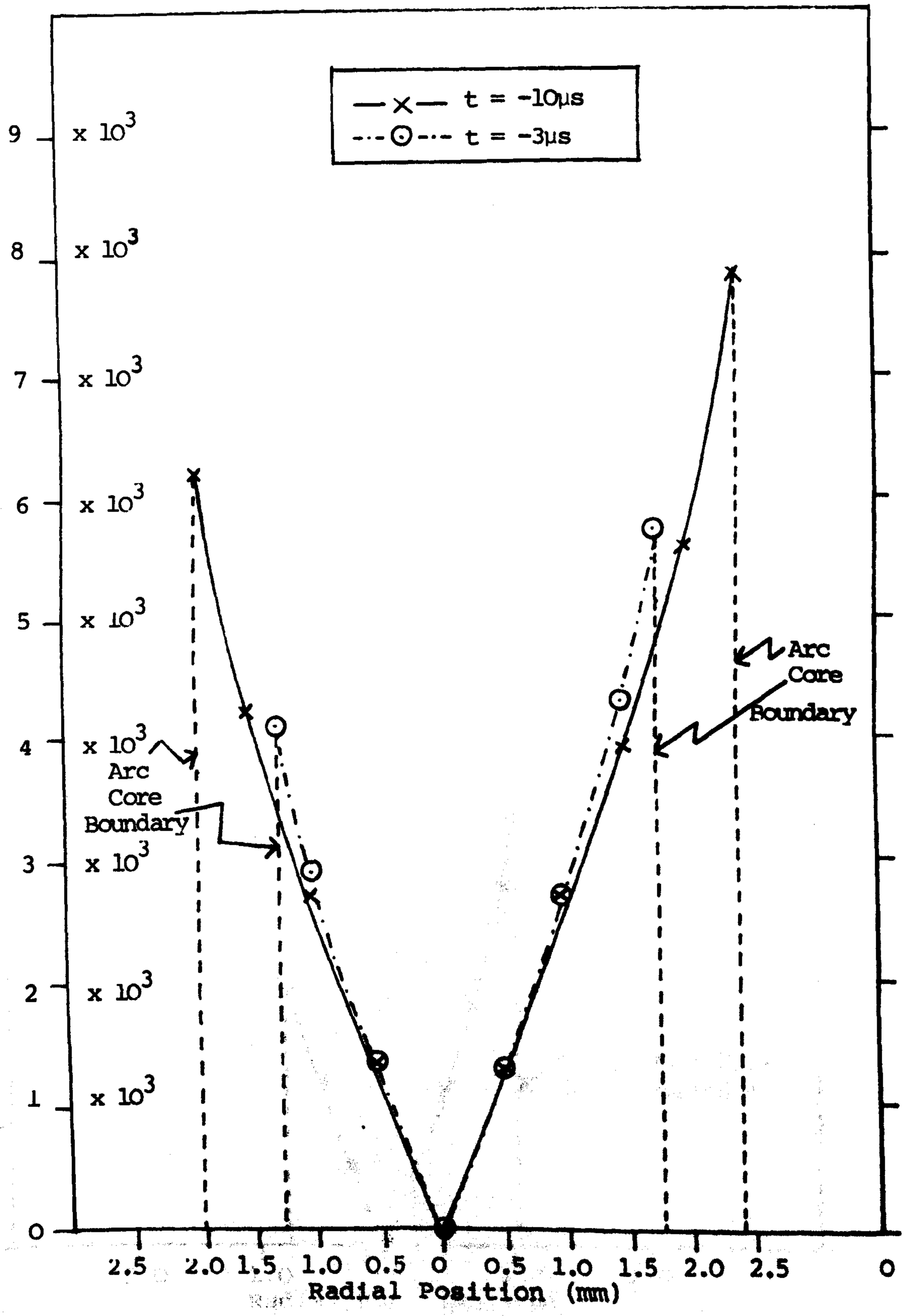

Fig. A.3.2 The Radial Profile of the Thermodynamic Quantity (ρhr) Used in the Core Energy Equation (i) Low di/dt

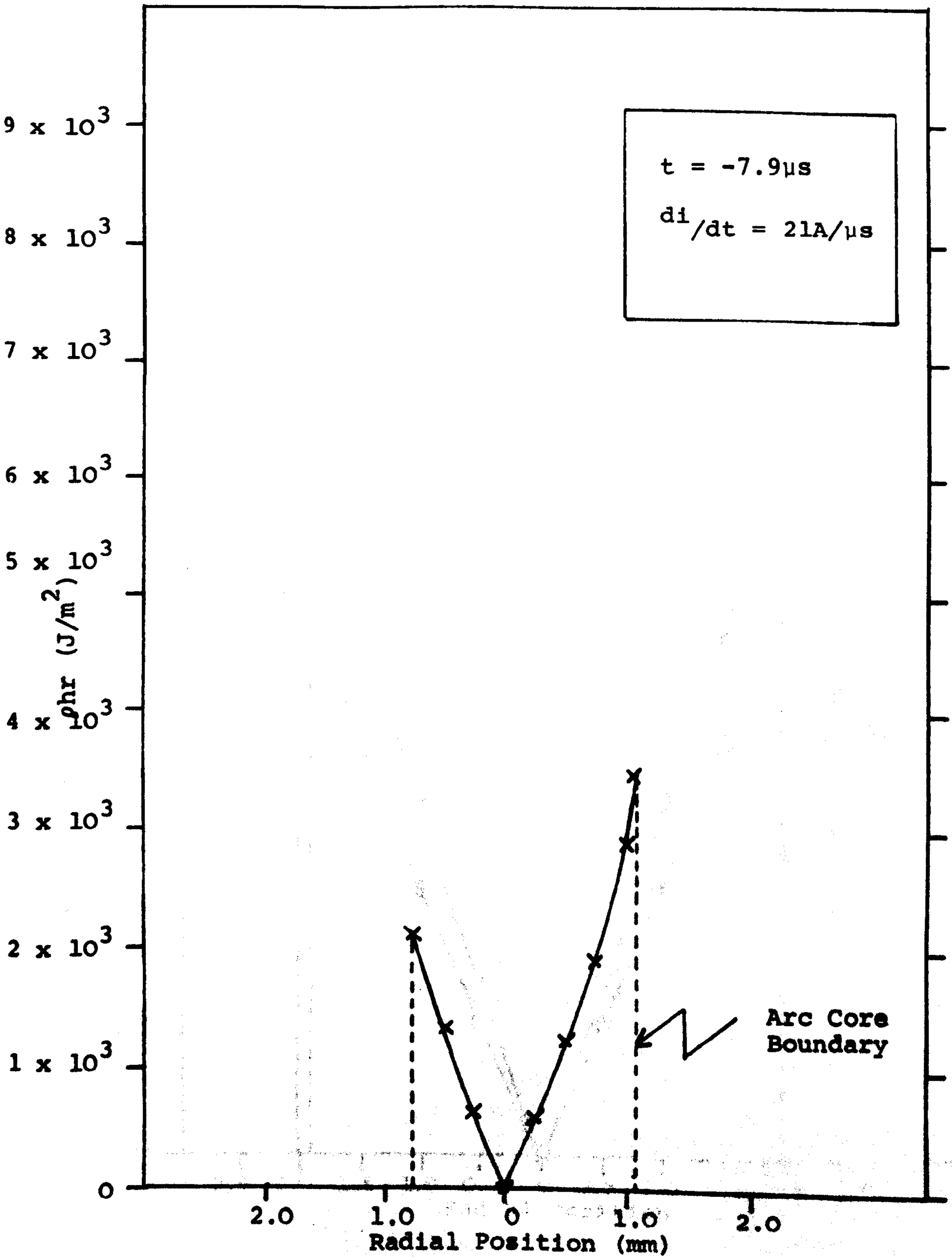

Fig. A.3.2 <u>(ii) High di/dt</u>

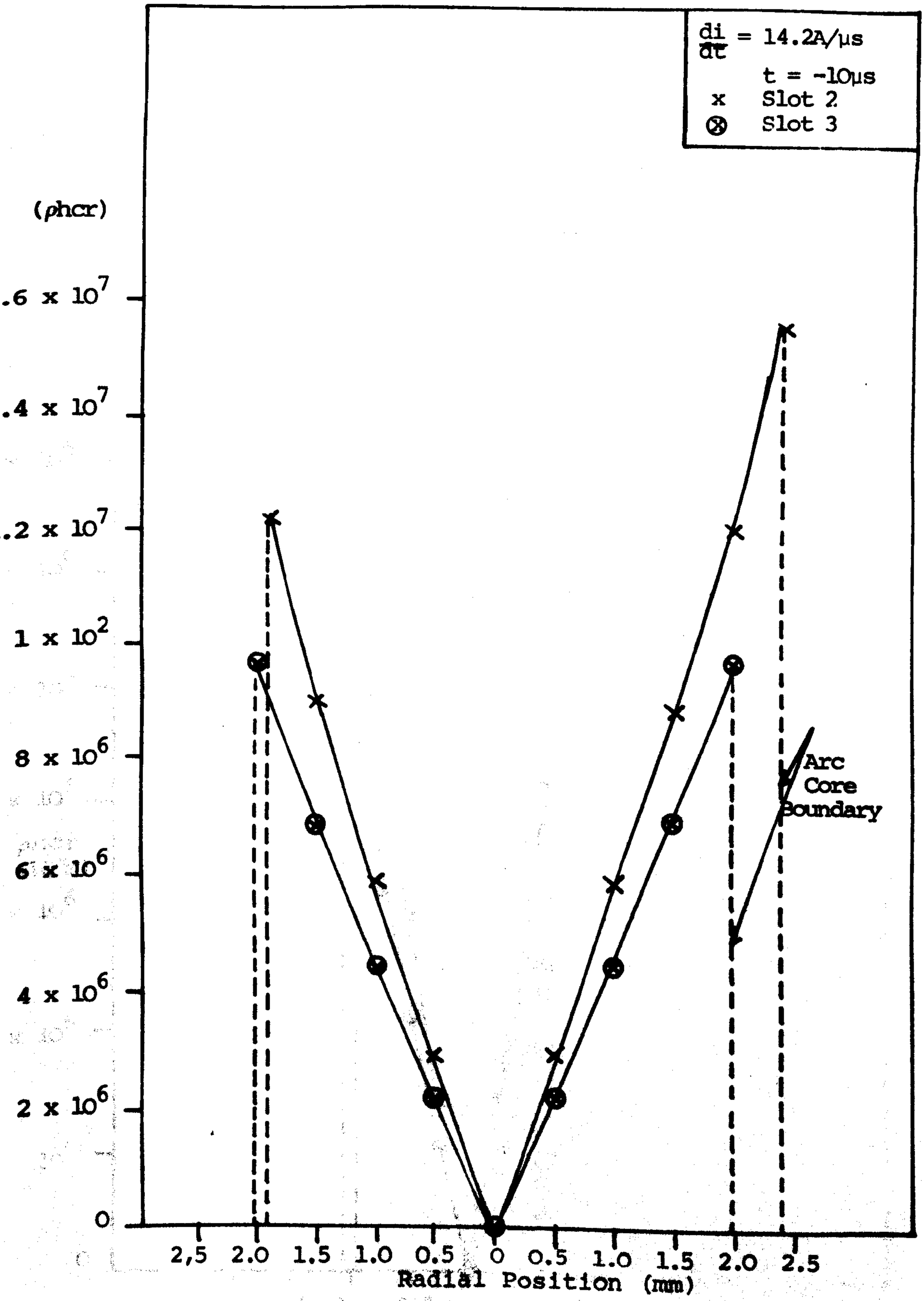

Fig. A.3.3 (i) Radial Profile of the Thermodynamic Quantity (ρhcr) Used in the Evaluation of the Core Energy Balance

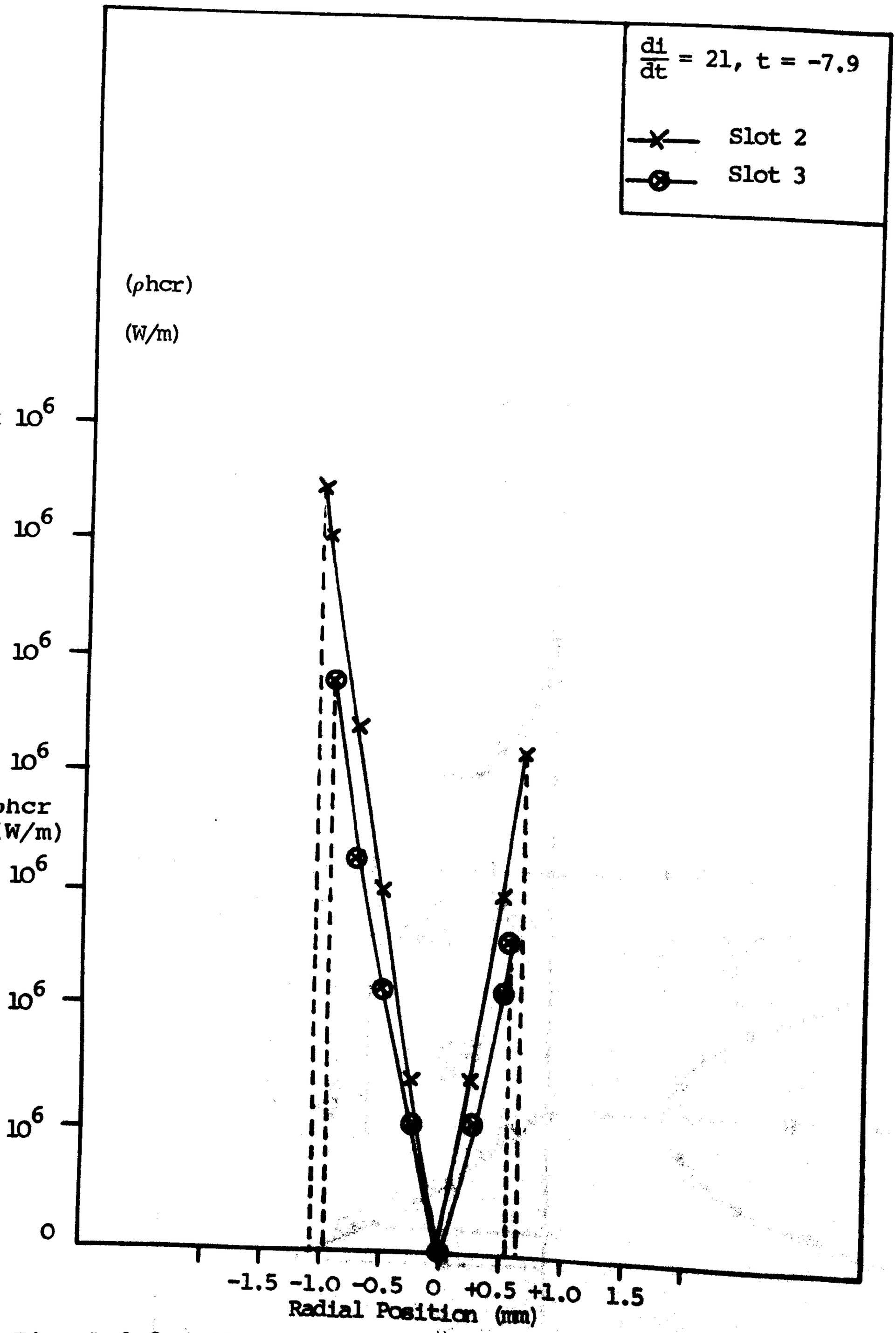

Fig. A.3.3 (ii) The Radial Profile of the Thermodynamic Quantity (ρhcr) Used in the Evaluation of the Core Energy Balance

Operating Conditions

$\frac{di}{dt}$ = 15A/μs, t = -2.2μs

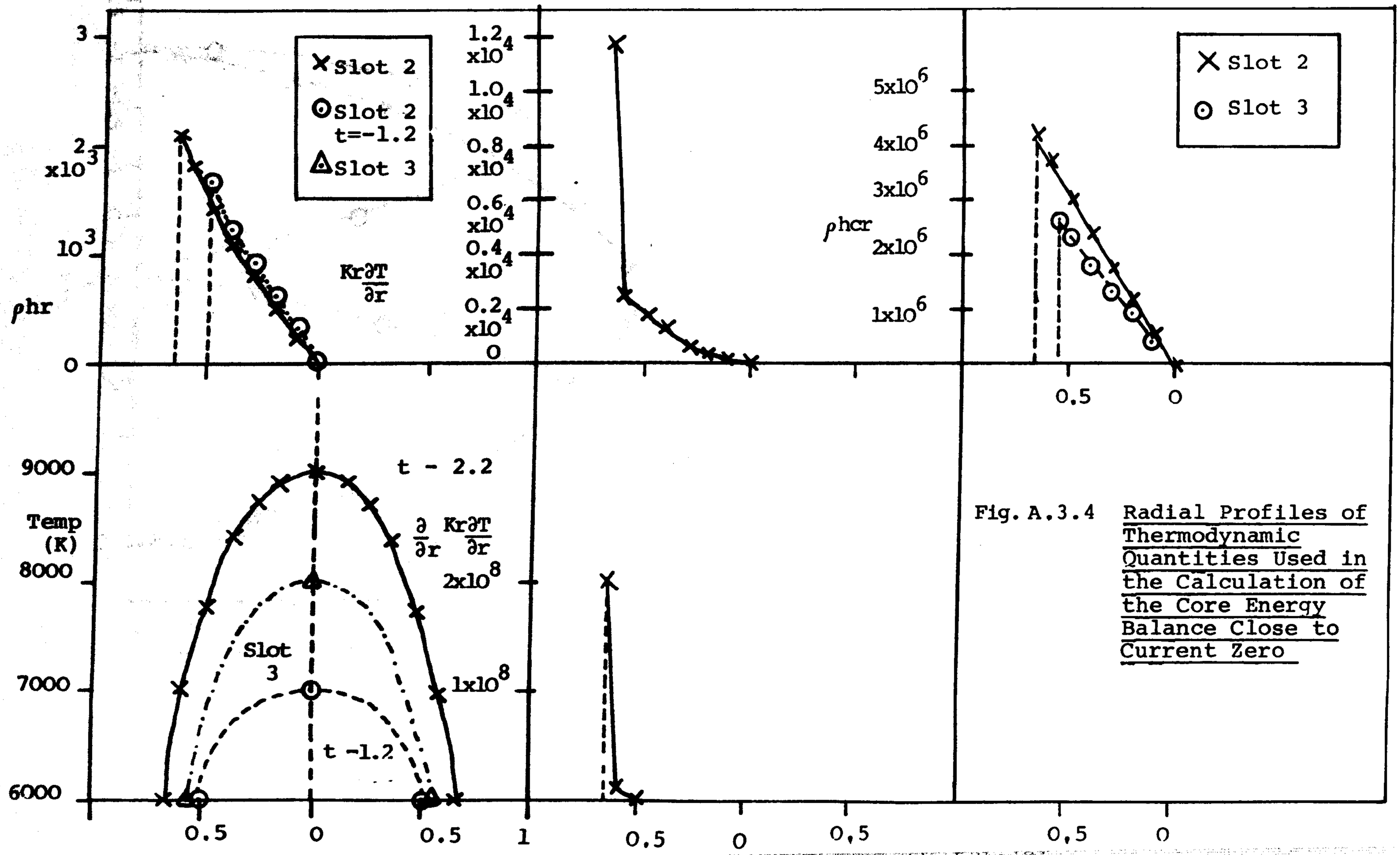

Fig. A.3.4 Radial Profiles of Thermodynamic Quantities Used in the Calculation of the Core Energy Balance Close to Current Zero

Fig. A.3.5 The Radial Profiles of the Electrical Conductivity and the Product r (i) di/dt = 14.2A/μs

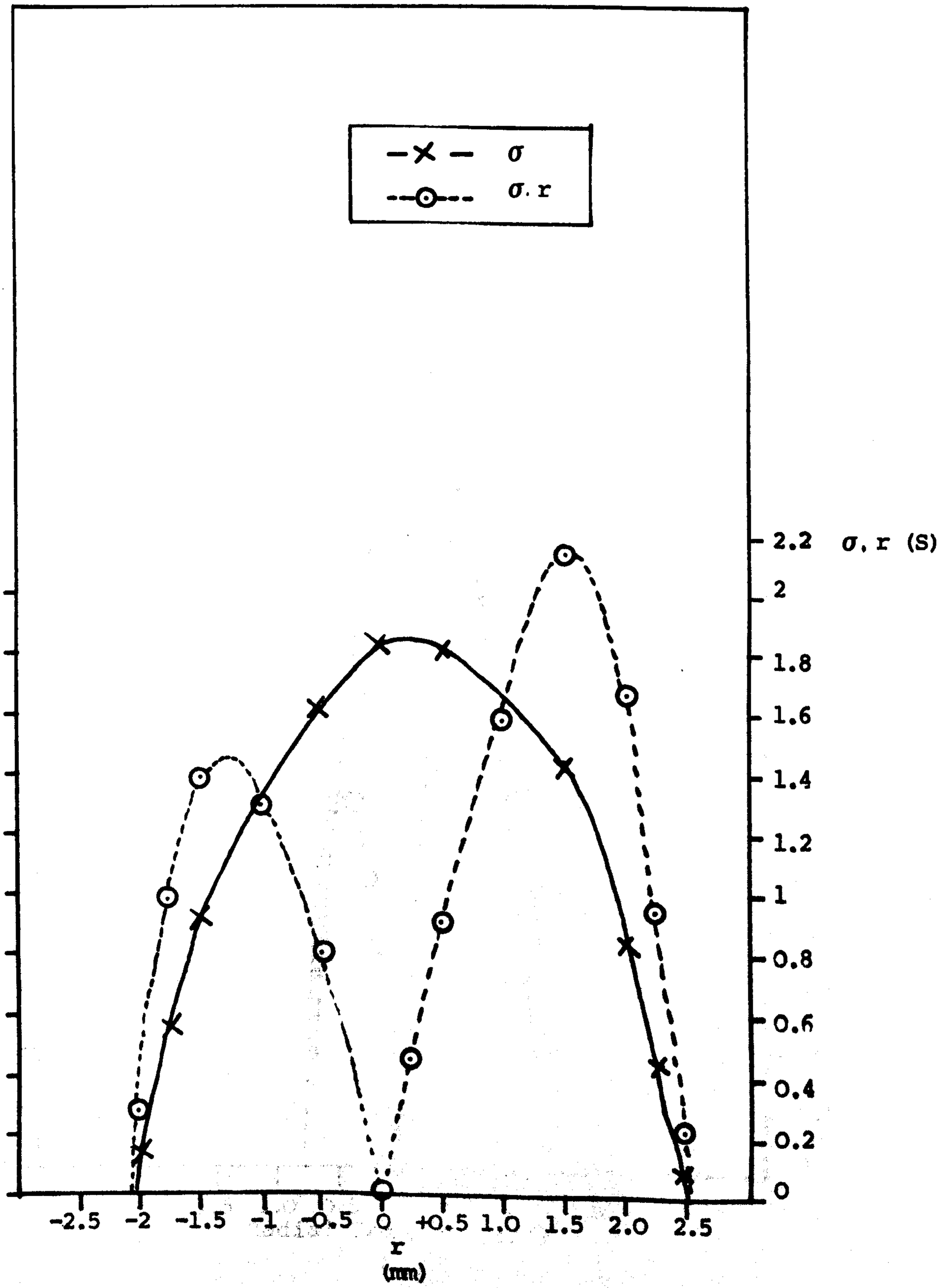

Fig. A.3.5 (ii) di/dt = 21A/μs

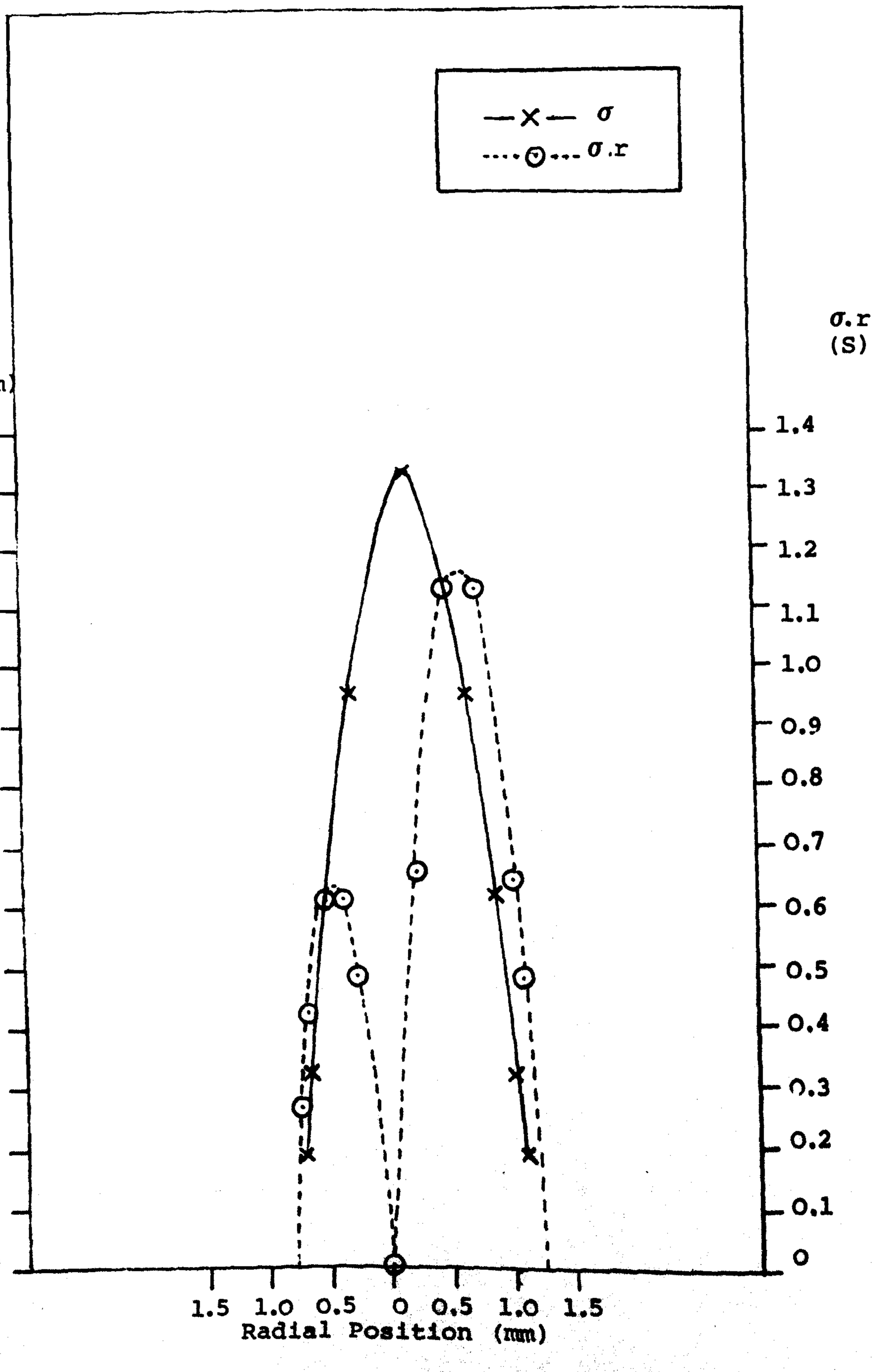

APPENDIX A.4

THE TOTAL RADIATION POWER LOSS DATA

The total radiation results during the current zero period of the full power arcs (Shammas, unpublished) are presented in this section. These results include two cases of $^{di}/_{dt}$ (fig. A.4.1 and A.4.2). A number of tests were carried out in both $^{di}/_{dt}$ cases which give rise to an experimental spread which is represented by the bands on figs. A.4.1 and A.4.2.

These are the results from which the total radiation power loss data for the current zero energy balance (chapter 8) was obtained.

Operating Conditions

$I_p \simeq 38KA$

$\frac{di}{dt} \simeq 18A/\mu s$

Fig. A.4.1 Total Radiation Results (Low $^{di}/_{dt}$). Source : Shammas (Private Comm.)

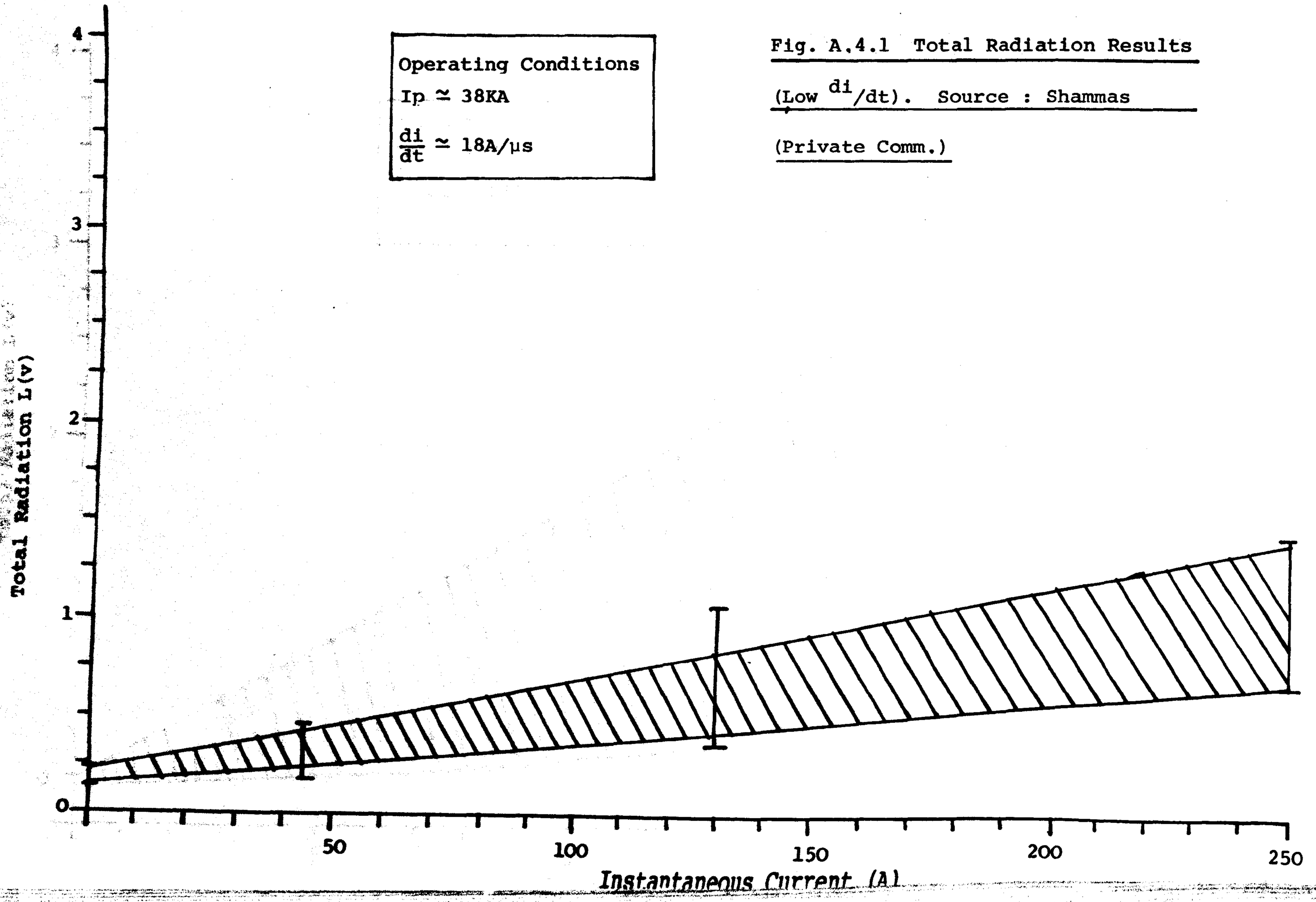

Fig. A.4.2 Total Radiation Results (Medium di/dt). Source : Shammas (Private Comm)

Operating Conditions
$I_p \simeq 43KA$
$di/dt \simeq 21A/\mu s$

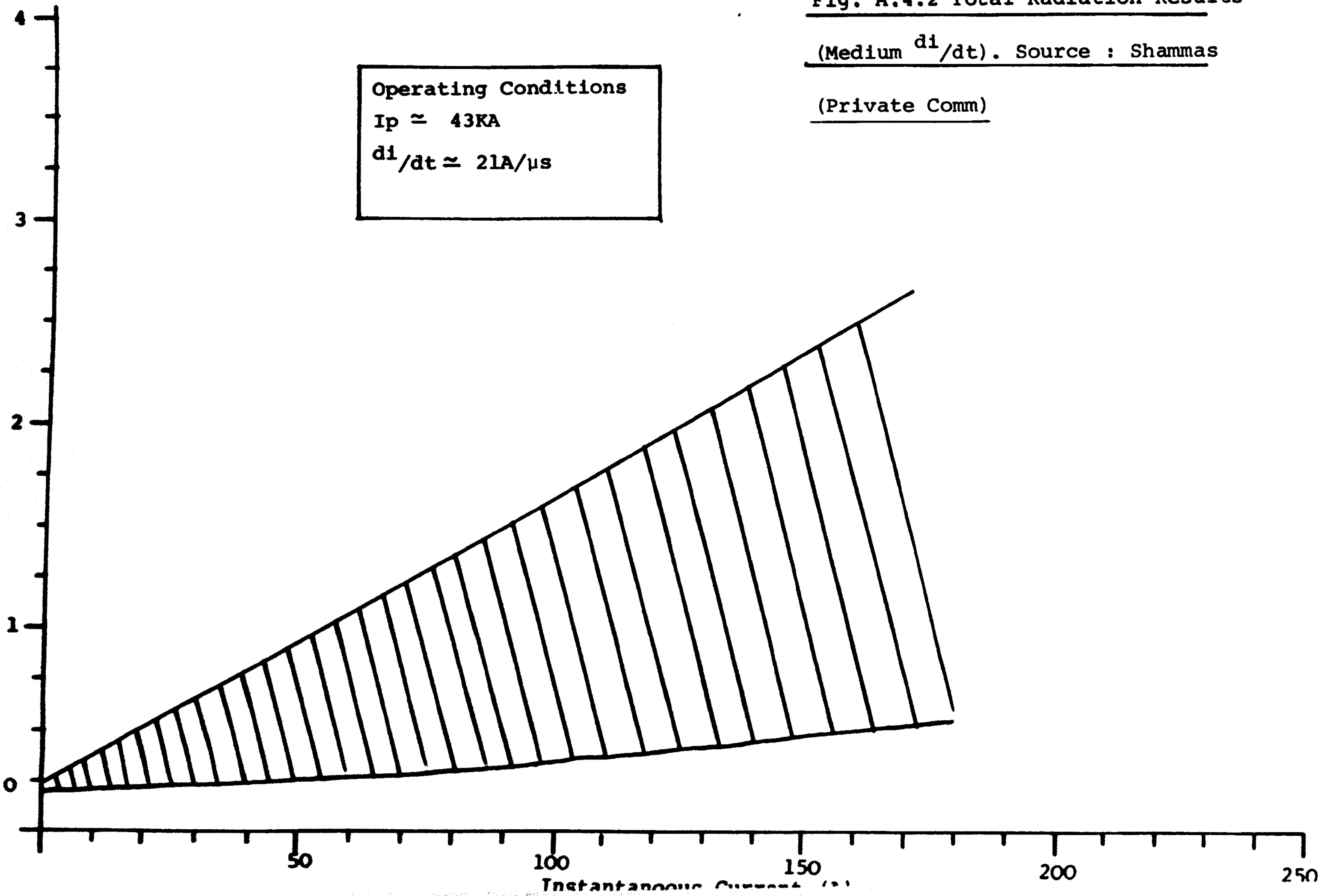

APPENDIX 5

TRANSPORT PROPERTIES OF SF_6

The transport properties of SF_6 used in the evaluation of the arc energy conservation were obtained from Frost and Liebermann (1971). The variation of the electrical conductivity, thermal conductivity enthalpy and density with temperature in the range 6,000K to 12,000K for a pressure of 4 ATM are shown on fig. A.5.1. The variation of sonic velocity with temperature in the range 6,000 to 10,000K for a pressure of 4 ATM is shown on fig. A.5.2.

Fig. A.5.3 shows the variation of Cu I species and electron density for various SF_6 and Cu plasma compositions (Kinsinger, unpublished). The data of fig. A.5.3 was used in the calculation of the optical depth in chapter 7.

Fig. A.5.1 The Transport Properties of SF_6

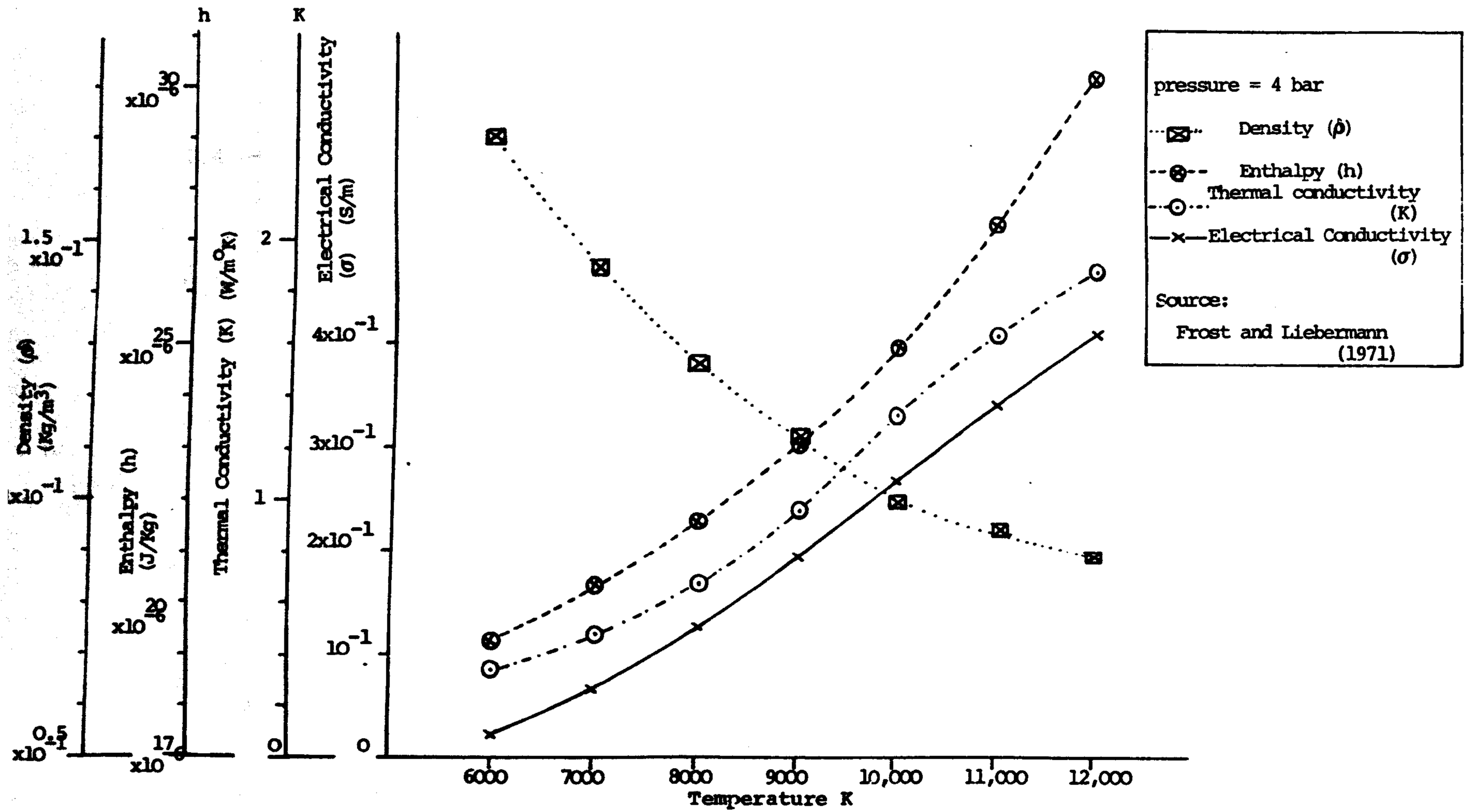

Fig. A.5.2 Variation of Sonic Velocity in SF_6 with Temperature

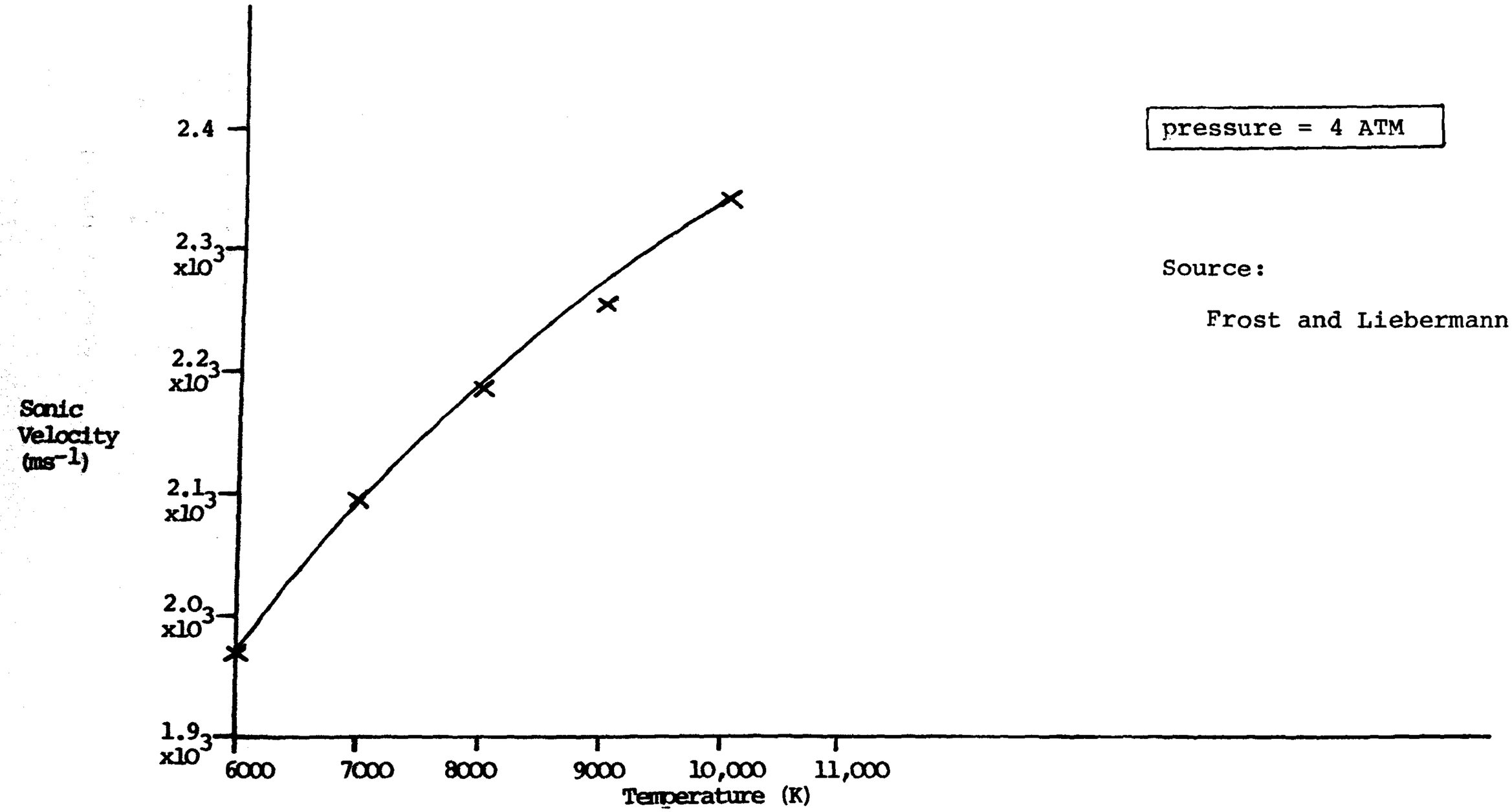

Fig. A.5.3 Cu I and Electron Densities for Different Plasma Composition

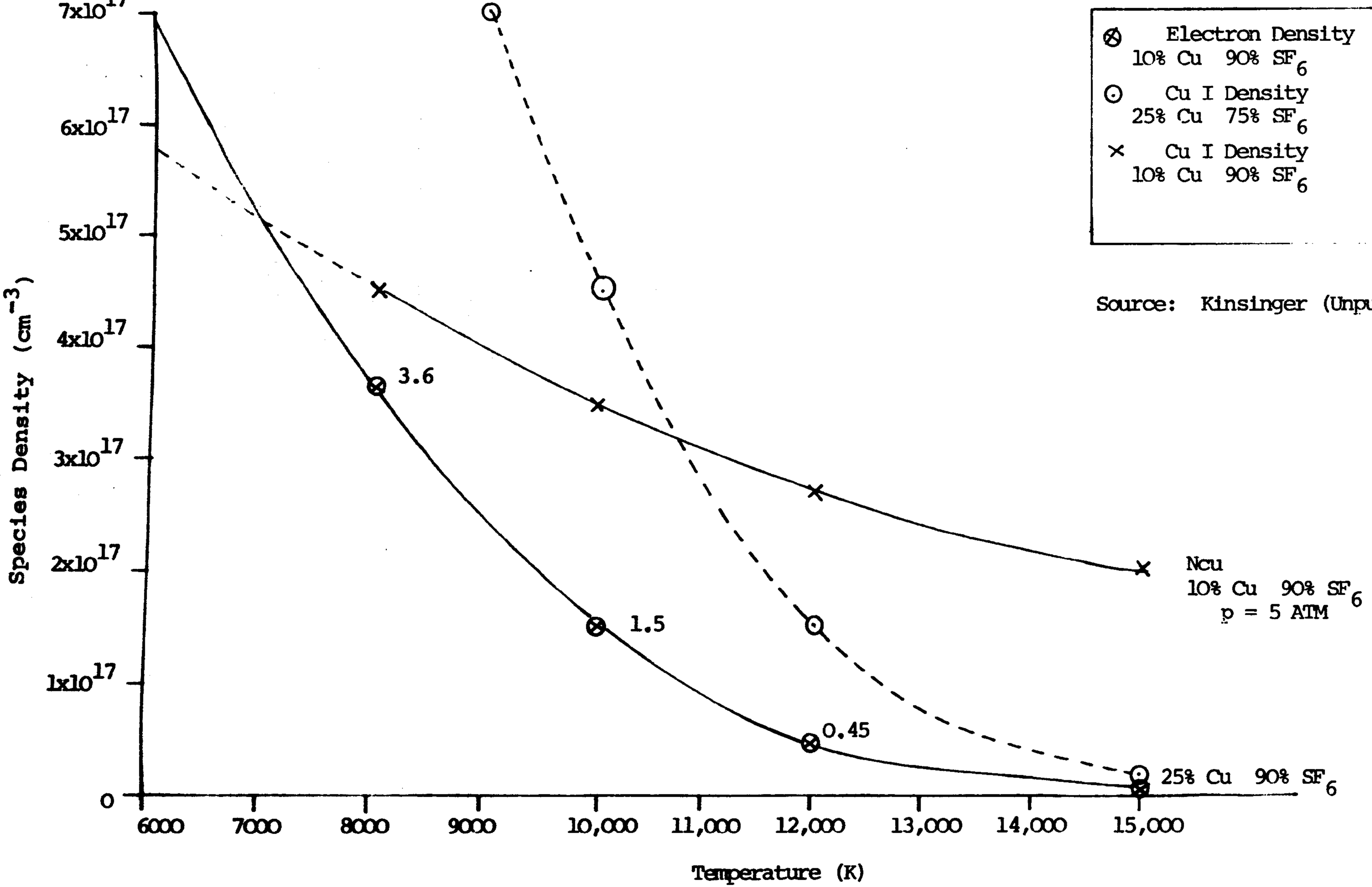

Source: Kinsinger (Unpublished)

APPENDIX A.6

ELECTRONIC CIRCUITS

This section is concerned with the description of some electronic circuits used in the present investigations.

The circuit diagram of fig. A.6.1 shows the opto-sensor used in the detection of laser pulses for speed sensing of the rotating shutter (chapter 4). The output pulses from this circuit were input to another circuit (fig. A.6.2) which detected the coincidence with a monostable pulse (coincident with the lst ignitron trigger pulse) for homing in on current zero (chapter 4). The unit which houses this circuit was referred to as the coincidence unit in chapter 4 which also includes a description of its function within the system.

Fig. A.6.3 shows the circuit diagram of the high voltage trigger unit for triggering the vidicon camera. The video output of the camera which corresponds to the scanning sequence of the vidicon (33ms active scanning period, 1.2ms blanking) was used as an input to the circuit of fig. A.6.4. This circuit converted the video signal to a pulse train of 33ms period and a 1.2ms pulse duration. These pulses were used in conjunction with the coincidence unit of fig. A.6.2 for the current zero triggering of the vidicon camera as described in chapter 4.

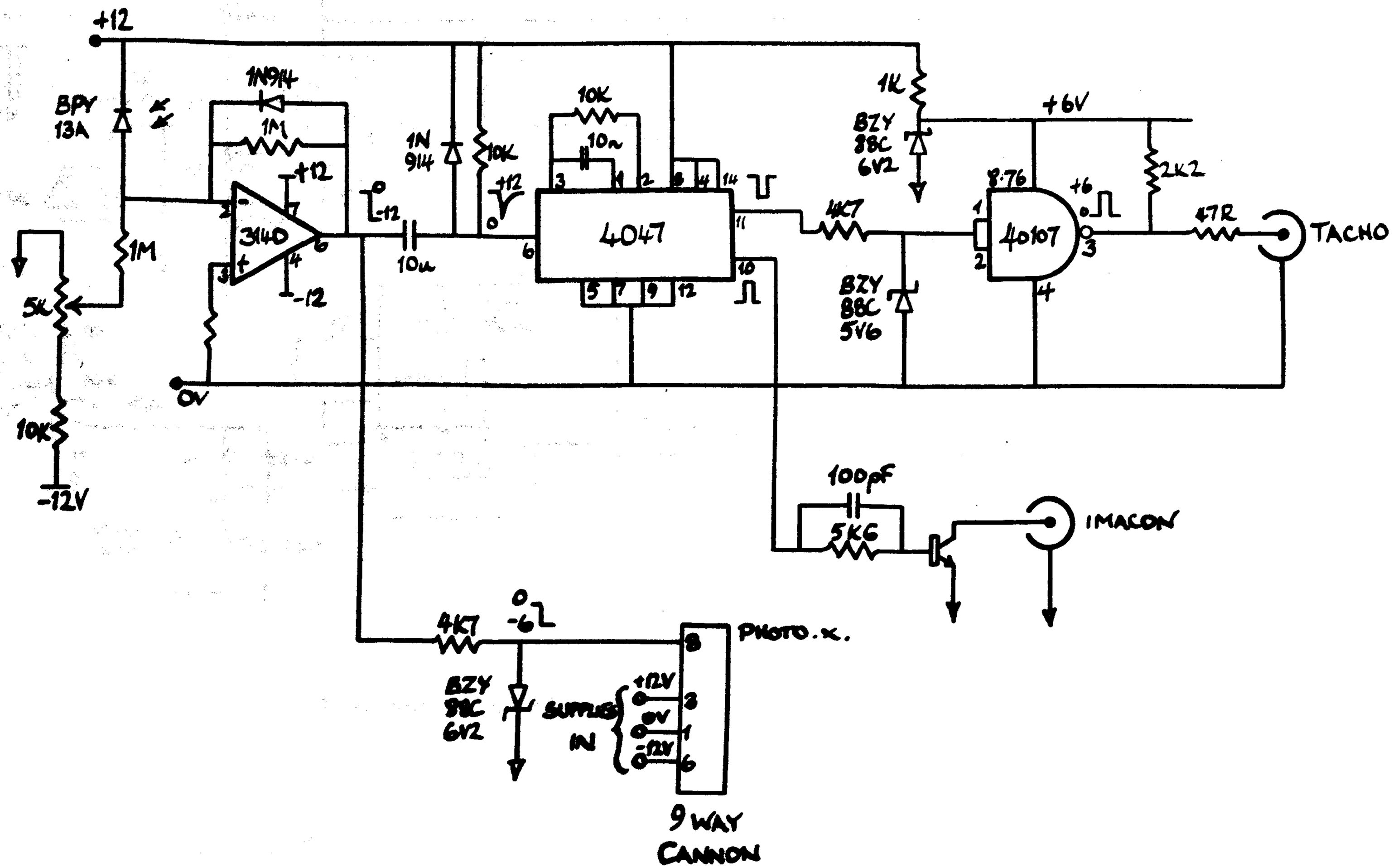

Fig. A.6.1 Opto Sensor for Rotary Shutter Speed Detection

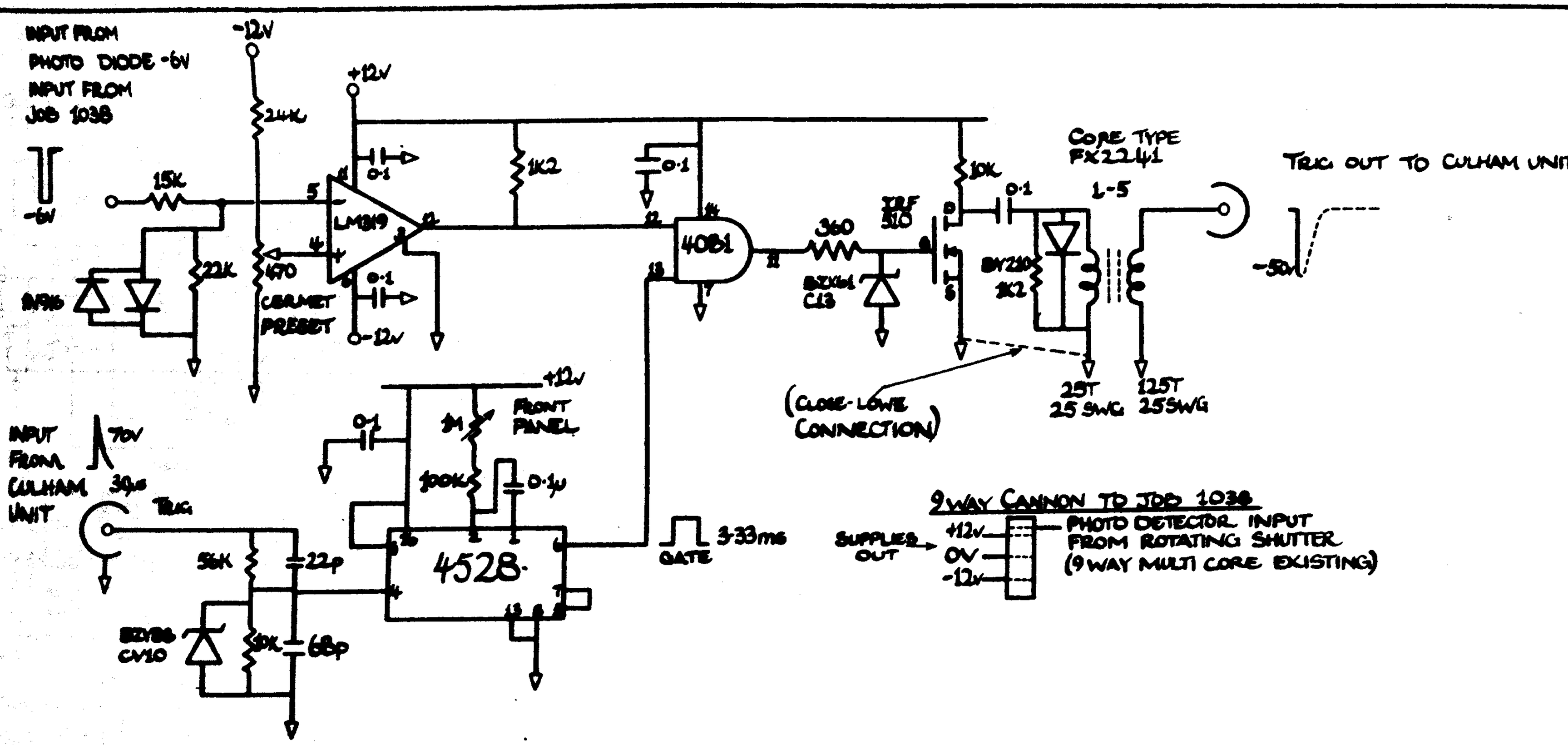

STANDARD ±12v REGULATOR AT 100mA

Fig. A.6.2 Coincidence Circuit for Rotating Shutter

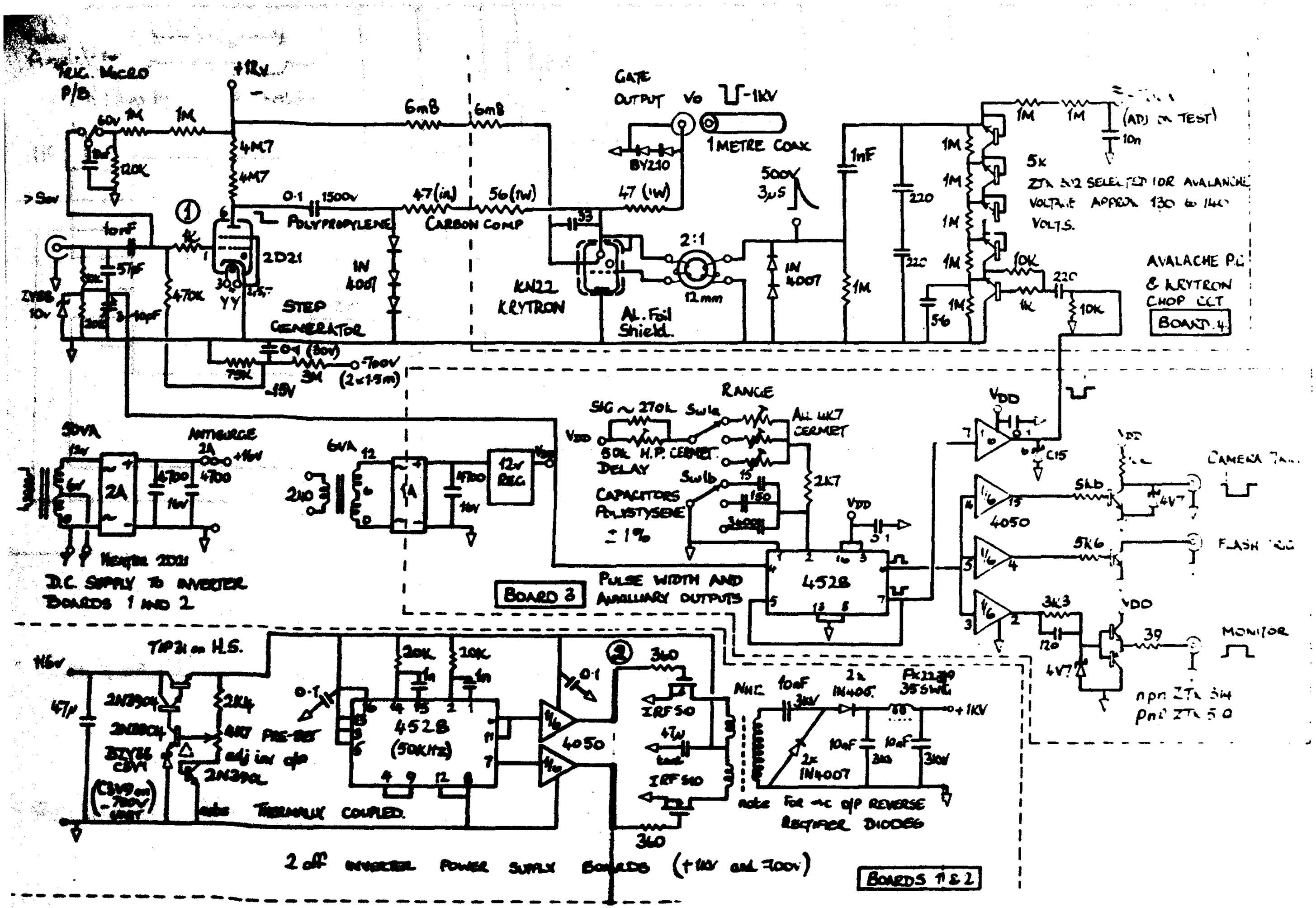

Fig. A.6.3 High Voltage Pulse Generator for the Vidicon Gate Trigger

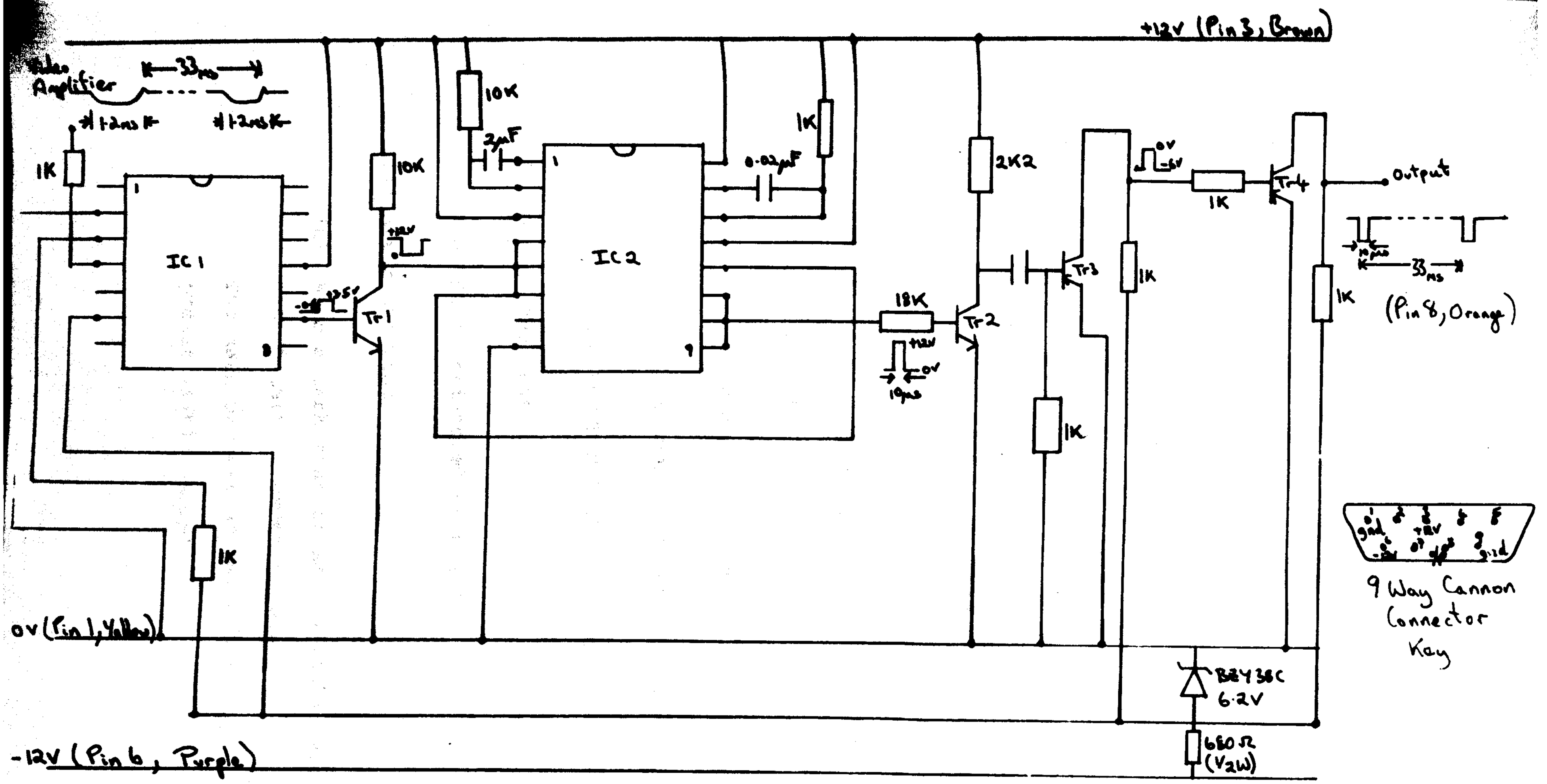

9 Way Cannon Connector Key

Fig. A.6.4 Interface for Vidicon Scanning Synchronisation

IC1 RS 710
IC2 CD4098
Tr1,2 BFX 85
Tr3,4 BFX 87

APPENDIX A.7

DIAGNOSTIC INSTRUMENTATION

In this section some of the operating parameters not described in detail in chapter 4 are included.

Primarily it is intended that the operating sequence and a general description of the 'call', '2D' and 'DEFINE' routines are presented. The full menu of the call, 2D and DEFINE routines including a brief description of each according to the manufacturer is given at the end of this appendix.

The sequence of operation of the OSA in order to obtain a radially averaged arc spectrum is as follows:

(i) Before the Test

(a) Choose an available memory M (e.g. 5)

(b) Preset the number of scans N (usually N = 3)

(c) CALL O ENTER M ENTER = initialise OSA for recording

(ii) During the Test

The OSA is triggered externally

(iii) After the Test

(a) Make a dark scan in an available memory

CALL O ENTER x ENTER - START

The dark current of the vidicon is scanned by the preset (i(b)) amount

(b) Subtract the dark current from the signal

CALL 1 ENTER M ENTER X ENTER

The result is in memory M and displayed

(c) The information can be transferred to the external computer using the following instructions

DEFINE 3 ENTER 9600 ENTER

CALL 6 ENTER M ENTER

In this case the external computer is the BBC which has to be initialised before this transmission using a separate program (OSA 1)

The sequence of operation of the OSA in order to obtain a radially resolved arc spectrum is as follows:

(i) Before the Test

(a) The 2D initialisation must be executed if not already done so. Usually the parameters for the 2DØ routine are as follows

2DØ ENTER 15 ENTER 5 ENTER 6 ENTER 10 ENTER 1

(b) A dark scan must be made. This is achieved by invoking the 2D2 routine as follows

2D2 ENTER START

The dark current is stored in memories 1 to 5.

This must be shifted out to other available memories by using the 2D8 routine as follows

2D8 ENTER 1 ENTER 5 ENTER X ENTER

The dark scan is now stored in memories X to (X + 4)

(c) The first 5 memories must be cleared for storage of arc spectra as follows

2D6 ENTER

(d) The accumulation program is invoked again, thus

2D2 ENTER

The OSA is ready for triggering externally to receive the DATA.

(ii) During the Test

The OSA is triggered externally.

(iii) After the Test

(a) The dark current is subtracted from each of memories 1 to 5 to obtain the true spectrum. The dark current records are stored in memories X to (X + 4), (i(b)) and can be subtracted from the corresponding data in 1 to 5 by repeated use of the CALL 1 routine.

(b) The spectra with dark current subtracted are shifted out to other memories using the 2D8 routine.

(c) These spectra can be transmitted to the external computer using CALL 6 with DEFINE 3 again set to 9600.

Another important parameter to be considered in the acquisition of the arc spectra is the reciprocal dispersion of the monochromator for various slit widths. This has been measured by Ibuki (1979) and is shown in fig. A.7.1.

OPERATING INSTRUCTIONS FOR CALL, 2D AND DEFINE PROGRAMS

(1) CALL PROGRAMMES

Call Ø: Accumulation Program

Entry:

CALL Ø ENTER X ENTER START possibly STOP.

Result: In memory X, after pressing the start key the pre-selected number of scans shown on the display screen will be accumulated. Whilst the accumulation proceeds, the red LED over the START key will light. Memory X will be automatically displayed on the XY display during and after the accumulation.

After initialisation with CALL Ø the accumulation can be effected as often as desired by pressing the START key, until a new instruction is entered.

The X-Y display control keys are blocked until the entry of a new instruction.

Call 1: Subtraction Program

Entry: CALL 1 ENTER X ENTER Y ENTER

Result: Memory Y is subtracted from memory X and the result is stored in memory X and automatically shown on the display.

Call 2: Accumulations and subtractions Programs

Entry: CALL 2 ENTER X ENTER START

Result: After pressing the START key the preselected number of presets will be accumulated in memory X (e.g. a signal spectrum). If the START key is again pressed, then the same number of presets will be subtracted from the contents of memory X with the scanned spectrum (e.g. dark spectrum). Memory X will nowcontain the signal spectrum corrected by the

dark spectrum. If on the display values around Ø and also around 65525 are held, then the Y offset must be shifted by the key until all points of the results spectrum are over Ø (the correction is necessary since the computer calculates without using sign so as not to lose dynamics i.e. for example, 2 - 3 = 65535).

Call 3: Alternative Presentation

Entry: CALL 3 ENTER X ENTER

Result: Alternative presentation of real time and memory X on the display, i.e. both spectra are shown in succession and therefore appear at the same time on the display. The intensities of the cursor channels are given alternatively for both spectra on the screen display.

Call 4: Standardisation

Entry: CALL 4 ENTER X ENTER

Result: Memory X is standardised at 12 bits, i.e. maxima of the spectra are set to 4095 and all other values to corresponding values, so that the values are multiplied by the same factor as the maximum value, or divided by the same factor as the maximum value.

Call 5: Addition Program

Entry: CALL 5 ENTER X ENTER Y ENTER

Result: Memory Y and memory X are added and the result stored in memory X and automatically shown on display XY.

Call 6: Serial Outputs

Entry: CALL 6 ENTER X ENTER

Result: Memory X between UG and OG (See define Ø/I) is output through the serial interface. Here in one line first the channel number, then the intensity, and finally Carriage Return are output. In addition, in the first "Memory X" as well as at the end the current integral and mean values are output. The coding of the individual symbols is in the ASCII code.

Call 7: Integral

Entry: CALL 7 ENTER

Result: Between UG and OG the integral of the spectrum shown on the display is calculated and given on the screen after Integral. The integral is calculated by adding the intensity values from UG to OG. The figure after the E gives the power of 10; e.g. 35,000 E 2 = $35{,}000.10^2$.

Call 8: Number of channels

Entry: CALL 8 ENTER XØØ ENTER

Result: By call 8, the number of channels by which the target is scanned, is altered. Possible values: 100, 200, 300, 400, 500. After entry of one value, the X axis is shortened to the display of n/5 where n = number of channels/100. Exactly as shown on the display, the target is now scanned from channel 1 as far as only n/5. It must be remembered here that the dwell time of the electron beam per diode (64µs) remains the same (i.e. the same amount of information collected as with 500 points), but the integration time of the light between scans is reduced to n/5 of 32ms (i.e. for steady state excitation - the same illumination strength) in real time the intensity of the spectral lines will be less.

If the scanning field is reduced, it is no longer possible to call X expand by the key operation. It is better in this case to set the optimum picture size by means of the Expand potentiometer adjacent to the X-Y display. Against the disadvantage of the reduced target area, the smaller number of channels has two advantages: the number of memories is increased to 150/n memories, i.e. for 100 channels a maximum of 150 memories is now possible. Then also in the 2D mode 150 tracks can be simultaneously stored in memory.

For uncooled systems in which with 500 channels only up to 5 tracks can be scanned without signal overlap by dark currents, this number is increased to 5 x (6 - n) tracks.

Call 9: Alternative Program

Entry: CALL 9 ENTER X ENTER Y ENTER

Result: Alternative presentation as for program Call 3, but presentation of two memories X and Y.

Call 10: Cushion correction

Entry: CALL 10 ENTER X ENTER

Result: This program corrects the memories X and Y by the values of a correction spectrum, which is programmed in. (See chapter 5.1).

Call 11: Multiplication Program

Entry: CALL 11 ENTER X ENTER Y ENTER

Result: Memory X is multiplied by memory Y, the result stored in memory X and automatically displayed on the XY display. Since the result can be output over the 16 bit range, in such a case the result is shifted by so many bits that the maximum

can be covered by 16 bits.

CAUTION

Memory Ø is needed for the multiplication and for this reason neither be mulplicant nor multiplier.

Call 12: Division Program

Entry: CALL 12 ENTER X ENTER Y ENTER

Result: Memory X is divided by memory Y, the result is stored in memory X and automatically displayed on the XY display. In order to attain full accuracy, the result is shifted to the right by so many bits that the maximum no longer contains any leading zero figures.

CAUTION

Memory Ø is needed for the division, and for this reason should neither be dividend nor divisor.

Call 13: Erase all memories

Entry: CALL 13 ENTER

Result: Memory Ø to Memory 3Ø are erased.

Call 14: ASCII Output

Entry: CALL 14 ENTER

Result: An ASCII symbol is output as control symbol through the serial interface. This control symbol can be programmed in to customer's requirements.

Call 15: Average value

Entry: CALL 15 ENTER

Result: Between UG and OG the intensity average value of the

spectrum shown on the screen is calculated and output in the penultimate line of the screen.

Call 16: Delay and accumulation Program

Entry: CALL 16 ENTER X ENTER START

Result: Call 16 is used after, by DELAY N ENTER the number of seconds was entered during which light is to be collected at the target. Then Call 16 can be called and by X the memory in which accumulation is to be effected after the delay time is entered. After pressing START, the target will be exposed for the given number of seconds and the result stored in memory. It is possible to use START again as often as desired without re-initialisation.

Call 17: Dark keying

Entry: CALL 17 ENTER

This programme is at present only in software, but not available in hardware.

Call 18: Real-time Plot Program

(Only for systems with Floppy Disc Option)

Entry: CALL 18 ENTER S ENTER

By this program it is possible to have a real-time spectrum plotted out at specific intervals of time. S is the time period in seconds between the plotting of two real-time spectra. By pressing a command key the program is stopped.

CAUTION

The spectrum is plotted which is at that moment on the X-Y display, so that the real-time spectrum must be visible

there.

Call 19: Arithmetic with constants

Entry: CALL 19 ENTER Z ENTER V X X X X ENTER

Result: Memory A, according to the sign V (+, -, *, /) is automatically logically associated with the constants X X X X X (up to 5 places) and the result is stored in Z.

(ii) 2D Programs

(Only possible for detectors with 2D option)

Generally for the two-dimensional scanning of the detector: By the 2D initialisation the target area scanned will be split into the preselected number of tracks and each track in succession scanned by the electron beam, the scanning time for each track being 32ms, so that the total scanning time for the target is given by n - 32, where n = number of tracks. The difference between 1D and 2D scanning is shown below:

In 2D images with several tracks on the display the functions X-expand and Y-offset are not capable of alteration. Only for 2D4 (real full track) can Y expand be selected. If it is desired to show a stored track with spread, the memory *in which the track is held must be selected as a sole image* by DISPLAY X ENTER

2D Initialisation

Entry: 2D Ø ENTER U ENTER W ENTER X ENTER Y ENTER Z ENTER

Result: A 2D image is initialised by this entry with the following specification:

U-PT = Possible tracks = Number of segments, in which the target is split in the Y direction

W-NT = Number of tracks = number of tracks which are really to be scanned by the camera and then shown on the X-Y display.

NT must always = PT

X-ST = Start track = Number of track (as seen from above) which is to be scanned first. If PT = NT, then ST must equal 1.

Y-OT = Offset track = Distance between two tracks to be scanned. If FT = NT, then OT must = 1.

Z-IT = Intensified track = That track of which the intensity value on the display screen is to be shown for the corresponding cursor value. This track is scanned more brightly on the XY display.

The initialised values for PT, NT, ST, OT and IT, after completing the last entry, are shown on the display screen (lines 7 and 8).

If a 2D target picture is to be stored in memory, then NT should not be greater than 30, since only 30 memories are

available. If, however, the number of channels is less than 500, the possible figure for NT is increased to the maximum number of memories then available.

2D 1: Realtime

Entry: 2D 1 ENTER

Result: A 2D real-time image with the tracks shown on the screen. For the intensified track the cursor and intensity value are displayed. The tracks are scanned in succession on the target, each track in 32 ms.

2D2 2D Accumulation

Entry: 2D 2 ENTER START

Result: 2D accumulation in the memory predetermined by the tracks with the predetermined number of scans. Here every track initialised by 2D is accumulated in the memory having the same number as that representing the track i.e. Track 1 in memory 1 etc.

CAUTION

After Press Start Key appears in the second line, there should be a wait of at least 10 seconds before pressing START, since the discharge of the target to 2D scan must have decayed.

2D3 2D Plot Program

Entry: 2D 3 ENTER

Result: 2D program for an XY recorder in which the initialised tracks are plotted starting at the top and working down. The tracks are automatically recorded over each other and the pen lift switched at the end of each track, so that at the start of the next track it can be dropped again. Starting and

finishing channels for the recording process are determined by UG and OG. By pressing a command key the recording process can be stopped. Care must then be taken that with more than 16 tracks which are to be recorded on one sheet, the tracks overlap since the amplitude for one track on the display and on the plotter cannot be set smaller than for 16 tracks. Change of recorder speed see under Define 2.

2D4 Presentation of one track only in real time

Entry: 2D 4 ENTER X ENTER

Result: Only the track X is shown in real time on the display. Track X is now alone scanned in its correct position on the target. As against 2D real-time the track will now be scanned every 32 ms. (less dark current than with 2D real-time).

2D 5: 2D Memory image

Entry: 2D 5 ENTER

Result: A 2D memory picture with the tracks of corresponding memories, i.e. Track 1 in memory 2, track 2 in memory 2 etc.

2D6: 2D Clear

Entry: 2D 6 ENTER

Result: All the memories initialised by 2D Ø for track storage are erased.

2D7 2D Delay and Accumulation

Entry: 2D 7 ENTER START

Result: As a linkage of the programmes 2D2 (2D Accumulation) and Call 16 (1 D Delay and accumulation), after a certain delay time the target will be two dimensionally scanned and memorised.

Firstly, with DELAY N ENTER, the delay time should be entered (N = number of seconds).

Before the start of the delay time the target is scanned with NT. The start of the delay time (suppression of the beam) is recognisable by the stationary holding of the base line at the lower edge of the display.

2D8 Shift 2D images

Entry: 2D 8 ENTER X ENTER Y ENTER Z ENTER

With this program two 2D images which have been fed into the first memory, can be shifted by one command into the memory space behind. The parameters to be called signify:

X - ST Start track of the 2D memory image to be shifted.

Y - NT Number of tracks (memories) to be shifted.

Z - DT Destination track = lst memory of the memory range into which the 2D image is to be shifted.

(iii) DEFINE PROGRAMMES

Define Ø = Lower limit (UG or LL)

Entry: DEFINE Ø ENTER Z ENTER

Result: The lower limit for integral, plot, average value, and serial output is set at Z. Z must lie between 1 and 499. Z is set to 1 in the initialisation program.

Define 1: Upper limit (OG or UL)

Entry: DEFINE 1 ENTER W ENTER

Result: The upper limit for integral, plot, average value, and serial output is set to W. W must lie between 1 and 499, and in addition, W must be > Z. W is set to 499 in the

initialisation program.

Define 2: Plot speed

Entry: DEFINE 2 ENTER V ENTER

Result: The plot speed for plot and 2D plot is set to V. The greater V, the slower the plot speed. V is set to 2 in the initialisation program. The smallest value for V is V = 1.

Define 3: Baud rate

Entry: DEFINE 3 ENTER S ENTER

Result: The Baud rate for the serial interface is set to S. S can have any value between 1 and 9600. The initialisation value for S is set at 300 Baud.

Define 4: Lambda (Wavelength)

Entry: DEFINE 4 ENTER 1 ENTER

Result: By setting define 4 to 1, in line 3 of the screen display instead of the intensity the wavelength for the set channel (cursor position) is shown provided that the wavelength decoder option is incorporated in the instrument. Switching back to intensity by entering Ø (see chapter 5.2).

Define 5: Y Offset

Entry: DEFINE 5 ENTER Z ENTER

Result: By entry of a value for Z between-32767 and 32767 the Y offset is set to this value i.e. the zero line on the XY display is shifted by this value.

Define 6: Heating Off, Plot Relay, Dark scan of camera

Entry: DEFINE 6 ENTER W ENTER

Result: Setting of functions by input of the following values:

Function		Value
Switch in recorder output X-Y		65519
Plot relay (Pen down)	on	65503
Plot relay and recorder output	on	65487
Dark scan- Camera	on	65471
Vidicon heating (filament)	off	64511

All functions are reset by input of 65535

Define 7: Delay scans

Entry: DEFINE 7 ENTER N ENTER

Result: The target is both in real time and in 2D real time operating dark-scanned between every N scans i.e. the light integration time per diode column is raised from 32 ms to (N-U) U = 32 ms. In the programs Call 0 and 2D2, after pressing the start key the target is scanned dark N.32 ms before the read-out starts. The number N is seen on the display screen (line 12).

Define 8: Accu + memory erasure

Entry: DEFINE 8 ENTER 1 ENTER

Result: If the variable 8 is set to 1, the accumulation memory in which accumulation is to be effected on calling Call Ø is erased on each of Call Ø before pressing the START key. Reset of the function by entry of Ø.

Define 14: 2D variable

Entry: DEFINE 14 ENTER R ENTER

Result: The intensified track is changed to the value R.

Define 2Ø-49 Track number

Entry: DEFINE 2Ø ENTER P ENTER

Result: From Define 2Ø to Define 49, 30 tracks can be defined which order of their entry from define 2Ø on are then scanned on the target. In this way it is possible from 256 tracks to select any 30 which, also by means of 2D2, can be accumulated in the appropriate memory track of Define 20 in memory 1, track of define 21 in memory 2, etc.

REFERENCES

AIREY D.R.
Arc diameter in air blast interrupter nozzle at 45,000 Amperes
I.E.E. Second International conference on gas discharges 1972, pp. 70-72.

AIREY D.R.
Energy balance and transport properties of very high current SF_6 arcs
Ph.D Thesis, University of Bath, 1977.

AIREY D.R., KINSINGER R.E., RICHARDS P.H. and SWIFT J.D.
Electrode vapour effects in high current gas blast switchgear arcs
I.E.E.E. Trans, Vol. PAS-95, 1976, pp. 1-13.

ANCILEWSKI M.K., BURLIK A.C. and KING L.H.A.
Calculation of SF_6 interrupter performance for thermal reignition criteria
International conference on large high voltage electrical systems 1984, session Aug/Sept, 13-07.

BAGSHAW J.R., ELLIS N.S. and FITTON D.
Photographing the air flow in an air blast circuit breaker interrupter during arcing
Reyrolle review, Christmas 1969, No. 192.

BARRAULT M.R., BLACKBURN T.R., EDELS H. and SATANARAYANA P.
Investigations of a high current free burning electric arc
Int. conf. on gas discharges (I.E.E. conf. publ. 90)
London, 1972, pp. 221-223.

BIERMANNS J.
Arc recovery
I.E.E. Journal, Vol. 10, 1932, pp. 28-30.

BRIGGS A.C.
The contribution of axial and radial components of gas velocity to the thermal interruption capability of a gas blast circuit breaker
Proc. VIIth int. conf. on gas discharges and their applications (London) 1982, pp. 28-31.

BRIGGS A.C. and KING L.H.A.
I.E.E. Int. conf. on EHV switchgear, London, 1979.

BROWNE T.E.
A study of A.C. arc behaviour near current zero by means of mathematical models
A.I.E.E. Transactions, 1948, Vol. 67, pp. 141-153.

BROWNE T.E.
An approach to mathematical analysis of a.c. arc extinction in circuit breakers
A.I.E.E. Transactions, 1959, pp. 1508-1517.

CASSIE A.M.
Introduction to the theory of arc extinction and circuit severity in circuit breakers with post zero conductivity
ERA report, 1953, No. G/XT134.

CASSIE A.M.
A new theory of arc rupture and circuit severity
C.I.G.R.E., Vol. 10, 1939, paper 102.

CASSIE A.M. and MASON F.O.
Post arc conductivity in gas blast circuit breakers
C.I.G.R.E., report 103, 1956.

CHAN S.K., COWLEY M.D. and FANG M.T.C.
Integral methods of analysing electric arcs : III Shape factor correlation for low radiation and laminar flow
J. Phys. D., Appl. Phys., Vol. 9, 1976, pp. 1085-1099.

CHAPMAN A.
Ph.D Thesis
View of Liverpool, June 1977, pp. 139-153.

CHAPMAN A., JONES G.R., and STRACHAN D.C.
High current arc in an orifice air flow
5 : The overall electrical behaviour of a.c. arcs particularly near current zero
Univ. of Liverpool, Elec. Eng., Arc res. report, ULAPT36 (1975).

COWLEY M.D.
Integral methods of analysing electric arcs : I Formulation
J. Phys. D., Appl. Phys., Vol. 7, 1974, pp. 2218-2231.

COWLEY M.D. and CHAN S.K.
Integral methods of analysing electric arcs : II Examples
J. Phys. D., Appl. Phys., Vol. 7, 1974, pp. 2232-2245.

DHAR P.K., IRIE M. and BARRAULT M.R.
A radio frequency technique for measuring arc boundaries
Univ. of Liverpool, Elec. Eng., Arc res. report, ULAPT58, 1978.

DHAR P.K., BARRAULT M.R. and JONES G.R.
A multi-ring radio frequency technique for measuring arc boundary variations both at high currents and close to current zero
Univ. of Liverpool, Elect. Eng., arc res. report, ULAPT64, 1979

DRAWIN H.W. and FELENBOK P.
Data for plasma in local thermodynamic equilibrium
Gauthier-Villars, Paris, 1965.

FANG M.T.C. and BRANNEN D.
A current zero arc model based on forced convection
I.E.E.E. Trans., Vol. PS7, No. 4, 1979, pp. 217-229.

FRASER S.G.
Extinguishing an arc
in Haydon S.C. 'discharge and plasma physics'
ed. Haydon, 1964.

FRIEDRICH R.E. and YECKLEY R.N.
A new concept in power circuit breaker design utilising SF_6
Trans. Am. Inst. Elect. Eng. 76, pp. 906-909, 1957.

FRIND G.
Uker das abklingen von lichtbogen - I Theoretische uberlegungen
A. Angew. Phys., Vol. 12, No. 5, 1960, pp. 231-237.

FRIND G. and RICH J.A.
Recovery speed of axial flow gas blast interrupter : Dependence on pressure and di/dt for air and SF_6
Trans. I.E.E.E., PAS 93, 1974, pp. 1675-1682.

FRIND G, PRESCOTT L.E. and VAN NOY, H.H.
Current zero phenomena in an orifice type gas blast interrupter
Trans. I.E.E.E., PAS 99, 1980, pp. 268-278.

FROST L.S. and LIEBERMANN R.W.
Composition and transport properties of SF_6 and their use in a simplified enthalpy flow arc model
Proc. I.E.E.E., Vol. 59, 1971, pp. 474-485

GABRIEL A.H.
Journal of scientific instruments, Vol. 37, 1960, pp. 50.

GOLDSTEIN S.
Modern developments in fluid dynamics
Clarendon press, 1938.

GRAF H.P., MEILI H.P. and SCHOETZAU H.J.
Axially blown SF_6 arcs around current zero
Appl. Phys. B, Vol. 36, No. 1, 1985, pp. 33-40.

GRIEM H.R.
Plasma Spectroscopy
McGraw-Hill Inc., 1964.

GRIEM H.R.
Spectral line broadening by plasmas
Academic press, N. York and London, 1974.

HERMANN W., KOGELSCHATZ U., RAGALLER K., and SCHADE E.
Investigation of a cylindrical axially blown high pressure arc
J. Phys. D., Appl. Phys., Vol. 7, 1974(a), pp. 607-619.

HERMANN W., KOGELSCHATZ U., NIEMEYR L., RACALLER K. and SCHADE E.
Experimental and theoretical study of a stationary high current arc in a supersonic nozzle flow
J. Phys. D., Appl. Phys., Vol. 7, 1974(b), pp. 1703-1722.

HERMANN W., KOGELSCHATZ U., NIEMEYER L., RAGALLER K. and SCHADE E.
Investigation on the physical phenomena around current zero in h.v. gas blast breakers
I.E.E.E. Trans., Vol. PAS 95, No. 4, August 1976, pp. 1165-1176.

HERMANN W. and RAGALLER K.
Theoretical description of the current in H.V. gas blast breakers
I.E.E.E. Trans., Vol. PAS 96, No. 5, Sept/Oct 1977, pp. 1541-1555.

HERZBERG G.
Atomic spectra and atomic structure
Dover publications, New York, 2nd ed. 1944.

HOUSBY-SMITH C. and JENKINS J.E.
High current arcs in an orifice flow - spectroscopic measurements under quasi-steady state conditions
Univ. of Liverpool, Elec. Eng, Arc res. report, ULAP T54, 1978.

HUDSON A.A.
Effect of arcing on air flow through nozzle of a gas blast circuit breaker
The Engineer, Vol. 200, 1955, pp. 249-252 and 288-290.

HUDSON A.A.
Mass flow in nozzle of a gas blast circuit breaker - effect of nozzle geometry
The Engineer, Vol. 217, May 1964. pp. 933-939.

IBUKI
Ph.D Thesis, University of Liverpool, 1979.

IKEDA H., JONES G.R., IRIE M. and PRASAD A.N.
Spectroscopy of very high current convection arcs
I.E.E. seventh int. conf. on gas discharges and their applications, 1982, pp. 5-8.

JENKINS J.E.
(Private communication, 1984).

JONES G.R., LIDGATE D. and EDELS H.
Interaction between a high current arc and the air flow in air blast circuit breaker
Proc. I.E.E., Vol. 122, 1975, pp. 1443-1451.

JONES G.R., MELBOURNE C.R. and BLACKBURN T.R.
Pressure measurements in a high current arc burning in an orifice flow
Univ. of Liverpool, Elec. Eng., Arc res. report, ULAP T20, 1974.

JONES G.R., BALDWIN R.K. and EDELS H.
Thermal reignition of high pressure arcs
Proc. 2nd int. symposium on switching arc phenomena (Lodz, Poland), 1973.

KESSELRING F. and KOPPELMAN W.
Das schaltproblem der Hochsparinaunsteknik
Archir fur elektrotek, 1935, Vol. 29, No. 1, pp. 1-32.

KINSINGER R.E.
(Unpublished)

KOCK M. and RICHTER J.
Experimentalle Ubergang swahrs heinlichkeiten und die PT72, selare Haufigket des kupfers
Z fur Astrophysik, 1968, pp. 180-192.

KOGELSCHATE U. and SCHADE E.
Experimental investigation of a high pressure arc in a strong axial flow
Proc. Xth int. conf. on phenomena in ionized gases, Oxford 1971.

KOPPLIN H.
Das dynamische verhalten von lichthogen im wechselstrumkreis
Archiv fur elektrotechnik, Vol. 47, p. 47,

KOPPLIN H., ROLFF K.P. and ZUCKLER K.
Study of theeffects of gas flow on the performance of gas blast circuit breakers
Proc. I.E.E.E., Vol. 59, No. 4, 1971, pp. 518-524.

LELLERC J.L. and JONES G.R.
The radiative characteristic of gas blast circuit breaker arcs at very high currents
I.E.E. seventh int. conf. on gas discharges and their applications, London, 1982, pp. 1-3.

LEE T.H.
Physics and engineering of high power switching devices
M.I.T. press, 1975, pp. 233-235.

LEEDS W.M., BROWNE T.E. and STRAM A.P.
The use of SF_6 for high power arc quenching
Trans. Am. Int. Elec. Eng. 76, pp. 906-909, 1957.

LEONARD S.L.
in Plasma Diagnostic techniques
ed. Huddlestone and Leonard, Academic Press, N.Y., 1965, pp. 45-53.

LEWIS E., KOROTCHENKO V. and JONES G.R.
High speed photographic studies of gas blast switchgear arcs during the current zero period current ramp simulation
Univ. of Liverpool, Elect. Eng., arc res. report, ULAP T74, 1983.

LEWIS E., SHAMMAS N.Y. and JONES G.R.
The current zero SF_6 blast arc at high di/dt
Proc. int. conf. on gas discharges and their applications, pp. 35-38, 1985 (Oxford).

LEWIS E., PRASAD A.N. and JONES G.R.
Proc. int. conf. on gas discharges and their applications, pp. 31-34, 1985 (Oxford).

LIDGATE D.
Properties of the high current arc in an orifice air flow
Ph.D Thesis, Univ. of Liverpool, 1973.

LOCHTE-HOLTGREVEN W.
in Plasma Diagnostics (Lochte-Holtgreven)(ed)
North Holland Publishing Co., Amsterdam, 1968, p. 184.

LOCHTE-HOLTGREVEN W.
in Plasma Diagnostics (Lochte-Holtgreven ed)
North Holland Publishing Co., Amsterdam, 1968, pp. 139-141).

LOCHTE-HOLTGREVEN W.
Evaluation of plasma parameters pp. 184-188
In Plasma Diagnostics, ed. Lochte-Holtgreven, North Holland
Publishing Co., Amsterdam, 1968.

MAECKER H.
Arc measurements and results
in Discharge and Plasma Physics ed.
S.C. Haydon, 1963, pp. 266-288.

MAYR O.
Contributions to the theory of static and dynamic arcs
Archiv fur Elecktrotechnike, Vol. 37, 1943, pp. 588-608.

MITCHELL R.R., TUMA D.T. and OSTERLE J.F.
Transient two dimensional calculations of properties of
forced convection stabilized arcs
I.E.E.E. Transactions on Plasma Science, Vol. PS-13, No. 4,
Aug.1985, pp. 207-220.

PRINCE D.C., HENLEY J.A. and RANKIN W.K.
The cross air blast circuit breaker
Trans. A.I.E.E., 1940, Vol. 59, pp. 510-517.

RIEDER W.
Circuit Breakers
Scientific American, Jan.1971, pp. 76-84.

RIEDER W.
Arc circuit interaction near current zero and circuit breaker
testing
I.E.E.E. Trans. PAS 91, 1972, pp. 705-715.

ROBERTS D.E. and PRASAD A.N.
Spectroscopic investigation of the 10KA free burning arc
in air
Univ. of Liverpool, Elect. Eng., Arc research rep., ULAP T8,
1972.

ROBERTS D.E. and COWLEY M.D.
Spectroscopic investigation of the 10KA arc in efflux air
flow
Univ. of Liverpool, Elect. Eng., arc research rep., ULAP T18,
1973.

SCHLICHTING H.
Boundary Layer Theory
Magraw-Hill, New York, 1958.

SEATON M.J.
in Atomic and Molecular Processes (D.R. Bates ed)
Academic Press, N. York and London, 1962, p. 374.

SHAMMAS N.Y. and JONES G.R.
Total radiation losses from SF_6 circuit breaker arcs during the current zero period simulated with current ramps
Univ. of Liverpool, Elect. Eng., arc res. report, ULAP T70, 1982.

SHAMMAS N.Y.
Private communication (1982).

SHAYLER P.J. and FANG M.T.C.
The transport and thermodynamic properties of a copper-nitrogen mixture
Univ. of Liverpool, Elect. Eng., arc res. report, ULAP T45, 1976.

SKEATS W.F.
Discussion on the paper presented by Browne (1948)
A.I.E.E. Transactions, 1948, Vol. 67, pp. 141-153.

SLEPIAN J.
Extinction of an a.c. arc
A.I.E.E. Transactions, 1928, Vol. 47, pp. 1398-1408.

SLEPIAN J.
Extinction of a long a.c. arc
A.I.E.E. Transactions, 1930, Vol. 49, pp. 521-530.

SMITH M.R., BARRAULT M.R., JONES G.R., EL-MENSHAWY M.F., HOUSBY-SMITH C. and JENKINS J.E.
Spectroscopic investigations during the current zero period for arcs in an orifice gas flow
Univ. of Liverpool, Elect. Eng., Arc res. report, ULAP T61, 1978.

STRACHAN D.C.
Radiation losses from high current free burning arcs between copper electrodes
Univ. of Liverpool, Elect. Eng., Arc res. report, ULAP T14, 1975.

STRACHAN D.C.
Radiation losses from high current free burning arcs between copper electrodes
J. Phys. D : Appl. Phys., Vol. 6, 1973, pp. 1712-1723.

STRACHAN D.C.
A study of the radiative energy losses from an arc in efflux flow
Univ. of Liverpool, Elect. Eng., Arc res. report, ULAP T23, 1974.

STRACHAN D.C.
A study of the radiative energy losses from an arc in jet flow
J. Phys. D. : Appl. Phys., Vol. 8, 1975(a), pp. 703-713.

STRACHAN D.C.
High current arcs in an orifice air flow
4 Radiation loss measurement
Univ. of Liverpool, Elect. Eng., Arc res. report, ULAP T35, 1975(b).

STRACHAN D.C., LIDGATE D. and JONES G.R.
Radiative energy losses from a high current air blast arc
Journal of appl. phys., Vol. 48, No. 6, 1977(a), pp. 2324-2330.

STRACHAN D.C., JONES G.R., BOLTON A.W. and ATKINSON F.B.
An experimental test facility for the study of high current arcs in sulphur hexaflouride and air
Univ. of Liverpool, Elect. Eng., Arc res. report, ULAP T46, 1977.

SWANSON B.W. and ROIDT R.M.
Boundary layer analysis of an SF_6 circuit breaker arc
I.E.E.E. Trans., Vol. PAS 90, 1971, pp. 1086-1093.

SWANSON B.W. and ROIDT R.M.
Thermal analysis of an SF_6 circuit breaker arc
I.E.E.E. Trans., Vol. PAS 91, 1972, pp. 381-389.

SWANSON B.W., ROIDT R.M. and BROWNE T.E. jr
The effect of gas dynamics and properties of SF_6 and air on short line fault interruption
I.E.E.E. Trans., Vol. PAS 89, 1970, pp. 2033-2042.

SWANSON B.W., ROIDT R.M. and BROWNE T.E. jr
Arc cooling and short line fault interruption
I.E.E.E. Trans., Vol. PAS 90, 1971, pp. 1094-1102.

SWANSON B.W., ROIDT R.M. and BROWNE T.E. jr
Some numerical solutions of boundary layer equations for SF_6 arcs
Proc. I.E.E.E., Vol. 59, No. 4, 1971, pp. 493-501.

SWANSON B.W.
Nozzle arc interruption in supersonic flow
I.E.E.E. Trans., PAS 96, pp. 1697-1706, 1977.

TAYLOR S.
Data acquisition and analysis of circuit breaker arc measurements
M.Eng. Thesis, University of Liverpool, 1973.

TAYLOR S., WANG B., BLACKBURN T.R. and JONES G.R.
Thermal reignition performance limitations of a model SF_6 circuit breaker under full and scaled power conditions
Univ. of Liverpool, Elect. Eng., Arc res. report, ULAP T72, 1982.

TOPHAM D.R.
The electric arc in a constant pressure axial flow
J. Phys. D. Appl. Phys., Vol. 4, 1971, pp. 1114-1125.

TOPHAM D.R.
The characteristics of axial flow electric arcs subject to pressure gradients
J. Phys. D. Appl. Phys., Vol. 5, 1972(a), pp. 533-541.

TOPHAM D.R.
Scaling laws of the interaction of a gas blast circuit breaker arc with an electric circuit
Proc. I.E.E., Vol. 119, 1972(b), pp. 1469-1476.

TOPHAM D.R.
Measurements of the current zero behaviour of constant pressure axial flow electric arcs in nitrogen
Proc. I.E.E., Vol. 120, No. 12, Dec.1973, pp. 1568-1574.

WALMSLEY H.L., HAJI F.H., STRACHAN D.C. and JONES G.R.
High current arcs in an orifice flow
8 High speed photography of the luminous core under a.c. conditions
Univ. of Liverpool, Elect. Eng., Arc res. report, ULAP T42, 1976.

WALMSLEY H.L., JONES G.R. and BARRAULT M.R.
Properties of the thermal region of a gas blast a.c. arc particularly near current zero
Univ. of Liverpool, Elect. Eng., Arc res. report, ULAP T56, 1978(i).

WALMSLEY H.L. and JONES G.R.
Correlation of the integral analysis parameters for gas blast arcs, particularly near current zero
Univ. of Liverpool, Elect. Eng., Arc res. report, ULAP T57, 1978(ii).

WALMSLEY H.L. and JONES G.R.
The luminous structure of gas blast arcs at very high currents in air and SF_6
Univ. of Liverpool, Elect. Eng., Arc res. report, ULAP T60, 1978(iii).

ZUCKLER K.
Reciprocal influence of the gas flow and arc in gas blast circuit breakers
Z. Angew Phys., Vol. 22, 1967, pp. 155-164.

ZUCKLER K.
Contribution to the clogging problem in high voltage power breakers
ETZ-A, Vol. 90, 1969, pp. 711-714.

Photomultiplier tubes radiant energy coverage data
(c) EMI electronics limited 4/72.

Absorption curve of a typical filter
Ilford Ltd., technical information sheet F26.1

ABSTRACT

High speed photographic and time and space resolved spectroscopic investigations have been undertaken to quantify the processes governing arc thermal reignition phenomena.

A fixed nozzle and electrode geometry was used with SF_6 as the host gas. A sonic flow of gas at the nozzle throat was sustained using an upstream vessel pressure of 7.8 psig.

A 35.5mF capacitor bank was used to supply electrical energy for reduced and full power arcing tests using different circuit configurations.

Sophisticated optical diagnostic instrumentation has enabled photographic and spectroscopic investigations with high time and space resolution to be made during the current zero period of both the full and reduced power arcing cases.

The results of above experimental investigations are of value in determining the thermal structure and the processes governing thermal reignition of the circuit breaker arc of the present investigation. In particular, temperature profiles derived from the above investigations have been used to quantify the important terms of the dynamic current zero energy balance.

Experimental investigations have thus been performed during the critical current zero period of a full power circuit breaker arc. The significance of these results has been realised in evaluating the current zero temperature profiles and subsequently the energy conservation equation terms for severe circuit breaking conditions.

Persistent lines of the elements, C.R.C. Handbook of Chemistry and Physics, 48th Ed. Publ. The Chemical Rubber Co., 1967-1968, pp. E148-151.

Fig. A.4.2 Total Radiation Results

(Medium $^{di}/_{dt}$). Source : Shammas

(Private Comm)

Operating Conditions

Ip ≃ 43KA

$^{di}/_{dt}$ ≃ 21A/μs